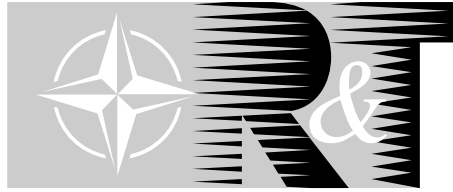


NORTH ATLANTIC TREATY ORGANIZATION



RESEARCH AND TECHNOLOGY ORGANIZATION

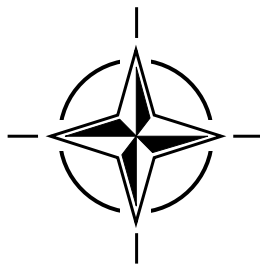
BP 25, 7 RUE ANCELLE, F-92201 NEUILLY-SUR-SEINE CEDEX, FRANCE

RTO MEETING PROCEEDINGS 61

Space-Based Observation Technology

(les Technologies de l'observation spatiale)

*Unclassified papers presented at the RTO Sensors and Electronics Technology Panel (SET)
Symposium held on the Island of Samos, Greece, 16-18 October 2000.*



Published October 2000

Distribution and Availability on Back Cover

Form SF298 Citation Data

Report Date <i>("DD MON YYYY")</i> 01102000	Report Type N/A	Dates Covered (from... to) <i>("DD MON YYYY")</i>
Title and Subtitle Space-Based Observation Technology		Contract or Grant Number
		Program Element Number
Authors		Project Number
		Task Number
		Work Unit Number
Performing Organization Name(s) and Address(es) Research and Technology Organization North Atlantic Treaty Organization BP 25, 7 rue Ancelle F92201 Neuilly-sur-Seine Cedex, France		Performing Organization Number(s)
Sponsoring/Monitoring Agency Name(s) and Address(es)		Monitoring Agency Acronym
		Monitoring Agency Report Number(s)
Distribution/Availability Statement Approved for public release, distribution unlimited		
Supplementary Notes		
Abstract This volume contains the unclassified papers presented at the Sensors and Electronics Technology Panel symposium held on the Island of Samos, Greece on 16, 17 and 18 October 2000. All aspects of space-based observation including the satellite, support systems, sensors, data handling etc. Topics covered included: Operational requirements/trade-offs Spaceborne radar technology On-board/real-time processing Specific space systems issues Special features of optronics systems		
Subject Terms Spaceborne detectors; NATO; Spaceborne radar; Synthetic Aperture Radar; Space reconnaissance; Space surveillance (spaceborne); Electrooptics; High resolution radar; Optical detection; Imaging; Radar detection; Image processing; Target acquisition; Optronics; Target recognition; SBR (Space Based Radar); Artificial satellites; Remote sensing; Real time operations		
Document Classification unclassified		Classification of SF298 unclassified

Classification of Abstract unclassified	Limitation of Abstract unlimited
Number of Pages 246	

REPORT DOCUMENTATION PAGE			
1. Recipient's Reference	2. Originator's References RTO-MP-61 AC/323(SET)TP/14	3. Further Reference ISBN 92-837-1050-9	4. Security Classification of Document UNCLASSIFIED/ UNLIMITED
5. Originator	Research and Technology Organization North Atlantic Treaty Organization BP 25, 7 rue Ancelle, F-92201 Neuilly-sur-Seine Cedex, France		
6. Title	Space-Based Observation Technology		
7. Presented at/sponsored by	the RTO Sensors and Electronics Technology Panel (SET) Symposium held on the Island of Samos, Greece, 16-18 October 2000.		
8. Author(s)/Editor(s) Multiple			9. Date October 2000
10. Author's/Editor's Address Multiple			11. Pages 244
12. Distribution Statement	There are no restrictions on the distribution of this document. Information about the availability of this and other RTO unclassified publications is given on the back cover.		
13. Keywords/Descriptors	<div style="display: flex; justify-content: space-between;"> <div> Spaceborne detectors Spaceborne radar Space reconnaissance Electrooptics Optical detection Radar detection Target acquisition Target recognition Artificial satellites Real time operations </div> <div> NATO Synthetic Aperture Radar Space surveillance (spaceborne) High resolution radar Imaging Image processing Optronics SBR (Space Based Radar) Remote sensing </div> </div>		
14. Abstract			
<p>This volume contains the unclassified papers presented at the Sensors and Electronics Technology Panel symposium held on the Island of Samos, Greece on 16, 17 and 18 October 2000.</p> <p>All aspects of space-based observation including the satellite, support systems, sensors, data handling etc.</p> <p>Topics covered included:</p> <ul style="list-style-type: none"> • Operational requirements/trade-offs • Spaceborne radar technology • On-board/real-time processing • Specific space systems issues • Special features of optronics systems 			

NORTH ATLANTIC TREATY ORGANIZATION



RESEARCH AND TECHNOLOGY ORGANIZATION

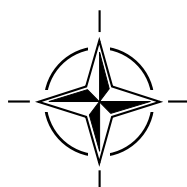
BP 25, 7 RUE ANCELLE, F-92201 NEUILLY-SUR-SEINE CEDEX, FRANCE

RTO MEETING PROCEEDINGS 61

Space-Based Observation Technology

(les Technologies de l'observation spatiale)

*Unclassified papers presented at the RTO Sensors and Electronics Technology Panel (SET)
Symposium held on the Island of Samos, Greece, 16-18 October 2000.*



The Research and Technology Organization (RTO) of NATO

RTO is the single focus in NATO for Defence Research and Technology activities. Its mission is to conduct and promote cooperative research and information exchange. The objective is to support the development and effective use of national defence research and technology and to meet the military needs of the Alliance, to maintain a technological lead, and to provide advice to NATO and national decision makers. The RTO performs its mission with the support of an extensive network of national experts. It also ensures effective coordination with other NATO bodies involved in R&T activities.

RTO reports both to the Military Committee of NATO and to the Conference of National Armament Directors. It comprises a Research and Technology Board (RTB) as the highest level of national representation and the Research and Technology Agency (RTA), a dedicated staff with its headquarters in Neuilly, near Paris, France. In order to facilitate contacts with the military users and other NATO activities, a small part of the RTA staff is located in NATO Headquarters in Brussels. The Brussels staff also coordinates RTO's cooperation with nations in Middle and Eastern Europe, to which RTO attaches particular importance especially as working together in the field of research is one of the more promising areas of initial cooperation.

The total spectrum of R&T activities is covered by 7 Panels, dealing with:

- SAS Studies, Analysis and Simulation
- SCI Systems Concepts and Integration
- SET Sensors and Electronics Technology
- IST Information Systems Technology
- AVT Applied Vehicle Technology
- HFM Human Factors and Medicine
- MSG Modelling and Simulation

These Panels are made up of national representatives as well as generally recognised 'world class' scientists. The Panels also provide a communication link to military users and other NATO bodies. RTO's scientific and technological work is carried out by Technical Teams, created for specific activities and with a specific duration. Such Technical Teams can organise workshops, symposia, field trials, lecture series and training courses. An important function of these Technical Teams is to ensure the continuity of the expert networks.

RTO builds upon earlier cooperation in defence research and technology as set-up under the Advisory Group for Aerospace Research and Development (AGARD) and the Defence Research Group (DRG). AGARD and the DRG share common roots in that they were both established at the initiative of Dr Theodore von Kármán, a leading aerospace scientist, who early on recognised the importance of scientific support for the Allied Armed Forces. RTO is capitalising on these common roots in order to provide the Alliance and the NATO nations with a strong scientific and technological basis that will guarantee a solid base for the future.

The content of this publication has been reproduced directly from material supplied by RTO or the authors.

Published October 2000

Copyright © RTO/NATO 2000
All Rights Reserved

ISBN 92-837-1050-9



*Printed by St. Joseph Ottawa/Hull
(A St. Joseph Corporation Company)
45 Sacré-Cœur Blvd., Hull (Québec), Canada J8X 1C6*

Space-Based Observation Technology

(RTO MP-61)

Executive Summary

Observation of the earth by use of spacebased sensors has a large number of advantages compared with ground-based or airborne sensors. It is, therefore, a primary requirement of future reconnaissance systems, and is thus also a primary requirement of future reconnaissance systems of NATO. There is a tendency worldwide to place in space many reconnaissance functions that have so far been fulfilled by airborne systems.

Spaceborne sensors are in essence optical and radar sensors. Optics have the property of high geometric resolution, but fail during the night and under adverse weather conditions. Radar can penetrate weather, dust and even foliage. The resolution achieved nowadays with Synthetic Aperture Radar (SAR) technology comes close to that of optical resolution. SAR offers additional features such as classification based on Doppler or polarimetry, moving target detection, 3D-imaging etc.

Sensors installed on a spacecraft have to fulfill various conditions which have to do with the space environment. Light weight, low-power power consumption, small size are prerequisites. Moreover, components have to be space-proof. Signal and image processing techniques and technology for on-board real-time processing have to be considered as well.

Starting from operational requirements this symposium summarizes aspects of spaceborne radar, including the required technology as well as special features, signal and data processing, optronics instrumentation and detector technology, so as to cover the whole range of spacebased observation technology based on radar and optronics. Various existing or planned observation satellite projects are described.

les Technologies de l'observation spatiale

(RTO MP-61)

Synthèse

La technique de l'observation de la terre à partir de capteurs spatiaux offre de nombreux avantages par rapport à l'observation à partir de capteurs terrestres ou aériens. Elle est, par conséquent, l'une des premières caractéristiques souhaitées pour les futurs systèmes de reconnaissance et à fortiori pour les futurs systèmes de reconnaissance de l'OTAN. Il existe une tendance universelle à faire réaliser des fonctions de reconnaissance remplies jusqu'ici par des systèmes aéroportés, par des systèmes spatiaux.

Les capteurs spatiaux sont des capteurs radar et optiques. Les capteurs optiques offrent une haute résolution géométrique, mais ils sont inexploitable de nuit et par mauvais temps. Le radar peut pénétrer les nuages, la poussière et même les feuillages. La résolution obtenue par les radars à ouverture synthétique (SAR) aujourd'hui est presque aussi bonne que la résolution optique. Le SAR a également d'autres fonctionnalités telles que la classification basée sur les techniques Doppler ou la polarimétrie, la détection des cibles mobiles, l'imagerie 3D etc...

Les capteurs installés sur les véhicules spatiaux doivent remplir certaines conditions en relation avec l'environnement spatial. Légèreté, dimensions réduites et faible puissance absorbée sont des éléments indispensables. En outre, les composants doivent être résistants à l'environnement spatial. Il faut également considérer les techniques et technologies de traitement de l'image pour le traitement embarqué en temps réel.

Prenant comme point de départ les besoins opérationnels, ce symposium fait le point des différents aspects des radars spatiaux, y compris les technologies, les fonctionnalités spéciales, le traitement du signal et le traitement des données, l'instrumentation optronique et les technologies de détection, de façon à couvrir l'éventail des technologies d'observation spatiale basées sur le radar et l'optronique. Différents projets de satellites d'observation, existants ou prévus, sont décrits.

Contents

	Page
Executive Summary	iii
Synthèse	iv
Theme	ix
Thème	x
Sensors and Electronics Technology Panel	xi
	Reference
Power for the New Century in Space by Y. Jones King	1*
Advanced Technologies for High Resolution Space-Based SAR Instruments by J. Wiedmann, W. Gilg, J. Link and R. Zahn	2*
Design Approach for Space Bistatic Illuminator by M.E. Davis, E. Jones and M. Hartnett	3*
Phase Scintillations Modelling on Earth-space Path and Evaluation of Some Effects Affecting High Resolution SAR Image Quality by L. Denise, O. Ravard, N. Caouren and J-G. Planes	4*
HR Target Feature Extraction by RELAX Extension by L. Vignaud	5*
High Resolution Processing of Low Incidence Angle ISAR-Images for Target Recognition by M. Peichl, T. Kempf, S. Dill and H. Suess	6*
Space Based GMTI – Technical Issues and a Possible Solution by D. Muff, R. Bird, J. Laycock and R. White	7*
A New Approach for Distributed Multi-Sensor Hyperspectral E-O and SAR CFAR Detection by G.A. Lampropoulos and J-M. Garneau	8*
A New GMTI Method for Radar Space-Based Surveillance by G.A. Lampropoulos	9*
Paper 10 withdrawn	

* These papers are to be published in a Classified Supplement. NB Since the printer has not yet received them, the details when published may differ slightly from those given here.

How Capable are Commercial Radar Satellites Compared to Passive Microsatellites for Maritime Surveillance? by T. Wahl	11†
Paper 12 withdrawn	
Constellation Orbit Design Criteria for a Dual Use EO System by P. Spera and A. Gallon	13
COSMO – SkyMed Mission Overview by F. Caltagirone, P. Spera, G. Manoni and L. Bianchi	14
Naval EarthMap Observer (NEMO) Hyperspectral Remote Sensing Program by T. Wilson, R. Felt and R. Baugh	15
The European Office of Aerospace Research and Development’s Small Satellite Propulsion System Research Program by T.J. Lawrence	16
An Innovative Approach to Satellite Technology by J.F. Janni, Y. Jones King and G. Witt	17
Paper 18 withdrawn	
The Production of Contamination on Spacecraft Surfaces by Hypervelocity Debris Impacts by Ch. Stein, R. Roybal and P. Tlomak	19
Space Power Generation Technology Development at the US Air Force Research Laboratory by K.C. Reinhardt	20*
Earth Observation from a High Orbit: Pushing the Limits with Synthetic Aperture Optics by L.M. Mugnier, F. Cassaing, G. Rousset and B. Sorrente	21
High Resolution Imaging from the Geostationary Orbit by M. Cecconi, S. Cesare and C. Dionisio	22
Paper 23 withdrawn	
Compact High Resolution Imaging Spectrometer (CHRIS) by M.A. Cutter	24
Sagem & Reose Space Observation Technology Trends by R. Geyl	25†
Compound Semiconductor Devices for Space Applications by S. Kayali	26
Development of Critical Technologies for the COSMO/SkyMed Hyperspectral Camera by D. Labate and F. Svelto	27

* These papers are to be published in a Classified Supplement. NB Since the printer has not yet received them, the details when published may differ slightly from those given here.

† Paper not available at time of printing.

Characterization of Infrared Detectors for Space Applications by D. Dantès	28
Quantum Well Infrared Focal Plane Arrays for Ballistic Missile Defense and Space Applications by M.Z. Tidrow and W.R. Dyer	29
Multi-Spectral HgCdTeIR Focal Plane Technology by J.P. Omaggio and J.R. Waterman	30*
Space Observation at Sofradir by J-P. Chatard, M. Vuillermet and J-P. Chamonal	31
X-SAR/SRTM – Part of a Global Earth Mapping Mission by W. Keydel, D. Hounam, R. Pác and M. Werner	32
The Shuttle Radar Topography Mission by T.G. Farr and M. Kobrick	33
ENVISAT ASAR – Design and Performance with a View to the Future by M. Hutchinson and M.D. Gibbons	34
Performance Analysis for the SRTM-Mission by R. Schroeder, K-B. Klein and H. Suess	35
High Resolution X-Band SAR Constellation for Risk Management by C.C. Lin, S. Ramongassié, M. Jérôme and L. Phalippou	36
The ‘SARLUPE’ Instrument Concept by C. Heer, R. Loewens and K-L. Blitzer	37*
Paper 38 combined with Paper 37	
Infoterra and TerrSAR, a New Operational Commercial Solution for Military Mapping and Intelligence by D. Davidson, C. Japp, J. Herrmann and Y. Munro	39†
Analysis of P-band Synthetic Aperture Radar for Airborne and Spaceborne Applications by A. Potsis, N. Uzunoglou, P. Frangos, R. Horn and K. Lamprecht	40
Paper 41 withdrawn	
The RF PRISM Concept for Pushing Forward the Antenna Size Barrier in Space Based Radar by J.P. Aguttes	42
Exploitation of Space/Frequency/Phase Diverse Waveforms to Resolve Range, Doppler, Spatial Ambiguity in Distributed Array Radar by J.W. Garnham	43*

* These papers are to be published in a Classified Supplement. NB Since the printer has not yet received them, the details when published may differ slightly from those given here.

† Paper not available at time of printing.

Enhanced-Spotlight Mode for High Resolution Image Acquisition in Alenia Aerospazio SAR2000 by A. Torre, L. Borgarelli and P. Ammendola	44†
Computer Simulations of Canada's RADARSAT2 GMTI by S. Chiu and C. Livingstone	45
Design and Performance of an Active Phased Array Antenna for the ENVISAT ASAR by M.D. Gibbons and R. Tucker	46†
A Real-Time SAR Processor Using One-Bit Raw Signal Coding for SRTM by F. Impagnatiello, A. Gallon, F. Buscaglione, M.N. Ferrara and F. Nirchio	47
Interferometric Processing of Spaceborne SAR Data in Advanced SAR Imaging Modes by J. Mittermayer and A. Moreira	48
Linear Features' Detection in SAR Images Using Fuzzy Edge Detector (FED) by A. Dimou, N. Uzunoglou, P. Frangos, G. Jäger and U. Benz	49
Image Content Dependent Compression of SAR Data by U. Benz, J.V. Fischer and G. Jaeger	50†
An Embedded Fusion Processor by J. Rooks	51
Fusion of the Multi-sensor Data of the COSMO-SkyMed Mission by F. Melgani, S.B. Serpico, F. Caltagirone and R. Vigiotti	52

† Paper not available at time of printing.

Theme

For many years, spaceborne observation and reconnaissance systems have been of high importance to NATO countries. The military and political changes of the past years lead to a situation where precise and fast reconnaissance is a primary requirement. Moreover, verification of disarmament treaties will become a major task in future years. This RTO-SET symposium will cover the specific aspects of space-based observation technology with emphasis on both radar and optronics systems.

Currently many high performance satellites use optronics technology for applications such as meteorology, terrain mapping, environmental monitoring, surveillance, reconnaissance etc. The rapid evolution of optronics technology in the fields of optics, detectors, and image processing will have significant influence on the design of the next generation of satellites. In addition to high-resolution target identification, optronics even allow the nature of their materials to be identified. While passive optronics detection systems are more or less “stealthy” in nature, active optronics may be used to distinguish real targets from false targets and decoys.

Compared with optical and IR sensors, radar technologies offer complementary capabilities such as all-weather, day/night operation, long range performance, penetration of obscurants such as dust, fog and smokes. Multispectral and multipolarization operation in the microwave domain are additional options for detection and classification. Geometrical resolution of less than 1m has been demonstrated by synthetic aperture techniques. The next generation of spaceborne radar will include active phased array antennas in conjunction with synthetic aperture processing, thus offering high efficiency, reliability and the potential of spatial signal processing for image enhancement, MTI, ECCM.

The high resolution of today’s optronics and radar technology makes the application of novel pattern recognition techniques such as artificial intelligence or neural networks possible. The complementarity nature of radar and optronics should be exploited for detection, localization and identification of targets in hostile environments, and should lead to highly reliable automatic or automated recognition systems. This symposium is proposed for Fall 2000. At that time several new space-based systems are expected to be in operation: SEAWIFS (USA) together with MOS on IRS (DLR); SRTM (Shuttle Radar Topography Mission, USA, Germany); ENVISAT/ASAR (ESA) together with ERS-2 (interferometric), SPOT5 (F+D). Fruitful interactions between these experiments and the proposed symposium can be expected.

The symposium will deal with all aspects of space-based observation including the satellite, support systems, sensors, data handling etc.

Topics to be covered include:

- Operational requirements/trade-offs
- Specific space systems issues
- Spaceborne radar technology
- Special features of spaceborne radar
- Spaceborne optronics technology
- Special features of optronics systems
- On-board/real-time processing

Thème

Une grande importance est accordée aux systèmes d'observation et de reconnaissance spatiaux par les pays membres de l'OTAN depuis de nombreuses années. Les changements politiques et militaires qui sont survenus ces dernières années ont conduit à une situation où il est impératif de disposer de données de reconnaissance précises et à jour. De plus, la tâche de vérification des traités de désarmement est appelée à s'amplifier dans les années à venir. Ce symposium RTO-SET traitera d'aspects spécifiques des technologies de l'observation spatiale, en mettant l'accent sur les systèmes radar et optroniques.

Aujourd'hui, bon nombre de satellites à hautes performances font appel aux technologies de l'optronique pour des applications telles que la météorologie, la cartographie de terrain, la surveillance de l'environnement, la surveillance, la reconnaissance, etc... L'évolution rapide des technologies de l'optronique dans des domaines tels que l'optique, les dispositifs de détection et le traitement de l'image aura une influence non négligeable sur la conception de la prochaine génération de satellites. L'optronique, en plus de sa haute résolution, permet d'identifier la nature des matériaux constitutifs des cibles. A la différence des systèmes de détection optroniques passifs, qui sont par nature plus ou moins « furtifs », l'optronique active est capable de distinguer entre « vraies », « fausses » cibles et leurres.

Comparé aux senseurs optiques et infrarouges, le radar offre des performances complémentaires telles qu'un fonctionnement tous temps, jour et nuit, une longue portée et la capacité de voir au travers d'obscurements tels que la fumée, le brouillard et la poussière. Le fonctionnement multispectre avec multipolarisation dans le domaine des hyperfréquences sont des options supplémentaires pour la détection et la classification. Des résolutions de moins d'un mètre ont été démontrées par le biais des techniques d'ouverture synthétique. La prochaine génération de radars spatiaux sera dotée de radars à antenne réseau active associés au traitement d'ouverture synthétique, de façon à assurer un haut niveau d'efficacité et de fiabilité avec la possibilité d'un traitement du signal spatial pour l'amélioration de l'image, ainsi que des capacités MTI et CCME.

La haute résolution autorisée par les technologies actuelles de l'optronique et du radar permet la mise en oeuvre de techniques novatrices de reconnaissance de formes, telles que l'intelligence artificielle et les réseaux neuronaux. Le caractère complémentaire du radar et de l'optronique doit être exploité pour la détection, la localisation et l'identification de cibles en environnement hostile, et devrait conduire à la réalisation de systèmes de reconnaissance automatiques ou automatisés hautement fiables. Ce symposium est proposé pour l'automne 2000. L'entrée en service de plusieurs nouveaux systèmes spatiaux est prévue avant cette date, à savoir : le SEAWIFS (USA) avec le MOS sur IRS (DLR); le SRTM (mission de topographie radar par la navette spatiale, USA, Germany); l'ENVISAT/ASAR (ESA) avec l'ERS-2 (interferométrie), le SPOT5 (F+D). Des interactions fructueuses entre ces expériences et le symposium proposé sont à prévoir.

Le symposium traitera de tous les aspects de l'observation spatiale, y compris les satellites, les systèmes de soutien, les senseurs, le traitement des données etc..

SUJETS A TRAITER :

- besoins opérationnels/compromis
- questions spécifiques à l'utilisation des systèmes spatiaux
- technologies des radars spatiaux
- caractéristiques particulières des radars spatiaux
- technologies de l'optronique spatial
- caractéristiques particulières des systèmes optroniques
- traitement embarqué en temps réel

Sensors and Electronics Technology Panel

CHAIRMAN

Dr L MARQUET
Director CECOM Research
Fort Monmouth
New Jersey 07703-5201
USA

DEPUTY CHAIRMAN

Dr D FAUBERT
Director General
Defence Research Establishment
Val-Belair, Québec G3J 1X5
CANADA

TECHNICAL PROGRAMME COMMITTEE

CO-CHAIRMAN: R. KLEMM, FGAN-FHR/EL (GE)
M. SIRIEIX, SAGEM SA (FR)

COMMITTEE MEMBERS:

D. CARTER, Matra Marconi Space	(UK)
G. CERUTTI-MAORI, Alcatel Space	(FR)
F. CHRISTOPHE, ONERA	(FR)
R. COIRAULT, ESTEC	(NE)
F. DAVARA, WEU Satellite Centre	(SP)
P. DENNIS, DERA	(UK)
W. DYER, BMDO/TOR The Pentagon	(US)
J-M. GARNEAU, DREV	(CA)
J. GRANONE, Army Space & Missile Command	(US)
W. HOLOTA, Dornier Satellite Systems	(GE)
A.K. HYDER, University of Notre Dame	(US)
Y. JONES KING, AFOSR	(US)
W. KEYDEL, DLR	(GE)
D. LIANG, DREO	(CA)
A. MARIANI, Alenia Defence	(IT)
F. RUBERTONE, Alenia Space	(IT)
R. ZAHN, Dornier Satellite Systems	(GE)

HOST NATION LOCAL COORDINATOR:

Prof. K. KIOULAFAS & Prof. N. UZUNOGLU
(INEAG, Research Institute, Samos &
University of Athens, Greece)

PANEL EXECUTIVE

Lt. Colonel A. SALZANO

From Europe:

RTA-NATO
Attn: SET Executive
7 rue Ancelle
F-92200 Neuilly-sur-Seine

From the USA or Canada:

RTA-NATO
Attn: SET Executive
PSC 116
APO AE 09777

Constellation Orbit Design Criteria for a Dual Use EO system

(13)

P. Spera, A. Gallon
Alenia Spazio SpA- Remote Sensing Engineering
Via Saccomuro 24, 00131 Roma Italy

Introduction:

In this paper the work concerning the definition of specific criteria for the orbit design of a Dual Use Earth Observation satellite constellation is presented.

These criteria have been derived by considering a wide range of civilian applications (e.g. risks management, agriculture/forestry, marine/coastal, geology) and military applications (surveillance, intelligence, crisis management, mission planning). In fact, for each of the application areas and the relevant EO products, a list of specific observation constraints have been identified and discussed in order to address optimal solutions allowing the timely generation of products characterised by a high level of quality and information content.

On the other hand, implementation/operational constraints and system complexity evaluation have been also considered in the constellation design process.

From the identification of candidate specialised orbits (elliptical orbits, inclined orbits and circular orbits) a specific system level trade-off has been performed in order to identify the best satellite constellation configuration in terms of orbit type, orbit planes, satellite phasing which allows to maximise the main performances (coverage and revisit times) for a given number of operational satellites.

This trade-off takes in to account the payload type (i.e. optical or SAR), the payload characteristics and constraints (e.g. field of view, resolution, dimension, power demand, illumination condition, interferometric capabilities and system complexity), the payload operational modes and spacecraft limitations due to drag effects and propulsion.

A detailed parametric analysis will be provided by showing the relationships between the system performances and the main design drivers.

Mission requirements for Dual-Use systems:

A dual use EO system shall be configured in order to satisfy specific needs of civil (institutional, commercial) and military users.

Given the wide range of applications to be covered, a dual use scenario calls for a mission which implements in an harmonic fashion several different operational modes characterised by a different priority with a suite of multi-mode/flexible sensors with an high thematic content, allowing to meet the military and the civil

objectives at the same time. User needs analyses have shown that such missions ask for a correct mix of optical and SAR sensor observations. The sensors should be based on multi-satellite EO system combined with a fast data reception and delivery capability.

The user needs can be characterised in terms of level of service to be provided (privileges, type and number of products, etc) and required applications. Each application is related to specific acquisition requirements and constraints, as shown in fig. 1, where two main design parameters are indicated: revisit time and spatial resolution with respect to the possible application areas of EO remote sensing products. As function of the application to be covered, one may have a fairly wide range for these parameters. The most demand for revisit time and high and very high spatial resolution is related to **Risk Management** and **Defence**. In the case of **Coastal applications** high revisit time are requested too, but the spatial resolutions are generally in the order of tens of meters. For **Marine observation** (i.e. open ocean and sea ice) the temporal resolution remains very high but the spatial resolution is coarser. Hinterland application such as **Agriculture and Forestry** generally require revisit time around 1 week. All other application (c.g. geology) require less frequent revisit time (up to seasonal) but the spatial resolution is quite variable.

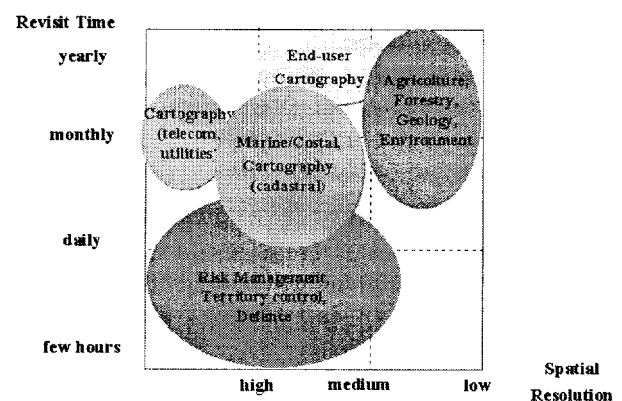


Fig. 1 - EO data applications vs. Revisit Time and Spatial Resolution

In addition to the revisit time and the spatial resolution requirements, there are other constraints on the imaging condition to be considered such as: image size, local time, incidence angle, access area, etc. All these design parameters have to be considered in the constellation design, in fact, for each specific application/product to

be satisfied, there are very different constraints (e.g. some products may require quasi-nadir observation, while for other products it is preferred to have high incidence angles). In order to cope with these different acquisition constraints, an optimisation process has to be performed based on some design criteria as indicated in the following sections.

System drivers identification:

The system drivers identify the main mission parameters or characteristics which can influence the optimisation of performance achievements vs. cost, risk and schedule for both space and ground segment.

In a Earth Observation satellite constellation the system performance which directly or indirectly impact on the orbit design process can be summarised in a limited number of peculiar figures of merit. These figures are:

- Accessible area
- Response time
- Revisit time
- On-ground resolution
- Swath

These figures of merit can be correlated to the system parameters as indicated in the following table.

Key Parameters	Involved Parameters
Accessible area	<ul style="list-style-type: none"> - Number of satellites - Payload field of regards - Altitude - Orbit
Response time	<ul style="list-style-type: none"> - Number of satellites - Altitude - Access region - Communications - Ground station locations - Re-scheduling / Processing time
Revisit time	<ul style="list-style-type: none"> - Number of satellites - Altitude - Access region
On-ground resolution	<ul style="list-style-type: none"> - Wavelength/Aperture (Optical) - Antenna length/Bandwidth (SAR) - Altitude - Off-nadir pointing angle
Swath	<ul style="list-style-type: none"> - Telescope FOV - Focal Plane array size - Data rate - Satellite agility (Optical) - Antenna area - Data rate (SAR)

Tab. 1 - Key design parameters

The main parameter to be considered as cost driver is the number of operating satellite to be deployed. Therefore this important parameter shall be quantitatively related to the system performance in

order to allow a clear understanding of the achievable performance w.r.t. the number of operating satellite.

Orbit and constellation design criteria:

The orbit and constellation design processes for the optical satellites and for the SAR satellites can be independently optimised. This assumption is justified by the different characteristics, acquisition constraints and operative modes of the corresponding payloads.

Few design criteria are in general applicable and therefore they are here below discussed.

Candidate Specialised Orbit

All orbits that have been considered are low Earth orbits, having an altitude ranging from 500 km up to 700 km. This restriction to the orbit altitude values is imposed by the specific optical and SAR payloads limitations (upper bound) and the drag decay effects (lower bound):

- for an optical payload this upper limitation is due to the difficulty to maintain both high resolution and limited instrument dimensions with the increasing of the altitude (for a fixed optical aperture the ground spatial resolution linearly decreases with the altitude)
- for a SAR payload this upper limitation is due to the difficulty to maintain both high SNR and limited power demand with the increasing of the altitude (for a fixed transmitted power the SNR decreases with the cube of the altitude)
- the exclusion of too low orbit altitudes is due to the drag effects that may limit the spacecraft lifetime and/or impose severe constraints on the propulsion.

Starting from this assumption the following types of orbits can be investigated:

- Elliptical orbits
- Inclined orbits
- Circular Sun-Synchronous orbits

The use of optical and SAR satellites in elliptical orbits has been investigated specially due to coverage advantages in a specific terrestrial hemisphere. In fact, when the orbit is elliptical, the satellite stays for a greater period at the apogee crossing, so allowing a major coverage in the corresponding hemisphere.

Because of the altitude range restrictions already discussed the maximum apogee altitude that can be considered is 700 km and the minimum perigee altitude that can be considered is 400 km.

So the bigger elliptical orbit that can be considered has an eccentricity equal to 0.022. This orbit presents very small eccentricity, and consequently, presents also very few advantages in terms of coverage of a specific

terrestrial hemisphere, while, on the other hand, presents all environmental perturbations problems joint to the elliptical orbits.

Therefore the use of elliptical orbits is not considered applicable for remote sensing applications, where non-uniform coverage or satellite altitude and velocity variations do not always guarantee adequate instrument performance and, on the other hand, do not provide significant advantages.

Since the use of elliptical orbits is discarded, only low Earth circular orbits will be considered.

The use of inclined orbits has been proposed specially for optical satellites in military application but:

- they cover only a limited latitude belt around the equator
- the orbit plane rotation induced by the RAAN-rate causes a variation of the illumination conditions of the target sites during the satellite passage. This means the incapability for an optical payload to acquire a target image during the dawn-dusk orbit periods (up to two months of duration)
- for the SAR satellite these orbits increase the system complexity (thermal control, solar arrays, etc) and costs

and therefore also the use of inclined orbits is discarded for EO satellites.

The use of circular SSO is definitely assumed since they allow:

- high latitude accessibility
- uniform coverage
- limited satellite altitude and velocity variations
- uniform Sun illumination conditions

Circular Sun Synchronous Orbits

In a SSO orbit the nodal regression is equal to the apparent motion of the Sun about the Earth (i.e. RAAN rate = $0.98563^\circ/\text{day}$ eastward) and the ground track pattern is completely defined by the number of orbits per day Q . By indicating with D the repeating cycle (number of days) it is possible to express Q as:

$$Q = [Q] + I / D \quad [.] \equiv \text{integer part}$$

where I is an integer number ($I < D$).

By indicating with S the fundamental interval (i.e. the angular equatorial distance between two successive satellite tracks) and with S_i the sub-interval (i.e. the angular equatorial distance between trace patterns day by day) we have:

$$S = 360^\circ / Q \quad \text{and} \quad S_i = S / D$$

The appropriate choice of I and D allows the selection of the desired observation scheme.

The choice of:

$$I = 1 \text{ or } I = D - 1 \text{ (i.e. direct orbits or drifting orbits)}$$

allows to achieve a good sampling in space but not in time of the pointed targets (e.g. $I / D = 15 / 16$)

The choice of:

$$n \cdot I \pm 1 = D \text{ or } n \cdot (D - I) \pm 1 = D \text{ (i.e. skipping orbits)}$$

allows to achieve a good sampling in time with a lower spatial resolution. In this case I / D approximates a fraction with a smaller denominator, that is:

$$I / D = I / (n \cdot I \pm 1) \approx 1 / n \text{ or}$$

$$I / D = [(n - 1) \cdot D \pm 1] / (nD) \approx (n - 1) / n$$

and the orbit is said to have a sub-cycle equal to n -days, that is to be a near- n orbit (e.g. $I / D = 13 / 16 \approx 4 / 5 \rightarrow$ near 5 orbit).

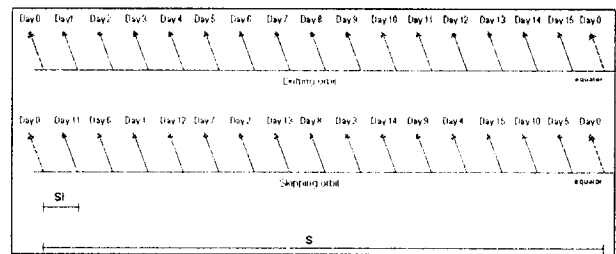


Fig. 2 - Example of ascending ground-tracks pattern at equator for a drifting orbit (e.g. $14+15/16$) and for a skipping orbit (e.g. $14+13/16$, near-5 orbit)

Altitude and Inclination

In a SSO the altitude and inclination are directly related (i.e. the inclination is function of the orbit altitude). For low Earth circular orbits, the sun-synchronous inclination is between 96° and 100° .

Therefore the selection of the orbit inclination shall take into account the limitations imposed by the available altitude range and the latitude belt to be covered.

For EO mission it has been assumed an altitude range of $500 \div 700$ km, allowing the satellite ground tracks to access all sites up to $\pm 82^\circ$ latitude.

Argument of Perigee and Eccentricity

A frozen orbit is selected for EO satellites. This type of orbit, its mean elements, specifically, argument of perigee ω and eccentricity e , have to be selected to maintain constant values with the time (or nearly constant).

The line of apsides is maintained fixed (no perigee rotation) with an argument of perigee frozen at 90° .

The advantage for remote sensing satellite is related to:

- a constant altitude profile over the oblate Earth from revolution to revolution, with very small altitude variation over the northern hemisphere;
- a tight longitudinal control of the ground trace (no longitudinal variations of the ground trace due to perigee rotation).

An argument of perigee of $+90^\circ$ results in an de/dt equal to zero (constant eccentricity).

A first guess of the eccentricity value can be obtained so that $d\omega/dt$ due to first two zonal harmonics J_2 and J_3 is zero.

The approximated value for the eccentricity (conservative) is here below given [RD 2]:

$$e \approx -J_3 \cdot R \cdot \sin(i) / (2 \cdot J_2 \cdot a)$$

where:

$$J_2 = 1.08263 \cdot 10^{-3}$$

$$J_3 = -2.536414 \cdot 10^{-6}$$

$$R = 6378.144 \text{ km, equatorial radius of the Earth}$$

$$a = \text{semimajor axis}$$

$$i = \text{inclination}$$

It is clear that active manoeuvre within the operative life of the satellite to maintain a frozen orbit shall be in any case performed, for example to compensate the drag effects on the orbit altitude and other perturbations affecting the orbital inclination (e.g. out-plane perturbation due to solar-lunar effect) and the orbital eccentricity (e.g. in-plane perturbations due to solar radiation effects).

SAR Constellation in Sun-synchronous Orbits: Orbit Selection

The most important feature of SAR payloads is their independence from the sun illumination conditions: this allows injecting the satellite in orbits which are strongly unfavourable for optical satellites. Moreover, since images can be obtained during the night and in presence of heavy cloud cover, the SAR satellites can operate for a good percentage of the satellite orbit period, spacecraft bus resources permitting.

The SAR payload is required to operate in multiple modes trading-off, for example, geometric resolution with swath width, or geometric resolution with radiometric resolution. This allows matching the characteristics of the sensor to the specific task to be performed during each orbit period, and from orbit to orbit.

A possible solution in order to increase the SAR constellation performance, in terms of coverage and revisit time performance limiting at the same time the number of satellites and the spacecraft bus resources, is to implement a double image side capability (left-

hand/right-hand) by manoeuvring the whole satellite. This means that access area is also doubled. The time required for this manoeuvre is an effective outage time and the manoeuvre cannot be performed when overpassing an area where multiple images must be taken. Therefore, all manoeuvres must be planned in advance and the spacecraft must enter the operational time slot already with a pre-set attitude.

According to the criteria addressed in previous sections the specific analysis concerning the SAR satellite orbit and constellation design is based on the following initial assumptions:

- use of circular Sun-Synchronous Orbits
- altitude ranging between 500 ÷ 700 km
- single dawn-dusk orbit plane for all the satellites

The next steps consist in the selection of a specific satellite orbit and then in the optimisation of the number of SAR satellites and their phasing on the orbit plane assuming as "key design driver" the capability of the system to guarantee adequate performance w.r.t. the number of operating satellites.

This design driver implies, in addition to a single orbit plane constellation choice, that some others orbit selection criteria should be applied:

- The global accessibility shall be achieved with only one operating satellite. For a SAR instrument this condition is surely achieved if the instrument access area at the equator is greater than the orbit basic sub-interval, that is:

$$\text{Access Area} > \text{Basic Sub-Interval } Si$$

Next figure depicts this concept:

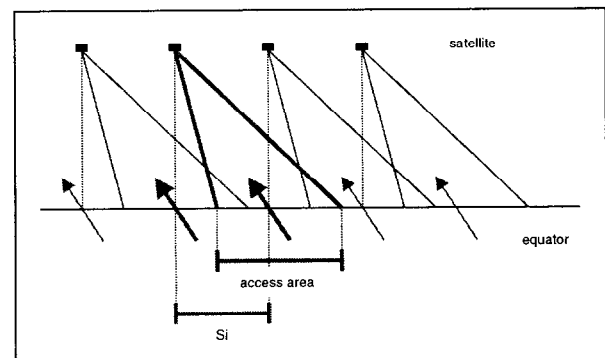


Fig. 3 - SAR instrument access area and basic sub-interval geometry

It should be pointed out that this is a very restrictive approach since in this way only the ascending or the descending orbits have been considered for the accessibility analysis. In fact, if this criteria is satisfied (i.e. Access Area > Basic Sub-Interval), all the points over the Earth's surface will be accessed either by an ascending orbit and a descending orbit during the orbit cycle. In other words this criteria

guarantees the global accessibility for two times during the whole orbit cycle.

- High repeat cycle length permits to implement incidence angle diversity. In fact higher is the repeat cycle length (D) and lower is the extension of the basic sub-interval (Si), allowing the SAR instrument to acquire the same target more times during the orbit cycle and with different incidence angles. The following figure depicts this concept:

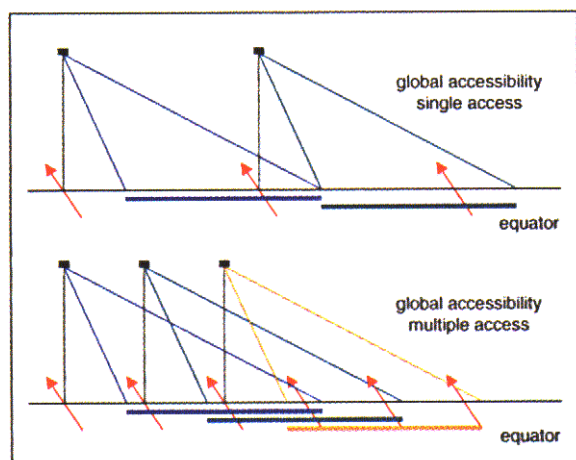


Fig. 4 - SAR instrument incidence angle diversity concept

Once that the global coverage criterion is satisfied with one satellite, the maximum revisit time is no greater than the repeat cycle interval. Within the set of orbits satisfying the global coverage criterion this would suggest to choose the orbit with the shorter repeat cycle.

On the other hand the selection of an orbit with a repeat cycle interval which exactly fits the required revisit period is usually not preferred since, in such way, a certain site would be always viewed at the same incidence angle, in contrast with the consideration of the second criterion.

Therefore, the preferred orbit shall be a skipping orbit having a near repeat cycle sufficiently small in order to provide an acceptable revisit time also in the case of availability of one operational satellites, and an effective repeat cycle sufficiently high in order to implement multiple incidence angle imagery.

Optical Constellation in SSO: Orbit Selection

The spectral observation regions covered by the optical payloads (VIS, IR and UV/Vis regions) imply some inherent limitations for the images acquisition. In particular, they can only sense the sunlight part of the Earth (except for IR bounds), this means that more than one half of each orbit is useless for images acquisition.

Moreover, the image acquisition for the polar regions during solstices is critical due to the poor illumination condition of the scene.

In particular at winter solstice all latitudes above 67° north cannot be accessed by the optical instrument, and assuming 15° degrees the minimum sun incidence angle allowing a reliable image acquisition only targets below 52° north can be effectively acquired.

As a result, an optical satellite can only take images during, theoretically, less than 40 % of the orbit period in average.

The necessity to optimise the illumination condition of the Earth scene drives the selection for optical satellites of near-noon sun-synchronous orbits. In fact, these orbits provide sufficient and near constant sun illumination of the Earth surface (for the orbit portion that is out of eclipse).

The cloud cover represents also a possible limitation for optical images acquisition. The cloud cover is known to be in the order of 30% to 70% of the time at all latitudes, except for very arid climatic zones. This effect further reduces the useful portion of the orbit period for optical satellites.

According to the criteria addressed in previous sections the specific analysis concerning the optical satellite orbit and constellation design is based on the following initial assumptions:

- use of circular Sun-synchronous orbits
- altitude ranging between $500 \div 700$ km
- single near-noon orbit plane for all the satellites

In particular the local time will be chosen between 10:00÷11:00 am for image acquisition performed during the descending orbits, or between 01:00÷02:00 pm for image acquisition performed during the ascending orbits, in order to image areas at high latitudes with the highest sun incidence (i.e. near noon).

The next steps consist in the selection of a specific satellite orbit and then in the selection of the number of optical satellites and their phasing on the orbit plane assuming as “key design driver” the capability of the system to guarantee adequate performance w.r.t. the number of operating satellites.

As already seen for the SAR constellation this design driver implies, in addition to a single orbit plane constellation choice, that some others orbit selection criteria should be applied:

- the global accessibility shall be achieved with only one operating satellite. For an optical instrument this condition is surely achieved if the instrument access area at the equator is greater than the orbit basic sub-interval, that is:

$$\text{Access Area} > \text{Basic Sub-Interval } Si$$

Next figure depicts this concept:

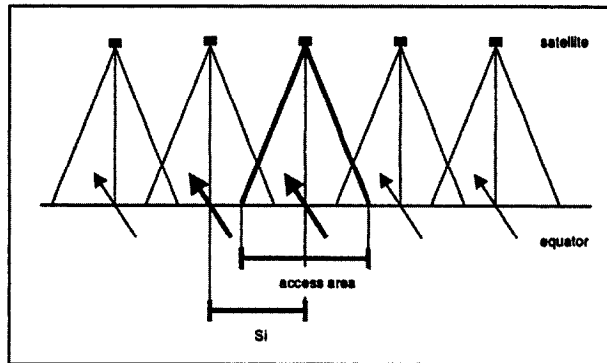


Fig. 5 - Optical instrument access area and basic sub-interval geometry

- All the accessible sites should be potentially observed during the repeat cycle at least once time with a quasi-nadir observation geometry (i.e. low off-nadir looking angles) in order to reach the maximum performance (maximum spatial resolution, minimum image degradation due to the off-nadir observation). Moreover, high repeat cycle length permits to implement incidence angle diversity. In fact higher is the repeat cycle length (D) and lower is the extension of the basic sub-interval (S_i), allowing the optical instrument to acquire the same target more times during the orbit cycle and with different incidence angles. This is particular important in observing targets casting shadows depending from the sun vector angle. Incidence angle diversity can also be exploited by multispectral acquisition, for classification tasks: in fact the response of vegetation in the various bands does also depends from the sun vector incidence. The following figure depicts this concept:

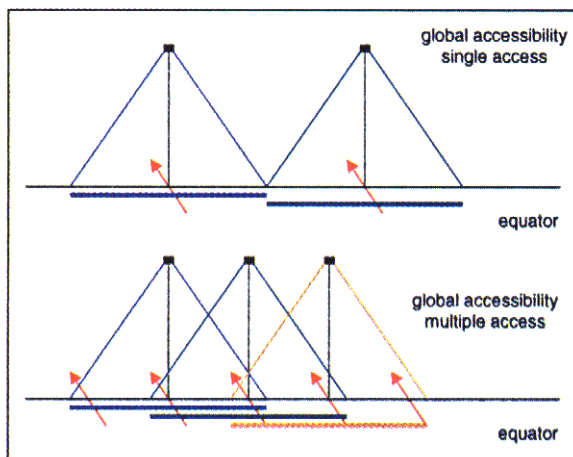


Fig. 6 - Optical instrument incidence angle diversity concept

Once that the global coverage criterion is satisfied with one satellite, the maximum revisit time is no greater than the repeat cycle interval. Within the set of orbits

satisfying the global coverage criterion this would suggest to choose the orbit with the shorter repeat cycle.

On the other hand the selection of an orbit with a repeat cycle interval which exactly fits the required revisit period is usually not preferred since, in such way, a certain site would be always viewed at the same incidence angle (up to 35° off-nadir, with a high image degradation), in contrast with the consideration of the second criterion.

Therefore, the preferred orbit shall be a skipping orbit having a near repeat cycle sufficiently small in order to provide an acceptable revisit time also in the case of availability of one operational satellites, and an effective repeat cycle sufficiently high in order to provide a quasi-nadir observation capability of the accessible sites within the orbit cycle.

The selection of a candidate orbit with the sub-cycle equal to the required revisit period and with a longer repeat cycle entails that the global accessibility shall be achieved by one operating satellite within the sub-cycle. This means that the following stronger condition must be verified:

$$\text{Access Area} > \text{Sub-Cycle Basic Sub-Interval}$$

Number of Satellites

The number of satellites is a driver factor for the overall system cost. Therefore the selection of the number of satellites shall be minimised considering the result of a trade-off between the achievable figures of merit (in terms of coverage and revisit time) and the system cost and complexity.

Number of Orbit Planes for each Constellation and Satellite Phasing

The number of orbit planes is one of the principal characteristics of any satellite constellation. It is important to guarantee adequate performance w.r.t. the number of operating satellites, this means that one would like to achieve some performance level as soon as the first satellite is operative and to raise that level of performance with each succeeding satellite.

In terms of constellation growth and degradation a single-plane constellation has some advantages w.r.t. constellations with multiple orbit planes:

- a new performance plateau is reached for each added satellite
- if a satellite fails, we may re-phase the remaining satellites with limited propellant consumption (in-plane manoeuvring) leading to a graceful degradation of the system. Re-phasing a satellite in a multiple plane constellation may be prohibitive (high propellant consumption for out-of-plane

manoeuvring and/or excessive time for manoeuvring completion).

In terms of optical and SAR payloads mission a single-plane constellation has some advantages w.r.t. constellations with multiple orbit planes:

- using a single near-noon orbit plane the optical payloads will acquire the images with the better and the same illumination conditions
- using a single dawn-dusk orbit plane for the SAR satellites allows the maximisation of the orbit period out of the eclipse, satisfying the spacecraft high power needs and, as a second instance, allowing a simplification of system complexity in terms of thermal control and solar arrays (sizing and Sun pointing)

The phasing of the satellites on the orbit plane is selected in order to achieve the optimisation of the performance in terms of coverage and revisit time.

The following table resumes the design variables that shall be addressed during the EO constellation design:

Design Variables	Major Effects	Selection Criteria
Altitude	- Coverage - Revisit time	System level trade-off (payload complexity, lifetime, etc.)
Inclination	- Latitude distribution of coverage	SSO: related to altitude
Number of Satellites	- System Cost - Coverage - Revisit time	Minimum number w.r.t. required figures of merit
Number of Orbit Planes	- Performance plateaus - Constellation growth and degradation	Constellation building/launch strategy
Satellite Phasing	- Coverage - Revisit Time	Performance optimisation

Tab. 2 - Selection criteria

A case study:

It is now possible to apply these general criteria to a specific case study. In particular for the system drivers deriving from the optical and the SAR payload characteristics we have considered as a reference the experience already made within the COSMO-SkyMed space program [RD 3] for the SAR and Optical constellation design.

According to these system drivers it is assumed that the SAR payload measurement geometry allows an off-nadir access between $22.7^\circ \div 44.3^\circ$ (only right looking) and that the Optical payload has a Field Of View wrt. nadir of $\pm 35^\circ$. Next figures show the corresponding observation geometry.

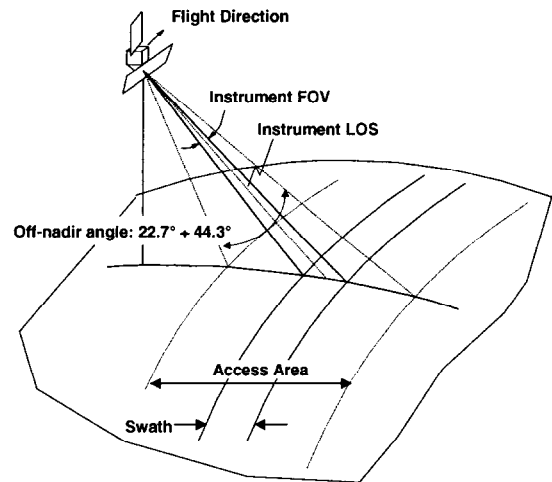


Fig. 7 - SAR payload observation geometry

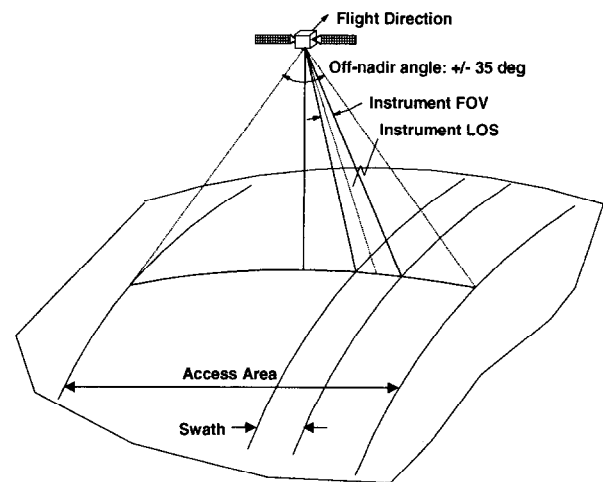


Fig. 8 - Optical payload observation geometry

SAR Constellation

In the following table the basic sub-interval and the satellite access area extensions are shown for SSO having an increasing repeat cycle (i.e. $D = 2, 3, \dots, 10$) and an altitude between the imposed range (i.e. $500 \div 700$ km) and assuming an off-nadir angle ranging between $22.7^\circ \div 44.3^\circ$.

I	N	D	Q	H (km)	Si (km)	Access Area (km)
14	1	2	14,50	720	1381	446
14	2	3	14,67	666	910	409
14	3	4	14,75	639	679	392
14	4	5	14,80	624	541	381
14	5	6	14,83	613	450	374
14	6	7	14,86	606	385	369
14	7	8	14,87	600	336	366
14	8	9	14,89	596	299	363
14	9	10	14,90	592	268	360

Tab. 3 - SAR instrument access area and basic sub-interval extensions

The table shows that this condition automatically excludes the orbits with repeat cycles less than 8 days, in fact, orbits with repeat cycle less than 8 days have a resultant access area smaller than the basic sub-interval.

As already observed this is a very restrictive approach since it consider only the ascending or the descending orbits have for the accessibility analysis. Access simulations have shown that orbits having a near repeat cycle ≥ 5 provide an acceptable revisit time also in the case of availability of only one operational satellites (i.e. about 90% target accessibility within the cycle).

According to the design criteria addressed the final selection is performed by identifying the SSO that:

- has a repeat cycle ≥ 8 days (i.e. global accessibility)
- has an access area at least two times greater than the basic sub-interval in order to guarantee global accessibility to the Earth's surface with at least two different incidence angles (i.e. incidence angle diversity)
- has a near repeat cycle equal to 5 days (i.e. revisit time optimisation with one satellite)

According to the above mentioned rational design criteria the following candidate orbit has been selected:

$$Q = 14.8125 \text{ orbits per day SSO}$$

$$(i.e. 14+13/16, h=619.6\text{Km}, i=97.86^\circ, e=0.00118, AOP=90^\circ)$$

In fact it guarantees an operational altitude in the range of 500-800 Km, global accessibility with one satellite, incidence angle diversity and the lowest near repeating cycle. The values selected for the eccentricity and the argument of perigee guarantee a frozen orbit solution.

The selection of the number of satellites is minimised by performing a trade-off between the achievable figures of merit and the system cost. For the selected orbit simulation analyses are performed in order to find the average and the maximum revisit times for different latitudes. These performances have been computed by taking into account one, two, three or four operational satellites being elements of the final SAR constellation placed on the same orbital plane and with the following phasing among the satellites:

Number of Satellites	True Anomaly
1	0°
2	0°, 180°
3	0°, 120°, 240°
4	0°, 90°, 180°, 270°

Tab. 4 - SAR satellites phasing

Next figures provide the results:

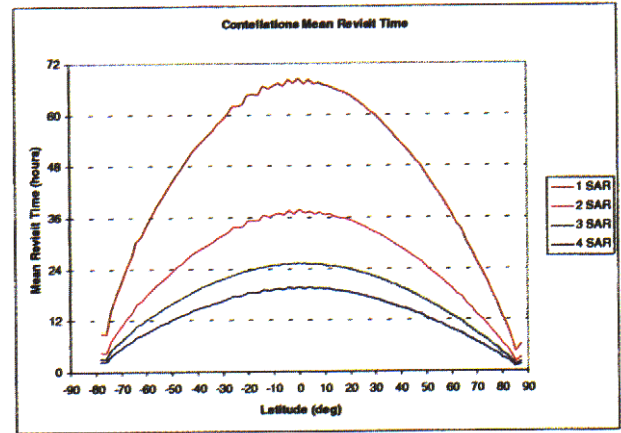


Fig. 9 - SAR constellation mean revisit time vs. satellite number

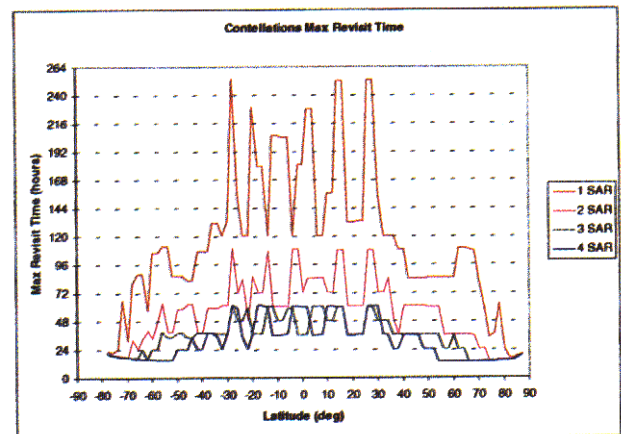


Fig. 10 - SAR constellation maximum revisit time vs. satellite number

The following table summarises the achievable performance in the latitude range $20^\circ \pm 60^\circ$ wrt the number of operating satellites.

1 satellite	37 ÷ 64 h	mean
	< 252 h	max
	38% (24h)	access
2 satellites	19 ÷ 35 h	mean
	< 108 h	max
	41% (12h) 64% (24h)	access
3 satellites	13 ÷ 24 h	mean
	< 60 h	max
	62% (12h) 84% (24h)	access
4 satellites	10 ÷ 18 h	mean
	< 60 h	max
	80% (12h) 95% (24h)	access

Tab. 5 - SAR constellation (@ 619.6 km: summary of performance results

Optical Constellation

In the following table the basic sub-interval, the satellite access area extensions and the squint degradation factor (i.e. ratio of the achievable spatial resolution at nadir and the resolution at the FOV angle limit, that is at half basic sub-interval) are shown for SSO having an increasing repeat cycle (i.e. $D = 2, 3, \dots, 10$) and an altitude between the imposed range (i.e. $500 \div 700$ km) and assuming an instrument FOV of $\pm 35^\circ$.

I	N	D	Q	h (km)	Si (km)	Access Area (km)	Squint degrad.
14	2	3	14,67	666	910	959	54,0
14	3	4	14,75	639	679	919	31,6
14	4	5	14,80	624	541	897	20,8
14	5	6	14,83	613	450	880	14,8
14	6	7	14,86	606	385	870	11,0
14	7	8	14,87	600	336	861	8,6
14	8	9	14,89	596	299	855	6,8
14	9	10	14,90	592	268	849	5,6
14	10	11	14,91	589	244	854	4,6
14	11	12	14,92	587	224	851	3,9
14	12	13	14,92	585	207	848	3,4
14	13	14	14,93	583	192	845	2,9
14	14	15	14,93	582	179	843	2,5
14	15	16	14,94	580	168	841	2,2

Tab. 6 - Optical instrument access area and basic sub-interval extensions

The table shows that this condition automatically excludes the orbits with repeat cycles less than 3 days, in fact, orbits with repeat cycle less than 3 days have a resultant access area smaller than the basic sub-interval.

A squint degradation factor next to one means a quasi constant performance over the entire accessible area.

Therefore the selection can be performed by identifying the orbits that:

- have a repeat cycle ≥ 3 days (i.e. global accessibility)
- have a squint degradation factor lower then 2% (i.e. a quasi-nadir observation capability)
- have a near repeat cycle equal to $3 \div 5$ days (i.e. revisit time optimisation with one satellite)

Therefore, as a result of this trade-off these two candidate orbits has been deeply analysed:

- the $Q = 14.8125$ orbits per day SSO
(i.e. $14 + 13 / 16$, $h=619.6$ km)
- the $Q = 14.6875$ orbits per day SSO
(i.e. $14 + 11 / 16$, $h=659.3$ km)

They both guarantee an operational altitude in the range of 500-700 Km, low off-nadir degradation factor (lower then 2%), incidence angle diversity and a near repeating cycle of 5 and 3 days respectively for a global accessibility. This means that also when only one

satellite is operational the maximum waiting time for each point on the Earth surface is 5 and 3 days respectively. Therefore the second orbit guarantees a better revisit time but with an higher altitude degradation factor.

The selection of the number of satellites is minimised by performing a trade-off between the achievable figures of merit (in terms of coverage and revisit time) and the system cost.

For the selected orbits the fundamental interval S is 2705 km and 2728 km at equator and the access area is 899 km and 957 km respectively. As a consequence three satellites equi-phased on a single orbit plane are sufficient to provide a revisit time less than 1 day in both cases, that is a maximum revisit time of about 24 hours for the visible channels (and less than 12 hours for IR channels). This is the minimum value achievable for an optical payload with a SSO. Therefore the optimum satellite number to be analysed is in the range of $1 \div 3$.

For each of the selected orbits simulation analyses have been performed in order to find the average and the maximum revisit times for different latitudes, and for different optical constellation configurations and sensor operation modes. These performances have been computed by taking into account one, two or three operational satellites being elements of the final optical constellation placed on the same orbital plane and with the following phasing among the satellites:

Number of Satellites	True Anomaly
1	0°
2	$0^\circ, 180^\circ$
3	$0^\circ, 120^\circ, 240^\circ$

Tab. 7 - Optical Satellites Phasing

Next figures provide the results:

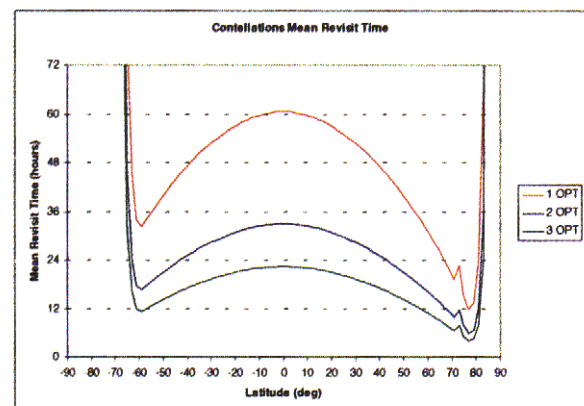


Fig.11 - Optical constellation (@ 619.6 mean revisit time vs. satellite number

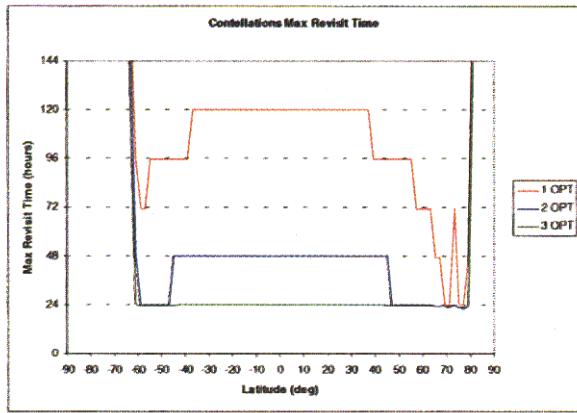


Fig. 12 - Optical constellation @ 619.6 maximum revisit time vs. satellite number

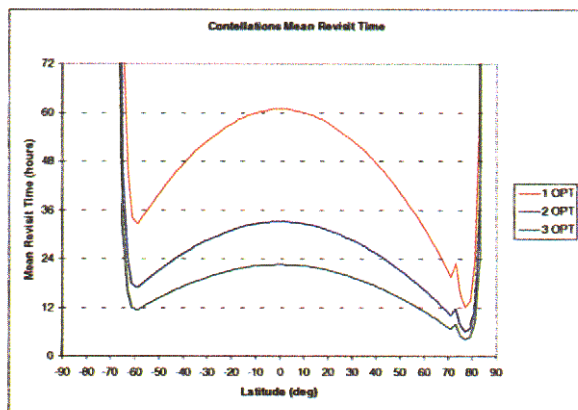


Fig. 13 - Optical constellation @ 619.6 mean revisit time vs. satellite number (nominal mode)

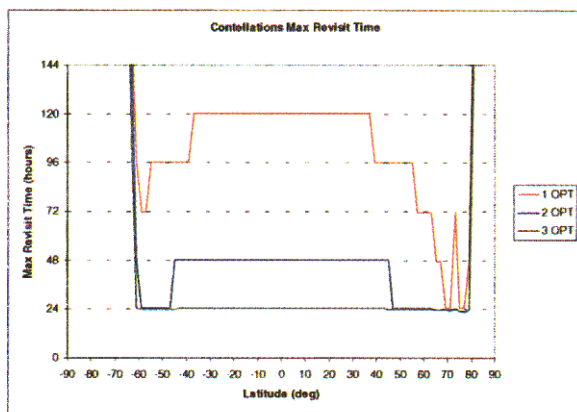


Fig. 14 - Optical constellation @ 619.6 maximum revisit time vs. satellite number (nominal mode)

The following tables summarise the achievable performance in the latitude range of 20° to 60° wrt the number of satellites for both selected orbits.

1 satellite	$32 \div 53$ h	mean
	< 120 h	max
	48% (24h)	access
2 satellite	$17 \div 31$ h	mean
	< 48 h	max
	89% (24h)	access
3 satellite	$11 \div 21$ h	mean
	< 24 h	max
	100% (24h)	access

Tab.8 - Optical constellation @ 619.6 km: summary of performance results

1 satellite	$30 \div 54$ h	mean
	< 72 h	max
	51% (24h)	access
2 satellite	$16 \div 29$ h	mean
	< 48 h	max
	92% (24h)	access
3 satellite	$11 \div 20$ h	mean
	< 24 h	max
	100% (24h)	access

Tab. 9 - Optical constellation @ 659.3 km: summary of performance results

Conclusions:

The design concepts described in this paper have been already applied in space projects where satellite constellations features have been exploited.

The optimisation process as here outlined can be easily adapted for other mission studies simply modifying the corresponding driving criteria and the payload characteristics.

References:

- [RD 1] Casey D., Way J. "Orbit Selection for the EOS Mission and its Synergism Implications" IEEE Trans. On Geoscience and R.S., Vol. 29, N° 6, Nov 1991.
- [RD 2] Chobotov V. A. "Orbital Mechanics" 2nd ed. AIAA
- [RD 3] Caltagirone F. et alii "COSMO-SkyMed Mission Overview" this symposium.

COSMO - SkyMed Mission Overview

F. Caltagirone *, P. Spera *,
G. Manoni **

Lt Col Lucio Bianchi ***

* ALENIA SPAZIO SpA - Remote Sensing Engineering

Via Saccomuro, 24 - 00131 Rome (ITALY)

** ITALIAN SPACE AGENCY (ASI)

Viale Liegi, 26 - 00198 Rome (ITALY)

*** ITALIAN MINISTRY OF DEFENCE

Via XX Settembre, 123 - 00187 Rome (ITALY)

SUMMARY: COSMO - SkyMed is an end-to-end Earth Observation System dedicated to the remote sensing and data exploitation for Dual (military and civil) Use applications.

Main mission objective is therefore the provision of data, products and services relevant to the:

- monitoring, surveillance and intelligence applications of MoD entities;
- environmental monitoring, surveillance and risk management applications of institutional entities;
- environmental resources management, maritime management, earth topographic mapping, law enforcement, informative / science applications of other institutional, scientific and commercial entities.

The program, presently funded by the Italian Space Agency (ASI), has been conceived since its very beginning to be implemented within an international scenario covering both the development of the infrastructures and utilisation of the system.

Purpose of this paper is to present an overview of the mission, the dual use concept design drivers, the current system architecture, the possible co-operation scenario, the deployment strategy and the current schedule.

INTRODUCTION

COSMO-SkyMed is an end-to-end Earth Observation system dedicated to the remote sensing and data exploitation for Dual (military and civil) Use applications.

COSMO-SkyMed is composed by space, ground and service segments.

Main mission objective is therefore the provision of data, products and services relevant to the:

- monitoring, surveillance and intelligence applications of MoD entities;
- environmental monitoring, surveillance and risk management applications of institutional entities;

- environmental resources management, maritime management, earth topographic mapping, law enforcement, informative / science applications of other institutional, scientific and commercial entities.

According to the user needs analysis the mission ask for a correct mix of Optical and SAR sensor observations.

The most required spectral characteristics are microwave (X-Band synthetic aperture radar, X-SAR), panchromatic (visible band, VIS), multispectral (VIS, near infrared band, NIR, short wave infrared band, SWIR) and hyperspectral (VIS, NIR, thermal infrared, TIR).

Moreover, the dual use scenario calls for a mission which implements in an harmonic fashion several different modes of operation, characterised by a different priority with a suite of multi - mode / flexible sensors with an high thematic content, allowing to meet the military and the civil objectives at the same time.

In this scenario, the development of new/innovative instrumentation in the radar field (e.g., multi-mode synthetic aperture radar's with a, very high resolution and a very high level of flexibility) and in the optical field (e.g. hyper-spectral sensor with variable spatial resolution and high sensitivity capability in the visible and infrared) have been included in the objectives of dedicated technological developments [1].

Because of its valuable panel of flexible, heterogeneous and complementary sensors, the COSMO-SkyMed mission belongs to the next generation of Earth observation systems for which innovative processing methodologies must be also considered [2].

In fact, the synergistic use of the numerous available sensors, which can be achieved by data fusion, allows to merge their advantages in order to obtain a richer information and to it reduces the uncertainty associated with the data from individual sensors.

USER NEEDS

User needs, which can benefit from space remote sensing techniques, have been identified, together with the relevant requirements.

It is worth to underline that the most important user needs are related to defence, national security and risk management applications, where space resources can provide a significant contribution to improve the tactical and strategic intelligence capability, minimise the vulnerability to disasters, et cetera.

In particular, risk management is evolving from pure post accident activities to prevention, preparedness and mitigation of crisis, so increasing the role of pre-crisis activities in order to avoid or mitigate the consequences of a disaster.

In this perspective risk management implies the applications relevant to the environmental monitoring and surveillance and can be subdivided into three major phases (namely, knowledge & prevention, warning & crisis and post crisis phases), each one having its own information and timeline needs.

Therefore the COSMO-SkyMed main civil applications can be identified in the disciplines of risk management, geology, forestry and agriculture, marine & inland water, ice, land use, landscape ecology, law enforcement, et cetera.

As an example, during the warning and crisis phases of the risk management, the users ask for images "as prompt as possible", "as accurate as possible" and "as synoptic as possible". In particular during such a phase the highest impact for disaster monitoring is accomplished if, few hours after the event, data are acquired over wide areas with low resolution. After such a period it is more relevant to acquire narrow swath coupled to very high resolution data.

Moreover, high resolution images with large swath are of great value also for routinary services, as topography updating, urban areas maps, land use maps at large scale, etc.

Most of these products are requested also for commercial purposes.

DUAL USE OPERATIONAL REQUIREMENTS

As previously mentioned, the system shall be able to support a Dual Use scenario which foresees various user classes both military and civilian in a national and international context.

In other words the system shall be able to provide the required/agreed level of service to each user, asking for the capability to be configured in a

flexible and expandable way for supporting new users.

The system overall co-ordination function shall be centralised (and based on priority rules).

To adequately support a Dual Use utilisation scenario main design criteria have been identified and here below summarised:

- Direct Control of the National Resources, control of the deployed infrastructures, management of the necessary operation to keep the system functional, including planning of the mission and compilation of the priority acquisition, if necessary.
- Interface with Different Class of Customers, the system shall interface with:
 - High Priority Customers*, as privileged users of the system.
 - Standard Customers*, as routine users of the system.
- Management of conflicts, the system shall be able to resolve conflicts relevant to the planning on the basis of specified priorities and agreed procedures
 The system shall be able to accept two type of user requests:
 - High priority Customers requests*
 The system shall be able to accept up to N high priority requests per day.
 The N high priority requests prepared by the military/institutional user, shall be always included in the overall task schedule to be executed by the system.
 - Standard Customers requests*
 These requests are characterised by a relatively long response time.
 Therefore, routine requests shall be included in the medium/long term planning of the system.
 In case of conflict between the military, institutional and /or commercial routine requests the corresponding time deadline associated to each request will be used as key parameter to solve the conflict.
- Approval of the tasking, The system shall be able to implement the current acquisition constraints given by National Security Authorities.
- Integrated Co-ordination and Planning Entity, the system has to foresee a co-

ordination and planning entity devoted to co-ordinate and harmonise, from an operational point of view, the different requests coming from the different users.

- Military Observer , military representatives could be located at the national and at the integrated planning facility with the specific task of checking the correct implementation .of the procedures.
- Confidential nature of the information, the system shall guarantee the confidential nature of acquisition request (both high and low priority) and the integrity of the information.
- Data Encryption, the command up-linked to the satellites, as well as all the down-linked data has to be encrypted.
- Restricted access to the activity schedule, the planned and the final schedule shall be restricted to authorised personnel.

COSMO-SKYMED ARCHITECTURE

COSMO-SkyMed mission will be based on a multi-satellite Earth observation system acquiring remote sensed data of very high quality from the spectral, temporal, spatial and radiometric points of view.

In particular, the fulfilment of the mentioned dual use applications calls for the following general performance characteristics:

- fast response time (up to the final users)
- very good image quality, to allow a robust image interpretability at the requested scale of analysis
- all weather and day/night acquisition capability
- collection of large areas during a single pass capability
- along-track stereo during a single pass capability
- global coverage
- acquisition of a sufficiently large and interpretable image in a single pass
- acquisition of homogeneous and comparable multi-temporal data set, characterised by adequate spatial and spectral resolution suitable to perform analyses at different scales of detail

Space Segment

The COSMO-SkyMed space segment is based on a constellation of seven small satellites combined with a fast data reception capability. Such a provision of data on an operational basis with the associated implications of continuity and quality is an essential characteristic of the system.

Three satellites of the constellation carry optical instruments such as a panchromatic camera, a multispectral camera and a hyperspectral camera, providing imagery with a valuable information content.

The four other satellites are equipped with a Synthetic Aperture Radar (SAR) to give an insight in the microwave range and, consequently, to provide all weather and day/night acquisition capability unreachable by optical sensors, but at the price of a more limited spectral information content.

The constellation will be deployed in two orbital planes (one orbit plane for optical satellites and one orbit plane for SAR satellites) allowing to the SAR satellites the collection of the maximum solar radiation (sun-synchronous dawn-dusk) to face their relevant power demand and to optical satellites to operate the in stationary illumination conditions (sun-synchronous near noon). optimising the imaging performance.

The orbit parameter have been selected taking into account the following additional aspects:

- Optimisation of the revisit time interval versus the number of the satellites;
- Implementation of incidence angle diversity;
- Global accessibility starting from one operating satellite.
- Graceful degradation in case of failure of one or more satellites;
- Optimisation of the mission lifetime versus the sensor achievable performances in term of radiometric resolution of the microwave instrumentation and spatial resolution of the optical instrumentation;

Therefore, the best promising constellation has been identified and the relevant characteristics are here below summarised [3].

SAR Satellites Selected Orbit
Orbit: Dawn-dusk SSO
Total satellite Number: 4
Altitude: \cong 600 km
Revisit Time: 12 hours

Optical Satellites Selected Orbit
Orbit : Near-noon SSO
Total satellite Number: 3
Altitude: ≈ 600 km
Revisit Time: 24 hours

The SAR Payload is an X-band Radar which offers the best compromise among several constraints due to the application requirements, technological issues, mission target cost etc.

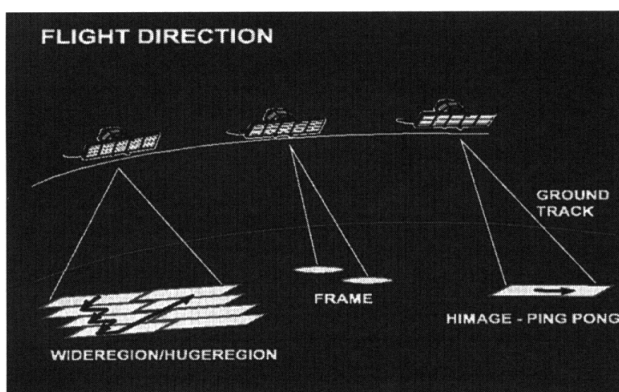
The fundamental characteristics of the Synthetic Aperture Radar instrument operative modes are summarised as follows:

Modes with one polarisation selectable among HH, VV, HV or VH:

- FRAME
 - resolution: order of the m and less
 - spot width: several tens of km²
- HIMAGE
 - resolution: few m
 - swath width: several tens of km
- WIDERECTION
 - resolution: few tens of m
 - swath width: hundreds of km
- HUGEREGION
 - resolution: several tens of m
 - swath width: few hundreds of km

Modes with two polarisation selectable among HH, VV, HV or VH:

- PING PONG
 - resolution: few m
 - swath width: several tens of km



Fundamental characteristics of the X-band Synthetic Aperture Radar Payload operative modes

The main SAR Payload characteristics which will necessitate technological consideration

throughout the duration of the relevant development activities are:

- spatial resolution and flexibility of the operative modes, developing and qualifying an X-band active antenna with range and cross-range steering capabilities;
- development and qualification of low mass and low power consumption technologies to make consistent the accommodation on small platforms.

The principle items which are affected by critical technologies are listed hereafter gathered for each Radar S/S:

- *Antenna*
 - Multi Polarisation Radiating panel
 - T/R Modules
 - Tile Digital controller
 - Tile power supply
 - Mechanical structure
 - Hold-down and release mechanism
 - Deployment mechanism
- *Radio Frequency S/S*
 - Up Conversion/Down Conversion Chains
 - Frequency Generation Unit
 - Calibration Network
- *Radar Signal Conditioning:*
 - Wide Band Chirp Generator
 - High Speed Analogue-to-Digital Converter
 - Hi-Rate Data Formatting Section
- *Instrument Control S/S*
 - Core Control Unit
 - Time Base Generator
 - Master Beam Controller

The High Resolution Panchromatic and Multispectral Camera (HRC) is designed to provide high spatial resolution images of the exposed risk area in order to support the defence, national security and risk management applications. The HRC is also capable to take a large area of the entire scene with a single pass using a mosaic technique.

The Hyperspectral Camera (HYC) is mainly devoted to the water pollution management, vegetation mapping and geological application. These activities are of great importance to assess the vulnerability of the environment during the knowledge and prevention phase of the natural and anthropic risk management. The TIR channels are devoted to monitor surface, sea temperature, forest fires and volcanic activities.

The fundamental characteristics of the optical

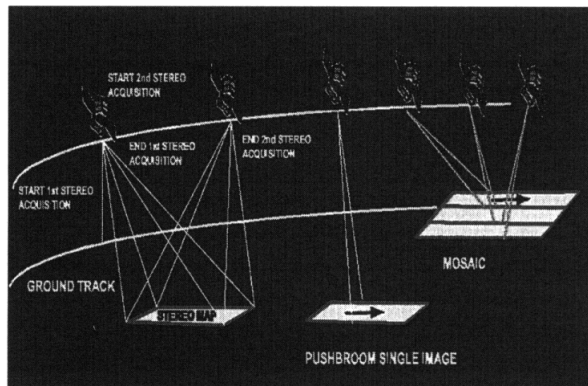
instrument operative modes are summarised as follows:

High-Resolution Camera:

- Type:
push broom imager operating in 6 different and simultaneous spectral channels
- Multispectral bands and resolutions:
 - 1: 0.5-0.90 μm (PAN) order of the m at nadir
 - 2: 0.45-0.52 μm (blue) few m at nadir
 - 3: 0.52-0.60 μm (green) few m at nadir
 - 4: 0.63-0.69 μm (red) few m at nadir
 - 5: 0.76-0.90 μm (NIR) few m at nadir
 - 6: 1.55-1.75 μm (SWIR) few m at nadir
- Swath : tens of Km
- Access region : $\pm 35^\circ$ (across-track)

Hyperspectral Camera:

- Operational modes:
 - Wide mode - Low resolution
 - Narrow mode - High resolution
- Resolutions: 20 m to 300 m (VIS, NIR)
50 m to 300 m (IR)
- Swaths: 20 Km to 300 Km
- Access region: $\pm 35^\circ$ (across-track)



Fundamental characteristics of the Optical Payloads operative modes

Payload Data Handling and Transmission

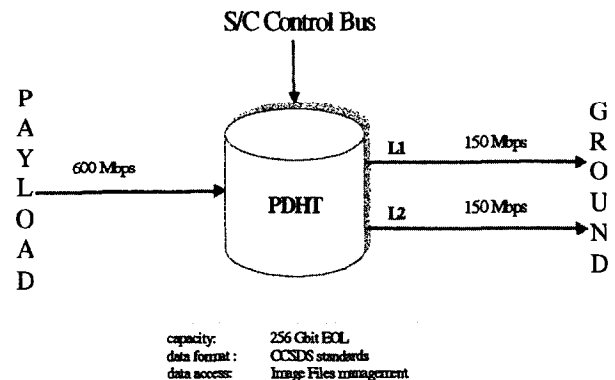
The PDHT comprises all functions necessary for the real-time acquisition, storage and handling of science data generated by the Payload, and for their transmission to the ground station.

The PDHT shall provide the following Mission Modes of operation:

- Store Only: Payload Data currently acquired (Image Segment File) are stored.
- Down-Link Only: Payload data previously stored (Image Segment Files) are down-linked (play-back).
- Store and Down-Link: Payload Data currently

acquired (Image Segment File) are stored, and simultaneously Payload data previously stored (Image Segment Files) are down-linked.

- Pass-Through: Data currently acquired (Image Segment File) are down-linked in near real-time on one of the two Links (L1 or L2).



PDHT Configuration: Data Volume and Data Rate

Spacecraft Bus General Architecture

The Spacecraft Bus functions can be summarised as follows:

- to support the Payload mass (on ground, during launch and in orbit);
- to keep the Payload at the right temperature.
- to put the Payload in the right orbit and keep it there;
- to provide correct pointing to the Payload;
- to provide the requested electric power to the on-board equipment and instruments;
- to provide interface with ground through telecommands and telemetry.

All the above functions have to be provided to comply with the spacecraft bus needs themselves, too.

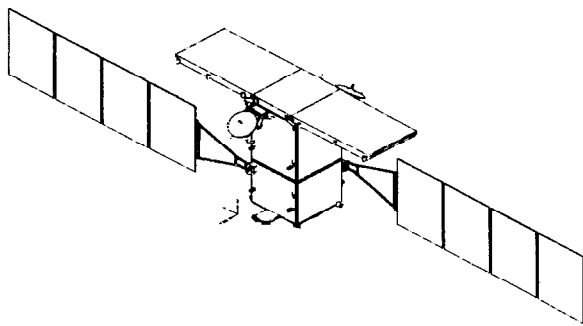
Here below the Spacecraft Bus subsystems main architectural features are recalled:

- Structure S/S: Structural Frame by machined aluminium with aluminium Sandwich Panels.
- Thermal Control S/S: Passive Control System augmented by use of Heaters.
- Integrated Control S/S (ICS), including the Attitude and Orbit Control (AOC) and the Data Handling (DH) functions.
- Propulsion S/S: Mono-propellant (Hydrazine) Blow-Down System.
- Electrical Power S/S: Unregulated Bus (23-35 V) with NiH2 Battery and GaAs Cells Solar Array.
- TT&C S/S: Standard totally redounded S-Band Transponder with Antenna.

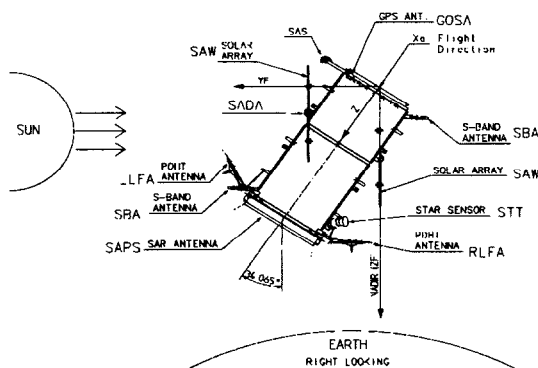
The nominal attitude of the optical satellite is nadir pointing, with a fast repointing capability up to $\pm 20^\circ$ in the pitch axis and $\pm 35^\circ$ in the roll axis, according to the various imaging modes.

The attitude control of the SAR satellite is in charge for the SAR antenna boresight pointing at $\cong 38^\circ$ of incidence on the right side of the ground track, for the yaw steering of $\pm 2^\circ$ (with orbital cycle) and for the repointing of antenna boresight also on the left side (mode available for a limited time interval to improve the accessibility and to support emergency requests).

The pointing accuracy and knowledge are quite stringent due to the high resolution and imaging quality of the embarked sensors.



SAR Satellite in the deployed configuration



SAR Satellite in the orbit configuration

Ground Segment

The COSMO/SkyMed ground segment provides all the infrastructures needed to support the COSMO/SkyMed Mission in the Dual Use scenario.

It is devoted to perform the main functions/operations at ground level needed to manage the COSMO-SkyMed mission both in terms of constellation control and global data management.

The COSMO-SkyMed ground segment

components located out to fulfil the high level requirements of the COSMO/SkyMed mission are the following:

- One Mission Planning and Control Centre (CPCM) which is in charge of co-ordinate on-board and ground activities, perform overall mission planning, allocate resources and solve conflicts;
- One Satellites Control Centre (CCS) which provides all the functions devoted to Monitor & Control the satellite constellation (including Flight Dynamics operations);
- TT&C Stations (directly controlled by the CCS and not necessarily co-located with it) which provides the primary link service between the COSMO/SkyMed Satellites and the Ground Segment;
- One or more Civil facilities which are devoted to manage Civil User requests, to acquire, archive, process and deliver the data received from the COSMO-SkyMed Satellites by means of co-located and/or remotely located X-band acquisition stations;
- One or more Military facilities, having own capabilities for the Payload data acquisition, archiving and processing.

A dedicated communication network will guarantee the connections between the different COSMO-SkyMed Centres/Stations in a secure, reliable and efficient way.

Service Segment

The nature of the service is quite variable w.r.t the application field and must be designed and implemented taking into account the peculiarities of each application. The key points related to service segment needs addressed by end-users in the field of risk management, having very stringent peculiarities, are :

- the access to information products derived from EO data: this access should be easy and fast, and from the point of view of end users, totally transparent with regard to EO data sources – i.e. data providers;
- the suitability and the accuracy of information products: this concern implies that the quality of the generated products is checked in order to assess their relevance compared to the initial user requirements, taking into account the limitations related to the characteristics of current space missions and image processing algorithms;
- the reproducibility: it is important for the customers that an approach, which has been successfully applied in one case, can be used

for another area. This point not only concerns the image processing algorithms themselves, but also the selection process applied to identify the relevant EO data or the type of ancillary data used to reach the required information product;

- the reliability and the robustness of the service: some users put the emphasis on the fact that the service must be available 24 hours a day and 365 days a year. Their own activity is related to crisis phase and may require information at any moment and with the shortest delivery time.

The following concepts are considered as design drivers:

Service Continuity: For many applications (e.g. defence applications, risk management, marine and coastal observation) the service must be available 24 hours a day and 365 days a year, for any activities related to crisis phase and which require information at any moment and with the shortest delivery time.

Space based Geo-Information must be obtained and secured in all weather and day/night conditions.

One of the most stringent requirements is the fast reaction in case of a disaster.

However this imply that at user site there is an operational entity which can interact with the system to require the acquisition of data. This also implies that the system is integrated in the decision process of the crisis management. Therefore, as an example, in case of an earthquake, the request for acquisition has to be issued very quickly, even before that epicentre is exactly determined. This imply the definition of an operational procedure within risk management entities to fully exploit the provided services and the implementation of specific means HW and SW in the system to support the operations. In this case, the distribution of a part of the processing capability to the user facilities could be a solution. In this perspective, the crisis management centres could be equipped with terminals able to order, acquire, provide quick-look images and process the data up to the level suitable for interpretation.

Archiving: The amount of data to be archived depends on the type of application.

In the case of risk management, land use mapping is a major activity used as a component of the vulnerability to create risk maps. In this activity, radar or optical raw data and intermediate products must be archived. Concerning optical data only

images with less than 10-20% cloud shall be archived. Some argue that only warning images (just before the crisis) must be archived. This option seems to be too restrictive as it is necessary to archived damage images and normal situation images. Therefore, the archiving facilities shall supply the customers with a recent image at the best quality. Then, these images will be used as reference data with eventually additional images acquired during the crisis.

In the case of risk management, again, for areas where a high level of risk can be detected (historical events reasons), some final products should be archived in order to have very quickly a product which allows comparison during the crisis and just after. Other specific areas must take into consideration and be archived as Final end-user products such as River and intermediate surrounding, increased urbanisation areas (e.g. rural/urban boundaries), etc. For these reasons, the archiving facilities shall describe these specific areas in order to provide, when requested, data that allowing to identify rapidly the potential vulnerable areas. This is an important feature of the archiving for the updating of the Risks & Vulnerability maps and may be less costly than a full Land Use/Cover product.

The multi-temporal acquisition feature raises the problem of the complexity of the requests. In order to facilitate the user requests, the archiving facilities shall archive together (i.e. with a same event reference) all the data worked out before, during and after the crisis. This will facilitate the retrieve operations and give a full set of data to the customers.

Confidential Archiving facilities of the sell products must be supported.

Cataloguing: This is an important issue of accessing the service. The catalogue access must be very efficient (time constraints) and Internet (web sites) seems to be the current better solution excepted in case of crisis where powerful and secured means shall be provided. Nevertheless, the data access in case of crisis must remain with the same user interface (what ever the request) but will include "short cut" in order to improve the access delay and to manage the priority requests. The hardware and/or software means used in these situations must remain totally transparent for the users. Confidential cataloguing facilities of the sell products must be supported.

Priority: In general, serving a various and large number of customers, necessitates a queue management process. This is generally based on

demands priority classification . Priorities need to be determined by events and the need for priority is related to urgency in the crisis phase. In this case, the following criteria are to be considered: the estimated duration of the crisis, the size and the location of the area, the availability of archive data, etc. These requirements will impact directly on the priority management facilities at different levels:

- planning of new acquisition ;
- priority of processing ;
- priority of delivery (in particular when the real-time product is requested) ;

Customisation: The goal is to have as much as possible off the shelf products, but in some cases customisation might be necessary. Identify rough estimates of customised products with respect to standard products to different types of customers, in the same application field). This will permit to identify the necessity to implement or not

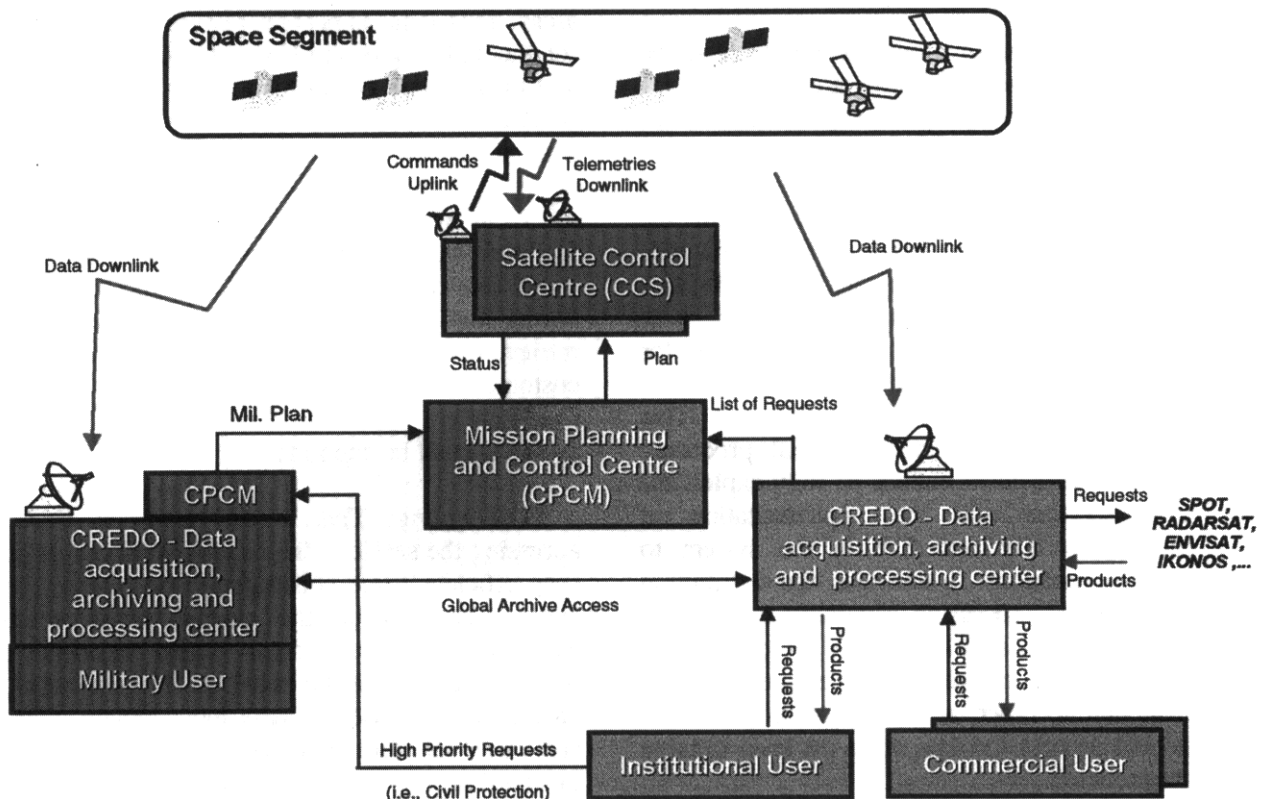
development facilities.

Data Dissemination: Risk management when a crisis occurs, requires fast reaction, which can be guaranteed much better in case of direct broadcast of sensed data to the crisis management centre. The satellites using access security features (e.g. encryption keys to guarantee the information) will broadcast only data acquired by sensors providing useful information for crisis management.

However some products may require direct “in-situ” product delivery. This raises the problem of the size of the data to be transmitted and the geo-location and calibration in case of providing data with reception capability directly from the satellite.

COSMO-SkyMed overall conceptual architecture is shown here below.

Dual Use Architecture



- [1] A. Torre, L. Borgarelli, P. Ammendola, "Enhanced spotlight Mode for High Resolution Image Acquisition in Alenia Spazio SAR2000", this symposium
- [2] F. Melgani , S. B. Serpico F. Caltagirone , R. Vigliotti, "Fusion of the Multi-sensor Data of the COSMO-SkyMed Mission", this symposium
- [3] P. Spera, A. Gallon, "Constellation Orbit Design Criteria for a Dual Use EO System", this symposium

Naval EarthMap Observer (NEMO) Hyperspectral Remote Sensing Program

Thomas Wilson and Robert Felt

Naval Research Laboratory, 4555 Overlook Avenue, S.W., Washington, D.C. 20375

Rebecca Baugh

Praxis Inc., 4875 Eisenhower Avenue, Suite 210, Alexandria, Virginia, 22304

Abstract

The NEMO hyperspectral remote sensing program will provide unclassified, space-based hyperspectral passive imagery at moderate resolution that offers substantial potential for direct use by Naval forces and the Civil Sector. NEMO merges Navy-developed technology with commercial technology and provides a space-qualified hyperspectral imager with the coverage and sensitivity required to collect broad-area synoptic imagery over land and ocean on a global basis. NEMO is a joint government and industry effort between the Naval Research Laboratory (NRL) and its industry partner Space Technology Development Corporation (STDC). NEMO is sponsored by the Office of Naval Research (ONR) and DARPA's Joint Dual-Use Application Program (JDUAP). NRL provides the design and integration of the NEMO sensor imaging payload with a commercial satellite bus as well as bus modifications, the on-board imaging processor, feature extraction and data compression software, and systems engineering. In addition, data products and algorithms are being developed by the Navy. STDC and its industry partners will provide the commercial satellite bus, launch services, commercial processing facilities, and long-term flight operations.

The NEMO program is currently in the hardware fabrication stage, concentrating on the manufacture and testing of flight hardware. NEMO will carry the Coastal Ocean imaging Spectrometer (COIS) which will provide images of littoral regions with 210 spectral channels over a bandpass of 0.4 to 2.5 μm . Since ocean environments have reflectances typically less than 5%, this system requires a very high signal-to-noise ratio (SNR). COIS will sample over a 30 km swath width with a 60 m Ground Sample Distance (GSD) with the ability to go to a 30 m GSD by utilizing the systems attitude control system to "nod" (i.e., use ground motion compensation to slow down the ground track of the field of view). Also included in the payload is a co-registered 5 m Panchromatic Imager (PIC) to provide simultaneous high spatial resolution imagery. A sun-synchronous circular orbit of 605 km allows continuous repeat coverage of the whole earth. One unique aspect of NEMO is an on board processing system, a feature extraction and data compression software package developed by NRL called the Optical Real-Time Spectral Identification System (ORASISTM). ORASISTM employs a parallel, adaptive hyperspectral method for real time scene characterization, data reduction, background suppression, and target recognition. The use of ORASISTM is essential for management of the massive amounts of data expected from the NEMO Hyperspectral Imagery (HSI) system, and for developing Naval products.

The combined HSI and panchromatic images will provide critical phenomenology to aid in the operation of Naval systems in the littoral environment. The imagery can also satisfy a number of commercial and science community requirements for moderate spatial and high spectral resolution remote sensing data over land and water. Specific areas of interest for the Navy include bathymetry, water clarity, bottom type, atmospheric visibility, bioluminescence potential, beach characterization, underwater hazards, total column atmospheric water vapor, and detection and mapping of subvisible cirrus. These data support requirements for Joint Strike and Joint Littoral warfare, particularly for environmental characterization of the littoral ocean. Demonstrations of timely downlinks of near real-time data to the warfighter are also being formulated. The launch date for NEMO has not been set yet. The commercial partner continues to seek necessary commercial capital to complete the program.

1. Background

The Navy is in the midst of a fundamental shift away from open ocean deep water operations to joint littoral warfare. To support that effort, the Navy and Marine Corps need more precise information in denied areas regarding shallow water bathymetry, bottom type composition, detection of underwater hazards, water clarity, and visibility¹. Visible radiation is part of the electromagnetic spectrum that penetrates the water, and passive optical systems can provide these products from space.

To address the problems of the coastal ocean, NRL scientists have been working since 1990 using the Airborne Visible/InfraRed Imaging Spectrometer (AVIRIS)^{2,3} which is operated by the Jet Propulsion Laboratory and flown on an ER-2 operated by NASA. AVIRIS data provides 20 m spatial resolution and 220 spectral bands covering a 0.4 to 2.4 μm spectral range at 10 nm resolution. In a collaborative effort with the University of South Florida, NRL has demonstrated the use of AVIRIS data to separate the chlorophyll signal from bottom reflectance in the clear waters of Lake Tahoe⁴ and the turbid waters offshore from Tampa Bay⁵. In addition, spectral signals from resuspended sediments and dissolved organic matter have been interpreted for the Tampa AVIRIS images^{5,6}, and for suspended sediments and kelp beds for AVIRIS images of the San Pedro Channel⁷. These results lead to a general semi-analytical model for decomposition of the spectral signatures^{8,9}.

Similar progress has been made on the land applications of imaging spectrometer data since the value of that data was first highlighted in an article in *Science* in 1985¹⁰. Primarily using AVIRIS data, applications have been developed for the retrieval of atmospheric properties and for assessing crop status, environmental quality, and mineral exploration (e.g., *Remote Sensing of the Environment*, Vol. 44(2-3), Special Issue on Airborne Imaging Spectrometry). In particular, mineral exploration has become a hot topic. Several companies now provide services interpreting AVIRIS or other aircraft hyperspectral data for mineral exploration. NEMO will provide the first data from space suitable for this application.

Multispectral imagers, such as Landsat and SeaWiFS, do not have sufficient spectral bands to resolve the complex spectral signatures in the coastal ocean or the spectral signatures used for mineral exploration. Imaging spectrometers do resolve those signatures and are an ideal tool to fill these requirements, but they have not been used to date because of cost and the demands of processing the data. Both these problems have been overcome in recent years.

Multispectral sensors image several wide discontinuous spectral bands (usually 3 to 5); hyperspectral sensors image at least 60, 10 nm wide contiguous spectral bands. As defined by Goetz et al¹⁰ each pixel within a hyperspectral image contains a continuous spectrum used to identify materials by their reflectance or emissivity. This allows identification of components within a scene (i.e., types of minerals, trees, crop health, bathymetry, composition) versus multispectral, which can only identify major features of a scene (i.e., rocks, trees, crops, water). Figure 1 gives a description of the imaging spectrometry concept.

2. Navy Program Objectives

For the Navy, the central focus of the NEMO program is to develop and fly a satellite-borne earth-imaging HSI system to provide HSI data and to process the data to meet Naval and commercial requirements. The mission objectives are as follows:

- Demonstrate use of hyperspectral imagery for the characterization of the littoral battlespace environment and littoral model development.
- Demonstrate automated, on-board processing, analysis, and feature extraction using ORASIS™
- Demonstrate the value of hyperspectral data for DoD operations and commercial applications.
- Demonstrate support to the warfighter with real-time tactical downlink of hyperspectral end products directly from the spacecraft to the field.

2.1 Naval Requirements. NEMO meets the unique requirements of Naval Forces by imaging the littoral regions of the world in 210 spectral bands over a 0.4 to 2.5 μm bandpass with a very high SNR. NEMO has the goal of characterizing the dynamics of the littoral environment through the use of hyperspectral imagery and the development of coupled physical and bio-optical

models of the littoral ocean. The collected images provide critical phenomenology to model the littoral environment. Specific areas of study for the Navy include water clarity, bathymetry, underwater hazards, currents, oil slicks, bottom type, atmospheric visibility, tides, bioluminescence potential, beach characterization, atmospheric water vapor, and subvisible cirrus along with terrestrial images of vegetation and soil. These data support identified requirements for Joint Strike and Joint Littoral warfare, particularly for environmental characterization of the littoral ocean and intelligent preparation of the battlespace for amphibious assault.

3. Commercial Program Objectives

Earth Search Sciences Inc. (ESSI) acquired Space Technology Development Company (STDC) and the commercial rights to the NEMO Program's hyperspectral satellite and data system. The current stated commercial program objectives are:

- Develop the next generation of HSI sensor.
- Develop improved data collection and processing to provide near real-time products from large quantities of data (includes use of the Navy's ORASIS™ software).
- Form a joint venture with one or more aerospace partners to complete the NEMO project and develop additional satellite based imaging systems.
- Aggressively exploit and market end-to-end hyperspectral data and products to domestic and international clients.
- Deploy ESSI's web-based TERRANET imagery delivery system.
- Develop a next generation of spaceborne hyperspectral instrument to replace NEMO at the end of its useful life.

4. NEMO Mission Description

The NEMO spacecraft will be launched into Low Earth Orbit (LEO). The spacecraft will be placed in a sun-synchronous, 97.81° inclination orbit at 605 km altitude with a 10:30 a.m. ascending equator crossing. This orbit will provide a 7 day repeat coverage ability to allow, at a minimum, weekly access to any point on the earth. The 10:30 a.m. orbital crossing ensures consistent image quality and minimal cloud cover. Table 1 provides a general overview of the NEMO program mission characteristics. The sensor complement flown on the NEMO spacecraft includes a Coastal Ocean Imaging Spectrometer (COIS) and a co-registered Panchromatic Imaging Camera (PIC). The primary challenges in the COIS design are the wide field of view ($>2.5^\circ$) and the very high SNR, particularly near the blue end (0.4 μm) of the spectrum required for ocean imaging. NEMO also employs NRL's Optical Real-time Adaptive Spectral Identification System (ORASIS™), an automated end-to-end HSI data processing system that will significantly reduce the amount of data NEMO must transmit to the ground. Figure 2 shows the current NEMO sensor deck concept.

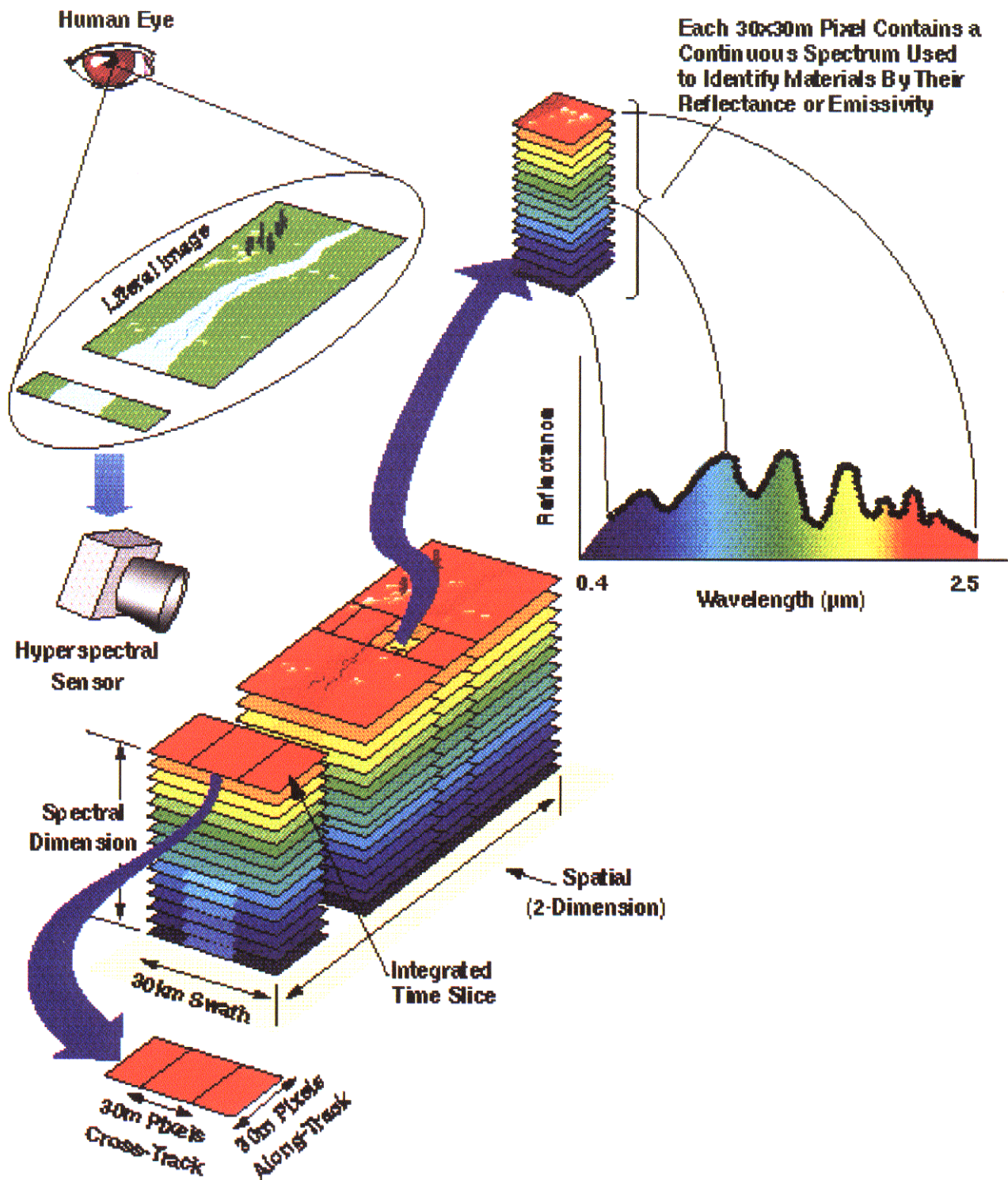


Figure 1. Imaging Spectrometry Concept

Table 1. Mission Characteristics

Item	Parameter
Orbit	<ul style="list-style-type: none"> 605 km sun synchronous (97.81° inclination) 10:30 am equatorial crossing (ascending)
Repeat Global Coverage	<ul style="list-style-type: none"> 7 day repeat, 2.5 day global average re-access
Spectral Range	<ul style="list-style-type: none"> 0.4 to 2.5 μm at 10 nm spectral resolution (210 bands)
Signal-to-Noise	<ul style="list-style-type: none"> >200 to 1 over 0.4 to 1.0 μm for a 5% reflectance target
Weight	<ul style="list-style-type: none"> 574 Kg
Power	<ul style="list-style-type: none"> 1,500 Watts
Lifetime	<ul style="list-style-type: none"> 3 year mission life 5 year design life
Data Rates	<ul style="list-style-type: none"> 150 Mbps X-Band imagery and telemetry downlink 1 Mbps S-Band imagery downlink for tactical demonstration 2 kbps S-Band command uplink
Data	<ul style="list-style-type: none"> Maximum capability of ≈ 105 Gbytes/day
On-Board Processing	<ul style="list-style-type: none"> Real-Time feature extraction and classification with >10x data reduction using ORASIS™

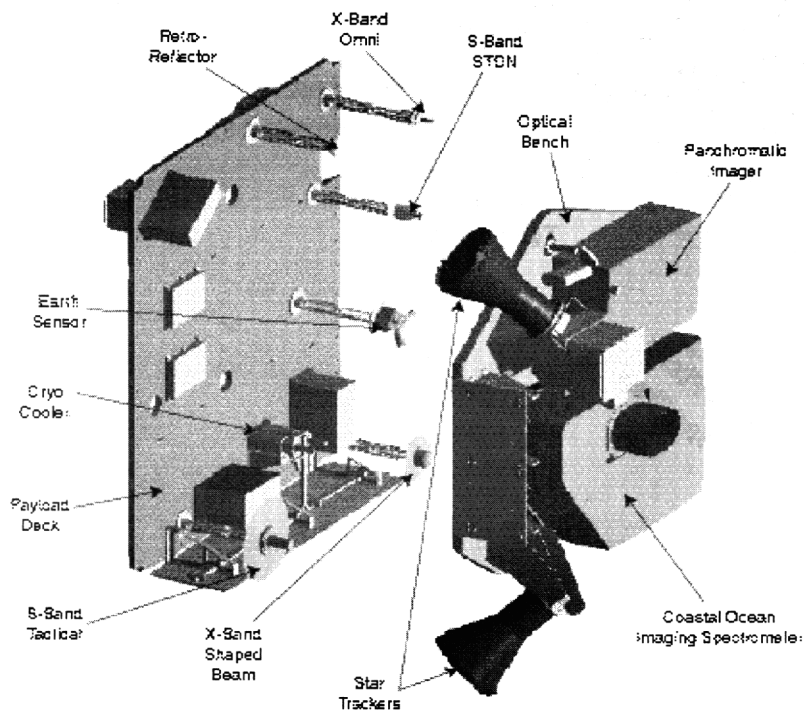
**Figure 2. NEMO Sensor Deck Concept**

Table 2. Sensor Systems Characteristics

	VNIR	SWIR	PIC
Ground Sample Distance (GSD)	30 m with 5:1 GMC 60 m with no GMC	30 m with 5:1 GMC 60 m with no GMC	5 m (with or without GMC)
Spectral Range	0.4 to 1.0 μm	1.0 to 2.5 μm	0.545 to 0.769 μm
Spectral Bands	60	150	1
Signal to Noise Ratio	>200 to 1 @ 5% Reflectance	>100 to 1 @ 30% Reflectance	>200 to 1 @ 30% Reflectance
Swath Width	30 km	30 km	30 km
Swath Length	200 km @ 30 m GSD continuous @ 60 m GSD	200 km @ 30 m GSD continuous @ 60 m GSD	Continuous
Field of View	2.86 degrees	2.86 degrees	2.86 degrees
Ground Swath Width	30 km	30 km	30 km
Aperture Diameter	15 cm	15 cm	16.4 cm
Focal Length	36 cm	36 cm	120 cm
F#	2.4	2.4	7.32
Pixel Size	18 μm	18 μm	10 μm
# of Pixels/Spectral Band	6	6	N/A
FPA Material	Si	MCT	Si
On-Orbit Sparring	1 for 1 Spare	1 for 1 Spare	1 for 1 Spare

4.1 Coastal Ocean Imaging Spectrometer (COIS).

The present design of the COIS instrument employs a three-mirror-off-axis anastigmat (TMA), 12 cm aperture telescope and two spectrometers to image a 30 km wide ground swath at a 30 m GSD. Table 2 provides the characteristics of the HSI sensor system. The two spectrometers used in the COIS are:

The Visible Near Infrared (VNIR) spectrometer that disperses the 0.4 to 1.0 μm light into 60 spectral channels (10 nm wide) and onto the Focal Plane Array (FPA). This provides a resolution of 1.0 to 1.5% of the band and 60 spectral bins.

The Short-Wave Infrared (SWIR) spectrometer that disperses the 1.0 to 2.5 μm light into 150 spectral channels (10 nm wide) and onto the FPA. This provides a resolution of about 0.6% of the band and 150 spectral bins. To achieve high SNR performance, the SWIR requires active cooling by a cryocooler.

COIS provides very high SNR environmental products for imaging the low-reflectivity ocean surface. The NEMO spacecraft implements Ground Motion Compensation (GMC) sufficient to reduce the apparent ground speed by a factor of 5. This provides the required dwell time to give a similar high SNR at a GSD of 30 m. COIS is also capable of producing 60 m GSD, high SNR data products without GMC by using spatial binning of the hyperspectral FPAs. Figure 3 shows the baseline COIS optical design.

4.2 Panchromatic Imaging Camera (PIC).

The PIC is a separate instrument that uses a similar off-axis telescope to simultaneously image the same 30 km swath as the COIS instrument onto a 6000 pixel long linear array to produce a panchromatic image in the 0.45 to 0.67 μm wavelength range at a 5 m GSD. The moderate COIS GSD matches the spatial scale of natural objects in the littoral zone, while the high resolution PIC provides simultaneous context and sharpening and supports commercial land imaging requirements. The 30 km ground swath of COIS and PIC spans the near-shore land, beach, and ocean. COIS and PIC use a single optical bench to minimize optical boresite drift. Table 2 provides the characteristics of the PIC sensor system and the sensor designs are described in a previous paper¹². The COIS and PIC sensors are presently in fabrication by SAIC.

4.3 Optical Real-time Adaptive Spectral Identification System (ORASIS™).

The NEMO program employs NRL's automated end-to-end HSI data processing system called ORASIS™. ORASIS™ offers automated and adaptive signature recognition capability, improving the operational efficiency to analyze both military and commercial data sets. It is important to note that while ORASIS™ is fully automated, it is also computationally intensive, requiring the NEMO satellite to have an on-board processor with multi-GigaFLOP capability.

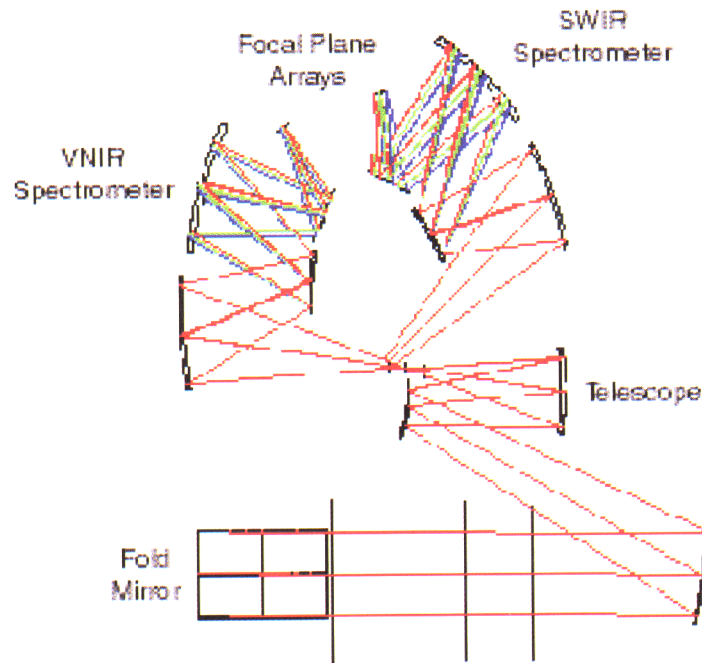


Figure 3. COIS Optical Design

ORASISTM is a high-speed processing system that identifies the spectral signatures corresponding to physical objects in the scene without supervision or *a priori* knowledge. The approach is to analyze each spectra in the scene sequentially, discarding duplicate spectra, and working only with the unique spectra and the map of their location in the scene. Using convex set methods and orthogonal projection techniques each observed spectrum is then analyzed in terms of the set of vectors that represent the physically meaningful basis patterns that have combined to make the observed spectrum. Then matched filters (Filter Vectors) are created and used to demix the image^{14,15}.

ORASISTM processing on board NEMO minimizes subsequent ground processing for data exploitation and maps of identified features, and enables the on-board production of data products. An important benefit of ORASISTM processing is a greater than tenfold data compression (lossy), relieving hyperspectral data bottlenecks of on-board data storage and transmission to the ground. An early version of ORASISTM was successfully flight demonstrated in a tactical environment in the 1996 COVERED LANTERN exercise, using hyperspectral images from a Pioneer Uncrewed Aerial Vehicle (UAV). This test proved ORASISTM compression and detection capabilities.

For NEMO, ORASISTM is implemented on the Imagery On-Board Processor (IOBP), an advanced high speed

computer consisting of a highly parallel array of digital signal processors, capable of sustaining 2.5 GigaFLOPS. The ORASISTM algorithm and the radiation tolerant IOBP allow the first demonstration of real-time processing of hyperspectral data in space. The NEMO on-board implementation of ORASISTM is described in detail in a previously published paper.¹⁵

ORASISTM will also be used under the NEMO program as the basic spectral decomposition tool for analyzing the HSI data and producing Naval products.

4.4 Spacecraft Characteristics. The spacecraft system architecture consists of eight hardware subsystems plus a software subsystem, which collectively accommodate the spacecraft payload and meet the mission and science requirements. These subsystems are: (i) the Attitude Determination and Control Subsystem (ADCS); (ii) the Electrical Power Subsystem (EPS); (iii) the Reaction Control Subsystem (RCS); (iv) the Thermal Control Subsystem (TCS); (v) the Structural Subsystem; (vi) the Mechanisms Subsystem; (vii) the Command, Telemetry, and Data Handling Subsystem (CT&DH); (viii) the Communications Subsystem; and (ix) the Flight Software Subsystem.

Figure 4 shows a concept of the NEMO spacecraft in orbit. Table 3 provides an overview of the subsystem characteristics of the NEMO spacecraft.

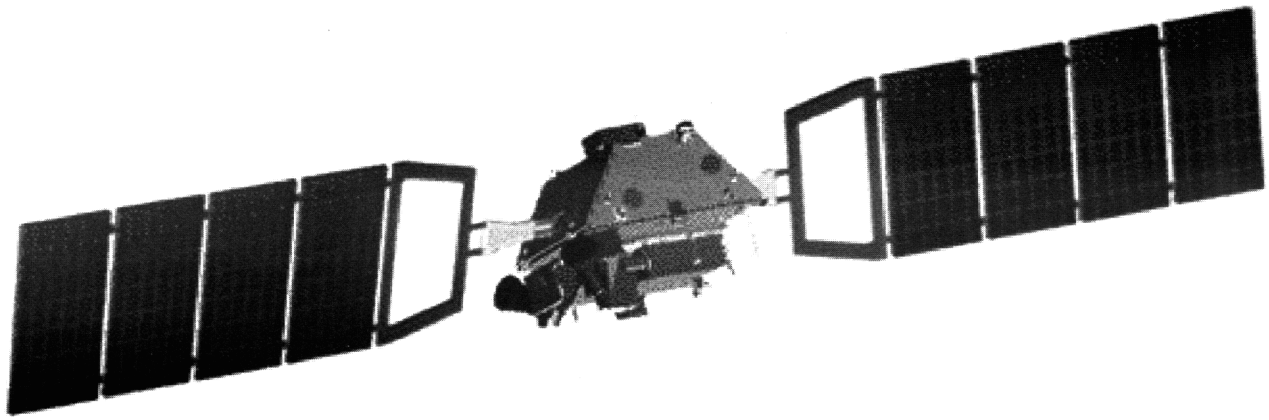


Figure 4. Spacecraft Concept

Table 3. NEMO Spacecraft Characteristics

Subsystem	Characteristics
Attitude Determination and Control	<ul style="list-style-type: none"> 3-Axis stabilized for all modes; 0.07 degree control Geolocation: 30 m with a Circular Error of Probability (CEP) of 0.9 2 star trackers and 1 inertial measurement unit for attitude determination 4 reaction wheels and 2 electromagnetic torquers for attitude control
Electrical Power	<ul style="list-style-type: none"> 2 gimbaled (single axis) solar array panels 4 for 3 redundant power control box 64 Ah nickel hydrogen battery Approximately 1500 watts
Reaction Control	<ul style="list-style-type: none"> Monopropellant hydrazine blowdown system 1 propellant tank (76.5 kg capability) 5 x 1N thrusters for orbit correction/orbit maintenance
Thermal Control	<ul style="list-style-type: none"> Passive thermal control with heater augmentation Battery and payload panels thermally isolated from bus
Structures	<ul style="list-style-type: none"> Primary structure is a combination of a rigid aluminum tubular frame and aluminum honeycomb shear panels Kinematically decoupled optical bench Space vehicle mass: ≈ 496 kgs dry; ≈ 574 kgs wet; payload ≈ 292 kgs
Mechanisms	<ul style="list-style-type: none"> Optical bench launch restraints Contamination covers for sensors Solar array drive mechanisms for gimbaling arrays Launch vehicle separation Two redundant main electrical umbilical connectors
Command, Telemetry, and Data Handling	<ul style="list-style-type: none"> NEMO Spacecraft Controller (NSC): Mongoose V (radiation-hardened processor) NEMO Payload Controller (NPC): R3000 processor Imagery On-Board Processor (IOBP): multiple SHARC processors in a parallel array 56 Gb solid state data recorder
Communications	<ul style="list-style-type: none"> Command and Telemetry Uplink: S-Band 2kbps, 2074.18 MHz Primary Imagery Data Downlink: X-Band 131 Mbps 8.2 GHz, with telemetry embedded Tactical Demonstration Imagery Downlink: S-band, 1.024 Mbps 2252.5MHz (DMSP frequency)
Software	<ul style="list-style-type: none"> On-board task scheduling capability Embedded fault detection, isolation, and recovery (FDIR) Attitude control interface and functionality Spacecraft Command Language (SCL) for enhanced "macro" commanding

4.5 Mission Operations. The NEMO program will use a combination of commercial operations and existing Defense infrastructure to provide the Naval, DoD, and commercial communities easy and timely access to data

collected by the NEMO spacecraft. The NEMO program concept for data handling on the ground is shown in Figure 5. The Navy operations concept is shown in Figure 6.

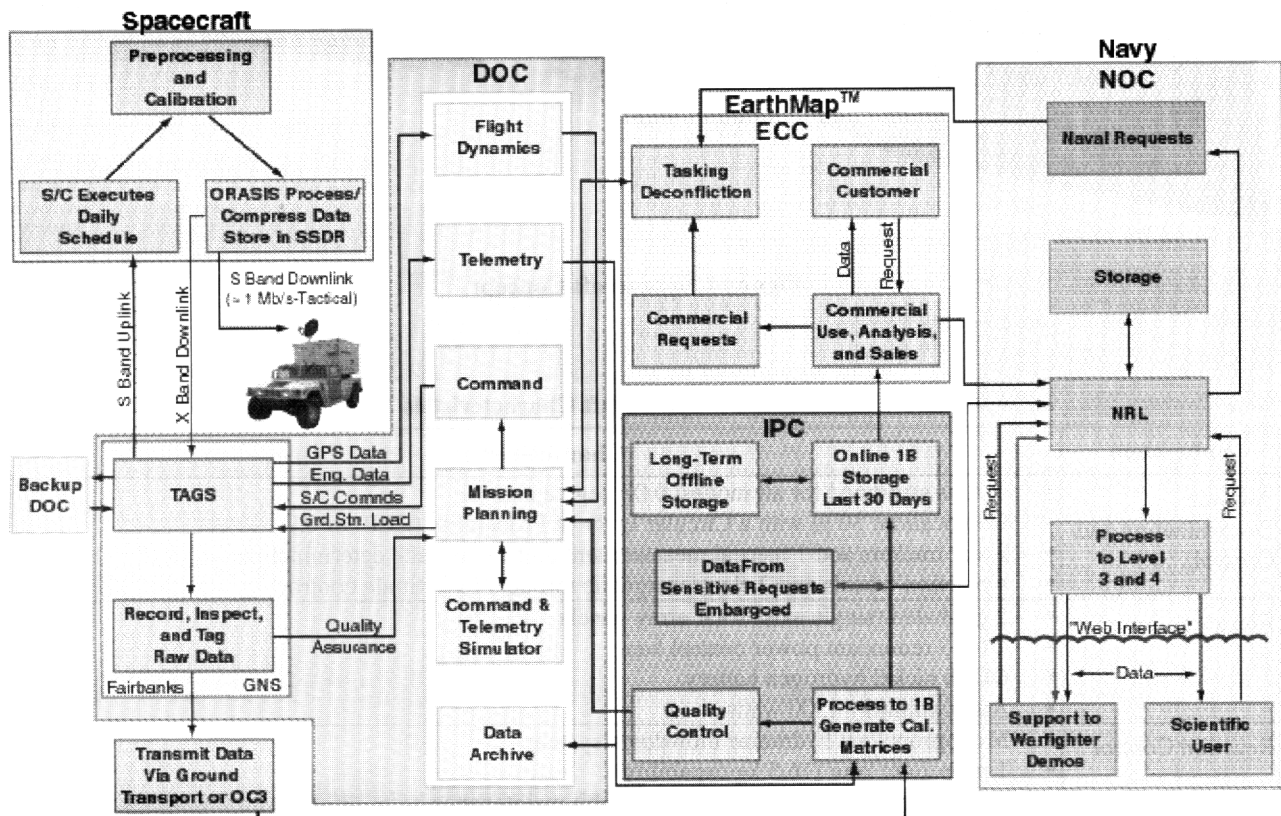


Figure 5. NEMO Mission Operations Block Diagram

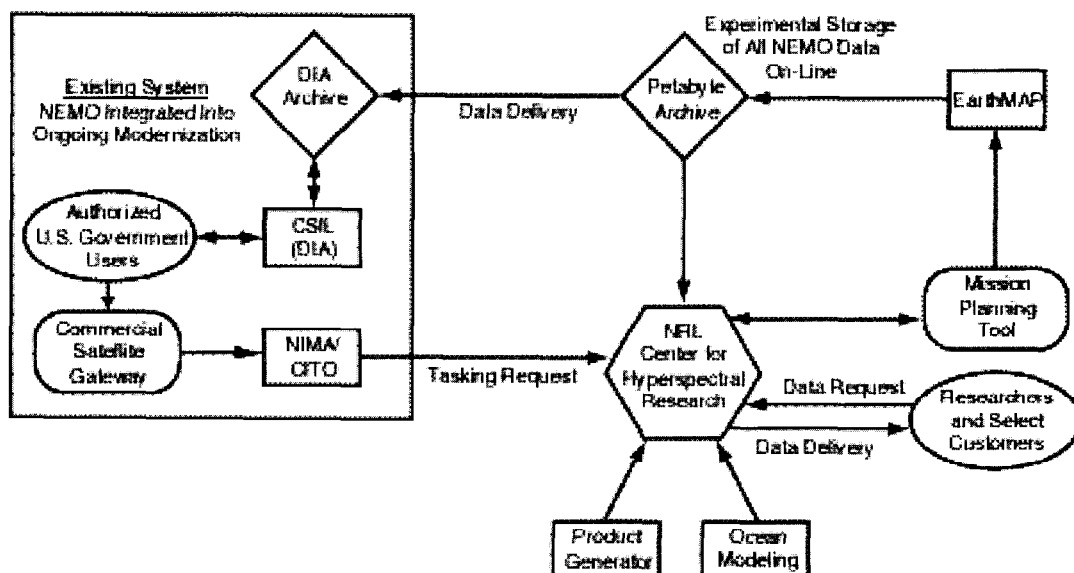


Figure 6. Ground Data Handling Concept Block Diagram

NEMO operations will be handled through the Advanced Spacecraft Operations Center (ASOC) which will be the central hub for NEMO mission planning, S/C operations, downlink data processing, command generation, and S/C and payload state-of-health monitoring.

The ASOC communicates with the S/C through Transportable Autonomous Ground Stations (TAGS) located in Fairbanks, Alaska, and at another site yet to be determined. The primary feature of the ASOC is that it consists of similar but enhanced elements of existing facilities. This approach effectively combines the cost savings benefits provided by reuse with the productivity enhancements of advanced technology. The ASOC also includes late-model, high-end work stations and PCs. These platforms have the capability to drive the operation of several automated ground stations and provide simultaneous displays for multiple satellites.

The TAGS tracks the NEMO S/C, sends commands to the satellite from the ASOC via S-Band uplink, and receives satellite health and welfare data embedded in the primary payload image data via X-Band downlink. Downlinked data is maintained on mass storage devices at the TAGS until final receipt at the Image Processing Center (IPC) is verified.

The Image Processing Center (IPC) interfaces with the ASOC to receive telemetry and imagery data. The IPC performs the image quick-look (quality control), data processing to Level 1B, and data archive functions. Activities also include fault tolerant data storage, analysis, and retrieval and in-flight sensor calibration.

The NRL Center for Hyperspectral Research (NCHR) is the Naval and scientific hub for the NEMO program. The NCHR performs the tasking for the Navy of the NEMO spacecraft and data distribution function for the Naval segment of the mission, and is the focal point for Naval Hyperspectral research.

4.6 Navy Tactical Demonstration. Currently NEMO is being designed with the ability to downlink directly to the "field" to demonstrate the use of hyperspectral data to the warfighter. An S-Band 1 Mbps transmitter along with the IOBP and ORASIS™ will allow real-time processing and downlinking of data products. The current demonstration scenario is as follows:

The NEMO spacecraft is pre-programmed with an image target command from the Fairbanks ground site.

The NEMO S/C enters the "demonstration area" and images the pre-programmed 30 x 5 km area. Imaging takes about 4 seconds.

In real-time the IOBP processes the image using the ORASIS™ processing algorithm. It crops the image down to a 5 x 5 km area of interest, then processes it into an ORASIS™ product. ORASIS™ reduces a 470 Mbit raw image into a much more manageable 60 Mbit product.

The result is downlinked to a deployed field station via a 1 Mbps S-band antenna. This takes about 60 seconds.

A custom interface to the deployed field station will be provided by the NEMO team. This interface will have all the tools required to exploit the hyperspectral imagery.

4.7 On-Orbit Calibration and Product Validation.

The NEMO program requires the routine imaging of 50 sites to maintain the calibration of the COIS instrument and for the development, validation and demonstration of coastal ocean products. Characterization and careful laboratory calibration to National Institute of Standards and Technology (NIST) standards of the COIS and PIC instruments will be conducted before flight and during thermal-vacuum testing. NRL will team with the instrument builder to establish the necessary tests and measurement procedures which will be incorporated as part of the instrument acceptance testing. The results will be used to create the initial calibration matrices, and software necessary to correct for any identified instrument abnormalities. On orbit COIS is designed to be stable to better than 1% per month. COIS calibration will be maintained on orbit by monthly imaging of the near full moon, daily stability checks using an on-board calibration lamp, and weekly imaging of large uniform ground reference targets, such as the Sargasso Sea and the Bonneville Salt flats, which have known and monitored reflectances. Moon imaging makes it possible to image reflected sunlight off of a known reflectance target without having to correct for the atmosphere. The moon imaging is currently being used by the SeaWiFS program,¹⁶ the MODerate resolution Imaging Spectrometer (MODIS) program. Imaging known reflectance targets on the earth provides a means for checking the combined accuracy of calibration and atmospheric correction. NEMO will use a new atmospheric correction algorithm based on the Ahmed and Fraser¹⁷ radiative transfer code which includes a correction for sun glint reflected off of the sea surface for water scenes¹⁸.

An additional ten coastal ocean sites will be used for the development, and validation of the standard ocean products and models. Standard products include phytoplankton chlorophyll, colored dissolved organic matter, suspended sediments, Kd(490) (diffuse transmission of light at 490 nm), bathymetry and bottom types. Measurements of these parameters from ships and moorings will provide ground truth for validation of the algorithms. Advanced products, such as spectral absorption and beam transmission, will also be developed at these sites as part of the NRL Hyperspectral Characterization of the Coastal Ocean (HCCO) program and the ONR Hyperspectral Coastal Ocean Dynamics Experiment (HyCODE). Those programs include the use of the NEMO products in the development and validation of coupled bio-optical physical models of the dynamics of the coastal ocean. The ultimate goal is the development of models for the prediction of the coastal ocean environment that are similar to today's weather forecasts for the atmosphere. An iterative process for the development of these models is outlined in Figure 7. The products and models will then be applied to additional sites of interest for science and naval applications.

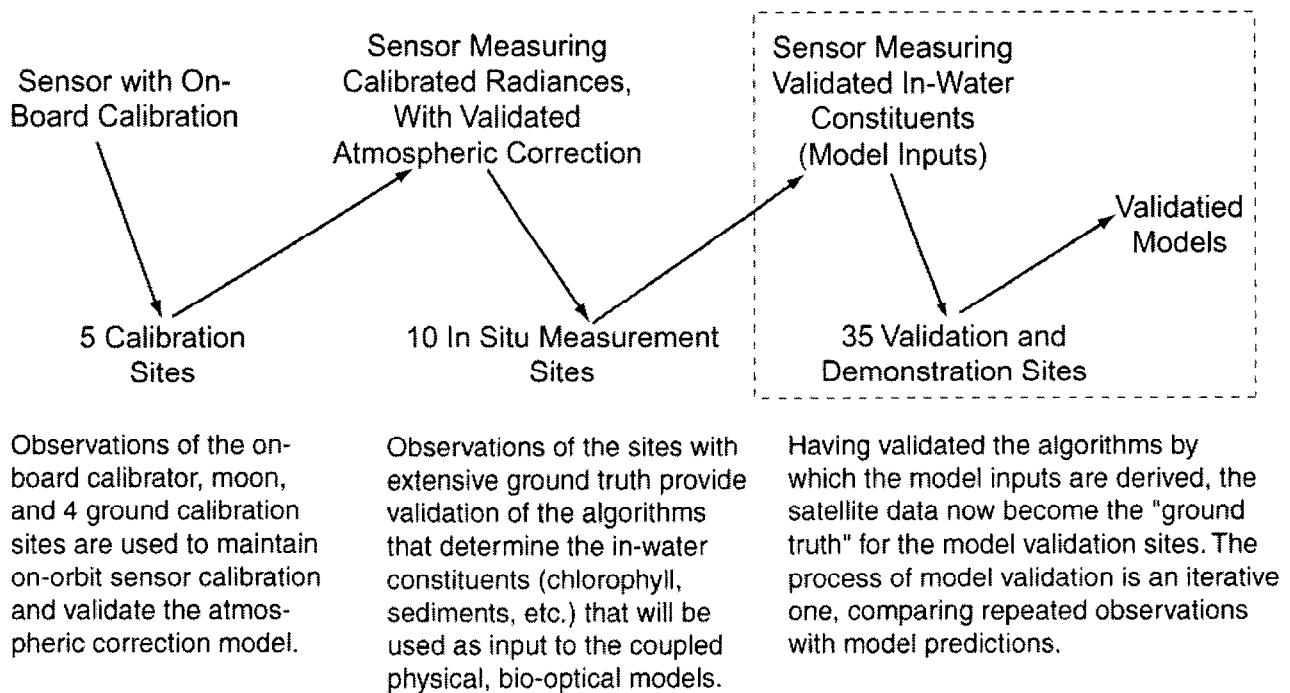


Figure 7. NEMO COIS Sensor Calibration, Product Validation and Model Development

5. Summary

The NEMO program will provide the Navy and DoD with the ability to test and demonstrate the utility of environmental hyperspectral remote sensing to support the warfighter. In addition, the NEMO program along with the NEMO spacecraft provides the opportunity to apply several important technologies to dual-use remote sensing missions. These include innovations in sensors and algorithms; experience in low-cost, high-volume satellite data production; experience in small-staff, automated ground operations; and innovations in image processing and data distribution. The launch date for NEMO has not been set yet. The commercial partner continues to seek necessary commercial capital to complete the program.

6. Acknowledgments

We wish to thank John Antoniadis, Pete Palmadesso, John Fisher, Mark Baumbach and Jeff Bowles for providing insight into instrument design and the ORASIS™ processor. Support from Dr. Curt Davis, Ron Contillo, Dr. Lee J Rickard and Dr. Phil Schwartz are appreciated. This work was funded by ONR and NRL.

7. References

1. Marine Corps Headquarters Letter 3000 of 7 December 1992 validated by CNO (NO96) Letter 3140 Ser 960/3u567444 of 15 January 1993; Special Operations Command letter of 16 April 1991 validated by CNO (NO96) Letter 3140 Ser 960/2u567322 of 22 January 1992.
2. Porter, W.M. and H.T. Enmark, "System overview of the Airborne Visible/Infrared Imaging Spectrometer (AVIRIS)", *Proceedings of the SPIE*, V834, pp. 114-126, 1987.
3. Vane, G.R.O. Green, T.G. Chrien, H.T. Enmark, E.G. Hansen and W.M. Porter, "The Airborne Visible/Infrared Imaging Spectrometer (AVIRIS)", *Remote Sens. Environ.*, 44, 127-143, 1993.
4. Hamilton, M.K., C.O. Davis, W.J. Rhea, S.H. Pilorz and K.L. Carder, "Estimating chlorophyll content and bathymetry of Lake Tahoe using AVIRIS data", *Remote Sens. Environ.*, 44, pp. 217-230, 1993.
5. Carder, K.L., P. Reinersman, R. Chen, F. Muller Karager and C.O. Davis, "AVIRIS calibration and application in coastal oceanic environments", *Rem. Sens. Environ.* 44, pp. 205-216, 1993.
6. Carder, K.L., Z.P. Lee, R.F. Chen and C.O. Davis, "Unmixing of spectral components affecting AVIRIS imagery of Tampa Bay", *Proceedings of the SPIE*, V 1937, pp. 77-90, 1993.
7. Davis, C.O., M.K. Hamilton, W.J. Rhea and J.M. van den Bosch, K.L. Carder and R. Steward, "Spectral analysis of an AVIRIS image of San Pedro Channel", *Proceedings of the SPIE*, V 1937, pp. 64-76, 1993.
8. Lee, Z., K.L. Carder, S.K. Hawes, R.G. Steward, T.G. Peacock and C.O. Davis, "A model for interpretation of hyperspectral remote-sensing reflectance", *Appl. Opt.*, 33(24), pp. 5721-5732, 1994.
9. Lee, Z.P., K.L. Carder, T.G. Peacock, C.O. Davis and J. Mueller, "A method to Derive Ocean Absorption Coefficients from Remote-Sensing Reflectance", *Appl. Opt.*, 35(3), 453-462, 1996.

10. Goetz, A. F. H. G. Vane, J.E. Soloman and B.N. Rock, "Imaging Spectrometry for Earth Remote Sensing", *Science*, 228, 1147-1153, 1985.
11. Gao, B-C., K. H. Heidebrecht, and A. F. H. Goetz, "Derivation of scaled surface reflectances from AVIRIS data", *Remote Sens. Env.* 44, 165-178, 1993.
12. Myers, A., "NEMO satellite sensor imaging payload", *Proceedings of the SPIE*, V 3437, 29-40, 1998.
13. Palmadesso, P., J. Antoniadis, M. Baumbach, J. Bowles and L. Rickard, "Use of filter vectors and fast convex set methods in hyperspectral analysis", *Proceedings of the International Symposium on Spectral Sensing Research*, November 26- December 1, 1995, Melbourne, Australia, 1996.
14. Bowles, J.H., "NEMO on-board processor an ORASIS™ real-time hyperspectral analysis system", *Proceedings of the SPIE*, V 3437, 20-28, 1998.
15. Bowles, J. H. , et al., "New results from the ORASIS™/NEMO compression algorithm", *Proceedings of the SPIE*, V 3753, In Press.
16. Barnes, R.A., R.E. Eplee , and F.S Patt., "SeaWiFS measurements of the moon", *Proceedings of the SPIE*, V 3498, 311-324, 1998.
17. Ahmad, Z., and R.S. Fraser, "An iterative radiative transfer code for ocean-atmosphere systems", *J. Atmospheric Science*, 39, 656-665, 1982.
18. Gao, B-C., M. Montes, C.O. Davis, and Z. Ahmad, "Atmospheric correction algorithm based on vector radiative transfer modeling for hyperspectral remote sensing of ocean color", *Proceedings of the SPIE*, V 3753, In Press.

**The European Office of Aerospace Research and Development's Small Satellite Propulsion System
Research Program**

Major Timothy J. Lawrence, Ph.D.
Space Technology
EOARD
Edison House
223/231 Old Marylebone Road
London
+44 207 514 4285 (phone)
+44 207 514 4960 (fax)
tim.lawrence@london.af.mil (email)
12 April 2000

**Prepared for Space Technology and Management Panel
NATO SET Symposium, 16-18 October 2000, Samos, Greece**

Abstract

A spacecraft needs propulsion for attitude control, stationkeeping, and orbit maneuvering. Traditionally, these needs have been satisfied by the following system options:

- Cold-gas propulsion – mainly using nitrogen for attitude control
- Hydrazine-based systems – for attitude control, station-keeping and orbit maneuvering
- Solid rockets – for orbit maneuvering

However, the space industry trend to build smaller and cheaper spacecraft (10 – 300 kg) have created propulsion system integration requirements and constraints unique to these niche applications. The European Office of Aerospace Research and Development (EOARD) has started a program with 3 European institutes to investigate these niche systems for future Air Force small satellite propulsion missions:

- **Nitrous oxide monopropellant, University of Surrey, UK:** a self-pressurizing, nitrous oxide catalytic decomposition technique is suggested for re-startable spacecraft propulsion. More than 50 different catalysts have been tested. Catalyst activation temperature of 250°C has been achieved with mass flow rates above 1.1gm/s. Decomposition temperatures in excess of 1500°C have been attained. Electrical power input (for heating the

catalyst up to its activation temperature) as low as 24W has been applied. The time required to heat the catalyst from ambient to activation temperature was as short as 3min. A catalyst lifetime in excess of 76min. has been demonstrated. Work will continue to find the optimum catalyst to meet spacecraft lifetime requirements.

- **100 W Stationary Plasma Thruster (SPT), Fakel Design Bureau, Russia:** An SPT works by developing an axial electric field between discharge electrodes. Due to the lower power, Fakel decreased the thruster size to 50-mm diameter x 40 mm in length (size of a 35-mm roll of film). They also varied the xenon flow density and magnetic field intensity to try to increase the performance. Fakel also developed a cathode (no heat required compared to other cathode designs) that is roughly the size of a standard ink pen. The thruster total mass is 350 g. Thruster tests covering a total of 9.5 hours at various settings were observed, including the following significant results (all stated efficiencies include the cathode): Input power: 94.5 W Thrust: 4.7 mN Specific Impulse: 1000 sec Efficiency: 24 %

- **Modification of the T-27 Thruster for 100 W Use, Tsniimash, Russia:** Tsniimash varied the flow and power conditions of their existing 200 W SPT T-27 thruster and operated it at 100 W. Although the efficiency decreased from 35 % to 23 % for the lower power operation, the thrust and Isp were good for small satellite application at 5 mN and 981 sec respectively.

The paper will go into greater description of these programs and will conclude with future work planned.

Introduction

The success of small satellite missions depends on low-cost launch opportunities. So far, the majority of small satellite missions have been as secondary payloads deployed into LEO (low Earth orbit). Unfortunately, until now these spacecraft lacked one critical system that would allow them to exploit fully emerging opportunities in LEO and beyond—a propulsion system. Propulsion systems are a common feature on virtually all larger satellites. However, until now there has been no need for very small, low-cost satellites to have these potentially costly systems. As secondary payloads, they were deployed into stable, useful orbits and natural orbit perturbations (drag, J2, etc.) were acceptable within the context of the relatively modest mission objectives.

Over the years, these pioneering small satellite missions have proven that effective communication, remote sensing and space science can be done from a cost-effective platform. As these missions have evolved, various technical challenges in on-board data handling, low-power communication, autonomous operations and low-cost engineering have been met and solved. Now, as mission planner's look beyond passive missions in LEO to bold, new missions which require active orbit and attitude control, a new challenge is faced—cost-effective propulsion.

In order to compete in the commercial market, small satellites have other unique constraints compared to larger spacecraft:

1. Cost < £4 million
2. Mass - < 500 kg
3. Volume - < 600 mm outer diameter x 800 mm length
4. Power - < 150 W on orbit average in LEO
5. Integration - safety, logistics of propellant transfer to launch site and handling of non-toxic propellants
6. Thrust - attitude control thrust < 1 N vs. high drag orbit thrust > 1 mN

Table 1 shows a comparison of various propulsion systems for a 100 kg spacecraft requiring a ΔV of 200 m/s. This mission velocity could move a 100 kg spacecraft from an circular orbit of 200 km to 600 km altitude or provide initial separation and phasing, 3 years stationkeeping, and deorbiting for each spacecraft in a 4 – 6 sunsynchronous constellation.

System	N ₂ Cold Gas	N ₂ O Liquid gas	100 W Nitrous Oxide Resistojet	Nitrous Oxide Monoprop.	Hydrazine Monoprop.	100 W Stationary Plasma Thruster (Hall Effect)
Propellant Mass (kg)	26.9	29.6	14.5	11.3	8.9	2.0
Propellant Volume (l)	330.4	38.1	18.7	14.5	8.0 + press.	3.4
Time (hours)	23.5	23.5	23.5	23.5	23.5	747.4

Table 1: Comparison of Various Propulsion Systems for a 100 kg satellite, $\Delta V = 200$ m/s

Table 1 presents interesting results. Current off-the-shelf cold gas systems would offer little/no

volume for the payload. The nitrous oxide monopropellant system gives similar

performance to hydrazine (48 bar vapor pressure requires no pressurant), but is non-toxic which makes it much better to handle logistically. The Stationary Plasma Thruster (SPT) offers very good performance, but will require more time to get the satellite on station. All of the other systems are scalable to different thrust levels with little impact on performance (except for the resistojet, which will require more power to maintain performance at a higher thrust). I assumed 100 mN since that would allow integration into a 100 kg spacecraft with little impact on the attitude control system (disturbance torques can be controlled by wheels and magnetorquers).

Figure 1 shows a comparison of the various systems as a function of density specific impulse and amount of power needed from the satellite to produce thrust. Density specific impulse is defined as the specific impulse of the propellant (mass performance) multiplied by its average specific gravity in its storage state. The ideal system for a small satellite would produce a high density specific impulse and require no power, which would be in the upper left hand corner of the figure. The goal of the EOARD propulsion program is to investigate such a system, but also keep the cost below current off the shelf hydrazine systems.

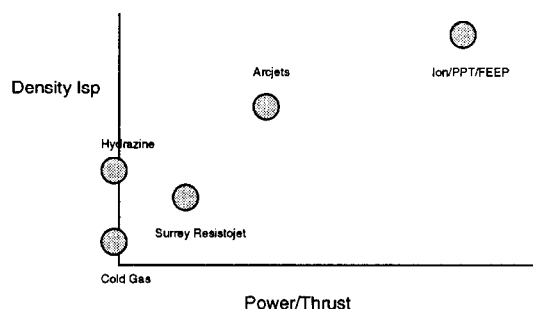


Figure 1: Power/Thrust ratio versus Density Specific Impulse

Nitrous Oxide Monopropellant

The University of Surrey, Guildford, UK started an investigation into low cost propulsion systems for their microsatellites (50 – 100 kg) in 1995. After analyzing the various options, they discovered that water and nitrous oxide resistojets looked attractive for its future missions. In 3 years of development time, they

produced the Mark IV thruster. This thruster was flown on the UoSAT-12 (University of Surrey 300 kg satellite) and flight qualified for the USAF MightySATII.1 program – work sponsored by AFRL/PRRS and EOARD. Figure 2 shows the two thrusters. Figure 3 shows a sectioned view of the thruster. It can be seen that the thruster is itself very simple in construction, which leads directly to the low unit cost feature, which was very much the design aim from the beginning. The key science problems solved was in the choice of bed material for heat transfer and material compatibility, high heat transfer to the working fluid at low power, and optimum nozzle size due to friction losses.

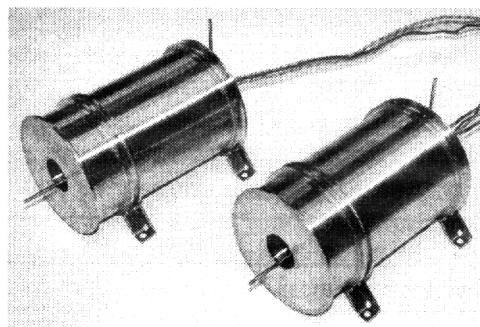


Figure 2: Mark IV standard thrusters

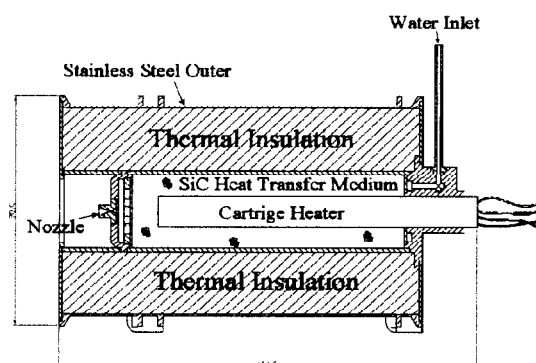


Figure 3: Section view of resistojet

To date two applications have been found for the Mark IV resistojet. The USAF intended to fly

one version on their MightySat II.1 program. The system was designed to operate with water as propellant. For various reasons this system was deselected as a baseline and the spacecraft will fly no propulsion system.

The other application was Surrey's own R&D spacecraft UoSAT-12. This system already had a cold gas nitrogen propulsion system as its baseline. However there was sufficient mass budget available to add an experimental nitrous oxide resistojet system at a late stage of the build program.

Table 2 below details both flight systems: -

Life duration testing using deionized water. From 13th to 30th June 2000 at SSC under ambient conditions. A total lifetime of 423 hours demonstrated with throughput of 29 kg of water. Post testing performance checks did not show any anomalies. The thrust results are shown in Figure 4.

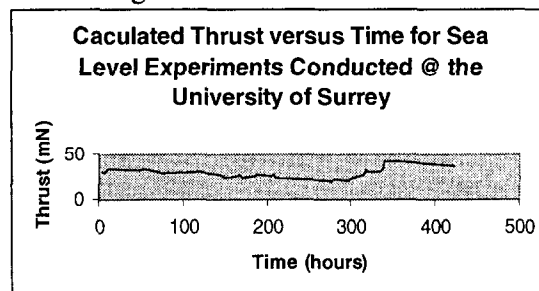


Figure 4. Endurance Test of Mark IV thruster

Item	UoSAT-12 Specifications	MightySat II.1 Specifications
Working fluid	Nitrous Oxide	Water
Chamber pressure	10 bar (~48 bar storage)	5 bar (10 bar inlet)
Mass flow	0.0001 kg/s	0.000066 kg/s
Power	91 W @ 28 V	100 W
Resistojet mass	1.2 kg	1.2 kg
Expulsion system mass	10.75 kg	6 kg
Propellant mass	2.3 kg	1.1 kg
Isp at steady state	127 sec	152 sec
Thrust	125 mN	75 mN
ΔV	~ 9 m/s	16 m/s
Nozzle	0.4 mm throat spark eroded	0.3 mm
Assembly	Electron beam welded	Electron beam welded

Table 2: Mark-IV System Specifications for the UoSAT-12 and MightySATII.1 Missions

MightySat II.1

An Engineering Model (EM) thruster was supplied to the USAF, however a flight unit was not supplied as the program was put on hold. Upon restart an alternative system was selected since the program office decided that MightySATII.1 no longer required a propulsion system. The EM was returned to SSC to allow a life demonstration program to be performed. Vibration testing of the unpowered EM took place on 31st May 200. Sine testing was up to 100 Hz and 15 g, and random vibration at 0.3 g²/hz (19.5 overall grams).

UoSAT-12

UoSAT-12 is a 300 kg experimental minisatellite. It was launched on a Dnepr launch vehicle from Baikonour, Khazakstan in April 1999. A Nitrous Oxide supply system with a Mark IV resistojet was fitted to the spacecraft.

The schematic of the propulsion system is shown below in figure 5. 2.3 kg of Nitrous Oxide was stored in three propellant tanks.

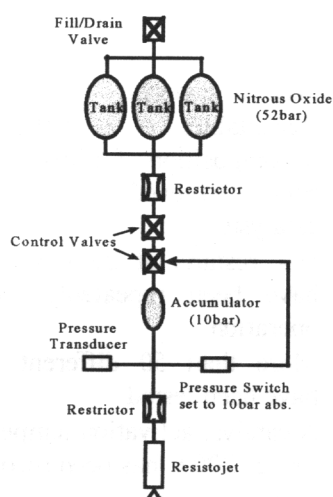


Figure 5: Nitrous Oxide feed system

Nitrous oxide is perfectly suited to this type of system as it is stored as a liquid, under its own vapor pressure of approx. 48 bar at room temperature; hence no pressurization system is required. Tank pressure is regulated to 10 bar using a pressure switch to control a solenoid valve giving a “bang- bang” regulator.

Since the system is designed for 100 W, one hour of continuous power is feasible during specific solar cycles of the orbit.

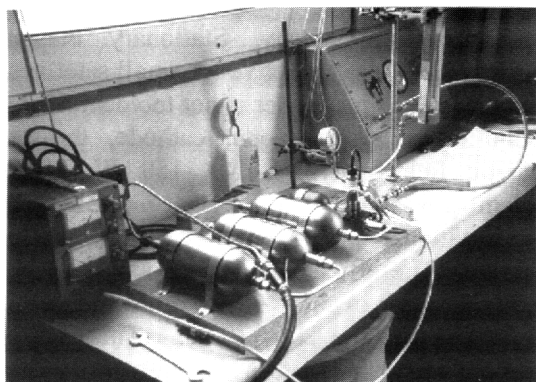


Figure 6: Polyflex Expulsion System

Figure 6 shows the expulsion system fabricated by Polyflex Aerospace Ltd, Cheltenham, UK. The system was shown to be able to support the 7 hour life time at the desired flow rate. Qualification tests were conducted in September 1998 with integration beginning in October of 1998 and were finished in December 1998.

The first on-orbit flight test was conducted on 26th July 1999. The thruster was fired for 15

seconds and produced an Isp of 93 sec, thrust of 95 mN, at a power of 91 W. Unfortunately the thrust vector was not aligned perfectly with the spacecraft C of G (off-set measured to be approximately 2.6 cm). The ADCS subsystem was not set-up for a torque to be generated by this firing and the result was to destabilize the attitude estimator filter, causing the AOCS not to remain nadir pointing. Spacecraft control was quickly regained, however no further firings were undertaken at that time. Investigation showed that the pressure reading saturated at 13 bar (maximum limit) compared to 10 bar which the pressure switch should have controlled to. It was concluded that the commercial grade pressure switch had failed and that the pressure control valve was permanently open. Since there is a viscojet in the system, this restricted the flow somewhat, but recent analysis shows the mass flow has increased from 0.1 to 0.13 g/s.

This phenomenon was confirmed by a longer firing on 11th April 2000. The performance results of this firing are shown in Figure 7. Subsequent to this it was decided to reprogram the control system, such that the pressure control solenoid valve was opened in a predetermined sequence. The valve sequence was programmed to be 100 milli seconds open and 10 seconds closed. On 16th June 2000 this sequence was run with the resistojet switched off (as no power was available). The pressure peaked out at over 10 bar with a saw tooth form giving 1 bar peak to peak. It was decided to reduce the ON time to 50 m sec to obtain a nominal thruster inlet pressure of 5 bar hence reduce the thrust to a level which would give a disturbance torque low enough for the AOCS to still be able to retain control of the spacecraft due to the CG offset. Further hot fire tests are planned for September 2000 when the spacecraft has available power.

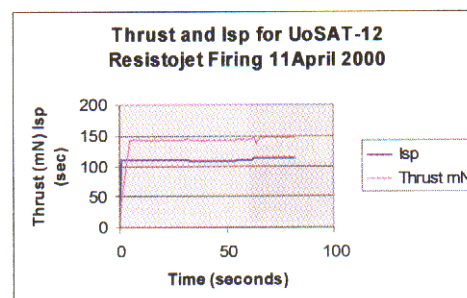


Figure 7: Thrust and Isp for 11 April UoSAt-12 Nitrous Oxide Resistojet Firing

One of the intriguing results that emerged from the Surrey resistojet research program was the exothermic decomposition of nitrous oxide. This was first observed in a resistojet test at Edwards AFB in January 1998. The thruster, similar design to the Mark-IV design described above, was initially heated to 600 C using the power system, and then the electric power was shut off and the system produced a steady state Isp of 148 seconds for 18 hours. The mechanism of this exothermic decomposition was thermal. It was noted that if catalytic decomposition could occur, the subsequent activation energy could be lowered and the reaction started at a lower temperature. This would be very attractive to small satellites since less power would have to be consumed. EOARD started a research program with the University of Surrey to investigate various catalysis in October 1999.

This thruster concept is based upon the catalytic decomposition of nitrous oxide and requires input energy at start-up, but then produces a self-sustaining reaction that runs as a function of the catalyst lifetime. Theoretical performance of the reaction is 206 sec. The University of Surrey has produced a ~ 1 N, 175 sec experimental apparatus that has been tested for 76 minutes continuously using a rhodium based catalyst. A picture of the apparatus is shown in Figure 8. The electrical power input was 24 W for 3 minutes, and then the reaction ran itself for the remaining 73 minutes.

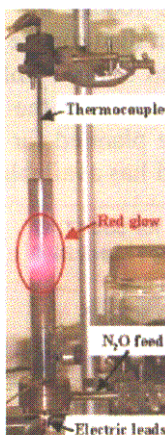


Figure 8: Nitrous Oxide Experimental Apparatus

Besides this accomplishment, the program has also achieved:

- Proof of concept was demonstrated
- Repeatable, self-sustaining, decomposition of nitrous oxide has been achieved using different catalysts
- Hot restarts at zero power input have been repeatedly shown in operation
- More than 50 different catalysts have been tested
- A catalyst activation temperature as low as 200 C has been recorded
- Nitrous oxide mass flow rates above 1.1 g/s have been supported
- Decomposition temperatures in excess of 1500 C have been demonstrated
- Electrical power input as low as 15 W has been used

The University plans on building a prototype thruster for vacuum testing in autumn 00. EOARD will investigate future collaboration in this program. EOARD also plans on co-sponsoring the upcoming ESA Green Propellants Conference in June 2001 at ESTEC.

Stationary Plasma Thrusters

As discussed previously, Stationary Plasma Thrusters (SPT) are attractive for small satellites, as long as their input power is not too demanding for the entire system (ppu, cathode, thruster magnetic field, valve) i.e. < 150 W. The problem is as the SPT's are scaled down from their traditional power of 1 kW, the losses dominate. The efficiencies of the kW thrusters are on the order of 50 – 60 % while the 100 – 150 W thrusters are 20 – 30 %. This loss in efficiency is attributed to a decrease in thruster size, which reduces the path for ionization and requires an increase in the flow density. The lower size also causes a higher magnetic field intensity and requires a different magnetic system.

However after discussions with Design Bureaus in Russia, efficiency is not as important a concern in small satellites. For low input power (~ 100 W), it is more desirable to increase the thrust and lower the Isp and efficiency. These results were obtained in the research programs.

The first effort was with TSNIIMASH Export, Moscow, Russia and was a characterization of the performance of their existing T-27 thruster, operating at lower than design power conditions. They investigated the changes in performance due to variations in thruster power, mass flow rate, and magnetic field strength at powers ranging from 40 – 150 W. Their goal was to increase the ionization efficiency at a lower mass flow density and voltage. They deduced that the losses were too high even with these changes, and a new thruster had to be developed if a power < 100 W is needed. However the physics of small hall thruster operation were produced with an understanding of the important variables from this study. A picture of the T-27 is shown in Figure 9.

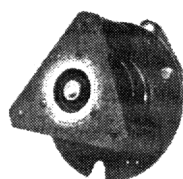


Figure 9: TSNIIMASH T-27 thruster

Fakel Design Bureau, Kaliningrad, Russia developed a new thruster to operate for the under 100 W power level. This thruster was a modification of the T-20 thruster that had been produced before, optimized for this power level and also required the development of a “heaterless” hollow cathode that could operate up to 1000 hours of operation. The thruster is shown in Figure 10 and produced the following results in 9 hours of tests at Kaliningrad:

Power: 94.5 W

Thrust: 4.7mN

Isp: 1000 sec

$\eta = 24\%$ (includes cathode and other “system” power)

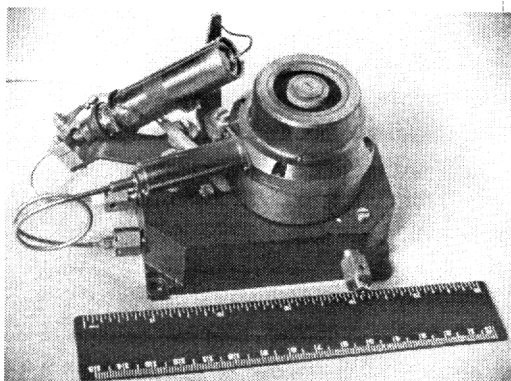


Figure 10: Fakel 100 W Thruster

This thruster has been delivered to Edwards AFB where it will undergo testing at the AFRL Electric Propulsion Laboratory to characterize its performance and estimate lifetime. Results of both of these programs will be published as EOARD reports through DTIC. Future work is also planned with Fakel in continuing the low power investigation.

EOARD is also working in SPT modeling research. Work has started with the University of Madrid to investigate 1 D modeling of the thruster plume. The University of ROMA is investigating the performance impacts of using superconductors on high power SPT's.

Future work is planned with Tsniimash to investigate the clustering of D-55 thrusters. Three thrusters will be fired continuously with different geometry locations and cathode placement. The plumes and power systems will be monitored to study the impact of “cross talk”. The application of clustered thrusters and resultant modeling could enable future high powered SPT systems to be designed in modules.

Conclusion

This paper has shown some of the work sponsored by EOARD in small satellite propulsion. EOARD's mission is to directly support AFRL research goals by:

- Providing liaison with members of the European scientific community.
- Facilitating contact between AF scientists and their European counterparts.
- Contracting with European scientists to conduct research or support conferences and workshops

This basic research work will have an impact in helping to decide future propulsion systems for USAF, university, and commercial small satellite missions.

Acknowledgements

The author would like to acknowledge the following individuals: Daron Bromaghim, Ron

Spores, Capt Jason LeDuc, Greg Spanjers, Mike Fife and Capt Rich Salasovich of the AFRL Electric Propulsion Laboratory; Dave Gibbon, Vadim Zakirov, Malcolm Paul, and Gary Haag of the University of Surrey; Randy Kahn, Capt Mike Rice, and Capt Rich Neufang of the MightySat Program Office; Pete Thomas and Robert Davis of the Aerospace Corporation; all of the MightySat team at Spectrum Astro; John Fumo and Bruce Moore of Trisys, Inc.; Royal Ordnance Wescott UK; Dr Ron Humble of the United States Air Force Academy; John Blandino of the Jet Propulsion Laboratory; Dr Boris Arhkipov and Vladimir Kim of Fakel Design Bureau, Kaliningrad, Russia; Alexander S. and Sergei T. of Tsniimash Design Bureau, Moscow, Russia; and Polyflex UK.

low cost Resistojet", 36th Joint Propulsion Conference, Huntsville, Alabama.

7. Spanjers, G., Birkan, M., and Lawrence, T. "The USAF Electric Propulsion Research Program", 36th Joint Propulsion Conference, Huntsville, Alabama.
8. Zakirov, V., Sweeting, M., Lawrence T., and Sellers, J. "Nitrous Oxide as a Rocket Propellant", IAF Conference, Oct 2000, Rio, Brazil.

References

1. Lawrence T.J., "Research into Water Resistojets for Small Satellite Application", MPhil. /Ph.D. Transfer Report, Department of Electrical Engineering, CSER, University of Surrey, Guildford UK, Sep 1996.
2. Lawrence, T., Sweeting, M., Paul, Drum, J., Humble, R., and Sellers, J. "Results of Cold Gas and Resistojet Research for Small Satellite Application", 11th Annual AIAA/USU Small Satellite Conference, Logan, Utah, September 1997.
3. M.N.Sweeting, T.Lawrence, J.Leduc. "Low-cost Orbit Manoeuvres for Minisatellites using novel Resistojet Thrusters", Proceedings of Institution of Mechanical Engineers, Volume 213, part G.
4. Lawrence, T. "Research into Resistojet Rockets for Small Satellite Applications", Ph.D. Thesis, Department of Electrical Engineering, CSER, University of Surrey, Guildford, UK June, 1998.
5. LeDuc, J.R., et. al. (1997), "Mission Planning, Hardware Development, and Ground Testing for the Pulsed Plasma Thruster (PPT) Flight Demonstration on MightySat II.1", 33rd Joint Propulsion Conference, Seattle, WA. AIAA 97-2779
6. Gibbon D., Lawrence, T. "The Design, Development and In-flight qualification of a

An Innovative Approach to Satellite Technology

Joseph F. Janni, Yolanda Jones King and Gerald Witt

Air Force Research Laboratory
Air Force Office of Scientific Research
801 N. Randolph Street, #732
Arlington, VA 22203-1977 USA

Introduction: Innovation and rapid prototyping using advanced technologies are the hallmarks of new initiatives coming from the USAF Research Laboratory's Office of Scientific Research (AFOSR).

University Nanosatellite Program. AFOSR, in conjunction with DARPA, is sponsoring ten universities, formed into small teams and challenged with paving the way to novel space capabilities. The satellites leverage innovative thinking within our universities, leading to flight experiments of state-of-the-art technologies and advanced mission concepts. Experiments range from micro-propulsion to formation flying. These miniaturized satellites will be prototyped and launched. We describe the philosophy, approach, and results to date of the program.

TechSat21 Program. Recent progress in the miniaturization of key satellite technologies enables innovative solutions for space missions. AFOSR, in conjunction with AFRL's Space Vehicles Directorate, has developed the TechSat 21 program. This low-cost, lightweight cluster of cooperating microsatellites may eventually replace today's heavy and more expensive systems. Each microsatellite will communicate with other members of the cluster to share information and mission functions, thus comprising a "virtual" satellite. TechSat 21 offers the flexibility to incorporate cutting edge technology in a reconfigurable constellation. This unusual approach offers multi-mission capability as well as a reduced life cycle cost. It is envisioned that new technology may be inserted by replacing members of the cluster with enhanced versions. Research and technology investments include sparse aperture sensing, local communications in space and microsatellite bus technologies. The investment in innovative basic research areas to make TechSat 21 a viable alternative as well as the overall program approach will be covered. Many of the techniques and technologies being demonstrated in the University Satellite program have application to the TechSat21 program.

University Nanosatellite Program Summary: The Air Force Office of Scientific Research (AFOSR) and the Defense Advanced Research Projects Agency (DARPA) are jointly issuing research grants centered on the design and flight experiments of nanosatellites. (Satellites sized 1 - 10 kg). These grants over two years have been awarded for universities to design, assemble, and conduct on-orbit experiments for these satellites. Universities are to pursue creative low-cost space experiments to explore the military usefulness of nanosatellites in such areas as formation flying,

enhanced communications, miniaturized sensors, attitude control, and maneuvering.

The Air Force Research Laboratory is developing a deployment structure, integrating the nanosatellites, securing a launch, and providing such advanced microsatellite hardware as high efficiency solar cells and micropropulsion. NASA Goddard has also teamed with the universities to provide funding to demonstrate such formation flying technologies as advanced crosslink communication and navigation hardware and flight control algorithms. Numerous industry partners are also supporting the universities with hardware and providing design and testing services. Information on the program and presentations from the kick-off meeting can be seen at the website, <http://www.nanosat.usu.edu/>.

The universities selected for the program are: Arizona State University, University of Colorado at Boulder, and New Mexico State University (Three Corner Sat); Stanford University and Santa Clara University (Emerald); Boston University (Constellation Pathfinder); Carnegie Mellon University (Solar Blade Nanosat); Utah State University (USUSat); Virginia Polytechnic Institute and State University (VTISMM); University of Washington (UW Nanosat). Descriptions of their satellite programs follow.

Three Corner Sat Constellation (3 Δ Sat): This project is a joint effort among Arizona State University (ASU), University of Colorado at Boulder (CU), and New Mexico State University (NMSU). Aptly named Three Corner Sat (3 Δ Sat), the proposed constellation of three identical nanosatellites will demonstrate stereo imaging, formation flying/cellular-phone communications, and innovative command and data handling. In addition, each University in the 3 Δ Sat constellation has the opportunity to fly an individual unique payload should it desire.

The primary science objective of the 3 Δ Sat constellation is to stereo image small (< 100 meter), highly dynamic (< 1 minute) scenes including deep convective towers, atmospheric waves, and sand/dust storms. These stereo images will enable the computation of range to within 100 meters giving accurate data regarding the shape, thickness and height of the observed phenomena.

Stereo imaging from space has several advantages over conventional imaging, the most obvious being the ability to derive range data. This range data can be substantially more accurate than range data acquired by other more usual means and also can cover a much

greater area. Stereo imaging involves correspondence matching between an image pair and calculation of the resulting disparity. From the disparity, triangulation can be used to determine range data, and three-dimensional images and depth maps can be created. Accurate depth maps with range resolutions of about 100 meters enable the study of relatively small-scale, short-lived atmospheric events such as cumulus-cloud towers.

To accomplish the science objectives, a "virtual formation" is proposed as part of this program. The virtual formation is a cooperative effort between satellites operating as a network where targeting and data acquisition are accomplished and results transmitted to the ground segment and to the other satellites via communications links without the need for strict physical proximity of the satellites. In this mode, the communications links carry the command and control data necessary to accomplish the mission regardless of the physical location of the satellites. For the mission to be accomplished, the locations of the satellites will need to be "in range" and mutually known in order for each to support its portion of the mission, but physical proximity is not a requirement for the formation network.

For stereo imaging, a nominal spacing of tens of kilometers between the satellites is required. With a controlled deployment to achieve this initial spacing, the satellites will remain within range for the suggested four-month lifetime of the mission. Therefore propulsive capability is not needed.

LEO satellites utilizing cellular telephone constellations is a new concept but one in which there is considerable interest in the government and private-sector space communities. This natural extension to the use of ground-based systems will be explored not only to

demonstrate the utility of this mode of communications but also to act as an experiment to characterize the constellation itself and the limits on the operations. A technology goal of 3^ASat is to perform the first steps in this characterization.

The 3^ASat constellation will consist of three satellites flying in a linear follow-formation with relatively constant separation from each other. The separation distance selected is based on altitude and camera field of view (FOV), with final determination based on the chosen launch vehicle. The mounting configuration within the launch vehicle will depend upon the launch vehicle and other satellites selected. The satellite will use gravity-gradient (GG) forces for stabilization with ± 5 degrees pointing accuracy.

All satellites will be identical, except for a standard payload envelope where each university will have the option to fly its own unique experiment after the primary science objective has been met. The spacecraft structure will be low-cost and reliable. The exterior envelope of the structure is a six-sided disk structure consisting of tubular supports and machined end caps to hold the bulk of the loading (Figure 1). The design will feature a number of modular, removable trays, allowing for on-the-spot modifications without extra machining or irreversible processes.

EMERALD: Stanford University and Santa Clara University are jointly developing EMERALD, a low SSDL (Space Systems Development Lab) and Santa Clara University's SCREEM (Santa Clara Remote Extreme Environment Mechanisms Laboratory) are working as a unified team to develop, construct, test and eventually operate the EMERALD spacecraft. The formation flying experiments will be coordinated through Stanford's ARL (Aerospace Robotics Lab).

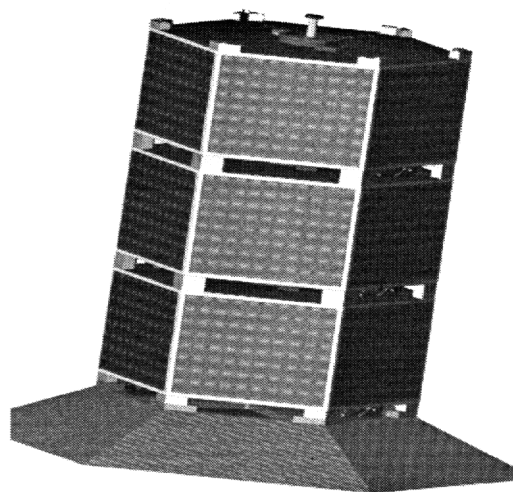


Figure 1. Spacecraft Overview

The Emerald Mission is divided into three distinct stages, that progress from a simple single satellite to two free flying satellites in a coarse formation. Using a building block experimental strategy, the research payloads first will be characterized in isolation. Then, they will be coordinated and combined to permit simple demonstrations of fundamental formation flying control functions such as relative position determination and position control.

At release, the two spacecraft will be stacked together and will travel as a single object. This will allow initial checkout, calibration, and some limited experimentation.

During the second stage of operation, the satellites will separate and a simple tether or flexible boom will uncoil, linking the two vehicles. This tethered stage will allow full formation flying experimentation including on-orbit relative position determination and simple closed loop relative position control using the drag panels and micro-thrusters.

During the final stage of operation, the tether will be cut in order to permit true two-body formation flying for a limited period of time. The tether will have a simple sub-satellite at its midpoint. Upon ground command, the two halves of the sub-satellite will separate. Each satellite will retain half of the tether and half of the sub-satellite, providing very rough gravity gradient stabilization.

The two EMERALD spacecraft will demonstrate several critical technologies for future formation flying missions: GPS-based positioning, Inter-satellite communication, advanced colloid micro-thrusters, and passive position control devices. In addition to these

mission critical payloads, Emerald will support a couple of auxiliary payloads: VLF receivers and the MicroElectronics Radiation In-flight Testbed.

These experiments will be built into a 12-inch tall, 18-inch diameter hexagonal bus adapted from heritage designs at SSDL. The structure employs a modular, stackable tray structure made of aluminum honeycomb. Inside, command and data handling is provided by a Motorola 68332-based processor built into a student developed radiation tolerant architecture. Ground communication will be handled by a 9.6 kbs packet communications system. The heritage power system consists of body mounted Silicon cell solar panels and a single Ni-Cad battery. This system will provide 7 Watts of average power to components via a 5V regulated bus.

Constellation Pathfinder: This program between Boston University and Draper Lab will demonstrate fabricate and launch one to three, <1 kg satellites that are capable of collecting and returning quality scientific and engineering data for one to four or more months. The particular satellite to be used is based on one developed over the past two years through a NASA-supported study called the Magnetospheric Mapping Mission (MMM) at Boston University. That study objective has been to assess the feasibility of placing hundreds of satellites equipped with magnetometers, into orbits extending into the tail of the magnetosphere, thereby obtaining a much more detailed three-dimensional picture of dynamic phenomena in geospace than has been possible previously. The Constellation Pathfinder proposal will take the first pathfinding step toward such an ultimate implementation. A proposed simplification of the current conceptual design is that the launch mechanism is provided by the Shuttle

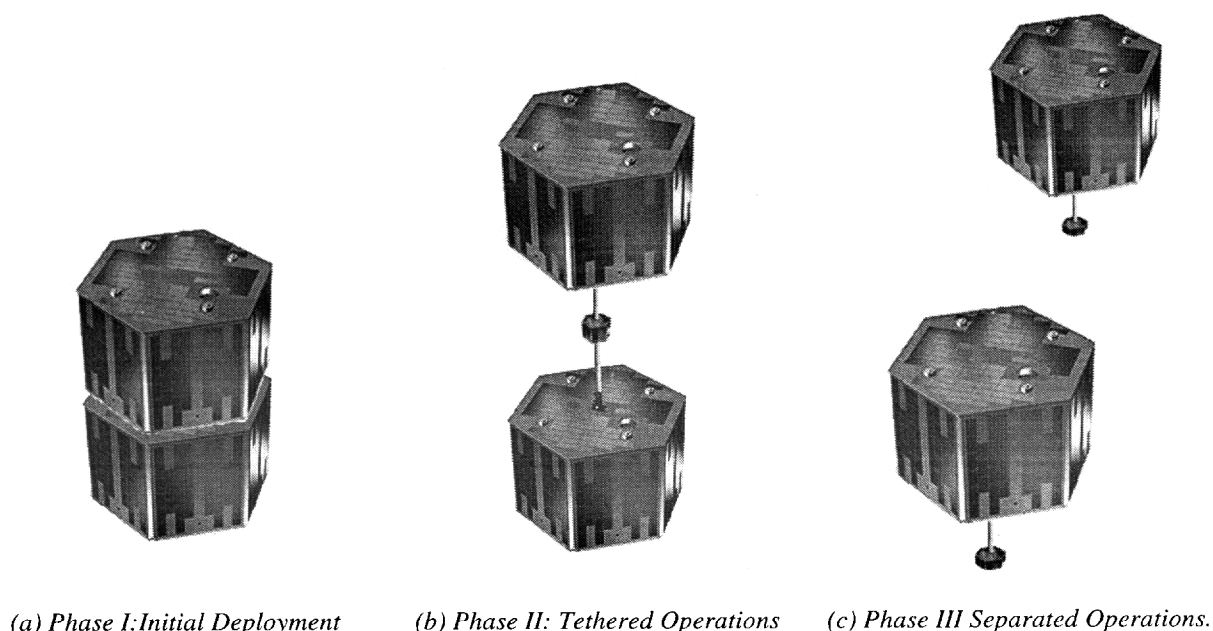
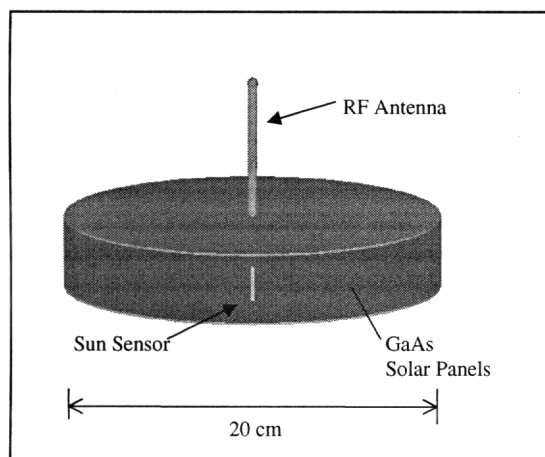


Figure 2: Mission Sequence

Hitchhiker. The magnetometer will be measuring larger (and therefore easier to measure) fields in the Earth's ionosphere, the lower altitude reduces RF communication requirements as does relaxation of the required data transmission rate, and the natural radiation environment will be much lower. The hardware demonstration of building and flying such a satellite, or small suite of satellites, will provide a proof of principle that will be helpful in many scientific and strategic applications where a fleet of coordinated small satellites is required. Satellite-to-satellite communication may also be accomplished.

The nanosatellite configuration is shown below. The outer cylindrical surface consists of power-providing GaAs solar cells. The RF antenna is along the axis of the cylinder. Satellite spin will maintain the orientation of both the antenna and the solar cells within 10 or 20 degrees of the ecliptic plane assuming that one can select the shuttle orientation at the time of release to be in this range. The satellite electronics including batteries will be concentrated in the center. The magnetometer location is chosen to minimize contamination by spacecraft magnetic fields and will be located within the cylindrical volume. The sun sensor looks radially outward and will be used to determine the phase of rotation. Additionally in conjunction with the magnetometer it will determine the direction of the spin axis.



Solar Blade Heliogyro Nanosatellite: Solar sail concepts have existed for decades, but their implementation has been elusive, and none have flown. The primary difficulty has been the need for great surface area relative to mass. Traditional spacecraft designs with hundreds of kilograms of mass led to rationalize, build, and fly. Nanosat technology drastically reduces mass and makes heliogyro design eminently practical and flyable.

Carnegie Mellon will develop and fly the first solar sail, a spacecraft which utilizes solar radiation pressure as its only means of propulsion and attitude control. The solar pressure will enable altitude changes, attitude precession, spin rate changes and orbital position changes.

The Solar Blade Heliogyro Nanosatellite has the appearance of a Dutch windmill and employs control akin to a helicopter. Four solar reflecting blades mount radially from a central spacecraft bus and actuate along their radial axis. The satellite uses collective and cyclic pitch of these solar blades relative to the sun's rays to control its attitude and thrust. The spacecraft weighs less than 5 kilograms, and, when stowed, is a package approximately the size of a fire extinguisher.

This satellite experiment includes attitude precession, spin rate management, and orbital adjustments, after which it will spiral out past the orbit of the moon. For the Solar Blade Nanosat, plane change maneuvers will be most efficient when the sun is furthest out of the orbit plane. This increases the magnitude of the orbit-normal component of force that can be used for the plane change maneuver. Plane change maneuvers can also be conducted if the sun lies in the orbit plane by orienting the solar blades at an angle relative to the orbit plane, optimally 45°. Unlike eccentricity changes, which can be implemented throughout the orbit using a single solar blade orientation, plane change maneuvers must change polarity on opposite ends of the axis of plane rotation. This is not possible unless the sun is in the plane of the orbit (the solar blades cannot produce a positive orbit normal force if the sun is above the orbit plane). Therefore, in most situations, plane change maneuvers will be conducted over an orbital arc on one side of the orbit near the axis of desired orbit rotation. In addition to attitude and orbital maneuvering, the ultra-light spacecraft will communicate with the Earth, uplinking commands and relaying orbital and attitude information to ground stations.

Solar cells embedded on the flanges of the C-beam frame provide up to 28 Watts of power. The spacecraft computer, communication system, and station-keeping sensors at the center of the square connect to the frame through thin lenticular beams. Wiring between the solar cells and the other subsystems consists of thin-film flexible printed circuits.

USUSat: This project will be built at Utah State University supported by faculty, professional engineers, and through the use of existing space engineering curriculum in both the Mechanical and Aerospace Department and the Electrical and Computer Engineering Department.

The USUSat program has four technology goals or science objectives: 1) Develop a 3-axis attitude controlled nanosatellite. The limited power available on a nanosatellite poses a challenge for 3-axis attitude control. This challenge will be met with an all magnetic torquer system where permanent magnets on stepper motors are used instead of traditional torquer coils. The attitude determination will be achieved by a combination of Earth horizon and sun sensors, giving three axis control to approximately two to three degrees; 2) Demonstrate that coarse orbital control maneuvers can be achieved by using the spacecraft's attitude to control the aerodynamic force vector on the spacecraft. In effect, the attitude control system acts to modulate the

aerodynamic drag to change orbital position; 3) Modulate the aerodynamic drag to fly as a formation with the nanosatellites being developed by University of Washington and Virginia Tech. The primary objective is to demonstrate that drag modulation can be used for relative in-track station keeping; 4) Make the first multi-satellite electron density measurements of the Earth's ionosphere using USUSat and the nanosatellites being developed by University of Washington and Virginia Tech. Each of the nanosatellites will carry a probe for measuring electron density built or designed by Utah State University. The multi point measurements of a constellation provides additional information required to answer questions about ionospheric density disturbances that can not be addressed by single satellite measurements.

The entire spacecraft will be covered with solar cells, with the exception of the areas designated for the possible plasma thruster systems. This design requires no deployable structures. The combined sun and horizon sensors will extend from the body in small pods, while the antenna is expanded to be either a 1/8th dipole or a set of patch antennas. The structure is hexagonal with an approximate width of 18 inches and height of 5 inches. This configuration can be modified as needed to meet the specific launch environment conditions. The power subsystem will be a typical solar cell/battery design. Unused solar cells from a GPS satellite solar panel will be individually tested and reassembled into the solar panels for USUSat. The power regulation electronics will make use of components developed commercially for portable laptop computers. The telemetry system will be a low-cost S-Band system developed at USU and includes all components from antennas to encoders. A 14-foot tracking antenna at USU will be used for the ground control station.

University of Washington Nanosatellite: The University of Washington will design, develop, and operate a nanosatellite, focusing on mission objectives that would benefit TechSat21 and future Air Force missions. The UW has partnerships established with Utah State University (design, science, research), Primex Aerospace Corporation (design, coop students), Honeywell Space Systems (design, research, coop students).

The program objectives and descriptions for the UW nanosatellite are as follows:

1) Basic research mission of investigating global ionospheric effects which affect the performance of space based radars, and other distributed satellite measurements.

The science objective is to understand ionospheric density structures that can impose large amplitude and phase fluctuations on radio waves passing through the ionosphere. This study contributes to TechSat21 basic research mission of investigating global ionospheric effects that affect performance of space based radars, as well as broader Air Force interests in navigation and communication links.

The satellite instruments (most likely plasma frequency probes) will determine the global distribution of plasma structure in both the quiet and disturbed ionosphere. The UW will fly the same instrument as Utah State. These instruments will be extremely useful for a number of interesting targets:

a) F region irregularities, especially at the equator, but also at mid latitudes. Several probes with km-scale spacing permit a superb sequence of "space-like" traces.

b) With high latitude field aligned structures, the satellites will on occasion pass through auroral arcs. The formation of satellites should provide superb space-like snap shots of density through the arcs.

In the latter case, the UW will operate a 100 MHz radar to detect these irregularities from the ground, and permit simultaneous calibration of the transmitter, as well as fluctuations in phase associated with irregularities associated with hundred meter structures on an integrated path.

2) Formation flying and local communication in a constellation, including upgrade of a nanosatellite into a constellation already flying in formation.

The need for small, low cost satellites that can fly in formation and perform collaborative mission objectives is becoming increasingly important. Future applications include surveillance (Space Based Radar), earth science and mapping (ionosphere and magnetosphere), astrophysics (stellar interferometry, and communications (laser). In addition, formation flying, on-orbit maintenance and communications, and other distributed satellite capability are enabling technologies to be demonstrated in TechSat21. The UW will use the USU nanosatellite to examine local communications between satellites, leader-follower demonstrations, and decommission and/or upgrade demonstration.

3) Baseline potential new technologies including microthrusters, miniaturized solar arrays, a thin-film polymer modulator for an optical communication link, or satellite autonomy.

Two versions of microthrusters are currently in conceptual phases. Primex is researching a number of options in the micro-Newton range, and will fly a prototype if available during the design of the UW nanosatellite. These include micro pulsed plasma thrusters, and micro-hydrazine thrusters. The launch choice will obviously affect this decision, as will the maturity of the technology. The UW and Primex are committed, however, to flying a prototype microthruster.

Dr. Larry Dalton of the UW is exploring the development of thin-film polymer modulators for optical communication links (good up to at least 200 GHz). Polymer materials have become increasingly important for electro-optic devices because of their low dispersion and fast electronic response. These modulators are unique in that they are low weight (plastic), low power (less than 1 W), and capable of beam steering and forming. The technology will not be

used for the communications subsystem, but simply as a low cost technology demonstration between nanosatellites.

VTISMM: The Virginia Tech Ionospheric Scintillation Measurement Mission (VTISMM) is a multiple spacecraft design, build, and fly space project. It comprises two small satellites flying in close proximity, using a GPS receiver for position determination, microsensors for attitude determination, interlink communications for data transmission and relative position determination, and GlobalStar for telemetry, tracking, and commanding. Additionally, VTISMM uses an amateur space-to-ground link as an alternative to the GlobalStar communications link; this space-to-ground link takes advantage of Virginia Tech's Satellite Tracking Laboratory, which is used in teaching undergraduate astrodynamics and space systems courses. The VTISMM science mission focuses on collecting and analyzing GPS data to characterize ionospheric scintillation effects on the communications signals.

The VTISMM system will be designed, built, and operated by undergraduate students in Aerospace Engineering and Electrical Engineering, using existing facilities. Undergraduates are participating in the project through capstone design courses and special project technical electives supervised by the principal investigators. The principal investigators have active research programs involving key aspects of the VTISMM concept, including flight dynamics, space system design, satellite communications, computer systems, power systems, and the effects of ionospheric irregularities on communications signals. These research projects are funded by the National Science Foundation, NASA, AFOSR, and industry.

The VTISMM system is in the preliminary design phase, with a team of juniors and seniors from aerospace, electrical, and computer engineering working towards a formal preliminary design review in May 1999. The two satellites, called Sulu and Uhura, have a common bus design for simplicity, but have different payloads. Sulu (the navigator) has a GPS receiver for its payload, and Uhura (the communicator) has a GlobalStar communications set for its payload. Both spacecraft buses include a flight computer, intersatellite communications, and attitude sensors. One (possibly both) spacecraft also includes an amateur band communications system as an alternative to the GlobalStar communications link. This link communicates with the existing satellite tracking station at Virginia Tech, using amateur satellite frequencies, or other frequencies as appropriate. Uhura also includes a small digital camera.

TechSat 21 Project Description: TechSat-21 consists of a cluster of small satellites that orbit in formation to create a distributed aperture. This cluster of satellites forms a "virtual satellite" which performs radar functions that typically require a large heavy antenna. The distributed aperture provides high angular

resolution that offsets the disadvantage of large clutter spread arising from each satellite's small aperture. By providing highly accurate angular information, the ambiguity in Doppler between "stationary" ground clutter and moving targets can be resolved. The additional angular resolution is enabling for multi-mission modes of operation, dramatically increasing military value and utility. Furthermore, having many satellites in the cluster offsets the small signal to noise ratio of each satellite. This approach can be cost effective due to economies of scale (large production runs of small satellites), the adaptability of the system, the capability to reduce launch costs by using smaller launchers and rides of opportunity (piggyback other missions), and its inherent robustness. This approach leverages space industry investments in large constellations of small communications satellites (e.g. Iridium, Teledesic).

TechSat -21 is inherently robust to on-orbit failures since the loss of a single satellite in a cluster will cause only a small decrease in performance. It enables line replaceable unit maintenance for the virtual satellite by replacing/adding satellites to the cluster. Constellation performance upgrades (similar to aircraft block changes) are possible by adding new satellites to the cluster with better individual performance to improve the virtual satellite performance.

A combined AFOSR basic research and AFRL applied research program is underway to develop the scientific and technology basis for this concept. Initial analysis has shown the technical and scientific feasibility. The follow-on research program will refine and expand the scientific and technical knowledge base to enable demonstration of this concept.

TechSat -21 is a revolutionary approach to space based surveillance. It replaces a single large (and very expensive) satellite with a cluster of smaller satellites flying in formation. However, since each satellite has sufficient autonomy and collaborates effectively with the other satellites in the cluster, the cluster appears to be a single satellite or a virtual satellite from the point of view of the operator or user. Thus, the infrastructure for command and control of the TechSat -21 constellation is no different from an equivalent constellation of larger satellites.

A summary of the technologies of importance to TechSat -21 follows. AFRL/VS and AFOSR are investing in research projects in most of the less mature areas.

1) Antenna: Two-dimensional steerable (60° each axis) X-band phased array antenna, less than 4 kg/m^2 (current systems are typically 20 kg/m^2). Moderate bandwidth requirements of approximately 300 MHz.

2) Thin film solar array: Lightweight thin film photovoltaics that can yield solar arrays of greater than 200 W/kg and less than $\$100/\text{W}$. This improves weight and cost by a factor of four over conventional planar,

crystalline photovoltaic systems. Requires advances in thin film cell efficiency from approximately 7% to 14% (air mass zero).

3) DC/DC converters: 90% efficiency at 500 W/kg.

4) Parallel computers: Low mass, low power, high speed digital signal processors for parallel computation application. Need greater than 200 MFLOPs/W and greater than 5000 MFLOPs/kg. This represents an order of magnitude improvement over current technology.

5) Distributed radar phenomenology: Algorithms and techniques for processing sparse aperture data to produce radar images and detect moving targets are needed. STAP techniques appear useable, but require significant engineering to adapt to sparse aperture systems and to implement efficiently in a parallel environment. Other more optimal techniques from interferometry or information theory may improve performance or reduce the processing and data storage requirements.

6) Ionospheric effects: The spatial inhomogeneity of the ionosphere on the scale of this large aperture may affect radar operation. Models and measurements of the ionospheric structure and predictive tools for their effects need to be developed.

7) Micro pulsed plasma thrusters: Small impulse bit propulsion is required to maintain the geometry of the satellite cluster. The most promising propulsion technology is pulsed plasma thrusters because the fuel is solid and non-volatile (easing integration of the propulsion system since there are no fuel lines, valves, or tanks), it has good specific impulse, and it can be throttled. Miniature thruster devices are required to reduce weight by taking advantage of the small impulse requirements.

8) Multi-functional structure: Highly integrated electronics packaging and mass-producible lightweight interconnects and harnesses are required to achieve significant cost and weight reductions. Techniques for providing adequate thermal dissipation and mechanical support are required. The radiation shielding lost by eliminating massive boxes, harnesses, and connectors must be supplemented by integrating spot shielding, radiation shielding composite structures, and increased radiation hardness of parts.

9) Lightweight star sensor: Low cost, lightweight (less than 1 kg), moderate accuracy star sensors are required. Pointing accuracy of 0.02° and a field of view of at least 30° are required. Autonomous star acquisition is desired to minimize additional sensor requirements.

10) Inflatable boom: Highly packageable, deployable structures will greatly reduce the stowed volume of the satellite, allowing more effective packaging on existing launch vehicles. Lightweight booms capable of over 200:1 compaction ratios with deployed stiffness of greater than 1 Hz are needed to deploy the solar arrays and gravity gradient boom.

11) Lithium ion battery: High energy density and low cost are the key technology drivers. Specific energy densities of over 100 Whr/kg for 6 to 8 Amp-hr cells are required. Desired depth of discharge for 15 year LEO cycle life is 30%. Batteries that allow production in arbitrary shapes and form factors are desirable to provide compact satellite geometries.

12) Variable emissivity coatings: Electrochromic materials are required to permit voltage modulated control of infrared emissivity or solar absorptivity (from 0.2 to 0.8) in the 3 to 25 micrometer spectral band. Low power actuation of less than 0.2 W/m^2 at less than 5 VDC for full switching. Long life in a space environment is required, including multi-level stability, insensitivity to static charge, and greater than 15 year life.

13) Formation flying control: Techniques are required for autonomous and collaborative control of the satellite cluster for the life of the mission. Satellites must maintain a specified geometry within 10s of meters over separations of 100s of meters, manage cluster resources, perform collision avoidance, and permit cluster reconfiguration.

14) Satellite LAN communications: Inter-satellite communications is required for a dense network of satellites (up to 16 satellites per cluster) at high data rates (on the order of 100 Mbps). Multicast, CDMA, TDMA, FDMA, and other techniques are required for short haul space communications. Protocols that permit high throughput and low data latency are required. Miniature space quality LAN communications hardware will be required.

15) Relative navigation: Techniques and devices are required to provide relative three dimensional position knowledge of the satellites to within 1 cm. These approaches must be adaptable to variable numbers of satellites in the cluster, be space qualified, work in near real time (latency and update times consistent with the orbital drift of satellites out of the cluster formation), and be amenable to lightweight, low cost hardware solutions.

Summary: It is clear that the spacecraft of the future will have to be more affordable and innovative. The Air Force Office of Scientific Research has made significant investments in the basic research methods and space technologies required to enable the future space architects through our university programs. The combined efforts of the Air Force Research Laboratory through the TechSat 21 program will bring a more capable and more cost effective space system to reality. AFOSR is dedicated to the furthering of breakthrough technologies to benefit the US and its allies.

Acknowledgements: The authors thank the entire teams of the University Nanosatellite Program and the TechSat 21 Project for their contributions to this effort and to the paper. Special thanks to Mr. John Garnham at AFRL-Kirtland for his design and analysis supporting the TechSat 21 demonstration.

THE PRODUCTION OF CONTAMINATION ON SPACECRAFT SURFACES BY HYPERVELOCITY DEBRIS IMPACTS

Charles STEIN, Robert ROYBAL and Pawel TLOMAK

*Air Force Research Laboratory, Space Vehicles Directorate,
2050 Chanute Street, Kirtland AFB, NM, 87117-6008, USA*

Telephone: +1-505-846-4822; FAX: +1-505-846-7345; email charles.stein@kirtland.af.mil

ABSTRACT. *A study of the mechanical damage and the contamination produced by hypervelocity debris impacts on spacecraft was conducted in a space chamber capable of accelerating debris simulating particles to 7.5km/sec and other components of the Low Earth Orbit environment. Damage characteristics and the nature and extent of contamination generated by the impact of 3mm diameter, 3 micron thick aluminum particles, accelerated to 4.5 km/s, were investigated. Scanning electron microscopy, optical microscopy, and spectrophotometry were used to measure the mechanical damage and the loss of transmission through solar photovoltaic cover glass materials.*

1. INTRODUCTION

Spacecraft placed in low-Earth orbit (LEO) are exposed to a large flux of hypervelocity impacts by small particles which originate from micro-meteorites and man generated debris^{1,2,3}. At risk are multiple satellite constellation systems and proposed large inflatable space structures. Many of these satellite systems, which are primarily used for communications, will be placed in low earth, nearly polar, orbits. The amount of damage experienced by space based assets in LEO from hypervelocity debris impacts can be extensive and can decrease the performance levels of subsystems below critical specifications. In LEO, the particle flux existing in circular orbits at altitudes near 500 kilometers⁴ can be, for 1 cm size pieces, as low as 1 hit /m²/100,000 yr., while it can vary between 10 and 100 hits /m²/yr for particles of about 0.1 mm. The damage generated by debris particle impacts on solid materials can be grouped into three distinct phenomena: a) mechanical property changes due to cratering (which is often many times larger in diameter than the particle itself) and surface damage produced by direct hits; b) internal and back surface spallation of

materials resulting from the shock wave produced by the hypervelocity impact; and c) molecular contamination generated by hypervelocity debris particles which arises from the vaporization of the particle itself as well as that of the material struck. Particles traveling at hypervelocities generate temperatures in the range of 5,000K and pressures of several megabars when they strike a surface. Consequently, one would not expect that the constituents of the vapor produced by the impact would be the same as those produced under ambient conditions and that fragmentation of the contaminant may not proceed by the Rice-Herzfeld mechanism.

This paper presents results on research carried out to study the production of debris generated contamination on the surface of thin, large area, solar cell cover glass materials and the degradation of their optical transmission. Large area solar cell arrays are desirable because they reduce the cost and complexity of this subsystem, but are viable only if the toughness of the cover glass can be increased so that they can withstand the rigors of ground handling and launch and deployment stresses.

2. EXPERIMENTAL

The technique used in this work to accelerate the debris particles is a laser driven method which has been described by Roybal et al, elsewhere⁵. The method used to fabricate the metal-to-glass laminate to create the debris particle is critical to produce the acceleration desired. In the method which we have developed, a metal foil of the desired thickness for the debris particle, is tenaciously bonded to a glass substrate by atomic diffusion of the metal into the glass. Both elevated temperature and a DC voltage are applied across the laminate to produce a very tenacious bond.

The metal foil is vaporize by a laser beam focused at the glass/metal interface. The vapor pressure thus produced reaches levels in the giga Pascal range which cuts out and accelerates a metal disk the diameter of

the periphery of the laser beam. Velocities from 4.5 to 7.5 km/s have been achieved by the authors. This compact method is suitable for impacting targets at hypervelocities in a space environmental effects chamber which has the additional capability of exposing samples, simultaneously, to energetic electrons, ultraviolet radiation and atomic oxygen. In this work, impact testing was carried out on solar cell cover glasses using flat aluminum debris particles, 3mm in diameter and 3 microns thick. The cover glass targets, which were 40mm by 40mm in size, consisted of two thin glass sheets laminated together with a thin layer of Teflon or CV2500 resin between them. The debris particles, which traveled a distance of approximately 12 mm before impacting the target had their velocities determined by a laser interferometer system⁶ in which a small Doppler shift in the frequency of the laser beam, returned from the surface of the moving debris particle, is measured. Only one impact was made per target so that an assessment of the amount of re-deposited contamination attributed to the ejecta from a single impact could be determined. The damage observed in these experiments included: front surface cratering, front and rear surface radial and concentric cracks, rear surface uplift and spall; and contamination in the form of vaporized material ejected from the crater which re-deposited on the front surface. The mechanical damage to the targets was characterized using optical and scanning electron microscopy (SEM).

A neodymium-glass, pulsed laser with energies ranging from 2 -5 joules and a 18 ns pulse was used in this work.

3. RESULTS

Figure 1 shows a typical optical micrograph image of an impacted coverglass target in which the mechanical damage resulted from an impact at 4 km/s. Radial cracks extend from the impact crater to the edge of the 4 cm sample. The dashed circle in the center of the image represents the size and impact location of the 3 mm flyer. Figure 2 is a typical SEM image of the rear surface of an impacted target and shows that some glass material has been removed from the rear surface. The predominant damage observed on the rear surface of targets was cracking and uplifting of the glass, however the glass remains attached to the laminate, similar to common safety glass.

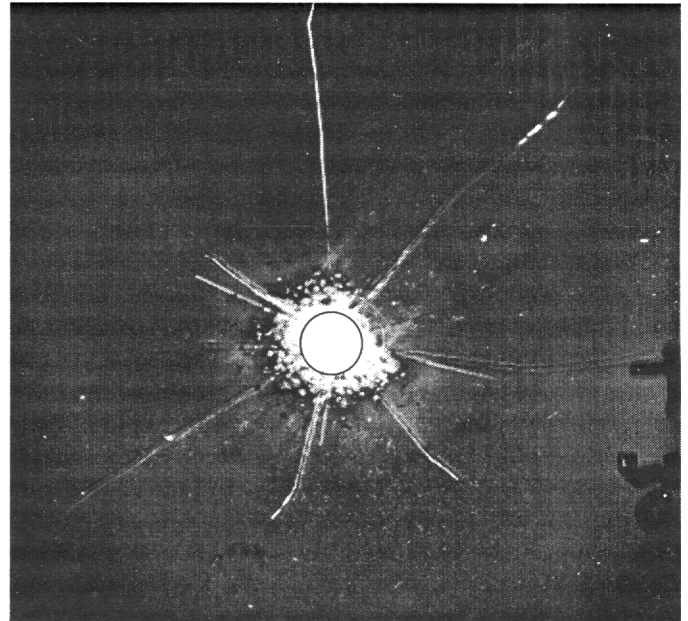


Fig. 1. 4X Optical image of a coverglass laminate.

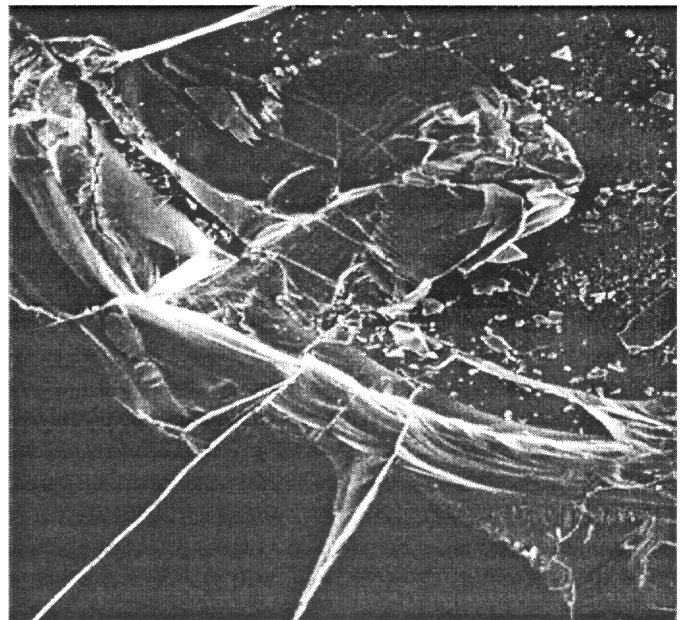


Fig. 2. A 40 X Typical SEM image of rear surface of a coverglass laminate.

Figure 3 shows a typical image of the cross-section of an impacted cover glass laminate sample. The impacted side, as well as the surrounding areas, suffered extensive damage to both layers of the glass laminate. The damage included extensive cracking of the glass layers and permanent deformation primarily within the impact area. Upon impact, the aluminum particle formed a crater concave towards the impact

direction. As a result, the glass on the impact side was extensively cracked but still remained attached to the deformed laminate. On the other hand, much of the

cracked glass on the rear side of the impacted cover glass was uplifted and spalled off.

IMPACT SIDE

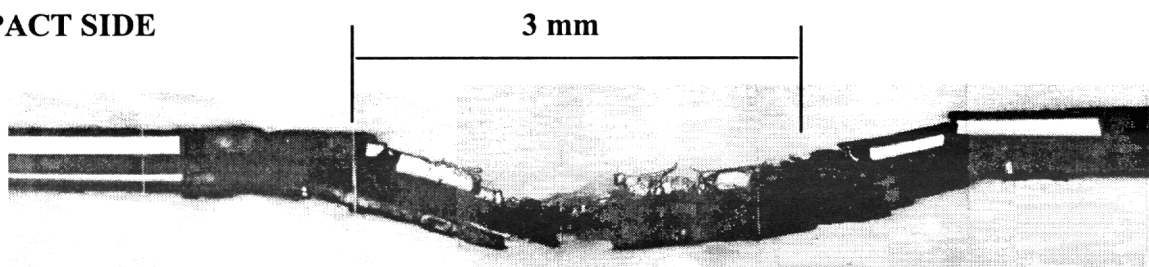


Fig. 3. Optical image of a cross section of an impact site on a coverglass laminate.

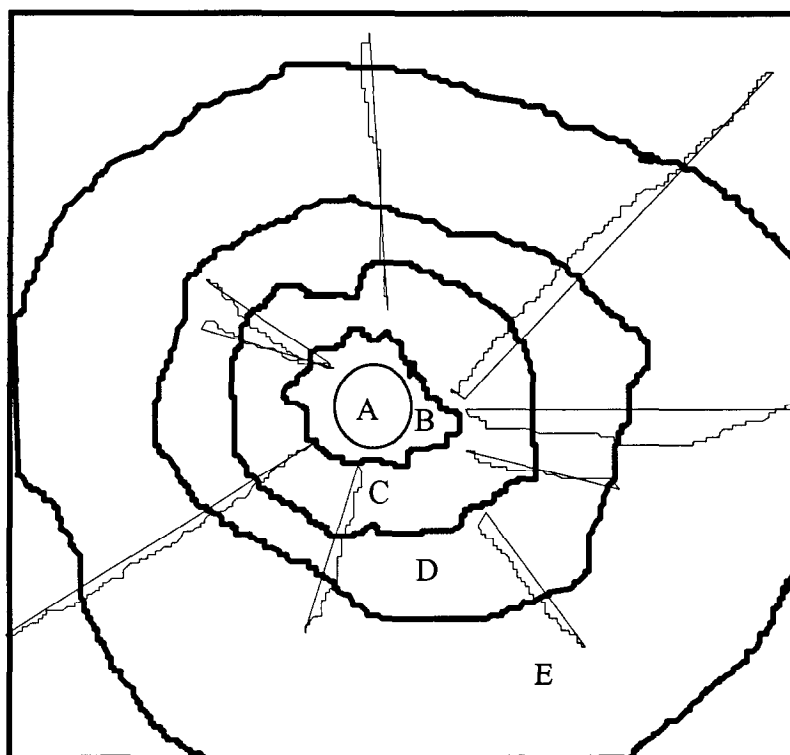


Fig. 4. Schematic of an impact area showing outlines of re-deposition regions.

When considering the overall efficiency of the solar cell, contamination from the vapor blown out of the impact crater may actually be the most serious consequence of damage to the cover glass. An interesting phenomena is seen when examining the deposition of ejecta from the impact crater onto the target surface. The ejected plasma forms bands of different material densities radiating out from the crater. Fig. 4 is a schematic diagram of the impacted sample shown in Fig.1, where area (A) represents

the size of particle impacting the surface; region (B) is the crater area in which material has been removed from the target; molten aluminum is found in area (C), where aluminum is also found on the entire sample in the form of trace deposited vapor; area (D) remained relatively free of re-deposition; and at a distance of over 1 cm from the impact site, area (E), the surface is heavily coated with the vapor removed from the crater.

An elemental analysis of the coverglass surface was completed using a PGT energy dispersive system attached to our scanning electron microscope, and produced the qualitative elemental analysis shown in Figures 5, 6 and 7. Figure 5 shows a "control" spectra consisting primarily of silicon and potassium for a coverglass sample that has not been impacted. Figure 6 is an energy dispersive spectra of the impact crater,

area (A). In the crater area, much of the glass has been removed, revealing the resin layer below which produces the resulting fluorine and carbon lines with reduced intensities of Si and K. The energy dispersive spectra in Figure 7 was collected for area (E) on the coverglass and shows the presence of carbon, fluorine, silicon and aluminum.

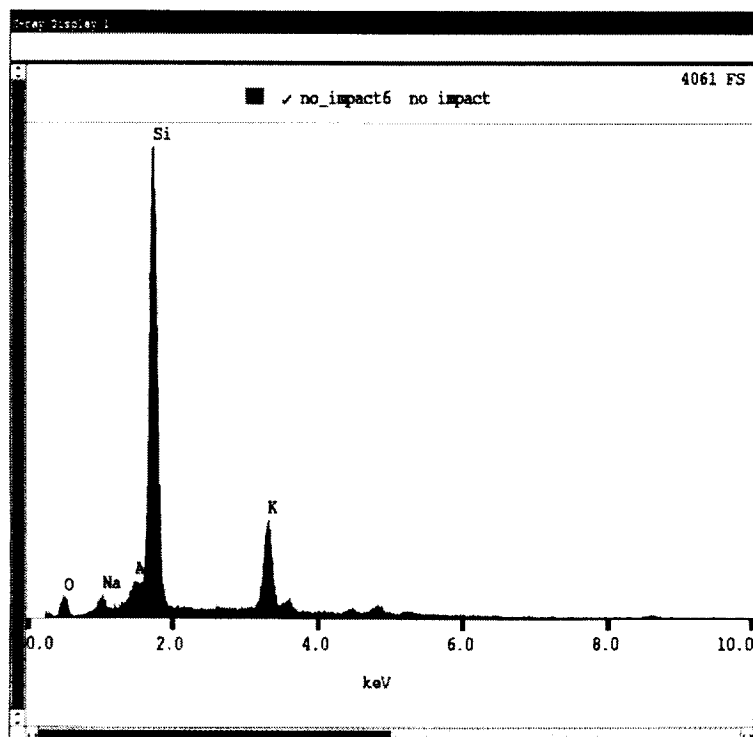


Figure5. Energy dispersive spectrum of a non impacted coverglass.

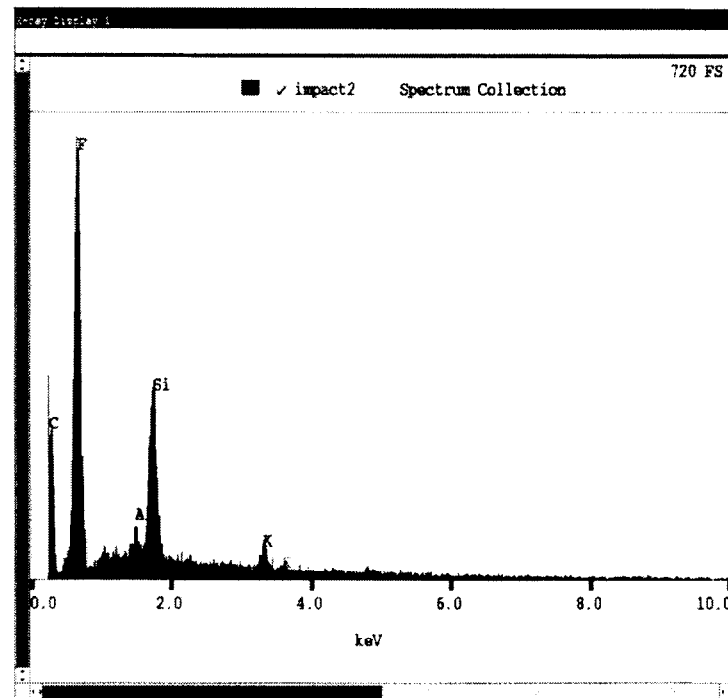


Fig. 6. Energy dispersive spectrum of the crater area (A) on an impacted coverglass.

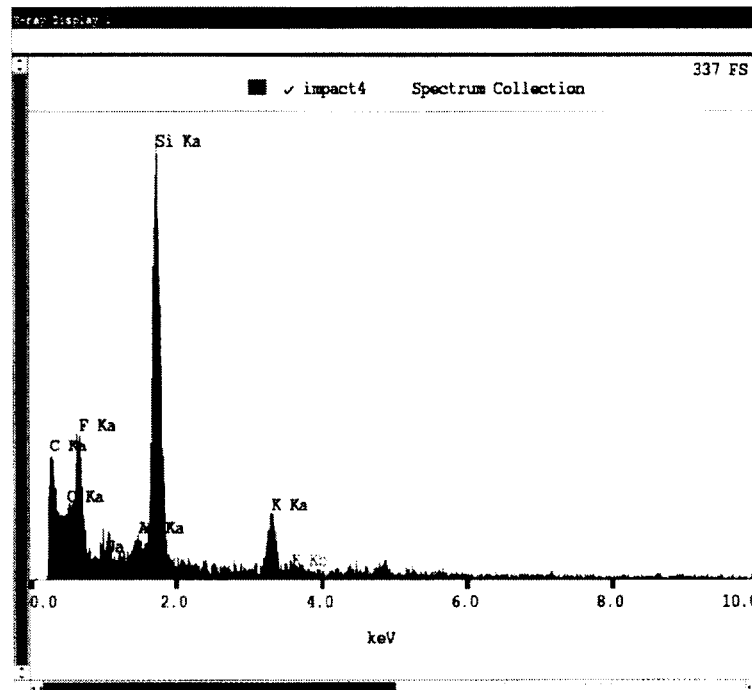


Fig. 7. Energy Dispersive spectrum of area (E) on an impacted coverglass.

The above spectra show that a deposition of fluorine, carbon, and aluminum are now present in regions of the once clean surface. The fluorine and carbon are generated from the vaporization and ejecta of the Teflon resin layer of the laminate. The probable source

of aluminum comes from vaporization of the aluminum flyer.

Light transmission measurements over the wavelengths from 300 nanometers to 1500 nanometers

were made using a Cray 5ev Spectrophotometer through impacted targets and control samples. This wave length range covers the useful solar spectra for solar cells. Figure 8 compares transmission spectra of an undamaged control sample to transmission spectra measured in area (E), 1.6 cm from the crater of an

impacted sample. These spectra show that a maximum transmittance of 90 percent exists at the wavelengths of interest in a control sample. However, degradation in the original sample transmittance by approximately 10 - 15% was measured across area (E) of the sample.

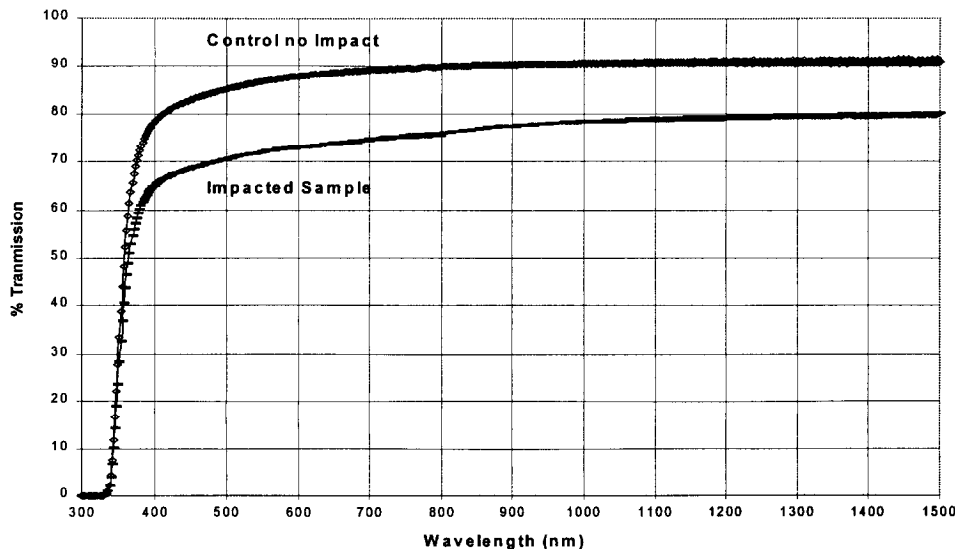


Figure 8 Transmission spectra of UV light through a coverglass target pre and post impact.

4. DISCUSSION AND CONCLUSIONS

The results of our investigations revealed a very complex morphology at the damage site of the cover glass samples exposed to hypervelocity impacts by aluminum debris particles at velocities ranging between 2.5 km/s and 5.0 km/s. The range of velocities and energy used in these experiments are relatively small and were limited by the configuration of the laser used in this set of tests. As such, the data reported in this paper are not sufficient to establish a quantitative relationship between the debris' velocity, its kinetic energy and the size and geometry of the post impact damage sites. Nevertheless, the results of our semi-quantitative analyses clearly indicates that there is a typical damage pattern consisting of both mechanical damage and contamination. Formation of the impact crater is accompanied by the presence of molten aluminum and post impact deposition of contamination on the surface of the damaged cover glass sample. The ejecta consists not only of the cover glass laminate material removed from the crater, but deposition of vaporized contaminant and some fragments of the aluminum debris particle as well. Over 90 percent of the 40mm X 40mm sample experienced at least a 10 percent loss in solar transmission. Degradation of the solar cell efficiency due to loss of solar transmittance may be more critical to the solar cell performance than the actual mechanical damage from impact. Results of the work presented in this paper were a part of our systematic

and comprehensive effort to investigate the response of nonhomogeneous and composite materials to the harsh space environment, including hypervelocity space debris impact damage.

REFERENCES

1. E. Schneider, "Micrometeorite Impact On Solar Panels. Proceedings of the 5th European Symposium: 'Photovoltaic Generators in Space', Scheveningen, The Netherlands, 30 September, (1986).
2. F. M. Rose, "Hypervelocity Impact On Solar Cells". NASA Technical Report, NASA-CR-192444, January (1993).
3. H. Dursch, "Results From Testing And Analysis Of Solar Cells Flown On LDEF". Proceedings of the LDEF Materials Workshop, NASA/Langley, Part 2, pp. 649-660, September (1992).
4. D. J. Kessler, R. C. Reynolds and P. D. Anz-Meador, "Orbital Debris Environment for Spacecraft Designed To Operate In Low Earth Orbit", NASA-TM 100471, September, 1988.
5. R. Roybal, J. Shively, C. Stein, and C. Miglionico, "Laboratory Simulation Of Hypervelocity Debris". Proceedings of the 19th Space Simulation Conference, a NASA Conference Publication 3341, Baltimore, MD, October 28 - 31 (1996).
6. L. M. Barker and R. E. Hollenbach, "Laser Interferometer For Measuring High Velocities Of Any Reflecting Surface", J. Appl. Phys. 43, pp. 4669-4675 (1972).

Earth Observation from a High Orbit: Pushing the Limits with Synthetic Aperture Optics

L. M. Mugnier, F. Cassaing, G. Rousset, B. Sorrente

Office National d'Études et de Recherches Aérospatiales
Optics Department / High Resolution Imaging Group
BP 72, 92322 Châtillon cedex, France

Abstract:

The resolution of a diffraction limited optical telescope is inversely proportional to its diameter; the latter is limited by the current technology to about 10 meters for ground-based systems, and even more limited by volume and mass constraints for space-based systems. Synthetic Aperture Optics (SAO) is a technique that allows the breaking of this limit; it consists in making an array of telescopes (or of mirrors) interfere, so that the data contains some high resolution information at spatial frequencies given by the separation of the telescopes (or "baseline") rather than by their sizes. In this communication, we first briefly review the two types of SAO instruments (called "Michelson" and "Fizeau") and the possible types of beam combination. We then study the possibility of obtaining wide-field interferometric imaging for a Michelson instrument. Then, we address the problem of optimizing the array configuration, which is an important problem for the design of a SAO instrument. We then give some insight on the image restoration, which is a necessary component of the observation system due to the shape of the PSF of a SAO instrument. We conclude that SAO is a promising technique for high resolution Earth observation, especially from a high orbit such as a geostationary one.

1 Typology of SAO instruments

Two types of optical interferometers (or SAO instruments) exist. A Fizeau interferometer contains a set of mirrors forming a virtually common primary mirror, whose light is combined onto a common secondary mirror (which can itself be segmented). The combination of the light beams coming from each piece of the primary mirror forms an image that is recorded in a common focal plane, in exactly the same way as for a monolithic telescope. The NGST [1] is an example of such an instrument. In contrast, a Michelson interferometer consists of a set of (so-called elementary) telescopes, whose light is brought by a set of periscopes into an additional (so called beam combination) telescope. The interferences are recorded in this beam combination telescope, either

in a pupil plane or in a focal plane. The ground-based interferometers built or being built for astronomy are Michelson-type interferometers. Figure 1 shows the two kinds of instruments, for the same input pupil (from [2]).

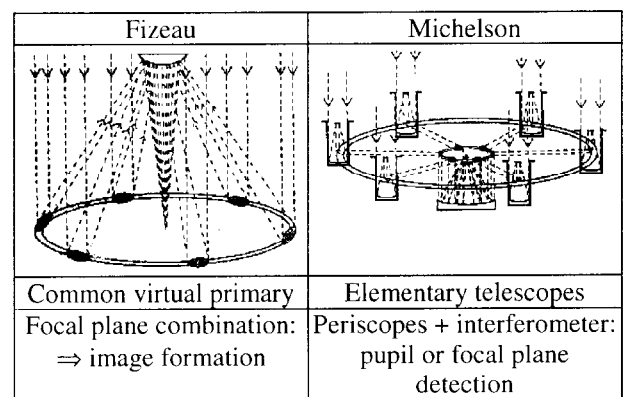


Figure 1: The two types of optical interferometers.

2 Wide-field imaging with SAO instruments

The Fizeau-type instrument is intrinsically an imager and has a wide field of view (FOV), which is limited by the optical design in much the same way as for a monolithic telescope. The Michelson instruments are usually not designed to produce images. In particular, when the data are recorded in a pupil plane, only a discrete set of spatial frequencies of the object (visibilities) is recorded; the field of view is then very limited (risk of field aliasing). In order for a Michelson to produce images, it is necessary to record an image in a focal plane, so that a continuum of spatial frequencies is recorded, and wide field is accessible.

We have studied the conditions under which wide FOV imaging is feasible with a Michelson. It is always possible to cophase at any field position the telescopes of a Michelson by adjusting delay lines and tip/tilt mirrors included for example in the periscopes. For imaging, correct phasing should be simultaneously ensured over a large field. This requires identical aplanetic telescopes, but also new requirements on the optical design.

A famous requirement is homothetic pupil mapping, known as the “golden rule” of SAO [3]: the exit pupil after the telescopes and periscopes should be an exact demagnified replica of the input pupil. For a smaller field, the subpupil demagnification by the telescopes can differ from the baseline demagnification by the periscopes, leading to a “densified pupil” as introduced by Labeyrie [4]. For a larger field, telescope distortion should also be controlled since the golden rule is only paraxial [5].

The effect of all these aberrations has been evaluated [6]. As expected, it can be shown that the cophasing complexity (i. e. the number and precision of optical parameters to control) increases with the field to resolution ratio, which is the number of resolved elements in the desired field. The results are summarized in Table 1.

Table 1: Complexity of an imaging Michelson-type instrument as a function of the field to resolution ratio (FRR).

FRR	Optical constraints
≈ 1	relative piston and tilt control
≈ 10	+ lateral base homothecy
≈ 100	+ complete (baseline+diameter) lateral homothecy
≥ 1000	+ longitudinal homothecy, + field curvature and distortion.

This analysis has been applied to the EUCLID RTP 9.2 study on the feasibility of Earth observation with SAO. The simulation of this 3-telescope Michelson instrument with an optical design software confirmed that by careful design of the telescopes, a very large field to resolution ratio can be obtained. A perspective view of the instrument is shown in Fig. 2. A thorough simulation of this instrument has been performed, whose results are given in Section 4.

Cophasing such an instrument is a major issue because of the large number of degrees of freedom. The most critical parameters to be controlled are on-axis tip/tilt and piston on each aperture. They are measured by an internal source sensor; this sensor analyzes the diffraction pattern of the 3-beam interferogram given by a point-like source retro-reflected by a common reference plane, which overlaps a small area of each aperture [7]. This setup ensures fast and accurate measurements to correct for instrument vibrations, but can be biased by aperture subsampling or by reference drifts.

The other parameters to be controlled in real-time are the lateral pupil position and the telescope magnification. Measuring these parameters requires sensors distributed in the whole FOV. Fortunately these parameters are less critical in terms of amplitude and can be measured at a lower frequency, directly on the observed object in order to minimize biases. These so-called external sensors are also used to correct for the slowly evolving bias of the internal sensor.

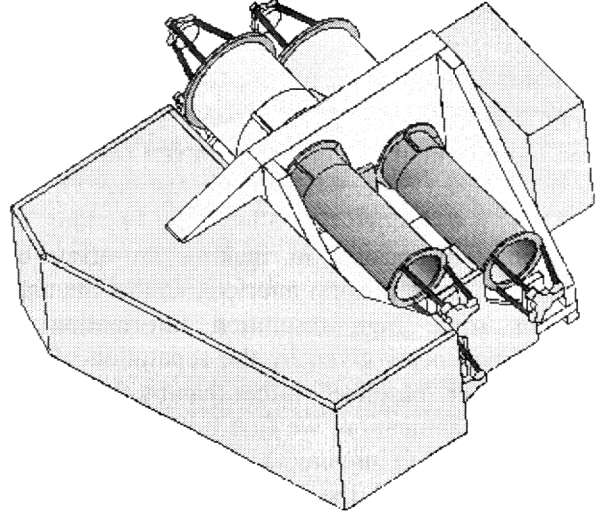


Figure 2: Perspective view of a SAO instrument for Earth observation.

3 Aperture configuration optimization

The choice of the positioning of the elements of a phased array of optical telescopes is an important point for the preliminary design of a SAO instrument, whether these elements be pieces of a primary mirror (Fizeau) or elementary telescopes (Michelson). A whole body of work exists in the literature on this subject, either based on shaping the PSF of the instrument, or on the idea of uniformity of the frequency coverage.

A more global approach consists in considering together the image acquisition and the restoration, and in optimizing the aperture configuration so that the restored image be as close as possible to the original observed object. This approach is usually referred to a “experiment design” in the signal processing community. Let o be the original object of interest, and $i = h \circledast o + n$ the recorded image, where h is the PSF of the instrument, \circledast denotes convolution and n is an additive noise. In order to keep the derivations tractable, the deconvolution is taken as a linear filter g (e.g., an inverse filter truncated to the

maximum spatial frequency of interest); the restored image, or estimated object, is then $\hat{o} = g^{-1} i$. If nothing is assumed about the noise statistics, then it can be shown [8] that the aperture configuration that leads to an \hat{o} that is closest to o in the least-squares sense is the one that maximizes the minimum of the transfer function \tilde{h} over the frequency domain of interest. One can note that this result gives a frequency-domain optimality condition, but this condition is not imposed *a priori* but, rather, derived from the described global approach, which considers the image restoration as part of the observation system.

Figure 3 shows the result of this optimization performed for 3, 4 and 5 elementary telescopes, for a given collecting surface and a given target resolution. The collecting surface is derived from signal-to-noise ratio considerations, and the maximum frequency of interest is derived from mission requirements. One can notice in particular that the four telescopes optimal configuration is not a square, which ensures a better frequency coverage.

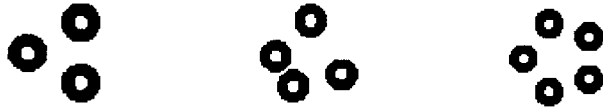


Figure 3: Optimal aperture configurations with 3, 4 and 5 telescopes, for a given collecting surface and resolution.

4 Image simulation and restoration

Due to the shape of the PSF of a SAO instrument, image restoration is a necessary component of the observation system. The data processing is similar to that of images taken by monolithic telescopes. The transfer function is lower than for a monolithic telescope, but does not go down to zero in the frequency domain of interest when the aperture configuration has been optimized as described in the previous section. The abovementioned Earth observation SAO instrument has been simulated, taking into account the optical and the detector transfer functions as well as photon and detector noises. The optical transfer functions includes design, fabrication and assembly aberrations, as well as cophasing residuals. Figures 4 and 5 show the object used in the simulation and the simulated noisy image respectively.

It is well-known that the restoration of the object using the sole data is an unstable process [9]. It is therefore necessary to add *a priori*

information on the solution into the restoration method. This can be done in a Maximum A Posteriori (MAP) framework: the object is endowed with an *a priori* distribution $p(o)$, and Bayes' rule combines the likelihood of the data $p(i|o)$ with this *a priori* distribution into the *a posteriori* probability distribution $p(o|i)$. If the PSF h is perfectly known, then the restored object can be defined as the most probable one given the data: $\hat{o}_{map} = \operatorname{argmax}_o p(o|i) = \operatorname{argmax}_o p(i|o) p(o)$. The prior information on the object that is incorporated into $p(o)$ is the available statistical knowledge on its spatial structure, its positivity and possibly its support. With gaussianity and stationarity assumptions both on the object and on the noise, this maximization has an analytical solution, which is the well-known Wiener filter estimate. This estimate is shown in Figure 6; the prior information used consists in a parametric model for the Power Spectral Density (PSD) of the object [10] and the noise variance, which can both be estimated from the image itself by, e.g., the maximum likelihood method. This simulation and restoration have been used to validate the instrument design.

If one wants to put such a SAO instrument into a high altitude orbit and to keep a high resolution, the size and/or the number of elements of the phased array must be increased. In order to keep these reasonably small, it is worth investigating the possibility to perform some spectral extrapolation from the image, i.e., to restore spatial frequencies that have not been recorded by the instrument.



Figure 4: Object used for the simulation.

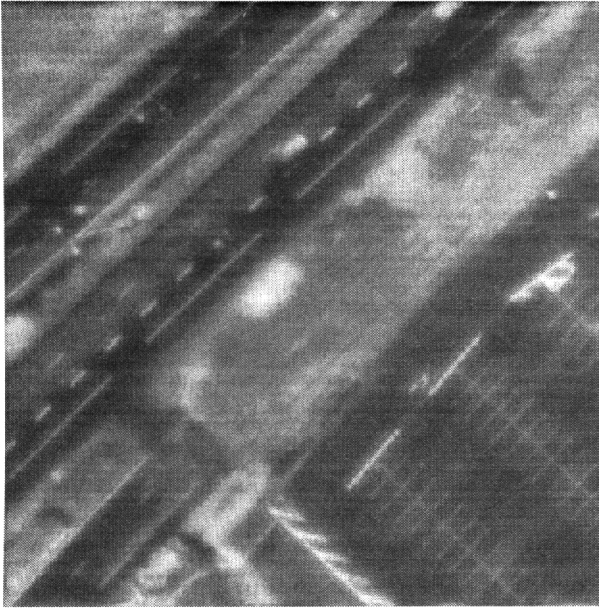


Figure 5: Simulated noisy image.

It can be shown that if the models for the object prior probability and for the noise are stationary and Gaussian, such extrapolation is impossible; indeed, the restored image is then a linearly filtered version of the recorded image. One must then resort to more advanced, non-linear restoration methods, which introduce non-gaussianity in the prior (e.g., edge-preserving priors [11-15], entropic priors, etc.) and/or non-stationarity (e.g., object support information). This has been validated on a one-dimensional simulation of a SAO instrument; figure 7 shows the transfer function corresponding to a two-telescope instrument having zeros before the cutoff frequency (left) and the considered object (right), which has a combination of smooth areas and spikes.



Figure 6: Restored image.

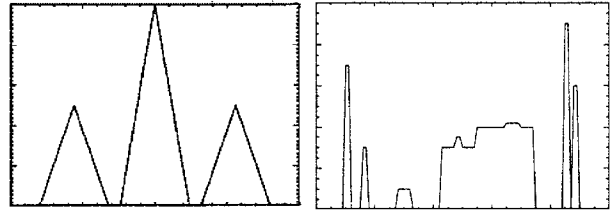


Figure 7: Transfer function of a diluted two-telescope instrument, and object considered for the simulation.

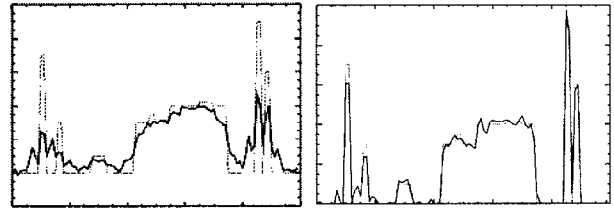


Figure 8: Simulated (left) and restored (right) images. The true object is recalled in dotted line.

The left part of figure 8 shows the image that would be recorded by such an instrument, with a 1% additive noise. The right part of the same figure shows the restored images obtained with an edge-preserving prior and a prior on the bounds of the object (constrained to be between 0 and 1). The object is quite well restored despite the missing frequencies in the recorded image. The inspection of the Fourier transform of the restored object (see Fig. 9) shows that these missing frequencies have indeed been restored by the use of the edge-preserving prior. One must note that this spectral interpolation (and extrapolation) works well only when the size of the frequency holes to be filled in is relatively small compared to the overall frequency domain of interest [16]. This is illustrated in Figure 10, where the telescope separation has been increased; the object's frequencies lying between the central peak and the interference peak are notably underestimated.

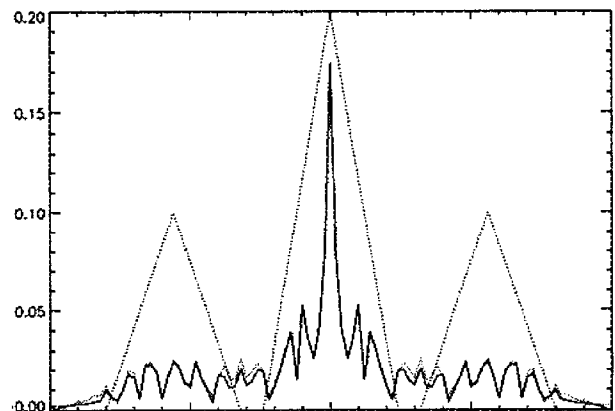


Figure 9: Spectrum of the restored image (continuous line); the spectrum of the true object (dots) and the transfer function (dashed line) are shown for comparison.

Another advanced image restoration problem of interest for a SAO instrument is the case when the instrument is not perfectly calibrated and the PSF is imperfectly known; this may be due for instance to thermal dilatation or to vibrations. A solution to this problem is known as “myopic deconvolution”; it consists in jointly estimating the object of interest and the PSF; this has already been demonstrated for long exposures in adaptive optics [10, 14] and for short exposures in speckle imaging [17, 18] and in deconvolution by wavefront sensing [15]. This myopic deconvolution gives good results provided one has some information on the PSF and its variability, in order to sufficiently constrain the estimation. For long exposures, this information is for instance the average PSF and the PSD of the PSF (i.e., error bars on the transfer function) [10]. For short exposures, an efficient way to constrain the estimation is to model the PSF through the phase in the pupil [15, 17, 18], which is similar to using phase closure in interferometry with very diluted apertures.

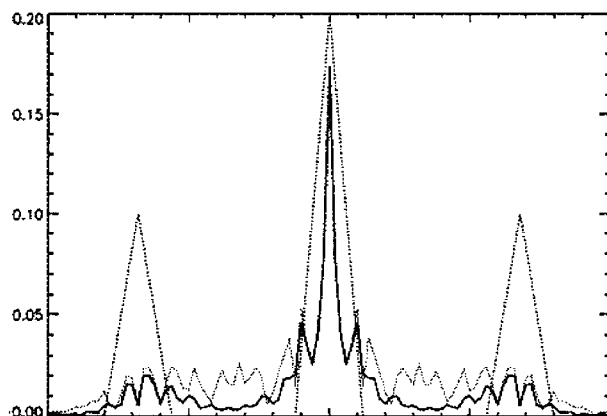


Figure 10: Spectrum of the restored image (continuous line) for an instrument with a very diluted aperture configuration; the spectrum of the true object (dots) and the transfer function (dashed line) are shown for comparison.

5 Conclusion

In this communication, we have studied the possibility of wide-field imaging with a synthetic aperture optics instrument. We have shown that this possibility exists both for a Fizeau and for a Michelson instrument, a necessary condition being the recording of the data in the focal plane and not in a pupil plane. We have shown some key elements of a study of the design of a Michelson for Earth observation, in particular the possibility and the strategy for wide field cophasing.

We have developed a tool for aperture configuration optimization and we have simulated the whole acquisition and processing chain.

We have also mentioned some possibilities for the processing of images coming from a diluted aperture instrument or from an imperfectly calibrated instrument.

In conclusion, we believe that SAO is a very promising technique for Earth observation from a high-altitude orbit; in particular a SAO instrument on a geostationary orbit would allow the permanent monitoring of a given zone while having a resolution comparable to that of current Low Earth Orbit satellites, as already noted by ONERA in the conclusions of the EUCLID RTP 9.2 project.

As a final note, we would like to point out that in the course of this work, it has become more and more apparent that even the early design of the instrument must incorporate the data processing as a key subsystem of the global observing system, because this processing can have a strong impact on the design.

6 References

- [1] P.-Y. Bely. The NGST "Yardstick mission". In *The Next Generation Space Telescope: Science Drivers and Technological Challenges*, ESA SP-429, Liège, Belgium 1998.
- [2] M. Faucherre, F. Merkle, and F. Vakili. Beam combination in aperture synthesis from space: Field of view limitations and (u,v) plane coverage optimization. In Jean-Pierre Swings, editor, *New Technologies for Astronomy*, volume 1130, pages 138–145. Proc. Soc. Photo-Opt. Instrum. Eng., 1989.
- [3] W. A. Traub. Combining beams from separated telescopes. *Appl. Opt.*, 25(4): 528–532, 1986.
- [4] A. Labeyrie. Resolved imaging of extra-solar planets with future 10-100 km optical interferometric arrays. *Astron. Astrophys. Suppl. Ser.*, 118:517–524, September 1996.
- [5] T. W. Stuhlinger. All-reflective phased array imaging telescopes. In *International lens design conference*, volume 1354, pages 438–446. Proc. Soc. Photo-Opt. Instrum. Eng., 1990.
- [6] F. Cassaing. Analyse d'un instrument à synthèse d'ouverture optique : méthodes de cophasage et imagerie à haute résolution angulaire. PhD thesis, Université Paris XI Orsay, December 1997.
- [7] F. Cassaing, L. M. Mugnier, G. Rousset, and B. Sorrente. Key aspects in the design of a

- synthetic aperture optics space telescope for wide field imaging. In N. Duric, editor, *Catching the perfect wave*, number 174 in Pub. Astron. Soc. Pacific, Albuquerque, June 1998.
- [8] Laurent Marc Mugnier, Gérard Rousset, and Frédéric Cassaing. Aperture configuration optimality criterion for phased arrays of optical telescopes. *J. Opt. Soc. Am. A*, 13(12):2367–2374, December 1996.
 - [9] Guy Demoment. Image reconstruction and restoration: Overview of common estimation structures and problems. *IEEE Trans. Acoust. Speech Signal Process.*, 37(12):2024–2036, December 1989.
 - [10] J.-M. Conan, L. M. Mugnier, T. Fusco, V. Michau, and G. Rousset. Myopic deconvolution of adaptive optics images using object and point spread function power spectra. *Appl. Opt.*, 37(21):4614–4622, July 1998.
 - [11] P. J. Huber. *Robust statistics*. John Wiley & Sons, 1981.
 - [12] P. J. Green. Bayesian reconstructions from emission tomography data using a modified EM algorithm. *IEEE Trans. Med. Imag.*, 9:84–93, March 1990.
 - [13] Charles Bouman and Ken Sauer. A generalized gaussian image model for edge-preserving map estimation. *IEEE Trans. Image Processing*, 2(3):296–310, July 1993.
 - [14] J.-M. Conan, T. Fusco, L. Mugnier, E. Kersalé, and V. Michau. Deconvolution of adaptive optics images with imprecise knowledge of the point spread function: results on astronomical objects. In *Astronomy with adaptive optics: present results and future programs*, Sonthofen, September 1998. ESO/OSA.
 - [15] L. M. Mugnier, C. Robert, J.-M. Conan, V. Michau, and S. Salem. Regularized multiframe myopic deconvolution from wavefront sensing. In *Propagation through the Atmosphere III*, volume 3763, Denver, CA (USA), July 1999. Proc. Soc. Photo-Opt. Instrum. Eng.
 - [16] André Lannes, Sylvie Roques, and Marie-José Casanove. Stabilized reconstruction in image and signal processing; part I: Partial deconvolution and spectral extrapolation with limited field. *J. Mod. Opt.*, 34(2): 161–226, 1987.
 - [17] T. J. Schulz. Multiframe blind deconvolution of astronomical images. *J. Opt. Soc. Am. A*, 10(5):1064–1073, 1993.
 - [18] E. Thiébaud and J.-M. Conan. Strict *a priori* constraints for maximum-likelihood blind deconvolution. *J. Opt. Soc. Am. A*, 12(3):485–492, 1995.

High Resolution Imaging from the Geostationary Orbit

Massimo Cecconi (*), Stefano Cesare (*), Cesare Dionisio (**)

(*) ALENIA AEROSPAZIO, Divisione Spazio, C.so Marche 41, 10146 Torino, Italia
Fax 011-7180998, scesare@to.alespazio.it, mceccconi@to.alespazio.it

(**) ALENIA AEROSPAZIO, Divisione Spazio, V. Saccomuro 24, 00131, Roma, Italia
Fax 06-4191391, c.dionisio@rmmail.alespazio.it,

Introduction

The geostationary orbit (GEO) is commonly used for telecommunication and meteorological missions, rarely for scientific missions, within certain limit for remote sensing. For this purpose, low orbits (LEO), typically between 500 to 1,000 km in altitude, are employed in order to get higher spatial and radiometric resolutions. However the GEO offers several advantages for the earth observations, which are: possibility of a continuous observations of the same geographic area of interest, coverage of the whole hemisphere and possibility of re-visiting in a short time the same region, real-time dissemination of the data towards the users and constant observation angles. These features are particularly important in the tactical and strategic surveillance.

The distance from the Earth (about 36,000 km) represents the main obstacle to the full exploitation of the GEO orbit for the remote sensing. This implies that, to achieve a given spatial resolution and to collect a given photon flux at a given observation wavelength, an instrument with aperture tens of times larger than those employed in LEO must be utilized in GEO. For example, to perform ground observation at very high spatial resolution of about 1 meter in the visible spectral band with a monolithic-mirror telescope, an aperture of about 30-m would be required.

With a monolithic-mirror telescope the resolution increase associated to a large aperture is paid first of all in terms of instrument mass. A large primary mirror implies, in addition, the need of the availability of a large volume under the launcher fairing for the accommodation of the instrument.

A solution to the problems related to the large aperture, in the cases when the issue is the high resolution and not the light collection (like for the observation of a portion of the Earth surface), is represented by the synthetic aperture technique. It consists in the reconstruction of the original image of an object starting from that formed on the common focal plane of a set of telescopes (or a

multi-aperture telescope). To this purpose, the set of telescopes (sub-apertures) must observe simultaneously the object while maintaining constant, within a fraction of wavelengths, the phase of the various wavefronts, which are combined together (so to fulfill the coherence and co-phasing conditions, and to operate consequently like an interferometer). The utilization of an optical system constituted by a set of smaller apertures equivalent for resolution to a single monolithic mirror telescope brings considerably advantages in terms of mass saving and reduction of the storage volume.

The scope of this paper is to present concept for a high resolution imaging system, based on the utilization of an optical interferometer and the aperture synthesis technique, for future military surveillance missions from GEO.

High resolution imagery from GEO

The maximum theoretical angular resolution provided by an aberration-free optical system characterised by an aperture of diameter D observing an object at a distance $R \gg D$ at the wavelength λ_0 is given by λ_0/D . This means that an object with a size $l = R \cdot \lambda_0/D$, belonging to a given scene emitting radiation at the wavelength λ_0 , is still distinguishable inside the scene itself, when the latter is observed from a distance R with a telescope of aperture D (in the assumption that the collected radiation is sufficient to get a $SNR \gg 1$).

Figure 1 shows the maximum theoretical on-ground spatial resolution achievable at the sub-satellite point for observations from LEO (800 km = Envisat-1 mean orbit altitude) and from GEO, as function of the telescope aperture diameter and for different observation wavelengths, belonging to visible (VIS: central wavelength $\lambda_0 = 0.63 \mu\text{m}$), near infrared (NIR: $\lambda_0 = 0.86 \mu\text{m}$), mid infrared (MIR: $\lambda_0 = 3.7 \mu\text{m}$), thermal infrared (TIR: $\lambda_0 = 10 \mu\text{m}$) bands.

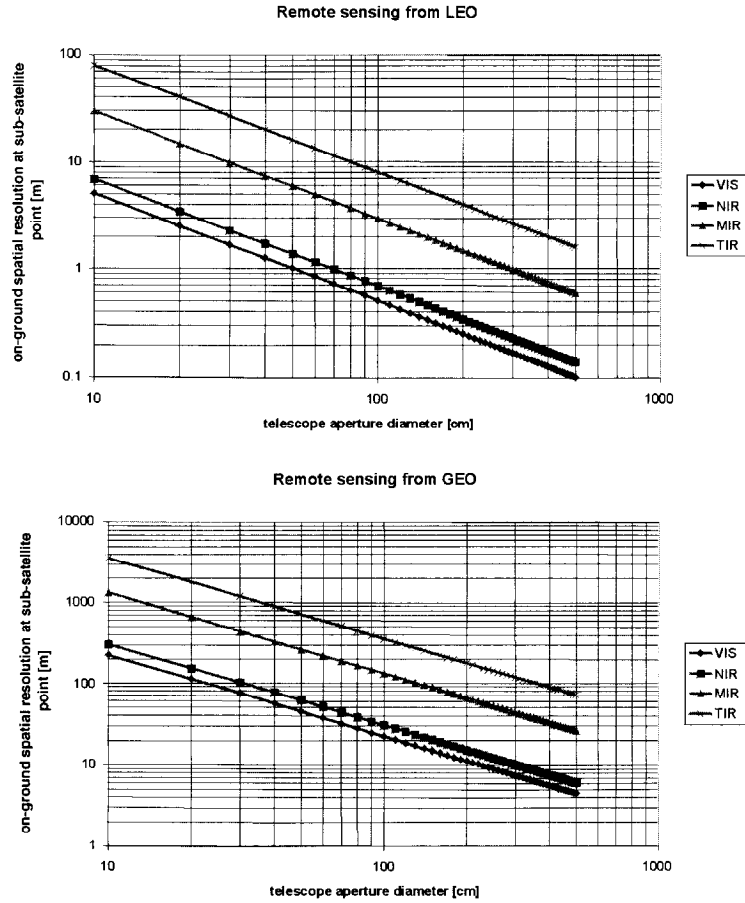


Figure 1 – Maximum theoretical on ground spatial resolution versus telescope aperture diameter for different observation wavelength. VIS = visible (central wavelength $\lambda_0 = 0.63 \mu\text{m}$), NIR = near infrared ($\lambda_0 = 0.86 \mu\text{m}$), MIR = mid infrared ($\lambda_0 = 3.7 \mu\text{m}$), TIR = thermal infrared ($\lambda_0 = 10 \mu\text{m}$).

The photon flux N collected by an optical system with aperture diameter D from a portion of Earth surface with area A_s , lying at the sub-satellite point, behaving like a lambertian sources characterized by a radiance L , and observed from a distance R along the surface normal (with $R \gg$ surface portion size), can be approximated by the expression:

$$N = \frac{L A_s \pi D^2}{4 R^2}$$

where L is expressed in photons/ $\text{m}^2/\text{s}/\text{sr}$.

By considering the value of the Earth radiance per unit wavelength measured by the ERS2 GOME instrument ($\sim 2 \cdot 10^{13}$ photons/ $\text{cm}^2/\text{s}/\text{sr}/\text{nm}$ around $\lambda_0 = 0.63 \mu\text{m}$) the collected photon flux in a 1-nm band from a telescope of aperture D in LEO

(800 km altitude) and GEO has been computed for different areas of the observed scene.

The results are reported in the plots of Figure 2.

From these computations it turns out that even if a relatively small 1-m aperture is sufficient to collect a good photon flux ($\sim 10^4$ photons/s) from a 10 m^2 portion of the Earth surface (in a $\Delta\lambda = 1\text{-nm}$ band around $\lambda_0 = 0.63 \mu\text{m}$), an aperture of 2.25 m is required to resolve that portion of the Earth surface from GEO at the same wavelength. This discrepancy becomes more evident moving towards the infrared region of the spectrum, since the spatial resolution for a given telescope aperture decreases as the wavelength increases (an aperture $D = 2.25 \text{ m}$ provides a resolution of $\sim 14 \text{ m}$ at $\lambda_0 = 0.86 \mu\text{m}$, $\sim 60 \text{ m}$ at $\lambda_0 = 3.7 \mu\text{m}$, $\sim 160 \text{ m}$ at $\lambda_0 = 10 \mu\text{m}$).

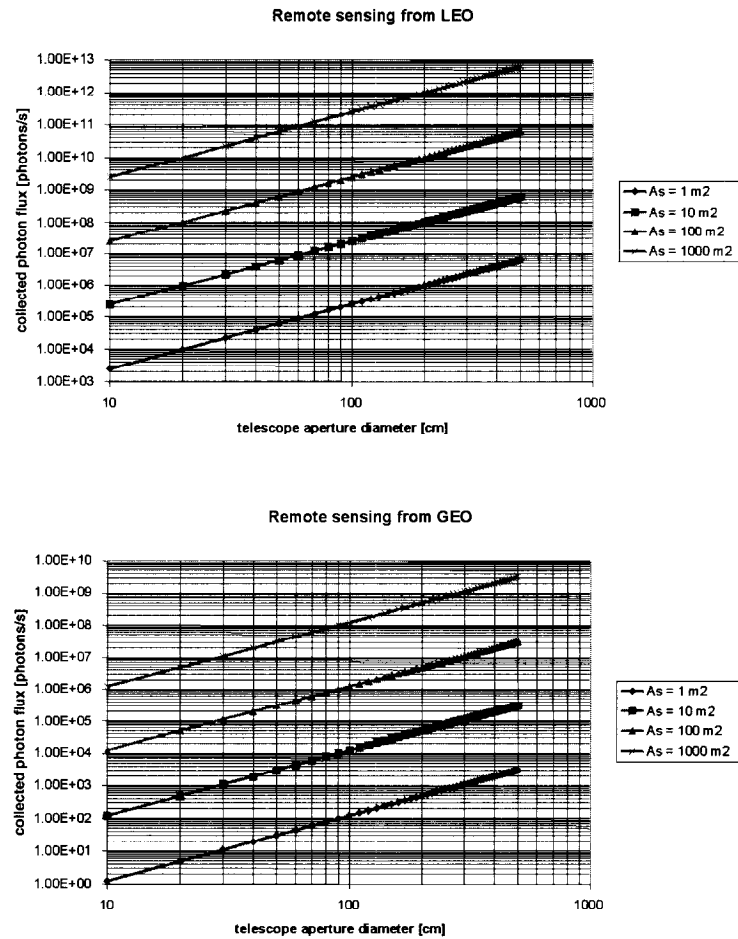


Figure 2 – Collected photon flux in a 1-nm band around $\lambda_0 = 0.63 \mu\text{m}$ versus telescope aperture diameter, for different areas of the observed Earth surface portion (located at the sub-satellite point and observed along the surface normal).

The optical aperture synthesis concept

With a monolithic-mirror telescope the resolution increase associated to a large aperture is paid in terms of instrument mass and storage volume. Even using the current techniques for the construction of ultra-lightweight mirrors, the mass of a 2.25 m diameter optic would be about 500 kg (see Figure 3 and ref. [1]). By comparison, the mass of the 2.48 m primary mirror of the Hubble Space Telescope is 773 kg.

A large primary mirror implies, in addition, the need of the availability of a large volume under the launcher fairing for the accommodation of the instrument.

A solution to the problems related to the large aperture, in the cases when the issue is the high

resolution and not the light collection, is represented by the synthetic aperture technique. This technique consists in the reconstruction of the original image of an object starting from that formed on the common focal plane of a set of telescopes (or a multi-aperture telescope) observing simultaneously the object while maintaining the Optical Path Differences (OPDs) between each interferometric arms much less than the so called coherence length $l_c = \Delta\lambda/\lambda_0^2$ (to generate a fringe pattern) and the residual OPDs much less than a fraction of wavelength λ_0 (to freeze the generated fringe pattern). That is, a multi-aperture telescope (or interferometer) can correctly work only if its telescopes are coherenced and co-phased.

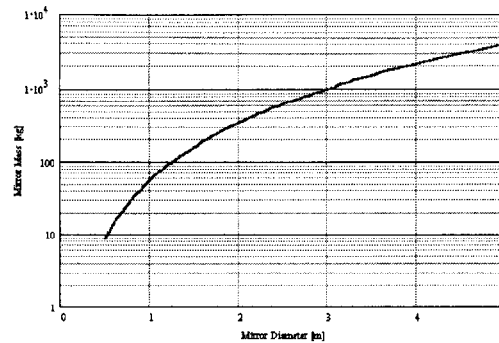


Figure 3 – Mass versus diameter relationship for ultra-lightweight mirrors (from ref. [1])

Neglecting the noise introduced by the detector, the image I of an object on the focal plane of a single-mirror telescope is given by the convolution of the “geometrical” image O of the observed scene with the Point Spread Function (PSF) H of the instrument, defined as the Fourier transform of the aperture function of the instrument:

$$I = H \star O$$

This relationship holds also for the image taken by a set of telescopes correctly coherenced and co-phased. In this case the image I directly produced by the interferometer can appear even very dissimilar from the observed scene O . The latter, however, can be reconstructed through the inverse of the operator H , which exists if the Modulation Transfer Function (MTF), defined as the modulus of the Fourier transform of the PSF never drops to zero in the domain of spatial frequencies in which it is defined [2]. In this case, the reconstructed image turns out to be equal, in terms of spatial resolution, to that formed by a single-mirror

telescope with an aperture containing the set of apertures forming the interferometer.

Thus, it is possible to obtain by aperture synthesis an high spatial resolution by using in place of a large, single-mirror telescope a set of small-aperture telescopes (or a multi-aperture telescope) operating like an interferometer, provided that the total collecting areas of the smaller apertures is sufficient to guarantee a sufficient SNR on the detectors.

Two types of optical interferometer exist (see Figure 4): Michelson type interferometer, constituted by a set of single-mirror independent telescopes, and Fizeau type interferometer, constituted by a set of mirrors obtained as parts of a virtual large monolithic mirror. In the cases in which the interferometer must maintain a relatively large field of view (FOV), and the overall size of the instrument is limited to few meters, the Fizeau configuration is the solution to be preferred.

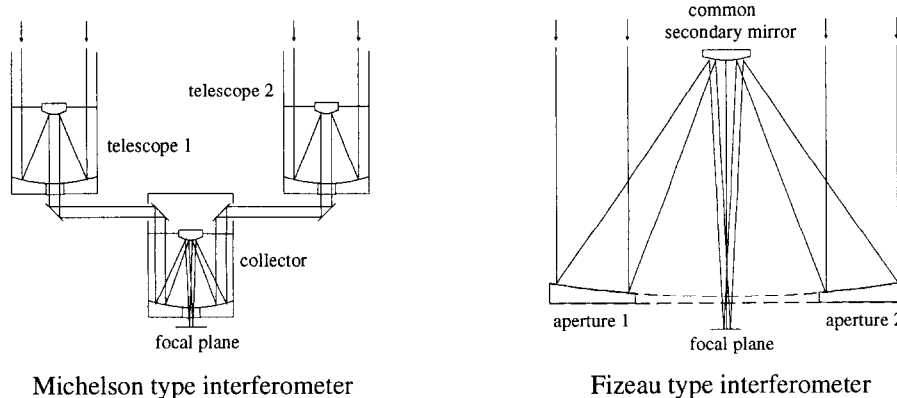


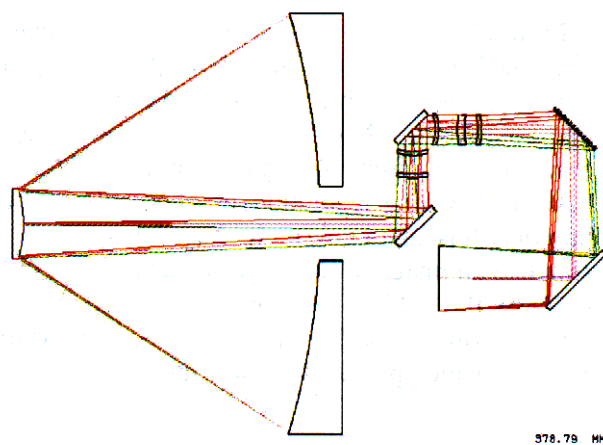
Figure 4 – Scheme of a two-mirror interferometer in Michelson and Fizeau configuration

An example of Fizeau interferometer fulfilling the $MTF \neq 0$ criterion, has been built starting from a monolithic telescope with 2.25 m aperture designed according to the following criteria:

- diffraction-limited optical system at $\lambda_0 = 0.63 \mu\text{m}$ over the instrument FOV;
- $FOV = 0.25^\circ \times 0.25^\circ$ (corresponding to $\sim 150 \times 150 \text{ km}$ at the sub-satellite point from GEO);
- effective focal length = 81 m (so that a $10 \times 10 \text{ m}$ object has a size on the focal plane = $22.5 \times 22.5 \mu\text{m}$)

The configuration of this telescope is shown in Figure 5. It is a two-mirror telescope with a 5-lens camera after the secondary mirror for the correction of the residual aberrations to achieve the diffraction limit condition over the $0.25^\circ \times 0.25^\circ$ FOV at $\lambda_0 = 0.63 \mu\text{m}$, and a focal length of 81 m in a compact configuration.

Such a telescope can be adapted to feed several focal-plane instruments (like imagers, radiometers, spectrometers) operating in different spectral bands by replacing the camera by a set of dichroic beamsplitters for routing the light beam towards the payloads. In this case each instrument shall be equipped by its own optical system (including lenses, mirrors, prisms, gratings, polarisers,...) for matching the light beam to the features and functions of its detector. The same optical system can be designed to include the function of selecting a particular portion of the overall FOV to be observed by the detector from time to time and to change the width of the FOV seen by the detector (zoom function).



In Figure 6 the Fizeau interferometer obtained from the 2.25 m aperture monolithic telescope is shown. The large primary mirror has been replaced by a set of 4 smaller mirrors (0.7 m diameter each). Their size and relative position has been selected so to obtain a “compact” interferometer configuration, namely with $MTF \neq 0$ over all the spatial frequencies sampled by the interferometer (the smallest of which, λ_0/D , corresponds to the resolution of the equivalent monolithic telescope, from which the interferometer has been obtained) and “non redundant”, namely without repetitions (in modulus and direction) among all the possible baselines joining the centers of the various mirrors (so to reduce at minimum the number of mirrors utilised).

In Figure 7 the normalized PSF and MTF of the interferometer are shown. Note that the MTF never drop to zero in the domain of spatial frequencies in which it is defined. This implies that the original scene O observed by means of this interferometer can be reconstructed through the inverse of the operator H , and the image so obtained has the same resolution as if it was taken by a 2.25 m monolithic telescope.

The set of 4 primary mirrors of the Fizeau interferometer has a total collecting area of 1.54 m^2 (equivalent to that a single 1.4 m diameter mirror) and a total mass of about 82 kg (estimated with the relationship of Figure 4), about 6 times smaller than that of the single 2.25 m mirror. This dramatic mass saving, together with the possibility of folding the four mirrors in a compact launch configuration allows to accommodate a large optical system on a relatively small spacecraft.

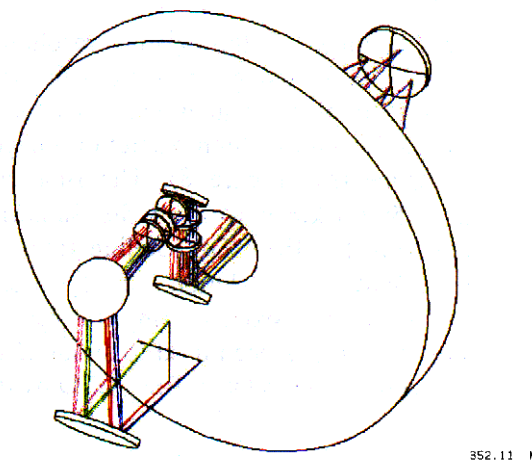


Figure 5 – The telescope with the 2.25 m monolithic primary mirror, from which the Fizeau interferometer has been obtained. After the secondary mirror the light is passed through 5-lens camera and reflected by 4 folding mirrors before the focal plane (the first folding mirror can be rotated so that the following optical system remains parallel to the plane of the primary mirror).

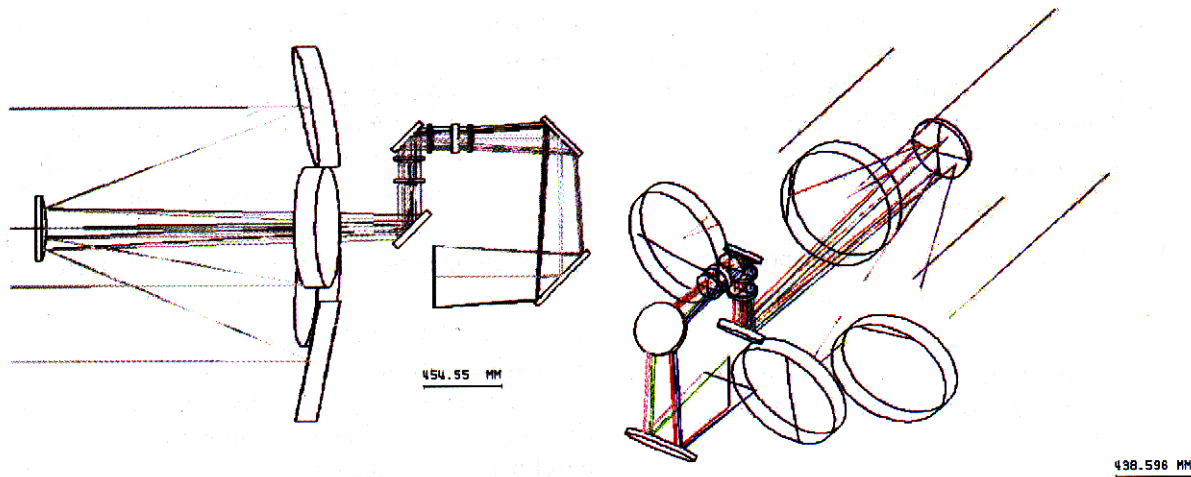


Figure 6 – Four-mirror Fizeau interferometer obtained from the 2.25 m monolithic telescope. The optics after the secondary mirror can be designed to distribute the light to various instruments.

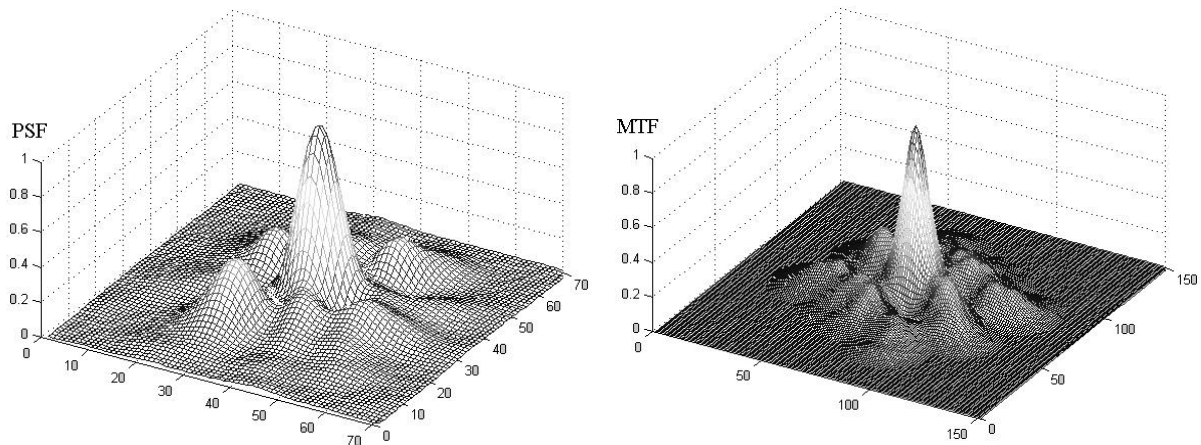


Figure 7 - Normalized PSF (left) and MTF (right) of the 4-mirror Fizeau interferometer

Simulation results

Some first examples of the spatial resolution achievable from GEO using an instrument with 2.25 m aperture (real or synthesized) have been produced starting from two high resolution images taken from space (see Figure 8). The first one contains a $\sim 3.5 \times 2.6$ km portion of the Santorini island taken from the IKONOS satellite (altitude ≈ 780 km) with a resolution of 4 meters (ref. <http://www.spaceimaging.com/level2/level2gallery.htm>). It has been used to simulate an image of the same scene as taken from GEO by the

2.25 m telescope in visible and near infrared bands ($\lambda_0 = 0.63 \mu\text{m} \pm 0.1 \mu\text{m}$, $\lambda_0 = 0.86 \mu\text{m} \pm 0.1 \mu\text{m}$), which provides a higher resolution. The second one contains a $\sim 20 \times 20$ km scene of a volcanic eruption taken from the Space Shuttle (altitude ≈ 220 km), with a resolution of about 30 m (ref. <http://earth.jsc.nasa.gov/>). It has been used to simulate an image of the same scene as taken from GEO by the 2.25 m telescope in mid and thermal infrared bands ($\lambda_0 = 3.7 \mu\text{m} \pm 0.1 \mu\text{m}$, $\lambda_0 = 10 \mu\text{m} \pm 1 \mu\text{m}$), which provides a lower resolution.



Figure 8 – High-resolution images of the Santorini island (left) and of the eruption of the Klyuchevskaya Volcano (right) taken from LEO, and used to simulate the observation of ground scenes by a GEO telescope.

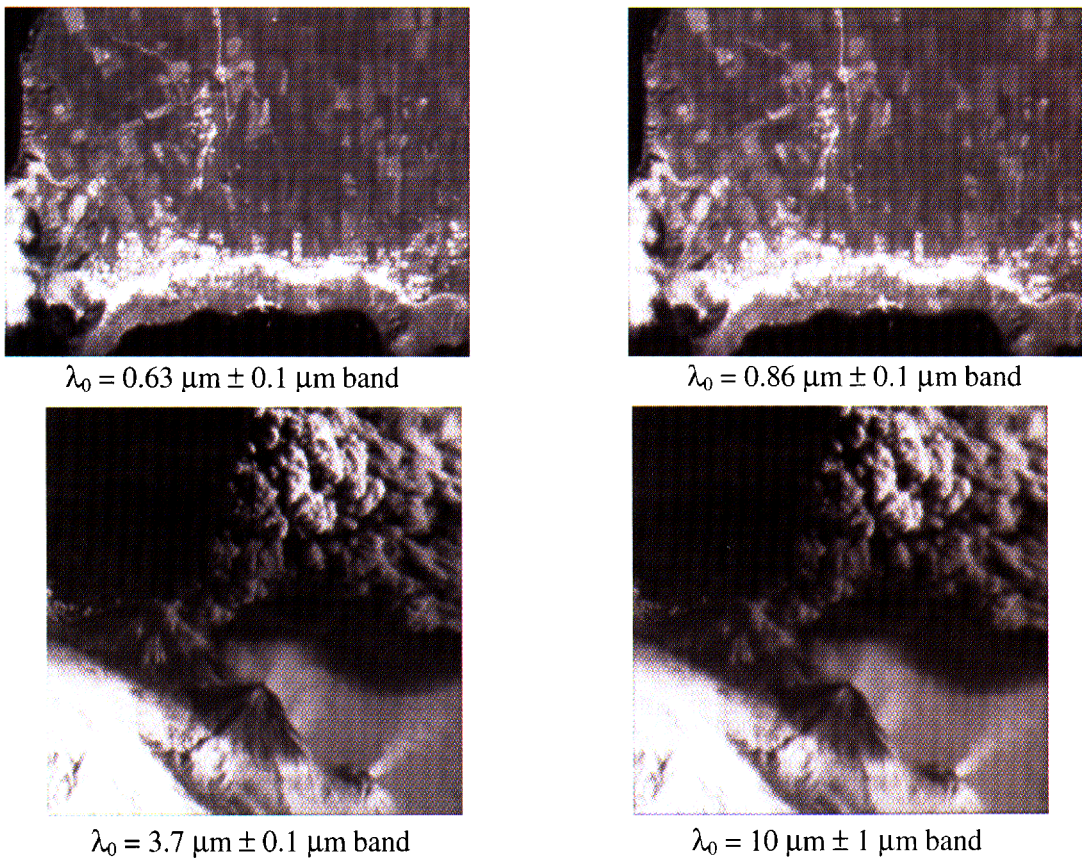


Figure 9 – Images of the Santorini island (up) and of the eruption of the Klyuchevskaya Volcano (down) as taken from GEO by a 2.25 telescope in different spectral bands (representative in terms of spatial resolution only).

These images have been convoluted with the PSF of the 2.25 m designed telescope (which includes also the residual optical aberrations) computed for the different spectral bands, and reported to the same scale of the geometrical size of the scene on the focal plane of the instrument when the latter is in GEO. The result of this operation is

representative, in terms of spatial resolution¹, of the image of the scene as seen by instrument from GEO, which is the same obtainable from the interferometer shown in Figure 6, if the latter is correctly coherenced and co-phased and no errors are introduced in the scene reconstructed through the inverse of the PSF operator.

¹ The original images are taken in visible light. Therefore the simulated images so obtained can be considered fully representative of the scene seen by the GEO telescope only in the $\lambda_0 = 0.63 \mu\text{m} \pm 0.1 \mu\text{m}$ band. In fact, no radiance

map relative to the emission in the infrared wavelengths has been applied to the scene for the simulation of the images in the NIR, MIR, TIR bands. The latter images, however are representative in terms of spatial resolution.

The resulting images are shown in Figure 9. The excellent image quality (in terms of spatial resolution) still achievable from GEO with a 2-m class telescope is apparent.

Implementation and technology to be developed

The main technical problem related to the operation of such an instrument is related to its coherencing and co-phasing, i.e. the equalisation of the optical path length (OPL) of the light from the interferometer apertures to the focal plane equal within a small fraction of the coherence length ($OPD_{ij} = |OPL_i - OPL_j| \ll \lambda_0^2/\Delta\lambda$; λ_0 , $\Delta\lambda$ = central wavelength and width of the observation spectral band) and its stabilisation within a small fraction of λ_0 ($\Delta OPD_{ij} \ll \lambda_0$) during the image acquisition and over the whole FOV. For instance, for an observation in the visible band, with $\lambda_0 = 630$ nm and $\Delta\lambda = \pm 100$ nm, and considering a factor 100 for the fulfilment of the above inequalities: $|OPL_i - OPL_j| = \lambda_0^2/(\Delta\lambda \cdot 100) \approx 20$ nm and $\Delta OPD_{ij} = \lambda_0/100 \approx 6$ nm.

The information for the equalisation of the OPLs within the coherence length can be achieved by analyzing the image of a point-like source on the instrument focal plane, with the same technique defined for the coherencing of the mirror segments

of the Next Generation Space Telescope or of the ground optical interferometers, like the VLTI. For this operation the instrument can be temporarily pointed towards a bright star (since the angular size of the full Earth seen from GEO is 17.4° , a relatively small slew manoeuvre is required to move the interferometer boresight axis from the Earth disk to the starry sky and vice versa).

For instance, with reference to the 2.25 Fizeau interferometer design described in section “High Resolution Imaging from the Geostationary Orbit”, a star image produced by the instrument once the coherence condition has been achieved shall look like that shown in Figure 10.

The OPLs equalisation can be performed by moving the primary mirrors in three DOF's (one piston along the mirror axis and two tilts of the mirror plane) by means of 3-DOFs tip-tilt mechanisms, like, for instance that shown in the Figure 11. Each mechanisms is composed by three linear actuators, placed at 120° around the mirror. Each actuator is made in two stages: a long-range coarse stage, constituted by a stepper motor (covering a millimeter-level stroke with micrometer resolution) and a short-range fine stage, constituted by a piezoelectric translator (covering a micrometer-level stroke with nanometer resolution).

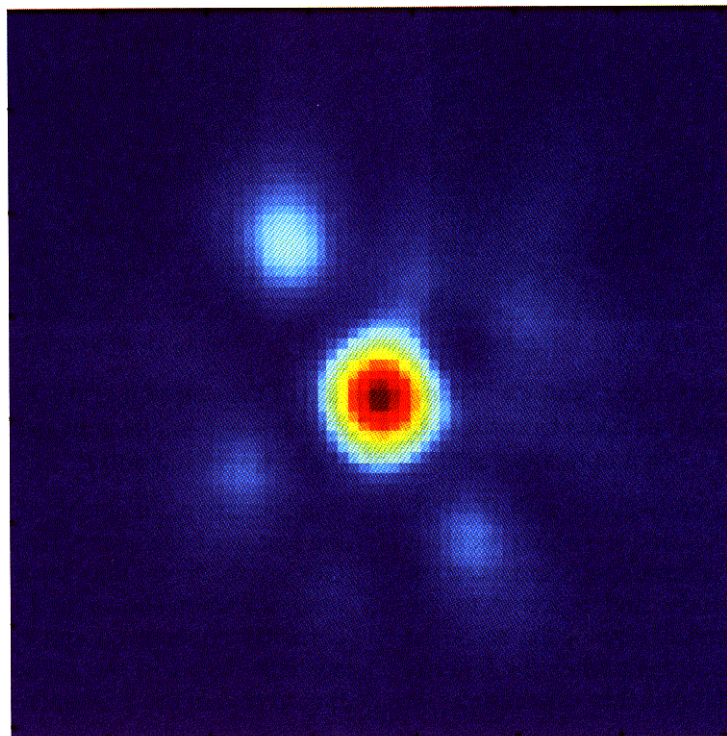


Figure 10 – Image of a pointlike source produced by the 2.25 m Fizeau interferometer after the equalisation of all the optical paths lengths of the light from the apertures to the focal plane.

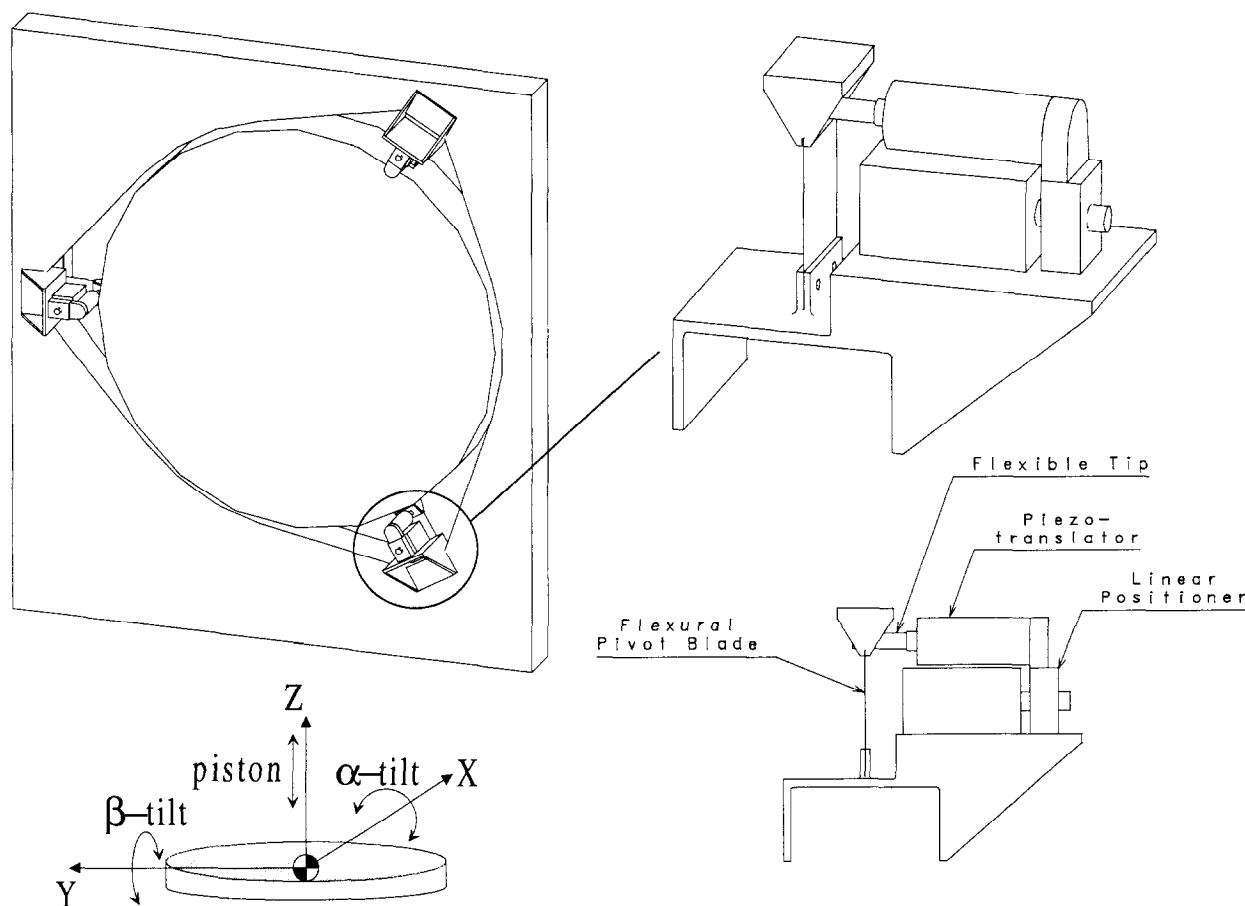


Figure 11 – Example of tip-tilt mechanism for the control of the interferometer primary mirrors

Once the coherence condition has been achieved, the co-phasing condition can be maintained without reference to external sources, by measuring by means of laser interferometers the relative position between optical reference markers suitably placed on the primary and the secondary mirrors (see Figure 12) and commanding the tip-tilt mechanisms so that to maintain stable the measured distances. In fact, the optical path from the secondary mirror to the focal plane is mostly common to light entering through all the interferometer apertures, therefore significant optical path difference can be originated only between the primary mirrors and the secondary mirror.

While the interferometer co-phasing is maintained in this way, the instrument can be re-pointed towards the Earth to perform the planned remote-sensing observations.

The possibility of achieving the coherence condition by means of tip-tilt mechanisms and to maintain the co-phasing by means of such an optics active control system (based on laser metrology and tip-tilt mechanisms) has been demonstrated by Alenia Aerospazio, by means of

analyses and simulations performed by suitable software tools, within the ESA TRP contract “Active Pointing of Large Telescopes and Attitude Measurement Transfer Systems”(APLT & AMTS) for a two-aperture Fizeau interferometer designed for the future astrometric mission GAIA (ref. [3]). Within the same study, a laboratory prototype of the optics active control system has been implemented and tested on a special test-bed (named Control Optics Structure Interaction - COSI – Test-bed). The metrology system consists of three Fabry-Perot interferometers fed by a Nd:YAG laser source at 1064 nm, frequency stabilised against a reference optical cavity using the Pound-Drever technique. The test purpose was the verification of the system performance in the stabilisation of the distances between three pairs of optical elements placed on two $\varnothing = 57$ cm plates (simulating two GAIA mirrors) at a 0.5 m relative distance (see Figure 4). The achieved distance stabilisation was better than **3 pm**, under the seismic and acoustic vibrations coming from the laboratory environment and the application of sinusoidal disturbances with 1 μm amplitude to one of the plates (ref. [4]).

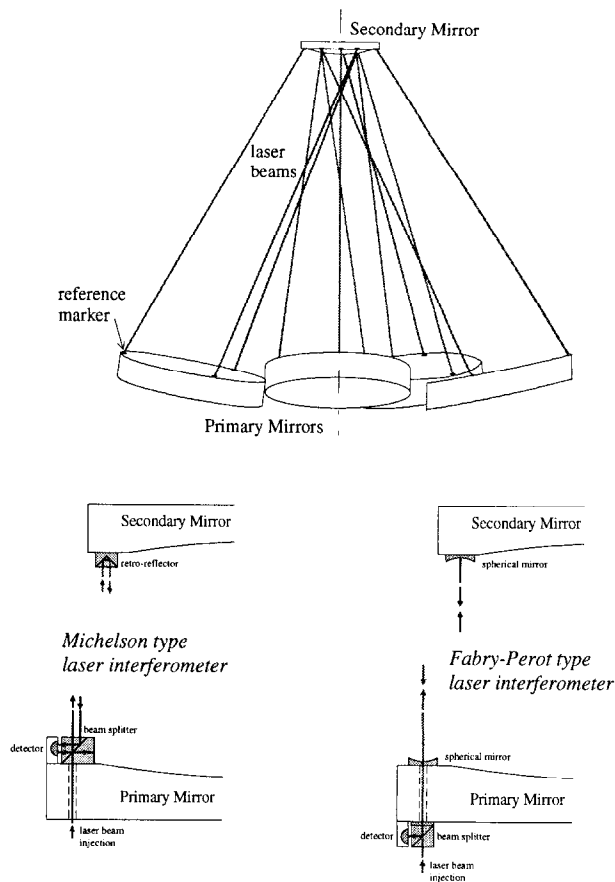


Figure 12 – Example of laser metrology system for the distance measurement between reference optical markers placed on the primary and secondary mirrors, to be used for the interferometer co-phasing. The laser interferometer utilised can be of two types: Michelson (concept shown on the left), or Fabry-Perot (concept shown on the right).

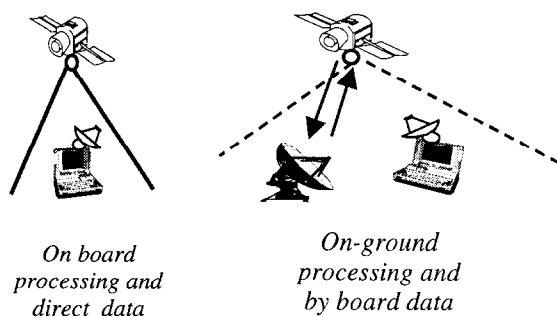


Figure 13 – Data processing and dissemination concepts

Conclusions

From the military and risk management applications point of view the availability of a continuous observation capability and a real time data delivery constitute an invaluable asset. Despite the one meter spatial resolution needs 25 meters diameter optic, for a five meters resolution only five meters telescope would be necessary. Then effective change detection can be implemented to support EW, treaty verifications, law enforcement, fire detection, disaster monitoring, etc. Five meter diameter value fits with the Ariane V firing dimension therefore the system can be launched avoiding complex folding architectures. The data processing and dissemination take benefit from the specificity of Geo orbit that permitting the direct transmission of the data to ground in a raw format or after the on board processing (see fig. 13). Alenia Spazio is studying the system concepts and the technologies to implement the such GEO system which could be deployed in 7-10 years from now.

References

- [1] Valente T. M. – *Scaling laws for light-weight optics* – Cryogenic Optical Systems and Instruments IV, SPIE Vol. 1340, 1990
- [2] J. W. Goodman – *Introduction to Fourier Optics* – McGraw-Hill, New York, 1968
- [3] S. Cesare, C. Philippe – *Developments of enabling technologies for the GAIA mission* – Proceedings of the 49 International Astronautic Congress, IAF-98-Q.1.06, September 1998
- [4] M.Bisi et al. – *Investigation of enabling interferometric technologies for the GAIA astrometric mission* – Proceedings of SPIE "Interferometry '99", Vol 3744, September 1999.

COMPACT HIGH RESOLUTION IMAGING SPECTROMETER (CHRIS)

Dr Mike A Cutter
Sira Electro-Optics Ltd,
South Hill,
Chislehurst,
Kent, BR7 5EH,
England

SUMMARY

This paper describes a hyper-spectral imaging system known as CHRIS (Compact High Resolution Imaging Spectrometer) which has been designed for operation on a spaceborne platform. CHRIS is designed to take images of the Earth in multiple spectral bands over the spectral region 415 to 1050nm. Band selection is programmable. The instrument is planned to be launched, in 2001, on an agile small satellite of the 100kg class. This satellite will operate in a sun-synchronous, high inclination orbit with an altitude in the range 700 to 830km. The instrument can provide 19 spectral bands with a spatial sampling interval of 25m at nadir and 37 bands at 50m, at an altitude of 830km. The field of view of CHRIS is 19 km from 830km altitude. Attitude control of the platform will allow access to non-nadir targets, multi-angle observations of selected targets and improved radiometric resolution.

1 INTRODUCTION

Sira Electro-Optics Ltd has completed the development of a hyper-spectral imager known as CHRIS (Compact High Resolution Imaging Spectrometer), to be flown on a small satellite in late 2001. The CHRIS instrument has been designed principally to provide remote sensing data for land applications, although its high spatial resolution provides potential for monitoring applications in littoral region. The CHRIS instrument is scheduled to be flown on a small satellite platform in sun-synchronous polar orbit, at an altitude of in the range 700 to 830km. The candidate platform is a highly manoeuvrable small satellite, capable of large, rapid rotations on pitch and roll axes, with fine control over pitch and roll rates.

2 OBJECTIVES

The observational objective for the CHRIS instrument is to provide data on Earth surface reflectance in the visible/near-infrared (VNIR) spectral band, at high spatial resolution. The instrument will use the platform pointing capabilities to provide Bidirectional Reflectance Distribution Function (BRDF) data (variation in reflectance with view angle) for selected targets on Earth surface. The instrument will be used mainly to provide images of land areas, and will be of interest particularly in recording features of vegetation and aerosols. Interests include observation of littoral regions and validation of techniques for future hyper-spectral imaging missions, particularly with respect to sub-pixel classification techniques.

The technology objective of the instrument is to explore the capabilities of imaging spectrometers on agile small satellite platforms and to provide a demonstration unit for future small satellite missions.

3 CONCEPT

The instrument is an imaging spectrometer, with a "telescope" forming an image of Earth onto the entrance slit of a spectrometer, and an area-array detector at the spectrometer focal plane. The instrument will operate in a push-broom mode during Earth imaging. The detector will be a thinned, back-illuminated, frame-

transfer CCD. CCD rows will be assigned to separate wavelengths, and CCD columns to separate resolved points in the Earth image.

The platform will be required to provide pointing in both across-track and along-track directions, for target acquisition and for BRDF measurements. The platform will also be required to provide slow pitch during imaging in order to increase the integration time of the instrument. This increase in integration time is needed to achieve the target radiometric resolution, at the baseline spatial and spectral sampling interval.

The spectral waveband covered by the instrument will be limited to the band 415nm to 1050nm, which can be achieved using a single CCD area-array detector. The design form selected for the spectrometer is capable of extension to cover the whole spectral range from 415nm to 2500nm by addition of a SWIR detector array.

The instrument will be calibrated in flight, for radiometric response, by use of (a) a dark scene, (c) vicarious techniques and (c) sunlight deflected into the instrument field, through optics of stable transmission and geometrical spread. This will provide data in calibration mode that will be used for flat-fielding and for absolute and relative spectral response measurement. Wavelength calibration will be corrected using data generated in flight from the atmosphere oxygen absorption band at 762nm.

3.1 CHRIS Design

The instrument optical design is shown in figure 3.1-1. The system comprises a catadioptric telescope and an imaging spectrometer. The system has no moving parts.

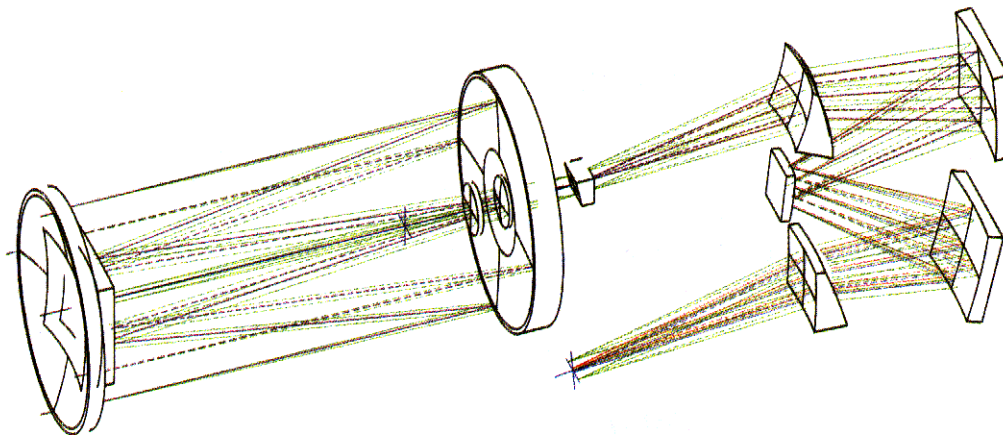


Figure 3.1-1 Instrument optical design

3.2 Telescope

A catadioptric design is utilised for the telescope this provides the required spectral range without aspherics or off-axis elements. For an altitude of 830km, the focal length of the system is set at approximately 746mm, and the aperture diameter at 120mm (f/6).

All refracting elements in the present design are made of fused quartz. The secondary mirror, which is cemented to the first large refracting element, is also fused quartz. The telescope primary mirror is made in a common optical glass. This choice is made, in order to athermalise the telescope.

The telescope is axially symmetrical and has only spherical surfaces, so that conventional construction methods can be applied.

3.3 Spectrometer

The spectrometer is a design recently patented by Sira. It uses "prisms" with curved surfaces integrated into a modified Offner relay. The design has only spherical surfaces, and uses only one material - fused quartz - for the prisms. The spectrometer mirrors will be made in a common optical glass. The design, shown in figure 3.1-1, has three mirrors and two curved prisms. As for the telescope, all surfaces are spherical. The dispersion of the spectrometer varies from approximately 1.3 to 12nm across the spectrum with the highest dispersion at 415nm and the lowest in the near infrared at 1050nm.

The spectrometer design will provide registration to better than 5% of the pixel in both spectral and spatial directions, with resolution limited essentially by the detector pixel size.

3.4 Detector

The CCD detector is an MAT (formerly EEV) device. It has the following features:

- CCD area array,
- frame transfer,
- thinned and back-illuminated, (providing good blue response)
- 748 nominal resolved elements per swath width
- 576 lines in exposed region (approx. 200 active for spectral resolution - others used for smear/stray-light correction),
- dump gate (providing fast parallel dumping)

The total frame time for 25m ground sampling is 12.7 ms.

3.5 Electronics

The instrument electronics includes:

- programmed line integration and dumping on chip for spectral band selection
- pixel integration on chip for spatial resolution control
- correlated double sampling (noise reduction circuit)
- dynamic gain switch for optimum usage of the ADC resolution
- 12 bit ADC.

The option for an image buffer exists.

4 OPERATIONAL, PLATFORM & ORBIT ASPECTS

The platform will receive demands from ground control for:

- target location - requiring roll manoeuvres to point across-track
- viewing directions for each target in one orbit - requiring pitch manoeuvres to point along-track,
- spectral bands and spectral sampling interval in each band,
- spatial sampling interval.

The platform will perform the required pitch and roll manoeuvres and transmit control signals to CHRIS to initiate and terminate imaging, with the required spectral and spatial characteristics.

The platform will receive digitised data from CHRIS, store the data in a mass memory unit and transmit to ground on command. Options exist for data compression in a Digital Signal Processing (DSP) unit.

The currently anticipated ground station has a nominal down link of 1 Mbit/s. However, this will be reduced by various link margins. With a single ground station it may take up to three over-passes to down load a set of 5 images (19 km x 19 km) assuming no on-board data compression. Additional ground stations may be used to improve the overall down link.

The platform is currently anticipated to operate at an altitude between 700 and 830 km in a polar and sun-synchronous orbit.

5 CHRIS SPECIFICATION

The provisional specification for CHRIS is as follows:

spatial sampling interval @ 830km	25m (nadir), integration to 50m.
swath width	19 km at nadir
spectral range	410nm to 1050nm
spectral sampling	1.3nm to 12nm
spectral bands	19 band readout @ 25m spatial sampling (nadir) 37 bands readout @ 50m spatial sampling (nadir)
radiance range	albedo 1
radiometric resolution	0.5% @ 20% albedo

The platform is designed to provide across-track and along-track pointing angles of $\pm 30^\circ$ and $\pm 44^\circ$ at ground level.

The instrument has an envelope of approximately 200x260x790mm, a mass of less than 14kg and a power consumption of approximately 9W.

6 ACKNOWLEDGEMENTS

The authors would like to acknowledge the support of the British National Space Centre for partial funding of the CHRIS instrument. Additional thanks go to the two Principal Investigators, Dr Jeff Settle of Reading University and Prof. Mike Barnsley of Swansea University, for support in defining the scientific programme.

The current plans are to launch on a small satellite provide by the European Space Agency.

Compound Semiconductor Devices for Space Applications

Sammy Kayali
 Jet Propulsion Laboratory
 California Institute of Technology
 4800 Oak Grove Drive, M/S 303-200
 Pasadena, CA 91109
 USA
 Tel. (818) 354-6830
 FAX (818) 393-4559
 Email: Sammy.A.Kayali@jpl.nasa.gov

Abstract

Application of semiconductor devices in high reliability space systems requires a thorough understanding of the reliability and failure mechanisms associated with the selected devices. This paper provides a description of the reliability and qualification issues related to the application of compound semiconductor devices in critical space systems. A discussion of common failure mechanisms, radiation effects and other reliability concerns is provided along with a discussion of methods for technology qualification for high reliability space applications.

Introduction

The recent growth of the compound semiconductor industry has resulted in substantial improvements in processing methods, fabrication yield, and overall quality of commercially viable compound semiconductor devices. This coupled with large volume production and the utilization of statistical process control has greatly reduced the infant mortality population without having to impose traditional high reliability part specifications. However, reproducibility of a product does not guarantee reliability in the intended application. For critical space applications where the success or failure of a mission hinges on the lifetime and performance of a single device; it is critical that all aspects of the reliability and the various known failure modes and mechanisms be addressed prior to the insertion of the component in the application [1, 22].

The selection and application of microelectronic components in high reliability space systems requires knowledge of the component design, fabrication process, and applicable tests. In addition, reliability analysis and detailed knowledge of the application environment is

necessary in order to determine the suitability of the selected component for the application. These issues are of particular importance for the application of compound semiconductor devices in high reliability systems due to the need for the utilization of large numbers of these devices at the upper limit of their performance and stress capabilities.

The user of compound semiconductor devices must gain an understanding of not only the technology performance capabilities but also of the limitations of the technology and must employ methods to utilize it in a reliable fashion. The user must also understand that many of the failure mechanisms associated with silicon devices do not apply to GaAs and other compound semiconductors, and new device structures bring new failure mechanisms. In addition, many of the traditional assumptions for mean-time failure rate predictions do not hold for those new devices. Thus, today's high reliability user must be more aware of measurement based predictions of long term failure rate over calculation based predictions.

This article provides a brief overview of reliability issues relating to compound semiconductor devices and some common practices for determining suitability of these devices for application in high reliability space systems.

Reliability and Qualification for Space Applications

Device reliability involves probability statistics, time, and a definition of failure. Given a failure criterion, the most direct way to determine reliability is to submit a large number of samples to actual use conditions and monitor their performance against the failure criteria over time. Since most applications require device lifetimes of many years, this approach is not

practical. To acquire device reliability data in a reasonable amount of time, an accelerated life test at high temperatures is used. This type of accelerated test is based on the observation that most failure mechanisms are thermally activated. By exposing the devices to elevated temperatures, it is possible to reduce the time to failure of a component, thereby enabling data to be obtained in a shorter time than would otherwise be required. Such a technique is known as "accelerated testing" and is widely used throughout the semiconductor industry. The rate at which many chemical processes take place is governed by the Arrhenius equation:

$$R = A \exp (-E_a/kT)$$

Where

R = rate of the process

A = a proportional multiplier

E_a = activation energy, a constant

k = Boltzmann's constant, 8.6×10^{-5} (eV/K)

T = Absolute temperature in Kelvin

This equation has been adopted by the semiconductor industry as a guideline by which the operation of devices under varying temperature conditions can be monitored. Experimental data obtained from life tests at elevated temperatures are processed via the Arrhenius equation to obtain a model of device behavior at normal operating temperatures. Rearranging the Arrhenius equation allows the temperature dependence of component failure to be modeled as follows:

$$\ln t_2/t_1 = E_a/k (1/T_2 - 1/T_1)$$

where

$t_{1,2}$ = time to failure

E_a = activation energy in electron volts

T = absolute temperature in Kelvin

Qualification can be defined as the verification that a particular component's design, fabrication, workmanship, and application are suitable and adequate to assure the operation and survivability under the required environmental and performance conditions.

Traditional qualification methods require extensive test and characterization of the specific component using a predetermined set of tests and characterization conditions. This approach has been very costly in schedule and expense and

typically results in very little interaction between the device manufacturer and the user.

A methodology for qualification based on continual interaction between the device manufacturer and the user is described in this paper. This interaction results in a detailed understanding of the device design, fabrication, and limitations along with the specific application conditions and expected operating environment. The methodology is divided into three main categories; Process Qualification, Product Qualification, and Product Acceptance.

Process Qualification: Is a set of procedures the manufacturer follows to demonstrate the control of the entire process of design and fabrication using a specific technology (MESFET, HEMT, HBT, etc.). It addresses all aspects of the process including the acceptance of starting materials, documentation of procedures, implementation of handling procedures and the establishment of lifetime and failure data for devices fabricated using the process. Since the goal of process qualification is to provide assurance that a particular process is under control and known to produce reliable parts, it needs to be performed only once, although routine monitoring of the production line is standard. In addition, any significant changes in the process may require re-qualification of the process. It is critical to remember that only the process and basic circuit components are being qualified. No reliability information is obtained for particular component designs.

Although process qualification is intended to qualify a defined fabrication procedure and device family, it must be understood that the technology is constantly evolving, and this technology evolution requires the continual change of fabrication procedures. Thus, strict application of the commonly used phrase, "freezing the production process," does not apply.

The qualification process also involves a series of tests designed to characterize the technology being qualified. This includes the electrical as well as the reliability characteristics of components fabricated on the line. Some of these tests are performed at wafer level and include the characterization of Process Monitors (PM), and Technology Characterization Vehicles (TCV). Other tests require the mounting of circuits or elements into carriers.

In reality, the manufacturer will already have an existing and defined process with established reliability and qualification procedures and practices. Therefore, it is the user's responsibility to become knowledgeable of these practices, get involved in the activities of the Technology Review Board (TRB), and to become aware of the necessary qualification steps. All of these tests and the applicable procedures are an integral part of the qualification program and provide valuable reliability and performance data at various stages in the manufacturing process.

Product Qualification: is the verification that a component will satisfy the design and application requirements under the specified conditions. The information sought after in this approach is design specific and applies to devices fabricated on qualified process lines. This qualification step is composed of Design Verification and Product Characterization.

Design Verification is one of the best ways of reducing engineering costs and improving reliability. Design reviews with the participation of the device manufacturer and the device user are a means of accomplishing this verification of model or simulation and layout of the design prior to fabrication. Verification of circuit design is only applicable to custom designs and requires detailed knowledge of the design tools, device physics, layout tools, fabrication, and test which requires the participation of personnel from the various disciplines.

Product characterization is another important aspect of product qualification. Thermal analysis and test to determine the thermal characteristics of the design, along with ESD sensitivity tests, voltage ramp tests, and temperature ramp tests are all essential in obtaining an understanding of the limitations and characteristics of the design. These characterizations are applicable to both custom and standard designs and are an accepted practice for establishing product qualification.

Product Acceptance: Although devices may be designed by highly qualified personnel, fabricated on a process qualified production line, and verified through measurements to meet the design goals; parts with poor reliability characteristics still may exist. This may be due to variations in the fabrication process, or material flaws that were undetected, or, as is more often the case, to the device package and stress

imposed on the device during packaging. Regardless of the cause, these weak devices must be found and removed before they are integrated into the system. Therefore, manufacturers of high reliability systems require the devices to pass a series of product acceptance screens, whose sole purpose is to increase the confidence in the reliability of the devices. This step in the qualification methodology is the major difference between space-qualified devices and commercial grade devices.

The level of testing performed under product acceptance is a function of the form of the deliverable. For example, the first level of acceptance testing, called "wafer acceptance test" is performed at the wafer level to assure the uniformity and reliability of the fabrication process through a wafer to wafer comparison. "Lot acceptance test for die" is a second level of testing that provides further reliability information, but only on a sample of the devices because of the difficulty in performing full characterization on non-packaged devices. "Packaged device screen" is performed on 100% of the devices if the deliverable is a packaged product.

Failure Modes and Mechanisms

Failures in electronic devices can be classified as either catastrophic failures or degradation failures. The exact mechanism, which causes the failure is normally dependent on the material structure, processing methods, application, and stress conditions. Device bias, resultant channel temperature, passivation, and material interactions may all cause or contribute to different failure mechanisms. Furthermore, device handling, choice of materials for packaging and the application environment may also cause failures[2]. Some common failure mechanisms affecting the device at die level:

Gate-Metal Sinking: The performance of GaAs-based devices relies heavily on the quality of the active channel area of the device. The Schottky gate metal-to-semiconductor interface directly influences the device electrical parameters, such as the drain saturation current and reverse breakdown. The gate structures are based on the industry standard multi-layer Au/Pt/Ti or Au/Pd/Ti on GaAs. Inter-diffusion of gate metal with GaAs results in a reduction of the active channel depth and a change in the effective channel doping. This effect is termed "gate

sinking.” This process is affected by the surface conditions of the GaAs material at the time of deposition, the deposition parameters, and the choice of deposited materials [3,4].

Ohmic Contact Degradation: The most common system for ohmic contacts is AuGe/Ni, which is alloyed into the GaAs at temperatures in excess of 400°C to provide the necessary low contact resistance (0.1 to 0.5 Ω/mm). A thick Au layer is then deposited on top of the alloyed contacts to provide conduction. This structure, employed at the drain and source contacts, has been shown to degrade at elevated temperatures (>150 °C). The degradation is the result of Ga out-diffusion into the top Au layer and the diffusion of Au into the GaAs causing an increase in the contact resistance. The Ni layer used in the ohmic contact is intended as a Au- and Ga-diffusion barrier. Some other materials such as Cr, Ag, Pt, Ta, and Ti have been used as barrier materials with varying degrees of success[16]. The activation energy associated with ohmic contact degradation varies between 0.5 eV and 1.8 eV. This activation energy may provide reasonable contact life at low operating temperatures (<100 °C) but it also indicates rapid deterioration at elevated temperatures [5].

Channel Degradation: Degradation observed in device parameters can sometimes be attributed to changes in the quality and purity of the active channel area and a reduction in the carrier concentration beneath the gate Schottky contact area. These changes have been postulated to be a result of diffusion of dopants out of the channel or diffusion of impurities or defects from the substrate to the channel. Deep level traps have also been postulated to cause similar degradation in MESFETs [17].

HEMT devices, being strongly dependent on the properties of the interface of the AlGaAs/GaAs heterostructure, can suffer a related failure mechanism. A decrease in electron concentration in the channel, caused by a de-confinement of the 2-Dimensional Electron Gas (2DEG), was postulated to be the cause of the observed failure mechanism.

HEMT devices can also suffer from metal-diffusion-related mechanisms, which are manifested as channel-related degradation. Lateral diffusion of Al into the gate recess region changes the conduction band discontinuity and consequently the confinement of the channel

electrons. Gold diffusion from the ohmic contact into the active channel region under the gate can also cause similar degradation. Lastly, vertical diffusion of Al from the AlGaAs donor layer and Si from the n^+ AlGaAs layer into the channel layer causes an increase in the impurity scattering in the undoped GaAs, thus deteriorating the high electron mobility of the 2DEG [6].

Surface State Effects: The performance of GaAs-based devices depends highly on the quality of the interface between metal and GaAs or the passivation layer (Si_3N_4 or SiO_2) and GaAs. The quality of the interface can depend on the surface cleaning materials and procedures, the deposition method and conditions, and the composition of the passivation layer. As shown in Fig. 4, the main effect of an increase in surface state density is the lowering of the effective electric field at the drain/gate region, which results in an increase in the depletion region and a change in the breakdown voltage.

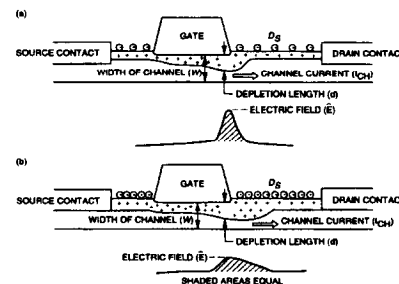


Figure 4. Schematic cross section of a MESFET with different surface charges. (a) with low density of surface states, and (b) with high density of surface states[13].

Unpassivated devices can be susceptible to surface oxidation and loss of arsenic, which may result in an increase in gate leakage current and a reduction of the breakdown voltage. Devices passivated using SiO_2 may experience surface erosion due to the interaction of SiO_2 with GaAs [7].

Electromigration: The movement of metal atoms along a metallic strip due to momentum exchange with electrons is termed electromigration. Since the mechanism is dependent on momentum transfer from electrons, electromigration is dependent on the temperature and number of electrons. Therefore, this failure mechanism is generally seen in narrow gates and

in power devices where the current density is greater than $2 \times 10^5 \text{ A/cm}^2$, which is normally used as a threshold current density for electromigration to occur. As shown in Fig. 5, this effect is observed both perpendicular and along the source and drain contact edges and also at the interconnect of multilevel metallizations.

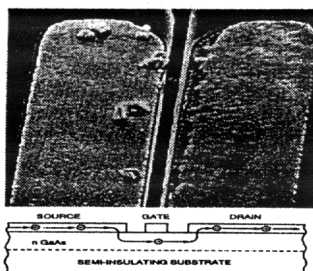


Figure 5. Depletion and accumulation of material in AuGeIn source and drain ohmic contacts induced by electromigration.

The metal atoms that migrate along the line tend to accumulate at the grain boundaries. The accumulation of metal at the end of the gate or drain contact can create fingers of metal that can short the device. Material accumulation and void formation perpendicular to the source and drain contacts can cause hillock formation over the gate structure. This may result in shorting the gate to the source or drain which may result in catastrophic failure.

Hot Electron Trapping: Under RF drive, hot electrons are generated near the drain end of the channel where the electrical field is the highest. A few electrons can accumulate sufficient energy to tunnel into the Si_3N_4 passivation to form permanently changed traps. As shown in Fig. 6, these traps can result in lower open-channel drain current, transconductance, and higher knee voltage, leakage current, and breakdown voltage. Since the traps are located above the channel, there is usually little change in the dc or small signal parameters near the quiescent point. Further, since the traps are located beside the channel, Schottky-barrier height and the ideality factor often remain constant. This selective change in device characteristics helps distinguish hot-electron effects from thermal or environmental effects [8].

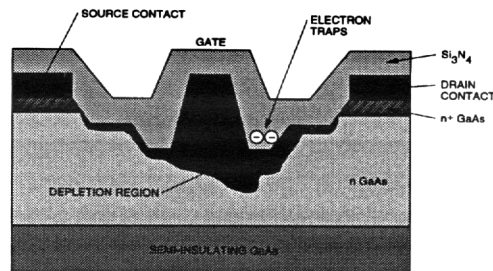


Figure 6. Schematic cross section of a degraded MESFET showing hot-electron-induced traps in the SiN passivation layer.

Hydrogen Effects: Degradation in I_{DSS} , V_p , g_m , and output power was observed on GaAs and InP devices tested in hermetically sealed packages or under hydrogen atmosphere. The source of the degradation has been attributed to hydrogen gas desorbed from the package metals (Kovar, plating, etc.). The exact mechanism by which hydrogen degrades the device performance and the path by which hydrogen reaches the active area of a device are not known and have been under investigation [9].

Earlier research, [18], on GaAs transistors identified the diffusion of atomic hydrogen directly into the channel area of the device where it neutralizes the silicon donors as the possible mechanism. It is believed that atomic hydrogen diffuses into the GaAs channel and forms Si-H , thereby neutralizing the donors. Experiments have shown that exposure of Si-doped GaAs to RF hydrogen plasma results in neutralization of the Si donors. Infrared spectroscopy data have also given evidence of $(\text{SiAs}_3)\text{As-H}$ complexes[19].

The neutralization of donors can decrease the carrier concentration in the channel, which, in turn, can decrease the drain current, transconductance, and gain of the device. Hydrogen effects in FETs with either Pt or Pd gate metals have been observed. Recent research has concluded that the diffusion of hydrogen may occur at the Pt side-walls and not at the Au surface of the Au/Pt/Ti gate metal[20].

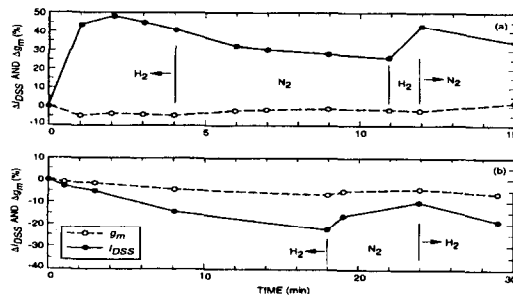


Figure 7. Changes in peak transconductance, g_m , and drain current at zero bias, I_{dss} , of (a) InP HEMT and (b) GaAs PHEMT under nitrogen and 4% hydrogen treatment at 270°C[21].

Other research, an example of which is shown in Fig. 7, on GaAs PHEMT and InP HEMT in a hydrogen atmosphere has shown that the drain current may increase in some cases. This observation has led to the conclusion that the hydrogen diffuses into the semiconductor surface where it is thought to change the metal-semiconductor built-in potential.

Manufacturers and users of GaAs devices used in hermetically sealed packages are currently pursuing an acceptable solution to this problem. Some of the possible solutions include thermal treatment of the packaging materials to reduce the amount of desorbed hydrogen after the seal, the use of hydrogen getter materials in hermetically sealed packages, and the use of barrier materials that do not contain the Pt/Ti or Pd/Ti structure. These solutions have limitations and possible instability problems that must be fully understood prior to implementation in high reliability systems.

Packaging Effects: The package serves to integrate all the components required for a system application in a manner that minimizes size, cost, mass and complexity. In doing so, the package must provide for mechanical support, protection from the environment, a stable thermal dissipation path, and electrical connection to other system components. For compound semiconductors, the package must satisfy all these characteristics and allow for reliable device performance over a wide range of conditions.

Understanding the packaging effects on the reliability of compound semiconductors is essential to attaining a reliable space system. In most applications, packaging of compound semiconductor devices is similar to that

developed for silicon based technologies. However, the choice of packaging materials plays more of a critical role due to differences in the coefficient of thermal expansion. In addition, compound semiconductors are more fragile and may exhibit mechanical stresses causing device degradation and failure.

The stability and reliability of the die attach is largely determined by the ability of the structure to withstand the thermomechanical stress created by the difference in the Coefficient of Thermal Expansion (CTE) between the die and the packaging material. These stresses are concentrated at the interface between the die and the die-attach material and the interface between the die-attach material and the package[12]. The Coffin-Manson relation relates the number of thermal cycles a die attachment can withstand before failure:

$$N_f \propto \gamma^m \{2 \cdot t/L \cdot \Delta CTE \cdot \Delta T\}$$

Where;

γ = shear strain for failure

m = constant dependent on the material

L = diagonal length of the die

t = die-attach material thickness

The number of thermal cycles before failure can be significantly reduced by the presence of voids in the die attach material, since voids cause areas of concentrated localized stress which can lead to premature die delamination. In addition, voids cause localized heating which in turn causes an increase in the thermal resistance of the die attach material leading to device degradation and possible catastrophic failure.

Infrared imaging techniques can provide for a qualitative and sometimes a quantitative measure of the adequacy of the thermal path and a visual representation and mapping of possible void locations. Figure 8 shows a comparison of an optical and an Infrared image of the same die.

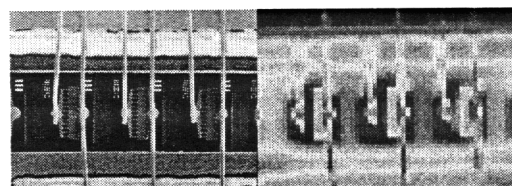


Figure 8. Optical(left) and IR image (Right) of the same die. The IR image shows thermal gradient and location of hot spots and possible void locations.

Radiation Effects: The use of microelectronic devices in both civilian and military spacecraft requires that these devices preserve their functionality in the hostile space environment throughout the mission life. An important feature of this environment is the presence of radiation of various types, including that from man-made sources. Unlike other aspects of reliability, radiation is unique and is not a requirement for nearly all other high-reliability applications, such as automotive, medical and terrestrial communications. Thus, because of the distinctive nature of the radiation environment, it is important to understand the effects of radiation on microelectronic devices and circuits used in space systems.

From the radiation point of view, the most important feature of GaAs is the lack of SiO₂ dielectric layers as gate insulators or as isolation insulators. In addition, the very high surface state densities typically found in the AlGaAs/GaAs system pin the Fermi level at the surface and effectively prevent radiation-induced surface inversion and its associated leakage currents from occurring. These differences result in GaAs devices being immune to total dose effects until very high doses are reached where the rare displacement damage events caused by Compton electrons formed from Co⁶⁰ gamma rays finally have an effect. GaAs being a direct band gap material, leads to the minority carrier lifetimes in GaAs being much less than those for Si. Thus, more displacement damage is required to affect GaAs devices that depend on minority carrier lifetime for their successful operation. The best example of this is the increased radiation hardness of GaAs solar cells relative to Si solar cells. In addition, the ability to perform "band gap engineering" in which layers of various materials can be grown on each other with little change in lattice constant, provides increased flexibility in the case of III-V materials relative to Si [10].

Ionizing Radiation Effects: As noted above, GaAs devices in general are relatively immune to total dose effects resulting from the deposition of ionizing energy. This is due to the absence of an oxide that can trap charge and alter the operation of the device. Tests have shown immunity to total dose effects up to 100 Mrad (GaAs). In contrast with the relative immunity of GaAs devices to total-dose effects, transient, high-dose-rate pulses can severely affect these devices. GaAs devices and circuits are typically

fabricated on semi-insulating GaAs substrates, which afford a natural isolation between individual transistors on the chip. However, in a transient radiation environment, this attractive feature becomes a liability because the transient photocurrents generated in the substrate are much larger than the transients generated elsewhere in the device as shown in Figure 9. In addition, if the semi-insulating substrate contains significant densities of deep traps, transient photo current effects can persist for a very long time.

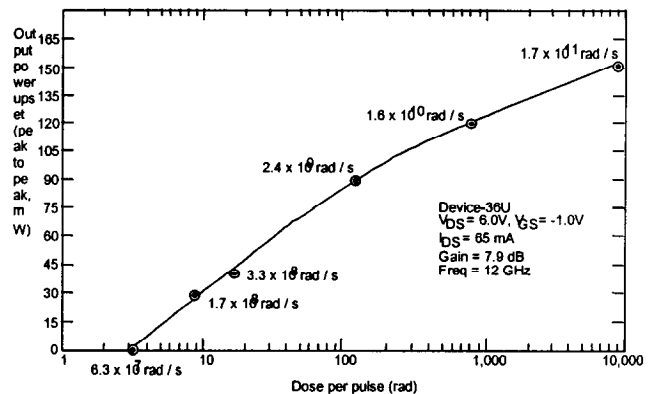


Figure 9. Response of MMIC amplifiers to transient electron pulses [14].

During the ionizing pulse, the large excess carrier densities that are generated in the semi-insulating substrate temporarily cause it to be a good conductor, allowing shunting of the transient photocurrent across transistor sources and drains. Under these conditions, upset levels in GaAs devices can be of the order of 10^{10} rad (GaAs)/s, or even less. Fortunately, these effects can be minimized by properly placing bonding pads and metal interconnects, and using various types of blocking layers [11].

Displacement Damage Effects: As pointed out earlier, GaAs devices are relatively insensitive to displacement damage effects when compared to Si devices. Generally, this is due to the shorter minority carrier lifetimes and higher doping levels found in GaAs devices and circuits. Since displacement damage introduction into the semiconductor material reduces the minority carrier lifetime, the mobility, and the carrier concentration, device properties that depend on these parameters will be affected by displacement damage. Generally, the longer the lifetime, the higher the mobility, and the smaller the carrier concentration the more effective

displacement damage is in altering these parameters. Thus, semiconductor devices with short lifetimes, low mobility, and high carrier concentrations will be relatively immune to displacement damage effects. GaAs has the characteristics of short lifetimes and high mobility. Therefore, we can expect GaAs device to suffer from reduction in mobility and carrier concentration as a result of displacement damage. Note, however, that greater amounts of displacement damage are usually required to cause carrier removal and mobility degradation.

Single Event Effects: Studies of charge collection in GaAs devices have shown the charge generated by a single particle can be collected by a greater variety of mechanisms than in Si devices. In GaAs MESFETs, the collection from deep within the device is limited because the recombination rate in GaAs is high and because the diffusion length is short due to small minority carrier lifetimes. However, relative to Si, this is offset by the fact that more regions of the device are sensitive than in the case of a Si MOSFET. In a GaAs MESFET, the source and drain regions are sensitive to upset as well as the gate region. Collection mechanisms for the various regions in the device are shown in Figure 10 and include a back channel turn-on mechanism, a bipolar source-drain collection mechanism, and an ion shunt mechanism. Fortunately, as in the case of photocurrent transients mentioned above, "band gap engineering" through the deposition of various blocking layers can minimize single event effects.

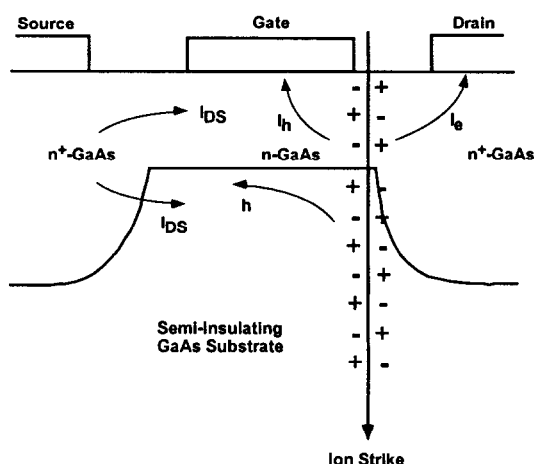


Figure 10. Single-particle-induced charge collection mechanisms in a GaAs MESFET [15].

Summary

The reliability and application of compound semiconductor devices in high reliability space systems requires a thorough understanding of the technology's reliability issues, failure mechanisms, relevance to the application, and methods for risk mitigation and qualification. Failure mechanisms related to materials, processes, environments and application of the devices should be considered. Also, an understanding of the effects of the radiation environment and the implementation of a meaningful qualification program is essential to assure successful insertion of this technology.

Acknowledgement

The work described in the paper was conducted at the Jet Propulsion Laboratory, California Institute of Technology, under contract with the National Aeronautics and Space Administration

References:

- (1) Kayali, S., Ponchak, G., and Shaw, R., *GaAs MMIC Reliability Assurance Guideline for Space Applications*, JPL Publication 96-25.
- (2) Ponchak, G., Kayali, S., and Huang, H., "The Development of a GaAs MMIC Reliability and Space Qualification Guide," *Monolithic Circuits Symposium Digest*, San Diego, CA, pp. 69-72, May 1994.
- (3) C. Canali, F. Castaldo, F. Fantini, D. Ogliari, L. Umena, and E. Zanoni, "Gate Metallization Sinking Into the Active Channel in Ti/W/Au Metallized Power MESFETs," *IEEE E. Dev. Lett.*, Vol. EDL-7, pp. 185-187, 1986.
- (4) J. Wurfl and H. L. Hartnagel, "Thermal Stability and Degradation Mechanisms of Ti-Pt-Au, Ti-W-Au and WSi₂-Ti-Pt-Au Schottky Contacts on GaAs," *Proc. 4th Int. Conf. Quality in Electronic Components*, Bordeaux, pp. 133-138, 1989.
- (5) J. C. Irvin, "Reliability of GaAs FETs," Ch. 6 in *GaAs FET Principles and Technology*, J. DiLorenzo and D. Khandelwal, Editors, Artech House, Mass., pp. 348-400, 1985.
- (6) A. Christou, "Reliability of High Speed HEMT Integrated Circuits and Multi-2DEG Structures," *Semiconductor Device Reliability*, A. Christou, and B. A. Unger eds., Kluwer Academic, pp. 454-555, 1990.
- (7) P.H. Ladbroke and S. R. Blight, "Low Field Low Mobility Dispersion of Transconductance in GaAs MESFETs with Implication for Other Rate-Dependent Anomalies," *IEEE Trans. El. Dev.*, Vol. ED-35, pp. 257-267, 1988.
- (8) Y. A. Tkachenko, Y. Lan, D. Whitefield, C. J. Wei, J. C. M. Huang, L. Aucoin, and S. Shanfield, "Hot-Electron-Induced Degradation of Metal-Semiconductor Field Effect Transistors," *Proc. Of IEEE GaAs IC Symp.*, pp. 259-262, 1994.
- (9) S. Kayali, "Hydrogen Effects on GaAs Device Reliability," *Int. Conf. On GaAs Manufacturing Technology*, San Diego, CA, pp. 80-83, 1996.

- (10) C. Barnes, and L. Selva, "*Radiation Effects in MMIC Devices*," Ch. 10 in *GaAs MMIC Reliability Assurance Guideline for Space Applications*, S. Kayali, G. Ponchak, and R. Shaw, editors, JPL Publication 96-25.
- (11) A. Meulenbergh, H-L. Hung, J. Singer, and W. Anderson, ""*Total Dose and Transient Radiation Effects on GaAs*," IEEE Trans. Elec. Dev., Vol. 35, p. 2125, 1988.
- (12) T. Tuhus and A. Bjorneklett, "Thermal Cycling Reliability of Die Bonding Adhesives", 1993 IEEE Annual International Reliability Physics Symposium. Digest, pp. 208, March 23-25, 1993.
- (13) F. Magistrali, C. Tedesco, E. Zanoni, and C. Canali, "Reliability Issues of Discrete FETs and HEMTs" Reliability of GaAs MMICs, A. Cristou, ed., John Wiley & Sons, New York, 1992.
- (14) A. Meulenbergh, H-L Lung, K. Patterson, and W. Anderson, " Total Dose and Transient Radiation Effects on GaAs" IEEE Trans. Elec. Dev., Vol. 35, P.2125, 1988.
- (15) J. Schwank, "Basic Mechanisms of Radiation Effects in Natural Space Environment" in 1994 IEE Nuclear and Space Radiation Effects Conf. Short Course, p.II-2, New York, 1994.
- (16) J.F. Bresse, "Reliability of the Structure Au/Cr/Au-Ge/Ni/GaAs in Low Noise Dual Gate GaAs FET," Microelec. Reliab., Vol.25,pp.411-424, 1985.
- (17) M. Omori, J. Wholey, and J. Gibbons, "Accelerated Active Life Test of GaAs FET and New Failure Mode," Proc. International Reliability Physics Symposium, pp.134-9, 1980.
- (18) J. Chevallier, W. Dautremont-Smith, C. Tu, and S. Pearton, "Donor Neutralization in GaAs(Si) by Atomic Hydrogen," Appl. Phys. Lett. 47, p.108, July 1985.
- (19) A. Jalil, J. Chevallier, J. Pesant, and R. Mostefaoui, "Infrared Spectroscopic Evidence of Silicon Related Hydrogen Complexes in Hydrogenated n-Type GaAs Doped with Silicon," Appl. Phys. Lett., Vol.50, No. 8, p.439, February 1987.
- (20) D. Eng, R. Culbertson, and K. Mac Williams, "The Effects of Hydrogen and Deuterium Incorporated on the Electrical Performance of GaAs MESFETs," Proc. 1995 GaAs IC Symposium.
- (21) P. C. Chao, M. Kao, K. Nordheden, and A. Swanson, "HEMT Degradation in Hydrogen Gas," IEEE Elec. Dev. Lett., Vol.15, No. 5,p.151, May 1994.
- (22) S. Kayali "Reliability of Compound Semiconductor Devices for Space Applications", Microelectronics Reliability, Vol. 39, P. 1723-1736, 1999.

Development of critical technologies for the COSMO/SkyMed Hyperspectral Camera

D. Labate*, F. Svelto§

* Alenia Difesa - Officine Galileo - Space B.U.
Via A. Einstein 35, I-50013 Campi Bisenzio (FI), Italy
Tel. +39-055 8950526 – Fax +39-055 8950613
email: demetrio.labate@officine-galileo.finmeccanica.it

§ Agenzia Spaziale Italiana
Viale Liegi, 26 - 00198 ROMA
Tel. +39-06 8567338 – Fax +39-06 8567328
email: svelto@asi.it

Summary

COSMO/SkyMed is a spaceborn program primarily dedicated to Earth observation, remote sensing and data exploitation for risks management, defence and intelligence applications and coastal zone monitoring. This program is going on under a contract of Agenzia Spaziale Italiana (ASI) that foresees also the development of critical technologies.

In the frame of this program, Officine Galileo is involved in some technological studies devoted to finalise the design of a hyperspectral camera (HYC) that will be part of the mission payload.

An instrument with state-of-art performance but with reduced mass, volume and power budgets is the challenging aim of these studies.

The major tasks performed are:

- manufacturing of very light mirrors with special emphasis on Silicon Carbide (SiC) material technology.
- development of electronics blocks at high integration level with the necessary speed for the acquisition and processing of the large amount of hyperspectral data
- testing of high quantum efficiency array detectors

The developed or under test subsystems are all parts of the HYC.

This paper presents just an overview of the camera design and it will focus on these subsystems development studies.

Introduction

Hyperspectral space imagery is an emerging technology but it has already proven it can support many scientific, civil and operational applications.

As technology of more sensitive detectors is rapidly evolving, the design of state-of-the-art hyperspectral imagers is getting more and more a challenge for sensor builders.

Officine Galileo is actively involved in this field [1] and in the development of relevant critical technologies.

In particular, at the moment Officine Galileo is developing a Hyperspectral Camera that will be part of the optical payload of the COSMO/SkyMed mission.

To improve the know-how background in the specific field, Officine Galileo has recently set up a program of technological development. This program, currently going on, was defined with the support of ASI.

Many issues have been dealt with during the study, but the major efforts have been devoted to:

- Review and implementation of state-of-the-art manufacturing techniques for light components (SiC or lightweighted Zerodur mirrors, carbon fiber structures).
- High velocity electronics components at high integration level (including digital and analog ASICs).
- Performance testing and verification of detectors with high quantum efficiency (CCD Backside illuminated and Hybrid CMOS). This is an essential requirement to get high SNR levels from a hyperspectral instrument with small spatial and spectral resolution.

At the moment all these studies are in the final phase of testing of the manufactured or purchased components.

The results obtained in terms of innovative design, improvements in manufacturing technique and breadboarding activity are presented in the next paragraphs following a short description of HYC.

Hyperspectral Camera Overview

The HYC is an instrument that utilises a pushbroom technique to get strip spectral images over the VNIR ($0.4 \div 1.0 \mu\text{m}$) and SWIR ($1.0 \div 2.5 \mu\text{m}$) regions.

The camera includes also a complementary Panchromatic Channel (PAN) ($0.4 \div 0.75 \mu\text{m}$).

Fig.1 shows a block scheme of the instrument, while Table 1 summarises its main characteristics.

The design of the HYC camera utilises a TMA (Three Mirrors Anastigmat) Telescope, common to all three channels, composed of three lightweight aspherical mirrors, with entrance aperture of 150 mm.

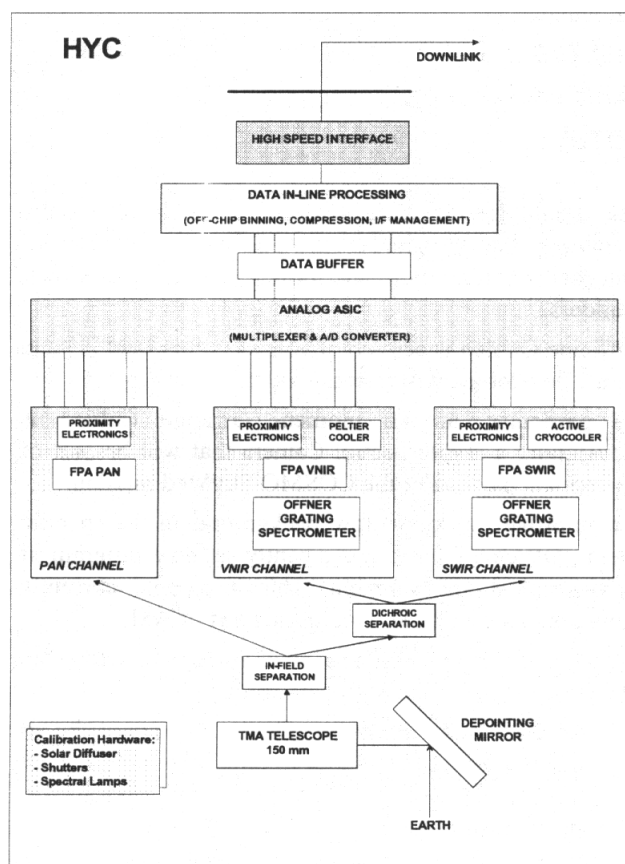


Fig. 1 - HYC Block Diagram

The telescope images a 20 km wide ground swath onto a beam slitting element that performs two different operations:

- In-field separation between PAN and VNIR+SWIR channels
- Spectral separation before spectrometer entrance slits between VNIR and SWIR

Each image taken during the acquisition time captures the spectrum of a line perpendicular to the satellite motion and a ground sample distance (GSD) at nadir of 20 m for VNIR, 40 m for SWIR.

The light spectral dispersion is obtained by two Offner grating spectrometers with nominal spectral resolution of 10 nm for both channels.

Therefore the maximum number of available spectral channels of 210 (60 for VNIR, 150 for SWIR).

The detectors used are :

- VNIR: backside illuminated CCD-2D or Hybrid CMOS matrix array (1000 x 120 useful pixels);
- SWIR: CMT-2D focal plane (500 x 150 useful pixels) cooled by pulse tube Stirling cycle cryocooler.

For applications for which a better radiometric accuracy (e.g. sea measurements) is preferable respect to a high spatial resolution, it is possible to combine up to 4 pixels in VNIR band and up to 2 pixels in SWIR. In this case a lower spatial resolution of 80 m in both bands is obtained. Moreover, better SNR performances can be obtained also by means of spectral bands combination (spectral binning) so that larger spectral resolutions can be selected.

The PAN channel, that produce images at about 7 m GSD, utilises a 4000 pixel long linear array placed into the telescope focal plane.

A pointing mirror, that can be pointed $\pm 22^\circ$ in the across track direction, allows the extension of the viewed area up to ± 250 km (with the assumption of an altitude of 619 km). The quite large dimension of this mirror (quasi elliptical shape - 320 x 160 mm) makes mandatory the use of light material.

Two different operating modes are foreseen for the HYC (Fig. 2):

- **Strip mode:** the pointing mirror is kept in the selected angular position and a spectral image of a strip 20 km in width is provided.
- **Mosaic mode:** the mirror motor can be controlled in a predefined sequence of angular positions, so that the area of interest is covered with a mosaic image. The mirror needs just 3 sec to change its orientation and this allows quick switches in observed zone.

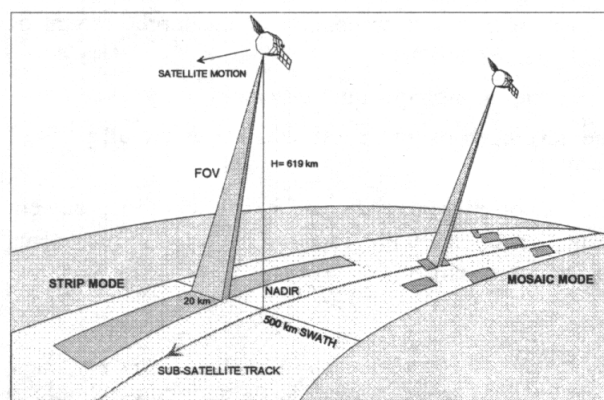


Fig. 2 - HYC Operating Principle

<i>HYC Parameters</i>	<i>VNIR Channel</i>	<i>SWIR Channel</i>	<i>PAN Channel</i>
Scanning Mode	Pushbroom		
Spectral Range [nm]	400-1000	1000-2500	400-750
Spectral Resolution [nm]	10-20	10-20	NA
Swath Width [km] / FOV	20 / 1.85°		
GSD [m]	20-80	40-80	7.7
Covered Area [km]	500		
Spectral Bands	60	150	1
Aperture Diameter [mm]	150		
Focal Length [mm]	557		
F#	3.7		
Detector Pixel Size [μm]	18	18	7
Array Dimension (useful pixel)	1000 x 120	500 x 150	4000 x 1
FPA Type	Si CCD Backside	Cooled CMT	Si CCD
Quantization [bit]	12	12	12

Table 1 - HYC Main Specifications

The manufacturing of the pointing mirror and of the telescope (aspherical mirrors and structure) with lightweight materials was one of the main subject of the technological developments.

The HYC is essentially composed of the following units:

- Optomechanical head (HO) which includes:
 - Scanning Mirror and motor/encoder assembly
 - Telescope
 - Spectrometers (VNIR and SWIR)
 - FPAs (VNIR, SWIR, PAN)
 - Calibration Hardware
 - Baffles
 - Thermal control components (radiator, coolers, thermal blankets)
- Three FPA proximity electronics boxes (one for each detector)
- Main electronics box for:
 - Digital electronics
 - PDU & Mirror control

Fig. 3 and Fig. 4 show respectively the optical system layout and the optomechanical structure of the HO.

The optical systems and the proximity electronics elements are housed in a mechanical structure realised with CFRP (carbon fiber) trusses and plates. The main optical elements, i.e. telescope and spectrometers mirrors, will be realised in light material as SiC or lightweight ceramic glasses (e.g. Zerodur™ Schott).

The overall dimension of the optical head is about 1080 x 550 x 590 mm.

The instrument mass, including all the electronics boxes (main and proximity electronics) is less than 100 kg.

The power consumption is:

- 115 W during acquisition mode
- 110 W in calibration mode
- 60 W in standby mode

The Signal-to-Noise ratio (SNR) of this instrument has been estimated at different radiance conditions using a radiometric model that accounts for the characteristics of the optical system, focal plane arrays and electronics, including digitization.

Table 2 reports some typical SNR values at nominal GSD and spectral resolution.

<i>Channel</i>	<i>SNR</i>
VNIR (0.55 μm -0.70 μm)	200
SWIR (1.0 μm -1.05 μm)	100
SWIR (1.20 μm -1.25 μm)	100
SWIR (1.55 μm -1.60 μm)	100
SWIR (2.10 μm -2.15 μm)	50
PAN	300

Table 2 – HYC SNR

Assumption: 30% Surface reflectance, 60° Solar Zenith, 45° Latitude Scene, Atmospheric Model: Mid Latitude Winter, Aerosol model: rural visibility 23 km.

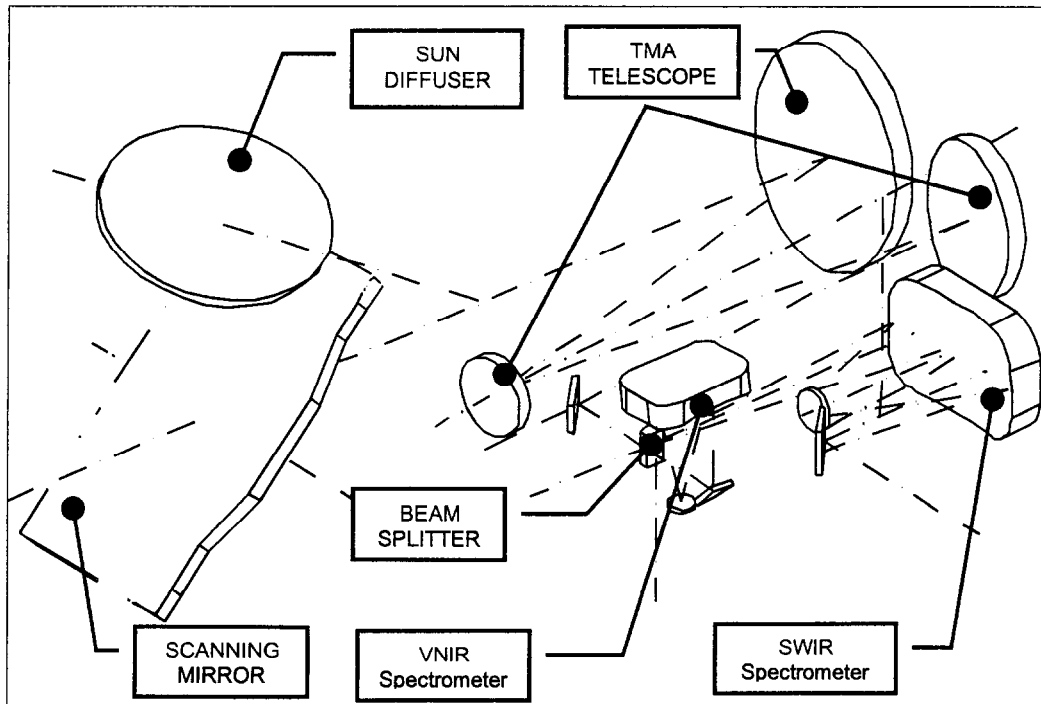


Fig. 3 – Optical System Layout

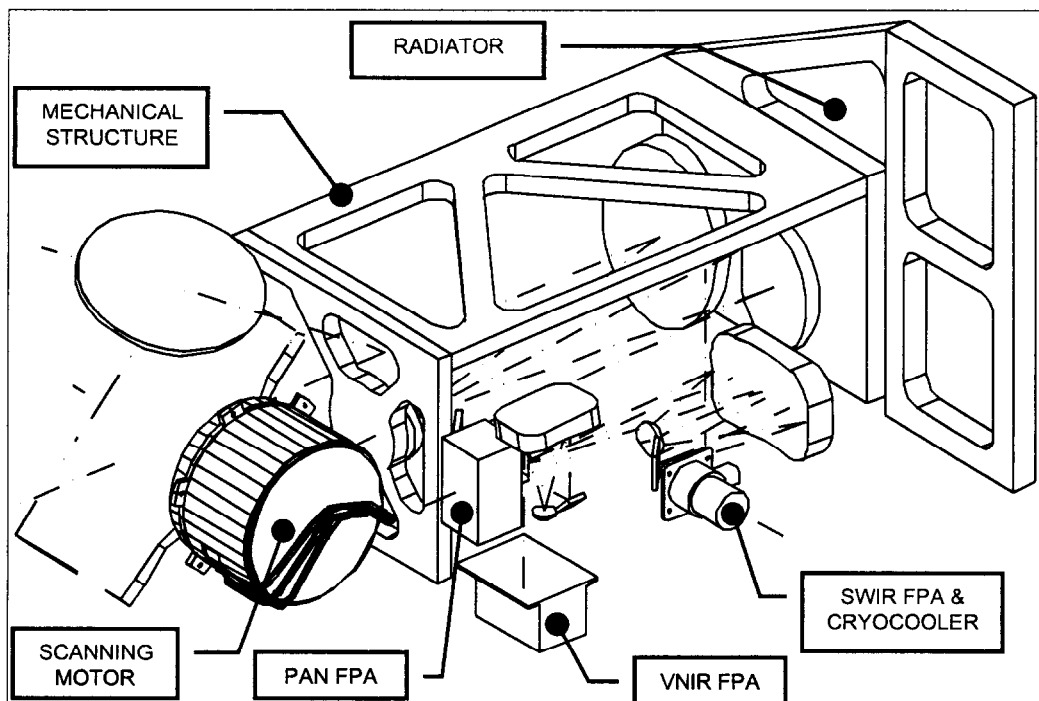


Fig. 4 – Optomechanical Layout

Lightweight Structures Development

An area of research and development has been dedicated to selection design solutions, materials and to development of processes for lightweight optomechanical structures.

A special emphasis was given to the use of SiC as substrate for reflective optics and for optics supports.

SiC offers a unique combination of critical properties, relative to other more traditional optical materials: high stiffness, high toughness, low thermal distortion, low toxicity and potential cost and schedule advantage.

There are several forms of SiC (i.e. Cold Pressed or Hot Pressed Sintered, Reaction Bonded, CVD-Chemical Vapour Deposited) corresponding to different manufacturing processes of the blanks.

The Cold Pressed-Sintered SiC has been selected as baseline process for the HYC pointing mirror (Fig. 5).

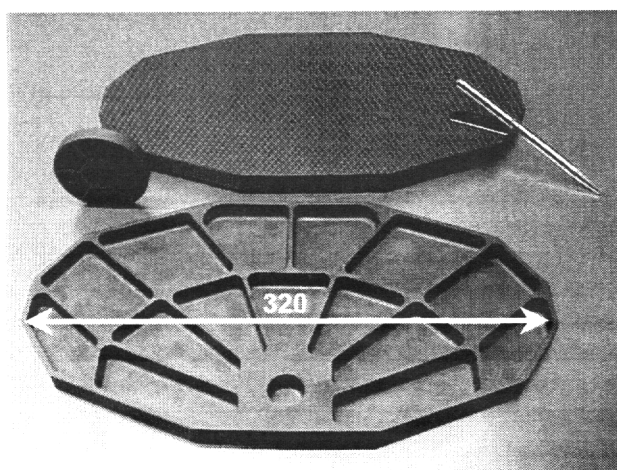


Fig. 5 - Prototypes of the SiC Pointing Mirror

This SiC can be bare polished up to the required specification of roughness. If necessary, it is also possible to further reduce the residual light scattering of the optical surface by coating the SiC substrate with the best polishable SiC-CVD layer that is without any CTEs (Coefficient Thermal Expansion) mismatch. Performance at cryogenic conditions of the mirror has been tested by interferometers placed in front of a vacuum chamber. In case of narrow operative temperature range, the expensive SiC-CVD layer can be substituted with electroless nickel plating, by using processes specially developed to deposit the nickel on SiC surfaces.

An alternative and more sophisticated technological solution has been considered also for mirror substrates, formed by a sandwich structure composed of two SiC face sheets deposited on a foam core of the same material (Fig. 6) [2]. Using this process to manufacture

mirrors it is possible to reach even better performance in terms of weight and stiffness. The potentiality of this technology and its advantage respect to the traditional manufacturing techniques becomes accentuated as the size of the mirror blank increases. The realisation and test of prototypes of the pointing mirror with this solution are in progress also. The above mentioned solutions has been developed in collaboration with Italian manufacturers of ceramic products.

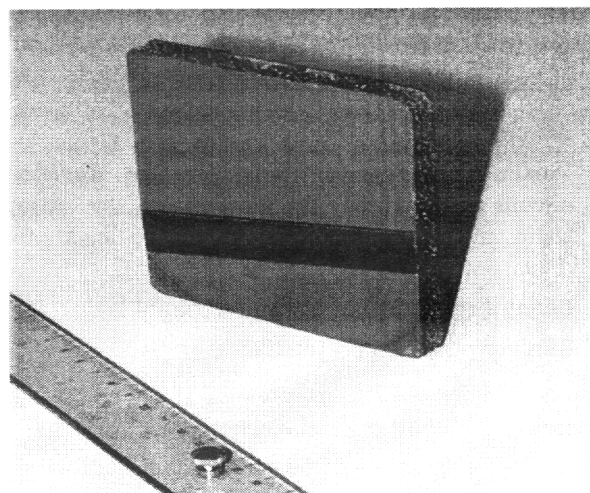


Fig. 6 - Mirror Substrate in SiC Foamed-core Sandwich

For what concerns the TMA Telescope of HYC, a more traditional solution has been adopted for the baseline, using mirrors in Zerodur™ and a metering structure in CFRP. Nevertheless, a dedicated investigation was carried out to get the highest lightening factors on the Zerodur mirror substrates. Several samples of the TMA telescope mirrors were realised to test the manufacturing capabilities and the achievable performance (Fig. 7).

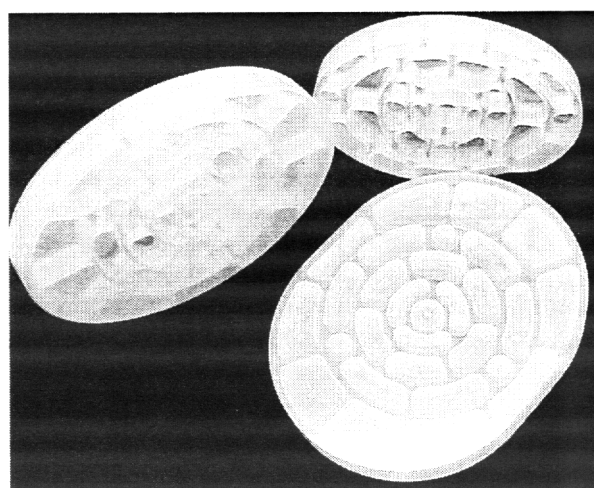


Fig. 7 - Lightweight substrates in Zerodur for TMA telescope mirrors

VNIR Electronics and Focal Plane Development

A very critical point of the design of hyperspectral instruments is the need to manage a great amount of data coming from the detectors.

For this reason particular effort was devoted to the development of the entire electronics chain. The study has started with the design of the VNIR channel, but many of the results of considerations presented here after can be applied also to the SWIR one.

The block diagram of the VNIR channel is reported in Fig. 8:

The electronics contains the following main parts:

- detector
- Proximity Electronics, formed by the front-end circuits to drive and bias the detector, the analog chain and signal processor up to the analog-to-digital conversion
- timing sequencer and acquisition control logic
- data and power supply interfaces

The task of the VNIR channel electronics is:

- to capture the image of the earth in its field of view
- to provide the downstream electronics with the amplitude of the pixels belonging to the addressed wavelengths [spectral editing] with the commanded grouping/binning

Considering the high data rate of the hyperspectral channels, the electronic architecture has been based on the possibility to put in parallel modules both for analog processing and for data in-line processing.

This approach allows increasing of N times the spatial resolution on ground of the instrument, where N is the number of modules in parallel. In fact it's impossible to begin a new readout of the detector before the end of the previous one, therefore the readout time represents a lower limit for the exposition time. To obtain the requested spatial resolution of 20 m, a maximum exposure time of about 2.9 msec is needed. The pixel acquisition rate of the analog processor is 3 MSPS. Hence, the complete readout of the maximum detector window of interest, formed by 120 lines with 1000 pixel per line, takes about 40 msec, giving a minimum spatial sampling interval of about 280 meters.

Using a N-ports (taps or outs) detector, the analogue processor throughput can be increased by N and the spatial sampling interval can be decreased approximately by N. For a detector with 4 outputs, the equivalent pixel rate becomes 12 MSPS with a readout time of 10 msec and a SSI of 70 meters. Consequently, as shown in Table 3, a 16 outputs detector is needed to obtain the requested spatial resolution of 20 m.

<i>N° of Detector Outputs</i>	<i>Readout Time</i>	<i>Maximum Spatial Resolution</i>
1	40 msec	280 m
4	10 msec	70 m
8	5 msec	35 m
16	2.5 msec	17.5 m

Table 3 – Resolution vs. detector number outputs

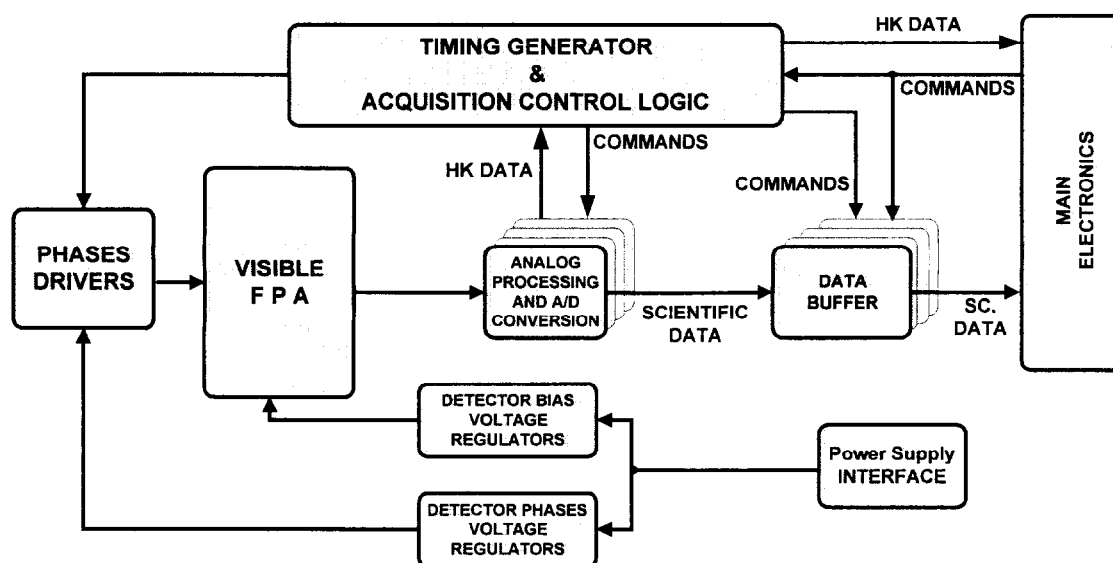


Fig. 8 – VNIR Focal Plane Electrical Architecture

Analog processing

The design of the analog processing electronics is essentially formed by modules already used and qualified in previous programs, with the addition of a new developed analog ASIC for detector signal conditioning, sampling and digitalisation.

The use of this ASIC is in line with the trend to reduce the size, weight and power consumption of digital imaging sensors and electronics for spaceborne systems. This trend is emerging in the market, due to the improvement in the micro-electronics technology and to the introduction of the 3D technology. The goal of this approach is to produce a 10x reduction in imaging sensor size, weight and power over the today's focal plane units.

As it can be seen from the block diagram (Fig. 9), the new analog ASIC contains all the main functions necessary to process a signal outgoing a photodetector. A CDS channel is provided to be used with CCD detectors, while 7 High Speed Sample and Hold channels are provided to be used with CMOS detectors. These channels can also be used to process and convert housekeeping (HK) signals. All the channels are equipped with a Programmable Gain Amplifier (x1 – x4). A multiplexer stage selects one of the 8 channels to be converted with 12 bits resolution. A 6 bits control code (Hamming) is provided together with the output. In the ASIC is also integrated a D/A converter, that can be useful for many practical applications. The component is realised in DMILL technology, it's latchup free, and it can withstand a total dose of about 1Mrad(Si).

The main characteristics of the new analog ASIC, are listed below:

- 12-Bit 3 MSPS A/D Converter
- 12-Bit 200 nS D/A Converter
- 1 integrated CDS with programmable gain amplifier (PGA, x1 – x4)

- 7 High Speed S/H channels with programmable gain amplifier (PGA, x1 - x4)
- 8:1 Multiplexer
- 12 bit output with 6 bit Hamming code
- Low power consumption: 400/500 mW max.
- RH Device: DMILL Technology.
SEU tolerance $\geq 70 \text{ MeV/mg/cm}^2$.
Total Dose $\geq 1 \text{ Mrad(Si)}$.
Latchup free.

At this moment this ASIC is going to be delivered to Officine Galileo for the testing phase.

Detector

In the frame of the technological program, several kinds of detectors have been taken in consideration. A market survey has been performed on COTS components, and finally two detectors have been selected to be tested in OG: the Sarnoff VCCD512H (512 x 512 Back Side Illuminated CCD) and the Rockwell TCM6600 (640 X 480 Hybrid CMOS).

The Sarnoff VCCD512H is a multiport detector with split storage architecture, projected to work with very low noise levels and high readout frequencies. The architecture of the device is illustrated in Fig. 10.

Each of the two readout registers presents 8 outputs, for a total of 16 outputs, each provided with an integrate CDS amplifier, eventually by-passable to use an external CDS circuit. This type of architecture, together with an elevated charge transfer rate, allows obtaining an extremely high frame rate (up to 800 frames/sec with binning and grouping X2). The detector structure is of back side illuminated type, with a silicon thickness of about 10 μm , and it allows to obtain a very high level of quantum efficiency in a spectral range from 350nm to 1000nm.

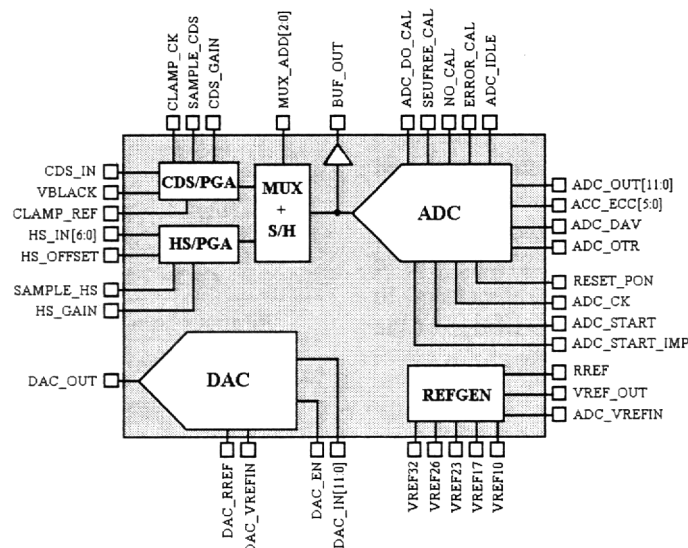


Fig. 9 – Analog ASIC functional block diagram

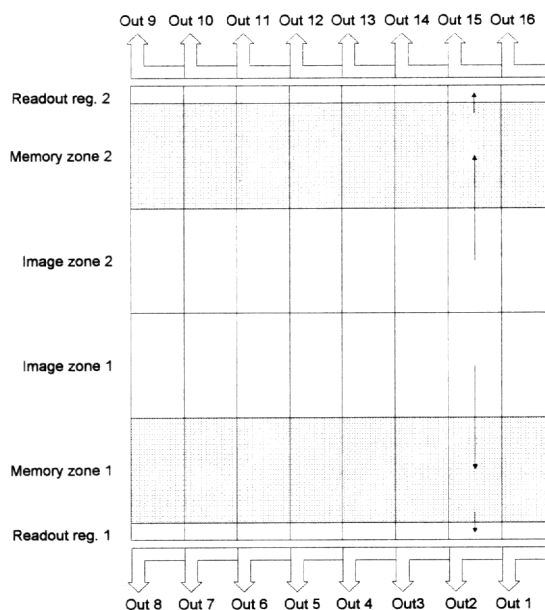


Figure 10 – VCCD512H architecture

The dimensions of the pixel are $18\mu\text{m} \times 18\mu\text{m}$, and the optic fill factor is about 100%. In the device a lateral anti-blooming drain is present on each pixel, that guarantees a good control on overexposure levels of up to 5000X. The manufacturing process used by Sarnoff guarantees a level of dark current in the order of 0.5 nA/cm^2 at ambient temperature without the use of MPP technology.

These technical characteristics match very well with those required for the VNIR channel, with the only difference in the number of pixels. In fact, the image zone has to be formed by at least 120 lines with sensitive 1000 pixels, but the technological step doesn't seem critical.

The Rockwell TCM6600 is a Hybrid detector, in which a matrix of revealing PIN is connected at pixel level to a CMOS readout multiplexer (ROIC) by means of Indium bumps. This allows the PIN diodes to inject the accumulated photocharges in the ROIC, where the input circuits, realised with a CTIA architecture (capacitive Trans-Impedance Amplifier), can convert them in a voltage signal. The pixel signals are then multiplexed and put out one at a time. The maximum frame rate is 100 frames/s, involving a pixel rate of about 5.5 MHz. The dimensions of the pixel are $27\mu\text{m} \times 27\mu\text{m}$. Also in the TCM6600 an anti-blooming structure is present. In Table 4 are summarised the main characteristics of the two detectors.

Test equipment

A complete equipment, that allows to obtain all the necessary measures in a totally automatic way, has been developed for both the detectors. In Fig. 11 a schematic block diagram of the test equipment 11 is depicted.

The system is based on the possibility to drive the focal plane electronics and to acquire the outgoing frames with a PC, using some appropriate I/O boards. In this way it is possible to program an appropriate sequence of acquisitions and to process the outgoing data in the PC.

It has been developed a dedicated software that allows to acquire the necessary images, with the requested operating conditions (window of interest, gain, offset, scan sequence), and to run the appropriate procedures on the outgoing data.

Thanks to the use of an optical bench, it is possible to obtain all the illumination conditions requested by the procedures. In this way, all the required measures can be obtained in a fully automatic way.

<i>Parameter</i>	<i>VCCD512H</i>	<i>TCM6600</i>
QE (600-800nm)	$\geq 60\%$	$\geq 80\%$
Full Well	$\geq 700 \cdot 10^3 \text{ el.}$	$\geq 650 \cdot 10^3 \text{ el.}$
PRNU	$\leq 5\%$	$\leq 5\%$
DSNU	$\leq 10\%$	$\leq 10\%$
Dark Current (293K)	$\leq 500 \text{ pA/cm}^2$	$\leq 1 \text{ nA/cm}^2$
Fixed Pattern Noise	None	$\leq 5\%$ of Qsat
CTE	$\geq 96\%$	NA
Readout Noise	$\leq 30 \text{ el.}$	$\leq 100 \text{ el.}$
Pixel Pitch	$18 \mu\text{m}$	$27 \mu\text{m}$
Output Taps	16	1

Table 4 – Main characteristics of the selected detectors

The test activities are currently in progress.

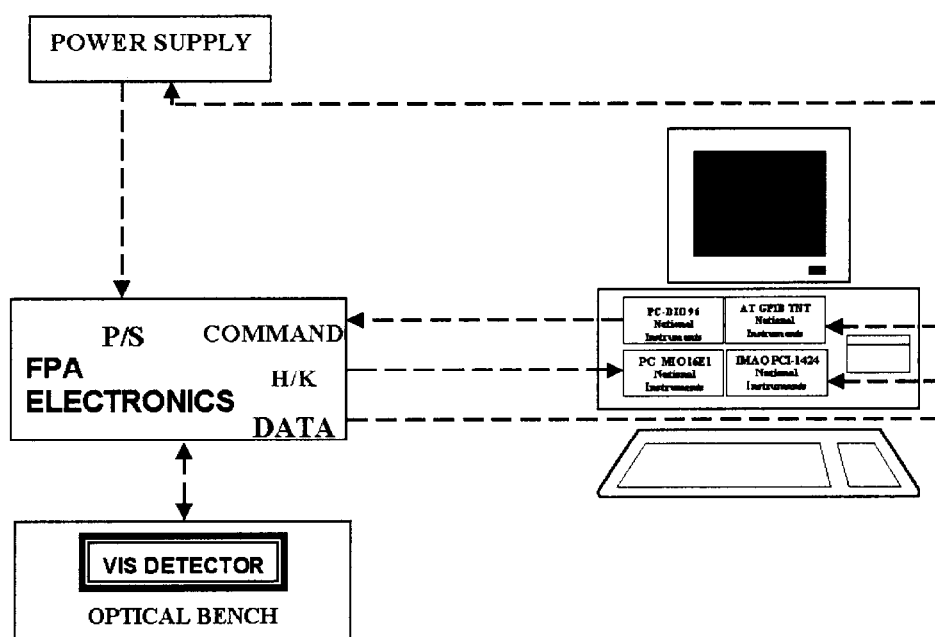


Figure 11 – Test equipment block diagram

Conclusion

The development currently going on will provide Officine Galileo with part of the technological background necessary to set up a challenging remote sensing mission.

The innovations coming from the study are enabling Officine Galileo to design and realise a flexible state-of-the-art instrument.

First use of this instrument will be the demonstration of the potentiality of the satellite hyperspectral technique that in a near future could satisfy different needs for a wide range of applications ranging from scientific studies of the Earth to civilian/military uses.

Acknowledgements

The authors of this paper represent all the people involved in the technological developments and design of this instrument. This work virtually belongs to them.

In particular, we would like to mention the following people of Officine Galileo:

Giuseppe Basile, Giovanni Cherubini, Fabio Fabbri and Massimo Attino for their contribution in the definition of the mechanical aspects and servomechanism design; Moreno Stagi, Francesca

Moretti and Stefano Puccini for the electronics design and ASIC development; Andrea Romoli for the optical system design.

The authors wish to particularly thank Andrea Novi and Fabio Brandani for their direct contribution to the drawing up of this paper (not to mention their considerable design and development work).

This work was carried out in the frame of ASI contract for COSMO/SkyMed Technological Development.

References

1. R. Bonsignori, M. Dami, D. Labate, A. Mariani "Hyperspectral Sensors for Earth and Planetary Observation at Officine Galileo", *50th International Astronautical Congress, 4-8 October 1999, Amsterdam, The Netherlands*
2. O.Citterio, A.Novi, R.Buzzi, G.Parodi "Light Weight SiC Foamed Mirror for Space Applications", *Liegi, June 1998, ESA- NGST Proceedings, Vol. SP-429, pag. 189-193*

Characterization of infrared detectors for space applications

Didier Dantès

Alcatel Space Industries, 100 Bd du Midi, 06156 Cannes la Bocca Cedex, FRANCE

ABSTRACT

Over the past decade, Alcatel Space Industries has become Europe's leader in the field of optical payloads for space applications : earth observation in the infrared spectral range, early warning systems, optical payloads for meteorology and sciences. This position was made possible by Alcatel Space Industries' will to develop the assets required for mastering the key performances of optical payloads, i.e. geometrical, modulation transfer function, radiometric and spectral performances. Infrared detectors have a heavy weigh in the performances of infrared payloads, and this leaded Alcatel Space Industries to perform very accurate characterization of infrared detectors.

This paper looks at those figures of merit of infrared detectors which are of interest to optical payload's performances. These parameters are detector sensitivity and associated dispersions, temporal noise and associated dispersions, contributors to spatial noise (pixel to pixel variation of non linearity, spectral response, 1/f noise, dark level variation versus temperature,...), frequency response, modulation transfer function, geometrical detector performances.

The techniques required for detector characterizations compliant with the required accuracies for each of these parameters are described. Performances of test benches available at Alcatel Space Industries are presented, with associated performances: vacuum chambers and cooling test sets, optical sources for radiometric and MTF measurements, electronics for detector power supply, clock generation, video and image processing.

Keywords : infrared detectors, detector characterization, detector performances

1. INTRODUCTION

Alcatel Space has developped a wide experience in the field of infrared for several type of applications, scientific, meteorology, and military. In each of these applications, the detectors have a very important weigh in the performances of the optical payload, requiring very accurate characterizations of infrared detectors.

A first part of this paper presents the detector figure of merits which are of interest to optical payload's performances, focusing on the radiometric performances for which the detector is the main contributor in most applications.

The test benches used to perform the characterizations and the associated performances are described in a second part of this paper.

2. DETECTOR FIGURES OF MERIT

In any type of application the performances of optical instrument may be resumed by:

- its radiometric and spectral performances,
- its MTF performances,
- its geometrical performances.

These performances impact directly the image quality expected by user, even if each of them have a different weigh with respect to the type of application. It is possible to identify the detector figures of merit which contribute to each of these instrument level performances.

2.1 Geometric parameters

Detector geometric performances are not easly described by generic figures of merit, and depend closely of the application and of the detector type. Single monoelements or several associated monoelements geometry description may be very different from linear or 2D arrays. However, for detectors having a large number of photoelements, several families of geometric parameters may be identified:

- Parameters describing the photoelement: they are related to the detector MTF described hereafter, and give the sensitivity in each spatial direction.

- Parameters describing the distribution of the photoelements centers. These directly impact the instrument geometric performance. These parameters are defined with respect to the theoretical distribution of the pixel centers, and will have at least maximum and standard deviation in each direction (x and y).
 - Parameters describing the flatness of the detector: they have an impact on the instrument MTF.
 - Parameters describing the coordinate of "average detector" (1D or 2D) with respect to mechanical origin and axes.
- The test sets dedicated to the measurements are not described in this paper, as they are closely dedicated to a specific application.

2.2 MTF parameters

Detector MTF is related to several other figures of merit which are used to characterize infrared detectors.

In the previous paragraph, we have already identified that the geometrical sensitivity of the photoelements in the x and y direction are closely related to the detector MTF. The shape of this sensitivity curve is directly related to the MTF, the vertical edges being associated with the theoretical MTF for a given pixel size.

Parameters like diaphoty (detection in neighbouring pixels due to photon/optical effects), diaphony (detection in neighbouring pixels due to electron/electrical effects) and crosstalk (summing effects of diaphoty and diaphony) also contribute to MTF performance but do not contribute to a better understanding of detector performances, unless in case of high photon flux for which MTF may be difficult to measure directly.

Diffusion is also a parameter which contributes to detector MTF, and quantifies the signal in the non illuminated zones due to optical reflexions or to electrical diffusion inside the detector.

All of these parameters may be required to be measured depending upon the type of applications. Nevertheless, in applications for which the capacity to discriminate spatial frequencies is of interest, the MTF is the most representative of detector performances, and include all the possible effects.

The accuracy which can be obtained in the measurement of infrared detectors MTF with classical methods are given in the following paragraphs.

2.3 Spectral parameters

Spectral parameters are in most of the applications closely related to the radiometric performances. The most important are:

- Spectral response, which contributes to the instrument selectivity of a specified spectral range.
- Pixel to pixel spectral response dispersion, which contributes to the instrument radiometric performances and has to be taken into account in the instrument calibration philosophy.

The methods used in Alcatel Space to measure these parameters are based on on-the-shelves test sets, and will be described very briefly in this paper.

2.4 Radiometric parameters

Radiometric requirements can be very different from one application to another. However, it is possible to identify the detector parameters which will be of interest for any of these applications, with different weights for each case.

The detector sensitivity may be expressed in several unities which are all strictly equivalent and which are chosen according to the type of detector and for the performance which is of interest:

- Responsivity in V/W or A/W.
- Quantum efficiency.
- Detector signal output (in V, A, e-) for a given optical energy.

For infrared detectors, like several other parameters, the detector sensitivity closely depends upon its temperature. The accuracy obtained in the measurement of the detector sensitivity and its associated temperature are described in the following paragraphs.

Two sources of noises can be identified: the temporal sources and, for detectors having a number of pixels higher than one, spatial sources coming from a non perfect correction of the pixel to pixel sensitivity dispersions.

Temporal sources of noise that must be taken into account in most of the applications may be resumed by:

- photonic shot noise, due to optical signal and stray light,
- detector dark current, Johnson and 1/f noises,
- detector readout electronics Johnson, kTC and 1/f noises,
- thermal regulation noise.

The theoretical values for each of these noises depends on the type of detector (thermal, quantum photovoltaic or photoconductive), on the type of readout electronics (CCDs, CMOS multiplexors, amplifiers adapted to the detector impedance) and of the spectral range (in most of the cases thermal constraints increasing with the spectral range). However, these terms may be used to characterize any detector for space applications, and the theoretical approach must be completed by measurements, with an accuracy which will be described in the following paragraphs.

Spatial sources of noise are related to a non perfect correction of the pixel to pixel dispersions. These type of noises concern applications using detectors with a large number of pixels, long linear arrays or 2D arrays, and they increase with the spectral range. The detector parameters which must be quantified in order to master the contribution of spatial noise in a given application are:

- Dark current variation with temperature and associated pixel to pixel dispersion.
- Signal variation with temperature and associated pixel to pixel dispersion.
- Non linearity of the signal with respect to the optical flux, and associated pixel to pixel variation.
- Pixel to pixel differential 1/f noise.

The measurement of such parameters are closer from accurate signal levels measurements than from noise measurements. The techniques used to measure these parameters and associated accuracy will be described in the following paragraphs.

The measurements related to other detector parameters which are more specific to one application are not described in the present paper: frequency response, saturation, effect of polarization on the sensitivity. The figures of merit which are a combination of sensitivity and noise, Noise Equivalent Power, Noise Equivalent Irradiance, Specific Detectivity are not discussed in the present paper and not commonly used in detector characterizations in Alcatel Space, as we consider that they are not the best suited figures of merit for a deep understanding of the detector performances.

3. CHARACTERIZATION OF INFRARED DETECTORS

3.1 Detector characterization

For each of the parameters described in the previous paragraph, several types of test sets and test procedures can be identified. The tests sets available in Alcatel Space are described in § 3.2, and the performances achieved in the measurement of the detector parameters are described in § 3.3.

Measurement of the spectral parameters may be performed by a monochromator associated with a blackbody and a reference detector, or by a Fourier transform spectrometer using the interferences from two reflecting surfaces to detect the energy at a given wavelength. Even if comparison have been made between the two methods which shows that the spectrometer allows a better accuracy, the well known and mastered monochromator solution is currently used for our applications.

For measurements of detector MTF, several tests sets are possible: spot scanners, line scanners and knife edges. trade offs have been performed and the knife-edge configuration has been the most currently used due a better accuracy in the detector MTF for a given spatial frequency and the characterization of detector behaviour for a higher number of spatial frequencies.

For measurements of radiometric parameters, the most accurate configuration uses a blackbody whose radiance can be accurately calculated from its temperature, with no focusing optics inserted between the blackbody and the detector under test. In any radiometric test configuration, the blackbody has to operate in vacuum to prevent degradations of radiance due to convection and atmospheric transmission effects.

In most of the cases, the infrared detector has to be operated at a low temperature and requires to be mounted in a dewar. For radiometric measurements, the blackbody also needs to be cooled and requires a vacuum chamber.

The vacuum chambers available in Alcatel Space allow all possible configurations: detector and blackbodies in the same vacuum chamber operating at two different temperatures, detector in its own dewar coupled with optics in a vacuum chamber. In any case, the solution retained for cooling any of the devices is based on the use of liquid Nitrogen and Helium associated to a thermal regulation, and has the advantage compared to active coolers solutions to be more flexible and adapted to any application, well mastered and easy to operate.

3.2 Test sets in Alcatel Space

Figure 3.2.a shows a classical radiometric test configuration. The main subsystems are described hereafter.

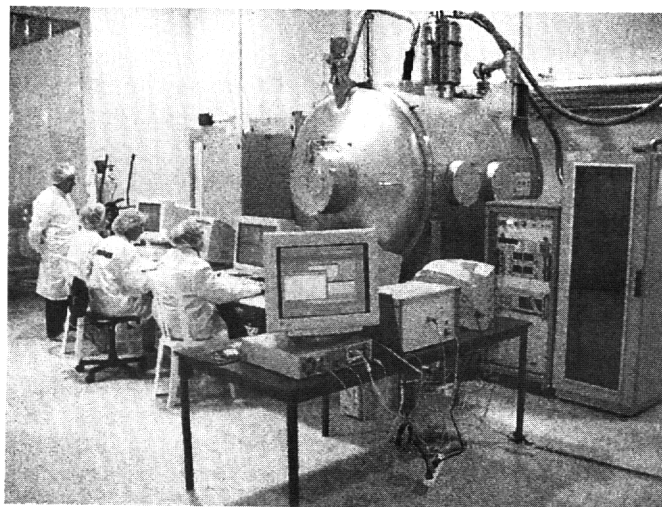


FIGURE 3.2.a: radiometric test configuration

3.2.1 Vacuum chambers

Figure 3.2.a shows one of the several 1m^3 vacuum chambers available in Alcatel Space for operation of infrared detectors and associated cooled optics. These chambers have useful volumes between $\varnothing 0,4\text{ m} \times 0,5\text{ m}$ and $\varnothing 0,9\text{ m} \times 0,9\text{ m}$. Each of them are compatible with temperatures from 4 K to 300 K with liquid Nitrogen or Helium associated with an active thermal regulation, and pressures between 10^{-5} and 10^{-7} Torr are reached by using turbomolecular, diffusion pumps, or cryopumps. Each of these chambers is equipped with connectors with a minimum of 7 x 37 wires. Several optical windows can be adapted according to the requirements of each test.

One of these vacuum chambers is connected to a class 100 clean room for integration of unprotected detectors or of optics requiring this cleanliness.

One additional 1m^3 vacuum chamber which can reach 80 K is coupled with an optical bench for infrared camera alignment. Larger vacuum chambers are available at Alcatel Space, ranging from 10 m^3 to 550 m^3 , which are used for configurations more complex than single detector testing.

3.2.2 Blackbodies

In most of the configurations, the blackbody is maintained by a tape on the chamber. The best fitted blackbodies in term of emissivity are cavity types with diffuse walls and large area-to-opening ratio. However, this type of device has the drawback of taking a longer time to stabilize to a given temperature, due to the larger mass and volume. A compromise solution has been chosen for nearly every of our test configuration, which is a disk with a roughened surface covered with high emissivity painting. This solution leads to a blackbody whose temperature can be stabilized in typically half an hour, but with an emissivity reduced typically to 0,95. In order to limit the risk of possible stray light linked to this emissivity lower than 1, the blackbody is shielded at LN2 or LH2 temperature.

3.2.3 Electronics

Electronics are constituted of several subunits which are flexible and adaptable to various type of detectors operating in a wide frequency range.

The preamplifiers are generally specific to the detector and application. The video processing has an accuracy of 16 bits and can operate at a frequency of 1 MHz. For frequencies up to 10 MHz, the accuracy of the video chain is 14 bits. For detector having a CCD multiplexor, a correlated double sampling can be implemented in the video chain.

A subunit is dedicated to the generation of low voltage detector power supplies. Up to 24 power supplies can be generated in the range [0-20 V]. The grounding of the system has been optimized and noise levels of $10nV/\sqrt{Hz}$ are obtained on several MHz.

An other subunit is dedicated to generation of clocks which can be necessary to operate the detector. Up to 32 clocks at frequencies below 50 MHz can be generated. The level shifting of the low and high level of each clocks can be performed up to 20 V. Rise and fall time can be adjusted with precision of 1 ns for optimization of detector operation.

Digitized datas can be processed with software which allow to extract the figures of merit that have been discussed in the previous paragraphs.

This electronic test set allows to operate most of the possible detectors with a very few hardware and software adaptation.

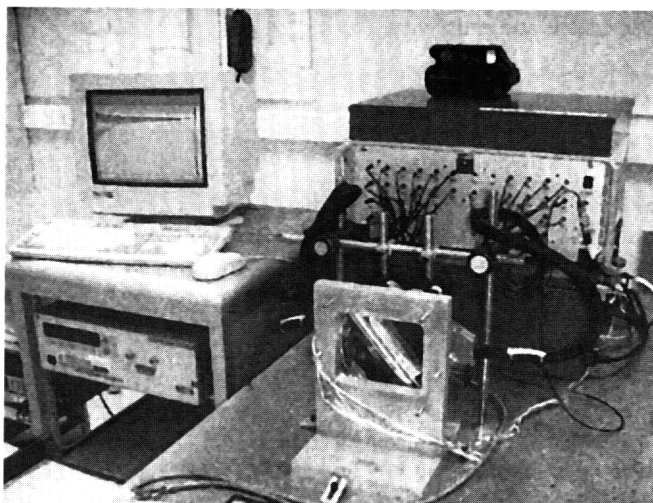


FIGURE 3.2.b: detector test with frame grabber

3.2.4 Temperature measurements

Temperature measurements are made in most of the case using Platinum Resistance Thermometers using the four lead method. The readout is performed by a high performance voltmeter, HP 3458 type.

These temperature measurement are necessary for the detector temperature, in particular to identify with a high accuracy the dispersions linked to detector temperature unstability for spatial noise estimation, and also for monitoring the blackbody temperature, in particular for detector linearity measurements.

3.3 Test sets performances

To the described test sets correspond an accuracy for the detector parameters described in the previous paragraphs: radiometric, spectral and MTF parameters and detector temperature.

3.3.1 Radiometric parameters

The accuracy on the detector sensitivity parameters (responsivity, quantum efficiency, detector signal output) can be degraded by the 5 following factors:

- temporal noise on signal,
- non-linearity of the video processing electronics,
- digital data processing,
- knowledge of the gain of the preamplifier and of the video processing electronics,
- detector thermal stability.

The first factor is made very small by averaging a sufficiently high number of acquisitions. The linearity of the video processing electronics is better than 2 LSB on 16 bits, and does not degrade significantly the signal measurements. Digital data

processing and detector thermal stability are neglectable beside the most significant factor which are the knowledge of first the preamplifier gain and second the video processing chain. Taking into account these factors of degradation, the accuracy is approximately 2 %.

To these electronic factors, it is necessary to add the factors inducing unaccuracies on the knowledge of the photon flux used for sensitivity measurements: the contributors are in this case the errors on:

- blackbody emissivity,
- filters and optical windows transmissions and emissivity,
- wavelength digitization,
- blackbody temperature,
- windows temperature stability,
- diaphragm diameter,
- detector/diaphragm centering,
- detector/diaphragm parallelism.

The error on the blackbody emissivity is the most important, and after comes the error due to the necessity to digitize the wavelength for the signal responsivity calculations, and the errors on optics transmissions. These factors lead to an accuracy of approximately 5 %.

Electronic and optical contributors being independant, one may consider that the accuracy obtained on the sensitivity of the detectors is approximately 5,5 %.

For the detectors parameters which have to be quantified to master the contribution of spatial noise, ie pixel to pixel dispersions, the accuracy of the measurements is degraded by a combination of temporal noises on the signal and of detector thermal stability. The pixel to pixel variation of optical flux is related to the geometrical field of views and does not have to be considered as an error contributor. In order to reduce the temporal noise, the number of acquisitions is increased, which also increase the time of acquisition, and so the detector stability which can be critical for some detector and cooling system configurations. An optimum has to be found for the number of acquisitions to perform, and an accuracy of 2.10^{-4} is commonly reached for the measurement of such parameters.

Detector linearity measurement can be degraded by the 4 following factors:

- temporal noise on signal,
- non-linearity of the video processing electronics,
- digital data processing,
- detector thermal stability.

Non-linearity of the video processing electronics, more specifically the preamplifier and the clamp when it is required, is the most important contributor and allows an accuracy of 5.10^{-5} which will depend on the level of signal.

To these electronic factors, have to be added the optical factors which contribute to the degradation of the linearity measurement:

- wavelength digitization,
- blackbody temperature,
- window temperature stability.

The highest weigh factor is the mastering of the blackbody temperature in the range required for the linearity measurements. The accuracy obtained is 2.10^{-4} which will also be the accuracy of the linearity measurements.

Accuracies on the noise measurements are lower than for the signal. It is possible to estimate the accuracy on the noise measurement B by the following expression:

$$\frac{\Delta B}{B} = \frac{\sqrt{B^2 + 4.(\Delta S)^2} - B}{B}$$

The accuracies ΔS on the signal measurements have been defined, and give an accuracy on the noise level which will be better if the signal uses all the dynamics of the acquisition chain. The typical levels obtained are between 5 % for signals which use most of the dynamics, and 50 % for low level signals.

3.3.2 MTF parameters

The most important sources of error applied to the knife-edge method for measurements of the MTF parameters are:

- the spatial sampling when defiling the edge on the detector,
- the focusing optics MTF,
- the microvibrations,
- the focusing unaccuracies due to unparallelism between detector and optics mount.

Optics MTF is often the preponderant factor. Depending on the summation rules, the MTF parameters are measured with an accuracy between 3 and 6 %.

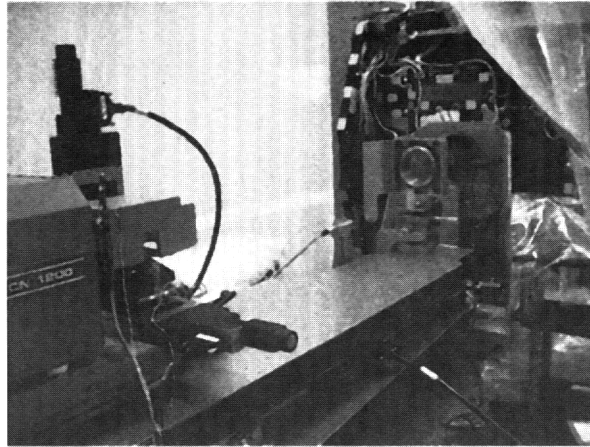


FIGURE 3.3.a: detector MTF test configuration

3.3.3 Spectral parameters

The precision of the monochromator method is mainly due to the accuracy of the reference detector. The contribution of the wavelength resolution may be a significant factor for some applications, like the atmospheric transmission if no precautions are taken on this point. The possible accuracy depends a lot of the wavelength range of interest, the value of 5 % being the typical value for the relative spectral response, and of 0,1 % for the pixel to pixel spectral response dispersion.

3.3.4 Temperature measurements

The accuracy of the temperature measurements are mainly due to the Platinum Resistance Thermometers using the four lead method. The temperature measurement accuracy is 200 mK on a 300 K temperature range, and an accuracy of 10 mK on a 50 K temperature range.

4 CONCLUSIONS

The main infrared detectors figures of merits have been identified in this paper. These parameters are of interest for most of the optical payloads for space applications in Alcatel Space. The assets available in Alcatel Space to characterize infrared detectors have been briefly described, with the accuracies achievable for the most important parameters. These accuracies are resumed on the table 4.a.

Detector figure of merit	Typical accuracy achieved
Responsivity/quantum efficiency	5,5 %
Pixel to pixel response dispersions	0,02 %
Linearity	0,02 %
Temporal noise	5 to 50 %
Detector MTF	3 to 6 %
Relative spectral response	5 %
Pixel to pixel spectral response dispersion	0,1 %

Table 4.a: Performances of the characterization test sets.

Quantum Well Infrared Focal Plane Arrays for Ballistic Missile Defense and Space Applications

M. Z. Tidrow and W. R. Dyer

Ballistic Missile Defense Organization, BMDO/ST
7100 Defense Pentagon
Washington, DC 20301-7100
USA

Abstract

Quantum Well Infrared (IR) Photodetectors (QWIP) have been developed very quickly and demonstrated large format focal plane arrays with low noise equivalent irradiance, high uniformity, and high operability. Using the high quality GaAs material systems, QWIPs have the potential for high production yield, low cost and low power consumption. Infrared focal plane arrays (FPAs) are widely used in ballistic missile defense (BMD) for surveillance, target detection, target tracking, and discrimination. These functions are performed from satellites, aircraft platforms, fixed locations or interceptors. Some ballistic missile defense sensor functions can be performed with single-color FPAs, while others require simultaneous measurements in two to four IR bands. The temperatures of most advanced BMD targets require FPA wavelengths in the mid-wave IR (MWIR), long-wave IR (LWIR), or very-long-wave IR (VLWIR) bands. Important FPA characteristics for future BMD FPAs will include large format, high sensitivity, low 1/f noise, good uniformity, and high operability. Due to the colder environment in space applications, VLWIR is very important for sensor design. QWIPs have lower sensitivity than mercury cadmium telluride FPAs at MWIR and LWIR wavelengths, but QWIP's performance at low temperature and very-long-wave IR makes it especially attractive for IR space systems. In addition, multicolor VLWIR sensing is important to eliminate the effects of earthshine in exoatmospheric discrimination. Superior multicolor capability has been demonstrated in QWIP manufacture. In this paper, an overview of the state-of-the-art of IR sensors will be given, and the advantages and shortfalls of QWIPs for BMD and space-based applications will be discussed.

Introduction

Infrared focal plane array (IRFPA) technology is very important to ballistic missile defense and space-based applications, as well as to other military and commercial applications. The IR spectrum can be divided into short wave IR (SWIR) (1 to 3 μm), MWIR (3 to 5 μm), LWIR (8 to 12 μm), and VLWIR (>12 μm). All BMDO supported Major Defense Acquisition Programs have urgent needs for high quality IRFPAs. Ballistic Missile Defense Organization (BMDO) has two major mission areas in ballistic missile defense: National Missile

Defense and Theater Missile Defense. Under these two umbrellas, BMDO has a number of programs, including Space Based IR System (-High Earth Orbit and -Low Earth Orbit), Navy Theater Wide, Navy Area Defense, Theater High Altitude Area Defense, and the Medium Extended Air Defense System.

In the functional areas, the missile defense systems are performed either in endo-atmosphere, or exo-atmosphere. Endoatmospheric interceptors and airborne surveillance sensors used for tactical applications typically observe warm targets with high background irradiance from heated windows, scattered sunlight, and the earth's surface. Such applications require accurate measurement and subtraction of background irradiance to detect the target's signal. In contrast, exoatmospheric interceptors and space based surveillance sensors used for strategic applications typically engage cool targets with low background irradiance levels. The targets are often far away and unresolved at the early stage of detection. For strategic applications where the scene is a space background and the targets are at relatively low temperatures, LWIR and VLWIR are very important wavelength bands. For tactical applications, the atmospheric transmission windows of SWIR, MWIR and LWIR determine the most important wavelength bands. Therefore, IRFPAs with high sensitivity, high uniformity, large format, and flexible wavelength are needed from SWIR to VLWIR. Multicolor capabilities are highly desirable for advance IR sensor systems. FPA stability, reproducibility, yield, cost, maintenance, and manufacturability are also very important issues.

IR Detectors and FPAs

At present time and in the near future, we expect all high performance IRFPAs for ballistic missile defense and space-based applications to be cooled IR photodetector arrays. Uncooled IR detector FPAs have been developed very quickly in recent years with large format arrays developed. They include both microbolometer and ferroelectric detector arrays. The thin film microbolometer structures directly built on Si readout circuitry are more mature than the thin film ferroelectric detector arrays at present time. Uncooled IR detector arrays have the potential to outperform cooled IR detectors at VLWIR. However, uncooled detectors developed so far are much less sensitive than the cooled detectors and require a relatively low frame rate. They

also have no intrinsic multicolor capability. Most commercial markets probably will be dominated by uncooled IR detector FPAs operating at room temperature, except for medical applications where high resolution and accuracy are needed. There are many commercial applications of IRFPAs, including medical, fire control, industrial quality control, environmental, surveillance, and driver's vision enhancement.

Current cooled IR sensor systems use material systems, such as InSb, PtSi, HgCdTe, and Si:As blocked impurity band detectors. The quantum well infrared photodetector is a relatively new technology to IR sensor applications. Among these cooled IR detector systems, PtSi FPAs are highly uniform and manufacturable. But they have very low quantum efficiency and can only operate in the MWIR range. InSb FPA technology is mature with very high sensitivity, but it can also only be operated in the MWIR range. Neither PtSi nor InSb has wavelength tunability or multicolor capabilities. Si:As has a wide band spectrum (0.8 to 30 μm), with no intrinsic tunability or multicolor capability, and it can only be operated at very low temperatures around 10-12 K. HgCdTe and QWIP offer high sensitivity with wavelength flexibility in MWIR, LWIR, and VLWIR regions, as well as multicolor capabilities. HgCdTe can also work at SWIR, while QWIP has to go to direct band gap scheme for SWIR. In this paper, the discussion is concentrated on QWIP technology on LWIR, VLWIR, and multicolor applications, especially those at low temperature and low background. The fundamental properties of each system and how they affect the device performance and applications are also discussed.

Multicolor FPAs

An important requirement for BMD missions is multicolor FPAs. Although many BMD functions can be accomplished using only one color, multicolor FPAs offer better performance in many cases, and some functions can be performed only with multicolor. Surveillance, target detection, and target tracking can be done using single-color FPAs if the targets are easy to identify. However, when the target and/or background are uncertain, or may change during an engagement, single-color design involves compromises that can degrade overall mission capability. Two or more spectral bands (colors) can greatly improve overall performance in such cases. For example, when a sensor must track a ballistic missile through booster burnout, much better detection and tracking will result if two colors are used—one before and one after burnout. Discrimination of targets from decoys and debris is greatly enhanced by using multicolor FPAs. While the irradiance measured by a single-color sensor is a useful discriminant, estimation of thermal characteristics requires two to four colors. The maximum number of simultaneous colors needed for future BMD missions appears to be four. It is desirable that each of the four colors be easily and quickly variable by changing a bias

voltage. This will permit simultaneous measurements in four bands optimized to target detection and background rejection, which is preferable to hyperspectral FPAs with many narrow bands.

Two-Color Temperature Estimation

Ignoring optical losses and spectral filtering, the power measured by a seeker of aperture area $S \text{ m}^2$ in wavelength band (λ_1, λ_2) meters from a gray body of emissivity ε , area $A \text{ m}^2$, and temperature $T^\circ\text{K}$, at a range of r meters is

$$P(T, \lambda_1, \lambda_2) = \varepsilon \frac{SA}{r^2} \int_{\lambda_1}^{\lambda_2} \frac{2hc^2 \lambda^{-5}}{e^{\frac{hc}{\lambda kT}} - 1} d\lambda \quad \text{Watts} \quad [1]$$

where $c=2.988 \times 10^8 \text{ m/sec}$ is the speed of light, $h=6.625 \times 10^{-34} \text{ J sec}$ is Planck's constant and $k=1.381 \times 10^{-23} \text{ J/K}$ is Boltzman's constant. It is not possible to accurately estimate the target's temperature T using only one wavelength band (λ_1, λ_2) , because ε , A , r and T are all unknown. However, if measurements are made simultaneously in two wavelength bands (λ_1, λ_2) , (λ_3, λ_4) , their ratio R cancels ε , A , S , and r , and can be used to estimate T . The ratio R is plotted in Figure 1 for two sets of wavebands. The ratio R is a monotonic function of T , which allows T to be found uniquely for every R . Also note from Figure 1 that the slope dR/dT is larger for the more separated wavebands. Hence, temperature estimation errors will be smallest when the wavebands are separated as much as practical, consistent with maximizing signal to noise ratio in both bands.

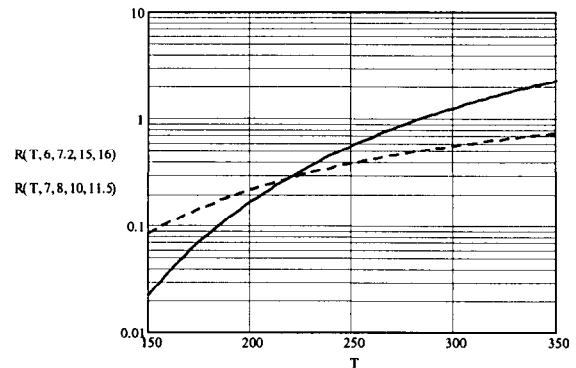


Figure 1. Ratio Of Measurements v Temperature T

Three-Color Temperature Estimation with Earthshine

While solar scattering can usually be ignored at wavelengths longer than 6 μm , temperature estimation generally will be complicated by earthshine reflected from targets at MWIR-VLWIR wavelengths. In this case, the measured irradiance is

$$P(T, \lambda_1, \lambda_2) = P_{\text{tgt}}(T, \lambda_1, \lambda_2) + \alpha P_E(\lambda_1, \lambda_2) \quad [2]$$

where α accounts for the view factor of the reflected earthshine and the subscripts *tgt* and *E* denote IR emitted

from the target and earthshine reflected from the target respectively. Equation [2] contains three unknowns, $P_{tgt}(T, \lambda_1, \lambda_2)$, $P_E(\lambda_1, \lambda_2)$, and α , but it is also a function of ε , A , and r , because the terms have forms similar to equation [1]. To make a temperature estimate, three measurements, $P_E(\lambda_1, \lambda_2)$, $P_E(\lambda_3, \lambda_4)$, $P_E(\lambda_5, \lambda_6)$ of the target are needed. In addition, three estimates $P(T, \lambda_1, \lambda_2)$, $P(T, \lambda_3, \lambda_4)$, $P(T, \lambda_5, \lambda_6)$ are made by looking directly at the earth or by measuring the earthshine reflected from a reference sphere near the target, with the same sensor used for the target measurements. With the P_E terms estimated, multiply $P(T, \lambda_3, \lambda_4)$ by the ratio of earthshine measurements $P_E(\lambda_1, \lambda_2)/P_E(\lambda_3, \lambda_4)$ and subtract the result from $P(T, \lambda_1, \lambda_2)$. The result is

$$D(T, \lambda_1, \lambda_2, \lambda_3, \lambda_4) = P(T, \lambda_3, \lambda_4) \left[\frac{P(T, \lambda_1, \lambda_2)}{P(T, \lambda_3, \lambda_4)} - \frac{P_E(\lambda_1, \lambda_2)}{P_E(\lambda_3, \lambda_4)} \right] \quad [3]$$

After calculating $D(T, \lambda_1, \lambda_2, \lambda_5, \lambda_6)$ the same way, form the ratio U , defined as

$$U(T, \lambda_1, \lambda_2, \lambda_3, \lambda_4, \lambda_5, \lambda_6) = D(T, \lambda_1, \lambda_2, \lambda_3, \lambda_4) / D(T, \lambda_1, \lambda_2, \lambda_5, \lambda_6) \quad [4]$$

$$= \frac{P(T, \lambda_3, \lambda_4)}{P(T, \lambda_5, \lambda_6)} \times \frac{\left[\frac{P(T, \lambda_1, \lambda_2)}{P(T, \lambda_3, \lambda_4)} - \frac{P_E(\lambda_1, \lambda_2)}{P_E(\lambda_3, \lambda_4)} \right]}{\left[\frac{P(T, \lambda_1, \lambda_2)}{P(T, \lambda_5, \lambda_6)} - \frac{P_E(\lambda_1, \lambda_2)}{P_E(\lambda_5, \lambda_6)} \right]}$$

Each term of U is a ratio of irradiance measurements, and hence is independent of ε , A , and r . Plots of U vs T are shown in Figure 2 for two sets of three bands. U is a monotonic function of T , and hence it provides a unique estimate of T for each value of U . As in the no-earthshine case, errors are reduced when the wavebands are separated as much as practical. Comparison of Figures 1 and 2 indicates that earthshine causes a reduction in the accuracy of the temperature estimates since the slopes of the dU/dT curves are smaller than those of the dR/dT curves.

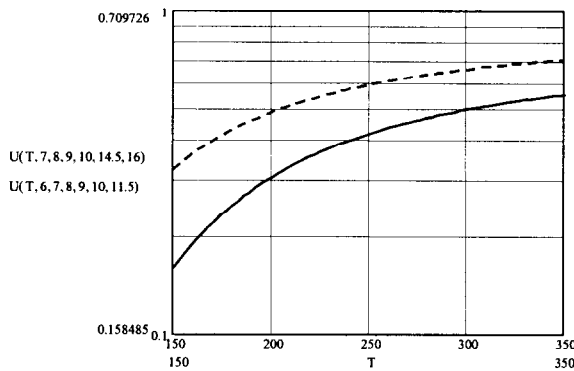


Figure 2. Ratio U vs Temperature T

Measured exoatmospheric data indicates that the accuracies of the earthshine ratio terms of [4] are maximized if one of the detector colors is chosen in a band where the earth's atmosphere partially blocks earthshine. There are three blocking bands in the

MWIR-VLWIR region that can be used: the water band ($5.5 \mu\text{m} - 7.5 \mu\text{m}$), the ozone band ($9.4 \mu\text{m} - 9.9 \mu\text{m}$), and the CO_2 band ($14 \mu\text{m} - 16 \mu\text{m}$). While none of these bands blocks earthshine totally, the CO_2 band offers the best combination of spectral width and earthshine blocking. The ozone band is narrow, and the lower portion of the water band should be avoided due to solar scattering. Best accuracy results when the color in the blocking band is between the other two colors. This makes QWIPs attractive because they can easily cover the CO_2 band and beyond.

If the targets of interest are not very reflective, it may be possible to ignore earthshine and use a two-color FPA with both colors in located separate earthshine blocking bands. The range of expected target temperatures and reflectivities determines the benefits of this approach, but it has the advantage of relative simplicity, and in some cases better accuracy. One of the blocking bands should be the CO_2 band due to its wide spectrum and good blocking characteristics. The solid curve of Figure 1 represents the potential of this method. Comparison with Figure 2 shows that the two-band approximation has larger slope and therefore may provide greater accuracy than the three-band method. After T has been estimated, target's emissivity-area product, εA , can also be estimated if an estimate of range r is available.

Four-Color Temperature Estimation of Non-gray Targets

The above two- and three-color developments assume a graybody target. If the target is non-gray (i.e., ε varies with λ), simultaneous measurements in four or more bands are needed. Spitzberg (1) has shown that graybody emissivity is coordinated well enough with wavelength that four uniformly spaced wavelength bands allow fairly good temperature estimation of non-gray targets between $5 \mu\text{m}$ and $25 \mu\text{m}$. Best results are obtained when $\varepsilon(\lambda)$ is expanded in an orthogonal series, and more bands improve the estimates somewhat. As in the graybody case, target's emissivity-area product, εA , can also be estimated if an estimate of range is available.

Quantum Well Infrared Photodetectors and Arrays

QWIPs are semiconductor devices operating at cooled temperatures decided by the cutoff wavelength. A typical QWIP consists of GaAs/AlGaAs 30 to 50 quantum well periods (2). Using GaAs as the well region and AlGaAs as the barrier region, confined quantum well structures can be formed when the well width is small. The thickness of the GaAs layer determines the well width, and the x value in $\text{Al}_x\text{Ga}_{1-x}\text{As}$ determines the barrier height. QWIP uses intersubband transitions within the quantum wells either in conduction band (n-type) or valence band (p-type). The well region has one bound ground state and one or more excited states, depending on the barrier structure. N-type QWIPs are donor doped,

resulting in a Fermi energy above the ground state. Electrons in the ground state can absorb IR photons with energy coinciding with the energy difference between the excited and ground states. Using either InGaAs or GaAs as well region, the detection wavelength of QWIPs can vary from 4 μm to larger than 20 μm . With different combinations of barriers and well structures, different detection wavelengths, detection bandwidths, and multicolor combinations can be achieved. QWIPs are usually operated in the photoconductive (PC) mode, and bias voltage (typically around 2 V) is applied to sweep the excited electron out of the well region.

QWIPs use III-V semiconductor material, mostly GaAs/AlGaAs. The advantages of the GaAs/AlGaAs material system are that it has superior bond strength and material stability, well behaved dopants, and thermal stability. Because of the maturity of GaAs technology, device processing and array fabrication for QWIPs is mature and repeatable. The outcome is highly uniform FPAs with high operability and high yield. One major disadvantage of the intersubband transition used in n-type QWIPs is that it has relatively low quantum efficiency as compared with other interband transition semiconductor devices such as HgCdTe, or InSb. Since the optical absorption is anisotropic; the absorption cross section is proportional to the square of the component of electric polarization perpendicular to the quantum well layers. This implies that a simple QWIP does not directly absorb normally incident light. Therefore, all n-type QWIP pixels for two-dimensional (2-D) arrays include a metalized diffraction grating or other similar structure to couple normally incident light into directions that are strongly absorbed by the quantum wells. The absorption quantum efficiency of the detectors is therefore a function of both the absorption strength of the quantum wells and the effectiveness of the coupling structure. Another characteristic of intersubband transition is the short carrier lifetime. A short carrier lifetime gives an intrinsically fast device speed, however, it also forces QWIP to operate at a lower temperature due to the higher dark current.

Currently, LWIR QWIP FPAs with up to 640x480 pixels have been demonstrated by Lockheed Martin (3) and JPL (4). JPL also demonstrated a 128x128 QWIP FPA at 15 μm (5). Multicolor 256 x 256 MW/LW and near infrared (NIR)/LW FPAs with sequential imaging were demonstrated by Lockheed Martin in 1993 and 1994, respectively (6). The most recent development in multicolor QWIP FPAs are two color MW/LW and LW/LW FPAs with simultaneous imaging capability at Lockheed Martin (6). The results of the LW/LW FPA have NEDT of 24 mK for the 8.6 μm and 35 mK for the 11.2 μm at 40 K with $f/2$ optics. The pixel operability in each color is >97 percent and has now improved to >99 percent.

QWIPs for BMD and Space Based Applications

Ballistic missile defense requires both tactical and strategic applications, while space based IR falls into the strategic category. In tactical applications, the scene usually has a high background (300K). The target temperature is high (>300K) and the distance is in the short to medium range. Due to the high background, the IRFPA performance is mostly background noise limited. For tactical applications, QWIP FPAs in the format of 320x256 are commercially available (Lockheed Martin) (7). QWIP is grounded on a commercial III-V material technology that is the basis of a multibillion dollar electronics industry). The substrates, MBE growth, and processing technology are very mature and a high yield can be achieved. The production of QWIP FPAs can also leverage other III-V semiconductor devices. Therefore the cost of QWIP FPAs are expected to be much lower than other cooled IRFPAs such as HgCdTe and InSb.

For space based IR systems, the scenario usually describes a very low background with far away targets. In countermeasures, the target can be cooled to a very low temperature, which gives very low IR signatures that peak in VLWIR spectrum. Therefore, VLWIR sensors are very important in strategic missile defenses and space applications. FPAs of 12 to 18 μm are very useful for the detection of cold objects such as ballistic missiles in midcourse. Using band gap engineering and mature GaAs technology, extension of tactical QWIPs to VLWIR is relatively easy because there is very little change in material properties, growth, and processing. At VLWIR, the intersubband spacing of a QWIP is relatively smaller than at LWIR. Due to the lower quantum well barriers, the dark current of thermionic emission dominates at a lower temperature. In order to achieve equivalent performance of a 10 μm cutoff QWIP at 77 K, the temperature needs to be cooled to 55 K for a 15 μm cutoff and 40 K for an 18 μm cutoff. An unoptimized 128 x 128 pixel QWIP FPA at a 15 μm cutoff wavelength has been demonstrated by JPL (5) with an NEDT of 30 mK at 45 K with 300 K background and $f/2.3$ optics. This initial array gives excellent images with 99.9 percent operability and uncorrected responsivity nonuniformity of 2.4 percent. Comparing QWIP with HgCdTe at 15 μm , QWIP has higher operability and uniformity, and higher yield.

In the situation of low background applications, the signal from the target is usually very weak due to a low irradiance and far distance of the target, besides peaking at a longer wavelength. In order to maintain the signal to noise ratio, high quantum efficiency and low noise is needed. In QWIP, thermally generated intrinsic dark current dominates the device performance at low background. The behavior of the dark current of a QWIP is well understood. It has three mechanisms with one mechanism usually dominating at one temperature range, even though all three mechanisms contribute at all

temperatures. At low temperatures ($T < 40$ K for 10 μm cutoff), the dark current is mostly caused by defect related direct tunneling (DT). With high quality III-V material growth and processing, this dark current is very small. In the medium operating temperature range (40 to 70 K for 10 μm cutoff), thermally assisted tunneling (TAT) dominates. Electrons are thermally excited and tunnel through the barriers, with possible assistance from defects in the triangle part of the barrier that forms under bias. At high temperature (>70 K for 10 μm cutoff), thermally excited electrons are thermionically emitted (TE) above the barriers. One can adjust the device structures, doping densities, and bias conditions to get optimum dark current and photoresponse for specific applications. However, when the device is TE dominated, which means the dark electrons have energy and transport mechanisms similar to photoelectrons, it is very hard to reduce the dark current without sacrificing the photoelectrons. A typical LWIR QWIP dark current density at 77 K is about 5×10^{-4} A/cm² for $\lambda_c = 9$ μm and bias voltage of -2 V. It usually reduces exponentially with inverse temperature with a reduction of three to five orders of magnitude between 77 K and 40 K. A dark current of 5×10^{-4} A/cm² is in the nanoampere for a 24×24 μm^2 pixel. Certain techniques, such as the E-QWIP (8) and C-QWIP (9), use coupling structures that are etched right through the QW stack. These schemes can maintain the detector optical area, while reducing the dark current by a factor up to 5. The fact that this can be done without introducing significant surface currents is further evidence of the low surface leakage along the unpassivated GaAs/AlGaAs surface.

IR detectors such as HgCdTe suffer from the tunneling dark current caused by defects when detector is operated at low temperature and at very long wavelength. The outcome is high nonuniformity caused by defect related dark current. Due to the high quality materials, there is a less problem for QWIP on defect related dark current when operating at low temperature and very long wavelength. However, there are some fundamental issues related to QWIPs for low background applications. First, due to the intersubband transition properties, the dark current of QWIPs is always higher than that of interband transition detectors, such as HgCdTe when operating at the same temperature. This is a fundamental limit, not due to technology immaturity as in the HgCdTe case. QWIP's dark current depends strongly on the doping density during the device growth. Reducing the doping could reduce the dark current. However, for low background applications, lowly doped QWIPs suffer from a long response time due to the depletion of the charged quantum well. A dielectric relaxation is also observed which is not yet well understood. The low quantum efficiency and gain product of QWIP also prohibits QWIP's ability to see very dim target at a very far distance which is most of the case for space based IR systems.

Summary

In summary, QWIP FPAs are mature for tactical applications and are commercially available. QWIP FPAs have many advantages for space based applications, such as high uniformity, high operability, high yield and low cost which are very important to space based IR systems. However, there are some fundamental limitations in QWIPs, which require them to operate at a relatively lower temperature compared to HgCdTe. Current QWIP's quantum efficiency and gain product is around 2 to 6 percent, which needs significant improvement for long range detection as in space based IR system. How much the uniformity and operability could compensate for the low quantum efficiency is yet to be determined. The future applications of QWIP also depend on the speed and maturity of other IR materials system development. Quantum dot infrared photodetectors (QDIPs) is a potential replacement for QWIPs (10). QDIPs have certain advantages over QWIP. First, no quantum selection rules prevent normal incident absorption in a QDIP, removing the need for grating. Second, higher photoconductive gain could be achieved in QDIPs due to longer lifetime of excited electrons. And third, there is the added potential of higher response due to the excited electron confinement in three dimensions, which results in a larger transition probability overlap integral and higher dipole matrix elements. The dark current in a QDIP is also smaller theoretically due to the three-D confinement. Therefore, a higher sensitivity is expected in QDIP than in QWIPs. However, QDIP is still in the developing stage and the technology is not even close to ready. QDIP also has intrinsically very narrow bandwidth, which might eliminate its potential of certain wideband applications.

References

- (1) Spitzberg, R.M. "Parameter Estimation for Gray and Nongray Targets: Theory and Data Analyses", Optical Engineering, July 1994.
- (2) Sheng S. Li and Meimei Z. Tidrow, "Quantum Well Infrared Photodetector", Chapter 9, Handbook of Nanostructured Materials and Nanotechnology, edited by H. S. Nalwa, Volume 4: Optical Properties, Academic Press, 2000.
- (3) L. T. Claiborne, S. L. Barnes, A. J. Brouns, F. C. Case, E. Feltes, T. A. Shater, K. L. Brown, M. Sensiper, R. J. Martin, C. Chandler, and P. Vu, in Proc. 1996 Meeting of the IRIS Specialty Group on Infrared Detectors, 1996.
- (4) S. D. Gunapala, S. V. Bandara, J. K. Liu, W. Hong, M. Sundaram, R. Carralejo, C. A. Shott, P. D. Maker, and R. E. Muller, SPIE (1997).
- (5) S. D. Gunapala, J. S. Park, G. Sarusi, T. L. Lin, J. K. Liu, P. D. Maker, R. E. A. Muller, C. A. Shott, and T. Hoelter, IEEE Trans. Electron. Devices 44, 45 (1997).

- (6) M. Sundaram, T. Faska, S. Wang, A. Reisinger, M. Taylor, R. Williams, K. Zabierek, R. O. D. Burrows, D. Walker, S. Wade, S. Duvall, R. Yanka, K. Nichols, A. Vera, D. Bingham, C. Cooke, J. Roussis, M. Winn, J. Ahearn, G. Milne, K. Brown, R. Martin, K. Reiff, and W. Spahr, in Proc. the IRIS Specialty Group on Infrared Detectors, Boulder, CO, 1998 (ERIM).
- (7) Private conversation with Lockheed Martin
- (8) M. A. Dodd, S. L. Barnes, A. J. Brouns, F. C. Case, L. T. Claiborne, and M. Z. Tidrow, in Proc. the 1997 Meeting of the IRIS Specialty Group on Infrared Detectors, , 1997.
- (9) C. J. Chen, K. K. Choi, M. Z. Tidrow, and D. C. Tsui, Appl. Phys. Lett. 68, 1446 (1996).
- (10) Xudong Jiang, Sheng S. Li, and M. Z. Tidrow, Physica E, 5, 27-35 (1999)

Space Observation at Sofradir

NATO – Research and Technology Agency
(Greece, 16-18 october 2000)

Jean-Pierre Chatard / Technical Director
Michel Vuillermet / Space Product Line Manager

SOFRADIR
43-47 rue Camille Pelletan
92290 Châtenay-Malabry / France

Jean-Paul Chamonal / Detector Technology Manager

CENG/LIR
17 rue des Martyrs
38054 Grenoble Cedex 9 / France

0. ABSTRACT

In the frame of space activities, Sofradir has developed a large know-how in the field of infrared detectors.

Thanks to some numbers of basic studies, thanks to its participation to the development and manufacturing of the Helios 2 program for which long linear arrays have been produced, Sofradir has established a Mercury Cadmium Telluride technology qualified for space applications.

Using MCT technology was a very good choice, not only for the level of performances but also for the flexibility of the material, as it is possible on the same base to manufacture SWIR, MWIR or LWIR detectors.

The purpose of the paper is to give some technical information and to present possible evolution of the detectors in regard of space observations.

1. INTRODUCTION

After several years of developing infrared detectors for the military tactical domain where quantities higher than 2000/year are now in production, Sofradir started to work in the field of space applications and especially in the earth observation domain.

Thanks to the work done with the support of the French Space Agency (Cnes), of the European Space Agency (Esa) and the French Ministry of Defence Sofradir has now a well-quality team of 15 people working on space programs.

In order to answer to the need of earth observations Sofradir propose the use of cooled and lightcooled Mercury Cadmium Telluride (HgCdTe/MCT) sensitive material which covers the spectral region from 1 μm to 14 μm [1] and the use of microbolometers which are sensitive in the long wave spectrum with the big advantage to be totally uncooled.

Thanks to these technologies developed by the French infrared research laboratory (Leti-Lir) and industrialised by Sofradir it has been possible to participate to key space technologies studies and to the largest military infrared program in Europe, Helios 2.

2. TECHNOLOGIES CAPABILITIES

2.1 Technology

The quality of the unique Mercury Cadmium Telluride (HgCdTe / MCT) process, which was transferred from CEA-LETI (LIR) in 1987, allows Sofradir to offer high performance IR detectors with respect to format and Electro Optical performance.

Based on the new generation concept of infrared detectors (FPA), this technology assembled photovoltaic (PV) MCT diode arrays with complex readout silicon circuit (ROIC) which includes integration, gain and offset control, sampling, multiplexing and specific features. The assembly is done thanks to a special indium bump hybridization technique (figure 2.1).

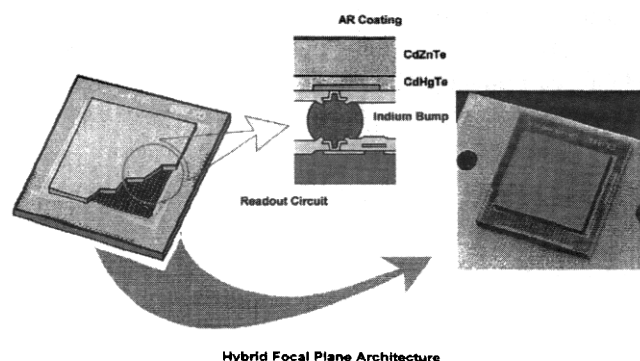


Figure 2.1 : dessin de la structure hybride

Sofradir technology key points are discussed in the following in order to highlight high performance technology parameters.

2.1.1 Wafer size

Sofradir substrates are issued from home-made Cadmium Zinc Telluride (CdZnTe) ingots sliced into crystal-oriented rectangular wafers. Since 1996, Sofradir has manufactured 60 mm (2.4") diameter CdZnTe ingots in which wafers are sliced.

Up to 1997, these wafers were standardized at 20 mm × 25 mm for the PV array manufacturing. Since 1998, the CdZnTe wafers have been increased to 36 mm × 38 mm at the production level, enabling larger detectors and/or more detectors per wafer (Figure 2.2).

This increase enabled for instance to step up the 2D array manufacturing from 30 μm pitch 320×256 arrays to 1 000×1 000 with 15 μm pitch.

The next step concerns processing of wafer size close to two inches diameter. This will be in production at Sofradir in 2001 for 2D staring arrays.

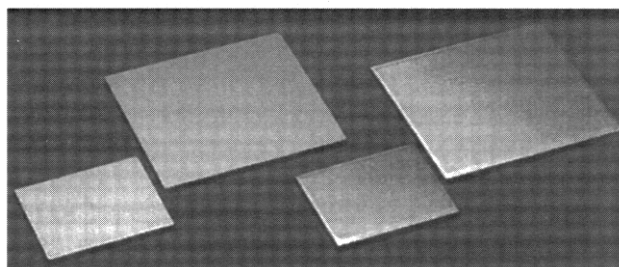


Figure 2.2: 20×25 mm² and 36×38 mm² PV wafers

(left : polished CdTe wafer ; right: with raw LPE grown detective HgCdTe layer)

2.1.2 HgCdTe process

On the detective process part, the Liquid Phase Epitaxy (LPE) growth of the HgCdTe layer has been the technological choice at Sofradir for more than 14 years. This process step is critical for the detection quality, spectral cut-off uniformity and reproducibility. It has been mastered and has demonstrated high yield and high reproducibility, making it the key point for the high performance detectors proposed by Sofradir.

Sofradir also investigates in cooperation with the CEA-LETI Infrared Laboratory (LIR) other technologies for detection array material manufacturing. The Molecular Beam Epitaxy (MBE) process on Germanium substrates is currently developed at LIR, for use on large arrays [2]. This enables even larger arrays than currently obtained with the LPE process, with a well mastered sensitive thin film thickness deposition.

2.1.3 Ion implantation process

Once the sensitive layer is grown and polished, the remaining step is to manufacture the photovoltaic (PV) diodes. The process chosen by Sofradir is the ion implantation process [3]. Unlike techniques like the diffusion process or the mesa structure process, the Sofradir ion implantation process enables the definition of sharp pixels with a planar technology (key point for an efficient passivation). The N on P homojunctions are implanted and provide a well controlled junction which combines with short diffusion lengths. This enables sharp diodes with high fill factor.

This is a Silicon-like planar technology which is now used at a large scale at Sofradir for more than 14 years.

2.1.4 Hybridization process

The Indium bump hybridization process at Sofradir is based on a unique reflow technique. This technique allows the HgCdTe array to be accurately and automatically self-aligned on its Silicon read-out circuit, and gives a perfect connection yield.

Moreover, it enables simultaneous multiple HgCdTe PV array hybridization on a single Silicon wafer [4], for producibility improvement and very large array manufacturing.

2.2 Specific means

2.2.1 Manufacturing means

General Sofradir front-end equipments are used to manufacture the retina. Some equipments were upgraded to work with some specific space application arrays.

In order to manufacture the space flight model in properly conditions of cleanness and confidentiality, all operations of assembly are performed in a dedicated clean room (figure 2.3).

Detector assembling is performed in class 100 areas with protection to avoid the electrostatic discharges.

This dedicated clean room is specially arranged with specific tools to operate very carefully on space products. Most of operations are performed with binocular vision and can be monitored by the customers in a meeting room with the help of a video system.

Pictures hereunder present main tools used for detector assembling. There are :

- visual control system (figure 2.4)
- gluing system for large arrays with very low defect of positioning between retina and package,
- automatic bond tool with a pull test (figure 2.5)
- optical three dimensional measurement system (figure 2.6)



Figure 2.3 : Clean room overview

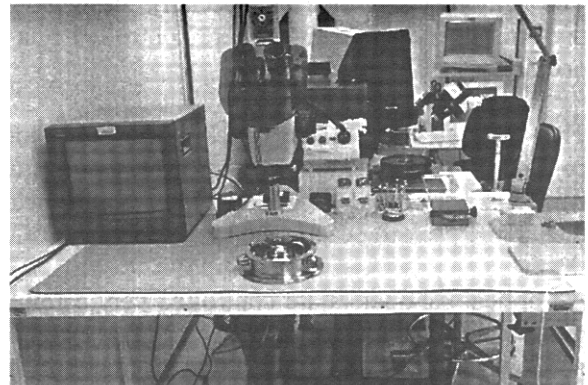


Figure 2.5 : Bonding tool

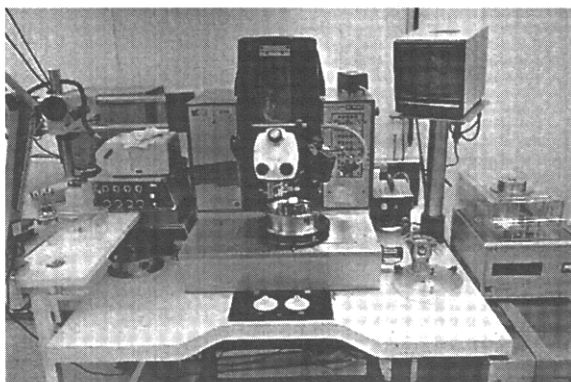


Figure 2.4 : Visual inspection station

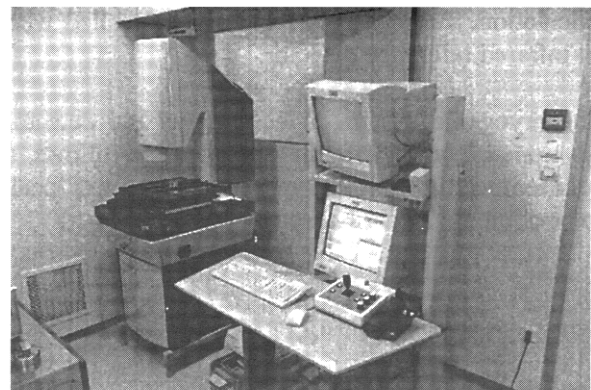


Figure 2.6 : Optical measurement system

2.2.2 Electrooptical test benches

The specific measurements performed to demonstrate the compliance with specification and the necessity to finely characterise the detector imposed the development of new test benches. Four electrooptical test benches were developed by Sofradir in less than two years.

It concerns :

- Radiometric
- Spectral
- Modulation Transfer Function
- Geometrical test benches.

Electronic system to operate detector and read the output signal was developed by Sofradir.

All test benches are regularly calibrated with a detector reference or other methods using specific detector of small dimension or material characteristics.

2.2.2.1 Radiometric test bench (figure 2.7)

The radiometric bench is specially designed to perform all measurements where controlled flux is necessary.

The main element of the bench is the blackbody confined into a vacuum chamber. The temperature control is better than 40 mK and the stability better than 3 mK peak to peak in the range $-20^{\circ}\text{C} / 60^{\circ}\text{C}$.

All optical parameters are controlled very carefully from the blackbody to the detector. For example, window temperature of the vacuum chamber and variation of blackbody emissivity, function of its temperature, are taken into account in the flux calculation. The bench is regularly controlled with an infrared reference detector.

The cryogenic system to cool down the detector developed under Sofradir specification allows a cold temperature stability of better than 5 mK peak to peak on the focal plane array.

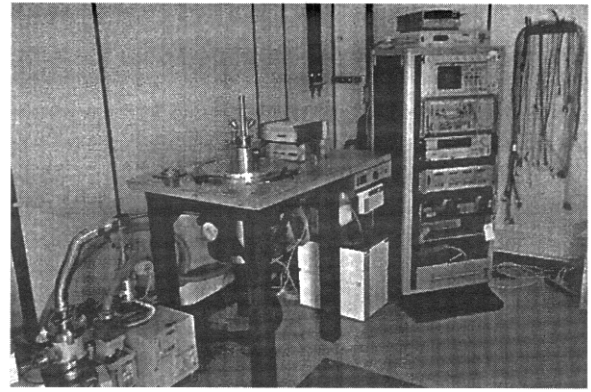


Figure 2.7 : Radiometric test bench

This test bench allows all radiometric measurement with very good conditions. For example, in case of Helios detector, linearity, signal to noise ratio, $1/f$ noise up to 0.5 Hz and electrical characteristics are measured with this bench.

The accuracy of signal on noise ratio measurement is better than 2% in full range of blackbody temperature.

2.2.2.2 Spectral test bench (figure 2.8)

The spectral test bench is based on a Fourier transform spectrometer modified with Sofradir specifications.

This test bench allows to perform spectral response in the bandwidth 1 to 14 μm . Thanks to its principle, spectral measurement can be done on the same time on more than 200 diodes. Therefore, the spectral response of all diodes of an array can be measured within a reasonable duration.

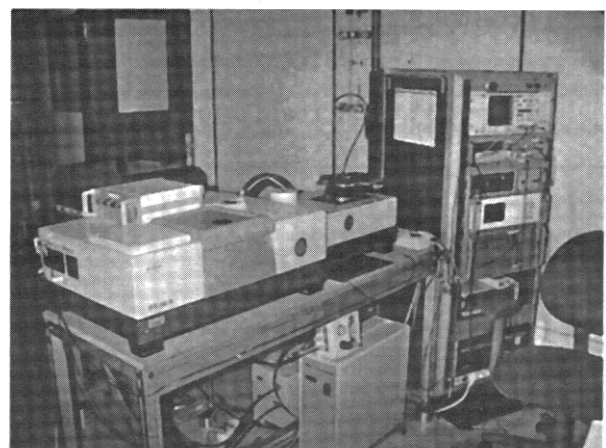


Figure 2.8 : Spectral test bench

2.2.2.3 Modulation transfer function test bench (figure 2.9)

The measurement of MTF is performed with the help of an edge shifted in front of the detector.

The detector MTF is calculated by Fourier transform of the detector response devised by the optical bench MTF. This last MTF is regularly measured with a small dimension detector ($2 \times 2 \mu\text{m}$).

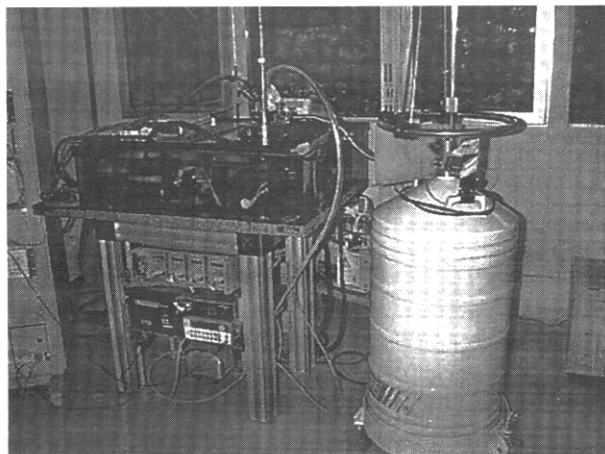


Figure 2.9 : MTF test bench

2.2.2.4 Geometrical test bench (figure 2.10)

This test bench was developed to measure the relative pixel position in the three axes.

For XY measurement the principle is to scan pixel lines from the first to the last pixel. The maximum of correlation function between two pixels response gives their relative position. Thanks to its high mechanical and optical control, the measurement accuracy is better than $0.5 \mu\text{m}$ from pixel to pixel and better than $5 \mu\text{m}$ all along the detector, up to 10 cm.

For Z measurement, the principle is to check by focalisation the maximum of pixel response. The method used allows an accuracy better than $2 \mu\text{m}$. As a consequence, the flatness accuracy measurement is better than $4 \mu\text{m}$.

Pixel spot scan, dynamic blooming and crosstalk measurements are possible with this bench.

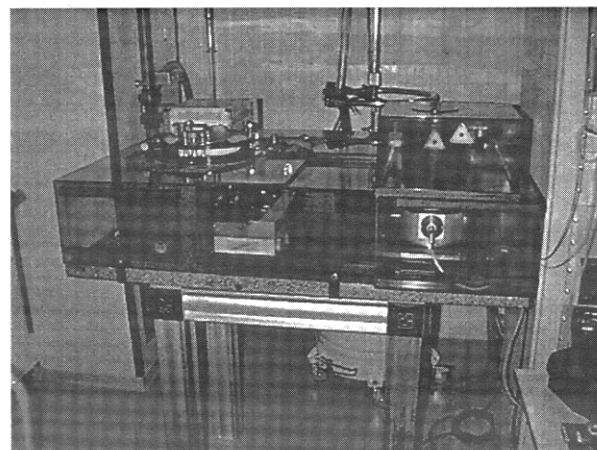


Figure 2.10 : Geometrical test bench

3. PROGRAMS

Different study programs have been done or are underway at Sofradir covering the spectral range from $1 \mu\text{m}$ to $14 \mu\text{m}$ using MCT material.

3.1 High Resolution Thermal Infrared Radiometric (HRTIR) [5] [6]

One of the most important Sofradir/Lir studies is certainly the HRTIR made in cooperation with Matra Marconi Space, Dasa and Officine Galileo under Esa support.

The principal aim of the HRTIR was to increase the understanding of energy, water and biogeochemical fluxes important in the study of land infrared processes. The HRTIR provides information on temperature and emissivity which is fundamental physical properties of terrestrial surfaces.

The detector works in the long wave region (8 to $12.5 \mu\text{m}$) where the technology is always difficult to manage.

The product demonstrator was an assembly of two subarrays of 256 pixels each operating at 55 K (figure 3.1).

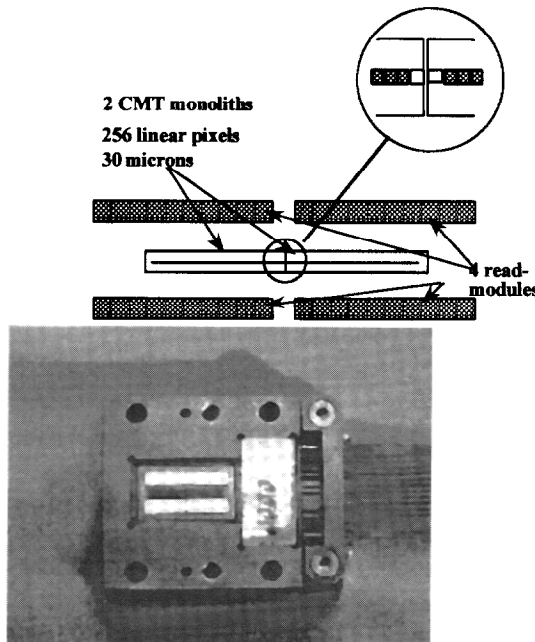


Figure 3.1 : LWIR HRTIR FPA breadboard

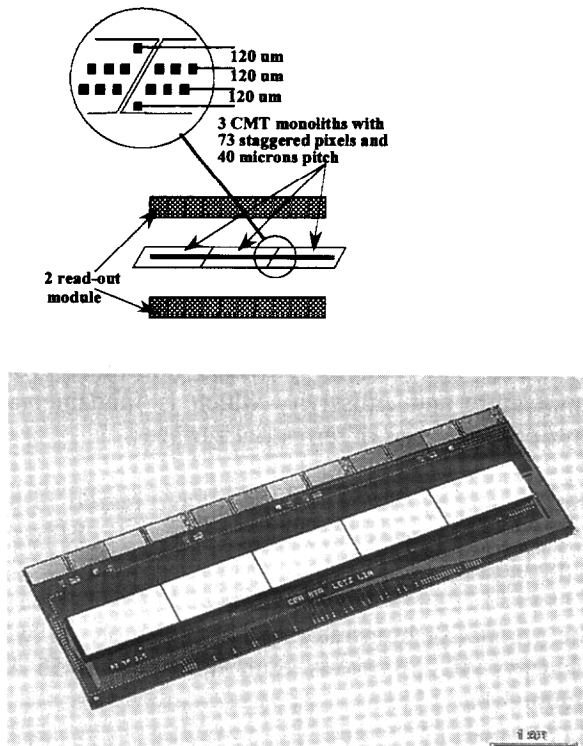


Figure 3.2 bis : 1500 x 1

Since that time Lir has demonstrated in the same spectral band an array of 1500 pixels by assembling 10 subarrays of 150 pixels (figure 3.2) with great success and no defect at the level of the buttings.

The technical objectives of the HRTIR detector breadboard manufacturing were to verify the performance of 12.5 μm cut off wavelength photodiodes operating at 50 K to assess the diodes operability and to check the self alignment of the subarrays.

The diode operability is a major issue for such thermal channels. Indeed, as the acquisition mode is based on the pushbroom principal, any defective pixel will lead to a dark column on the images.

The HRTIR detector breadboard shows that 97% of diodes are operational.

The dark currents (figure 3.3) are measured in a nearly zero background conditions when the FPA temperature can vary from 50 to 60 K. The mean dark current is 0.33 nA (30 μm^2 pixels).

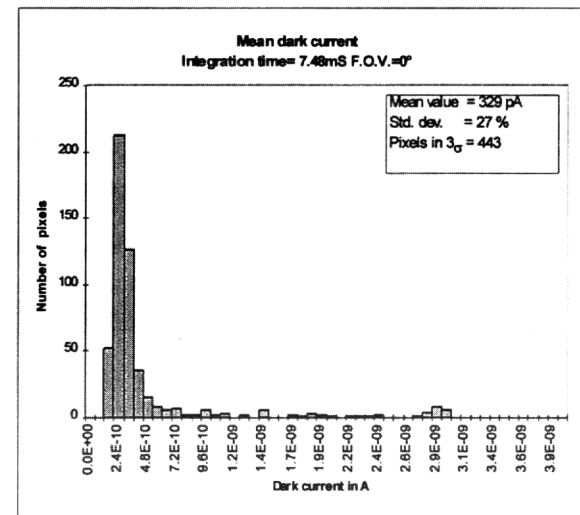


Figure 3.3 : Dark current distribution at 55 K

The dark signal uniformity defined by its standard deviation along the arrays is better than 27%. This figure can be improved a lot when the production phase will be considered. Figure 3.4 shows also the variation of the mean dark current versus the FPA temperature.

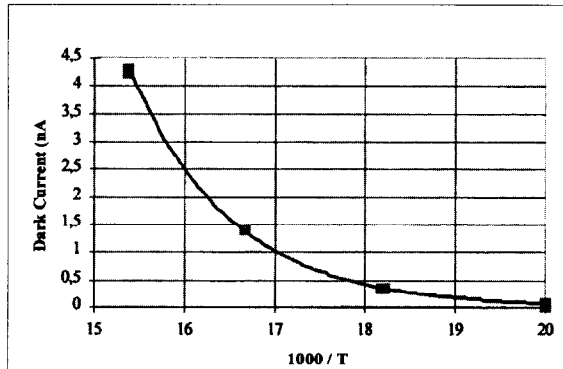
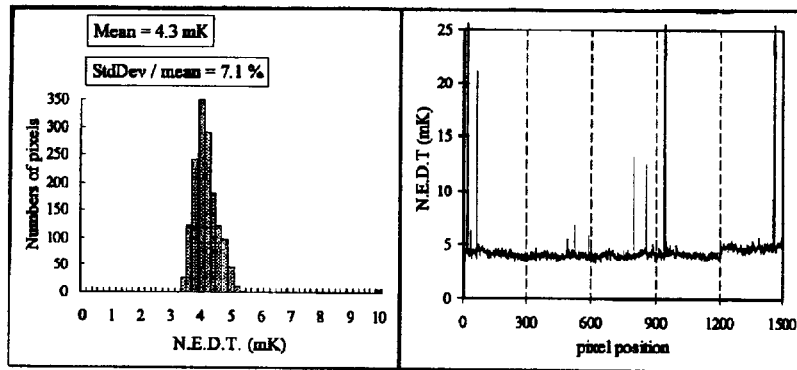


Figure 3.4 : Variation of mean dark current vs temperature in the 50-65 K range

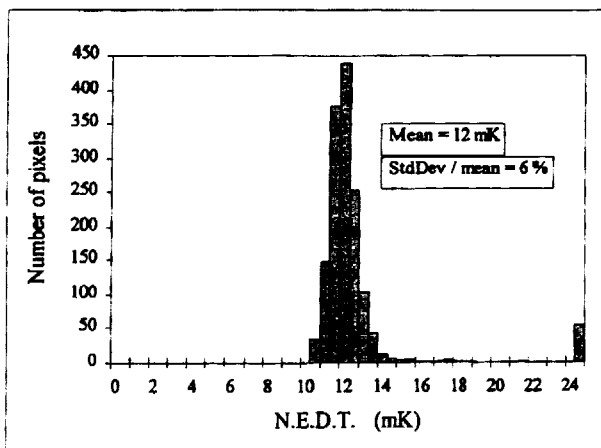
Since the end of the HRTIR program the butting technology which allows to loose no pixel at the butting has been improved at Lir. Then bigger components have been demonstrated showing a very low number of defect [7] either in MW or LW spectral region (figure 3.2) (figure 3.5, figure 3.6) (figure 3.7, figure 3.8).



**Figure 3.5 :
NEDT histogram**

**Figure 3.6 :
Spatial distribution of NEDT**

Operating temperature : 77 K
Field of view : 28°C
 λ_c : 5.5 μm
Frame frequency : 200 Hz
Integration time : 5 ms



NEDT histogram of the 1500 element linear LWIR butted array

Figure 3.7 : NEDT histogram of the 1500 element linear LWIR butted array

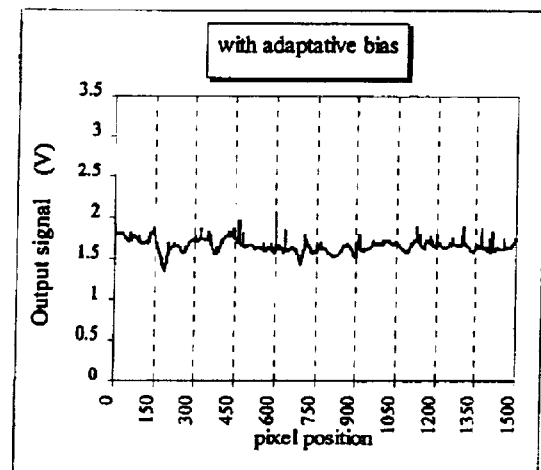


Figure 3.8 : Spatial distribution of NETD

Operating temperature : 78 mK
Field of view : 28°C
 λ_c : 10 μm
Frame frequency : 150 Hz
Integration time : 2,4 ms

Earth observation (from helicopter) has been done by Onera and it is possible to compare different pictures taken at different wavelengths (figure 3.9).

Valence 3-5 μm (day time) :



Valence 8-10 μm (day time) :



Figure 3.9 : Long linear MWIR and LWIR MCT detectors

3.2 Short wave infrared detector array for hyperspectral imagers

Sofradir starts the phase A of the Land Surface Processes and Interactive Missions (LSPIM) where a short wave large array is under development.

The large array of 256 rows of 1000 pixels with a pitch of 30 μm both directions is sensitive in the spectral bandwidth of 1 to 2.35 μm .

The program will be completed by end of 2001 with the delivery of prototypes.

This array will be a monolithic piece of HgCdTe hybridised to a ROIC. Whatever is the size of the array the standard technology will be used.

The selection of this approach is due to the good results obtained in the SWIR regions on diodes.

Figure 3.10 shows the prediction of the dark current versus FPA temperature and cut off wavelength as well as several experimental measurements which are in good accordance with the predicted figures.

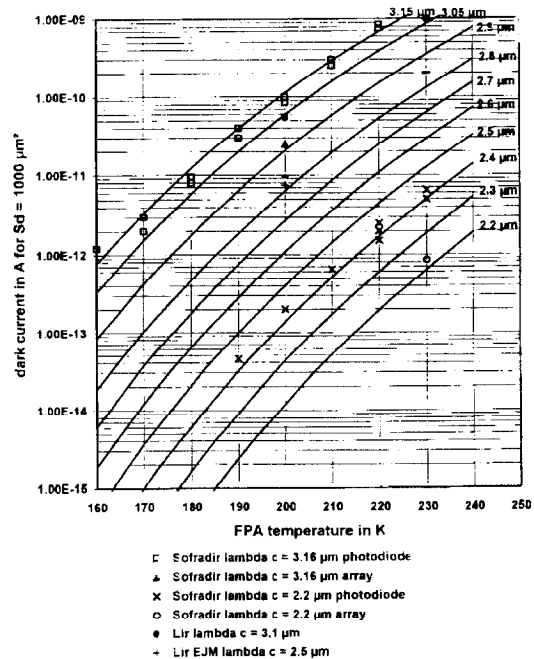


Figure 3.10 : dark current predictions

3.3 Large infrared linear array (Helios 2)

3.3.1 Summary of the development

The development of the infrared detector of Helios II (French military earth observation satellite) began in 1992 with the French Ministry of Defence. This development was based on the existing MCT and readout circuit technologies developed by the French Infrared Laboratory (LETI / LIR).

First, feasibility studies were supported by the Ministry of Defence. At the end of these studies the main choices concerning the detector, focal plane topology, infrared bandwidth, working temperature and number of pixels were done.

The detailed development began in 1994. Then, the direct customer was Alcatel Space Industries who is in charge of the detecting system. The first electrical breadboards was available at the end of 1995 to evaluate the main electrooptical and electrical performances.

The engineering model was delivered at the end of 1997.

Based on this detector, technology validation were made with success and the definitive design of the detector was presented in the middle of 1998.

The industrialisation and qualification models were available at the end of 1998 and the qualification test began in 1999.

Manufacturing of the flight model is in progress. The first flight model was delivered in June 2000. The second one and the extra model will be delivered this year.

3.3.2 Helios II detector characteristics

3.3.2.1 General characteristics

The Helios II detector is a large array of a large number of MCT photodiodes

MCT detecting modules and silicon readout circuit are hybridised by indium bumps onto an interconnection circuit.

The retina is integrated into a non hermetic packaging supporting filter, cold shield and thermal functions to control temperature and heat the detector for molecular decontamination. Two flex cables, one for retina functions and one for thermal functions, are implemented.

3.3.2.2 Electrooptical characteristics

3.3.2.2.1 Geometrical

System requirements concerning the geometrical characteristics of the detector are taken into account early in the detector development and were at the origin of lot of technological chooses.

Relative pixels location versus their theoretical locations is better than $1.0 \mu\text{m}$ along the detector. This high level of performance is insured by the technology used, hybridisation by indium bumps onto an interconnection circuit.

Low flatness of the detection array was one of the main parameters in the choice of the focal plane material. The challenge is to limit in the same time the thermo-mechanical deformation and the constraint in materials and assemblies.

In this case, thermo-mechanical deformation of the focal plane is less than $10 \mu\text{m}$ when the detector is cooled from the ambient to the cold temperature. This performance leads to a final detector flatness better than $20 \mu\text{m}$ at low temperature.

Absolute position of the detection line versus the mechanical interfaces is controlled by the assembling tools and is about $\pm 50 \mu\text{m}$.

3.3.2.2.2 Spectral (figure 3.11)

Spectral response is defined by a cold pass band filter located near the retina.

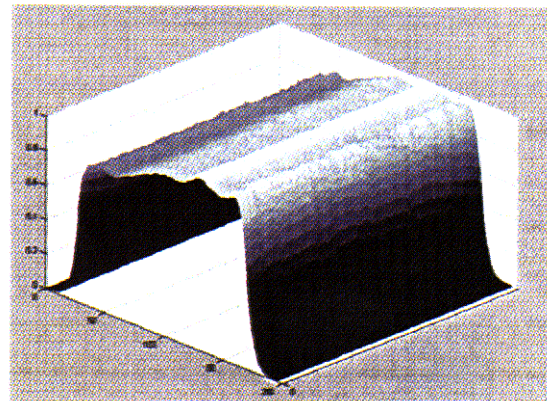


Figure 3.11 : Spectral response of all the diodes of the array

3.3.2.2.3 Radiometric

Low number of defects and high radiometric (signal / noise ratio) performances were required.

The high signal to noise ratio is mainly due to the high quantum efficiency and to the low noise level of MCT detectors. In term of noise, the readout circuit contribution is negligible and leads to a mean signal / noise ration very close to the theoretical limit.

The number of defects of a selected detector is very low. As an example the detector presented has zero defect. To obtain such performance, the detection modules were selected before hybridisation following their electrical characteristics measured on probe test bench and their visual aspect.

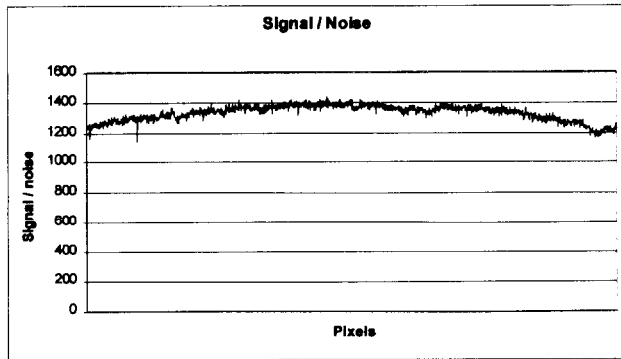


Figure 3.12

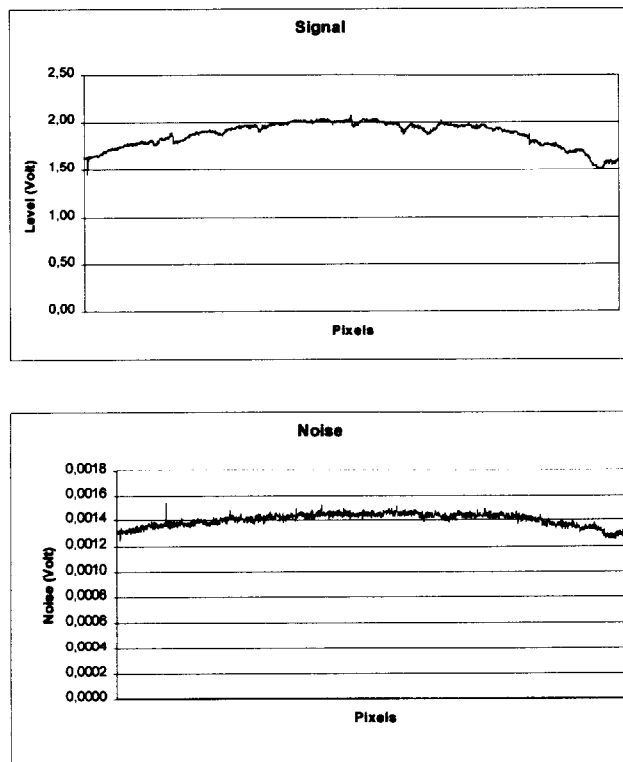


Figure 3.13

3.3.2.3 Environmental / Reliability

Detector reliability is better than 0.996 after 4 years of orbital life. This value was demonstrated based on Sofradir experience and specific tests.

For this detector, environmental characteristics before damage are :

Life time : ground life > 10 years
orbital life > 5 years

Working time > 5000 hours

Thermal cycles > 300
Radiation > 5 krad

4. BIBLIOGRAPHY

- [1] "Status and trends in detector development in SWIR, MWIR and LWIR wavebands" P. Tribolet et al.
- [2] Progress in HgCdTe homojunction infrared detectors, P. Tribolet et al., Journal of Crystal Growth 184/185 1262-1271 (1998)
- [3] Electrical doping of HgCdTe by ion implantation and heat treatment, G.L. Destefanis, Journal of Crystal Growth 86 (1998), 700-722
- [4] "Collective flip-chip technology for HgCdTe IRFPA" SPIE Vol. 2894 (1996)
- [5] Design and critical technology breadboarding of a high resolution thermal infrared radiometer" Dominique Dubet et al.
- [6] New development of a long linear array for 11.3 to 12.3 μm earth observatory" Olivier Saint-Pé et al.
- [7] "Long linear MWIR and LWIR HgCdTe infrared detector arrays for high resolution imaging" Jean Paul Chamonal et al- SPIE Vol 3553, 1998.

X-SAR/SRTM

Part of a Global Earth Mapping Mission

Wolfgang KEYDEL,
David HOUNAM, Regina PÁC, Marian WERNER

Institut für Hochfrequenztechnik & Radarsysteme
DLR Oberpfaffenhofen
82234 Wessling – Germany
Telephone: +49 8153 28 23 05
Fax: +49 8153 28 11 35
e-mail: wolfgang.keydel@dlr.de

Abstract

X-SAR/SRTM is Germany's and Italy's contribution to the Shuttle Radar Topography Mission (SRTM), which has been operated from February 12th 2000 to February 21st 2000. It is the X-Band radar interferometer, which operated in unison with SIR-C the C-Band interferometer of the US. Both technique and technology of X-SAR/SRTM will be described as well as both the internal and external calibration procedures. The error sources which influence the product quality will be shown as well as first X-SAR results.

1. Introduction

The Shuttle Radar Topography Mission (SRTM) has been launched on February 2nd 2000 with the Space Shuttle Endeavour (STS-99). The 13,6 tons of the payload consisting of 2 interferometric radar systems, a C-Band and a X-Band radar, orbited and mapped the Earth for 11 days. The whole mission mainly was sponsored from the US National Imaging and Mapping Agency (NIMA) as well as from the Italian Space Agency (ASI) and the German Aerospace Centre DLR. [1 to 6] The Mission Objectives were to use C-band and X-band interferometric synthetic aperture radar's

(IFSAR's) to acquire data over 80% of Earth's land mass (between 60°N and 56°S) and produce topographic products which meet Interferometric Terrain Height Data (ITHD), specifications: 30 m x 30 m spatial posting with ≤ 16 m absolute vertical linear accuracy and ≤ 20 m absolute horizontal circular accuracy at 90%.

The C-Band Radar-Interferometer was an US-Instrument, and the X-Band Radar-Interferometer X-SAR was Germany's and Italy's contribution to SRTM with DLR as the project lead responsible for system engineering, mission operation, calibration and data processing, *Dornier Satellite Systems GmbH* now renamed to ASTRION Co. was the main contractor for the development of the X-SAR flight instrument (X-SAR/SRTM).

Fig.1 shows both the C-SAR and the X-SAR coverage obtained during the eleven day mission. (The colored Fig's 1 - 4 and 7 - 10 are in chap 9).

2. The Shuttle Radar Topography Mission

[1, 2, 4, 5, 6]

The two-frequency (C-band and X-band) single-pass interferometric SAR's (Synthetic Aperture Radar) instrument were configured by simultaneously operating two sets of radar

Main mission characteristics

Orbital altitude	233,1 km,
Inclination	57,0 °
Flight duration	11 days, 166 revs
Flight attitude (roll, pitch, yaw)	301°, 180 °, 0 °, $\pm 0,1$ °,
Total payload weight	13405 kg
Total payload power/energy	7,14 kW, 9,8 kW peak/880kWh
Number of data tapes	320 equivalent to 2140 GByte
Crew members	G.Thiele, J.Kavandi, M.Mohri, K.Kregel, D.L.P.Gorie

antennas, each with a transmit/receive and a receive-only antenna separated by a 60 m baseline and two receiver channels. The 12 meter long and 40 centimeter wide X-SAR main antenna for transmit and receive (channel one) was mounted directly to a tiltable part of the 12 meter C-radar antenna truss structure in the shuttle's cargo bay. The second (receive-only) antenna was 6 meter long and was, together with the second 8 meter long C-band antenna, mounted onto the tip of a 60 meter long, deployable, stiff, boom structure perpendicular to the velocity direction of the space shuttle, to build the baseline. That configuration, the space shuttle with its 60-meter mast extended from the cargo bay was the longest structure ever flown in space.

Fig.2 shows that schematically, **Fig 3** shows a photograph of the deployed mast with both antennas at the end.

3. X-SAR as Part of SRTM, [1, , 5, 6]

Fig.4 shows the joint operation modes of both systems principally. X-SAR was not capable of operating in a ScanSAR mode like the C-radar which would also allow complete coverage of the Earth during the short orbiting period of 11 days or 166 orbits. X-SAR operated, in turn, in a higher-resolution mode with a smaller swath width of approximately 50 km placed inside the 250km SIR-C scan swath at an angle of 54.5 degrees off-nadir. The C-band and X-band could operate simultaneously or independently. For the most part, they operated together. The only disadvantage to that was that joint operations consumed more

power, but since the coverage of sites with both frequencies was desirable, the basic plan took this power usage into account. The advantage is the ability to crosscheck the maps produced by the two systems.

The primary antenna could be tilted in elevation to align its beam with the one of the secondary antenna. To accomplish an azimuth in-orbit alignment of both antennas an electronic beam steering of the receive antenna within a range of 0,9 degrees in steps of 0.3 degrees has been installed. However, it was not necessary to use this equipment during the mission.

The two-channel output data streams, with 90 Mbit/sec, produced by the X-SAR radar were multiplexed for recording on cassette tape recorders onboard or down linked at half the rate. These represent the raw amplitude and phase data for the two images to be processed to create the interferometric fringes on ground after the mission. For X-SAR alone more than 80 hours of data takes have been recorded on 110 cassette tapes.

The X-SAR operated in a higher-resolution mode but with a smaller swath width of 50 km than the C-Band radar. Only approximately 40% of the surface being flown over have been detected. Consequently the selection of the reference target locations is determined by the illuminated swaths of the X-SAR-System. The locations are positioned in regions of swath crossing points. Thus every reference target generally appears in two different SAR images.

Parameter	Main Channel	Secondary Channel
3 dB beam width elevation	5,3°	5,3°
3 dB beam width azimuth	0,14°	0,28°
Electronic beam steering range in azimuth		± 0,9° step 0,03°
Antenna gain	44,5 dBi	41,5 dBi
Noise figure	5,25 dB	2,52 dB
Transmit power peak at HPA output	3300 W	
Pulse length	40 µsec	
Pulse repetition frequency	1674 Hz	
DC power in transmit mode	886 W	290 W
DC power in pause mode	154 W	290 W
Data quantization	4 Bit I&Q	4 Bit I&Q
Data rate	45 Mb/s	45 Mb/s
Total energy	125 KWh	
Total mass	220 kg	123 kg

Tab. 1: X-SAR/SRTM Flight Instrument Characteristics

	X-Band Primary	X-Band Secondary	C-Band Primary	C-Band Secondary
Frequency	9.6 GHz	9.6 GHz	5.3 GHz	5.3 GHz
Polarization	VV	V	H, V	H, V
Polarization Isolation	39 dB		>25 dB	>25 dB
Adjustable Off-Nadir Angle	15° - 55° mechanical	54° -55° mechanical	15° - 55° electronical	15° - 55° electronically
Off Nadir during Mission	54.5°	55.5°	36.5°, 46.5°, 53°, 58°	36.5°, 46.5°, 53°, 58°
Adjustable Horizontal Angle	0°	0.9° step 0.3°		
Swath Width	45 km	45 km	225 km	225 km
Azimuth Res. (4 looks)	25 m	25m	30m	30m
Range Resolution				
10 MHz/20 MHz Bandwidth	20 m / 10 m	20 m / 10 m	25 m / 13 m	25 m / 13 m
Total Dynamic Range	60 dB	60 dB	60 dB	60 dB
Radiated Peak Power	3.5 kW		1.7 kW	
Main Antenna Area	0.4 m x 12 m	0.4m x 6m	0.7 m x 12	0.7m x 8m
Main Antenna Gain	43.5 dB	41,8 dB	42.8 dB	40,0 dB
Elevation Side Lobe	-20 dB	-21 dB	-18 dB	-19 dB
3 dB Beam Elevat. /Azimuth	5.5° / 0.14°	5,3°/0,28°	4.9° / 0.25°	4,9°/37,5°
Radiometric Resolution	2.5 dB	2.5 dB	1.5 dB	1.5 dB
Data Rate / Channel	45 Mb /sec	45 Mb /sec	45 Mb /sec	Mb /sec

Tab.2 Comparison of X-Band and C-Band flight instruments

4. The Calibration [1, 5, 8]

The accuracy requirements for the mission results claim for an extremely accurate system calibration. In total the SRTM calibration is divided into 5 phases:

1. Preflight concept definition phase including sensor characterization, calibration algorithm development and implementation
2. Ground campaigns during the mission
3. On board calibration measurements during the mission
4. A 6 to 8 month's commissioning phase for the generation of static and dynamic calibration files, and for analysis and modeling of parameter drifts with temperature and time which **is the present status**
5. Operational calibration and validation after the commissioning phase which **will be started at the beginning of next year**

The task of the on-ground calibration was to set up precisely surveyed control targets for both the radiometric and interferometric calibration, 22 calibration fields distributed all over the world have been established.

Hence, in the area from Bayreuth down to Füssen in Bavaria, a calibration field was set up encompassing 27 different locations, in which passive as well as active reference targets (trihedral corner reflectors and/or transponder) and calibrated ground receivers were erected. By using the ground receivers and the transponders, the antenna patterns of both the German-Italian X-SAR-System and the American SIR-C-Radar could be measured, which is required for radiometric calibration. The corner reflectors serve as reference points in the topographic data to calibrate the phase.

Some corner reflectors had to be moved between passes. All had to be pointed towards the shuttle before a pass. Furthermore, it was necessary to determine the geographical location of every corner site very precisely by using differential GPS.

The interferometric calibration concept for X-SAR considers instrument phase calibration and InSAR (Interferometric SAR) imaging geometry calibration also. A height error may result from errors due to uncertainties in the imaging geometry parameters, such as baseline length and tilt angle, and orbit data, and from phase variations caused by the instrument. The tables in **Fig 5** (following page)

X-SAR/SRTM Error Budget

X-SAR/SRTM Height Error Sources

- Baseline Tilt Angle Error
- Baseline Length Error
- Instrument Phase Error
- Random Phase Error
- Ambiguity Phase Error
- Atmospheric Error
- Position Error
- Calibration Error
- Slant Range Error
- Processing Error

Performance Requirements:

- Relative Height Accuracy (90 %) < 6 m
- Absolute Height Accuracy (90 %) < 16 m

Height Error Examples (Middle of Swath)

Error Type	Relative (30 seconds)		Absolute (11-days)	
	Accuracy	Error	Accuracy	Error
Baseline Tilt Angle	2 arcsec	3,0 m	9 arcsec	13,4 m
Baseline	1,3 mm	0,8 m	4,0 mm	2,6 m
Instrument Phase	4,0 deg	4,2 m	4,0 deg	4,2 m
Total (RSS)	5,5 m		14,4 m	

Fig.5 Error Sources and examples of height errors resulting from special error types

Deutsches Zentrum für Luft- und Raumfahrt

e.V.

Calibration Concept

- Estimation of systematic errors
- Monitoring of system parameters and instrument performance
- Characterization of instrument parameters
- Development of calibration models (parameter drifts as a function of time and temperature)
- Ocean as reference height (sea surface height model)

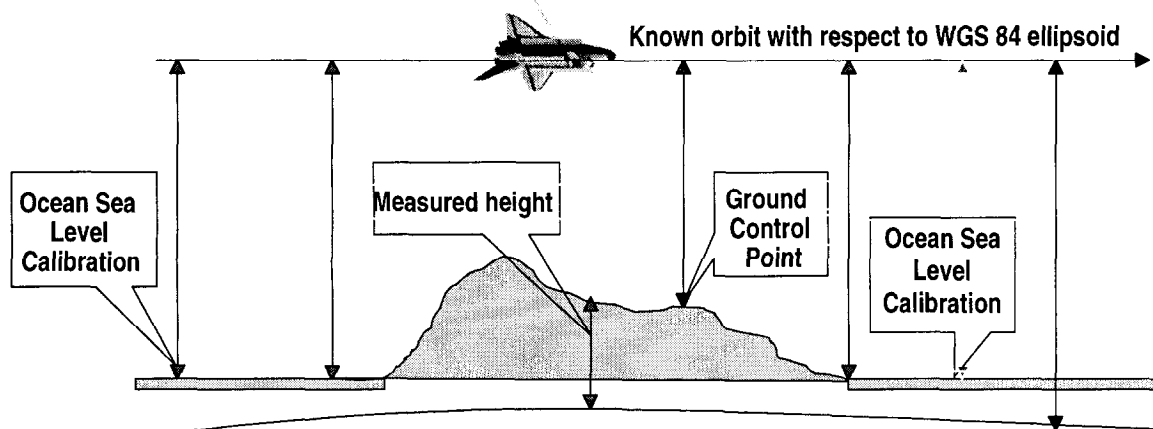


Fig. 6 Scheme of calibration concept

list the main error sources as well as the accuracy requirements which had to be fulfilled in order to reach the goals of the mission with respect to X-Band. A suite of sensors was responsible for measuring and controlling the proper alignment of the secondary antenna with respect to the main antenna and the attitude and position of the interferometric system in orbit.

A star tracker has measured the orientation of the interferometric system in orbit, which is supported by an inertial reference unit consisting of three 2-axis gyros. An optical tracker of the secondary antenna which is a video camera and LED targets, will allow a relative 3-axis measurement of the boom antennas. Additionally, GPS antennas on the secondary antenna structure will provide a 0.8m orbital position accuracy determination and, furthermore, a time reference for the radar with an accuracy of 100 microsec. In addition to the static misalignments, there is the dynamic reaction of the top of the boom to the space shuttle orbit and attitude control system and thermal displacements. An extremely stiff and thermal stable construction is foreseen using CRFP (Carbon Re-inforced Fiber Plastic) technology. The ocean surface serves as reference height. Before and after each continental pass, there was a calibration over the ocean (Fig. 6, previous page). Phase calibration has to be performed for time and temperature variations. Preflight characterization of the behavior of critical parts is required for estimating the residual calibration error. In certain cases these parameters in combination with temperature measurements can be sufficient for later correction.

5. Products, [1,3,5]

The final products of the SRTM mission are digital elevation products in a mosaic format generated from C- and X-band radar frequencies. X-band full coverage begins at latitudes greater than about 55° North/South. The C-band radar has completely cover the land surface between 60° North and 58° South with multiple overlap in the higher latitudes.

The complex SRTM data processing will require one to two years in order to convert the raw radar data into topographic maps. Resulting data formats will be compatible with standard cartographic data-analysis software and tailored to the needs of the scientific, commercial and operational user communities.

Detailed specifications of the X- and C-band derived DEM's and other elevation products are delineated in the box on top of the next page. Apart from digital terrain height maps in two different resolutions, there are multi-look images in ground range, single look images in slant range as well as terrain-corrected data and incidence angle masks. A height error map co registered to the elevation maps will be available indicating the quality of the interferometric DEM's pixel by pixel.

The measurement of topography in vegetated regions through SAR techniques causes in some areas deviations from the true terrain height because the short radar wavelengths of C- and X-band (5.3cm and 3.1cm, respectively) sense the very top of dense canopies or high buildings. In order to correct for these inconsistencies within the DEM, it is planned to provide a land cover classification map.

6. Results [1,3,5]

During the 11 day mission 69 data takes have been received and analyzed during mission with 72 Gigabytes of data, 99 interferogram's and 45 DEM's have been generated. The InSAR processing of a 45 km x 170 km area took 1 hour. The processing was done on a 12 CPU SUN E4000.

Fig .7 shows as the very first result obtained 11 hours after launch the interferometry fringes as well as the resulting (DEM) of an area around White Sands in New Mexico, United States. The DEM is color coded following the rules of normal geographic maps, i.e. increasing altitudes from light brown over dark brown up to white.

SRTM Data Produkts

DTED (Digital Terrain Elevation Data) ⇒ ITED (Interferometric Terrain Elevation Data)

- 1 degree x 1 degree cell; origin in SW corner
- elevations in meter
- intervals in Arc Seconds (DTED 1: posts every 3 arcsec, DTED 2: 1 arcsec)
- datum: vertical = mean sea level, horizontal = WGS 84
- Specification ITED level 2

	C-Band	X-Band	
horizontal absolute accuracy	< 20 m	< 15 m	(90% circular error WGS)
vertical absolute accuracy	< 16 m	< 10 m	(90% linear error WGS)

The **Fig 8** and **Fig 9** show exemplary a DEM of parts of Hokkaido, the northernmost of the four main islands of Japan. With an area 83.500 square kilometers it constitutes more than 20 percent of Japan's land area and comprises 90 percent of Japan's pastureland. The scene shows the northern and southern shores of Ushiura-wan (Volcano Bay). A distinctive feature is the volcano Komagatake just off the image center on the southern shore of Ushiura-wan. The lower image in Fig. 9 shows a three dimensional representation of the Komaga volcano.

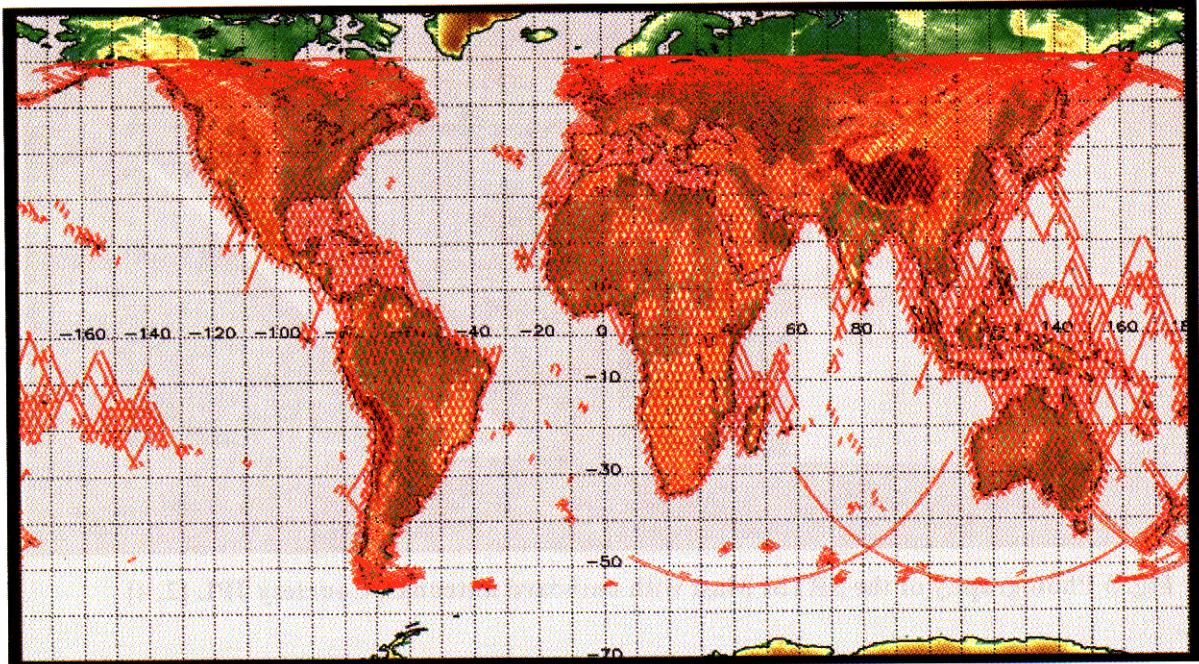
Fig. 10 shows in the upper image a X-SAR DEM as a perspective view over the Baia de Paranagua/Brazil with the Pico Parana in the upper left and in the lower image a photograph of that mountain.

7. Concluding Remarks

The whole Mission was successful and fulfilled the expectations up to 99.6%. The quality of the binary data as well as their homogeneity seems to be excellent [3], however, the final data quality can not yet be accomplished due to missing precision attitude and orbit data. The system and the processor as well presently deliver the expected parameters close to the theoretical limits.

8. References

- [1] DLR/DFD Homepage
<http://www.dfd.dlr.de/srtm/>
- [2] JPL Homepage: <http://www.jpl.nasa.gov/srtm/>
- [3] Eineder, M., R. Bamler, N. Adam, H. Breit, S. Suchandt, U. Steinbrecher: SRTM/X-SAR Interferometric Processing-First Results, EUSAR 2000, 3rd European Conference on Synthetic Aperture Radar, 23 – 25 Mai 2000, Munich, Germany, pp 233 -236
- [4] T. Farr and M. Kobrick, "The Shuttle Radar Topography Mission: A Global DEM", IGARSS Proceedings 2000.
- [5] Werner, M. Shuttle Radar Topography Mission (SRTM)-Mission Overview, Proc. EUSAR 2000, 3rd European Conference on Synthetic Aperture Radar, 23 – 25 Mai 2000, Munich, Germany, pp.209 - 212
- [6] Werner, Marian, Kay-Bodo Klein, Martin Haeusler. Performance of the Shuttle Radar Topography Mission, X-Band Radar System
- [7] WERNER, Marian, Operating the X-band SAR Interferometer of the SRTM
- [8] Zink, M., D. Geudtner: First Results from The Calibration of the Interferometric X-SAR System on SRTM, EUSAR 2000, 3rd European Conference on Synthetic Aperture Radar, 23 – 25 Mai 2000, p 223



D:\mpuser\work\p-or-c_data\takes.gif created 24-FEB-1999 18:02 GMT
G/T: 0/11:50:00.0 to 10/08:30:00.0

Fig. 1 Coverage Map: X-SAR/SRTM coverage during the 11-day shuttle mission.. The Internet link <http://isis.dlr.de/XSAR/srtm> will guide you to the geographic locations of the X-SAR swaths.[5,7]

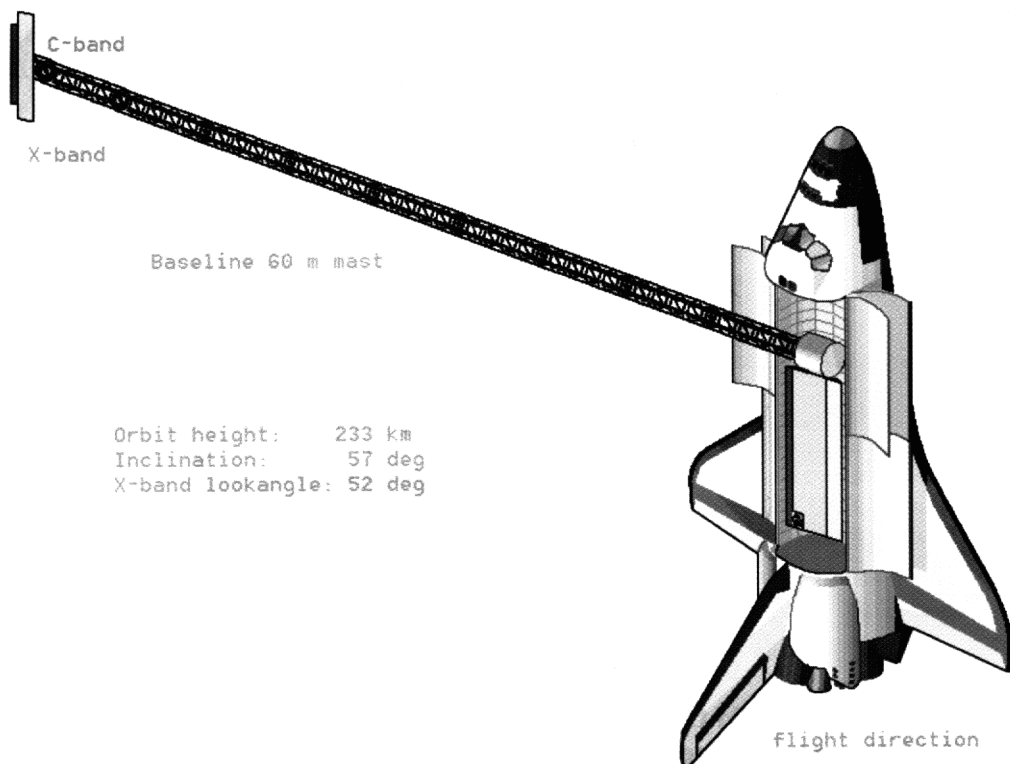


Figure 2: Drawing of the SRTM Configuration with the Secondary Antennas mounted on the Mast

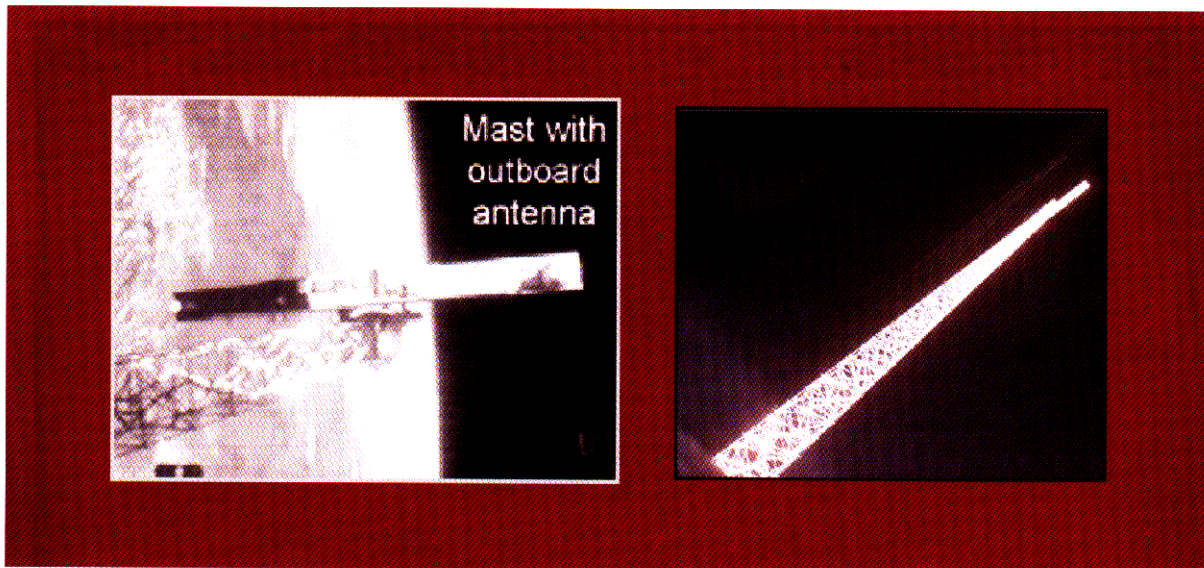


Fig. 3 Photography of the SRTM Mast with outboard antennas, Courtesy JPL [2, 4]

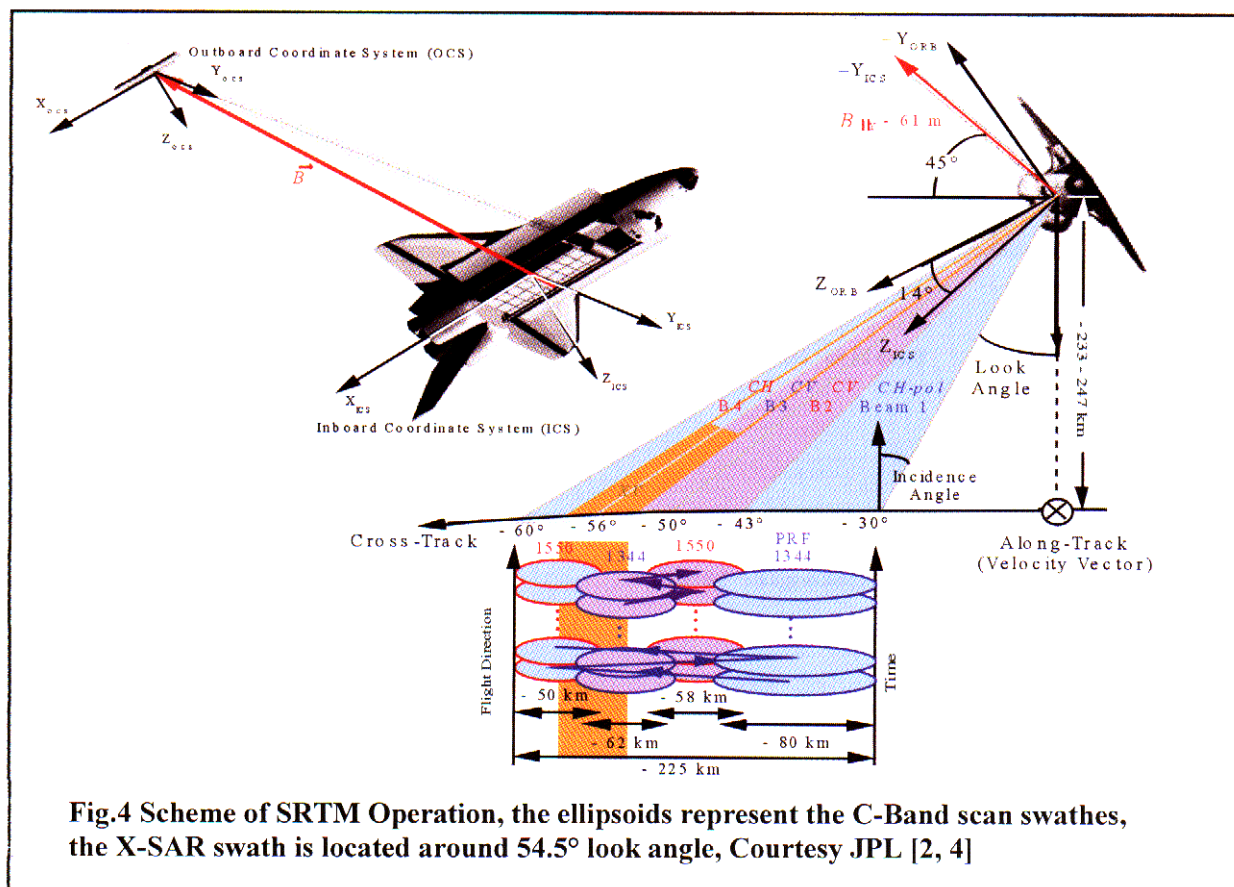


Fig.4 Scheme of SRTM Operation, the ellipsoids represent the C-Band scan swaths, the X-SAR swath is located around 54.5° look angle, Courtesy JPL [2, 4]

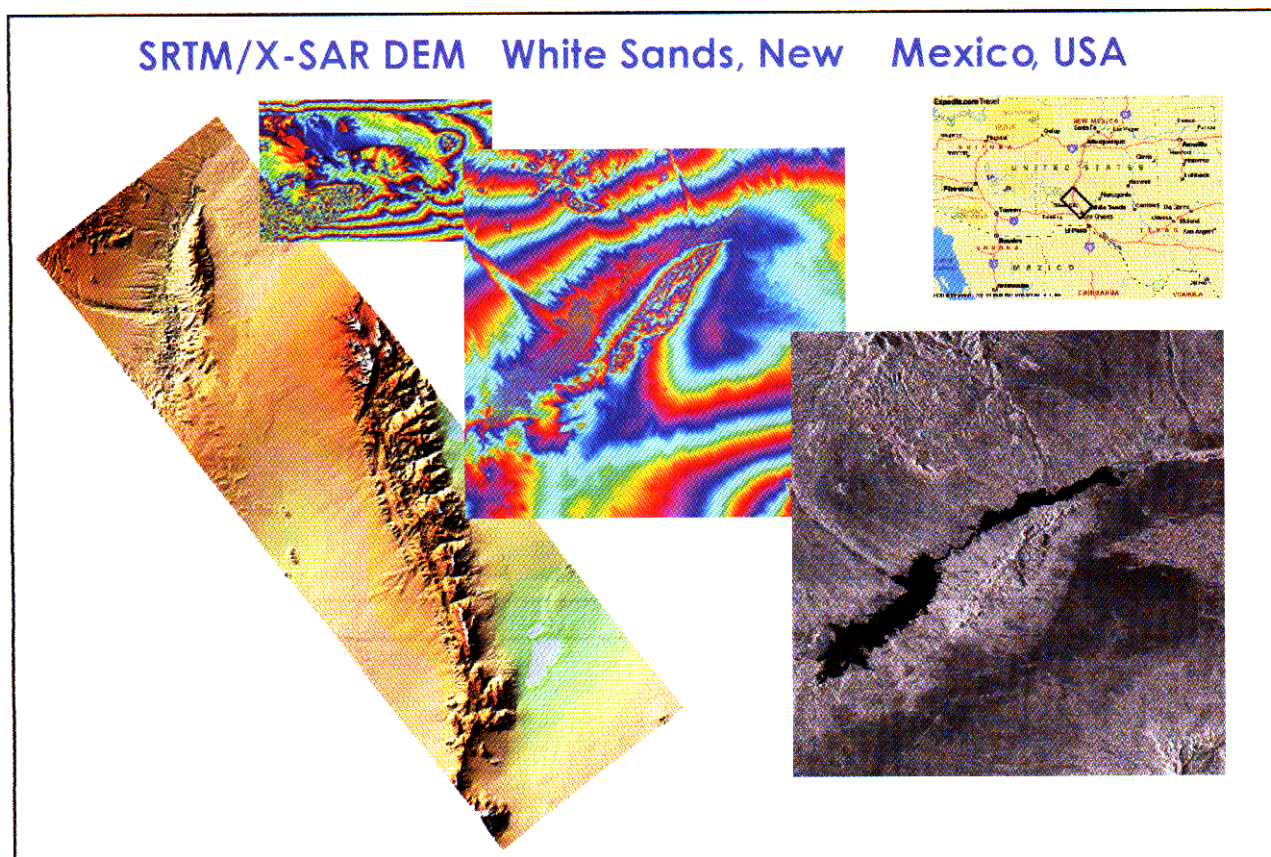


Fig. 7 Fringes, SAR-Image, colorcoded DEM of White Sands, New Mexico, map in the upper right corner [1]

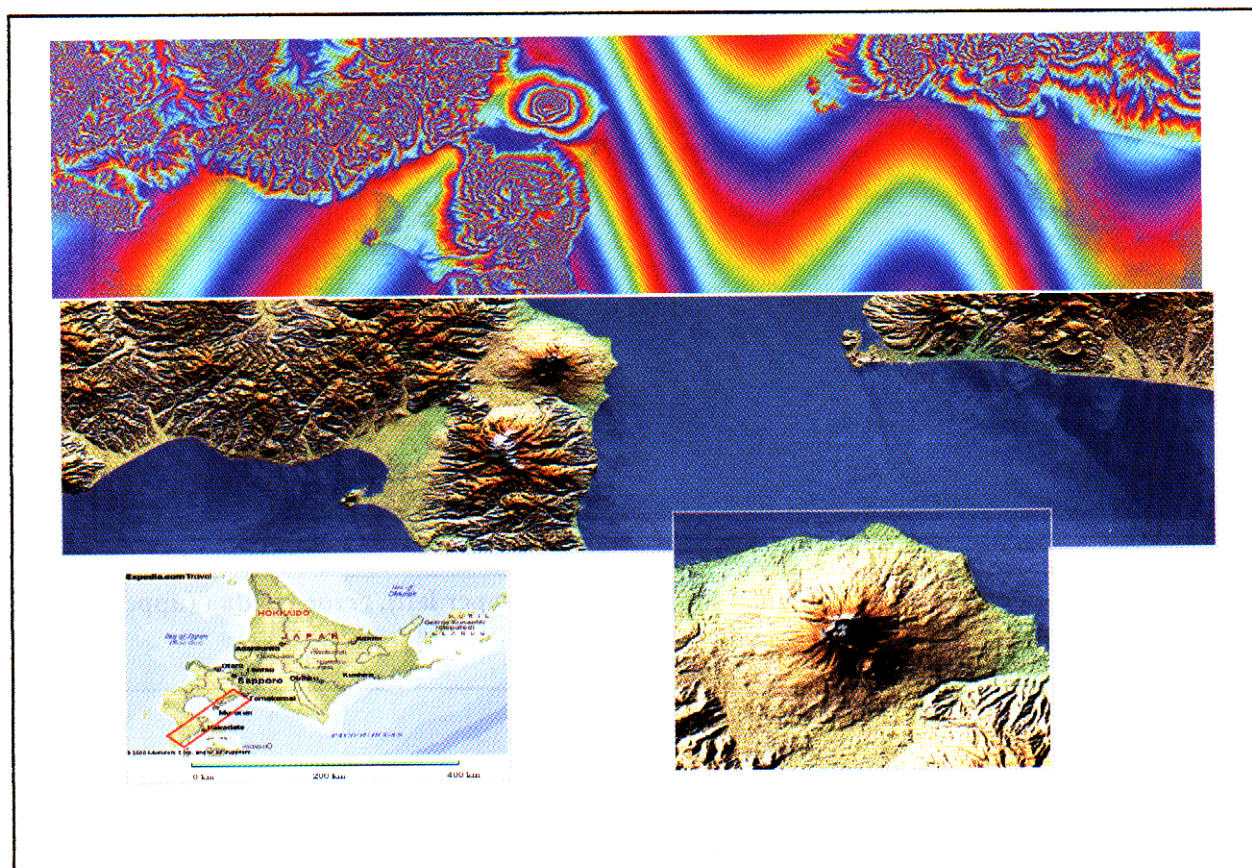


Fig. 8 DEM of Hokkaido Peninsula, Japan, with interferometry fringes with map, enlarged DEM of Kanaka-take Volcano [1]

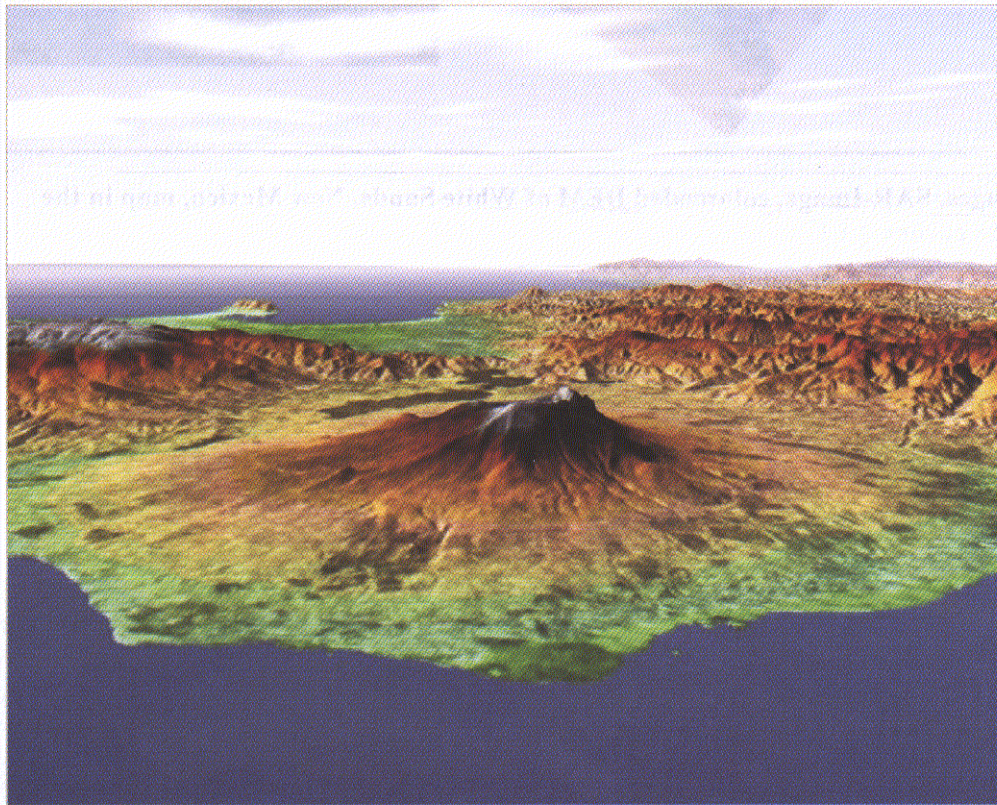
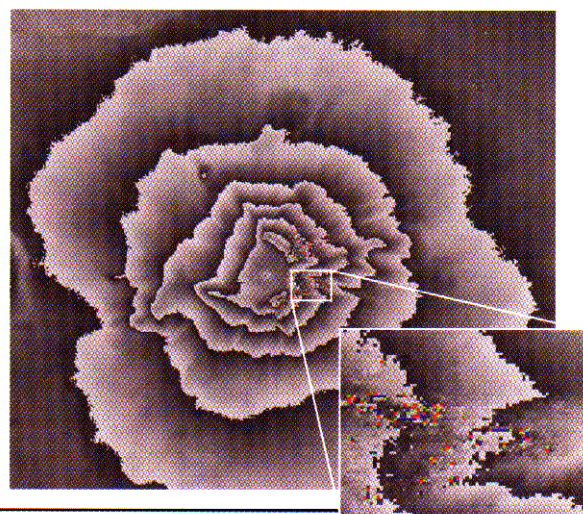
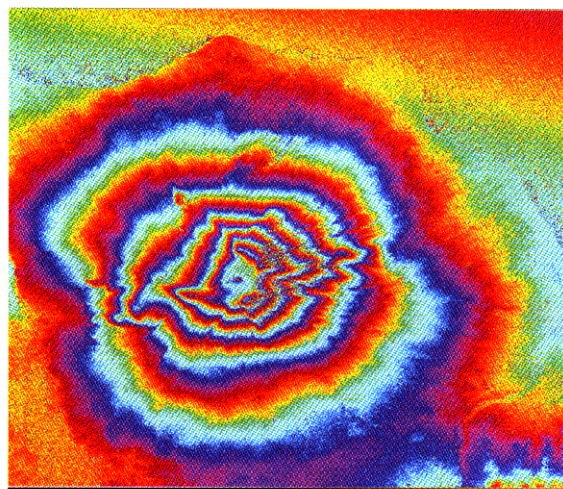


Fig. 9 :Kanaka-take Volkano, Hokkaido Japan: Fringes (upper left), error residua (upper right), 3-D representation (bottom) [3, 1]

Deutsches Zentrum für Luft- und Raumfahrt

e.V.

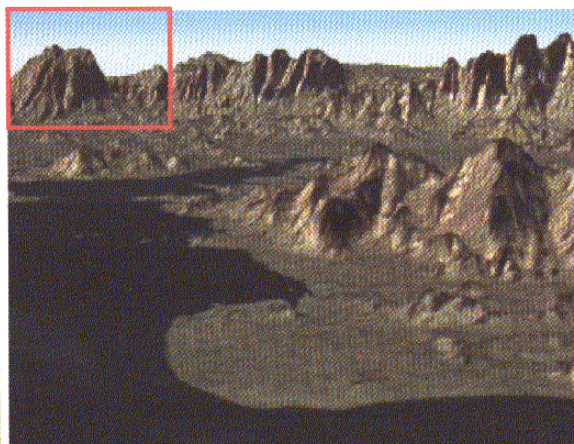


Foto: Marco Aurélio

Pico Parana, Paranaguá, Brazil.

Data are recorded over the Baia de Paranaguá/ Brazil, approximately 200km south-east of Sao Paulo located in the State of Paraná. Further inland the highest peak of the Serra do Mar Range, the **Pico Paraná (1922m)** is visible on the **upper left corner**. The Baia de Paranaguá is an estuary reaching 40km inland and comprises a total area of 667km².

Upper image :perspective view created from the **X-SAR DEM** over the Baia de Paranaguá towards the mountains in the West. Lower image: photograph of Pico Parana.

Data Take: 13.02.2000

Scene Center: 48° 36' West,
25° 24' South

The Shuttle Radar Topography Mission

Tom G. Farr, Mike Kobrick

Jet Propulsion Laboratory
California Institute of Technology
Pasadena, CA 91109 USA

On February 22, 2000 Space Shuttle Endeavour landed at Kennedy Space Center, completing the highly successful 11-day flight of the Shuttle Radar Topography Mission (SRTM). Onboard were over 300 high-density tapes containing data for the highest resolution, most complete digital topographic map of Earth ever made. SRTM is a cooperative project between NASA and the National Imagery and Mapping Agency (NIMA) of the U.S. Department of Defense. The mission was designed to use a single-pass radar interferometer to produce a digital elevation model (DEM) of the Earth's land surface between about 60° north and 56° south latitude. When completed, the DEM will have 30 m pixel spacing and about 15 m vertical accuracy. Two orthorectified image mosaics (one from the ascending passes with illumination from the southeast and one from descending passes with illumination from the southwest) will also be produced.

The technique to acquire this data set has been used for over a decade to produce accurate topographic and topographic change maps (Madsen and Zebker, 1998). Radar interferometry uses the fact that the sensor is phase-coherent, so that if two images are acquired at two slightly different locations, a phase-difference image can be produced that contains information on the topography. The two images can be obtained simultaneously, as with most airborne systems, or at different times, which is the case with all previous spaceborne systems. The main drawbacks to the repeat-pass mode is the need to know the baseline separation of the two images to the mm level, and changes in the

atmosphere and surface can occur between the two passes. The baseline can be determined by obtaining a few ground control points, however the other effects are much more difficult to alleviate. Water vapor in the troposphere adds a significant phase delay, which, if different at the two times of image acquisition, will cause large errors in the topographic map produced. This effect has been noted by many investigators; the only feasible way to counteract it is to acquire many pairs of images. Surface changes that degrade the interferometric measurement include incoherent sub-pixel motion such as the waving of leaves and branches on trees. This decreases the amount of correlation between the two images, increasing the error of the phase measurement. In extreme cases, complete decorrelation results in loss of the phase information.

To avoid the problems with repeat-pass interferometry, SRTM acquired its two images simultaneously. SRTM used the same radar instrument that comprised the Spaceborne Imaging Radar-C/X-band Synthetic Aperture Radar (SIR-C/X-SAR) that flew twice on Space Shuttle Endeavour in 1994 (Evans et al., 1997). SIR-C/X-SAR was a cooperative project between NASA and the German and Italian Space Agencies and obtained data for over 50 science investigations. To collect the interferometric data, a 60 m mast, additional C-band antenna, and improved tracking and navigation devices were added (Fig. 1). A second X-band antenna was also added by the German Space Agency, and collected higher resolution topographic measurements in strips nested within the full, C-band coverage (Werner et al., 2000).

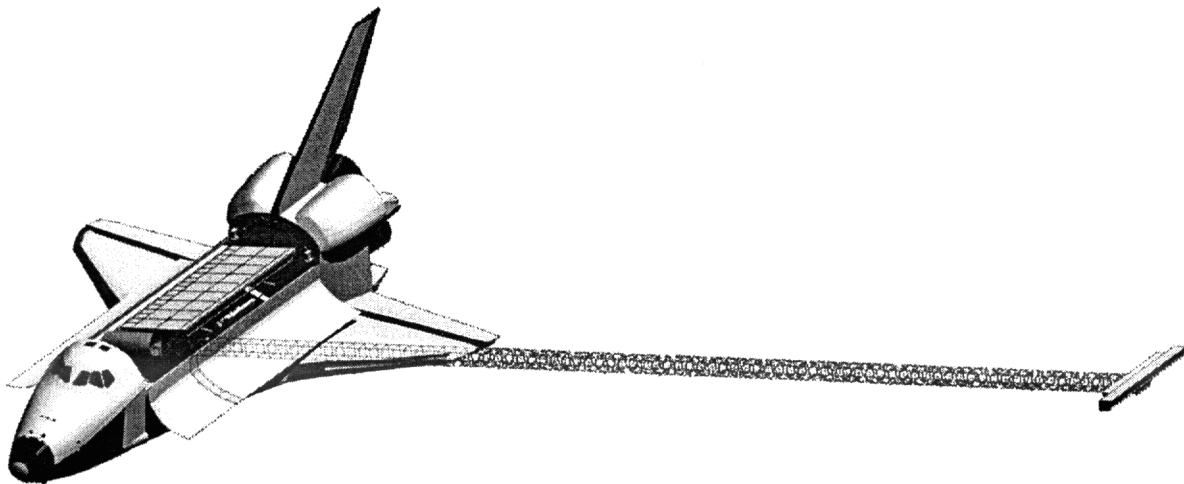


Figure 1. The SRTM payload in the Space Shuttle. The main antenna is seen in the payload bay and the outboard antennas are at the end of a 60 m mast.

The major part of the SRTM hardware resided in the payload bay of the Space Shuttle (Fig. 2). This included the main structure, supporting the L, C, and X-band antenna panels, the mast canister, and the Attitude and Orbit Determination Avionics (AODA).

Due to weight limitations, the L-band panels were removed. The C-band system was operated in a 4-beam scanSAR mode to acquire a 225 km swath, allowing complete coverage in 10 days, with a small overlap at the equator. Owing to the nature of the original SIR-

C/X-SAR digital data handling system, the scanSAR system was operated in a dual-polarization mode: two

beams were HH polarization and two were VV.

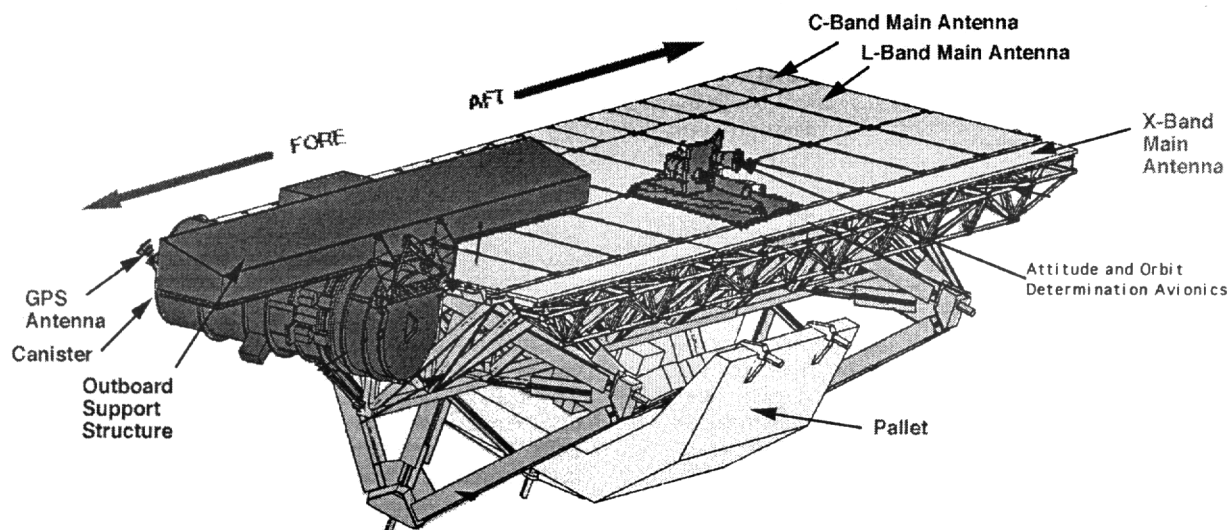


Figure 2. A detailed view of the SRTM hardware in the Space Shuttle payload bay. The 60 m mast is in its stowed configuration; the outboard antennas are folded back on top of the main antenna.

The 60 m mast was produced by AEC-Able Engineering, based on designs for the International Space Station. It consisted of carbon-fiber longerons forming cubes, or bays, with titanium wires under tension as cross-braces. There were 87 bays, each about 70x80 cm making up the full 60 m length. The mast was stored as a collapsed spiral in a canister 2.9 m in length. When deployed, the Shuttle with the mast was the largest structure ever flown in space.

An important addition to the original SIR-C/X-SAR hardware was the Attitude and Orbit Determination Avionics (AODA; Duren et al., 1998). This system was required to obtain data on the length and orientation of the mast and the location and orientation of the Shuttle in earth-centered inertial coordinates. These factors are critical to the creation of an accurate digital topographic map automatically without the necessity of ground control points. AODA occupied the place of one of the L-band panels on the face of the main antenna (Fig. 2). It consisted of an Astro Target Tracker, Electronic Distance Meters, Star Tracker, GPS receivers, and an Inertial Reference Unit. The Astro Target Tracker was a modified star tracker with new optics designed to allow it to track a set of LEDs mounted on the outboard antenna structure, recording data on the motions of the outboard antenna relative to the main antenna. The Electronic Distance Meters were off the shelf Leica surveying instruments modified for the space environment and set up to measure the length of the mast to better than 3 mm. The GPS receivers were built at JPL to measure the location of the Shuttle at 1 m accuracy using antennas on the outboard antenna structure (Fig. 2). AODA data were recorded continuously and stored on the Shuttle as well as sent to the ground for incorporation into the processing stream of the interferometric data.

Another important addition to the SRTM hardware was the presence of several laptop computers on the aft flight deck of the Shuttle. These monitored and archived AODA data and controlled the Payload High

Rate Recorders. AODA data were sent to one set of laptops so that the Shuttle crew could monitor mast motions. This also aided in the initial alignment of the inboard and outboard antennas by the astronaut crew. The recorders were the same as flew on the SIR-C/X-SAR missions, but due to a desire to more efficiently pack data onto a limited number of tapes and the fact that some data takes were longer than a single tape, a more sophisticated controller was needed. The laptop controlling the recorders sensed the approaching end of a tape, started the next recorder to produce overlapped data, and then handed over to the second recorder.

As the full C-band data rate of 180 Mb/s was about 4 times that of the Shuttle downlink capacity through the Tracking and Data Relay Satellite System, full interferometric data could not be downlinked in real time. However, during the mission some data were played back from tape at one-quarter speed and processed overnight at JPL and the German Space Agency. This provided an end-to-end check of the entire system.

SRTM launched aboard Space Shuttle Endeavour on February 11, 2000 and had a nearly flawless 11 day flight, landing on February 22 with over 10 terabytes of data on over 300 tapes. Upon landing, the flight data tapes were transferred to a secure area at Kennedy Space Center, copied, and delivered to JPL for processing. After a checkout and calibration period, full data processing will begin in spring 2001 and take approximately 1 year.

The ground data processing system is broken into 3 parts: Interferometric processor, which converts the raw radar data into strip height maps and radar image strips; Mosaic processor, which takes the myriad of strips from all over the world and compiles a mosaic of the height and image data a continent at a time, allowing block adjustments on that scale; and the Verification system, which tests the mosaics for quality, producing an accuracy map (Rosen et al.,

2000). Mosaics will be delivered to NIMA, where some validation of the data set will be done. The data will also be delivered to the civilian archive at the U.S. Geological Survey's EROS Data Center. Current agreements call for the full resolution data covering the United States to be publicly available, however for areas outside the U.S., the data will be averaged to 90 m pixels for public release. NASA and NIMA will review requests for scientific use of the full resolution data for areas outside the U.S. on a case by case basis.

An extensive program for calibration and verification of the SRTM data will be undertaken. The calibration of the interferometer will allow fully automatic processing of the data to absolute Digital Elevation Models (DEM). In addition to the measurements made by AODA, radar path delays were monitored by a phase-locked optically coupled calibration tone injected at the input to the receiver chains. These systems provided accurate relative calibration over short (less than the orbit period) time scales. Longer period errors in the mosaics will be evaluated with a globally distributed set of small, high-resolution DEMs, ground control points, and kinematic GPS surveys. Absolute calibration will be carried out through measurements at two ground control sites as well as of the ocean surface before and after every coast crossing, along with a few long deep-ocean passes.

Acknowledgements

Work performed under contract to NASA. More information about the Shuttle Radar Topography Mission can be found at: <http://www.jpl.nasa.gov/srtm/>

References

- Duren, R., E. Wong, B. Breckenridge, S. Shaffer, C. Duncan, E. Tubbs, and P. Salomon, 1998, Metrology, attitude, and orbit determination for spaceborne interferometric synthetic aperture radar, *Proceedings of SPIE, Acquisition, Tracking, and Pointing XII*, v. 3365, p.51-60.
- Evans, D.L., J.J. Plaut, E.R. Stofan, 1997, Overview of the Spaceborne Imaging Radar-C/X-Band Synthetic-Aperture Radar (SIR-C/X-SAR) Missions, *Rem. Sens. Env.*, v. 59, p. 135-140.
- Madsen, S.N., H.A. Zebker, 1998, Imaging Radar Interferometry, ch. 6 in Henderson, F.M., A.J. Lewis, ed., 1998, *Principles and Applications of Imaging Radar, Manual of Remote Sensing*, v. 2, Wiley, NY, 866 pp.
- Rosen, P., S. Hensley, J. Martin and E. Rodriguez, 2000, First Results from SRTM: The Beginning of the World's Digital Topography, abs., *IGARSS 2000*, Honolulu.
- Werner, M., D. Hounam and W. Keydel, 2000, X-SAR as Part of SRTM, abs., *IGARSS 2000*, Honolulu.

ENVISAT ASAR – Design & Performance with a View to the Future

Michael Hutchinson, Michael D. Gibbons

(Email: michael.hutchinson@astrium-space.com)

Astrium (UK) Ltd.

Directorate of Science and Earth Observation & Meteorology
Anchorage Road, Anchorage Park, Portsmouth, Hampshire PO3 5PU
England

Summary: The Advanced Synthetic Aperture Radar (ASAR) is a 'C' band dual linear polarized multi-mode terrain monitoring radar forming part of the environmental satellite (ENVISAT) mission. It is to be launched on Ariane 5 in 2001. With heritage from the highly successful ERS-1 & ERS-2 SAR instruments Astrium Ltd. have developed the system design of ASAR in order to provide polarisation diversity, flexible swath selection, and wide swath techniques providing a range of operating modes with data products to suit various needs. This paper describes the overall instrument architecture summarising the key technology areas and the characteristics of each operating mode. It also reviews the major technical challenges that were faced and how they were resolved. The ASAR design based on the use of an active antenna, with individual subarray temperature compensation and internal calibration loop, is complex but a breakthrough with respect to earlier passive antenna designs. The instrument calibration scheme is described and the predicted system performance presented for key parameters based on FM test results. Budgets for mass and power are also provided. The paper concludes with a review of the future SAR development activities that are currently in progress at Astrium Ltd (formerly Matra Marconi Space (UK)).

Introduction: Following the success of the ERS 1 & 2 missions the next generation ESA environmental satellite was conceived and would include a SAR instrument. The advanced SAR (ASAR) design was developed by Matra Marconi Space (UK) with the concept of an active antenna allowing a dramatic improvement in the flexibility of SAR operation. Demonstration equipments were built and tested to confirm the technology capabilities, following which the European Space Agency adopted the design for the ENVISAT program. Subsequently a full technology program was embarked upon involving 22 sub-contractors over 11 countries. This technological step has over recent years been a major contributor to the development of a stronger European Space community.

The original ASAR instrument brief was to provide performance equivalent to or better than that of ERS, while utilising the full flexibility of the active antenna architecture to provide selectable swaths and dual polarisation. The two basic modes of ERS were to be retained, ie. Image and Wave, but swath versatility opened the possibility for increased coverage using scansar mode; and polarisation diversity. The

complexity of the control system was therefore to be increased. Functionally the instrument will provide the capability of imaging a large range of incidence angles with high, medium and low spatial resolutions combined with a dual-polarisation. These features will assign to this sensor a role of primary importance for future microwave imaging requirements.

Architecture: The ASAR instrument consists of two main elements, the Central Electronics Sub-Assembly (CESA) and the Antenna Sub-Assembly (ASA). The whole being designed with a fully redundant electronics systems architecture and a life requirement of 5 years in the Low Earth Polar Orbit environment. The CESA provides control and RF signals, receive conditioning to IF and Baseband, and data processing. The ASA provides RF power generation, low noise receivers and antenna beamforming. The CESA equipments are situated on internal panel faces within the payload equipment bay of the satellite and the ASA is fitted on an angled mounting frame on the lower face of the satellite. Connection between these assemblies is achieved with the Instrument Distribution Subsystem (IDS), which includes the antenna feed waveguide (AFW). The satellite configuration is illustrated in Figure 1, which shows the orientation of the antenna lengthwise in the flight direction. The larger planar structure also depicted in Figure 1 represents the solar array.

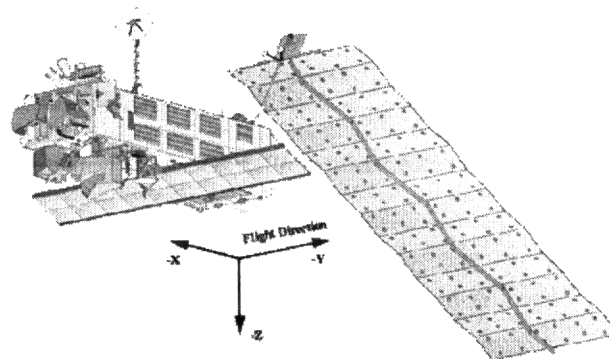


Figure 1 ENVISAT Illustration (courtesy of ESA)

The CESA hardware tree is provided in Figure 2. The instrument is interfaced to the satellite for command and control through the CSS, which comprises two cold redundant ICE units. These each contain a primary processor or CPU (central processing unit) and provide

the 'intelligent' interface, managing the derivation and distribution of the operational parameters (eg. transmit pulse characteristics and antenna beams among many others). It generates the instrument operation timeline and also provides routine monitoring and crisis management procedures. Command interfaces with the DSS and the TSS (part of the ASA) are provided by a MIL-STD-1553 bus. Control signals are routed via specific interfaces to manage the detailed pulse timing sequences of the radar.

The instrument transmit pulse characteristics are flexibly derived within the DSS based on parameters sent from the CSS. The output of the DSS is an up-chirp pulse centred at the IF carrier frequency (124 MHz). Within the RFSS this pulse is up-converted to the main transmission frequency (5.331 GHz) and amplified to provide the correct input power to the antenna.

In receive the RF echo signal from the ASA is delivered to the RFSS where it is filtered, amplified and downconverted again to IF. The receive gain of the RFSS can be commanded to optimise the signal levels over the ADC dynamic range. The received IF signal is passed to the DSS where it is coherently demodulated into In-phase & Quadrature (I & Q) components, which are passed through separate anti-alias filters and digitised using 8-bit A/D converters.

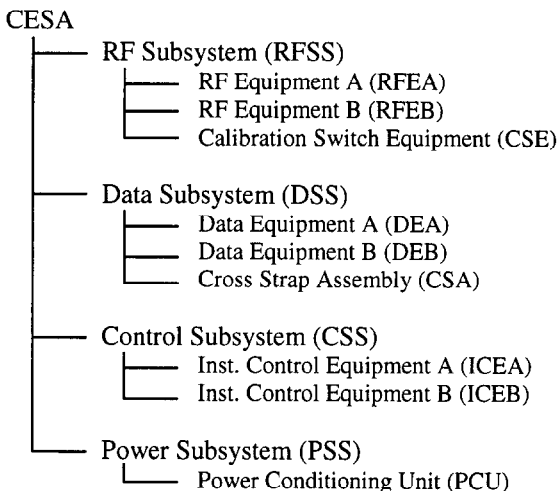


Figure 2 CESA Hardware Tree

Data compression is applied to the raw science data to reduce the data stream volume. This compression is performed using an FBAQ¹ (flexible block adaptive quantiser) that permits acceptable data rates with minimal degradation in image quality. It is achieved by using an algorithm optimised to the statistics of the radar signal, and implemented within an ASIC. It can be operated in three modes: Averaging (compressed), sign & magnitude (3 lsb) or Bypass (full 8-bit) depending on the type of data to be processed. The available compression ratios are 8/4, 8/3 and 8/2 bits depending on mode requirements. For the three on-board signal types to be digitised the default BAQ settings are as in Table 1.

As these functions and the general operation of the instrument results in varying internal data rates the DE also contains a pair of swap memory banks for the Science Data to be stored. Header information including on-board time and other information required by the ground processor is included with the compressed science data to form packets that are passed to the spacecraft interface.

Signal type	BAQ mode
Calibration pulse	Bypass
Noise samples	Sign/Magnitude
Echo (Signal + Noise)	Compressed 8/4 (8/2 Wave)

Table 1 BAQ Default Settings

The ASA provides the ASAR antenna, which is itself a significant feature and covered in detail within a separate paper². This is an active phased array antenna 1.3m x 10m comprising five 1.3m x 2m panels which are folded into a stack position for launch. It consists of a support and services structure carrying 20 tile equipments. Each panel houses four 0.65m x 1m tiles mounted in a lattice beam structure. The ASA hardware tree is provided in Figure 3.

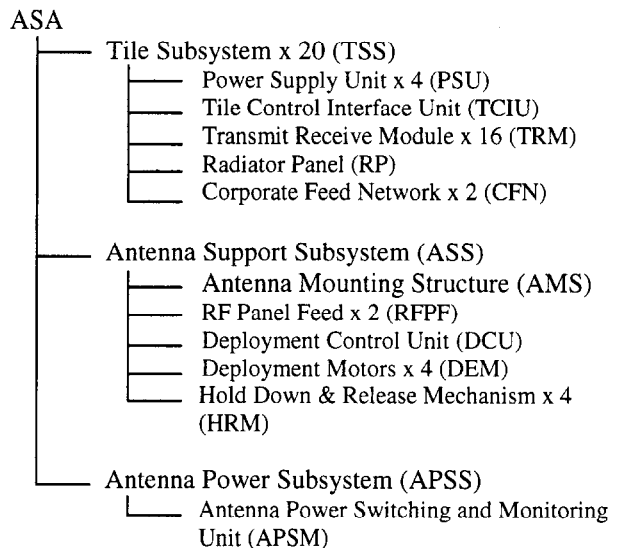


Figure 3 ASA Hardware Tree

The ASS provides the mechanical structure with five rigid Carbon Fibre Reinforced Plastic (CFRP) frames, hold-down and release, and deployment mechanisms (motors and latches). It also includes two RF distribution networks of CFRP waveguide running in parallel along the five panels to provide RF distribution for Radar and calibration signals.

In the launch configuration, the four deployable panels are folded over the fixed central panel and held together in compression by eight Hold-Down and Release Mechanisms (HRM). Each HRM consists of a retractable telescopic tube that is lever locked and tensioned in place by a kevlar cable assembly. Release is achieved using a thermal knife within each HRM that acts on the kevlar cable. Following release the panels

are deployed under the control of a Deployment Control Unit (DCU). Each of four stepper motors are activated in sequence to complete the deployment, which takes typically 1½ hours. Latching is achieved by using eight spring-loaded units built into the main longitudinal beams. When latched the structure achieves a high degree of rigidity and a planarity of better than $\pm 4\text{mm}$ over the full length.

Each TSS has 16 subarrays of radiating elements with each element being connected to a TRM. The TRM contains two TR chains to provide dual polarisation (V & H). These are internally switched according to the setting provided with the beam data. The TRM achieves phase and gain controls for beam steering as well as power amplification in transmit and low-noise reception. An ASIC handles the beam data and routes the internal RF signals accordingly, also setting the appropriate commands to the phase and gain control elements. The active circuits for transmit and receive are only powered during the period of transmission or reception respectively. The TRM phase and gain settings are updated by the TCIU at least twice each PRI to facilitate transmit and receive beams. Beam data is uploaded to the TCIU from the CSS prior to the start of the mode and includes data for all the mode swaths. Swath selection is carried out during the mode by command from the CSS. The TCIU provides feed-forward temperature compensation of the TR module characteristics to provide continual high performance beamforming. This is based on TRM temperature and a set of characterisation coefficients determined during on-ground test.

The radiator panel provides the TSS structure and supports on one side 16 subarrays, each comprising 24 dual-polarised low-loss radiating elements. The TSS equipments are mounted on the other side and the TRM are connected to respective subarrays through the panel using semi-flexible coaxial cable. The cable is fixed to the subarrays at one end and a blindmate connector at the interface with the TRM. A loop is included in the cable to take up mechanical deviations during assembly, vibration and thermal environments. Separate connections are provided for the two polarisations.

Transmit pulses are received from the signal RFPF, which provides a nominally co-time equi-amplitude signal to each of the twenty TSS. Within the TSS this signal is distributed to each of sixteen TRM by the microstrip corporate feed network and passed to the radiators. Receive signals pass through a reciprocal path although the internal routing of the TRM is obviously different. Calibration signals can be injected or coupled out at a point between the TRM circulator and the radiator interface. The calibration interfaces are distributed through a corporate feed network and RFPF that are separate from the signal feeds but virtually identical in design.

The APSM distributes the spacecraft antenna power bus to each of eighty tile PSU, providing individual switch-on, over-current protection, current and status monitoring facilities for each PSU. All PSU are

switched on in sequence with a delay no less than 200ms. In the event of over-current the supply to all PSU on the same tile will be disabled automatically. Status and current monitoring data is sent to the CSS for comparison with expected limits and telemetry purposes.

Calibration is an essential part of the process of accurately translating the instrument output data into absolute units of radar cross-section. Design of calibration techniques therefore form an important aspect of the instrument design, impacting the hardware and operational timeline. The science data from the instrument is a series of digital numbers related to the amplitude and phase of the received echo signal. Figure 4 illustrates the processes involved in providing a calibrated data product from the raw echo data.

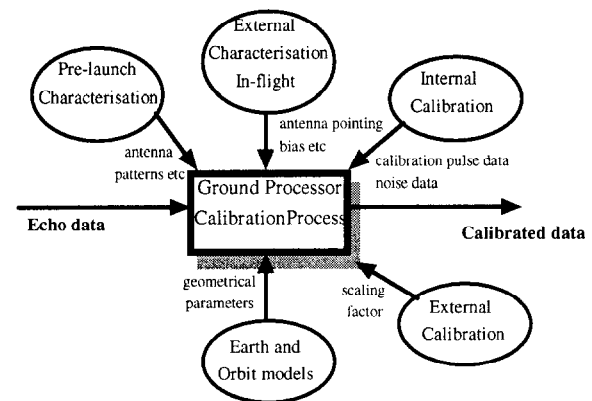


Figure 4. Calibration Data Flow

The ASAR modes are identified in Table 2 along with the associated antenna swaths used. With modes (a) to (d) the instrument is in either vertical or horizontal polarisation so there are 55 distinct mode-swath-polarisation combinations, which each need to be calibrated. Further information on ASAR modes of operation and calibration can be found in ref. 3.

Mode	Swath							Pol
	SS1	IS1	IS2	IS3	IS4	IS5	IS6	
a) Image		x	x	x	x	x	x	V.H
b) Wide Swath	x			x	x	x	x	V.H
d) Wave		x	x	x	x	x	x	V.H
c) Global Monitoring	x			x	x	x	x	V.H
e) Alternating Polarisation		x	x	x	x	x	x	-

Table 2 ASAR Mode / Swath Combinations

The basic requirement for instrument calibration system is to form an accurate reference, which is achieved using a target of known radar cross-section (RCS), and to monitor changes in the combined transfer function of the transmit and receive paths. These processes are separately termed external and internal calibration.

External calibration for ASAR will be carried out using three ground transponders each with an equivalent calibrated cross-section of 58 dBm^2 . These are arranged to be visible simultaneously within a single swath, and are viewed over several passes. The procedure will be

repeated no more frequently than once every six months.

The 55 individual mode/swath/polarisation states that need to be calibrated could, in principle be individually calibrated at one point in the orbit. This is not necessary because parts of the system are common to a number of mode/swath/polarisation states. External calibration will therefore primarily be performed in image mode with observations made over all swaths and both polarisation states.

Other modes use mostly the same swaths and the same paths through the instrument as image mode. The exceptions are wide swath mode and global monitoring mode, which operationally represent a significant departure from image or wave modes. Both modes have a similar principal of operation and utilise one different swath to all the others therefore it is expedient to include external calibration in wide swath mode. Hence the external calibration activity is confined to image and wide swath modes with effects in other modes taken into account by on-ground characterisation.

The external calibration process is subject to errors in both the instrument and the transponder and these limit the accuracy of the calibration. Also the calibration is only strictly valid for the specific operational parameters at that time. To achieve stability around orbit and calibration over the full swath width, and for the full period between external calibrations requires further techniques.

Internal calibration allows estimation of drifts in the instrument transfer function using calibration paths within the instrument. This is repeatedly carried out in each instrument mode continually throughout the life of the instrument. Noise measurements are also made periodically to allow correction of the power level of the raw instrument data.

The precise details of operation depend on the mode being used, but essentially the technique is common to each one. The aim is to characterise the central electronics gain drift and that of the active part of the antenna on a row by row basis for both transmit and receive using special calibration pulses and the calibration loop. The ground processor uses the measured amplitude and phase of the calibration pulses from each row of TR modules to estimate the instrument gain at a single reference point in the swath.

Figure 5 illustrates the calibration paths and shows that each TR module is connected independently by signal distribution networks and a coupled point close to the radiating element. Overall the distribution network and calibration hardware provide 640 paths from the modules to a single connection at the central electronics. These distribution paths are purely passive and are designed to be equi-time delay.

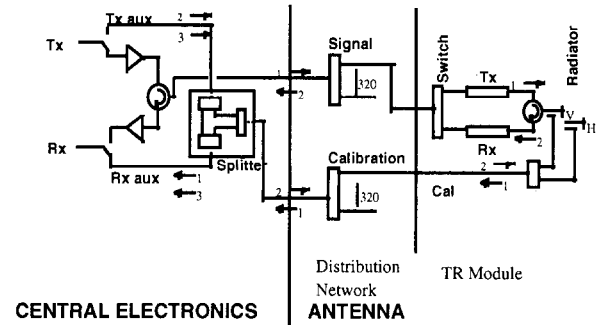


Figure 5. The Three Calibration Paths

The calibration loop around the antenna, along with the flexibility of the control system allows in-orbit monitoring of each TR module transmit and receive path, either individually or in groups. Monitoring and optimisation of the antenna performance throughout the mission is therefore possible. The loop also provides the facility to record an accurate replica of the transmitted chirp pulse waveform, which can be used for processing the SAR data. Hence, although it adds complexity and mass to the antenna the advantages are significant.

Calibration signals are routed from the auxiliary transmit path and into the auxiliary receive path through switches and a stable coupling network. The network consists of three hybrid splitters, which form a basic three way splitter with additional ports to accommodate redundancy. There are three calibration paths employed. Two of these pass through the antenna - path 1 for transmit and path 2 for receive, whereas path 3 is directed within the central RF electronics only. These are identified in Figure 5 where the path numbers are also used to identify the calibration pulses themselves.

Acquisition of the calibration pulses is carried out within different PRI during the instrument timeline and with minimal disturbance to the instrument measurement sequence. The pulses are digitized and sent to the ground processor along with the normal echo data. The Image mode timeline is summarised in Figure 6 to illustrate the typical calibration sequencing although this is not specific of all the modes.

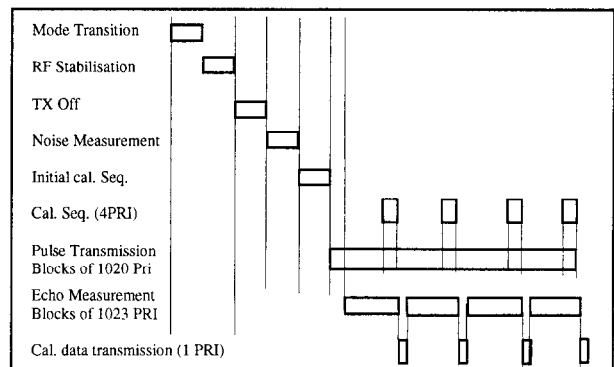


Figure 6 Image Mode Summary Timeline

The internal calibration procedure is carried out for all 32 rows of the antenna array in succession. Following initial calibration, the echo measurement within the mode commences. Continuous echo measurements are taken, interspersed with a periodic calibration sequence every 1024 PRI. Each periodic calibration calibrates a single antenna row, and although the sequence occupies four PRI, only one echo is corrupted due to the routing and timing of pulses. The periodic calibration serves to track changes relative to the initial calibration. In the ground processor the 32 calibration data sets for each of transmit and receive, are used to estimate the overall gain of the instrument (transmit and receive paths) at a reference elevation angle corresponding to a reference point within the swath. In most cases all calibration pulses are representative chirp signals, the exception is in Wave mode where because of data rate limitations the initial calibration is performed with CW pulses. This is valid for tracking gain variations, with replicas being generated from periodic calibration pulses.

External characterisation establishes certain in-orbit parameters where the conditions cannot be fully represented on-ground, e.g. deployment and zero-g effects. It involves measuring the transmitted amplitude and phase from each antenna row both directly using an on-ground receiver, and through the instrument using the calibration path and processed data output. In the context of calibration this procedure provides a relative measure of the on-board calibration signals with respect to the transmitted signals, and is used to correct the antenna calibration data. The direct on-ground measurement of each of the 32 row signals also serves to determine antenna elevation pointing errors by using relative phase information. The procedure aims to track changes in that part of the antenna that lies outside the calibration loop, and also in the calibration loop itself. External characterisation is performed using a dedicated instrument mode and will be carried out at nominally six month intervals throughout the lifetime of the instrument.

Instrument Imaging Modes: ASAR will exploit its flexibility through various operational modes. To enable the Instrument to provide these modes the on-board software and control architecture has to facilitate the complex timeline to provide swath selection along with measurements of target, calibration pulses and noise samples. Figure 1 illustrates the concept of the different operating modes and summarises the data product available in each case.

Image Mode generates high spatial resolution data products (30m) downloaded over the Satellite high rate science data link. The scanned area being selected from a total of seven available swaths located over a range of incidence angles spanning 15° to 45° . Typically this mode is expected to be used in 10 minute periods over less than $1/3^{\text{rd}}$ of the orbit due to the high data rate and relatively high power with resulting thermal profile.

Imaging is performed by transmitting a continuous series of pulses and receiving the echo information from regions on the ground. The coverage regions are defined

firstly by the antenna swath and secondly by the exact placement of the receive period within the pulse repetition interval (PRI).

Wave Mode generates vignettes of nominally 5km by 5km and spaced at 100 km intervals along-track with high spatial resolution (30m). The mode is effectively a segmented Image mode with alternating swath regions. The position of the vignettes can be selected to alternate between any two of the seven swaths as defined for Image mode. This mode offers a low data rate typically being used as part of a mode sequence around orbit, and specifically intended to monitor oceanic regions. The quiescent period between vignettes is used to transfer data to the data management system via the low rate data interface. Due to the relatively benign power requirements and thermal dissipation this mode may be of any defined duration.

Wide Swath Mode provides a 400km medium resolution (150m) ScanSAR product covering five sub-swaths over the nominal 15° to 45° angle of incidence and providing data over the High Rate data link. The instrument utilises a scan-SAR sequence that repeats after 5 subswaths, although the instrument capability is for 14.

Global Monitoring Mode is also based on the ScanSAR technique using five sub-swaths as for wide swath mode. This mode offers a low data rate wide swath products over 400 km ground range with spatial resolution of 1000 m.

Each of the above modes are typically operated in either of two orthogonal polarisations; HH (horizontal transmit, horizontal receive) or VV (vertical transmit, vertical receive). In contrast the **Alternating Polarisation Mode** provides two simultaneous images by application of interleaved sub-swath operation from the same area in HH and VV polarisations, HH and HV or VV and VH, with the same imaging geometry and resolution as Image Mode. Imaging is performed in any single swath as for Image mode, effectively utilising the ScanSAR technique but without varying subswath.

In-orbit performance parameters are not available through direct on-ground measurement, they have to be computed using a suite of algorithms and various inputs. The input parameters are either assumptions (eg. related to the earth model, ground processor operation, atmospheric characteristics) or characteristics of the instrument determined by analysis or test (eg. noise figure, temperature, thermal sensitivity, antenna patterns). Early performance predictions relied heavily on analytically derived instrument characteristics which necessarily included margin by virtue of either the values used or assumptions made in the analysis. These have since been replaced by direct measurement of the hardware where possible, although some inputs to the performance algorithms remain calculated from low level test data when direct measurement of the CESA, ASA or instrument is impractical. Figure 7 provides a list of all the major ASAR specification parameters and the range of values achieved across all swaths for each mode, using the flight model input data.

Parameter	Unit	Image	Alternating Polarisation	Wide Swath	Global Monitoring	Wave
Polarisation	-	VV or HH		VV or HH	VV or HH	VV or HH
Spatial Resolution (Az., El.)	m					
Near swath (IS1)		27.5, 37.6	28.7, 37.6	N/A	N/A	27.5, 37.6
Other Swaths		27.4, 29.6	28.6, 29.6	149.2, 145.7	942.3, 977.2	27.4, 29.6
Radiometric Resolution	dB	1.54	2.46 to 2.50	1.45 to 1.72	1.34 to 1.38	1.54
Point Target Ambiguity Ratio						
Azimuth Range		25.9 to 29.7 31.5 to 47.0	25.9 to 29.7 26.4 to 41.9	22.2 to 28.3 24.9 to 32.2	26.6 to 29.5 25.0 to 32.3	25.8 to 29.7 31.5 to 47.0
Dist. Target Ambiguity Ratio	dB					
Azimuth Range		22.6 to 24.7 17.0 to 40.2	18.1 to 24.6 17.0 to 40.2	20.3 to 35.0 17.0 to 31.5	24.3 to 27.3 17.0 to 31.5	22.6 to 24.7 21.2 to 48.6
Radiometric Stability (1 σ)	dB	0.33 to 0.43	0.50 to 0.58	0.34 to 0.46	0.46 to 0.56	0.57 to 0.67
Radiometric Accuracy (3 σ)	dB	1.18 to 1.48	1.81 to 2.14	1.21 to 1.56	1.54 to 1.82	1.83 to 2.14
Noise Equivalent σ	dB	-18.9 to -21.3	-18.6 to -21.2	-19.8 to -25.5	-30.1 to -34.0	-18.7 to -21.6
Noise Equivalent σ margin	dB	-1.0 to 6.0	-1.3 to 6.0	3.62 to 6.93	10.8 to 17.4	-0.7 to 17.0
Incidence Angle	deg	15 to 45	15 to 45	17 to 43	17 to 43	15 to 45
Swath width (quantity swaths)	km	103 to 58 (7)	103 to 58 (7)	406 (5)	406 (5)	5 (7)
Localisation Accuracy	m					
Azimuth Range		70.7 to 75.6 48.7 to 125.0	70.7 to 75.6 48.7 to 125.0	71.1 to 74.9 52.5 to 111.5	71.1 to 74.9 55.6 to 112.9	70.7 to 75.6 48.7 to 125.0
DC Power (Mean)	W	1358	1358	1195	640	555
Data Rate (Peak)	Mb/s	95.8	95.8	95.8	0.58	0.89

Figure 7: ASAR Performance Summary

Two of the key swath dependant parameters are distributed range ambiguity ratio and noise-equivalent sigma-nought. These have been plotted for all swaths in Image mode showing their variation over the full coverage region in Figure 8.

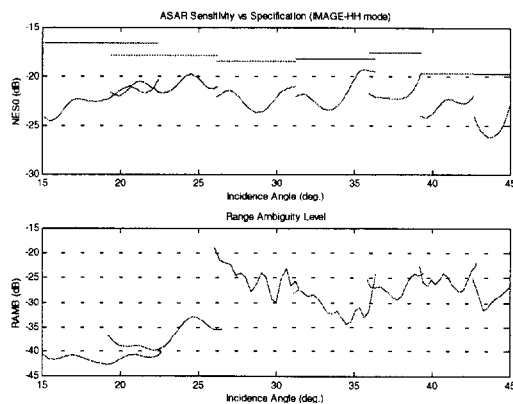


Figure 8: Sensitivity & Range Ambiguity

Notice that Figure 7 also provides NES0 margin with respect to the mid-swath surface model as this is the specified parameter

Notable Design Features of ASAR: Within the CESA a high degree of command robustness and independence has been built into the Control Sub-system (CSS) and the secondary processors of the Data Subsystem (DSS) and the Tile TCIU. Within the CSS the reception of Macro Commands from the ground are not only verified to eliminate corruption but are also checked for consistency of the data encoded and the compatibility of the command to the current operational mode. The CSS also holds default parameter settings for optimised performance, which are initialised on power-up. These settings may also be modified by ground command and retained in RAM (random access memory). The benefits of this approach are that the time from initial power up to normal operation is minimised and the telecommand budget is severely reduced.

Through digital chirp generation the CESA is able to provide signal characteristics matched precisely to the required swath, both in terms of pulse duration and

bandwidth. This efficiently facilitates the various needs associated with the variety of available operating modes of the instrument. Along with the many other comandable features this also allows for re-optimisation of performance during the instrument lifetime, or when a new operational scenario is envisaged.

Budgets: The instrument mass and power budgets are summarised for the main subassemblies in Table and Table respectively.

Item	Mass (Kg)
ASA (Structure)	239
ASA (TSS)	327
ASA (APSM)	17
ASA (Deployment, HRM, Harness)	155
CESA	58
IDS	20
Total Mass (Kg)	817

Table 3 Instrument Mass Budget

	Mode				
	Image	Wide Swath	Wave	Global Monitoring	Alternating Polarisation
Pulse Duty Cycle (%)	4.47	3.52	5.68	4.41	4.47
CESA (Watts)	131	131	131	131	131
ASA (Watts)	1234	1060	388	472	1234
Total (Watts)	1365	1191	519	603	1365

Table 4 Instrument Power Budget

Key technology areas: The development of the ASAR required a number of Technology developments to be completed to enable the performance of the instrument to be met. These were focussed in the components of the Data sub-system and in the Tile sub-system. The Data sub-system development required the procurement and incorporation of suitable components for the FBAQ and the digital chirp generator. These technologies were however at an appropriate degree of advancement at the time of design and a space qualifiable set of components were developed with less than the expected impact.

The Tile sub-system design and qualification was however more complex requiring the development of new processes as well as new ASIC, MMIC and hybrid components. The main endeavour centred on the Radiator and TR module development. Although the TR module architecture was established early on following development work at Astrium Ltd., the implementation of a qualified design proved to be difficult. These issues are addressed in a dedicated paper².

Challenges met during development: Aside from the technology development issues one of the more spectacular challenges in the ASAR design has been the development of the Antenna structure. Although not new technologically, the stowed panel design and deployment requirements to meet stringent planarity specifications have required interesting solutions to the problems of both design and handling. Designed for use in a zero-g environment the deployment hinges and motors are relatively delicate components, the stepper

motors having a low operating torque (80Newtons max). The demonstration of deployment and verification of compliance to the required antenna performance therefore demanded development of some ingenious devices. A deployment gantry with a variable geometry, which allowed the panels to be stowed and unfolded with near zero torque was one of the solutions. The further development of a 'zero-g' deployment test room where the Antenna is deployed in the horizontal plane supported on air bearings was a further challenge. This facility required construction of a resin floor some 14m x 5m having less than 1mm distortion in flatness. A factor in achieving this, related to the Portsmouth site location required the resin to be poured and set at the ebb of the tide!.

More generally though, technology developments created many challenges over the eight year development programme. To mitigate some of the risks posed by such development on those features that were characterisable in terms of performance, the system design was structured to allow software control of as many parameters affecting performance as possible. Thus tables of control parameters for such functionalities as the BAQ algorithms, beam steering, and tile characterisation coefficients have been not only stored in data tables but can also be easily modified by ground control. Furthermore chirp pre-distortion coefficients are made more accessible through being included within the mode 'set-characteristics' commands. This design approach in conjunction with calibration techniques was taken to allow for the optimisation of performance at any phase of design and use.

Given this built-in flexibility, the on-board software was several orders of magnitude more complex than previous designs, particularly with the need to minimise ground telemetry / telecommand budgets. This in itself formed a significant challenge, and in order to achieve a realistic schedule required the recognition that the effort and cost of software design had finally surpassed that of the hardware in which it was to be embedded. Due to schedule constraints and the unmeasured characteristics of the integrated instrument at software build date, the flexibility of the software was retained until the last minute by use of EEPROM. These are being replaced by PROM only just prior to final satellite integration acceptance test, since at the time of design EEPROMS were not available for space qualified use. Complexity of the software design was thus justified by the need to re-optimize the mode characteristics following resolution of the more major system design challenges.

Now having faced these major development undertakings in hardware, software and AIT the ASAR instrument has finally emerged as a successful and powerful instrument. It is currently at an advanced stage of integration with the ENVISAT spacecraft at ESTEC, which is depicted in Figure 9. Here the stowed antenna is clearly visible without MLI showing some of the harness and RFPF network.

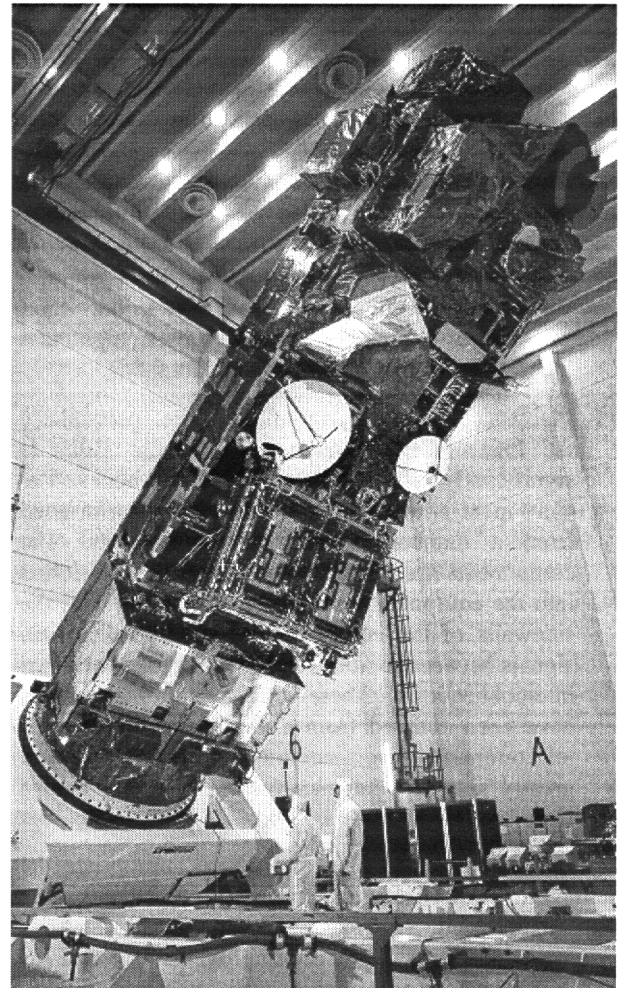


Figure 9 ENVISAT-1 Flight Model (courtesy of ESA)

Lessons learned and Further Developments: The design of the ASAR instrument, as of the ERS AMI before it, is a major step forward in the development of spaceborne SAR. Lessons learnt during both programmes have been exploited at Astrium Ltd.. In definition of the **CORE** (Common Radar Elements) development programme it is intended to form a flexible, adaptable SAR for use at frequencies from L to K band, and for integration into a number of platforms, including airborne vehicles. The **CRESS** (Core Radar Electronic Subsystem) has now been adopted as the Sensor Electronics for the SAR payload for the RADARSAT-2 programme. Examples of the enhancements introduced as a result of the ASAR experience are outlined below:

- Chirp predistortion was found to be a useful facility on ASAR. To improve the flexibility of the system further Core has adopted to store the waveform in memory to be uploadable by command as required.
- Both ASAR and ERS-1/2 AMI used the same IF frequency for Transmit and Receive. For Core different IF are used to ease isolation between transmit and receive.

- Block Adaptive Quantisation is used by Core, as for ASAR. However the algorithm has been refined and the faster technology has been adopted.
- The internal control bus used by Core is the CAN bus. This is used widely within the automotive industry, but has been flown by SSTL, and can be made with space qualified processes. The bus is used for collection of telemetry, saving harness mass and reducing routing problems. The CAN also has advantage in that it overcomes the 1553 problems of limited number of terminals, high mass transformer coupling and limited data fields.
- Mechanical construction of the Core, particularly the Intermediate Frequency Equipment (IFE) is significantly different from the ASAR boxes. The Core ideal is to enable a system to be constructed from a number of modular components. The components are the modules, which can be slotted into the equipment box. In the case of the IFE the sidewalls of the equipment are used to distribute signals between modules in order to reduce external interconnections. These construction techniques have been adopted from a number of commercial telecommunication satellite programmes and greatly simplify the manufacture of a number of Core-based systems.

This list is not exhaustive, and where appropriate the heritage of ASAR and its successful predecessors has been maintained. However, the Core/RADARSAT-2 systems will offer performance improvements over ERS AMI and ASAR, with significantly greater flexibility and adaptability, depending on the mission.

The FESS (Front-end Electronics Subsystem) includes the antenna radiators, RF distribution and power amplification. Architectures range from single polarized slotted waveguide fed by microwave power modules, to multi-polar integrated TR module and radiator structures, in many ways similar in concept to the ASAR antenna. Current work at Astrium Ltd. includes development of a generic TR module architecture to form a building block for multi-frequency, multi-polar applications. Future concepts that include higher levels of integration between the TR module elements, power and control distribution, radiating elements and structure are also being actively studied⁴.

The complexity of the ASAR antenna structure and deployment requirements has been a major impetus for the pursuit of a more efficient SAR spacecraft architecture. To this end Astrium Ltd. have patented a novel platform designated 'Snapdragon', which maximises utilisation of the launch vehicle payload volume and incorporates a large planar antenna with only one deployment hingeline. The design⁵ can be scaled according to launcher constraints and with

current launcher capabilities allows antenna areas in the range 11.7m² to 80m² for the basic configuration. Larger areas can be incorporated by additional deployable sections.

Conclusion: ASAR has faced many challenges both expected and unexpected, as could be anticipated with new technology applications. The major achievement has been to triumph over each one and thereby push forward the technology of the European space industry. Lessons learned are already benefiting new product developments and projects with the Core technology now forming the building blocks of the next generation of space-borne and air-borne equipments. Examples have been provided to show how the design and manufacturability of SAR systems has been improved and embodied in the Core Radar programme. Investment in this development is now reaping rewards with Core being adopted for missions such as the RADARSAT-2 Sensor Electronics.

The Astrium organisation is a new European company formed between two of the most significant contributors to the ENVISAT/ASAR programme and is able to call on all the extensive experience gained. Although there is no direct follow-on SAR program from ESA, industry is now in a position to take the technology forward.

Acknowledgements:

The authors acknowledge the work of colleagues in Astrium Ltd., Alcatel Espace, Alenia Spazio and many other subcontracting organisations in development of the ASAR Instrument. Also the support provided by Astrium GMBH and the ESA Technology Centre (ESTEC) as mission prime contractor and customer respectively.

References:

1. D.L.Hurd, G.Fowler, Optimisation of the ASAR Block Adaptive Quantisation Scheme, EUSAR '96, Königswinter, Germany 1996.
2. M.D.Gibbons, R.Tucker, Design & Performance of an Active Phased Array Antenna for the ENVISAT ASAR, NATO RTA Sensors & Technology Panel symposium on space based observation technology, Samos, Greece, 16-18 October 2000.
3. S.S.Hartley, M.D.Gibbons, ASAR – Calibration Aspects for a Multi-Mode Instrument, CEOS SAR Workshop 3-6 February 1998.
4. M.A.B.Cohen et al., Integrated Front End Subsystem Design Concept for Future Spaceborne SAR, EUSAR 2000, Munich, 23-25 May 2000
5. J.D.McCaughey et al., Instrument Carrier – SAR specific Polymorphic Configuration, EUSAR '98, Friedrichshafen, Germany, May 1998.

Performance Analysis for the SRTM-Mission

Reinhard Schroeder, Kay-Bodo Klein, Helmut Suess

Institute of Radio Frequency Technology
DLR Oberpfaffenhofen
P.O. Box 1116
82230 Wessling, Germany

Abstract:

The Shuttle Radar Topography Mission (SRTM) flown on the Shuttle Endeavour from 11th to 22nd February 2000 has produced the most excellent interferometric image products ever obtained by a spaceborne SAR system. Its final product the global high precision digital elevation map will benefit numerous military and civilian applications.

The X-SAR mission operations team included four radar positions for instrument monitoring, performance analysis, contingency handling and radar data analysis. A key step in the acquisition of the high quality radar raw data was the performance analysis of the SAR system. The work presented here considers the major tasks for the X-SAR Performance position in the preparation and the carrying out of the SRTM mission. During the mission the X-SAR Performance position was operated in the Payload Operations Control Center (POCC) of the Johnson Space Center, Houston.

I. Introduction

The purpose of the X-SAR/SRTM Mission was to acquire data of the surface of the Earth [1]. Due to the fact that this radar system was no free-flying space system but operated inboard the Space Shuttle the data had to be collected on data recorders onboard the Shuttle itself. Strong NASA mass requirements permitted only a total amount of 120 tapes for X-Band data recording. Therefore the radar system could only be operated over land and had to be initialized at the beginning of each data take. For this reason the performance related parameters had to be calculated depending on the mission timeline provided by the dedicated Mission Timeline System (MPS). As a next step all timeline data has been processed by the PEWITS tool (Performance Estimator With Integrated Time System) and has been resent to the MPS where the radar parameter settings were stored in a data base. The base for this tool was a software performance analysis and prediction tool called PE (Performance Estimator), developed within DLR with the experimental experience of more than a decade [2]. The software has been extended to the specific and operational needs of the X-SAR interferometer.

During the X-SAR/SRTM flight the performance has been observed with a tool called 'Performance Analyzer' (PA). This tool allowed observing whether

the pre-mission calculated parameter settings based on the mission timeline were sufficient regarding the required system performance.

II. The PEWITS Functionality

The PEWITS tool was designed to automate the process of setting SAR system parameters affecting the image quality with respect to the mission timeline. The mission timeline file included the information of land start and stop times, called 'data takes'. Figure 1 shows a typical data take over South America of the X-SAR/SRTM mission.



Figure 1: DT of South America.

Every data take consisted of at least four instrument commands: The first command has to set the radar system into transmit mode and to initialize the instrument parameters for the ocean calibration phase. The second command has to set the instrument parameters for data acquisition over land. The third command was provided for ocean calibration at the end of a data take, and the last command to set the radar instrument back to pause mode, marking the end of a data take. There could be more than those four commands depending on the Earth's surface which had to be mapped. Especially for large variations in the

the latitude of the calculated DT. This would help the operator to interpret changes of the DWP due to different look angles or wrong latitude values.

IV. Assessment of Interferometric Performance

A fundamental step in the development and optimization of a SAR system is usually performed by an analytical assessment of image quality parameters like e.g. spatial and radiometric resolution, signal-to-noise ratio and ambiguity ratios. For the X-SAR/SRTM mission a special focus had to be directed of course to the interferometric performance. Two important parameters defining this performance are the relative height error and the absolute height error in the digital elevation model. The typical performance calculation is an iterative optimization process, which is depicted simplified in Figure 5.

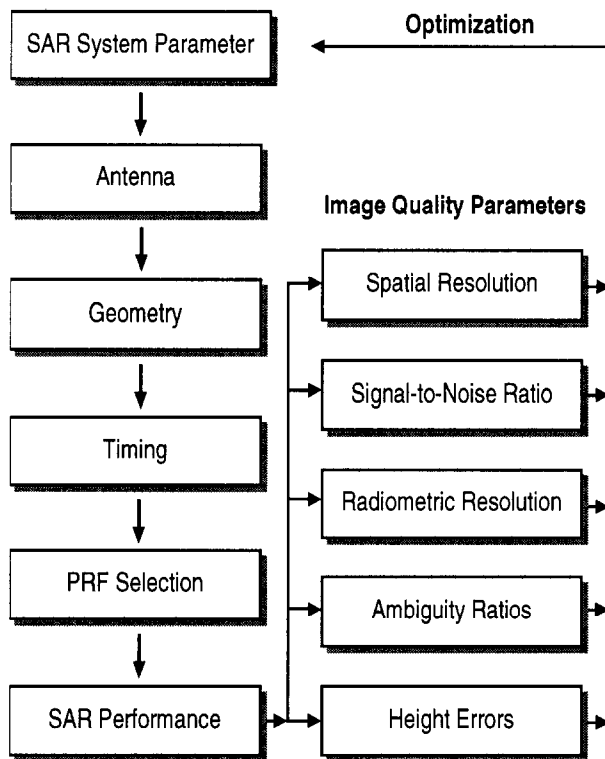


Figure 5: Approach of Performance Analysis.

One of the most important steps in the design process is the selection of the pulse repetition frequency (PRF), which is a highly restricted parameter. Once the PRF is determined the image quality parameters can be evaluated in an analytical way. By assessment of these quality parameters the SAR system parameters can be optimized.

V. System Parameters of the X-SAR Instrument of SRTM

In the beginning of the system parameter planning for the X-SAR system of SRTM the overall orbit constellations were developed. To cover the whole

landmass between +60 deg and -57 deg latitude within 11 days an orbit height ranging from 233 km to 249 km was necessary for the C-band Scan SAR system [3]. The variation of the effective height over ground was due to the trim burn maneuvers of the Space Shuttle and the deviations of the Earth's surface.

Due to the historical development from SRL 1/2 [1] the X-SAR system has the ability to operate just eleven different PRF modes ranging from 1240 up to 1736 Hz. The problem was to find a PRF that could be kept constant for the whole range of orbit heights. A change of the PRF during data takes was not acceptable for the interferometric processing. Additionally the swath width and image quality should be optimized. Figure 7 and Figure 6 illustrate the unacceptable PRF bands for the minimum and maximum orbit height. To perform a data take with a constant PRF, the data window area must remain within the pulse repetition interval for both constellations.

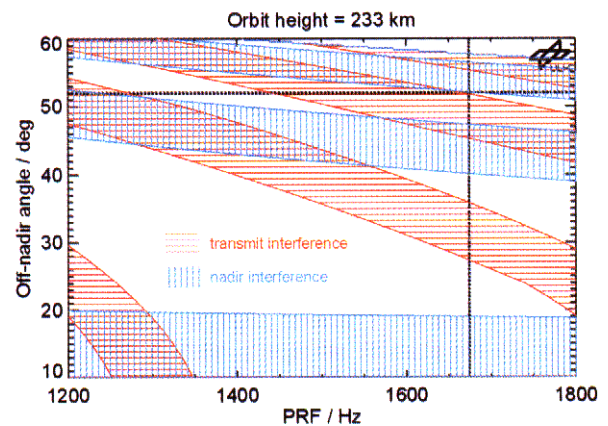


Figure 7: PRF restrictions at 233 km orbit height.

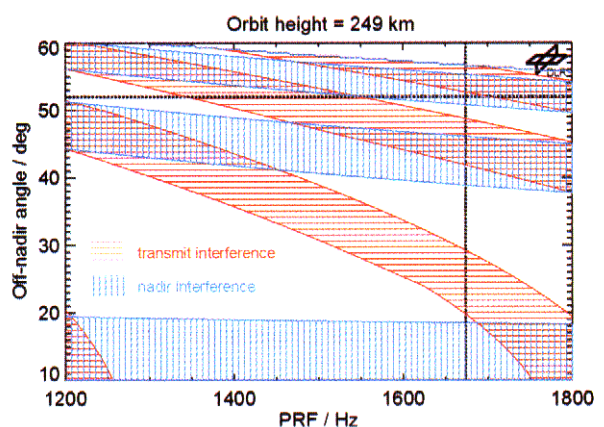


Figure 6: PRF restrictions at 249 km orbit height.

Further restrictions to the off-nadir angle resulted from the integration of the X-SAR main antenna next to the C-band radar antenna and the AODA system (Attitude and Orbit Determination Avionics) [4]. This configuration required a minimum off-nadir angle of

51 deg for the X-SAR main antenna. From Figure 7 and Figure 6 it can be seen, that combinations of PRFs with off-nadir angles above 51 deg, avoiding both transmit and nadir interferences, are possible just for PRFs less than 1350 Hz. PRFs in that order result in a poor azimuth ambiguity suppression in the secondary channel since the X-SAR outboard antenna has just half the length of the main antenna.

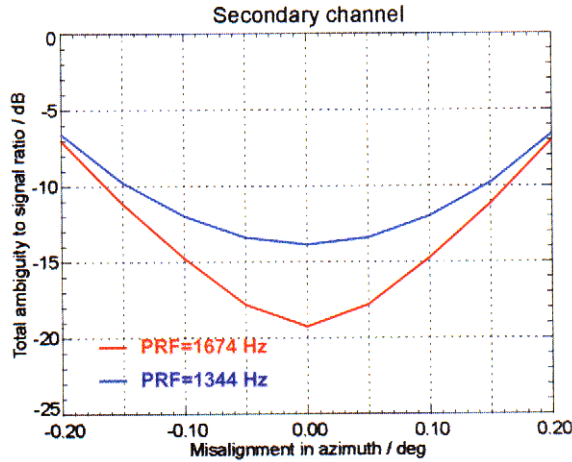


Figure 8: Ambiguity ratios of the secondary channel.

Figure 8 illustrates the difference in ambiguity suppression for the PRFs 1674 Hz and 1344 Hz in the secondary channel. The total ambiguity ratio is mainly driven by the azimuth ambiguity ratio. A misalignment of both antennas yields further degradations. Fortunately the accuracy and stability of the alignment experienced throughout the mission was less than 0.025 deg and better than expected [4]. The ambiguity ratios in both channels affect the overall height resolution of the interferometer. The estimated relative and absolute height errors are shown in Figure 9 for both PRFs. The degradation of height resolution at the low PRF is mainly given by the poor azimuth ambiguity suppression. For a perfect alignment the estimated relative height error is 6.4 m worst case, i.e. at the far range of the swath for the PRF 1674 Hz and 7.36 m for the PRF 1344 Hz. At near range the relative height error is expected to be about 5.2 m for the PRF 1674 Hz.

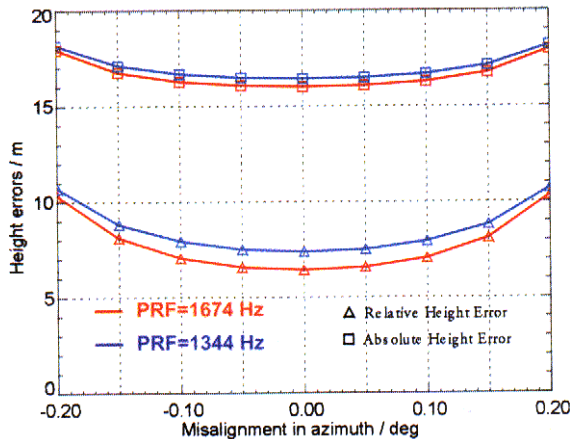


Figure 9: Relative and absolute height errors.

This shows clearly that the high PRF is more favorable for the interferometric performance. The remaining problem was the nadir interference. As depicted in Figure 10 the elevation patterns of the X-SAR antennas have a Tschebyscheff tapering yielding very low side lobes between 31 and 55 degrees off-nadir.

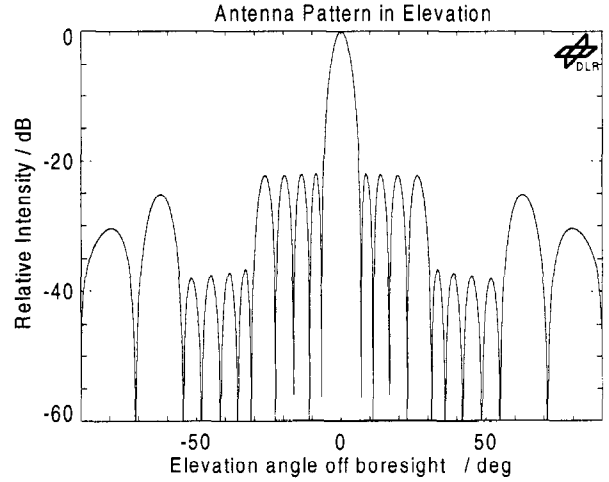


Figure 10: X-SAR antenna pattern in elevation.

This revealed the freedom to accept nadir interferences and to improve azimuth ambiguity suppression and hence height resolution significantly. The best possible choice turned out to be the PRF of 1674 Hz at a look angle of 52 deg. The preliminary radar data analysis during the mission confirmed that nadir echoes appeared noticeable just in few cases [5]. The detailed analyses of the first SRTM image products indicate that the average height resolution is in very good correspondence with the predicted values in Figure 9. The average height resolution may even exceed the estimated values.

VI. Mission Experience

The key system parameters were determined during the design phase of the project. The most important remaining parameters which have been calculated during the operating phase were:

- Receiver gain settings for both radar channels depending on the backscatter coefficient of the Earth's surface.
- Data window positions for both radar channels with respect to the terrain height (a rough model was used).

As a first result from post-mission processing of the radar data the signal standard deviation was about 35% below the maximum ADC amplitude [6]. This is close to the optimal value of 30% giving the best compromise between clipping and reduction of ADC quantisation noise. The gain settings for both radar receivers were optimally estimated by the Performance Estimator software but the maximum gain of both channels was limited to 80 dB. The receiver gain setting variation of the primary channel was between 74 and 80 dB, mostly at the maximum setting. The stronger secondary channel had a range of gains between 70 and 80 dB.

The only critical contingency that occurred during the SRTM mission was the failure of a thruster at the outboard antenna to compensate the Earth's gravitational forces on the mast. During the contingency handling different options were discussed. One option was to change the roll angle of the whole Shuttle to reduce these forces. A change of the roll angle would also have changed the look angle of the SAR system. In this situation it was vital to have a software tool like the Performance Estimator to find suitable system parameters for these hypothetical configurations in a very short period of time. These analyses were similar to the ones presented in chapter 5. The results were the basis for further decisions in the contingency management.

VII. Summary

In this paper, the software tools which were utilized for the performance estimation of the X-SAR interferometer in the preparation and the carrying out of the SRTM mission were presented. The functionality and the versatility of the software were demonstrated. The analyses of the first SRTM digital elevation models indicate that the average height resolution is as good as predicted or even better. A final comparison can be done after all data takes are processed.

VIII. References

- [1] Stuhr, F., Jordan, R., Werner, M., 'SIRC/XSAR A Multifaceted Radar', IEEE AES Systems Magazine, Oct. 1995, p.15-24.
- [2] Schroeder, R.; Suess H.; Zeller K.-H.: *Performance Analysis of Spaceborne SAR Systems*, NATO RTO-SET Symposium on "High Resolution Radar Techniques", 22.-24.3. 1999.
- [3] Farr, T.G.; Kobrick, M.: *The Shuttle Radar Topography Mission*, Proceedings of EUSAR 1998, pp. 307.
- [4] Werner, M.: *Shuttle Radar Topography Mission (SRTM)*, Proceedings of EUSAR 2000, pp. 209.
- [5] Buckreuss, S.; Scheiber, R.; Basler, C.: *The SRTM Radar Data Analyzer*, Proceedings of EUSAR 2000, pp. 219.
- [6] Steinbrecher, U.; Bamler, R.; Eineder, M.; Breit, H.: *SRTM Data Quality Analysis*, Proceedings of EUSAR 2000, pp. 217.

High Resolution X-Band SAR Constellation for Risk Management

C.C. Lin

ESTEC (APP-FPE), PO Box 299, 2200 AG Noordwijk, The Netherlands

S. Ramongassié, M. Jérôme and L. Phalippou

Alcatel, av. J.-F. Champollion 26, PO Box 1187, 31037 Toulouse Cedex 1, France

Summary:

This paper summarises the result of an ESA sponsored study on a Risk Management Earth Watch mission. The proposed system consists of a constellation of X-band SAR satellites so as to provide essential and complementary information with respect to other observing systems whether space or terrestrial. The mission requirements to meet both high spatial and temporal resolution, combined with fast data delivery led to two unique, alternative SAR-satellite designs which combine both the electronic and platform agilities.

1. Risk Management Mission

Risk management and monitoring constitutes one of the highest priority application fields of the European Remote Sensing Information Services (ERSIS [1]). It addresses specific aspects within various application areas such as resource monitoring (e.g. crops, forests, ship routing, geology, etc...) and assistance for the assessment of damage to environment, population and industries due to pollution and natural hazards (e.g. volcanic eruptions, earthquakes, hurricanes, floodings, etc...). The provision of information is required for assisting users throughout all three phases of risk management: namely the prevention, crisis and post-crisis phases.

Risk management and monitoring imposes most stringent observational requirements in terms of spatial resolution, temporal resolution and information delivery time. In particular, the high temporal resolution requirement inevitably leads to a satellite constellation including sensors in microwave spectral range in order to enable almost all-weather observations. A high-resolution SAR constellation therefore forms an essential component of such an observation system which shall also include sensors in optical spectral domain. The satellite-based system must be considered as providing complementary observations to those of terrestrial systems.

The potential users directly involved in the major disasters management are mainly public and governmental institutions, namely civil protections (national level), ministries (environment, defense, planning, fishery...), international and non-governmental organisations (UN, EU, Red Cross,...), scientific institutes, universities and specialised centres. There are also potential private users such as insurance, re-

insurance companies, utility and transportation companies, industry and service companies in the area of geographical information and communications.

2. System Requirements

Table 1 summarises the most important system requirements. The centre-frequency has been selected so as to enable a maximum use of the allocated band for active sensing. A single polarisation has been specified as no specific requirement exists for dual-polarisation capability.

Most stringent requirements are placed on the revisit time, allowing quick responses of the system in emergency cases. An equally important requirement is the frequent delivery of INSAR products ($\leq 1 \sim 2$ days) for estimating e.g. ground movements or flooding extent in real-time.

The spotlight mode was not deemed necessary as $2\text{m} \times 2\text{m}$ single-look resolution can be achieved in the strip-map mode. A noise equivalent σ^0 of ≤ -22 dB has been specified as a good mapping capability is required for large classes of surfaces. This value has been estimated from the published statistics of σ^0 over land [3]. A further effort is currently made by the Agency to analyse, to compile and to make available a statistical database of X-band σ^0 [4] for verifying the requirements.

The duty cycle/orbit/satellite will depend on the number of satellites in constellation: it can be as low as ≥ 5 min. for 6 satellites and increases to ≥ 10 min. for 3 satellites.

Frequency	9.65 GHz	
Polarisation	HH (or VV)	
Mean/max revisit	$\leq 12/24$ h	
INSAR mode	Repeat cycle $\leq 1 \sim 2$ days	
Imaged swath width	Strip-map	ScanSAR
	≥ 20 km	≥ 140 km
Spatial resolution	Strip-map	ScanSAR
	$\leq 2\text{m} \times 2\text{m}$ (single-look)	$\leq 25\text{m} \times 25\text{m}$ (≥ 6 looks)
Noise equiv. σ^0	≤ -22 dB	
Total ambig. ratio	≥ 20 dB	
Duty cycle	$\geq 5 \sim 10$ min/orbit/satellite	
Satellite life	≥ 5 years	

Table 1: System requirements

Further important requirements, which have been imposed on the system, are the cost efficiency and short time to mission implementation, implying a design with low technological risks and driven by cost.

3. Constellation Analysis

The revisit performance of the constellation is characterised by the mean and maximum revisit times which correspond respectively to the mean and maximum time intervals between two opportunities to image an arbitrary location on the Earth. They depend on the geographical location (latitude and longitude) and the selected orbit characteristics.

The requirement of global coverage imposes automatically polar orbits for the constellation. The remaining parameters are the number of satellites, whether sun-synchronous or not, the local nodal crossing time(s) if sun-synchronous, the mean altitude, whether the sensor shall view one side only or both sides of the satellite track, and finally the number of available incidence angles for any location. Sun-synchronous orbits with the 6PM/6AM Equator nodal crossing times have been preferred as they simplify the satellite power and thermal designs as well as they permit an identical design for all satellites, thus ensuring cost efficiency.

The most significant trade-off is between the number of satellites and the accessible swath-width for each satellite. The accessible swath width is necessarily limited through the requirements to meet the imaging performance (imaged swath width, spatial resolution, sensitivity and ambiguity ratio). A so-called Walker 6/1/0 constellation at 510 km offers an optimum solution with only one-sided viewing capability. It corresponds to a regular distribution of 6 satellites on a single orbital plane: each satellite has a 6-days repeat cycle with 91 orbits and the constellation has a one-day cycle with a circular permutation of the 6 satellites. This translates to a repeatable image acquisition geometry over any point on Earth every 24 hours by successive satellites, a particularly useful property for delivering INSAR products on daily basis. For global coverage, an accessible swath-width of 430 km is required, which is feasible from the 510 km orbit altitude. The resulting maximum revisit time is less than 15 hours for most of the latitude range and increases to 24 hours for polar regions.

A 430 km accessible swath width can be achieved by electronic beam-steering in the case of the active antenna based concept. A further extension of the swath is also possible by combining both the electronic and platform steerings in order to overcome the limitations of the active antenna such as grating lobes and gain losses for large steering angles. In this case, the incident angle range is expanded from 20°-53.7° to 10°-63° using roll-maneuvers of the platform, resulting in an accessible swath of 660 km. However, either the spatial resolution

or the sensitivity (noise equivalent σ^0) would be degraded in those extended accessibility regions. Despite the degraded imaging performance, the introduction of those extensions would permit to reduce the mean revisit time by a significant amount (from 12h to 7.5h over the Equator).

Finally, a two-sided viewing capability can further improve the revisit characteristics of the constellation at the cost of a more complex satellite design (mainly the attitude and thermal controls). This is achieved by re-pointing the platform through the nadir direction around the roll-axis. Alternatively, the number of satellites in constellation can be reduced, but at the same time conserving the same revisit characteristics as in the case of one-sided viewing capability. Thus, the higher complexity of the individual satellites can be traded-off against their number in the constellation.

Table 2 summarises the result of revisit analysis for different cases of constellation. One can notice that a constellation of 4 satellites with two-sided view has almost the same performance as 6 satellites with one-sided view only. A reduction to 3 satellites would still provide an acceptable revisit performance, a case of interest during a progressive deployment of the constellation, or in case of failure of a satellite. Therefore, the two-sided viewing capability has been baselined.

Constellation	Mean revisit	Max. revisit
6 satellites with one-sided view	≤ 7.5 hours	≤ 15 hours for most latitudes
3 satellites with two-sided view	≤ 14 hours	≤ 22 hours for most latitudes
4 satellites with two-sided view	≤ 8 hours	≤ 14.5 hours for most latitudes
6 satellites with two-sided view	≤ 6 hours	≤ 14.5 hours for most latitudes

Table 2: Revisit characteristics of different constellation cases (all cases assuming 10°-63° access range)

4. SAR Satellite Designs

A number of instrument concepts have been considered during the study and traded-off each others. The baseline concept is based on a planar active antenna which offers the largest flexibility in terms of operational modes and compliance to all of the requirements.

A second best option has also been studied in details as a complementary study [5] as it offered a lower cost alternative with a slightly compromised performance. This alternative concept is based on an array-fed reflector antenna which is combined with platform agility (rapid re-pointing capability) in order to enable large accessibility. Both of those designs are described below.

4.1 Active antenna based design

The concept based on an active planar antenna consists of a 4m by 1.9m non-deployable array accommodated on a Skybridge type platform (see Fig. 1). The spacecraft is a so-called "longitudinal flyer" with its largest surface occupied by the planar array for generating a steerable, side-looking fanbeam. As no spotlight mode is required, the beam-steering is performed only in elevation.

A number of options exist for accommodating a solar array, the most attractive one being the configuration shown in Fig. 1. The array is attached along a rear-edge of the spacecraft parallel to the flight direction. The 4 panels of the array can be folded and stowed along a side-wall of the spacecraft for launch. No rotation of the solar array along the orbit is necessitated as the sun-aspect angle remains constant for the 6PM/6AM orbit. Such a configuration also minimises air-drag as well as mass-inertia around the roll-axis for enabling rapid roll-maneuvers.

Fig. 2 depicts the antenna design. It consists of 6x5 sub-panels, each one composed of 2 rows of 16 subarrays. The amplification is fully distributed among the 960 T/R modules (30x32). The proposed SSPA technology is $\frac{1}{4}$ μ m PHEMT producing 7 W peak power with a duty cycle of 5 to 16.5 %. The subarrays are made of slotted aluminium waveguides which offer a low cost, but very low loss solution.

The instrument general block diagram is shown in Fig. 3.

The **processing unit** contains:

- a digital chirp generator followed by D/A converter and up-converter for achieving the required large bandwidth (≤ 220 MHz);
- a direct analogue quadrature demodulator followed by A/D converter and interpolator filter to reduce the sampling frequency.

The **RF unit** contains:

- an up-conversion chain to 9.65 GHz;
- a down-conversion chain to the baseband;
- Tx and Rx calibration circuits.

The **antenna subsystem** contains:

- an elevation power splitter followed by time-delay-lines for minimising signal dispersion while beam-scanning;
- 5 azimuth power splitters which feed the sub-panels;
- 30 sub-panels each of which contains a power booster, a sub-panel power splitter, 32 T/R modules and 32 subarrays;
- calibration power splitters.

Furthermore, the instrument contains a **radar control unit**, a **power unit** and a **500 Gbit solid state mass memory**.

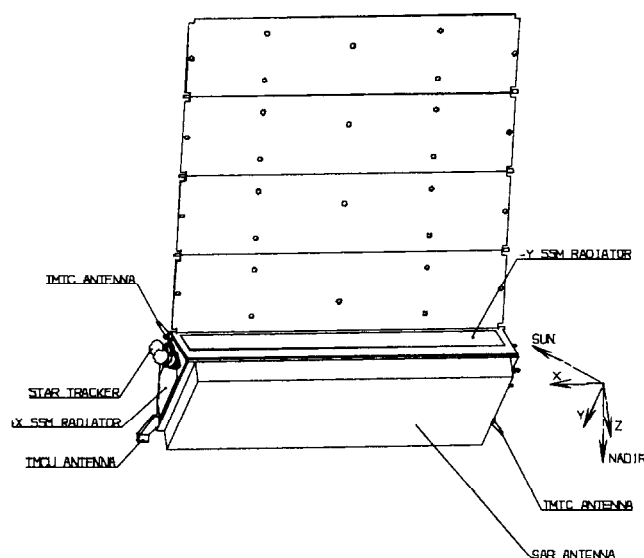


Fig. 1: SAR satellite configuration (active antenna based)

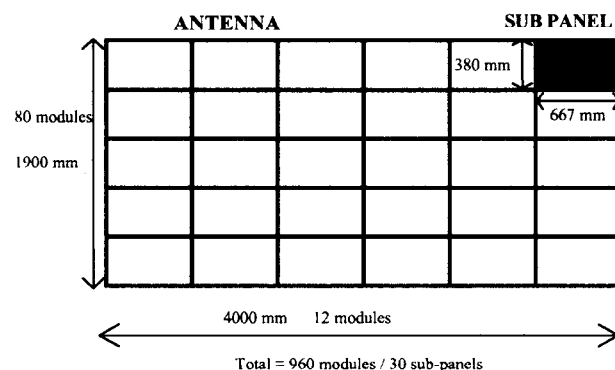


Fig. 2: Active antenna configuration

Two alternative architectures for the sub-panel design have been analysed. Those are:

1. A classical active antenna architecture where both the amplification and control (phase and amplitude) functions are imbedded within the T/R modules (see Fig. 4a).
2. An architecture borrowed from modern telecommunication satellite payloads where the control functions (phase and amplitude) are implemented within the sub-panel power splitter and the T/R modules are solely responsible for amplifications (see Fig. 4b).

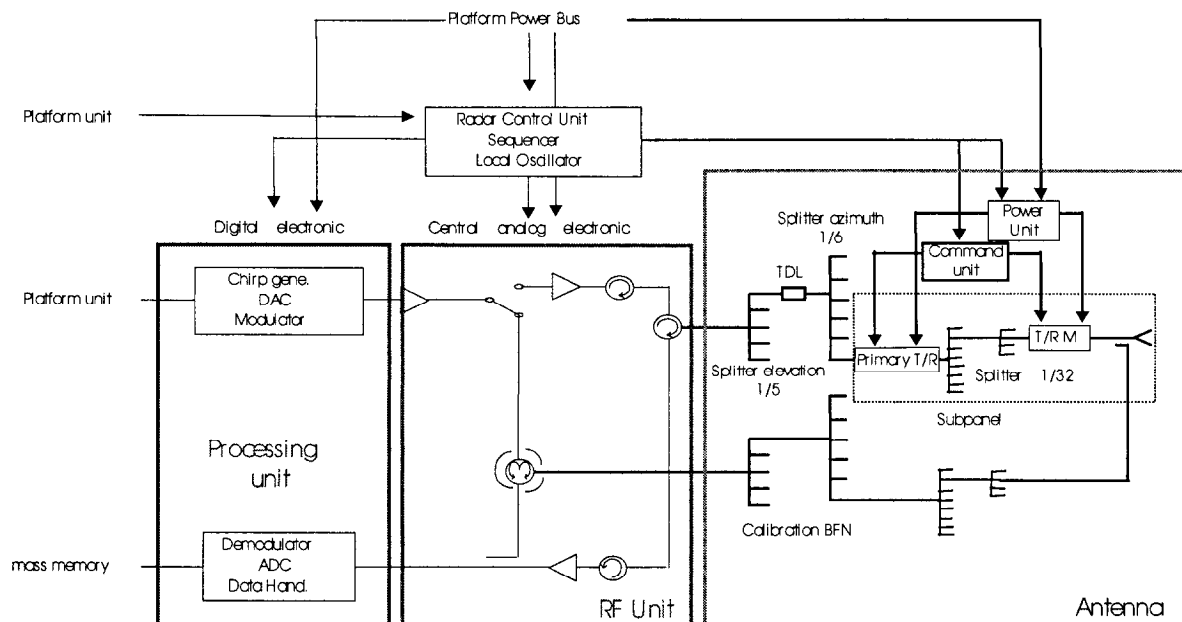
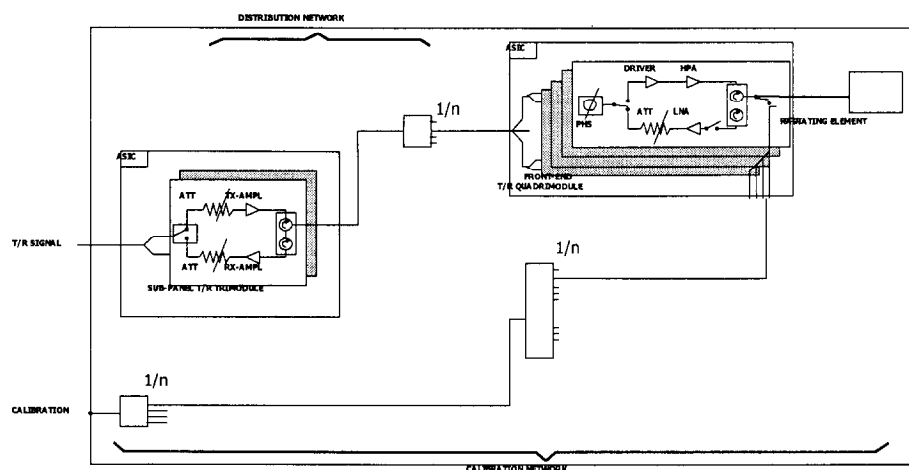
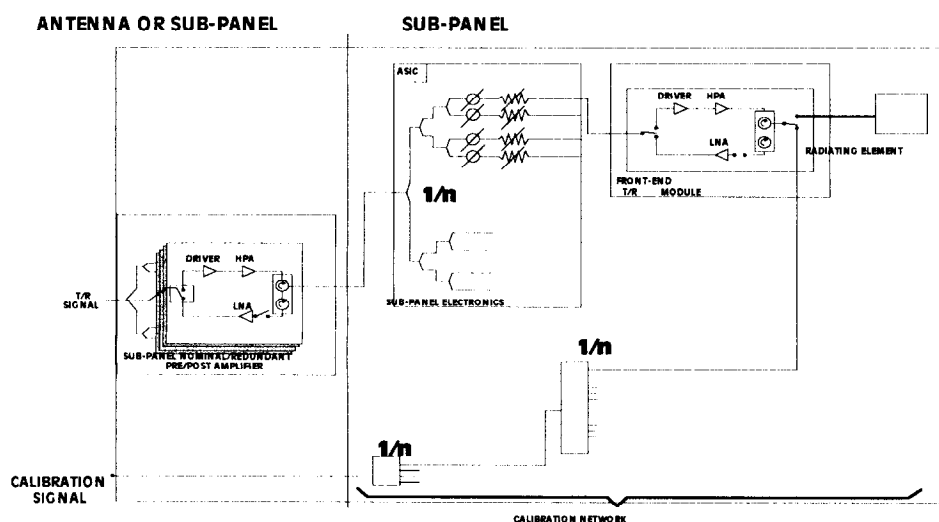


Fig. 3: SAR instrument general block diagram



a) Classical architecture with all functionalities implemented within the T/R modules



b) Alternative architecture where amplitude and phase control functions are moved from the T/R modules to the sub-panel power splitter

Fig. 4: Two alternative sub-panel architectures

The alternative architecture is particularly attractive for saving costs when the number of T/R modules is high as it minimises their complexity [6], which is the case for the considered SAR concept (960 T/R modules per satellite). By minimising the number of components which are required to be incorporated in the T/R module, their production costs can be reduced through:

- simpler design optimisation for serial production;
- shorter, thus faster assembly chain;
- shorter, thus faster verification and characterisation processes;
- higher yield, thus reduction of the overall number of T/R modules to be produced;
- simpler, thus faster identification of possible design flaws and simpler/faster design corrections.

From the instrument point of view, there are also significant advantages:

- reliability improvement of the T/R modules;
- reduction of the number of control cable connections to the individual T/R modules;
- phase and amplitude control circuits are placed in a better thermally controlled environment (away from the radiator surface and from the heat generated by the SSPAs).

The instrument parameters are summarised in Table 3. A maximum system bandwidth of 220 MHz is required for achieving a range resolution of 2 m at the lowest nominal incident angle of 20°. Below this limit, the range resolution will be degraded.

Orbit	510 km sun-synchronous 6PM/6AM Equator crossing
Accessible swath	20°-53.7° (electronic steering) 10°-63° (platform steering) Two-sided viewing capability
Nominal Antenna pointing	33° from nadir (right-hand-side of satellite track)
Satellite roll angles	+17°/-10°/-53°/-66°/-83°
System bandwidth	≤ 220 MHz
PRF	≥ 4550 Hz
Operational duty cycle	≤ 5 min. per orbit over 3 consecutive orbits
Instrument mass	≅ 480 kg
Power consumption	≅ 4600 W DC in imaging mode
Solar array area	≤ 16 m ²
Data rate	≤ 800 Mbits/s after BAQ 8:4
Data storage	≤ 500 Gbits

Table 3: Summary of instrument parameters

The upper limit of the PRF depends on the ability of the synthesised beam to reject nadir returns. If the suppression of the nadir returns was possible for all beam positions, the PRF increase can be limited to 200 Hz. If they had to be avoided by choosing appropriate timings, the PRF can increase by more than 1500 Hz which could cause large increase in data rate. Hence, the former case has been assumed for the estimation of the data rate.

The operational duty cycle is limited mainly due to the high data rate of the SAR instrument. The indicated duty cycle has been derived by assuming one downlink possibility per orbit at 240 Mbits/s transmission rate.

The predicted sensitivity as a function of the incident angle (continuous line) is presented in Fig. 5 against a 95 % detection probability derived from the existing data [3] (= Specification $\text{Ne}\sigma^0$). The sensitivity is excellent up to the incidence of 42°, but is somewhat marginal for the higher incidence range. Thus, the analysis has been repeated for a relaxed range resolution of 3 m (≈ 150 MHz system bandwidth). With the resulting improvement of 2 dB (broken line), the sensitivity becomes fully satisfactory.

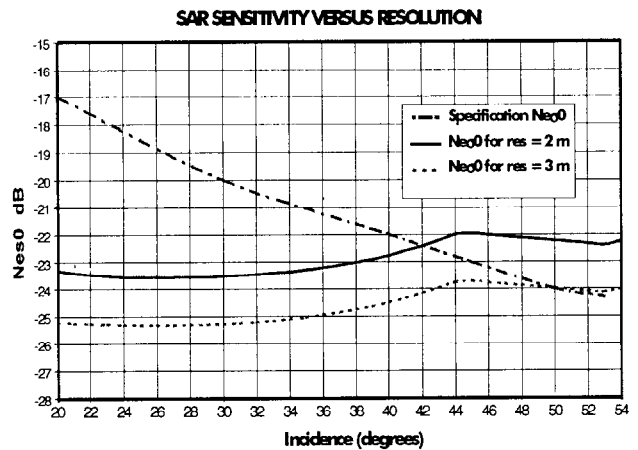


Fig. 5: Predicted noise equivalent σ^0 for 2 m and 3 m range resolutions

For a rapid deployment of the constellation, successive multiple launches are recommended for reducing the launch cost. The Skybridge launch approach can be adopted where the spacecrafts are attached to the launch keel dispenser through the $-z$ spacecraft facing deck by means of interface fittings (see Fig. 6). Up to 4 spacecrafts can be launched in such a configuration. Fig. 6 shows an example of 3 spacecrafts stowed under the Soyouz/Fregate launch fairing.

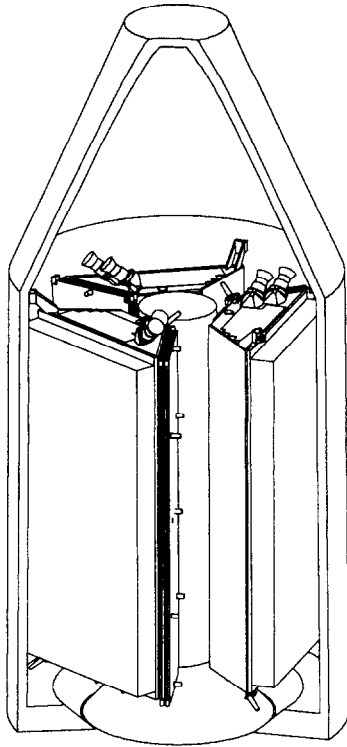


Fig. 6: Example of 3-spacecraft stowed configuration under Soyouz/Fregate launch fairing

4.2 Reflector antenna based design

The main motivation for studying a reflector antenna based alternative was its potential to achieve an acceptable performance at a significantly lower cost than the active antenna approach. The rationale for such a cost reduction is based on:

- the potential to achieve an instrument at much lower mass than the active antenna one, which should enable the electronic agility of the active antenna to be replaced by the spacecraft agility;
- possible exploitations of synergy with modern telecommunication payloads technology, particularly in the area of light-weight, deployable, multiple-beam reflector antennas.

The large beam scanning range of the active antenna ($\pm 15^\circ$) is difficult to achieve with a reflector unless it is oversized (e.g. 50 % increase in diameter). Consequently, the electronic scanning option has been discarded, which means that only the strip-map mode of the instrument is retained. This was felt to be acceptable as the constellation would still provide short revisit to progressively build up large area-coverages.

The selected solution consists of a 4 m diameter single offset reflector which is fed by a linear horn array (see Fig. 7). The degree of freedom offered by the array-feed enables synthesis of a beam with varying width which is

optimised according to the viewing incident angle. Such an optimisation is mainly driven by the sensitivity (noise equivalent σ^0) and range ambiguity ratio requirements.

A preliminary system optimisation assuming an orbit altitude of 510 km led to the necessity to reduce the imaged swath width to 16 km for meeting the image quality requirements. A high peak power of 6 kW at a maximum of 16 % duty cycle is required from a cluster of TWTs. This reduction of swath width is due to the inability of the analysed reflector design to meet the tight beam-shape and gain requirements for achieving 20 km swath. This limitation arises because of:

- 1) the lower aperture efficiency of the reflector as compared to a planar antenna of the same size, as the aperture illumination is necessarily tapered in the former to avoid excessive spill-over losses. In order to achieve a comparable beam quality, the size of the reflector needs to be increased by approximately 20 %.
- 2) the lower number of degrees of freedom offered by the array-feed of e.g. 7 horns as compared to the 80 rows of the planar active array.

The preliminary analysis also identified a narrower incident angle range within which the image quality requirements could be met. A first estimate gave a compliant $20^\circ - 50^\circ$ range which corresponds to a 370 km accessible ground range. This would impact the number of satellites required in the constellation to meet the revisit requirements.

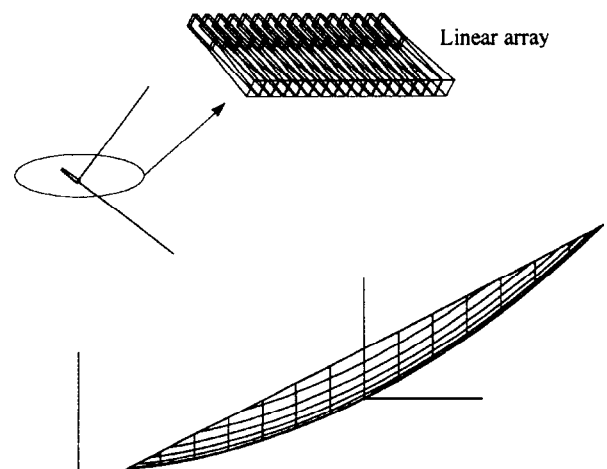


Fig. 7: Array-fed single offset reflector antenna configuration

A review of existing unfurlable reflectors has been carried out in order to find a solution for achieving a compact launch configuration for small satellites. The following 4 technology alternatives have been identified:

- Membrane-type reflector with flexible edges

- Thin stiffened reflector with foldable edges
- Wrap rib reflector
- Faggot or bundle using metallic unfurlable mesh

An analysis of platform accommodation showed that the faggot/bundle solution appears to be clearly the most convenient in terms of stowed dimension and ease of deployment. Two examples of accommodations using this solution are depicted respectively in Figs. 8 and 9 in deployed and stowed configurations. Fig. 8 shows a solution using a Skybridge type platform. In the stowed configuration, the faggot/bundle antenna has a form of a thin cylinder. Fig. 9 shows an accommodation on a Proteus type platform. Both of the configurations are so-called “transversal flyers”.

The parameters of the reflector based SAR instrument have not yet been fully optimised at the time of writing, but they nevertheless are summarised in Table 4. Those values should be understood to be very preliminary and further optimisations will be carried out in the on-going study. In particular, the assumption on the orbit altitude is subject to review in an attempt to improve the overall performance. Estimation of the interface values such as mass and power will be consolidated after a more detailed design.

Orbit	510 km sun-synchronous 6PM/6AM Equator crossing
Accessible swath	20°-50° (platform steering) Two-sided viewing capability
Imaged swath width	≥ 16 km
System bandwidth	≤ 220 MHz
PRF	≥ 4500 Hz
Operational duty cycle	≤ 5 min. per orbit
Instrument mass	$\cong 230$ kg
Power consumption	$\cong 3000$ W DC in imaging mode
Solar array area	≤ 12 m ²

Table 4: Summary of instrument parameters (preliminary)

5. Conclusion

This paper presented two alternative SAR designs for a Risk Management Earth Watch mission. The active antenna based solution meets all the requirements, but is a complex instrument to build, test and operate. Some alternative active antenna architectures have been investigated for reducing technological risks.

The reflector antenna based solution appears to offer an attractive alternative for reducing the system costs but at a price of descoped capability. The feasibility of the concept is conditional upon the availability of unfurlable large ($\cong 4$ m) reflector technology. Such a technology is readily available in the US and in Japan. Further

optimisations of the concept and assessment of technology are required before one could confirm the viability of this option.

Acknowledgement

The study has been performed by an industrial consortium led by Alcatel Space Industries, and EMS Technologies, ComDev Europe, System Engineering & Assessment as subcontractors.

References

- [1] RPT/ESS/000X/..., European Remote Sensing Information Services, ERSIS Final Dossier – Draft Version, June 2000.
- [2] ESTEC Contract No. 12948/98/NL/GD to Alcatel, Feasibility Study of High Resolution X-Band SAR Constellation for Risk Management.
- [3] Handbook of Radar Scattering Statistics for Terrain, F.T. Ulaby and M.C. Dobson, Artech House, 1989.
- [4] ESTEC Contract No. 13246/98/NL/GD to Univ. Wageningen, Study of Global X-Band NRCS Statistics for Land Surfaces and Sea Ice Using Airborne and Ground-Based Radar Data and Creation of a Database.
- [5] ESTEC Contract No. 13881/99/NL/GD to Alcatel, Reflector Antenna Based X-Band SAR Study.
- [6] F. Petz, J. Rosello-Guasch, C. Mavrocordatos and Ch.V. Narasimha Rao, “Modular Design of SAR Electronics,” Proc. CEOS SAR Workshop, 26-29 Oct. 1999, Toulouse, pp235-240.

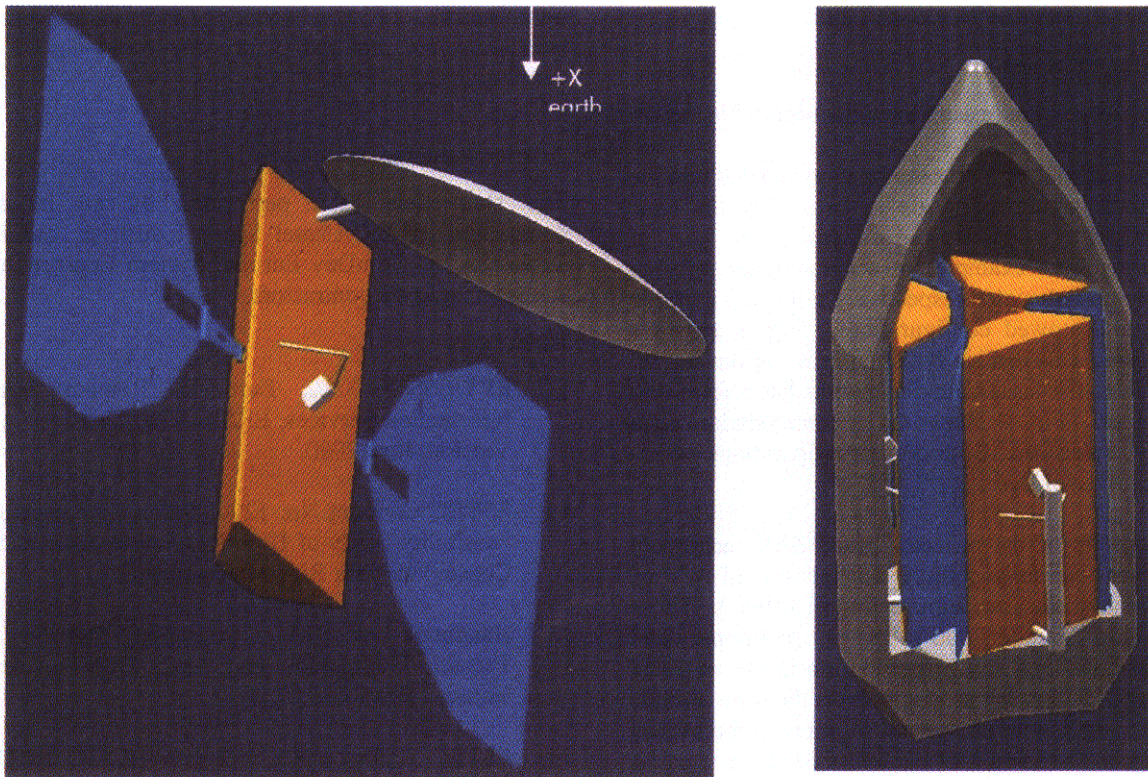


Fig. 8: Accommodation of faggot/bundle reflector antenna on a Skybridge type platform

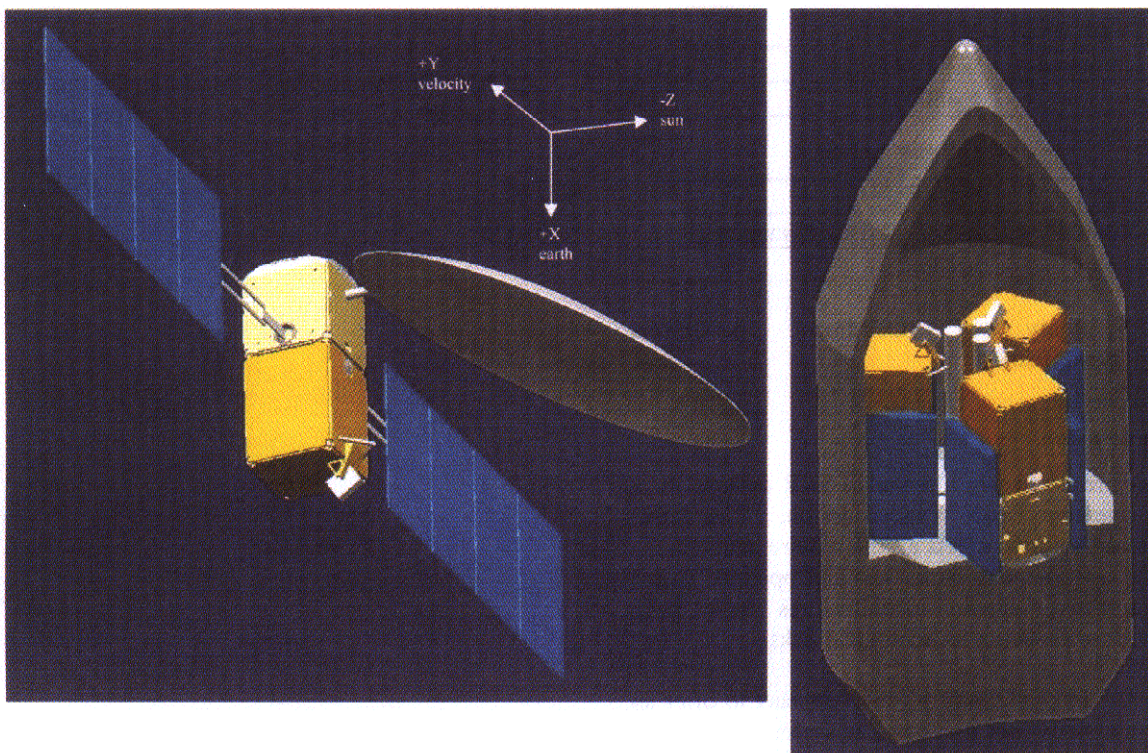


Fig. 9: Accommodation of faggot/bundle reflector antenna on a Proteus type platform

Analysis of P-band Synthetic Aperture Radar for Airborne and Spaceborne Applications

^{1,2}A. Potsis, ¹N. Uzunoglou, ¹P. Frangos, ²R. Horn, ²K. Lamprecht

¹National Technical University Of Athens. Department Of Electrical And Computer Engineering
9 Iroon Polytechniou Str.GR -15780 Zografos, Athens, Greece

²German Aerospace Center (DLR) Institute for Radio Frequency Technology.
D-82230 Oberpfaffenhofen, Germany. Tel/Fax (49)8153-282367/281135

Email: athanasios.potsis@dlr.de, nuzu@cc.ece.ntua.gr, pfrangos@central.ntua.gr, ralf.horn@dlr.de, katja.lamprecht@dlr.de

Summary: An increasing amount of interest has evolved in VHF/UHF SAR applications. These types of radars have proven to be a very powerful method for underground and obscured object detection. In this paper we analyze the possibility of a spaceborne P-band SAR system, based on the experience gained from the analysis of the experimental airborne P-band SAR (E-SAR) system of DLR. We address possible methods and filters for effective Radio Frequency Interference (RFI) suppression, polarimetric and radiometric calibration procedures. We also assess the problems concerning the image quality degradation due to ionospheric propagation effects based on several simulation models.

1. INTRODUCTION

In recent years a new class of Synthetic Aperture Radar (SAR) systems using low frequency have emerged. Behind these developments lie technological advances in antenna design, low noise amplifiers, bandpass filters, digital receiver technology as well as new processing algorithms. The combination of low frequency and high bandwidth, creates a variety of applications. Emerging military and civilian applications of P-Band radar systems include the detection of targets concealed by foliage and / or camouflage, detection of buried objects (like the Unexploded Ordnance (UXO) and underground communication and power lines), forestry applications, biomass measuring, archeological and geological exploration.

The above applications of a P-band SAR system have already been explored and demonstrated using mainly airborne systems [1],[2]. All this variety of applications makes the idea of opening a new low frequency spectral window from space for global coverage very attractive.

However the VHF/UHF portion of the spectrum is heavily used for commercial as well as military purposes. Therefore RF interferences (RFI) are typically encountered in the received radar signals. In most of the cases, the presence of RFI in SAR imagery diminishes the usefulness of the processed data [3],[4],[5]. Additionally, accurate calibration of both amplitude and

phase of quad-polarized SAR data is essential for most of the applications [8]. Especially calibration of quadpolarized SAR data is essential if we are to analyze and understand of what kind polarimetric signatures actually are, if we are to compare low frequency backscattered data between scenes and within scenes, and if we are to compare the observations with theory. These are some of the main problems appearing in an airborne P-band system.

In the spaceborne case, the structure and the composition of the ionosphere is strongly correlated to wave propagation performance. The ionosphere behaves as an anisotropic medium and influences the refraction index, which becomes a function of space and time. This has a strong impact on the propagating wave. Due to the changing refraction and diffraction properties and due to the resulting dispersion relation the ionosphere influences both the propagation path (the direction of the wave vector) and the properties of the propagating wave itself. These problems arising from the propagation effects of the VHF/UHF signal through the ionosphere are additive to the problems addressed in the airborne case [23].

In this paper we analyze the possibility of a spaceborne P-band SAR system, based on the experience gained from the analysis of the experimental airborne P-band SAR system of DLR. We address possible methods and filters for effective RFI suppression, polarimetric and radiometric calibration procedures as well as hardware modifications. We also assess the problems concerning the image quality degradation due to propagation effects through the ionosphere, as well as the possibility that a spaceborne SAR sensor will introduce RFI signals to the terrestrial communication channels.

2. E-SAR P-BAND SYSTEM

The E-SAR is a multi-frequency SAR system mounted on board a Dornier DO-228 aircraft (Figure 1), which is owned and operated by DLR [1]. Currently the radar is operational in the P-, L-, C- and X-Bands with selectable vertical or horizontal antenna polarization. SAR interferometry and SAR polarimetry are functional modes of the radar established in 1996 [2].

The resolution of the E-SAR image products is up to 1.5 m in slant range. Typical swath width are 3 and 5 km and the scene length is not limited in general. For motion compensation purposes the Dornier 228 aircraft is equipped with a CCNS4/ Aerocontrol navigation system coupled with DGPS and INS. This assures the measurement of the platform position with an accuracy of 0.1m rms, and of its attitude by 0.01 degrees. The system also gives the pilot an online control about the actual flight path to help keeping the nominal track with an accuracy better than 5m. This reduces the amount of motion compensation during SAR data processing by one order of magnitude.

Nevertheless, since the E-SAR system is installed on a very unstable platform on low altitudes having long aperture times, a proper processing algorithm with a convenient motion compensation approach, has been developed [2]. For the calculations of the motion compensation phase the imaged terrain is assumed to be flat at some reference level. This assumption is justified for a single-pass acquisition and moderate terrain elevation changes [2], but in the repeat pass a complete and accurate phase evaluation is performed.

E-SAR P-Band System	
<i>Parameter</i>	<i>Typical Value</i>
Center frequency [MHz]	450
Pulse bandwidth [MHz]	18 or 50
Chirp duration [μsec]	5
Sample rate [MHz]	60
Forward velocity [m/s]	80-95
PRF [Hz/channel]	500
Flight altitude [m]	3000-5000
Incidence angle [deg]	25-60
interferometric mode	Repeat-Pass
Across-track baseline [m]	Variable
Baseline tilt. vert. [deg]	Variable

Table 1. Basic operational parameters of the E-SAR P-band system.

In the last years a big effort has been made for improving the efficiency of the P- Band system (center frequency: 450MHz).

The system has been equipped with a new high power amplifier (HPA) of 53 dB gain and peak power of 200 Watts. Additionally a 60MHz band-pass filter was implemented before the low noise amplifier to avoid signal distribution by out-of-band broadcasting frequencies. The high isolation requirements between the four polarization channels was achieved by the implementation of a new 50 dB PIN switch.

As already mentioned before, in low frequency SAR systems it is very likely to have very strong signals due to the nadir echo as well as the radio frequency

interference. These strong signals drive the E-SAR 6 bit ADC's into saturation. In order to accommodate these strong signals the RF receiving path was modified to prevent the saturation of the ADC. According to these modifications most of the effective bits of the ADC were used to sample the low amplitude radar backscattered signals and as less as possible bits for the high amplitude RFI signals.



Figure 1. The E-SAR system mounted on a Do-228 aircraft. The antennas of the multi frequency SAR system are depicted in the yellow

The system performance is mainly determined by the antenna which consists of a 2mx4m microstrip element array at a center frequency of 450 Mhz. Azimuth beamwidth is 30° and elevation one of ~60°. The basic operating parameters of the E-SAR P-band system are depicted in Table 1. [8]

It the next section, the basic problems that scientists have to face in most of the cases in an airborne VHF/UHF SAR system, namely the presence of RF interferences, the high calibration requirements of interferometric applications and the low Signal-To-Noise ratio (over unvegetated areas), will be briefly discussed and the procedures applied in the E-SAR P-band system in order to overcome these problems will be presented.

3 AIRBORNE P-BAND

3.1 RADIO FREQUENCY INTERFERENCE FILTERING

As already mentioned above, the both requirements of wide bandwidth for high resolution and a low frequency range for foliage or ground penetration necessitate use of frequency bands occupied by other communication channels. As a result, radio frequency interferences (RFI) appear in the receive signal. In most of the cases, the presence of RFI in SAR imagery diminishes the usefulness of the processed data making extremely difficult any attempt for radiometric and polarimetric calibration. In the airborne P-band case we consider interferences coming from other communication sources operating at the same frequency

but for the spaceborne case we will analyze the case where a spaceborne P-band SAR will introduce interferences to the terrestrial communication systems.

E-SAR P-band data contaminated with RFI have been analyzed and several RFI filtering methods have been tested [3],[4],[5]. Two operational RFI suppression filters were the result of this effect.

The first is a very simple and robust frequency domain notch filter which removes the interference peaks by setting a small bandwidth around the detected peaks to zero. This RFI filter is very fast and gives quite acceptable quality data but it has all the disadvantages of a notch filter (sidelobe effects, removing a part of the SAR signal resulting in a degradation of the image quality).

The second RFI suppression filter is based on the least mean square estimation (LMS) algorithm. As described in [3] the algorithm models the RFI signals as a superposition of sinusoidal signals. The general model of the received signal is:

$$X(k) = S(k) + n(k) + \sum_{i=1}^N A_i e^{j(2\pi f_i k + \varphi_i)} \quad (1)$$

where $X(k)$ is the received signal, $S(k)$ is the 'pure' target return SAR signal, $n(k)$ is the noise signal (uniformly distributed random variables with zero mean) and the RF interference signals. According to the model (1), every interference signal was detected, estimated and coherently subtracted in each range line in the raw data. This filter provides better quality data than the notch filter as it achieves better signal preservation but it is slower.

The amplitude image and the interferogram of the VV channel of the test site of Gilching/Germany before and after RF interference filtering using the LMS algorithm filter are shown in Figure 2. From this figure becomes evident the "destructive" effect of the RFI signals to the SAR data especially at the interferogram which appears to be completely destroyed, and the filtering improvement.



Figure 2a

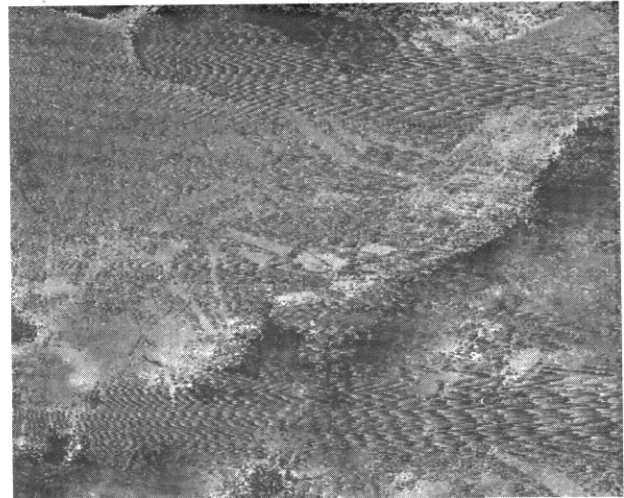


Figure 2b



Figure 2c

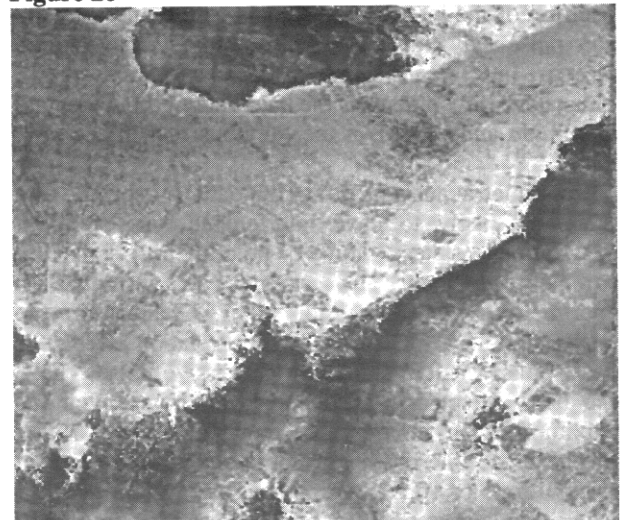


Figure 2d

Figure 2 a. The unfiltered amplitude image (VV channel) of the test site of Gilching/Germany. The RFI effect it is evident. **2b.** The interferogram of the same area (repeat pass interferometric pair with baseline of 40m). The destructive effect of the interference signals to the interferometric phase is here more than evident. **2c.**

The amplitude image after RFI filtering using the LMS algorithm with resolution in range, 4m and in azimuth, 3m and finally 2d. The interferogram after filtering. The biggest amount of the phase information has been successfully recovered. Near range on the left site of the image. This flight campaign was partially supported by DERA Farnborough UK.

A new mode of operation of the airborne E-SAR system called Listen Only (LO) channel mode of operation, gave us the opportunity to study and analyze the special characteristics of the interfering signals and how they effect the SAR data quality. The basic idea of the LO channel mode of operation is shown in Figure 3. From this Figure becomes evident that in order to be able to store the interfering spectrum between two successive radar pulses we have to implement a control signal [4].

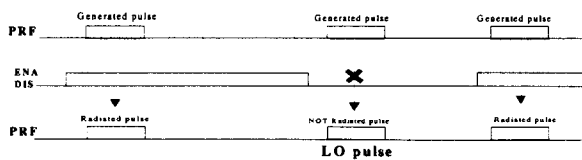


Figure 3: Basic idea of the LO channel mode of operation.

When this signal was set to high voltage (Enable-ENA) the generated chirp signal was directed to the antenna for radiation as in the usual operating mode but when this signal was set to low voltage (Disabled-DIS) the generated chirp was not transmitted. The new important information that this mode of operation provides to us, arises from the fact that the whole spectrum of the interference signals before and after the radar pulse is available. For the first time we have stored the entire interference signal, in all polarizations, and we can analyze how it distorts the backscattered radar signal (amplitude and phase) in the previous and in the next pulse.

Polarimetric analysis of the LO data [4] showed that it is very likely to have interference tones in both polarization states (fully polarimetric) making extremely difficult any attempt to introduce a polarimetric RFI suppression filter. Changes in the polarization state (and probably decorrelation effects) of the H polarized RFI signals in successive pulses have also been detected. Statistic analysis showed that the amplitude of the interferences remains almost constant for one range line but it can not be supposed to remain constant for 5 or 10 E-SAR range lines.

A simple notch filter which uses the frequency information of the LO pulse in order to filter the interferences in the next pulse (Radar+RFI) was finally implemented [4]. In general the filter detects in the spectrum the position of the interference (which most of the times appears as high picks) signal and then it sets to zero a small bandwidth of 50kHz at the same position at

the previous radar pulse which contains the back-scattered signal plus the interferences.

There are two main advantages of this filtering approach:

a) This method is very fast and can give filtered data almost in **real time**.

b) All the existing interference signals inside a radar pulse can be detected and successfully removed by the filter regardless of their corresponding amplitude. Without the LO mode it is almost impossible for any estimation algorithm to successfully detect and remove these small amplitude signals in a backscattered data line. This filter was applied on repeat pass interferometric polarimetric data collected by DLR's E-SAR System on the test site of Oberpfaffenhofen /Germany. The filtering results are depicted in Figure 4. From Figure 4 we can see that almost all periodic disturbances generated by interferences have been successfully removed.

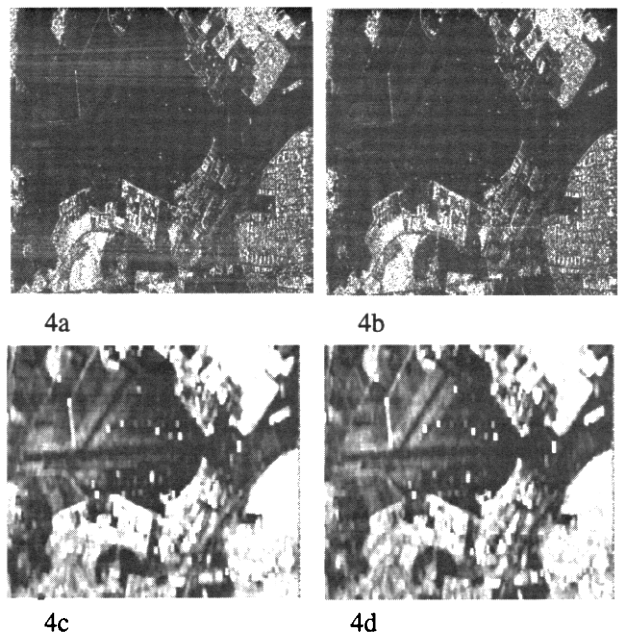


Figure 4: (a) Unfiltered amplitude image of Ch HH, (b) filtered data with a real time notch filter using interference information from LO Ch. H, (c) unfiltered coherence map of (a) and (d) the filtered coherence map. Near range on the left site of the image.

The experience gained from the airborne P-band RFI signal analysis, the filtering algorithms that have been already developed and successfully implemented, and especially the idea of the LO channel mode of operation, which can provide almost "real time" interference filtering, can be applied to a spaceborne P-band system ensuring interference free data.

3.2 RADIOMETRIC AND POLARIMETRIC CALIBRATION

As VHF/UHF SAR systems become more and more commonly available to the research community, the radiometric and polarimetric calibration of this kind of

systems becomes important. The high calibration requirements of interferometric applications and P-band characteristic problems as the low Signal-To-Noise ratio (over unvegetated areas) and, as already discussed, the presence of RF interferences make it necessary to adapt, modify, and extend the existing calibration methods, in order to establish a operational calibration [8].

Several calibration flights have been made recently using the modified E-SAR P-band system. The developed calibration procedure and the accuracy that has been achieved are described in this paper. In the next section, the special calibration demands and constraints the scientists have to face in a spaceborne P-band case mainly due to wave propagation effects through the ionosphere, are analytically discussed.

• Calibration of the RFI filtering effect

After the RFI filter has been applied, the total energy of each range line is reduced according to the amount of the subtracted interference signals. This energy reduction is compensated afterwards. In general, the gain of a filter $H(f)$ applied on a stationary (signal) process of power spectral density $A(f)$ is [13]:

$$k_{s,filter} = \frac{\int A(f) |H(f)|^2 df}{\int A(f) df} \quad (2)$$

This gain $k_{s,filter}$ caused by the LMS filter was calculated and corrected in every filtered range line in the raw data.

• Radiometric calibration.

Adequate radiometric corrections of the P-band E-SAR data require knowledge of the sensor-target geometry and the antenna elevation pattern. Preflight measurements have been performed and the P-band antenna patterns were checked, corrected and stored.

The intensity of the backscattered signal in the raw data and in the processed image can be written as: [8]

$$P = P_s + P_N, \quad I = I_s + I_N \quad (3)$$

Where P_s is the signal intensity in the raw data, P_N is the noise intensity in the raw data, I_s and I_N is the signal intensity and the noise intensity in the image respectively. According to [4], for one homogenous distributed area with "radar brightness" β^0 we get:

$$\bar{I} := \bar{I}_s + \bar{I}_N = K_s \bar{P}_s + K_N \bar{P}_N = K_s C_s \beta^0 + K_N \bar{P}_N \quad (4)$$

Where,

$$C_s = \frac{c}{2} \frac{\lambda^2}{(4\pi)^3} \frac{\varphi_a E_{TX} G_R G^2(\theta - \theta_i)}{R^2} \quad (5)$$

and K_s is the signal gain of the processor for distributed scatterers, K_N is the processor noise gain, λ is the wavelength, φ_a is the effective beam width of the azimuth antenna diagram, E_{TX} is the transmitted chirp energy (=transmit power x chirp duration), G_R is the receiver path gain, $G^2(\theta - \theta_i)$ is the two way elevation antenna pattern, where θ is the off-boresight angle and θ_i is the off-nadir look angle, and R is the slant range distance.

To assure that the signal gain remains constant in time and space the following equation must be valid:

$$K_s \propto \frac{1}{C_s} \propto \frac{R^3}{\lambda^2 \varphi_a E_{TX} G_R G^2(\theta - \theta_i)} \quad (6)$$

In the processor, using the stored antenna diagrams, all the range and azimuth corrections are applied after range compression using the radiometric calibration function (6).

Several calibration experiments have been made and more than five, three meter trihedral corner reflectors with known RCS value have been used for absolute radiometric calibration. The corner reflectors have been placed in different test sites (Ettersschlag and Gilching) and in incidence angles from 25° to 60° . Using the antenna elevation patterns, the corresponding boresight angle and the gain of the system receiving path, radiometrically corrected P band E-SAR data have been analyzed. The data have been processed to an absolute radiometric calibration factor of $K_s = 60$ dB.

The measured RCS, the signal to background ratio and the measured calibration factor for the two corner reflectors are presented in Table 2.

Track 1	Incidence angle (in deg)	Calibration factor [dB]	Theoretical RCS [dB*sqm]	Estimated RCS [dB*sqm]	signal-to-background ratio [dB]
Polarization state HH					
CR1 (near range)	36.62	61.01	28.75	29.74	25.86
CR2 (far range)	54.27	58.9	28.82	27.73	25.3
Polarization state VV					
CR1 (near range)	36.62	61.7	28.75	30.46	26.52
CR2 (far range)	54.27	58.8	28.82	27.39	26.45

Table 2: The measured RCS, the signal to background ratio and the measured calibration factor for the two corner reflectors in both polarization states.

From Table 2 we can conclude that the measured calibration factor is close to the expected one of the 60 dB (less than 1.5 dB variation). Considering the imbalance of the calibration constant, the measured RCS of the corner reflectors appear to be very close to the theoretical value [8],[9],[12]. Using RCS imbalance information from the corner reflector analysis the E-SAR antenna pattern was afterwards corrected.

A second evaluation has been performed concerning the stability from pass to pass. The same test site has been calibrated based on trihedral measurements of the first track. The pass to pass stability is observed to be in

the order of 0.3 dB, meaning that the system shows good temporal stability.[12]

More calibration experiments are planned for the near future. With this experiment we expect to increase our calibration knowledge and to improve even more the performance and the stability of the P-band E-SAR system.

• Polarimetric calibration

Qualitative and quantitative evaluation of the scattering matrix data acquired by the airborne E-SAR fully polarimetric P-band system, requires the estimation and elimination of the system induced distortions. This is necessary in order to identify and analyze the underlying scattering matrix.

A large number of polarimetric calibration methods based on different assumptions concerning the system distortion and utilizing backscattering properties of deterministic and distributed scatterers, can be found in the literature [11],[12]. For the polarimetric calibration of the modified P-band system we used the modified Quegan's calibration approach. According to [11], for the airborne SAR case with the absence of the ionospheric effects, the model which describe the systems effects is a two-stage liner distortion model for receive and transmit given by:

$$[O]=[R][S][T]+[N] \quad (7)$$

where $[O]$ is the 2x2 observed scattering matrix, $[S]$ is the target scattering matrix, $[R]$ and $[T]$ are 2x2 complex matrices describing amplitude and phase distortions in the receiver and transmit path respectively and $[N]$ is the system noise. The polarimetric calibration consists of the following steps:

i) Cross-Talk Removal

In order to accurately estimate the system cross-talk ratios ($w=R_{hv}/R_{vv}$, $u=R_{vh}/R_{hh}$, $z=T_{hv}/T_{hh}$ and $v=T_{vh}/T_{vv}$) two effects had to be taken into account. Firstly the areas which appear to have high correlation between the co- and cross polarized channels (>0.3) [11] have been masked out before the cross-talk estimation. The second effect is the low signal-to-noise ratio (SNR) especially over unvegetated areas which mainly effects the cross polarized channels. These noise affected areas have been excluded and an average $-\alpha-$ range profile for the whole scene was estimated and used for the cross-talk removal. Additionally the range profiles of the estimated cross-talk ratios were used in the correction procedure. Figure 5 depicts the $u=R_{vh}/R_{hh}$ and $v=T_{vh}/T_{vv}$ cross-talk ratios of the data of Figure 2, before and after cross-talk calibration. From this figure we can see that the cross talks can be improved in the order of 13dB resulting values from -33dB and even below -45dB.

ii) Symmetrisation

According to [11], symmetrisation of the cross polarised channels based on the least-square solution has been performed.

iii) Phase Calibration

The signal response from the trihedral corner reflectors deployed in the test sites in different ranges and incidence angles, with known ratio S_{HH}/S_{VV} was used in order to estimate the complex receive channel imbalance. Evaluation of the collected data showed that after the phase calibration the HH-VV phase imbalance reduces to the order of 10^0 which is, in most of the cases, acceptable for polarimetric applications [12].

iv) Absolute Inbalance Calibration

The amplitude imbalance ratio of HH and VV channels was derived from the same trihedral corner reflectors. In order to estimate the energy in both co-polar channels of the cross-talk corrected images the integral method was used [11]. Evaluation of the calibrated data showed that the amplitude imbalance takes values close to 0.1 dB.

The RGB representation of a Pauli [11] decomposition of an RFI filtered, radiometric and polarimetric calibrated E-SAR P-band data of the test site of Gilching / Germany, is depicted in Figure 6.

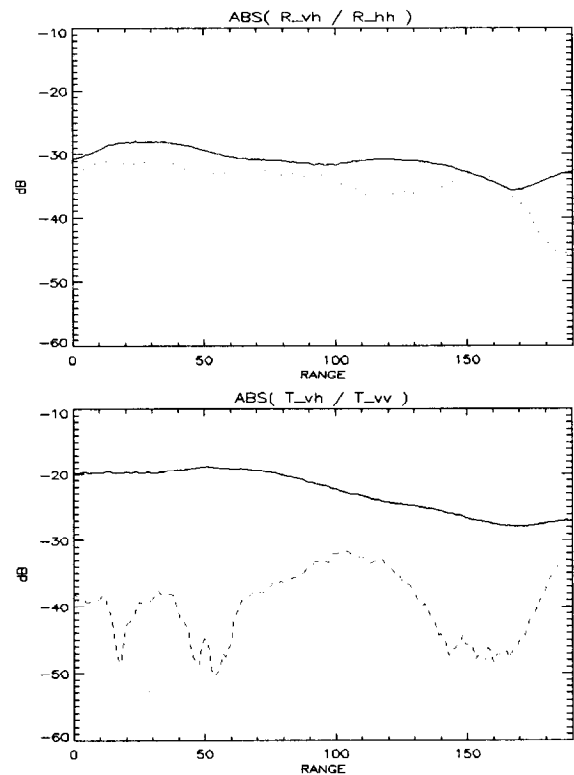


Figure 5: The estimated cross-talk ratios before (solid lines) and after (dash-dot) the calibration is performed.

4 SPACEBORNE P-BAND

Scientific fields and the several remote sensing campaigns by the E-SAR P-band system contributed intensively to the development of algorithms and understanding the sensitivity of interferometric fully polarimetric VHF/UHF SAR systems to surface and subsurface detection and parameter estimation. As already presented, the technological progress in

VHF/UHF SAR systems has resulted in the development of new hardware design, signal processing and RFI filtering algorithms, polarimetric and radiometric calibration techniques providing data that are fine tuned for detecting and measuring various Earth surface as well as sub-surface targets and parameters of great interest for the user community (military, forest management, Biomass estimation, archeology etc.).

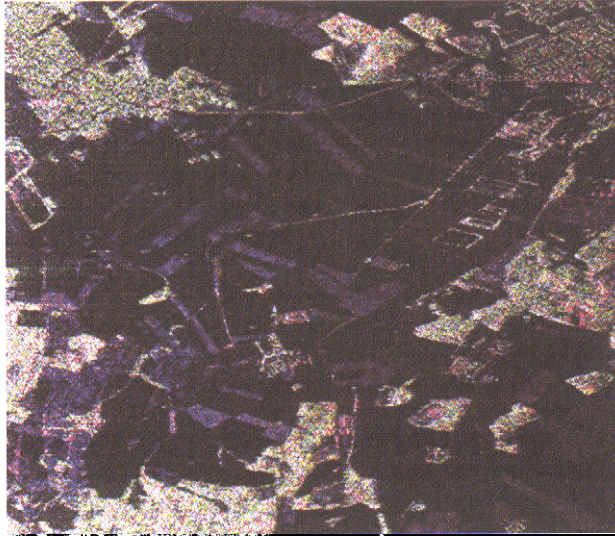


Figure 6: The RGB representation of a Pauli decomposition of a full polarimetric E-SAR P-band data set of the test area of Gilching/Germany (colors : Red: HH-VV, Green :2HV and Blue: HH+VV.) Near range on the left side of the image. This flight campaign was partially supported by DERA Farnborough UK.

The wave length used so far for space applications extend to L-band [23],[27],[30]. Adding a new band at longer wavelengths is only meaningful if only sufficient spacing between the wavelengths can be achieved so that the scattering properties of the radar waves become significantly different. The experience gained by operating the E-SAR P-band system with center frequency of 450MHz and 50MHz bandwidth, proved that P-band frequency is adequate as far as the scattering properties are concerned and it is technically feasible on small platforms like the Do-228 airplane. Hence, the frequency band from 400MHz up to 500MHz has been investigated.

But, as all the above variety of applications makes the idea of opening a new low frequency spectral window space for global coverage very attractive, at the same time, it becomes a great challenge for the scientists as the propagation effects of the electromagnetic waves, at VHF/UHF frequency caused by the ionosphere, become significant and can not be ignored.

Irregularities in the propagation medium can cause fluctuations in the phase, amplitude and polarization vector of the radar signal. These errors can be expressed as a sum of two terms, the first a mean value across the synthetic aperture, and the second a fluctuating component [15]. Especially the second one can cause severe distortions of the signal causing difficulties for

any attempt not only for radiometric and polarimetric calibration but also for the data processing itself.

The main parameters in a VHF/UHF SAR scenario which are affected by ionospheric propagation are the azimuth and range resolution, the image position and the orientation angle of the incoming polarized wave [15],[23],[24]. Additional problems in such a system design are the RFI introduced to the radar by the terrestrial communication systems and vice versa, as well as the frequency allocation problem. These problems as well as possible solutions will be analyzed in this section.

4.1 IONOSPHERIC EFFECTS

• Azimuth resolution

According to [23], the fluctuations of the refractive index and thus phase fluctuations of the signal due to the ionospheric turbulences affect the coherence length of the wave field. Depending on the value of the Total Electron Density (TEC) and the used frequency, it might be reduced below the equivalent aperture size $D/2$, as it happens for P-band frequencies, and thus the azimuthal resolution becomes larger than the half of the antenna aperture size ($D/2$).

According to [23], the azimuthal resolution of a spaceborne P-band system is very sensitive to the frequency. Changing for example the center frequency from 400MHz to 500MHz we can expect great improvement in the resulting azimuth resolution.

• Total Electron Density (TEC)

The Total Electron Density (TEC) is defined as the integration of the electron density over the vertical path from the ground to the upper ionosphere [17]. The value of the TEC changes with solar activities, and the differences can be found with a factor of 3.

The correct and as accurate as possible estimation of TEC variations is essential for the compensation of the ionospheric effects in the radar signal. Different methods have been already used, like satellites and high-altitude rockets, to estimate TEC. An important contribution to the ionosphere TEC mapping has the worldwide network of the Global Positioning System (GPS) [22],[18],[19]. According to [18], the accuracy of the generated TEC maps are restricted, beside hardware errors, by multipath of signal propagation at low elevation, by the limited amount of ground receiving station and by the used model for mapping slant TEC values to vertical values, like assuming a shell ionosphere with constant peak height [21], [18]. Special care has to be taken in using vertical TEC values of given TEC-references for slant path analysis. By measuring the GPS phase fluctuations, that means by measuring the time rate of differential phase of the dual frequency GPS signals, this network-based system enables to monitor the generation and the changes of the ionospheric irregularities continuously around the globe under various geophysical conditions. As described in [16] instead of measuring the TEC

values, several theoretical models can be applied and the TEC values can be estimated. The more accurate and detailed this knowledge is, the better we can estimate the appropriate time for remote sensing applications [20].

- **Range resolution**

The dispersion and to a lesser extend the multiple scattering due to ionospheric turbulence result in a pulse broadening. This has an influence on the range resolution, and the resolution cell in range can, depending on the TEC values, increase by a factor of 3 for a frequency of 400MHz [23]. The resulting pulse broadening is also a function of the used bandwidth. Due to changes of the pulse group velocity, the position of the image changes and undergoes a shift in range. This shift increases with the values of the TEC [23].

- **Faraday rotation**

In spaceborne applications, long wavelength imaging systems (like P-band systems) are strongly affected by Faraday rotation, an effect that arise due to the circular bi-refractive behaviour of the ionosphere caused by the earth magnetic field which results in different propagation constants for the two left- and righthanded polarized parts into which a wave can be split up. For a generally polarized wave the change of the ellipticity angle can be neglected, but not the rotation of the orientation angle. The amount of Faraday rotation depends on the Total Electron Density (TEC) profile, the Earth's magnetic field (increases with the inverse square of the radar frequency) and the elevation angle. Faraday rotation is also a function of time. For example the maximum likely Faraday rotation at a system operating at the frequency of 400MHz is 675° during the day and only 67° at night [30].

The Faraday rotation effect in VHF/UHF frequencies is quite strong and any attempt of polarimetric calibration of the collected data becomes very challenging. It is known [24] that for frequencies above 100MHz, the one-way Faraday rotation angle Ω is given by :

$$\Omega = K_F f^{-2} B_{propa}^- \int_{path} N_e ds \quad (8)$$

Where f is the system frequency, B_{propa} is a weighted mean value of the magnetic field component along the propagation direction, N_e is the electron density, s is the path length, and K_F is a constant. The integral express the TEC value along the slanted ray path.

For the spaceborne P-band case, including Faraday rotation, the model of equation (7) which describe the systems effects becomes:

$$[O] = [R][F][T] + [N] \quad (9)$$

where $[O]$ is the 2x2 observed scattering matrix, $[F]$ is the scattering matrix given by:

$$F = \Omega S \Omega \quad (10)$$

With the Ω Faraday rotation matrix given by:

$$\Omega = \begin{pmatrix} \cos \Omega & \sin \Omega \\ -\sin \Omega & \cos \Omega \end{pmatrix} \quad (11)$$

The sign of Ω is positive in the northern hemisphere in a right-handed coordinate system with $x=H$, $y=V$, and z toward the Earth [25]. $[R]$ and $[T]$ are 2x2 complex matrices describing amplitude and phase distortions in the receiver and transmit path respectively and $[N]$ is the system noise [25]. Like in the airborne case, the system calibration involves solving (9), using only the observed matrix $[O]$ and some knowledge of the scattering properties $[S]$, to obtain the distortion matrices $[R]$ and $[T]$ as well as the Faraday matrix.

The magnetic field can be assumed for practical reasons, to be both static and homogeneous over typical scenes and aperture formation types. However, spatial variability in B_{propa} occurs because the line-of-sight of the radar with respect to the magnetic field direction changes as the radar moves. This is one of the main sources of azimuth defocusing effects as already mentioned. The value of the resulting Faraday variations $\Delta\Omega_m$ over the synthetic aperture radar length L at an altitude h is given for $L \ll h$ by [25] :

$$\left| \frac{\Delta\Omega_m}{\Omega} \right| \approx \frac{L}{h} \sin \varphi_0 \cos \psi_0 \quad (12)$$

where φ and ψ are the angles between the aperture plane and the magnetic field direction respectively, as illustrated in Figure 7, with φ_0 and ψ_0 the corresponding mean values. For a relatively low SAR platform altitude of 600 km (as proposed for BioSAR [31])

$$\left| \Delta\Omega_m / \Omega \right| < 0.002L \quad \text{for all values of } \varphi_0 \text{ and } \psi_0.$$

The solution of (9) is quite complicate and it is under investigation.

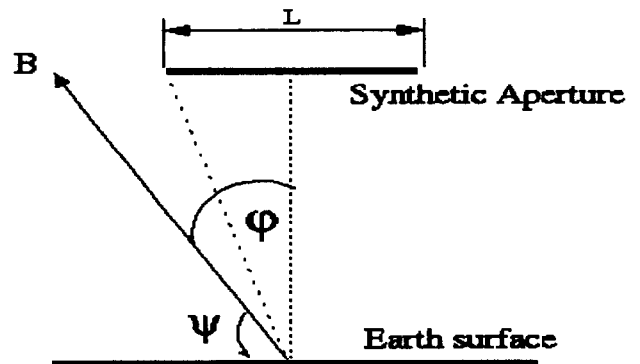


Figure 7: Imaging geometry of the imaging sensor and the magnetic field.

Once the Faraday rotation has been measured the SAR system may need to adjust the plane of the

transmitted polarization to achieve the wanted polarization on the ground (Figure 7).

Freeman in [24] modeled the Faraday rotation in a spaceborne SAR backscatter case and presented a new approach for estimating the Ω , while overcoming also the problem of the modulo 2π errors. The proposed approach improves the numerical solutions offered by Gail [25] and the approach of Rosen [26] which uses ground based corner reflectors.

The idea of using the RFI signal from the terrestrial communication channels to the SAR system [30] as reference signals for measuring the Faraday rotation does not seem to be valid any more as the LO analysis proved that it is very likely to have interference tones for both polarization states (fully polarimetric).

In order to overcome the problems introduced to the signal due to Faraday rotation, a common approach for a spaceborne VHF/UHF SAR system design is to use circular polarised signals. A circular polarised signal is less sensitive to the Faraday rotation but at the same time is limiting the use of a spaceborne VHF/UHF SAR system for applications like the Biomass estimation [30].

Using this circular polarised signal configuration, Shteishleiger et al [28] proposed a new approach for compensating the ionospheric distortions using a two dimensional adaptive filter in the receiver for chirp compression where the reference phase function is matched with the received signal that has passed through the ionosphere (and not with the radiated chirp signal). The 2D-compensation algorithm has been tested with real airborne VHF/UHF SAR data where ionospheric distortions have been simulated, with quite promising results.

Nevertheless, in the recent years, DLR has gained a lot of experience in calibration of X-SAR, SIR-C and recently SRTM space shuttle missions, and several calibration techniques have been developed and successfully implemented [13],[14]. Since night-time P-band Faraday rotation is predicted to be comparable with L-band day-time Faraday rotation, similar calibration techniques (like in L-band) could be easily developed for operating a spaceborne P-band SAR even at linear polarisation at night-time [30].

• RF Interferences in spaceborne P-band SAR

As already analysed in details for the airborne P-band SAR system, RFI are a mutual problem when frequency bands are shared between different services. Hence, for the spaceborne P-band case two types of interference will be discussed.:

1. RFI from the terrestrial communication services to the SAR imaging sensor and
2. RFI from the P-band spaceborne sensor to the terrestrial communication services.

1. As already analysed in section 3.1 the interference caused by the large number of interference sources within the SAR's field of view, will degrade the data quality (examples of this effect is shown in Figures 2a and 2b). The same algorithms (notch filter and LMS

estimation and subtraction algorithm) developed for the airborne E-SAR P-band system can be applied without any difference and with the same results in a spaceborne P-band sensor. Especially the application of the LO channel mode of operation can offer almost real time RFI filtering [3],[4],[5]. Additionally in order to increase the acceptability of the system, it is attractive to operate during the night when the communication services are used less.

2. The spaceborne SAR illuminates a strip beneath and to one or both sides of the satellite. The strip can be between tens and hundreds of kilometres wide and can be thousands of kilometres long. The revisit time (the time between passes of the satellite over the same geographic area) is normally between 3 and 30 days. Hence, during the illumination time, a big number of terrestrial communication stations will be within the scanned area, but interference caused by the radar will be less than once per day.

The operation parameters of a common communication channel (Table 3) and the system specifications of the proposed spaceborne P-band BioSAR (Table 4) system was analysed in order to determine the interference effect from a P-band spaceborne SAR sensor to the terrestrial communication links.

BioSAR is a fully polarimetric spaceborne P-band system design proposed to ESA by a group of companies as described in [32]. The basic aim of the proposed system is the measuring of the geophysical parameters like biomass, flooding condition, and land cover class. Using the design parameters of tables 3 and 4 the peak radiated field strength on the surface of the Earth P_{BioSAR} due to the spaceborne sensor is given by [31] :

$$P_{BioSAR} = \frac{\text{Peak Transmit Power}}{R \beta_{BioSAR} W_{BioSAR}} \quad (13)$$

Where for $\beta = 7^\circ$ becomes 1.310^{-6} W/m^2 and for $\beta = 9^\circ$ 1.06 W/m^2

Parameter	Symbol	Fixed Comm. Station	Mobile Comm
Transmit power	P_{COM}	100W	10W
Antenna Polarization		Vertical	Vertical
Antenna Gain (Horizontal)	G_{COM}	2dB	2dB
Antenna Gain (towards satellite)	$G_{COM-SAT}$	0dB	0dB
Receiver Noise Figure	F_{COM}	2(3 dB)	2(3 dB)
Transmit Bandwidth	B_{COM}	10kHz	10kHz
Transmit condition		continuously	continuously

Table 3. Operational parameters of a common fixed and mobile terrestrial communication service.

This calculated energy is spread over the whole bandwidth of the transmitted chirp pulse. For this reason, the effective strength of the received field within the bandwidth of the terrestrial communication system must be also calculated. Using the parameters of Table 3 we get [31] :

$$P_{BioSAR} \cdot \frac{B_{COM}}{B_{BioSAR}} = 1.6 \text{ or } 1.3 \cdot 10^{-9} \text{ W/m}^2 \quad (14)$$

In order to compare the strength of this interference signal with the corresponding strength of communication signal, the field strength of a fixed and a mobile communication transmitter for a distance $r=10\text{km}$, has been calculated.

$$P_{comm \text{ field strength}} = \frac{P_{COM} \cdot G_{COM}}{4 \pi \cdot r^2} \quad (15)$$

at a mobile receiver we get : $1.3 \cdot 10^{-7} \text{ W/m}^2$ and at a fixed station: $1.3 \cdot 10^{-8} \text{ W/m}^2$.

Comparing these values with (14) we see that the SAR signal is for a mobile station two order of magnitude below the communication signal level and one order for fixed station.

But in order to estimate the interference generation to the communication channels, the sensitivity of the communication receivers (the limiting field strength due to noise), must be calculated.

$$\frac{\text{Noise Density}}{\text{Effective Antenna Aperture}} = \frac{B_{COM} \cdot (F_{COM} - 1) 290 \cdot k}{G_{COM} \cdot \lambda^2 / 4 \pi} \text{ W/m}^2 \quad (16)$$

Where k is the Boltzman's constant, and λ is the systems wavelength. For BioSAR with $\lambda=0.689\text{m}$ (16) becomes equal with $8,38 \cdot 10^{-16} \text{ W/m}^2$. The resulting sensitivity is much smaller than the direct path strength of the transmitted SAR signal (as expected to be) [31].

BioSAR System Specifications		
Parameter	Symbol	Value
Spacecraft Altitude above Nadir	R	600 Km
Swath width	W_{BioSAR}	50 Km
Incidence angle at mid swath	ϕ	23°
Center frequency	F_{BioSAR}	435 Mhz
Chirp pulse bandwidth	B_{BioSAR}	8 Mhz
Antenna beamwidth (azimuth)	β_{BioSAR}	7° or 9°
Peak transmit power	P_{BioSAR}	50 W

Table 4. Basic BioSAR operating parameters.

Even though, the SAR signal has an average power comparable with the strong communication signals, and therefore will cause interference to the users, it is not so strong that the terrestrial communication links will be overloaded. We must also note that the reliability required by the mobile phone links is less than 10 minutes per year and therefore the disturbance caused by a spaceborne P-band SAR seem to be acceptable [31],[33].

• Frequency allocation

The final investigation subject of our spaceborne P-band SAR analysis is the problem of the frequency allocation. We let this problem last as it is more close to a politic decision and less a scientific/technological problem.

The frequency allocations for spaceborne applications are derived from the International Telecommunication Union (ITU). Unfortunately no primary or secondary allocation for active spaceborne sensors below 1GHz exists. The range up to 406 Mhz includes meteorological aids which can include weather radars with high transmit power and antennas pointing skywards. The band above 470 MHz is allocated to broadcasting, mainly TV stations with high continuous transmit power [31]. In between the band is allocated by fixed and mobile communication stations. As these services mainly use low power and antennas pointing horizontally, this band is mainly considered for the proposed P-band spaceborne SAR sensors (BioSAR). As already mentioned this band has no provision for operation by spaceborne SAR sensors, but as analyzed above the mutual interferences are tolerable. Hence, it shall not be too difficult to obtain permissions from the regulations authorities.

5. CONCLUSIONS

Low frequency fully polarimetric, interferometric Synthetic Aperture Radar has proven to be a very powerful method for underground and obscured object detection as well as for geophysical parameter estimation. In this paper the possibility of a spaceborne P-band SAR system, based on the experience gained from the analysis of the experimental airborne P-band SAR system of DLR is presented. Concepts like the low frequency SAR hardware design configuration, the algorithms used for polarimetric and radiometric calibration and finally RFI suppression techniques concerning the airborne P-band case have been discussed and analyzed. Extension of the advantageous low frequency remote sensing technique to a global scale by a spaceborne P-bands SAR sensor is addressed. For this case the several problems that ionosphere introduces to the system like the reduced azimuth and range resolution, the displacement of the imaged scene, the Faraday rotation, the necessity of accurate TEC measurement and the frequency allocation, have been analyzed and possible solutions are given.

The Radio Frequency Interference problem introduced from the terrestrial communication channels to the spaceborne sensor and vice versa have been analyzed. Especially, for the second case of RFI generation to the terrestrial communication channels, the design specifications of the proposed BioSAR sensor have been used and the analysis proved that the possible disturbance caused by a spaceborne system to a communication services seem to be acceptable.

6. ACKNOWLEDGMENTS

Mr. Potsis would like to thank DaimlerChrysler Aerospace and DaimlerChrysler Hellas for their financial support to his research.

Special thanks to the hardware department of the Institute of Radio Frequency Technology of the German Aerospace Center and mainly to B. Gabler for his work in the E-SAR P-band system and to Dr. M. Zink for his help in analyzing the radiometric calibrated data.

We would also like to thank P. Snoei from the Fokker Space company for his help providing all the necessary information of the proposed BioSAR system for RFI analysis.

Finally Mr. Potsis would like to sincerely thank A. Reigber and Prof. V. Makios of the University of Patras / Greece for supporting his research work.

7. REFERENCES

- [1] R. Horn : "The DLR Airborne SAR Project E-SAR." Proceedings of IGARSS'96 Lincoln, Nebraska USA. pp. 1624-1626, 1996.
- [2] R. Scheiber, A. Ulbricht, A. Reigber, K.P. Papathanassiou: "Airborne Interferometric SAR Activities in DLR". RTO Meeting, High Resolution Radar Techniques. Granada, Spain March 1999.
- [3] A. Potsis, A. Reigber, T. Sutor and K.P. Papathanassiou: "A phase Preserving Method for RF Interference Suppression in P-Band Synthetic Aperture Radar Interferometric Data." Proceedings of IGARSS'99 Hamburg, pp. 2655-2658, 1999.
- [4] A. Potsis, S. Buckreuss, R. Horn and N. Ouzunoglu : "P-Band Interference Study Using Information From The New E-SAR Listen Only Channel Mode Of Operation". Proceedings of USAR2000, Munich/ Germany, May 2000, pp 855-857.
- [5] S. Buckreuss and T. Sutor 1998 : "Suppression of interferences in P-band SAR data". International Radar Symposium, DGON Munich, Germany.
- [6] Ritcard T. Lord and Michael R. Inggs 1998: "Approaches for RF Interference Suppression for VHF/UHF Synthetic Aperture Radar." Proceedings IEEE South African Symposium on Communication and Signal Processing, COMSIG'98 , Cape Town, South Africa.
- [7] G. Cazzaniga, A. Monti Guarnieri 1996: "Removing interferences from P-Band airplane SAR data." Proceedings of IGARSS'96 Lincoln, Nebraska USA Vol.III. pp.460-463
- [8] A. Potsis, B. Gabler, R. Horn, K. Papathanassiou and A. Reigber: "End-To-End calibration Of Polarimetric P-Band Data of DLR Experimental SAR (E-SAR)" Proceedings of USAR2000, Munich/ Germany, May 2000, pp 855-857.
- [9] L.M.H Ulander May: 'Radar remote sensing for sea ice: Measurement and theory', Chalmers University of Technology, Goteborg, Sweden, Tech. report 212, 1991.
- [10] L.M.H Ulander: 'Accuracy of using point targets for SAR calibration', IEEE Trans. Aerospace Electron. Syst. Vol. 27, No.1, pp. 139-148, 1991.
- [11] K.P. Papathanassiou, M. Zink: *Polarimetric Calibration Of the Airborne Experimental SAR System Of DLR. Proceedings Of European Conference On Synthetic Aperture Radar*, Proceedings of EUSAR'98, Friedrichshafen, Germany, 1998.
- [12] A. Freeman, " SAR Calibration: An overview", IEEE Transactions On Geoscience and Remote Sensing, Vol 30, Nov 1992, pp 531-539.
- [13] M. Zink, R. Bamler: " X-SAR Radiometric Calibration and Data Quality", IEEE Transactions On Geoscience and Remote Sensing, Vol 33, Jul. 1995, pp 840-847.
- [14] M. Zink, D. Geudtner: "First Results from the Calibration of the interferometric X-SAR system of SRTM", Proceedings of EUSAR'2000, Munich, Germany, 2000.
- [15] S. Quegan, J. Lamont: " Ionospheric and Tropospheric effects on synthetic aperture radar performance", International Journal For Remote Sensing, no 7 1986, pp. 525-539.
- [16] Daniell, R.E., Brown, L.D., Anderson, D.N., Fox, M.W., Doherty, P.H., Decker, D.T., Sojka, J.J., Schunk, R.W., " Parameterized ionospheric model: A global ionospheric parameterization based on first principle models", Radio Sci, vol 30, 1499-1510 (1995)
- [17] Davis, K., "Ionospheric Radio Waves", Blaisdell Publishing Comp., Waltham, Massachusetts, (1969)
- [18] Ho, C.M., Wilson, B.D., Mannucci, A.J., Lindqwister, U.J., Yuan, D.N., "A comparative Study of ionospheric total electron content measurements using global ionospheric maps of GPS, TOPEX radar, and the Bent model", Radio Sci., vol 32, no 4, 1499-1512, July-Aug (1997)
- [19] Ho, C.M., Mannucci, A.J., Sparks, L., Pi, X., Lindqwister, U.J., Wilson, B.D., Iijima, B.A., Reyes, M.J., "Ionospheric total electron content perturbations monitored by the GPS global network during two northern hemisphere winter storms", J. Geophys. Res., vol 103, no A11, 26409-26420, Nov. (1998)
- [20] Iijima, B., Harris, I.L., Ho, C.M., Lindqwister, U.J., Mannucci, A.J., Pi, X., Reyes, M.J., Sparks, L., Wilson, B.D., "Automated daily process for global ionospheric total electron content maps and satellite ocean altimeter ionospheric calibration based on Global Positioning Systems data", J. Atmos. Solar-Terrestrial Physics, vol 61, 1205-1218 (1999)
- [21] Mannucci, A.J., Wilson, B.D., Edwards, C.D., "A new method for monitoring the earth's ionospheric total electron content using GPS global network", Proc. Sixth Int. Technical Meeting of the Satellite

Division of the Inst. of Navigation, Inst. Navig. Alexandria, Va., 1323–1333 (1993)

[22] Pi, X., Mannucci, A.J., U.J. Lindqwister, Ho, C.M., "Monitoring of Global Ionospheric Irregularities using the Worldwide GPS Network", *Geophys. Res. Letters*, vol. 24, no. 18, 2283–2286, Sept. 15 (1997)

[23] A. Ishimaru, Y. Kuga, J. Liu, Y. Kim, A. Freeman: "Ionospheric effects on synthetic aperture radar at 100 MHz to 2 GHz", *Radio Science*, Vol. 34, no 1, Jan–Feb 1999, pp. 257–268.

[24] A. Freeman, S. Saatchi: "The Effects of Faraday Rotation on Backscatter Signatures in SAR Image Data", *SPIE*, vol 3120, 1997 pp 37–44

[25] W.B. Gail: "Effect of Faraday Rotation on Polarimetric SAR", *IEEE Transactions On Geoscience and Remote Sensing*, Vol 34, no 1 January 1996, pp 301–307.

[26] P. Rosen, "Faraday Rotation", JPL memorandum.

[27] D.M. Vine, M. Kao: "Effects of Faraday Rotation on Microwave Remote Sensing from Space at L-band" *Proceedings of IGARSS'97 AUGUST 1997*, pp 377–379.

[28] V. Steinsheiger, A. Dzenkevich, V. Manakov, L. Melnikov, G. Mizezhnikov: "Quantative Characteristics of Two-Dimensional Adaptive Compensation for Ionospheric destructive Influence on VHF Spaceborne SAR Resolution". *Proceedings of EUSAR2000, Munich/Germany, May 2000*, pp 419–422.

[29] V. Blinov: "Preasence Refinement of Ionospheric Parameters For Function Securing Of Spaceborne VHS SAR", *Proceedings of USAR2000, Munich/Germany, May 2000*, pp 407–410 E.J. Rignot, R.

[30] R. Zimmermann, J. Van-Zyl: "Spaceborne Applications of P-band Imaging Radars for Measuring Forest Biomass" *IEEE Transactions On Geoscience and Remote Sensing*, Vol 33, no 5, 1995, pp 1162–1169.

[31] M. Chandra, D. Hounam: "Feasibility of a Spaceborne P-band SAR for Land Surface Imaging", *Proceedings of EUSAR'98, Friedrichshafen, Germany, 1998*.

[32] F.M. Seifert, P. Snoeij: "Biomass Mapping Satellite System (BioSAR)" *Proceedings of EUSAR2000, Munich/Germany, May 2000*, pp 81–84.

[33] S. Buckreuss, M. Chandra, D. Hounam: "Low Frequency SAR Criticalities", *Study for ESA-ESTEC 1997*.

The RF PRISM concept for pushing forward the antenna size barrier in space based Radar

Jean Paul AGUTTES

CNES (Centre National d'Etudes Spatiales), 31401 TOULOUSE, France.
(phone 33 5 61 27 41 28, jean-paul.aguttes@cnes.fr)

Abstract: RF PRISM is a new space antenna concept where an array is fed through a mesh of points on the antenna back face with RF signals transmitted (or received) by another satellite called illuminator and usually offset by 100 Km on the same orbit. Basically the PRISM deviates, amplifies, and beam forms the signals passing through it and travelling between the illuminator and the earth. Providing that the speed vector and the main earth viewing axis have equal incidence on antenna plane the antenna deformation control or knowledge requirement is relaxed by a factor 10. Moreover there are no longer cables between the antenna panels. RF PRISM therefore enables deployment of very large antenna in space. The illuminator satellite is not constrained by the illumination function (a few Watts and a 1m² antenna), but just by the central payload function moved away from the satellite bearing the antenna. This can be a micro-satellite.

Among others applications, this concept opens up new prospects for space-borne SAR requiring a very large antenna structure either for very low frequency (P-band), or for very high altitude (high revisit), or for single pass interferometry (two antennas). Optionally it can be combined with the SAIL that is an another concept circumventing large antenna constraints (vertical antenna with gravity stabilisation).

A short overview of the concept applied to Radar has already been presented at IGARSS 2000 (Honolulu) and published in proceeding (/2/). This papers goes more in details in term of practical implementation of the concept.

1 RF PRISM CONCEPT

1.1 Generic geometry

This concerns an active array antenna whose the signal supplying (supplied by) the radiators comes (goes) through the back of the antenna from (to) a more or less remote RF source (receiver). This type of approach as known to date is that of the RF lens and we know that this device leads to strong tolerance to deformations, provided that the antenna beam remains in a direction close to that of the illumination and that the source is sufficiently remote in relation to the antenna's dimensions. As a result, application to a large space antenna has a limited interest, as the source must be set on an extremely long mast.

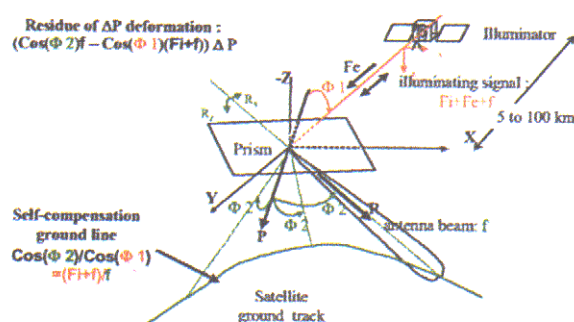


Figure 1: Generic geometry

In our study, the source is rejected far away on another satellite located on the same orbit (in front or

behind). The antenna does not work like a lens but like a prism as it achieves considerable deviation of the wave from a horizontal illumination axis to a vertical or oblique earth sighting axis. The deformation immunity is achieved when these two axis have an incidence (angle to the antenna plan vector) on the antenna plan that meet conditions detailed here after function of the frequencies used on illumination (back) side and on mission (earth) side, a particular case being the identity of the incidences.

Figure 1 shows the generic geometry. Illuminator I is located on axis -Y, the speed vector is on Y in any direction. The vector P is normal to the antenna plane. The antenna beam aims to ground a range set by the mission (vector R).

1.2 Internal and/or external frequency translation

Since the prism performs an amplification, a frequency translation in the prism is used on both transmit and receive links to earth.

The illuminating frequency is $F+f$, f is the frequency used by the mission on the earth side, F is positive or negative. In the generic case the frequency translation is the combination of two translations, one said internal using a translation tone of frequency F_i generated in the prism and an another said external using a tone of frequency F_e received from (or whose reference used for building it by multiplying is received from) the illuminator, and in that $F = F_i + F_e$. In presence of several illuminators (can occur for satcom application where a cluster of illuminators gives an equivalent

cluster of beams) only one called focus transmits the tone Fe.

1.3 Self-compensating geometry with respect to Antenna Deformations

Here we analyse the prism working on transmit path only. When $F_e = 0$, every thing applies to the receive path too as the means are reciprocal. The implementation of the external translation in receive mode is detailed in /1/. The preferred solution to get the same behaviour in receive as in transmit as is to use F_e with a negative translation (which move away from the desired frequency on the side of the prism) and to compensate that by an internal translation (or an increase of the internal translation) of value $2 |F_e|$.

We can model the antenna by a field of deformations about a mean plane (unflatness type) Δp along P. The coplanar deformations (normal to P) are by nature much less significant.

Self-compensation is obtained when, for any point of the antenna, the point projected on the wave plane normal to R sees the wave with an unchanged phase. That is when the projection of Δp on R has a phase value opposite to that of the projection of Δp on IA. For an illuminator sole or combined with the focus, the phase values of the two projections are respectively $-2\pi \Delta p \cos(\phi_2) f/C$ and $2\pi \Delta p \cos(\phi_1)(F+f)/C - 2\pi \Delta p \cos(\phi_1)F_e/C$, with ϕ_2 and ϕ_1 being respectively the incidences on the prism of R and AY. Self-compensation is obtained when: $\cos(\phi_2)/\cos(\phi_1) = (F+f)/f$.

The external translation does not play any role in the self-compensation geometry. The Earth sighting axis that meet the self-compensation condition are on a cone whose axis is normal to the prism.

The phase seen by the projection in the wave plane of any antenna point will not vary with deformation but the position of the projection in this wave plane will move. There are two cumulative shifts within the wave front plane, one related to the illumination path in $\Delta p \sin(\phi_1)$ and the other one related to the mission path in $\Delta p \sin(\phi_2)$. The validity of the concept may be affected in presence of a significant gradient for the phase and amplitude distribution within the wave plane. If this distribution is brought by the prism, only the downstream shift (at illumination side on receive path, at mission side on transmit path) counts. We will see later an option of the concept allowing for correcting theses shifts effects.

1.4 Self-compensation residue and mission field of view.

For a change $(\delta\phi_1, \delta\phi_2)$ of the geometry, the self-compensating residue is as $\Delta p (-\sin(\phi_1) (F+f) \delta\phi_1 +$

$\sin(\phi_2) \delta\phi_2 f)$. Only the second component is of interest here as it is that which results from the mission field of view requirement.

We consider a maximum residue of $0.1 \Delta p$, that is to say a reduction by 10 of the flatness requirement (from $\lambda/20$ to $\lambda/2$ for instance). For $F_i=0$, a solution can be $\phi_1 = \phi_2 = 45^\circ$ et $\delta\phi_2 = \pm 10^\circ$. For F_i positive, we can improve the mission field of view or the deformation relaxation. With $(F_i+f)/f = 5$, we have $\phi_1 = 79^\circ$, $\phi_2 = 11^\circ$ and there is not any more real limit on mission field of view for a 0.1 flatness relaxation factor. However, positive F_i made the position of self-compensation sighting more sensitive to prism attitude error.

The flatness requirement is typically relaxed from $\lambda/20$ to $\lambda/2$.

1.5 Electronic correction of deformations and attitude

If the deformation can be known or measured, the deformation residue $\Delta p (\cos(\phi_1)(F+f) - \cos(\phi_2)f)$ can be removed at the level of the antenna phase shifters. In this case the relaxation factor $(\cos(\phi_1)(F+f) - \cos(\phi_2)f)$ applies to the accuracy δp of deformation knowledge and there is not anymore requirement on flatness itself. Considering that a knowledge of $\lambda/2$ can be easily achieved, the electronic correction removes both flatness and mission field of view constraints. As an option, the measurement all along the antenna of the phase of the illumination signals provides an elegant way to determine the deformation. That enables also measurement and correction of the attitude pitch and yaw errors.

The electronic correction can also apply for the shift effects within the wave plane (see § 1.3) of the phase and amplitude distribution using the knowledge of the two components of the shift: $\Delta p \sin(\phi_1)$ et $\Delta p \sin(\phi_2)$. For that later correction, the concept provides no relaxation with respect to the case of a standard antenna. However, the shift effect correction is less exigent than the basic flatness effect correction, taking into account the low gradient of most of the distributions laws.

1.6 Geometry examples with $F_i = 0$

- Geostationary communication: We generally aim around the nadir. P vector is within the orbit plan and inclined by 45° with respect to the vertical. The deviation is simple. The relaxation factor is 10 (field of view $< \pm 10^\circ$). On both illumination and mission side the antenna area is used with an efficiency of 0.7.
- Low orbit, side looking, communication or radar: This is obtained from the previous geometry by a

roll tilt by 45° (roll field of view from 35° to 55°) since the prism working is independent of the roll position.

- SAIL (/3/,/4/) type satellite for radar or telecom on low orbit: The SAIL geometry is characterised by a vertical antenna plane (P is horizontal, orthogonal to AZ), one of its interests is the enable gravity gradient stabilisation of the antenna and therefore to ease large antenna flying. For a lateral main sighting axis inclined toward earth by 45° , as in the previous case, the self-compensation condition is obtained when P vector is deviated from the orbit plan by 55° . The wave deviation realised by the prism is combined. The efficiency for use of the surface is 0.57 both on illumination and mission side.
- Low orbit mission (radar or telecom) based on a swath mode. Similar geometry as geostationary telecom but with a field of view achieving a defiling swath. With P in the orbit plane, the cone of self-compensation sighting encounters the earth according to a line globally transverse to the satellite track. The deformation relaxation is total if the field of view is a swath that follows this line.

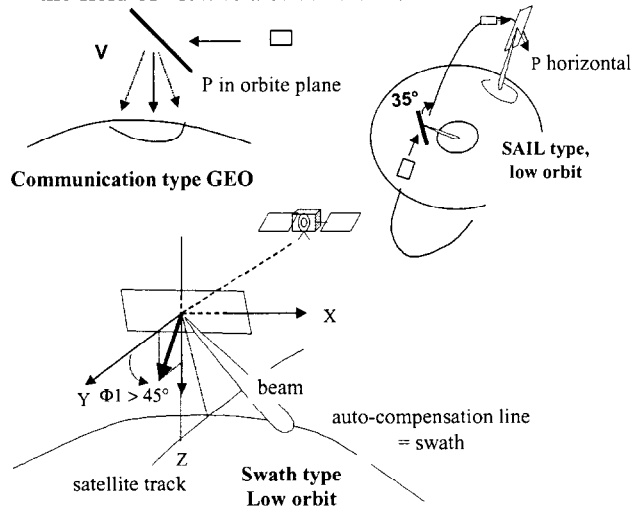


Figure 2: Geometry examples with $F_i=0$

1.7 Sampling of the coupling between prism faces

The antenna is divided into tiles containing a single coupling point between faces. This coupling point realises the frequency translation and the deviation of the wave. The later is based on a phase shifting and needs a delay line too (except in case of limited relative bandwidth). The local deformation within the tile is not compensated but the flatness control is above all a constraint at the scale of the whole antenna mainly because of the partition into deployable panels. Nevertheless, because of the overall deformation, perfectly flat tiles may deviate from the antenna main

plane and several tiles may be required per antenna panel, that depends on the deformation profile. With a deformation whose scale is the antenna dimension (wash-bowl profile, general case of thermal deformations) and the amplitude limited to $\lambda/2$, a single tile per panel is sufficient provided that there are at least 10 tiles in each dimension. (see figure 3)

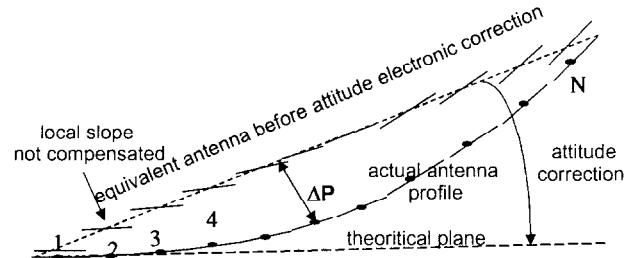


Figure 3: Local scale errors not compensated

If we know the deformation, the tile miss-alignments with respect to the main antenna plane can be corrected at the level of the phase shifters of the array antenna and the tile sampling can be relaxed or the deformation scale reduced. However, for these local corrections within the tiles, we do not benefit from the relaxation in term of knowledge accuracy as we do for the correction between tiles (cf §1.5). That is of little relevance since the knowledge is always much better locally as soon as a deformation model, even simple, is used (whether or not the knowledge relies also on measurements).

A cluster of illuminators gives a cluster of beams. With several illuminators the aperture of the cluster of beams also drives the sampling in order to limit the grating lobes. A $7\lambda \times 7\lambda$ effective (as seen once projected in the wave plane) sampling enables a 2° cluster aperture ($/1/$).

2 PRISM OPERATION IN PRESENCE OF ERRORS (ATTITUDE, ILLUMINATOR POSITION, , FREQUENCY) OR MULTIPLE ILLUMINATORS

2.1 Prism modelling as a modified lens

Let us refer to the projection of the prism on planes orthogonal to AY and R respectively as the equivalent rear and front faces of the prism. Generally, these transforms from the real faces to the equivalent ones do conserve neither length nor angle. In a simple deviation prism case, a line of the real face orthogonal to the plane (AY,P,R) is kept orthogonal to this plane with no length change. The other line of the real face orthogonal to the first one has got its transforms orthogonal to those of the first line but there is a ratio $\cos(\phi_1)/\cos(\phi_2)$ between the front and the rear transforms.

The prism's basic role can be decomposed as follows, no matter the order of the operations:

- Translation F_i with the same phase for all the points of one of the two equivalent faces. In reality, that translation is applied on the real face with addition of a delay or phase profile on the antenna as an inclined plane
- Translation F_e at the level of the equivalent or of the real rear face with the phase according which the translation signal is received on that real or equivalent rear face.
- Linking each point of an equivalent face to the corresponding one of the other equivalent face with a delay identical for all the point couples. In reality, the delay is applied on the real face according to a profile as an inclined plane.

2.2 Illuminator Deviation and Multi-illuminator Operation

It can be shown (/1/) that the prism works as a lens whose the illuminator would be located in a deviation frame R_xR_z (see figure 1) derived from the actual deviation frame XIZ by the same transformation as those which applies between the equivalent rear and front faces, followed by an amplification/reduction as $(F_i+f)/f$ for what is related to the deviation of the focus with respect AY axis and as $(F_i+F_e+f)/f$ for what is related to the deviation of the illuminator with respect to the focus.

2.3 Behaviour with Respect to Prism Attitude

A change in attitude of the prism combines two effects as far as the position on the beam footprint is concerned, with the effect induced by the movement of the illuminator in a reference system related to the prism and the direct effect (the only one for a conventional antenna) of the movement of the reference system. From what is said earlier, the induced effect related to any illuminator if $F_e = 0$ or to the focus is scaled by the actual motion of that illuminator in the prism frame, that is to say by the direct effect, and by the ratio $(F_i+f)/f$. For great value of $(F_i+f)/f$, the attitude sensitivity is therefore increased.

The roll effect of a prism remains unchanged as compared with a standard antenna. Only the direct effect applies since the illumination is invariant with roll. If the prism is in self-compensation geometry, an attitude error around an axis contained in the prism and orthogonal to roll axis has no effect since it can be considered as a deformation transverse to the prism plane. The induced effect scaled by $(F_i+f)/f$ impacts only for attitude error component orthogonal to the two

previous, that is to say on yaw for a satcom type prism, or on pitch for Sail type prism.

2.4 Effect of frequency unstabilities and of the $\Delta f/f$

In absence of F_i , the deviation between different illuminators or between an illuminator and the focus is affected by the f variation on account of the transfer function of the deviations as $(F+f)/f$. For $\Delta f/f$ of few % and a total cluster beam aperture of 2° , the impact is kept limited. In the case of a single illuminator located near the focus (if any), there is no sensitivity to $\Delta f/f$.

F_i instability adds an offset of the whole beam cluster, however it depends on F_i value and can be avoided by using a delay ramp rather than a phase ramp for the application of F_i on the real face (see § 2.1).

See /1/ for more details.

3 ANTENNA ARCHITECTURE

The prism antenna is a signal deviator. Mission related beam scanning is added on around a fixed base deviation. Deviation of the base must be obtained in principle by a delay (except in the case with a low relative band where phase shift is adequate for the entire deviation introduced at each point between the rear side and the front side. The delay function aims, by completing the geometrical delay already existing between two corresponding points of the front and rear equivalent sides, at make the total delay constant for all the couples of points. The delay function is the opposite of the geometrical delay, it is two-dimensional for a combined deviation. As the delay values are of the order of the antenna dimensions, we need to sample this function broadly to reduce the number of delays so as to be able to introduce them in the inside of the antenna. The antenna is divided into tiles containing a single coupling point. The deformations are not compensated for inside the tiles. However, this does not detract from the advantage of the concept, as stiffness is above all difficult to maintain on large dimensions (see §1.7)

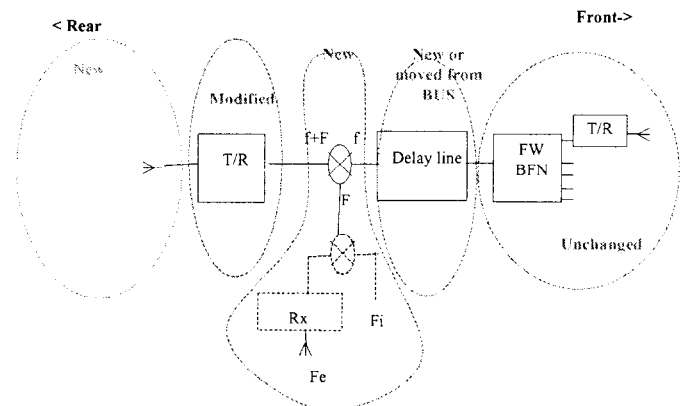


Figure 4: Tile RF Architecture

Figure 4 shows the architecture inside a tile. The tile can be seen as a tile of standard active antenna with added components.

The part forward of the delay remains unchanged as compared with a current array antenna (which also needs fixed and tunable delays but that we can leave in the platform). The beam forming network (BFN) is not made of equal length branches since it must reproduce the portion of the delay function seen in the tile. It can be shown (/1/) that the rear radiator can be very small ($1,4 \lambda_{F+f}$ per $1,4 \lambda_{F+f}$) and that the whole rear antenna is very lacunary. The rear BFN can be avoided or considered as an integral part of the rear radiating element. It is possible to keep the rear side available for possible heat protections or stiffeners as is usually the case. The Rear amplification / reception involves very low power levels (0.5 W, /1/) and can thus be seen as a modification of primary amplification/reception as found in standard active array antennas to relay signals from or to the platform.

We can conclude that:

- Putting aside the frequency translation, the only significant difference as compared with a conventional architecture is the introduction of a fixed delay inside the tile. The variable delay for which the need and the sizing remains unchanged (depending on the bandwidth and the mission off-steering around the base deviation) must also be in the tile here.
- In the case where the tile is the panel to be deployed, the fixed delay introduces no additional constraint, indeed rather the opposite in that it replaces the RF transmission/reception cable connecting the panel to the platform which makes for greater overall length and complicates deployment.

The principle must be applied with discernment in order to gain the maximum advantage. For example, in the case of an antenna with an elongated shape, we shall seek to compensate for deformations on the length only, all the more as the latter corresponds to the axis of deployment resulting in the main mode of deformation.

4 APPLICATION TO SAR

4.1 SAR prism geometry

The P vector of a space-borne SAR antenna is usually orthogonal to the speed vector V and tilted toward earth. As shown by Figure 5, a SAR prism is achieved by a second antenna tilt either on pitch or on yaw to enable the illumination, the SAR sighting range (vector R) being kept unchanged and orthogonal to V.

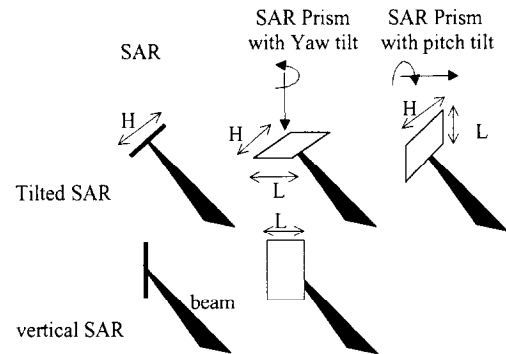


Figure 5: SAR prism as seen from the illuminator

In the case of the Vertical/ Sail Prism (see 1.6) the illumination with a yaw tilt keeps intact the other vertical or SAIL advantages. With $F_i=0$, the yaw tilt is limited (35°) and it is still possible to have solar cells on the back of the antenna on a dawn dusk orbit and to keep there another advantage of the SAIL concept (no need of solar array)

External translation is not necessary ($F_e=0$) in Radar since a single illuminator is generally used. A great F_i value reduces the illumination tilt and improves the deformation immunity or the field of view (see §1.4).

4.2 Fully self-compensated system

The Prism concept allows compensation or correction of all the deformations and attitude errors except the roll axis attitude. However the latter is the one that is the easiest to measure and to correct by the radar itself using the fact that the image radiometry is attached to the attitude and that the image geometry is not.

4.3 Radar Timing constraints

For radar, echo reception must occur outside transmissions. If the same illuminating frequency is used on transmit and receive, this timing condition must be verified both for the antenna and the illuminator. If that case the distance between the two satellites must be locked on a multiple of the ambiguity. A control error $\pm \delta d$ of that distance affects by $\pm 2\delta d/C$ the position of the echo in the timing diagram of illuminator. Transmit and receive are still separated at the illuminator level if the timing control considers that the echo at the level of the prism is virtually enlarged on each side by the value $2\delta d/C$ or that the swath is virtually enlarged of

$2 \delta d / \sin(i)$. This virtual swath enlargement applies only for the timing (not at all for ambiguity or any other swath related constraint) and affects the required range of relative tuning of the PRF on a one per one base (at least). Therefore, considering as worse case a mission with a 10 km swath at 30° incidence, a

doubling of the relative PRF tuning range enables a tolerance in inter-distance of $\pm 10 \sin(i)/2 = \pm 2.5$ km. For a mission of much larger swath this constraint is relaxed accordingly.

The constraints related to second F_i frequency have to be traded against those of the distance control.

5 P BAND SAR ($\lambda = 75$ CM)

5.1 Deployment of a very large antenna

The large antenna area is the main design constraint of a P band SAR satellite. At least 50 m^2 should be provided to enable significant incidence domain and revisit performance.

The Prism approach roughly removes all the flatness constraint. Indeed, the deformation constraint can be relaxed up to $\pm 37 \text{ cm}$ ($\lambda/2$). The constraint can even be totally freed since the poor deformation knowledge accuracy ($\pm 37 \text{ cm}$) required for the electronic correction can be obtained intrinsically or via rudimentary devices (angular coders at hinges for example). The $\pm 37 \text{ cm}$ control or knowledge envelop does not include the attitude error whose electronic correction (see § 1.5) needs phase measurement on only three or four distant points of the antenna.

Without flatness constraint the large antenna can be obtained with inflated structure or by rigid panels deployed with rudimentary mechanisms (eg: shape memory). Two other Prism advantages particularly ease the deployment of a large antenna: 1) There is not any more RF cable to circulate along the antenna. 2) The antenna can be made of several leaves not fully attached each other, which eases two-dimensional deployment as shown by figure 6.

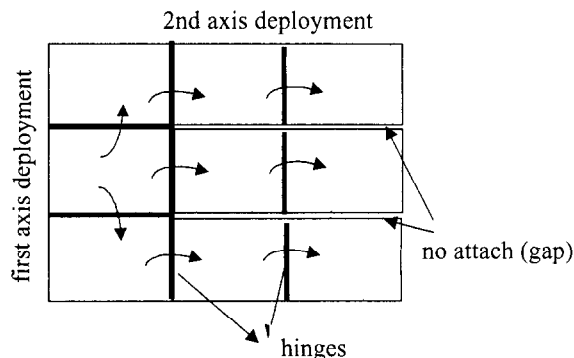


Figure 6: Two-dimensions deployment

5.2 Design options

Antenna folding and deployment are not the only satellite design constraints. The antenna has to be powered and attitude controlled. A SAIL type prism is advantageous from these view points but it may induce a significant extra antenna area if highest incidence is smaller than 55° and it does not fit well long antenna

and consequently large swath ($>50 \text{ Km}$). A tilted prism may optimise the antenna area but the attitude control (and stability) becomes a major concern. Indeed, such a large body in space is exposed to a significant gravity gradient torque and has low structural stiffness. The torque is the key sizing factor of the attitude control system in the tilted case whereas it does naturally most of the control job in the Sail case. The stiffness has to be kept compatible with the control system, which is much more difficult in tilted case as that control system is much more active. In tilted case, the limitation of the gravity torque leads to a long antenna (for a given antenna area) and to an illumination with yaw tilt.

6 SINGLE PASS INTERFEROMETRY (X BAND)

A straightforward way to exploit prism for single pass interferometry is to have the base and the two antennas within a common plane. Doing so, the single pass interferometry is mainly a matter of deployment and orbiting of a large planar structure, as for P band. There are however major differences. The frequency is at the other edge of the spectrum (X or Ku) because of the need to limit the base length. Consequently electronic correction should be implemented in order to relax the deformation control beyond the basic $\lambda/2$ (1.5 cm in X band) allowance offered by the self-compensation. The two antennas must use a distinct F_i translation in order to separate the two receive channels. The two antennas should be identical in order to enable the ping-pong mode (alternate pulse transmit on each antenna) which doubles the effective double length size.

The antenna is rather short with respect to the base, which enables the Sail Prism option. In Sail case the roll is cyclic at twice the orbit period, few interferometry images per orbit taken on flat areas (sea) enable a retrieval of the roll error.

However, the knowledge attitude accuracy may be insufficient for absolute DEM, moreover the system does not control or compensate the baseline length. The system can be focused on accurate relative DEM as, on account of the reduction of size constraints, the two X antenna can be large and the phase noise very small (good SNR and ambiguity protection).

7 A COMPOSITE RADAR MISSION: MULTIFREQUENCY, P BAND, X BAND INTERFEROMETRY.

We consider a planar structure terminated by two X band antenna (for interferometry purpose) with all the others other antenna panels employed for other radar mission, and possibly P band. The figure 7 gives a possible scenario X+P using the SAIL concept.

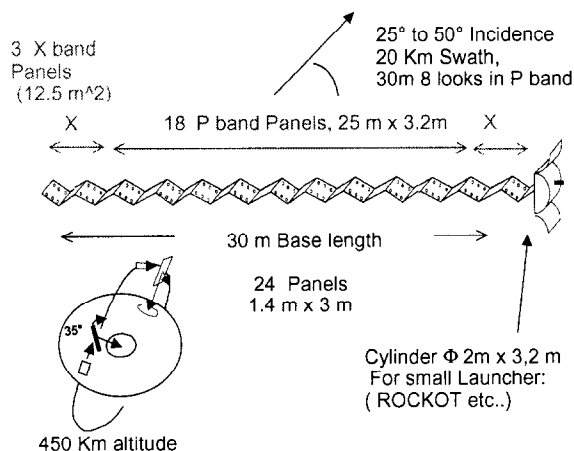


figure 7: Composite Radar Prism mission example

8 CONCLUSION

The RF Prism concept opens up new prospects for large antenna, particularly for two exciting SAR applications: P band and single pass interferometry. More work should be needed to get a full understanding of the opportunities offered by this concept in space based radar.

REFERENCES

- /1/ Satellite Prisme RF et son compagnon illuminateur (J.P. AGUTTES), Patent pending FR 99 08223- June 28
- /2/ The RF prism concept and its application to large antenna SAR satellite (J.P. AGUTTES), proceedings of IGARSS 2000, 24-28 July 2000, Honolulu)
- /3/ RADAR "SAIL" satellite concept and design, (J.P. AGUTTES. and All) ACTA ASTRONAUTICA Volume 46, N° 9, pages 565-576, 2000
- /4/ A radically new design of SAR satellite: the short vertical antenna approach, (J.P. AGUTTES), IEEE Transactions on Aerospace and Electronics Systems, in press.

Computer Simulations of Canada's RADARSAT2 GMTI

Shen Chiu and Chuck Livingstone

Space Systems and Technology Section, Defence Research Establishment Ottawa
3701 Carling Avenue, Ottawa, Ontario, Canada K1A 0Z4

Tony Knight and Ishuwa Sikaneta

MacDonald, Dettwiler and Associates Ltd.
13800 Commerce Parkway, Richmond, B.C., Canada V6V 2J3

Abstract

Canada's RADARSAT2 commercial SAR satellite will have an experimental operating mode that will allow ground moving target indication (GMTI) measurements to be made with received data. This mode is also called MODEX (Moving Object Detection Experiment). In the GMTI or MODEX mode of operation, the spacecraft's radar antenna is partitioned into two apertures that sequentially observe the scene of interest from the same points in space. Data is simultaneously and coherently received from both apertures and is down-linked in parallel channels for processing to extract moving target radial speeds in their SAR image context. This paper provides an analysis of SAR-GMTI performance based on computer modeling and simulations. Two SAR-MTI processing approaches are being explored. One utilizes the classical DPCA clutter cancellation technique to provide sub-clutter visibility for dim slowly moving targets. The other is based on the along-track (temporal) SAR interferometer technique, where amplitude and phase information of the slow-moving targets are exploited to extract them from the dominant clutter background. Performances of the two approaches are compared.

1.0 Introduction

A space based radar (SBR), operating at 800 km altitude, has an orbital speed of approximately 7.5 km/s. Under the RADARSAT2 antenna design constraints (this is a synthetic aperture radar satellite), acceptable range and azimuth ambiguity levels can be achieved for the two GMTI apertures at pulse repetition frequencies (PRFs) in the vicinity of 2000 Hz, for terrain grazing angles between 80° and 40° . The radar design allows PRFs up to 3800 Hz to be selected by accepting ambiguity level and swath width trade-offs. The available PRF and grazing angle ranges result in the majority of the received signal spectrum being occupied by strong clutter returns from the "stationary" terrain. Since the radar is fundamentally a SAR, there is no azimuth beam steering capability that would allow the radar beam to dwell on a point on the earth's surface more than the synthetic aperture time. Single channel GMTI measurements, based on the extraction of the target Doppler spectrum are severely constrained to large cross section, rapidly moving targets whose motion has a large radial component.

The detection probability and the estimation accuracy can be increased considerably by use of multiple aperture antennas. Space-time adaptive processing (STAP) techniques can be used to provide sub-clutter visibility for dim slowly moving targets. The displaced phase center antenna (DPCA) technique, which is a form of STAP, is well suited for SBR. This technique requires at least two antenna phase centers be arranged along the flight direction, each with its own dedicated receiver channel. The phase centers of the two sub-apertures are displaced physically in such a way that a pair of pulses from the two receivers appear to be generated from a stationary radar when an appropriate sampling rate (i.e. the PRF) is chosen. Since the clutter Doppler frequency from a stationary radar is concentrated at dc, a conventional MTI canceller can be used to null the background clutter. This is the classical DPCA two phase center clutter suppression technique. In this approach, the received signals from channels 1 and 2 are time shifted to register them spatially, then subtracted to cancel the background clutter. Target enhancement is limited by the noise floor and phase noise of the radar, by scene phase noise and by target fading.

This paper reports on a preliminary investigation of the GMTI performance of two SAR-MTI processors developed by the authors for RADARSAT2. The two SAR-MTI processing architectures are introduced in Sec. 2.0. This is followed by a discussion of the newly proposed RADARSAT2 GMTI mode in Sec. 3.0, including its sensor configuration and parameters. Sec. 4.0 looks at the SBR MTI simulation tool used to simulate realistic radar signals and Sec. 5.0 defines the experimental scenario to be used for this study. Simulation results are then presented in Sec. 6.0. This is followed by a discussion of some experimental airborne data and GMTI results in Sec. 7.0. The two GMTI approaches are then analyzed and compared in Sec. 8.0. Finally, Sec. 9.0 provides some conclusions. The results presented in this paper are based on the analysis of a single case.

2.0 MTI Processors

Three types of MTI processing are being considered for RADARSAT2 MODEX mode: SAR displaced phase center antenna (DPCA) processing, along-track interferometry (ATI), and space-time adaptive processing (STAP). In this investigation we will only consider the first two processors.

The proposed GMTI processors for RADARSAT2 MODEX are shown in Fig. 1. The first MTI processor, which we shall call the SAR/DPCA processor, is the limiting case of the two-beam DPCA clutter canceller. The pulses from the leading antenna are delayed by T , the integral pulse number needed to effectuate the DPCA condition. SAR processing is then performed on each channel. The outputs of the SAR modules are subsequently subtracted to yield a GMTI image. The stationary clutter signals are suppressed, and only signals from moving targets with sufficient radial velocity remain.

In true classical DPCA, target detection would be performed on the raw difference data. Performance may be improved by taking advantage of the SAR capability of the system and performing SAR processing on the difference data prior to detection. Due to theoretically perfect clutter cancellation of DPCA, any remaining targets in the image will correspond to moving targets. Since SAR processing is a linear operation, the SAR processing on the difference data is equivalent to performing SAR processing on the two apertures separately, and then taking their difference. The utilization of the SAR/DPCA technique to provide SAR and MTI simultaneously has also been discussed by other authors [1, 2].

In a similar way to classical DPCA, ATI uses two-displaced phase centers aligned along-track. Instead of taking the difference of the two channels, the interferometric phase is computed. This is done, as in other types of interferometry, by generating SAR images for each channel separately, and then estimating the interferometric phase by computing the phase (i.e., the complex argument) of the product of one image with the complex conjugate of the other (see Fig. 1b). The remaining phase is zero for stationary objects and non-zero otherwise. The application of the ATI technique to GMTI have also been discussed by other investigators [3, 4].

3.0 RADARSAT2 GMTI

At present time, no spaceborne radar system has a GMTI capability. Although all of the processes needed for full function GMTI have been developed for airborne systems, differences in platform velocity, range

to target, and accessible depression angles between airborne and spaceborne radars result in several unknown parameters for the optimization of spaceborne GMTI sensors. Cost, complexity, available technology, and design risk have all combined to preclude the construction and launch of a full-function space-based GMTI radar.

When the detailed properties of GMTI and SAR systems are examined, a restricted set of GMTI functions can be added as operating modes to an appropriately designed SAR with little impact on the radar design. The RADARSAT2 MODEX is thus the world's first attempt to implement such a limited-function GMTI aboard a commercial SAR satellite. Although the subset of possible GMTI operating modes available from a radar of this type is small, such a radar could be used to validate GMTI parameters and algorithms needed for more sophisticated radars.

RADARSAT2 is currently under development and is scheduled for launch in early 2003. Preliminary information on the RADARSAT2 MODEX configuration can be found in references [5, 6]. Table 1 lists some of the SAR-MTI sensor characteristics and design parameters.

Table 1: RADARSAT2 SAR-MTI Parameters

Parameter	Value
Orbit Description:	
Type	Circular
Inclination	98.6°
Altitude A	800 km
Active Array:	
Length × Width	15 m × 1.5 m
Number of sub-apertures	2
Orientation	Long-axis forward, Elevation boresight ±29.5° (selectable)
Look Geometry:	
Nominal Incidence Angle	10° to 60°
Search Type	Strip-map
Swath Size	150 km to 25 km
Azimuth Beam Width	Programmable from 0.21° to 0.63°
Detection Cell Size	Programmable from 25m×25m to 3m×3m
Waveform:	
Band	5.405 GHz
Bandwidth	10 to 100 MHz
Peak Power	2.4 kW (42 μs pulse)
	3.7 kW (21 μs pulse)
Duty Ratio	10 %
PRF	1300 to 3800 Hz
Burst Length	up to 500 ms
Receiver Noise Temperature:	695 K

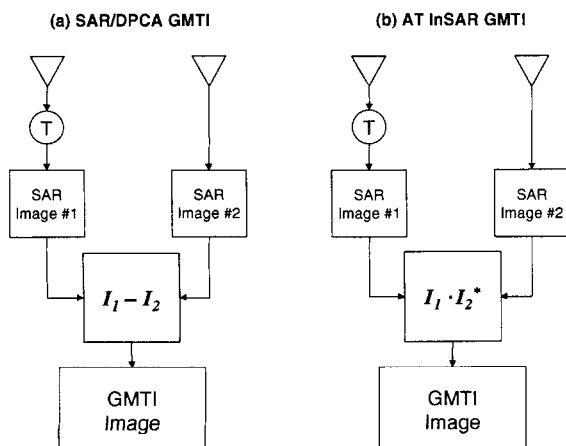


Fig. 1 Two simple SAR-MTI processors: (a) SAR/DPCA GMTI and (b) Along-Track InSAR GMTI.

Detection cell sizes are based on RADARSAT2's standard beams and the new ultrafine beam that operates at 100 MHz bandwidth to produce 3m×3m image resolution cells. The RADARSAT2 antenna looks broadside to track. While this limits the capability to dwell on an area of interest for theater defence applications, it should be well-suited as an experimental SAR-GMTI sensor, providing very useful real data.

The proposed "dual-receive" mode uses the full antenna on transmit, while the antenna is divided into forward and aft apertures on receive. The one-way phase center separation can be controlled by the number of columns used for receiving, but have a nominal value of 7.5 m. An "alternating-transmit mode" has also been considered, where pulses would be alternately transmitted from each aperture of the antenna. This mode would give a larger two-way phase center separation than the dual-receive mode. However, only the first "dual-receive" mode will be considered in this study.

4.0 SBR MTI Simulator

The simulation results described in the next section were obtained using a sophisticated space-based MTI radar simulator known as the SBRMTISIM, developed by Sicom Systems Ltd. for DND. The simulator provides an Environment Window showing a world map overlaid with the satellite ground track. The user can specify the look-geometry and define clutter regions and targets to create a scenario (see Fig. 2). Clutter is modeled as a set of regularly distributed scatterers with user specified cross-section, statistics and internal motion, and targets are modeled as point scatterers with user specified cross-section and fading statistics. Other windows are used to specify the radar and antenna parameters, and other parameters needed to characterize the system. Once the parameters are specified, the simulator generates high-fidelity, complex baseband signals representing the received signals for the SBR. The complete, two-way path of the signal is modeled from the transmitter, to the earth, and back to the receivers.

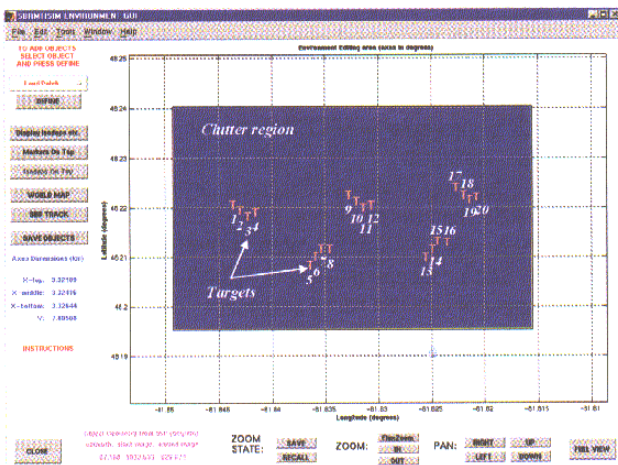


Fig. 2 SBRMTISIM Environment Window

The simulator then passes the generated data to a customized, built-in processing module, in which the architecture and algorithms are specified by the user. One of the processor options is the SAR/DPCA architecture as illustrated in Fig. 1a. The ATI processor option (Fig. 1b) has also been implemented, and a constant false-alarm rate (CFAR) detector suitable for the ATI processed signal output is currently under development. Some preliminary results are presented in Sec. 6.0.

5.0 Experimental Definition

One of RADARSAT2's beams known as a Wide Mode Beam provides swaths in the 120 km to 170 km range with multi-look ground image resolutions of about 25 m × 25 m. This mode is expected to be useful for GMTI surveillance for large strong targets [5]. In this paper, only the wide-mode beam is investigated for predicting the GMTI performance of RADARSAT2.

A carefully designed scene is created using the Environment Window (Fig. 2). A range swath of 1500 m was generated, which contains a 2.5 km × 5.0 m land-clutter patch with a reflectivity of $-10 \text{ dB m}^2/\text{m}^2$ and a spectral width of 0.1 m/s. The clutter amplitudes are Rayleigh distributed. The same target and clutter scenario is used for both SAR/DPCA and ATI processing architectures.

A total of 20 targets occupy the clutter region (Fig. 2), with key target parameters summarized in Table 2. The targets cover a typical range of radial speeds and target radar cross-sections.

Table 2: Target Parameters

Target Number	RCS (m^2)	Speed (m/s)
1	45	15 (east)
2	45	10 (east)
3	45	5 (east)
4	45	3 (east)
5	40	15 (west)
6	40	10 (west)
7	40	5 (west)
8	40	3 (west)
9	35	15 (east)
10	35	10 (east)
11	35	5 (east)
12	35	3 (east)
13	30	15 (west)
14	30	10 (west)
15	30	5 (west)
16	30	3 (west)
17	20	15 (east)
18	20	10 (east)
19	20	5 (east)
20	20	3 (east)

The satellite heading is approximately north with the right-looking geometry. The targets are heading either east or west; as a result, the moving targets have significant radial components toward or away from radar.

A waveform with a PRF of 1988 Hz is used, which provides the necessary DPCA condition for clutter cancellation. This PRF generates 750 ms of data for each of the two 7.5 m receive sub-apertures.

6.0 Simulation Results

The first test case is one where the 20 moving targets were present with both the land clutter and the thermal noise removed from the scene. The generated raw signal data were put through the SAR/DPCA processor and the targets were detected using a cell-averaging CFAR detector to produce a MTI image as shown in Fig. 3. As expected, the MTI image is very clean with no noise- or clutter-contributed false alarms. All 20 targets were detected irrespective of their RCS or speed. The positions of these targets were shifted in azimuth according to their respective radial speed. The targets-only MTI image serves as the reference for the subsequent full scenario simulation.

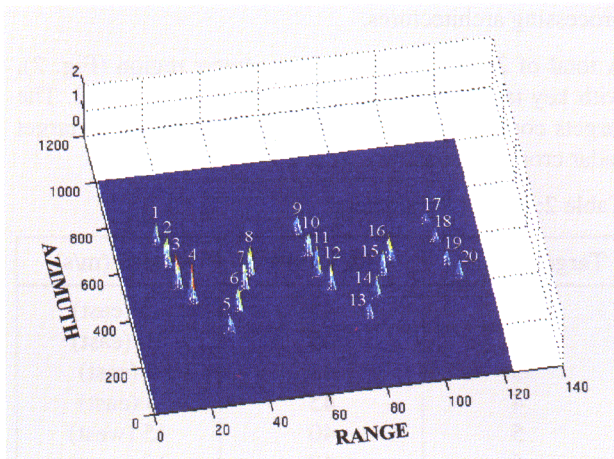


Fig. 3 MTI image of 20 moving targets without the land clutter and the thermal noise.

Next, a scenario with targets, clutter and thermal noise signals were generated. Each channel's signal data were SAR-processed separately to produce two SAR images. Fig. 4 shows the SAR image from channel 1. Most targets are below the background clutter, and no moving targets are detectable. This is expected since the brightest target in the scene has a signal-to-clutter ratio

(SCR) of only about 1.2 dB. Plotting the same SAR signal in the complex plane as shown in Fig. 5, one sees that the targets are completely buried in this clutter "noise ball," making the target detection virtually impossible.

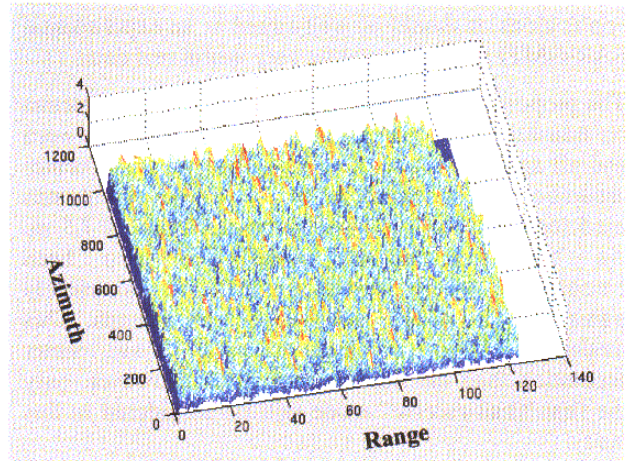


Fig. 4 Signals from channel 1 after SAR processing.

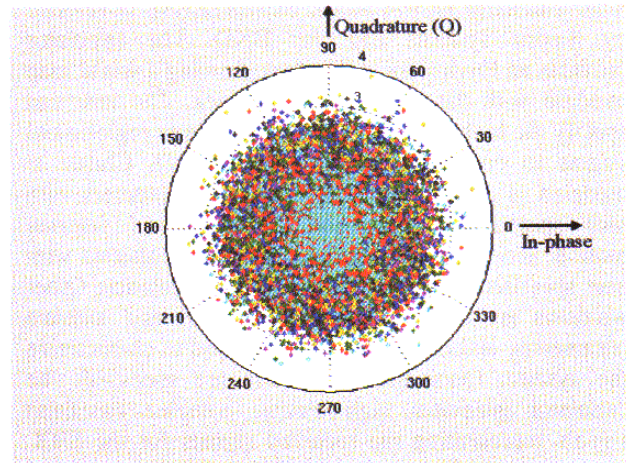


Fig. 5 Complex-plane plot of Channel 1 SAR signal.

Continuing with the signal processing chain, as depicted in Fig. 1a, the SAR signal of channel 1 is time shifted by an inter-pulse period T and then subtracted from channel 2 to produce a MTI image. As can be seen in Fig. 6, the stationary clutter signals are suppressed or whitened, leaving only the signals from the moving targets and the noise floor. The I-Q plot of the SAR/DPCA output signal is also shown in Fig. 7. The coherent clutter signal is clearly suppressed with most of the targets above the noise level.

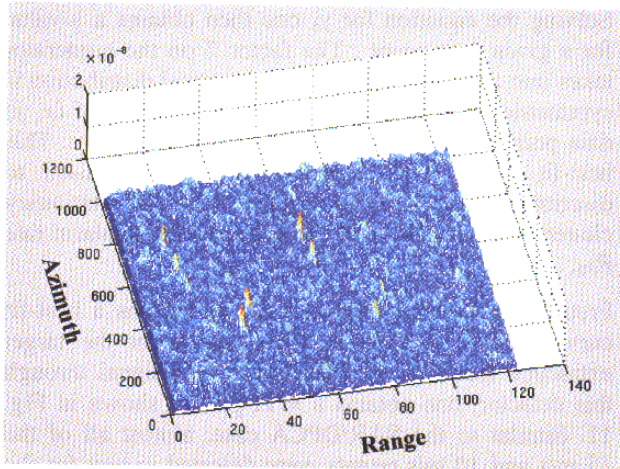


Fig. 6 Output signal from the SAR/DPCA processor, with clutter signal reduced to the noise level and some moving target signals clearly visible.

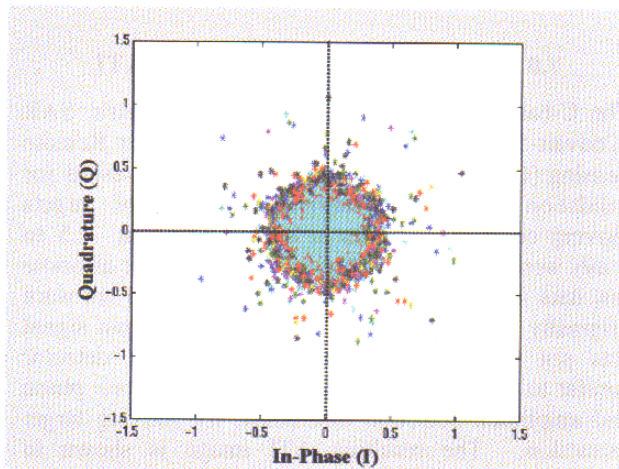


Fig. 7 I-Q complex plane plot of SAR/DPCA output signal. Dots lying outside the noise “ball” are the moving target signals.

Putting the SAR/DPCA signal through a CFAR detector, one obtains a MTI plot as shown in Fig. 8. In this case, almost all of the 15 m/s and 10 m/s targets were detected except for the 20 m² RCS target #17. However, all the 3 m/s targets were missed and only two of the five 5 m/s targets were detected. This is expected since the magnitude of the SAR/DPCA output signal or the “difference vector” is of the form $\sin(x/2)$, where x is directly proportional to the target radial velocity. Thus, slow-moving targets are attenuated or suppressed along with the stationary clutter. In this test, three of the four 20 m² targets were missed, indicating that long integration times provided by SAR are necessary for smaller targets and that MTI is also needed if reliable detection is to be achieved in clutter.

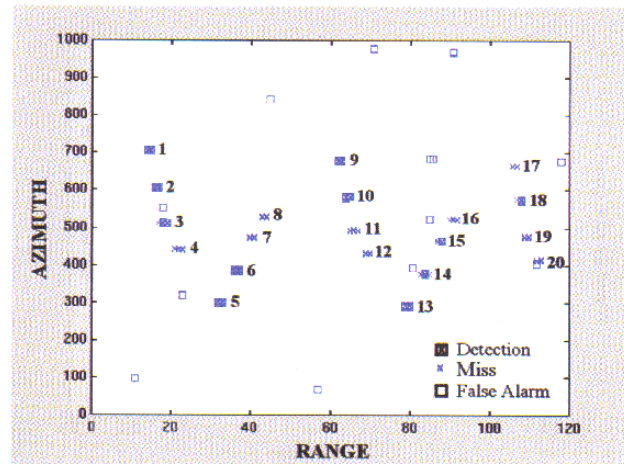


Fig. 8 Output of CFAR detector.

With the ATI processing architecture (Fig. 1b) the SAR signal from channel 1 is time shifted by an inter-pulse period T and then multiplied with the conjugate of the SAR signal of channel 2 to produce an interferometric SAR image. The I-Q plot of this ATI image signal is shown in Fig. 9. The clutter-signal phase is “cancelled” giving a mean zero phase. The phase spread of the main lobe clutter around the x-axis (or in-phase axis) is due to the thermal noise, the phase noise, and other noises of the system. Moving targets with finite radial velocities appear in the figure as vectors with non-zero phases. It is clear from the plot that those moving target vectors that reside outside the main clutter region can be detected using a suitably devised detection scheme. Here we would like to suggest a simple method based on empirically fitting a set of I-Q points derived from Q-component distributions of the signal data.

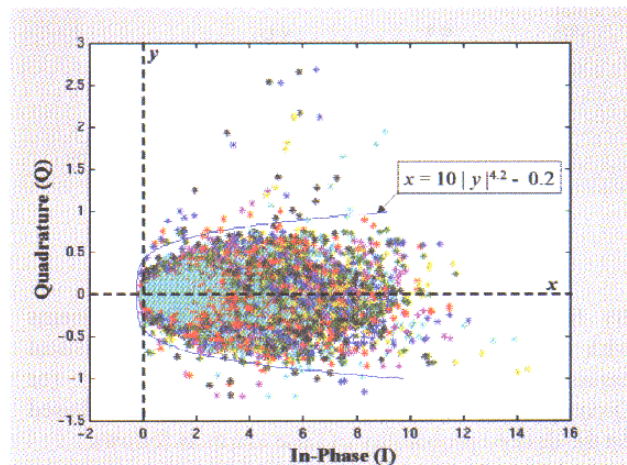


Fig. 9 Output signal from ATI processor, with clutter phases center around zero and moving target phases at non-zero values.

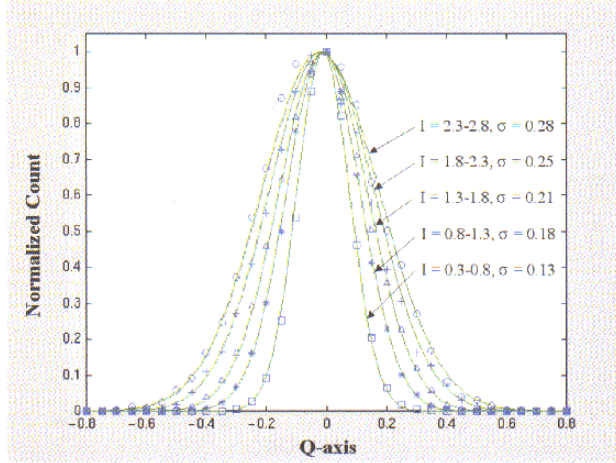


Fig. 10 Q-component distributions at different I-component range intervals.

We first proceed by dividing the x -axis into equally spaced segments and then plot the Q-component distribution of each of these segments as shown in Fig. 11. We found that the Q-component of the clutter has a Gaussian distribution. This may be expected since if the thermal noise is dominant noise component contributing to the main lobe clutter scatter and since the thermal noise is normally distributed in magnitude, we would expect also a normally distributed Q-component.

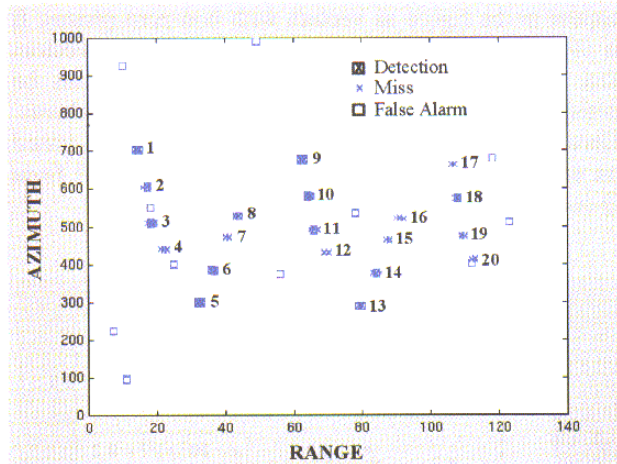


Fig. 11 Output of “ $10 \cdot |y|^{4.2} - 0.2$ ” detector

By fitting these normally distributed Q-components with best normal curves and deriving their statistical parameters, we can then calculate the y (or Q-component) values for each of the x segments based on the desired probability of false alarm as follows:

$$P_{FA} = \frac{2 \cdot \int_{y=y_0}^{y=+\infty} e^{-\frac{y^2}{\sigma^2}} dy}{\int_{y=-\infty}^{y=+\infty} e^{-\frac{y^2}{\sigma^2}} dy}$$

Solving the equation for y_0 , one then obtains a y -value for a given x segment. The factor 2 on the numerator takes into account the fact that the normal distribution is symmetric. The above procedure yields a set of (x, y) data points to which one can fit a $x = F(y)$ curve. This best-fit curve is the detector that can be used to discriminate the moving targets from the stationary clutter and that will yield the specified false alarm rate P_{FA} .

Proceeding with curving fitting, one obtains a best-fit curve “ $10 \cdot |y|^{4.2} - 0.2$ ” as the detector for the target extraction (see Fig. 9). Putting the ATI signal through this detector, one obtains a MTI plot as shown in Fig. 11. Similar to the SAR/DPCA case, almost all of the 15 m/s and 10 m/s targets were detected except for the 20 m² RCS target #17. All the 3 m/s targets were missed except for target #8 and only two of the five 5 m/s targets were detected. All of the 20 m² RCS targets were missed except for target #18, suggesting that detection is noise-limited.

7.0 Comparison of SAR/DPCA and ATI

The C-band airborne along-track interferometric SAR (Convair-580) operated by Canada Center for Remote Sensing (CCRS) was used to produce GMTI results for validation of the simulations. Two control targets moving on railway tracks at speeds of about 2.5 to 6 m/s were used in this set of experiments. The airborne raw data was processed using a modified ATI software originally developed by CCRS. The ATI output signal was put through a simple phase-amplitude detector similar to the one described above, with separate phase and amplitude detection thresholds, for moving target extraction. The resulting ATI image is shown in Fig. 12. As can be seen, the two control targets in the scene were both detected. They are also displaced in azimuth. A few vehicles on a highway and roads were also detected, also displaced in azimuth from their true positions on the highway or the roads.

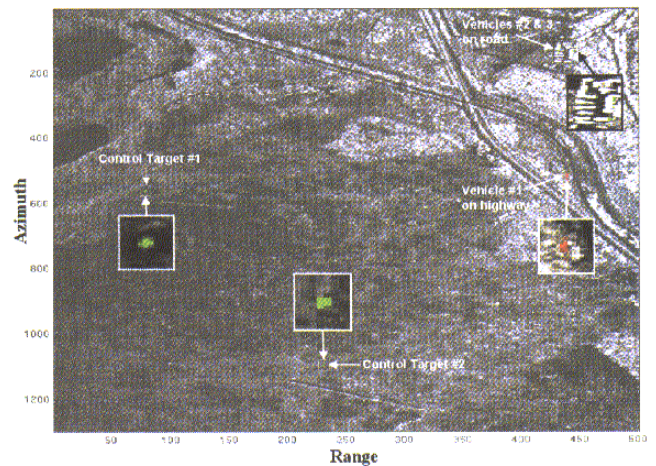


Fig. 12 ATI image showing moving targets being detected using a simple phase amplitude threshold detector.

The ATI output signal is plotted in a I-Q plot in Fig. 13. The phase-amplitude threshold detector, which has a key-hole shape in the complex signal plane, is also shown. This detector allows a moving target with phase and amplitude above certain threshold values to be declared as a detection. The amplitude threshold is necessary to minimize the noise contribution to false alarms. In this case, the two control moving targets in the scene are outside the main clutter region and are easily detected using this simple “key-hole” detection technique.

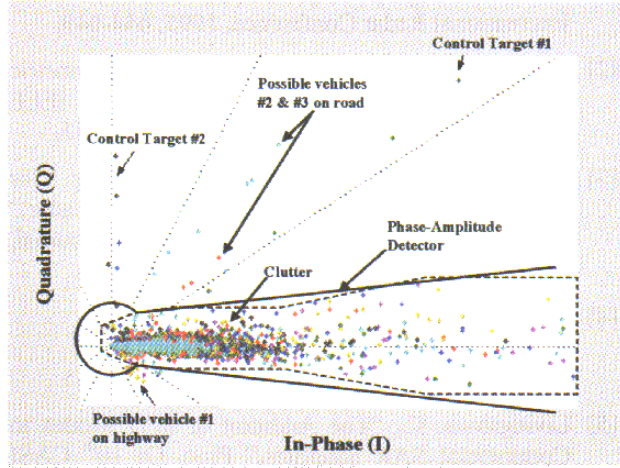


Fig. 13 Output signal from the ATI processor plotted on I-Q plane. Also shown is a simple phase-amplitude detector for moving target extraction.

The Q-component of this ATI airborne data was also found to have a Gaussian distribution as was found in the simulated data. Thus, a more sophisticated and optimized detector can be similarly constructed using the procedure described in the previous section to ensure that smaller, slower targets are not excluded from the detection region (i.e., outside the “key-hole” area).

8.0 Comparison of SAR/DPCA and ATI

At first, ATI would appear to have an advantage over SAR/DPCA in that the ideal PRF is no longer required. The two-antenna SAR/DPCA suffers the shortcoming of any two-pulse delay-line canceller in that its output signal is equal to the difference of two slightly different signal vectors and its magnitude is related to the target radial velocity as follows:

$$a = |S_1 - S_2| = |S(x, y)| \left| 1 - e^{j4\pi(R_2 - R_1)/\lambda} \right|$$

which simplifies to:

$$\begin{aligned} a &= 2 \cdot \left| \sin\left(\frac{2\pi(R_2 - R_1)}{\lambda}\right) \right| \cdot |S(x, y)| \\ &= 2 \cdot \left| \sin\left(2\pi \frac{V_r \delta t}{\lambda}\right) \right| \cdot |S(x, y)| \quad , \end{aligned}$$

where R_1 and R_2 are ranges from the forward and aftward phase centers, respectively, to the moving target, and V_r is the target radial velocity. δt is the “DPCA time,” which in this case is equal to the pulse repetition interval (PRI). Thus, slow-moving targets are significantly attenuated by the DPCA clutter rejection filter.

On the other hand, the ATI output is the signal power (as opposed to the signal voltage from the SAR/DPCA processor) and its magnitude is simply equal to $|S(x, y)|^2$. The targets are not suppressed along with the stationary clutter when one utilizes phase and amplitude information for target. Careful examination of the ATI processor shows that the ATI phase depends on the signal-to-clutter ratio (SCR). For example, in a $25 \text{ m} \times 25 \text{ m}$ resolution cell, target and clutter signal vectors will be added within the cell. Ignoring noise, the output image from the first channel can be written as

$$S_1 = V_{s,1} + V_c \quad ,$$

where V_c is the clutter and $V_{s,1}$ is the signal from the target of interest in channel 1. Similarly, for channel 2 we can write

$$S_2 = V_{s,2} + V_c \quad .$$

The estimated phase from the ATI processor output is

$$\text{Arctan}(S_1 \cdot S_2^*) \quad .$$

But the correct interferometric phase for the signal of interest is

$$\text{Arctan}(V_{s,1} \cdot V_{s,2}^*) \quad .$$

The estimated phase is “attenuated” by the clutter contained in the same resolution cell as the target. The smaller the SCR, the more likely the target will become buried within the main clutter region in the complex plane and less likely be extracted from the clutter. As illustrated in Fig. 12, the resulting signal vector within a resolution cell has a phase angle that is consistently smaller than the actual moving target’s signal phase. For a clutter vector that is of same size as that of the target vector, the resulting signal vector would have a phase value that is exactly half of that of the moving target. The effect will be most severe for low SCR targets. This is indeed observed for targets 17 to 20, where only target 18 has a confirmed detection. However, the clutter contamination effect can be mitigated by selecting radar resolution cell areas that are closer to the physical size of the target. For RADARSAT2 MODEX studies, cell sizes of $6 \text{ m} \times 6 \text{ m}$ and smaller may be needed to extract weak targets.

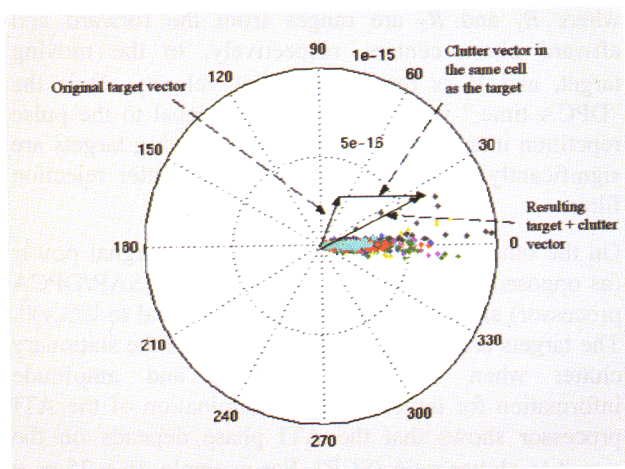


Fig. 14 The target signal phase within a resolution cell is being "attenuated" the clutter signal occupying the same cell.

In ATI processing, noise tends to scatter the clutter signal around zero phase and may obscure the nearby targets with smaller phase angles. High system noise could potentially present a problem for detecting bright but slow moving targets. However, the overall performance of ATI processor was shown to be about the same as that of the SAR/DPCA approach for the target and clutter parameters examined.

On the other hand, both ATI and SAR/DPCA suffer from the limited efficiency of the two-pulse canceller: to get high sensitivity, the two antennas have to be widely separated, but this leads to a comb of blind velocities $v_{blind} = kv_p\lambda/d$, where k is an integer, v_p is the platform velocity, and d is the antenna separation.

9.0 Conclusions

At first, it was expected that ATI would outperform classical DPCA when the SCR is high and that DPCA would be superior when the SCR is low. But this expectation does not appear to be supported by the present study. The two processor architectures both appear to perform well under the target and clutter parameters examined. Both approaches have difficulty detecting targets with radial speed below 5 m/s or RCS smaller than 20 m². The initial simulations and airborne ATI results here are encouraging, and suggest that detection of ground moving targets of sufficient radar cross section is possible with a sensor of the RADARSAT2 GMTI class. Further studies are expected to refine these performance data and characterize the full range of a space-based GMTI capability.

Acknowledgement

Special thanks to Dr. David Liang for his valuable advice and for his encouragement throughout this work and to Georgio Dinardo for his computer support. This work is carried out by the DREO Space Systems Group.

References

- [1] Coe, D.J., White, R.G., "Moving Target Detection in SAR Imagery: Experimental Results," IEEE International Radar Conference, 1995, 644-649.
- [2] Stockburger, E.F., Held, D.N., "Interferometric Moving Ground Target Imaging," IEEE International Radar Conference, 1995, 438-443.
- [3] Ender, J.H.G., "Space-Time Processing for Multichannel Synthetic Aperture Radar," Electronics & Communication Engineering Journal, 11, 1999, 29-38.
- [4] Yadin, E., "Evaluation of Noise and Clutter Induced Relocation Error in SAR MTI," IEEE International Radar Conference, 1995, 650-655.
- [5] Livingstone, C., "The Addition of MTI Modes to Commercial SAR Satellites," Proc. Of 10th CASI Conference on Astronautics, Ottawa, Canada, October 26-28, 1998.
- [6] Luscombe, A., "The Radarsat Project," IEEE Canadian Review, Fall 1995.

A Real-Time SAR Processor using one-bit raw signal coding for SRTM

(46)

F. Impagnatiello, A. Gallon, F. Buscaglione, M.N. Ferrara *
F. Nirchio **

*Alenia Spazio - Remote Sensing Engineering
Via Saccomuro 24, 00131 Roma Italy

** ASI - Agenzia Spaziale Italiana - Geodesy Space Centre
Loc. Terlecchia 75100 - Matera Italy

Summary

The great success of the two SIR-C/X-SAR missions and the lack of global topographic data are the reasons at the basis of third Shuttle Radar Topographic Mission (SRTM). The mission is a joint program among NASA NIMA, DLR and the Italian Space Agency. The SRTM mission aims is to create a tri-dimensional topographic map of the Earth's surface 30 times as precise as the best global maps in use today.

The sophisticated mission technology is able to produce topographic maps with a level of detail never achieved before and a very good height precision.

The technique used, based on microwave instruments with a synthetic aperture radar, is a totally new concept in geodesy, the science that studies the morphology of planet Earth and measures its characteristics.

The mission has been also a great opportunity to test in an operational contest a innovative one bit processing chain operating in the pure time domain. The processor focuses the X-SAR signum coded raw data applying a quasi-phase preserving algorithm. The equivalent computing power is about 8,000 billions operations per second.

The processor architecture is such to comply with the continuous data flow coming from the instrument delivering a striped image.

Alenia Spazio, beside the responsibility with Dornier of the design and realisation of the X-band radar, also in this case under ASI contract, has designed and realised a complete ground station organised as a X-band data Processing Chain installed and operated at JPL site. This includes a Real-Time SAR processor, a comprehensive data management system and finally a topographic post-processing station.

Astonishing results have been produced both as single-bit focused SAR images and digital elevation models, also thanks to the advanced capabilities developed in last years at University Federico II of Naples one of the more active research institutions in this field.

Background

X-SAR, X band Synthetic Aperture Radar, was developed by Alenia Aerospazio for Italian Space Agency (ASI), as part of the joint Italian, German and US space Shuttle Radar Laboratory (SRL) program.

It was designed for integrated operation with the SIR-C Synthetic Aperture Radar developed by JPL as part of the same mission.

The instrument was successfully qualified and validated through two space shuttle missions in 1994, where its challenging imaging performance at X band were proven.

It was the first X-band SAR developed for spaceborne applications, and provided a significant contribution to improve the knowledge of multi-frequency SAR imaging in co-operation with the L/C band of SIR-C instrument.

New Features

X-IFSAR is a radar interferometer based on a couple of Synthetic Aperture instruments, that share the transmitting antenna while hold separate the receiving channels including antennas, RF sections and digital data handling subsystems.

The X-Band acquisition is guaranteed providing all weather operation and night/day imaging and topographic mapping of about 35% of the Earth surface.

The Italian Processing Chain operated in connection with X-IFSAR in Pasadena (CA) at the Jet Propulsion Laboratory NASA centre.

The direct down-linked data was available for processing and delivering first absolute DEM products together with auxiliary functions aimed to instrument in-flight calibration and performance monitoring.

The X-IFSAR Processing Chain employees a revolutionary real-time parallel processor based on a proprietary ASIC solution. Each of the 128 ASICs,

developed using VHDL coding and Field Programmable Gate Array (FPGA) technology, endorses the Single Bit SAR coding and focusing algorithm, first conceived and analysed by the University of Naples "Federico II", Department of Electrical Engineering.

The Signum Code (SC) algorithm, together with state-of-the-art FPGA chip architecture, made the real-time operation possible, achieving full geometric resolution on SAR images and full height accuracy for DEM generation.

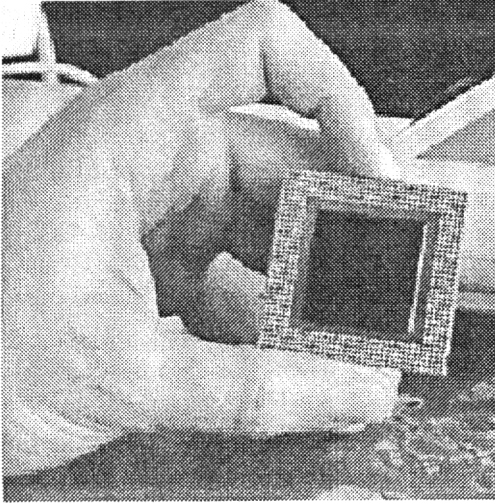


Figure 1 The TID Complex Correlator FPGA

Applications

X-IFSAR is derived from X-SAR whose primary application has been Earth surface imaging together with the study of the moisture connected to hydrology, geology, ecology and other disciplines.

The specific purpose of X-IFSAR is the measurement of ground height in order to deliver high resolution, high accuracy topographic maps all over the world. The planning of the 11-days SRTM mission constrained X-IFSAR to acquire about 35 % of the Earth surface within $\pm 57^\circ$ latitude boundaries.

The Italian Operational Processing Chain has been used within the mission-time frame for in-flight calibration purposes and absolute first product generation.

After SRTM conclusion, it has been installed at "Centro di Geodesia Spaziale" Matera - Italy - where all the SRTM data set has been available starting from November 1999. There the Processing Chain has been used for systematic fast product generation.

The comparison with the large data sets acquired during SRL missions in 1994 will also allow the observation of midterm geological process, soil erosion and deserts progression within a five years period.

The huge coverage granted during SRTM by X-IFSAR will allow once again the analysis of precipitation over tropical forest and ice properties and their variation and, finally, ocean large-scale dynamics.

Basic SC Arithmetic

The arithmetic operation that plays the central role in the novel SC data representation is the multiplication.

Given h and r two variables defined within the real field number (usually represented adopting the IEEE754 standard on conventional computer FPUs), two new variables can be associated as defined here below

$$h \rightarrow \hat{h} = \begin{cases} +1 & h > 0 \\ -1 & h < 0 \end{cases}$$

and

$$r \rightarrow \hat{r} = \begin{cases} +1 & r > 0 \\ -1 & r < 0 \end{cases}$$

The new variables, generated by means of a hard quantization, also belong to the real number field, but they can assume only two values.

Now the new variables can be re-coded using a more appropriate representation that accounts for true possible states. The binary representation is immediate.

Let's H and R be the codes corresponding to \hat{h} and \hat{r} :

$$\hat{h} \rightarrow H = \begin{cases} 1 & \hat{h} = +1 \\ 0 & \hat{h} = -1 \end{cases}$$

and

$$\hat{r} \rightarrow R = \begin{cases} 1 & \hat{r} = +1 \\ 0 & \hat{r} = -1 \end{cases}$$

The binary coding of hard quantized variables H and R is named **Signum Coding** shortened in this frame with the symbol **SC**.

Now let's examine how the signum coding works on arithmetic multiplication.

The h by r product generates the results s that can be represented using binary coding too.

It can be shown that the value of S , the SC of s , obtained by means of the negation of an exclusive OR between H and R , is exactly equal to the value got applying SC on the hard quantization of $s = h \cdot r$.

In term of mathematics this property can be written as:

$$\hat{s} = \hat{h} \cdot \hat{r} \Rightarrow S = \overline{R \otimes H}$$

which can be verified case by case looking into Table 1, where S , computed in the two equivalent ways, are systematically compared.

\hat{r}	\hat{h}	$\hat{r} \cdot \hat{h}$	R	H	$\overline{R \otimes H}$	\hat{s}
+1	+1	+1	1	1	1	+1
+1	-1	-1	1	0	0	-1
-1	+1	-1	0	1	0	-1
-1	-1	+1	0	0	1	+1

Table 1 – Real/Boolean relations for multiplication

If the True State Counter (TSC), or “1” occurrences counter, is defined using the symbol

$$\|S_j\|_{j,CNT}^{\{1\}} := \begin{array}{l} \text{counts the number of "Sj = 1"} \\ \text{occurrences while j varies} \end{array}$$

the sum of products s_j can be written using the equivalent SC coding

$$\sum_{j=1}^N \hat{s}_j = 2 \cdot \|S_j\|_{j,CNT}^{1,N} - N$$

where N , the number of added elements s_j , acts as a bias. N is sometimes called “magic number”.

Signum Code SAR Focusing Algorithm

Here the SAR processing algorithm based on the SC raw data representation is detailed as implemented within the X-SAR Processing Chain.

The time domain operation used for SAR focusing is the bi-dimensional correlation, performed using mono-dimensional correlation followed by results addition. This correlation is defined in the complex number field and can be decomposed into four real number field correlations.

Therefore the basic function is the real correlation, which is susceptible of signum coding representation.

Real Correlation

Let $r(*,*)$ be the input complex data matrix built of the aligned raw data radar echoes, and $h(*,*)$ be the complex bi-dimensional space-varying holographic SAR reference function.

The derived measurement $s(*,*)$ of local ground whet reflectivity can be computed in the native time/space domain as the correlation product :

$$s(i, j) = \sum_{p=1}^{Nr} \sum_{q=1}^{Na} r(i + p, j + q) \cdot h_{i,j}(p, q).$$

The space varying dependence of $h_{i,j}(p, q)$ is depicted by the i and j indexes. The hard quantization transforms the expression of $s(i, j)$ into

$$\hat{s}(i, j) = \sum_{p=1}^{Nr} \sum_{q=1}^{Na} \hat{r}(i + p, j + q) \cdot \hat{h}_{i,j}(p, q).$$

It is not relevant now how the $\hat{s}(i, j)$ and $s(i, j)$ expressions differ, because the theoretical SAR focusing performance is not a matter of interest here.

If the equivalence property of the sum products is applied, the $\hat{s}(i, j)$ can be immediately evaluated employing the SC representation and getting the relationship

$$\hat{s}(i, j) = 2 \sum_{p=1}^{Nr} \left\| \overline{R(i + p, j + q) \otimes H_{i,j}(p, q)} \right\|_{j,CNT}^{1,Nq} - N_p N_q$$

The bi-dimensional count operation is exploited into the sum in one dimension of mono-dimensional counts in the other one.

Complex Correlation

The complex correlation is similar to the real one analysed in the previous section. The mathematical definition of it is exploited by the following equation

$$s(i, j) = \sum_{p=1}^{Nr} \sum_{q=1}^{Na} r(i + p, j + q) \cdot h_{i,j}^*(p, q)$$

where $h_{i,j}(p, q)$, $r(i, j)$ and $s(i, j)$ are complex numbers instead of real numbers.

Note that the reference function $h_{i,j}(p, q)$ shall be conjugated in order to express a full significant correlation.

The complex multiplication between two complex numbers can be reduced into a set of four real multiplications and their proper combination for generation the real and imaginary part.

Given A and B the signum code representations of two complex numbers where, A^{Re} , B^{Re} , A^{Im} e B^{Im} stay for the four components, the complex multiplication of A by B* (* signifies complex conjugation function).

$$C = A \cdot B^*$$

is equivalent to the combination of six real field operations

$$C \rightarrow \begin{cases} C^{Re} = A^{Re} \cdot B^{Re} + A^{Im} \cdot B^{Im} \\ C^{Im} = -A^{Re} \cdot B^{Im} + A^{Im} \cdot B^{Re} \end{cases}$$

This relates to the complex product only. If the complex addition is introduced, the sum of complex products

$$c = \sum_j a_j \cdot b_j^*$$

can be translated in the real field according to the scheme here below

$$c \rightarrow \begin{cases} c^{Re} = \sum_j a_j^{Re} \cdot b_j^{Re} + \sum_j a_j^{Im} \cdot b_j^{Im} \\ c^{Im} = -\sum_j a_j^{Re} \cdot b_j^{Im} + \sum_j a_j^{Im} \cdot b_j^{Re} \end{cases}$$

Now, by applying the discussed rules and dividing by 2 (which does not break the generality of this property), the SC representation S of s can be computed as

$$C = \frac{c}{2} \rightarrow \begin{cases} C^{Re} = \left\| A_j^{Re} \otimes B_j^{Re} \right\|_{j,CNT}^{1,N} + \left\| A_j^{Im} \otimes B_j^{Im} \right\|_{j,CNT}^{1,N} - N \\ C^{Im} = -\left\| A_j^{Re} \otimes B_j^{Im} \right\|_{j,CNT}^{1,N} + \left\| A_j^{Im} \otimes B_j^{Re} \right\|_{j,CNT}^{1,N} \end{cases}$$

Note that the imaginary part C^{Im} only requires the bias compensation due to the presence of positive counters. On the other hand the biases of the two C^{Im} components compensate each other.

For the purposes of the SAR focusing application, the by 2 division does not break the validity of the property.

Non space-varying SAR focusing

The ideal SAR focusing scheme has been employed that fully respects the intrinsic space-variance of SAR acquisition system. In fact the reference correlation function $h_{i,j}(p, q)$ depends on the raw data sample position through i and j .

The implementation of full space-variant filter is not realistic and would lead to an extremely complex design resulting not compatible with real-time architecture and run.

The relationship that determines the translation from raw data to focused image shall be therefore simplified in some way.

Keeping the same meanings for $r(*,*)$ and $s(*,*)$ an alternate relation is derived that expresses $s(i, j)$ as

$$s(i, j) = \sum_{p=1}^{Nr} \sum_{q=1}^{Na} r(i + p, j + q) \cdot h_k(p, q)$$

where $h_k(p, q)$ is frozen in connection with a limited number of K values (K from 1 to 5 are reasonable) in such a way to assume a piecewise constant reference function. The validity region of each filter make the processing act as 'unfocused'.

The requirement baseline requests for one single correlation filter all over the swath that shall be matched in correspondence of the swath centre. The azimuth focusing degradation implied by that choices directly proportional to the swath width where the single filter operates a space-invariant correlation.

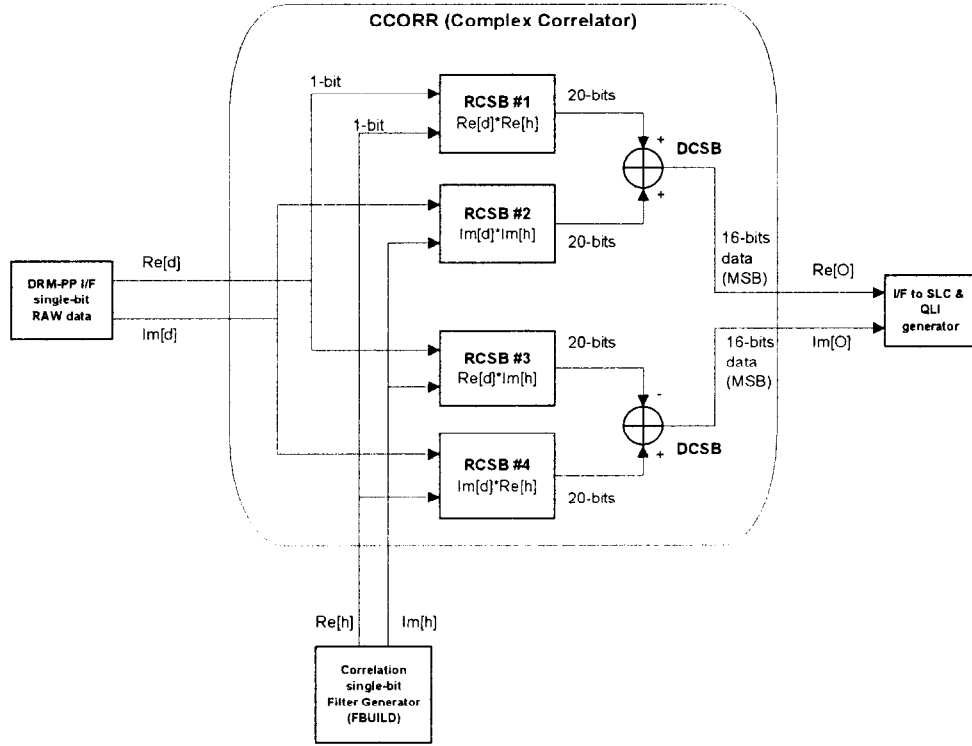


Figure 2 Time Domain Complex Correlator Architecture

Fast Filter Evaluation

If r_{CS} is the centre swath range, that is the distance between the antenna phase center and the swath center, the Doppler rate μ_A induced by the effective relative motion is given by:

$$\mu_A = -\frac{2 \cdot V'^2_{proc}}{\lambda \cdot r_{CS}}$$

where the negative sign is due to the physical change of radar-to-target distance during SAR motion.

The azimuth quadratic phase excess $\Phi_{Aq}(t)$, as function of flight time t computed at swath center, is then defined as

$$\Phi_{Aq}(t) = \pi \mu_A (t - t_0)^2 \quad \text{with } |t - t_0| < \frac{T_A}{2}$$

where t_0 is the flight time over a specified target placed at swath center and T_A is the coherent integration time. t is the flight time.

This is an exact expression at swath centre only and should be corrected for any other range position. The assumption of using a single reference filter consists in extending the validity of this quadratic phase shape to all ranges within the swath.

The total azimuth phase excess shall include also the linear term induced by the Doppler centroid, physically due to a slight skew in acquisition geometry. If f_{Dc} is the Doppler centroid frequency the azimuth linear phase term is given by

$$\Phi_{Al}(t) = 2\pi \cdot f_{Dc} (t - t_0) \quad \text{with } |t - t_0| < \frac{T_A}{2}$$

The range quadratic phase is instead determined by the chirp pulse bandwidth and duration. If T_p is the pulse

duration and Bp its bandwidth, the chirp rate μ_R is simply given by the ratio

$$\mu_R = \frac{B_p}{T_p}$$

then the range quadratic phase $\Phi_R(\tau)$, as function of echo fast time τ , can be computed as

$$\Phi_R(\tau) = \pi\mu_R(\tau - \tau_0)^2 \quad \text{with } |\tau - \tau_0| < \frac{T_p}{2}$$

where τ_0 is the centre of the chirp pulse.

The correlation filter $h_K(p, q)$ (this is not the signum coded filter but the full dynamic one) is defined over the 2D domain determined by the range axis (p index samples) and the azimuth axis (q index samples).

The relation between range index p and echo fast time τ is defined by the sampling frequency f_s

$$\tau_p = \frac{p}{f_s}$$

while the relation between the azimuth index q and the flight time t is determined by the pulse repetition frequency (PRF) as

$$t_q = \frac{q}{PRF} + t_{REF}$$

where t_{REF} is arbitrary and can be ignored without lacking of generality.

Assuming the following ranges for p and q:

$$p = 1, 2, \dots, N_r$$

$$q = 1, 2, \dots, N_a$$

the time centres t_0 and τ_0 are assumed in correspondence of

$$t_0 = \frac{1 + N_a}{2 \cdot PRF}$$

and

$$\tau_0 = \frac{1 + N_r}{2 \cdot f_s}$$

so that the total phase $\phi(t, \tau)$ over the filter, that can be computed in the 2D continuous domain as

$$\begin{aligned} \phi(\tau, t) &= \phi_{Aq}(t) + \phi_{Al}(t) + \phi_R(\tau) \\ \text{with } |\tau - \tau_0| &< \frac{T_p}{2} \text{ and } |t - t_0| < \frac{T_A}{2} \end{aligned}$$

is re-written according the expression

$$\begin{aligned} \bar{\phi}(p, q) &= \bar{\phi}_{Aq}(q) + \bar{\phi}_{Al}(q) + \bar{\phi}_R(p) \\ \text{with } p &= 1, \dots, N_r \text{ and } q = 1, \dots, N_a \end{aligned}$$

where

$$\bar{\phi}_{Aq}(q) = \pi \frac{\mu_A}{PRF^2} \left(q - \frac{1 + N_a}{2} \right)^2$$

$$\bar{\phi}_{Al}(q) = 2\pi \cdot \frac{f_{Dc}}{PRF} \left(q - \frac{1 + N_a}{2} \right)$$

$$\bar{\phi}_R(p) = \pi \frac{\mu_R}{f_s^2} \left(p - \frac{1 + N_r}{2} \right)^2$$

From the total phase $\bar{\phi}(p, q)$ the real and imaginary parts of the correlation filter $h_K(p, q)$ can be computed as:

$$\begin{aligned} h_K^{\text{re}}(p, q) &= \cos[\bar{\phi}(p, q)] \\ h_K^{\text{im}}(p, q) &= \sin[\bar{\phi}(p, q)] \end{aligned}$$

which are the full dynamic versions of the correlation filter required by Signum Code SAR focusing algorithm.

The Signum Code version can be immediately derived. Anyway, without computing the transcendent functions,

it is possible to generate the signum of cosine and the signum of sine using the simple verification rule based on the phase normalization.

A normalized phase Ψ is associated to the true phase $\bar{\phi}$ by means of:

$$\Psi = \text{mod} \left[\frac{2\bar{\phi}}{\pi}, 4 \right]$$

that furnishes Ψ in the range $[0,4[$. Then the sine signum S_{sine} and cosine signum S_{cosine} are immediately obtained looking for the integer value of Ψ achieving at the end:

$$Z = \text{int}(\Psi) \rightarrow \begin{cases} S_{\text{cosine}} = +1 & S_{\text{sine}} = +1 & \text{if } Z = 0 \\ S_{\text{cosine}} = -1 & S_{\text{sine}} = +1 & \text{if } Z = 1 \\ S_{\text{cosine}} = -1 & S_{\text{sine}} = -1 & \text{if } Z = 2 \\ S_{\text{cosine}} = +1 & S_{\text{sine}} = -1 & \text{if } Z = 3 \end{cases}$$

System Operation

The system operation was based on joint operation of an On-Board Segment, including the SAR sensor, with the Ground Segment, including the necessary equipment for mission planning, control and data image and DEM processing.

The On-Board segment includes the two X-band antennas (12 m and 6 m azimuth apertures), integrated with the C-band antennas, the RF and digital subsystems for interferometric radar operations. Digital data was formatted and stored on-board and a fraction (~2%) was down-linked to the Jet Propulsion Laboratory.

The Italian Processing Chain for X-IFSAR was supported by the mission and sensors planning operators. Most of instrument parameters, significant for final image and DEM performance, was monitored in conjunction with the German and US Ground Segments.

The X-IFSAR Processing Chain supplied the acquisition and monitoring of housekeeping data received from the sensor via the high-rate bit-multiplexed channels, as well as the real-time focusing processing of received scientific data through SAR images generation. All bit-stream synchronisation was performed using latest hardware and software available technologies.

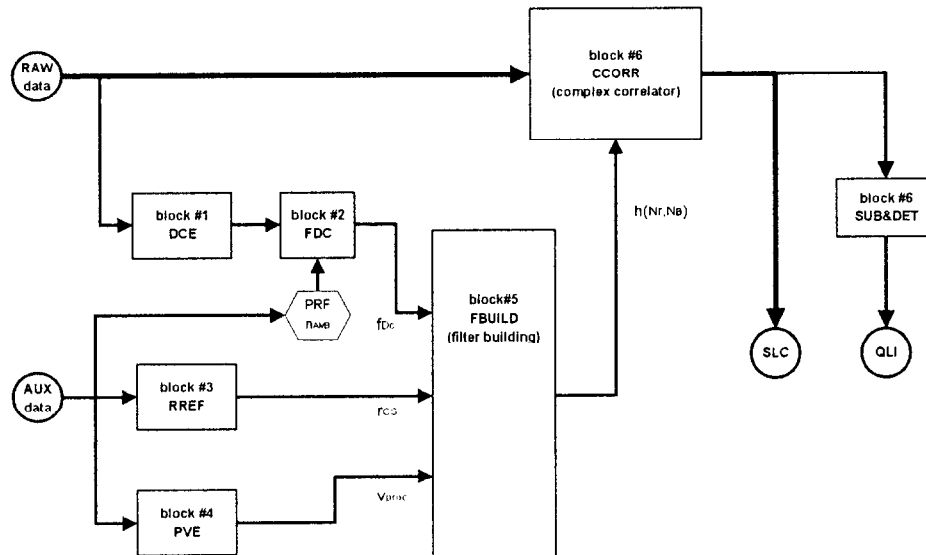


Figure 3 Overall SAR focusing SC algorithm block diagram implementation

Key Technologies

The emphasis of X-SAR development was put on application of the latest available space qualified technologies.

Now the technologies employed within the advanced X-IFSAR Italian Processing Chain are the key through the incoming Italian Space Programs, such as COSMO and SAR2000, that will benefit of the drawback of the developments and results achieved in the frame of SRTM program.

The present SAR processor is a machine that sizes as large as one VME crate cabinet (8 boards) that, thanks to the acquired know-how, will be miniaturised down to

a single double-Euro card and few tens of Watt power supply.

These feature and specifications in terms of envelope, mass and power enables the on-board implementation of the Signum Code SAR processing technique which is seen now as the switch-on gate toward new applications of spaceborne SAR instruments addressed to a larger base of users.

This is the key relevance of the Italian participation to SRTM where SRL experience and academic invention has been exploited.

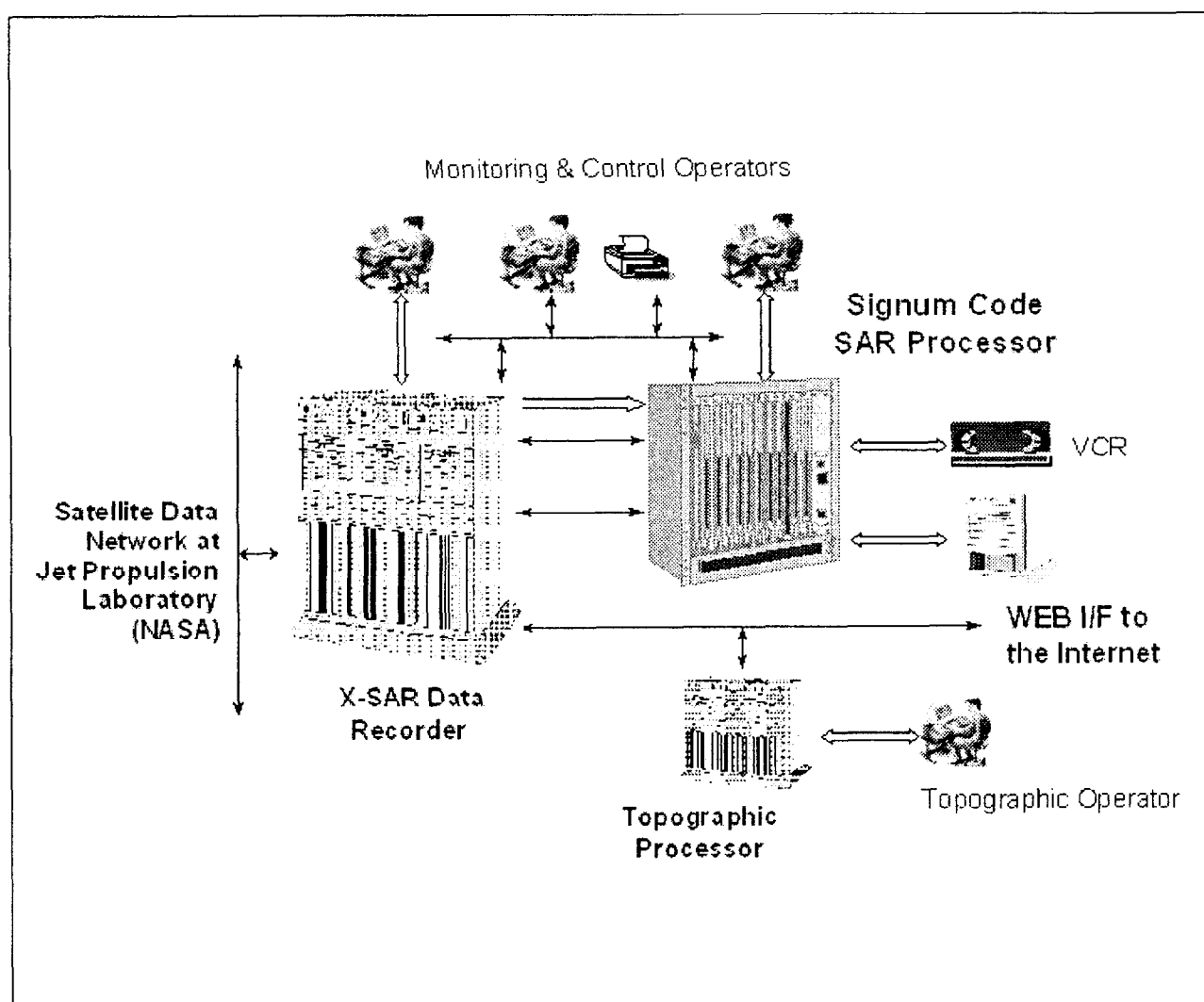


Figure 4 Overall Processing Chain Architecture as implemented at JPL site

Here are listed main specifications of the X-SAR Processing Chain components.

SAR Processor

Implementation	Full-custom
SAR Processor Algorithm	Time-Domain Signum Code
Operation Capability	Real-Time
Architecture	SIMD
CPU Technology	FPGA / BGA
Number of CPUs	128
Clock Frequency	30 MHz
Equivalent Computing Power	~ 6,500,000 Mops
Master Controller	Motorola 68060
RT Operating System	OS9k
Input I/F: raw data	IEEE 1284
auxiliary	RS232C
command	VME-PCI bridge
Output Interface	Fast Ethernet
Local Storage	63 GByte
Recording Autonomy	35 minutes

Chain Controller

Host Computer	IBM-PC
Platform Architecture	Intel PII @450 MHz
Operating System	NT 4.0
Control Environment	LabView 5TM
Local Control	full
Remote Control	operations
Thermal Control	on 128 CPUs
Fan Control	VME fans
I/O Control Interface	VME
RT Image Data Display	Viper550-TNT
On-Screen Resolutions	800x600
	1280x1024
	1600x1200
VCR	PAL (VGA)
System Printer	InkJetTM
Photographic Support	NP1600

Data Management Service

Host Computer	SUN E450 WS
Disk Storage	117 GByte
RAM Memory	1 GByte
CPUs	4 x 400 MHz - UltraSPARC
I/O Interfaces	Fast Ethernet
Tasks on X-SAR raw data	Syncho-Deformat - DQA/PE
Service Capability	60 minute/day
Network Services	FTP Server & WEB Server

Topographic Processor

Host Platform	SUN E450 WS
Disk Storage	33 GByte
RAM Memory	512 MByte
CPUs	4 x 300 MHz - UltraSPARC
I/O Interface	Fast Ethernet
Products	Fringes & DEM
Processing Capability	1 DEM / 2 hours
Algorithm & S/W Source	University of Naples

References

1. N.C.Currie, 'Radar Reflectivity Measurement: techniques and Applications', Artech House, 1989.
2. B.Porat, 'Digital Processing of Random Signals: Theory and Methods', Prentice-Hall, 1993
3. J.D.Taylor, 'Ultra-Wideband Radar Systems', Ed. U.S. Air Force, CRC Press, 1995
4. Bombaci, O., F. Rubertone, and A. Torre "Alenia Spazio Activities on SAR Interferometry: application on scientific mission," IGARSS '95, Florence, 1995.
5. Bombaci, O. and A. Torre, "Alenia Spazio Research Activities on SAR Interferometry," EUROPTO '95, Paris, Sept. 1995.
6. Bombaci, O., F. Impagnatiello, and A. Torre, "New features for on-line processing in interferometric applications" EUSAR '96, March 1996.
7. G. Franceschetti, A. Mazzeo, N. Mazzocca, E. Napoli, A. Strollo, P. Spirito, M. Tesauo, "A novel time-domain processor for real time SAR operation", PIERS'98 Conference 13-17 Luglio 1998 Nantes, Francia.
8. G. Fornaro, G. Franceschetti, R. Lanari, E. Sansosti and M. Tesauo. Global and local phase-unwrapping techniques: A comparison. Journal of the Optical Society of America A. vol. 14, pp. 2702-2708, 1997.

Interferometric Processing of Spaceborne SAR Data in Advanced SAR Imaging Modes

Josef Mittermayer and Alberto Moreira

Deutsches Zentrum für Luft- und Raumfahrt (DLR)
Institut für Hochfrequenztechnik und Radarsysteme
82234 Oberpfaffenhofen, Germany
T: +49-8153-28-2360, E-Mail: josef.mittermayer@dlr.de

Summary: The paper gives an analysis of ScanSAR and Spotlight data and identifies their common properties and the differences. A generic processing algorithm which consists of the Extended Chirp Scaling algorithm and the Frequency Scaling algorithm is proposed for high precision phase preserving processing of ScanSAR and SpotSAR imaging modes for future spaceborne SAR systems.

The ScanSAR processing performance is demonstrated by the interferometric processing of Radarsat ScanSAR data. The SpotSAR processing is validated using raw data from the airborne experimental SAR-System (E-SAR) of DLR.

I. Introduction

ScanSAR and SpotSAR are two operation modes of SAR systems, which improve the standard stripmap mode of operation in two different ways.

In ScanSAR, the scene size in range is extended by scanning the antenna in elevation and alternating illumination of several subswaths. The raw data of one illumination of a subswath are denoted by raw data burst. Like in stripmap SAR, the scene extension in azimuth is principally only determined by the length of the overflight. By the scanning in elevation, the synthetic aperture length is reduced to the burst length. The full synthetic aperture, which corresponds to the azimuth beamwidth θ_a , is shared between the subapertures T_{si} . Due to the short burst length, the achievable azimuth resolution is reduced. Figure 1 shows the geometry in the ScanSAR mode of operation.

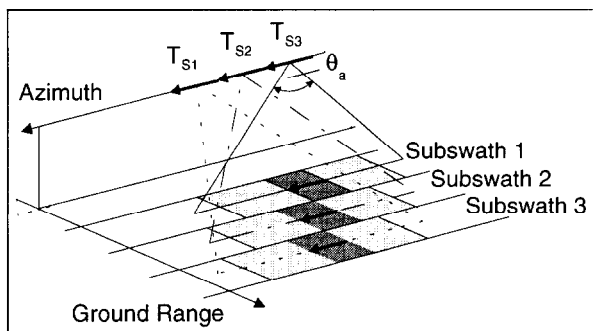


Figure 1: ScanSAR geometry

The basic difference between ScanSAR and conventional stripmap mode SAR is that each target is illuminated by different parts of the azimuth antenna pattern for a shorter time, the burst duration. This means each target has a different Doppler history depending on its azimuth position. ScanSAR shows a lot of interesting properties, which are for example discussed in [7].

In SpotSAR, the antenna is steered in azimuth direction in order to obtain an improved geometric resolution in azimuth. During the data acquisition, the antenna is constantly steered to scene center direction. This extends the illumination time and allows the generation of a long synthetic aperture, denoted by spotlight aperture in the following, which corresponds to a large Doppler bandwidth and thus, to a high azimuth resolution.

For a similar high range resolution, high bandwidth linear frequency modulated signals have to be transmitted. Due to the small range extension of a spotlight scene, the linear frequency modulation is usually removed before A/D-conversion in order to obtain a bandwidth reduction. This procedure is known as dechirp on receive (DOR) [2]. The DOR has two important impacts on the processing. First, it removes the linear frequency modulation, which for example prohibits a direct chirp scaling processing. Second, a quadratic phase term with range is introduced, which deteriorates the image quality if not compensated. This phase term is denoted by residual video phase (RVP) [1]. The RVP describes a range dependent time shift of the range signal.

As shown in Figure 2, the spotlight illumination in azimuth is fully described by the start and end squint angle, Ψ_{start} and Ψ_{end} , the scene center position and the azimuth beam angle θ_a . Instead of start and end squint angle, the start and end time of the illumination $t_{a,start}$ and $t_{a,end}$ can be used. The scene center defines the origin of the azimuth time and is located at the slant range position r_c .

The gray area in Figure 2 is the valid target area, which contains targets, constantly illuminated from $t_{a,start}$ to $t_{a,end}$. The bold lines show the limit of the azimuth illumination.

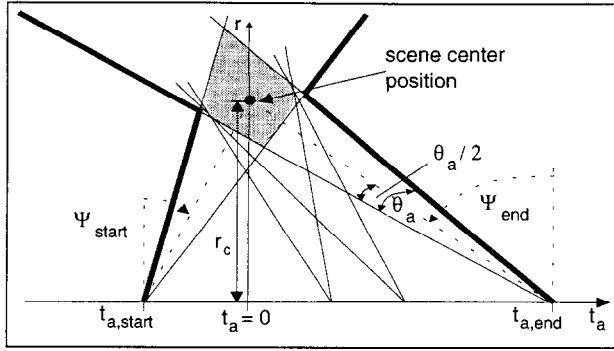


Figure 2: Spotlight illumination geometry

Due to the azimuth antenna steering in SpotSAR, the azimuth scene size is limited by the azimuth angle of the real aperture θ_a . The scene size in range is mainly determined by the antenna elevation pattern but also by the antenna steering. More information about the spotlight mode can be found for example in [4].

II. ScanSAR and SpotSAR Raw Data

The range modulation in SpotSAR and ScanSAR raw data is given by the modulation of the transmitted radar pulse, which is mostly a linear frequency modulation. In SpotSAR, often Dechirp on Receive is used before the A/D-conversion in order to transform the range signal into a superposition of sinusoidal signals with reduced bandwidth. In case of no Dechirp on Receive, the range modulation in SpotSAR and ScanSAR raw data is identical. Of course, the signal bandwidth in SpotSAR is normally higher than in ScanSAR.

The azimuth modulation in SpotSAR raw data and in one ScanSAR raw data burst is inherently very similar since in both modes the azimuth illumination for all targets has the same start and end time. The high resolution Spotlight mode consists only of one raw data burst with a high number of range echo lines, while ScanSAR raw data consist of several hundreds of bursts with only several tens of range echo lines. In the following, one ScanSAR raw data burst and a complete set of SpotSAR raw data is considered.

The azimuth signals are different for different target azimuth positions, in contrary to Stripmap data. ScanSAR and SpotSAR azimuth signals show a different Doppler history, a different Doppler centroid and also a slightly variation of the azimuth bandwidth dependent on the azimuth position of a target. In stripmap data, the Doppler history and centroid as well as the azimuth bandwidth are independent of the azimuth position of a target.

On the other hand, the azimuth signal length in ScanSAR and SpotSAR is independent of the target range position while in Stripmap SAR the azimuth signal length is increasing with range. Due to constant length of the synthetic aperture with range, the ScanSAR and SpotSAR

target azimuth bandwidth and resolution is strongly dependent on the targets range position. There is also a neglectable dependency on the target azimuth position. Stripmap mode data show an azimuth bandwidth and resolution independent on the range position. This is one of the well-known fundamentals of the standard stripmap SAR.

The following properties of the azimuth signals are identical in SpotSAR raw data and a single ScanSAR raw data burst:

- valid targets can be defined as targets with an azimuth illumination length equal to the full burst /spotlight aperture length
- the start and the end times of the azimuth illumination are equal for all valid targets independent of target range and azimuth position
- the azimuth signal is space-variant and depends on the azimuth position of the target
- the azimuth resolution is almost independent of the azimuth positioning of a target but shows noticeable dependency on the range position
- the azimuth processing can be performed by stripmap methods but this requires a large data overhead by zero padding, which makes the processing inefficient
- due to the constant illumination start and end times for all targets, SPECAN [9] is an efficient processing approach, which can be made highly accurate and phase preserving by azimuth scaling [4][7]

The target Doppler histories in a single ScanSAR raw data burst and in SpotSAR raw data are very similar, as is shown in Figure 3. The Doppler frequency is denoted by f_a , the azimuth time by t_a and the frequency histories are linearly approximated in the figure.

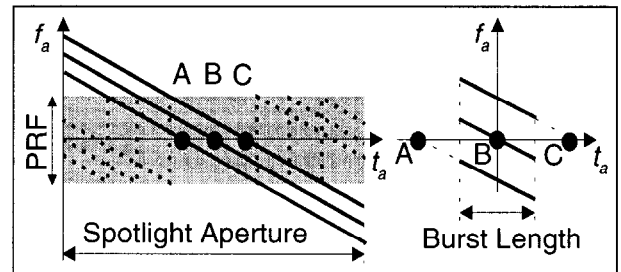


Figure 3: Doppler history in SpotSAR (left) and ScanSAR (right)

The left diagram shows the Doppler history of three targets A, B and C, located at different azimuth but identical range position for SpotSAR illumination. Spotlight raw data are acquired with a PRF sufficient for the instantaneous bandwidth, which corresponds to the azimuth beam angle, but which is smaller than the total bandwidth of the Spotlight scene. The signals in the Spotlight raw data are ambiguous in azimuth frequency

and are shown in dashed style. The continuous lines show the unambiguous signals for a theoretically very high PRF.

The right diagram in Figure 3 shows the Doppler history of three targets at different azimuth but identical range position in a ScanSAR raw data burst. From the figure it is obvious that a similar azimuth processing can be applied to both, ScanSAR and SpotSAR due to the constant start and end times of the illumination, if the spotlight azimuth signal is made unambiguous, i.e. by subaperture processing [4].

III. The Generic ECS for ScanSAR and SpotSAR

A generic processing approach is presented, which is denoted by generic Extended Chirp Scaling (ECS) for ScanSAR and SpotSAR. It is composed of the Extended Chirp Scaling for ScanSAR and the Frequency Scaling Algorithm for SpotSAR.

A processing kernel is introduced, consisting of chirp scaling or frequency scaling for range processing and SPECAN, combined with azimuth scaling for the azimuth processing. This kernel is applied to both, ScanSAR and Spotlight raw data.

The range processing is performed by chirp scaling for ScanSAR and Spotlight SAR without Dechirp on Receive. For Spotlight data with Dechirp on Receive, the frequency scaling operation is used. Both methods require only multiplications and FFTs and use partially equal analytical expressions, although the derivation of chirp scaling and frequency scaling is different. The azimuth processing is also free of interpolations. The proposed generic processing method is thus very suitable for high accurate and efficient image and interferometric processing.

Different processing steps are added before and after the kernel for either ScanSAR or Spotlight processing. In ScanSAR, different single look complex (SLC) subswath images are generated for each possible azimuth look. From the SLC subswath pairs complete subswath interferograms are generated, which are later coherently added for a reduction of the phase noise. The number of possible azimuth looks is defined by the scanning strategy. In SpotSAR, a subaperture processing is applied, which reduces the requirements on the PRF during the processing to the PRF-value in the raw data and enables data blocks with short azimuth extension inside the algorithm kernel.

The block diagram of the generic formulation of the ECS for phase preserving SpotSAR and ScanSAR processing is shown in Figure 4. All parts in black letters on white background are used in ScanSAR and SpotSAR processing. Black letters on grey background mean usage only in SpotSAR processing and white letters mean usage only for ScanSAR.

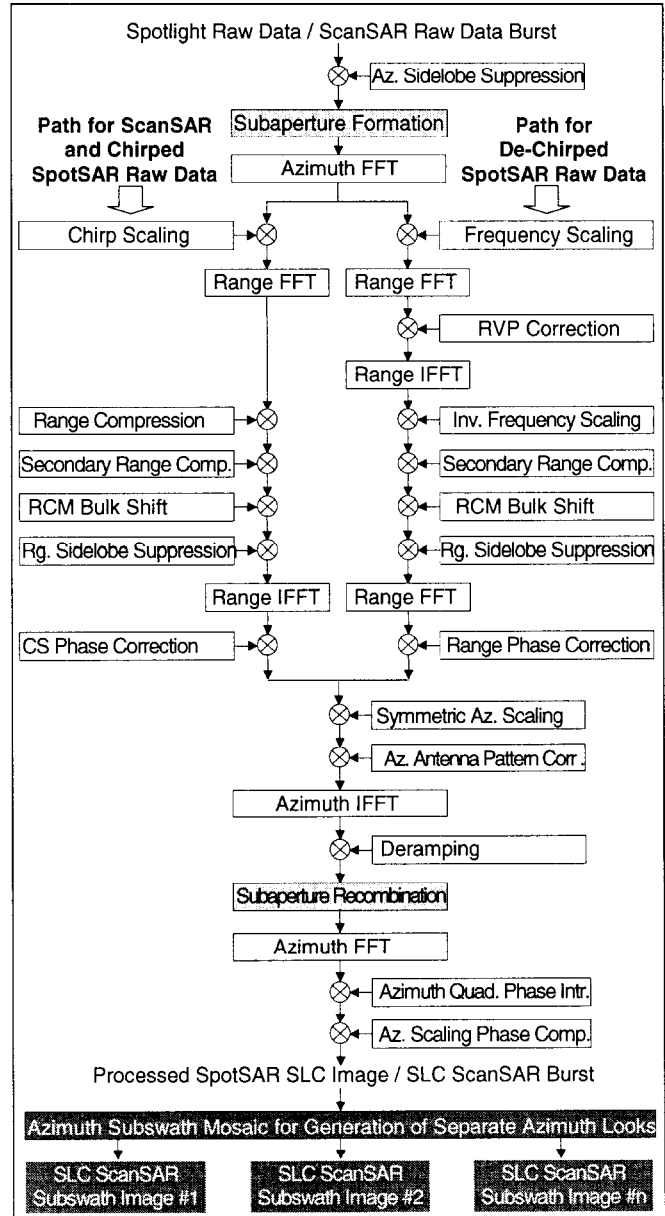


Figure 4: Block diagram of generic ECS for SpotSAR and ScanSAR

IV. Azimuth Processing

As shown in Figure 4, the azimuth processing starts with the weighting of the raw data for azimuth sidelobe suppression. This can easily be performed since in the raw data all azimuth signals are located at the same azimuth time position and the ECS is focussing in azimuth frequency domain. Next, the subaperture formation is performed in case of spotlight data for avoiding upsampling of the raw data in azimuth [4]. After transforming the data into range Doppler domain, either chirp scaling or frequency scaling is performed for full range compression and range cell migration correction, as will be explained in more detail in section V.

The azimuth processing is continued by azimuth scaling and the azimuth antenna pattern correction. The azimuth scaling transforms the azimuth modulation into a pure quadratic phase modulation which is independent of range [7] [4]. The possibility of selecting the final azimuth sampling distance during the azimuth scaling is very useful for exact co-registration of interferometric image pairs and for the mosaic of the single ScanSAR subswaths. The term symmetric azimuth scaling is due to an azimuth time shift during the azimuth scaling for a minimized symmetric azimuth time extension [4].

The azimuth pattern correction is important since the azimuth signal of a target is weighted by different parts of the azimuth antenna pattern dependent on the target azimuth position. If not corrected, an amplitude modulation is visible in the image. In ScanSAR, the pattern can be corrected accurately in azimuth frequency domain. For SpotSAR, the subaperture approach allows an approximated azimuth antenna pattern correction, which is the more accurate the smaller the subapertures are. The azimuth antenna pattern correction in SpotSAR can also be performed in the final image. The approximation there is the assumption that each target is always illuminated by the same portion of the antenna diagram.

After transforming the data into azimuth time domain, the deramping operation is performed by using a quadratic phase function, which is constant with range. In case of SpotSAR, the subapertures are recombined next. The azimuth compression is then performed by the final azimuth FFT, which is followed by a quadratic phase correction, required for phase preserving SPECAN processing and by an additional azimuth scaling phase correction, which is due to the azimuth time shift during the symmetric azimuth scaling.

After the phase corrections, the SpotSAR single look complex (SLC) image is available for further interferometric processing. In case of ScanSAR, the processed bursts have to be combined in order to form one SLC ScanSAR subswath image for each azimuth look. The number of possible azimuth looks is defined by the ScanSAR scanning strategy. From each interferometric SLC subswath image pair an interferogram can be generated and all these interferograms can be coherently added for phase noise reduction.

V. Range Processing

As can be seen in Figure 4, the range processing follows one of the two signal paths. The left signal path is for ScanSAR data and for SpotSAR data without Dechirp on Receive. The range processing in this path is performed analog to the range processing in the ECS algorithm [7] for stripmap. In case of spotlight with Dechirp on Receive, the right signal path has to be selected using the frequency scaling approach [4]. Both methods require only multiplications and FFTs and use partially equal analytical expressions. In case of chirp scaling, the

weighting for range sidelobe suppression is performed in range frequency domain while the weighting in the frequency scaling approach is performed in range time domain.

VI. Interferometric Spotlight Processing of E-SAR Stripmap Raw Data

The algorithm performance for SpotSAR is demonstrated using real raw data of the experimental SAR System (E-SAR) of DLR. However, the algorithm can easily be adopted to Spaceborne SpotSAR. The E-SAR is working in the stripmap mode but offers a wide beamwidth in azimuth and a high PRF. This allows the processing of relatively high resolution spotlight images. Figure 5 shows the principle of processing stripmap raw data in the spotlight mode.

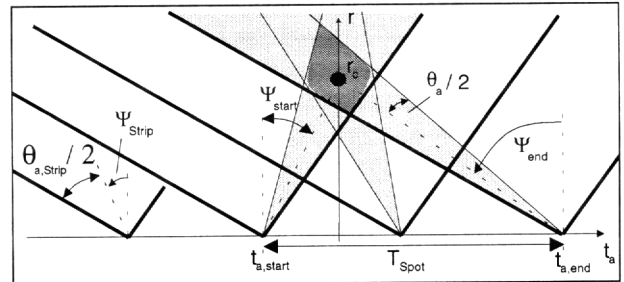


Figure 5: Processing stripmap raw data in spotlight mode

The thick lines in the figure show a stripmap illumination with fixed squint angle Ψ_{strip} and a beamwidth $\theta_{a,\text{strip}}$. For the spotlight image, the bright gray sectors have to be selected, which correspond to the spotlight beamwidth θ_a . This results in a different squint angle for each azimuth position within the interval $[\Psi_{\text{start}}, \Psi_{\text{end}}]$.

As a reference, the detected image of a stripmap processed E-SAR raw data set is shown in Figure 6. The azimuth beamwidth is 8° and the instantaneous bandwidth is 780 Hz, from which 270 Hz were processed to 0.42 m azimuth resolution. The range resolution is 2.16 m. The scene size is about 480 m in azimuth (horizontal) by 530 m in range. The spotlight image processed from the same raw data is shown in Figure 7. The spotlight beamwidth is set to 5.3° and the resulting squint angle variation is 2.8° . This means an azimuth bandwidth of 283 Hz in near and 257 Hz in far range, corresponding to azimuth resolutions of 0.40 and 0.44 m. The range resolution is as in the stripmap image.

A more conspicuous difference between the stripmap and the spotlight image is marked by the white circles. The edge of a building is more visible in the spotlight image. For the squint angle of the stripmap illumination, the reflection was less than for the squint angle of the spotlight illumination at this position in the image. Figure 8 shows the stripmap spotlight difference image. In the middle of the image, there is no difference visible since the focussing in stripmap and spotlight mode was over the same squint angle range. To the left and right side, the differences are

growing, due to the different squint angle ranges. Also the coherence map in Figure 9 shows the conformity in the middle of the images and the increasing non-conformity to the left and right side. High coherence is encoded towards white while low coherence is encoded towards black.



Figure 6: *Detected stripmap image*

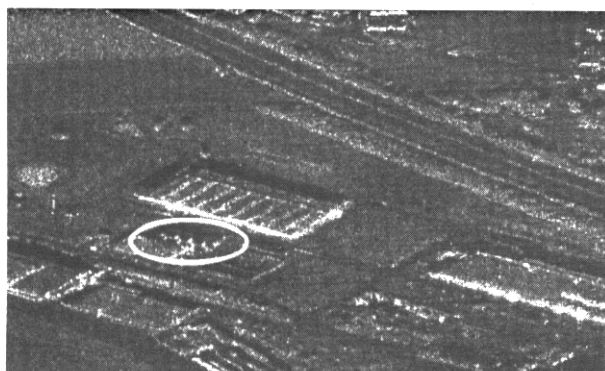


Figure 7: *Detected spotlight image*

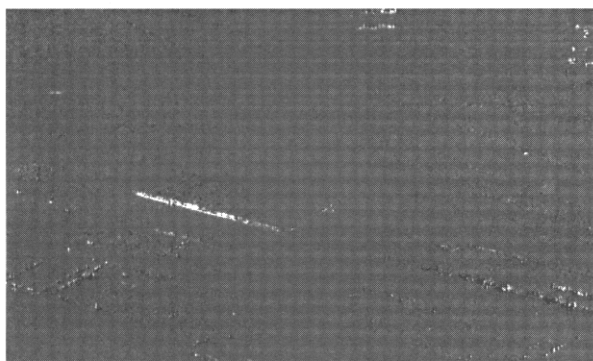


Figure 8: *Stripmap spotlight difference image*

The result of the interferometric Spotlight processing is shown in Figure 11 while Figure 10 shows the stripmap interferogram of the same scene as a reference. The stripmap spotlight difference interferogram is shown in Figure 12. The height information in the stripmap and spotlight interferogram is principally identical. Small differences exist for targets, which are only visible from a certain observation angle. Other differences arise in shaded areas, where only noise is processed from different squint angle ranges. Both interferograms are identical in the center of the image, since the center is focussed

over the same squint angle range and shows the same phase noise. To the left and right side, the difference in the phase noise is increasing since different spectral components are processed.

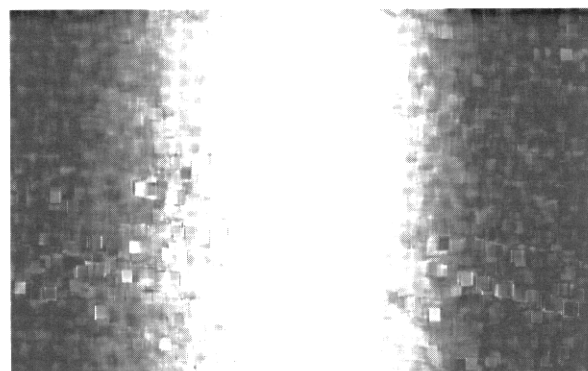


Figure 9: *Coherence map of stripmap and spotlight channel 1*

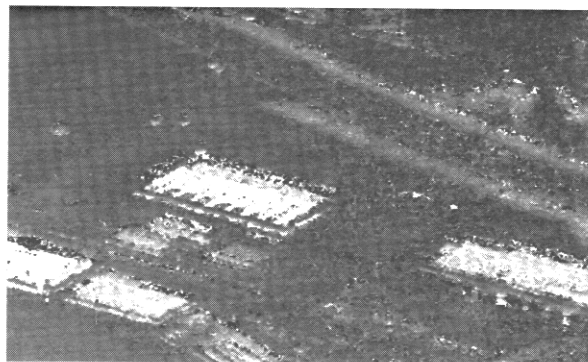


Figure 10: *Stripmap interferogram*



Figure 11: *Spotlight interferogram*

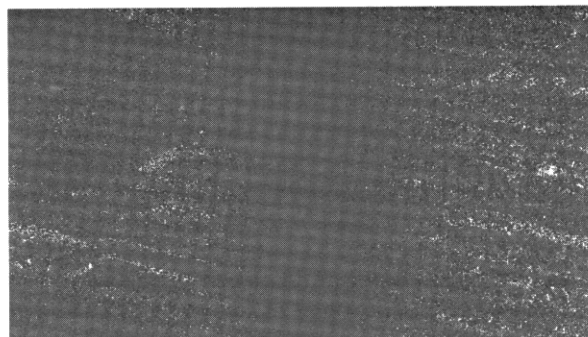


Figure 12: *Stripmap spotlight difference interferogram*

VII. Interferometric ScanSAR Processing

With courtesy from CSA, Radarsat ScanSAR data within the CCRS ADRO Proposal #500 were used for the processing. The same data had also been processed using an azimuth time domain convolution approach combined with DLR's BSAR processor [1].

After the subswath processing following the generic ECS of Figure 4, an image domain range multilooking was applied to one detected SLC subswath image and to the amplitude azimuth multilook image by a moving average with a window length corresponding to 3 range looks. The image detected from one SLC subswath is shown in Figure 13. Interesting image parameters are listed in Table 1.

number of processed bursts	137
corresponding scene extension azimuth	181 km
subswath W1 extension in slant range (196 km extension in ground range)	78 km
number of selected range echo lines within a burst	64
corresponding azimuth resolution	68m (near) 74m (far)
number of range looks	3
resolution slant range	11.6 m

Table 1: Subswath processing parameters

The image of a part of the Barthust Island in Canada shows land surface, ocean and ice areas. Compared to Figure 14, which shows the multilook image with 3 range and the two azimuth looks, more speckle is obvious in the single azimuth look image. The scalloping is much higher in the azimuth single look image but due to the lower speckle, the scalloping can be better observed in the azimuth multilook image.

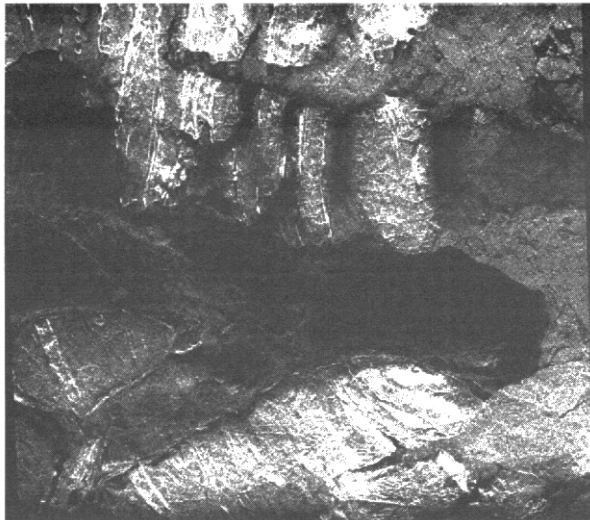


Figure 13: Image detected from one azimuth look

This can be seen in Figure 15, which shows the azimuth amplitude profiles of a part of the single azimuth look image at the bottom and the corresponding profile of the azimuth multilook image at the top.

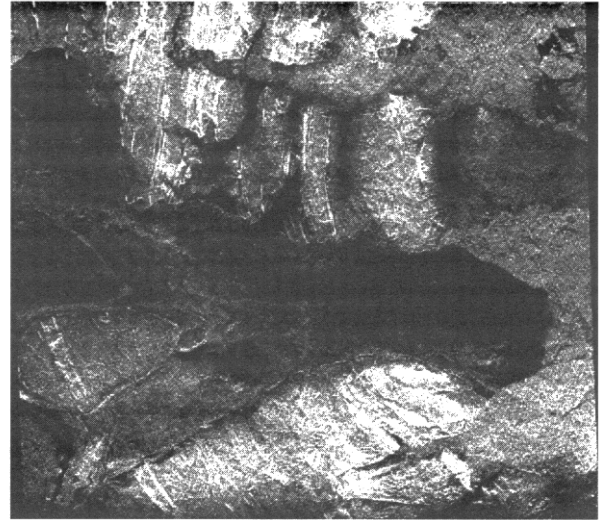


Figure 14: Detected image with azimuth multilook

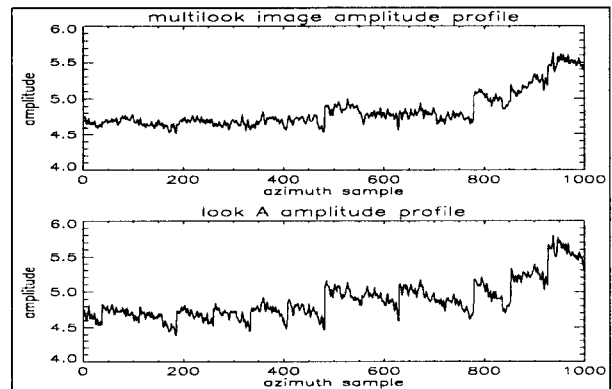


Figure 15: Scalloping shown by azimuth profiles

The interferometric processing starts already before the subswath processing by the selection of the raw data echo lines, which contribute to the same area on the ground [1]. For the processed Radarsat data set, this reduces the number of valid echo lines within a burst from 112 down to 64, corresponding to the azimuth resolution of about 70 m.

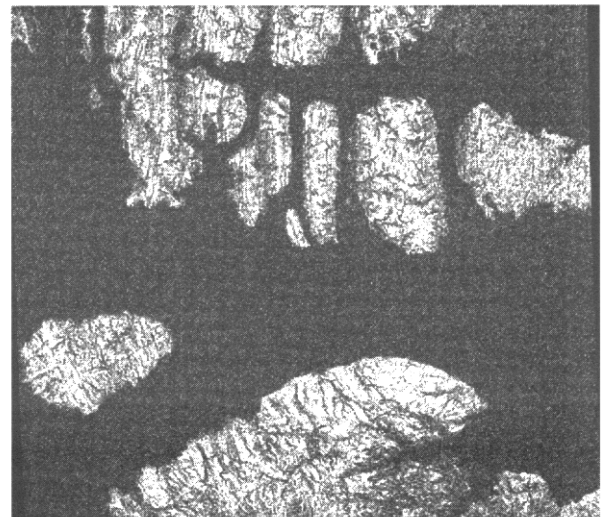


Figure 16: Coherence map of azimuth look 1

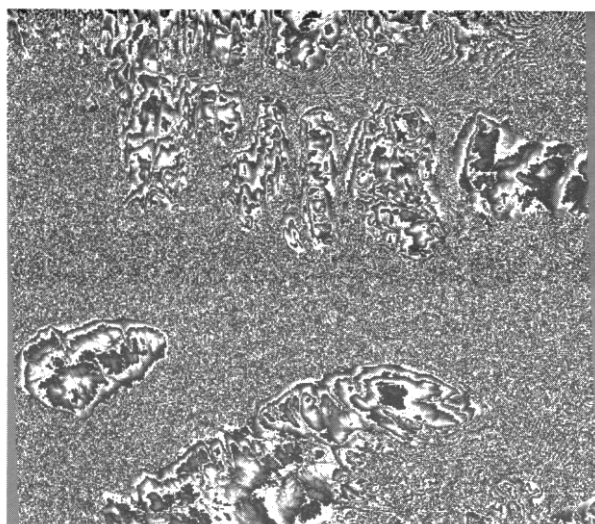


Figure 17: Interferogram of combined azimuth looks

A Range scaling [6] as well as the wavenumber shift [3] are applied during the subswath processing. We estimated a difference in the distance from near to far range of about 30 m between master and slave, which corresponds to 2.6 range samples. The introduced wavenumber shift was 2 MHz, while the transmitted bandwidth was 11.7 MHz.

After subswath processing, the interferometric multiplication of the master SLC subswath images with the conjugated slave SLC subswath images was carried out separately for each azimuth look. Then, after flat earth subtraction, a phase noise reduction was performed by a complex moving average in range on the two single azimuth look interferograms.

Figure 16 shows the coherency map of one azimuth look interferogram. The two data sets have been acquired with a time separation of 25 days and thus, almost only the land surface contributes to the interferogram. From the coherency histogram in Figure 18, a mean coherency of about 0.75 can be estimated for the land surface. The peak at 0.25 is due to the large ice areas with high temporal decorrelation.

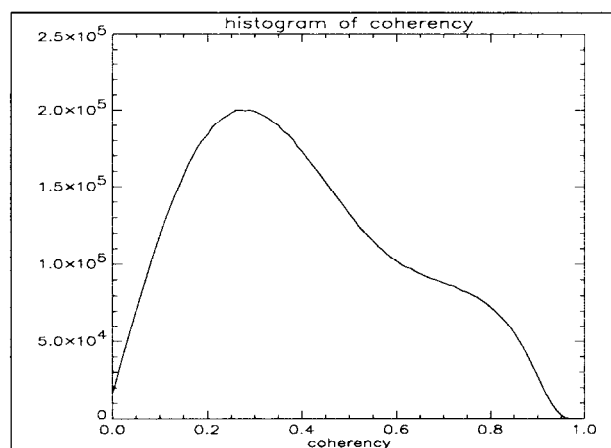


Figure 18: Histogram of coherency for look A

The multilook interferogram resulting from the coherent addition of the two SLCS interferograms is shown in Figure 17 after flat earth subtraction and a phase reduction by a moving average in range. The difference in the phase noise between azimuth single and multilook interferogram can't clearly be seen with the scale of Figure 17.

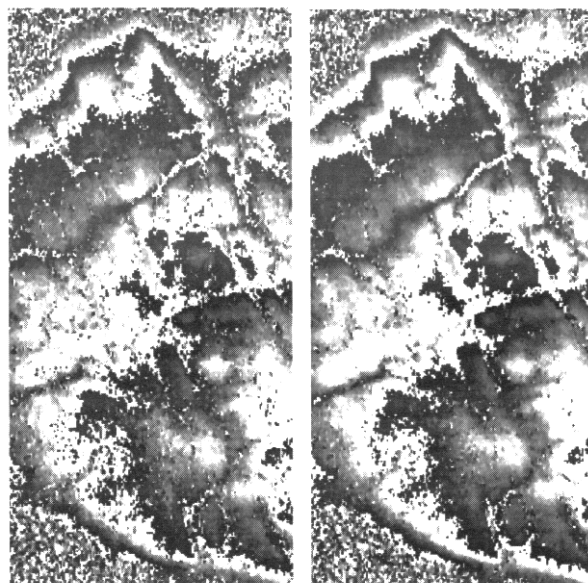


Figure 19: Single look (left) and multilook (right) interferogram

The small parts of the interferograms in Figure 19 allow a better observation of the difference in the phase noise. The single azimuth look interferogram is on the left and the multilook interferogram is on the right.

VIII. Conclusions

This paper shows the similarities between ScanSAR and SpotSAR and demonstrates how these similarities can be exploited by using a generic formulation of the ECS for the processing. The generic formulation provides advantages for the processor implementation in hard- or software and off-line or real-time since equal or very similar processor modules can be used for both, ScanSAR and SpotSAR data processing.

The good performance in interferometric ScanSAR and SpotSAR processing was shown by processing an interferogram from Radarsat ScanSAR data and from the generation of a SpotSAR interferogram from E-SAR data.

IX. References

- [1] R. Bamler et al.: "RADARSAT SAR Interferometry Using Standard, Fine and ScanSAR Modes", Proc. of Radarsat ADRO Final Symposium, Montreal-Canada, 1998.
- [2] G. Carrara, R. S. Goodman, R. M. Majewski: "Spotlight Synthetic Aperture Radar", Artech House Boston, London, 1995.
- [3] F. Gatelli et al.: "The Wavenumber Shift in SAR Interferometry", IEEE Transactions on Geosc., Vol. 32, No. 4, July 1994, pp. 855-865.
- [4] J. Mittermayer, A. Moreira, O. Lofeld: "Spotlight SAR Data Processing Using the Frequency Scaling Algorithm", IEEE Trans. on Geosc. and Remote Sensing, Vol. 37, No. 5, September 1999.
- [5] Mittermayer, J., A. Moreira and O. Loffeld: "Comparison of Stripmap and Spotlight Interferometric SAR Processing using E-SAR Raw Data". Proc. of EUSAR 2000.
- [6] Mittermayer, J., A. Moreira: "The Extended Chirp Scaling Algorithm for ScanSAR Interferometry". Proc. of EUSAR 2000.
- [7] A. Moreira, J. Mittermayer and R. Scheiber, "Extended Chirp Scaling Algorithm for Air- and Spaceborne SAR Data Processing in Stripmap and ScanSAR Imaging Modes", IEEE Trans. on Geosci. and Remote Sensing, Vol. 34, NO. 5, September 1996.
- [8] R. K. Raney, Runge, H., Bamler, R. Cumming, I. and Wong, F.: "Precision SAR Processing without Interpolation for Range Cell Migration Correction". IEEE Trans. on Geosci. and Remote Sensing, Vol.32, No.4, July 1994.
- [9] Sack, M., Ito, M.R., Cumming, I.G.: "Application of Efficient Linear FM Matched Filtering Algorithms to SAR Processing". IEE Proc.-F, Vol.132, No.1, 1985. pp. 45-57.

Linear features' detection in SAR images using Fuzzy Edge Detector (FED)

Alexandros Dimou^{1,2}, Nicolaos Uzunoglou¹, Panagiotis Frangos¹, Gunther Jäger², Ursula Benz²

¹ National Technical University of Athens
Department of Electrical and Computer Engineering, Division of Electrosience
GR-157 73 Zografou, Athens, Greece

² Deutsches Zentrum für Luft- und Raumfahrt (DLR) e.V.
P.O. Box 1116, D-82230 Wessling, Germany
Tel: ++49 08153 28 1168, Fax: ++49 08153 28 1449, E-mail: alexandros.dimou@dlr.de

Summary: Synthetic Aperture Radar (SAR) images exploitation is of great importance in remote sensing and Earth observation techniques, as well as in military surveillance and reconnaissance missions. One of the most important image-processing techniques is image segmentation. Segmentation subdivides an image into its constituent parts or objects. Edge detection is often an important first stage in many types of image segmentation. It can be used to simplify complex imagery in preparation for subsequent feature identification. Detection of linear structures (road network, airfields e.t.c.) is of great interest in a potential automated recognition system.

A new approach for edge detection in SAR images, which overcomes the necessity of choosing arbitrary thresholds is described in this paper. The Fuzzy Edge Detector (FED) not only discriminates between edge pixels and no-edge pixels, but assigns each image point a degree of being an edge point. This intermediate fuzzy output enables a very flexible post-processing and thus an efficient edge detection processing chain (e.g. non-maximum suppression and edge linking). Additionally, the edge direction information resulting from FED can be used for linear features' identification and extraction. The performance of the proposed edge detector on airborne and spaceborne SAR images that include linear features is presented.

1. INTRODUCTION

Edge detection is based on the concept that an edge is the boundary between two regions with relatively distinct gray level or textural properties and therefore the idea underlying most of the edge detection techniques is the computation of a local derivative operator. Traditionally, edge detection is regarded as a convolution operation. Usually, the edge detectors are divided into two groups based on the support of the convolution kernel. When the kernel has finite support, mask-based edge detectors are obtained, while when the kernel has infinite support, a different class of models (recursively implemented filters) arises. More recently, there have been studies of edge detection with learning models that mimic one style or another. This class includes both artificial neural networks and fuzzy reasoning systems [1].

In the case of SAR images, the speckle phenomenon has to be taken into account. Constant false alarm rate (CFAR) edge detectors deal with speckle noise. A characteristic example of this category of edge detectors is the normalized ratio (NR) to be applied on detected (intensity) data, either in its single-edge version, or the multiedge version [2][3]. More recently, edge detection in complex SAR images with correlated speckle is presented [4].

Features' extraction usually follows the edge detection process and makes use of the contours resulting from edge detection. The methods for identifying linear features can be roughly divided into two major categories: contour-tracing methods and structure-oriented hierarchical methods [5][6][7]. Contour-tracing methods try to directly exploit the edge detection result, having the advantage of resolution (the edge detection resolution), but being limited by the capabilities of the edge detector (e.g. its CFAR) in its performance. Structure-oriented methods use as starting conditions the results of the edge detection and build up structure hierarchies by composing complex structures from less complex structures. For this reason, a knowledge base is used and approximations concerning the comparison of the object form to its pattern are made. Within the framework of this paper the contour-tracing method was used, mostly due to the fact that FED [8] overcomes the necessity of choosing some arbitrary thresholds associated with false alarm rates (FAR). It has to be noted that the goal is to achieve good visual interpretation fulfilling the screening task mentioned in [6].

2. FUZZY EDGE DETECTOR (FED)

FED evaluates pixel by pixel the degree of being an edge pixel and the edge direction of this pixel. Fuzzy dissimilarity is calculated for two symmetrical neighborhoods moving in the opposite sides of each pixel to be resolved as an edge pixel. The bigger the dissimilarity, the higher the estimated degree of being an edge pixel. The dissimilarity measure is based on the difference (ratio) between certain features (statistical or geometrical) within the neighborhoods. FED's output denotes the degree of a certain pixel to be an edge pixel

and the possibility of the according edge to be a vertical, horizontal or diagonal edge.

FED is based on the general edge detection scheme of figure 1 but in all stages incorporates the fuzzy information output, which the edge-enhancing stage produces.

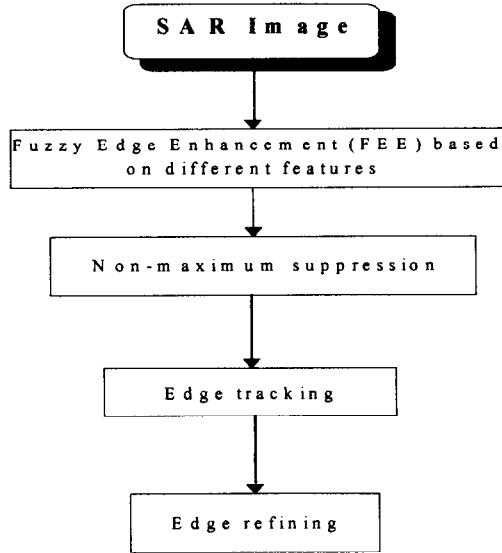


Figure 1: FED's edge detection scheme.

2.1 EDGE ENHANCEMENT

The concept of the edge enhancement stage is based on the movement of two symmetrical neighborhoods N_1 and N_2 in the opposite sides of each image pixel $p(x,y)$ to be resolved as an edge pixel following a scanning-window central-edge (SWCE) configuration [4]. The whole operation - for symmetrical 3×3 windows moving in the opposite sides of the pixel to be resolved as an edge pixel - is described in figure 2.

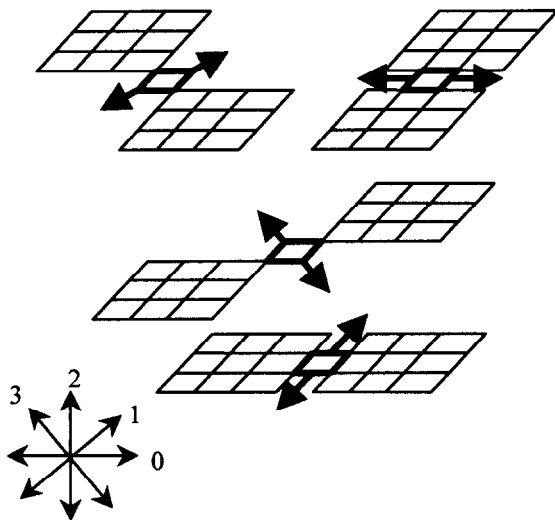


Figure 2: The four possible alignments of the two symmetrical windows moving around the pixel to be resolved as an edge pixel and direction index.

During this movement, the dissimilarity between the extracted features is assessed by fuzzy dissimilarity measures. Important parameters affecting the output of the fuzzy edge detector are:

- different fuzzy dissimilarity measures
- the extracted features in the neighborhoods
- the size and form of the neighborhoods
- the distance between the neighborhoods and the pixel to be resolved.

Finally, the edge properties (the edge strength and the edge direction) and the presence of speckle noise influence the output.

This process results in a description for every pixel, which includes two features:

- A four-dimensional feature vector $\vec{\mu} = [\mu_1 \mu_2 \mu_3 \mu_4]$. The components give the pixel's degree to belong to an edge with certain orientation according to figure 2.
- The degree of the certain pixel $p(x,y)$ being an edge pixel $e(x,y)$ - it is, in fact, the maximum component of the four-dimensional feature vector $e = \max(\vec{\mu})$.

The first step in edge enhancement is to extract the features out of the two symmetrical neighborhoods and then estimate the dissimilarity between them.

2.1.1 Fuzzy Dissimilarity Measures (FDM)

Fuzzy similarity measures estimate the similarity between two objects. We define a fuzzy dissimilarity measure D , by taking the complement of a fuzzy similarity measure S , where α and β are the feature vectors to be compared [9]:

$$D(\alpha, \beta) = 1 - S(\alpha, \beta) \quad (1)$$

In FED's case, the fuzzy dissimilarity measures project the dissimilarity between features to the interval $[0,1]$. This gives for each pixel a degree of being an edge pixel in the certain direction.

We compared the following four fuzzy dissimilarity measures:

$$D_1^k(\alpha, \beta) = 1 - \left[1 - \frac{\sum_{i=1}^n |\alpha_i - \beta_i|}{n \cdot 255} \right]^k, \text{ where } 1 \leq k \leq \infty \quad (2)$$

$$D_2(\alpha, \beta) = 1 - \frac{\sum_{i=1}^n (\alpha_i \wedge \beta_i)}{\sum_{i=1}^n (\alpha_i \vee \beta_i)} \quad (3)$$

$$D_3(\alpha, \beta) = \frac{\sum_{i=1}^n |\alpha_i - \beta_i|}{\sum_{i=1}^n (\alpha_i + \beta_i)} \quad (4)$$

$$D_4(\alpha, \beta) = 1 - \frac{\sum_{i=1}^n \alpha_i \wedge \sum_{i=1}^n \beta_i}{\sum_{i=1}^n \alpha_i \vee \sum_{i=1}^n \beta_i} \quad (5)$$

where $\vec{\alpha} = [\alpha_1 \dots \alpha_n]$ and $\vec{\beta} = [\beta_1 \dots \beta_n]$ are feature vectors to be compared.

Dissimilarity measure D_1^k incorporates a scaling factor k , which can control the contrast and therefore is capable of “adjusting” to a certain SAR image.

Dissimilarity measure D_2 together with dissimilarity measure D_4 constitute two promising edge detection tools for SAR images, as they incorporate despeckling properties (using the ratio between the two opposite regions it is possible to deal with multiplicative nature noise) [2].

2.1.2 Feature extraction

Up to now, the basic fuzzy tools for edge detection have been outlined. The major factor, though, determining the performance of a potential edge detector are the features to be extracted from N_1 and N_2 and used inside the dissimilarity measures. For this purpose some first features have been investigated with respect to their edge detection properties as well as taking under consideration some of the SAR image properties (presence of speckle noise). Those features are:

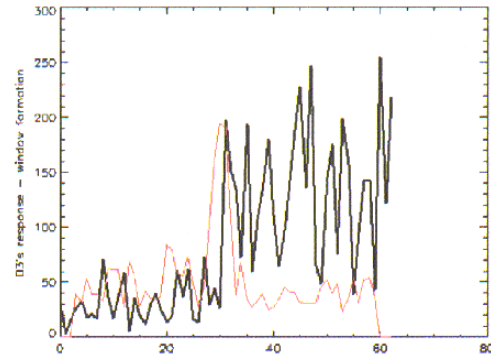
- *The M-dimensional vector of the sorted pixels within the neighborhoods:* the pixels are sorted from maximum to minimum.
- *The mean value of the neighborhoods:* this feature has good performance in the presence of speckle, due to the smoothing properties.
- *The median of the neighborhoods:* this feature has good performance in the presence of impulse noise [10].
- *The minimum and the maximum of the neighborhoods:* feature sensitive to “salt and pepper” noise.

In addition to this, texture measures could be used as features but this has not yet been verified.

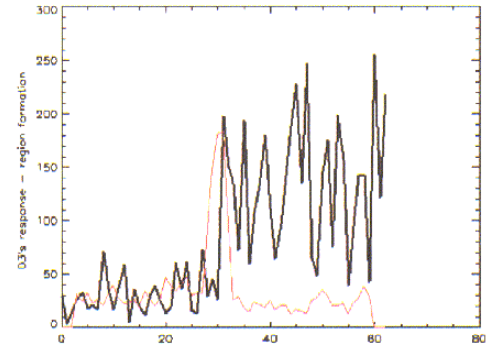
2.1.3 Form, size and distance of the neighborhood

One major concern is the symmetrical neighborhoods within the pixel’s area of investigation. The *form* of neighborhoods N_1 and N_2 on each side of the pixel is of

great importance for the capabilities of a potential fuzzy edge detector, concerning the edge orientation description. The neighborhood of the pixel can be divided e.g. a) into two contiguous regions by cutting out a line along the desired direction, or b) two windows in the opposite sides of the pixel (figure 2). Those two forms of neighborhood were particularly investigated within the framework of this paper. For understanding better the impact of these parameters, a speckled step-edge has been simulated [11] and then FEE with the two different forms has been applied. Figure 3 outlines the results.



(a)



(b)

Figure 3: FED’s response to a speckled step edge using 7×7 area of investigation, sorted pixels as feature and dissimilarity measure D_3 , for (a) region and (b) window formation.

The responses of figure 3 reveal a bigger sensitivity of edge detection to speckle noise if window form is applied. This is due to the smaller number of pixels used inside the symmetric neighborhoods for feature extraction.

The *neighbourhood size* is also a parameter under investigation, taking under consideration the nature of SAR images (presence of speckle, ambiguities, etc). Smaller neighbourhoods produce sharper responses to an edge (better resolution) with bigger sensitivity to the presence of noise, while bigger neighbourhoods have better immunity to noise, sacrificing resolution [2]. Figure 4 summarises the results.

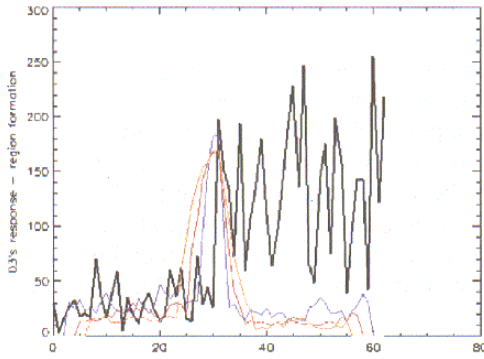
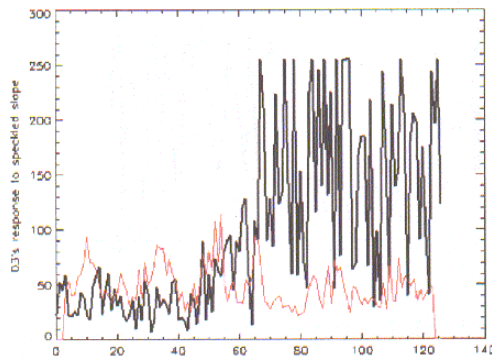
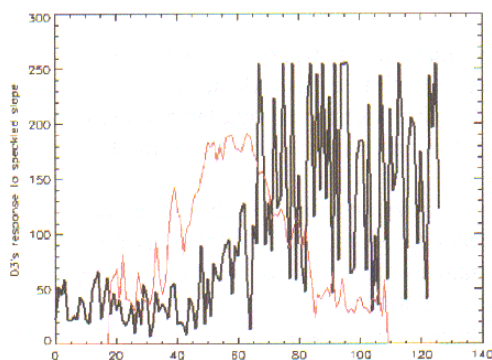


Figure 4: FED's response to a speckled step edge using sorted pixels as feature and dissimilarity measure D_3 for different region sizes (from a 7×7 area size having light blue color, up to a 15×15 area size having orange color).

Finally, the *distance* between the neighbourhood and the pixel to be resolved has to be considered. The bigger the distance, the broader the response of the edge detector becomes. One possible advantage of enlarging the distance is the better resolution of a slope edge. In this case, the distance may overcome the transition area and resolve better the edge, having of course broader response. Figure 5 summarises the results for a speckled slope edge.



(a)



(b)

Figure 5: FED's response to a speckled slope step edge (30 pixels transition area) using 7×7 area of investigation, region form, sorted pixels as feature and dissimilarity measure D_3 having (a) 0 and (b) 15 pixels distance between the pixel to be resolved and the symmetrical neighborhoods.

In figure 5(a) FED's response presents no edge enhancement of the slope edge or even the transition area for 0-pixel distance, while introducing the 15-pixels distance in figure 5(b) results in big edge enhancement of the transition area (slope edge). It also gives maximum response in the center of the transition area located in the 62nd line of the artificial edge. Nevertheless, equally big responses are produced in the vicinity of the maximum response, making the task of the non-maximum suppression stage harder.

2.2 NON-MAXIMUM SUPPRESSION

The maximum of each vector $\vec{\mu}$ is assigned to the edge map. As the maximum lies in the interval $[0,1]$, the edge map constitutes a 3D-surface.

Non-maximum suppression keeps for each edge only those pixels, which have maximum degree of being an edge. We use the fuzzy information resulting from FED to erase all pixels with less edge degree to the considered edge. The whole process is based on Canny's non-maximum suppression technique [12].

First, the edge direction has to be estimated. Instead of using gradient interpolation, the two most possible edge directions are used to approximate the actual edge direction. The estimated edge direction splits the 8-pixel neighborhood of $p(x,y)$ into two halves. In each half the edge degrees of the two closest pixels to the normal of the edge direction define together with $p(x,y)$ a plane. These two planes (each in every side of the edge direction) locally approximate the 3-D surface of the edge map. The value e of the center pixel is one common point of both planes. If it is the maximum value of all the five considered pixels, it is regarded as a local maximum point and $p(x,y)$ is kept as an edge pixel $e(x,y)$.

The output of this operation is, in fact, an extraction of FED's maximum response to an edge, located in the actual position of the edge. The whole procedure is described in figure 6.

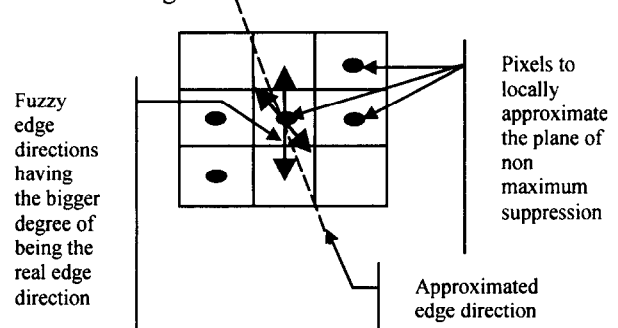


Figure 6: Non-maximum suppression scheme.

2.3 EDGE TRACING

After the non-maximum suppression stage, the edge map still presents some discontinuities along an edge line. An edge-tracing algorithm is applied to get continuous edge lines. We propose an edge-tracing scheme, which is divided into two major functions:

- *The endpoint searching function:* it evaluates if a certain $e(x,y)$ is actually a nominal endpoint. The tracing process starts from these points. This function incorporates also a refining property as edge pixels, representing forbidden profiles (e.g. junction points, thick edges), are erased. Figure 7 presents usual examples of valid and invalid endpoint pixels.

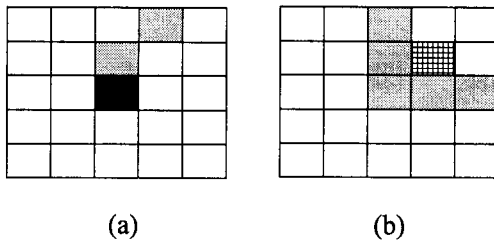


Figure 7: (a) valid endpoint pixel to be used by the edge linking function. (b) Invalid endpoint pixel to be erased from the edge map e .

- *The tracing function:* within the 8-pixel neighborhood of each endpoint, possible successors are selected taking into account the edge direction (and the pixels excluded due to this direction) and the fuzzy directions of the endpoint. The successor is selected by calculating the similarity of the feature vectors between the endpoint and the possible successors. To this end, a similarity measure S is applied. We used in our experiment the similarity measure $S_2 = 1 - D_2$. The whole concept is explained in figure 8.

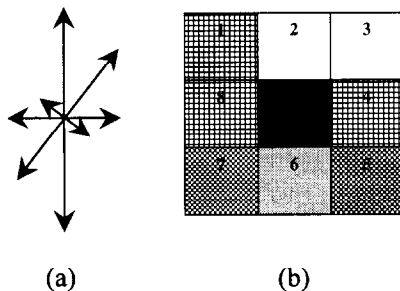


Figure 8: Successor pixels resolved with the use of the fuzzy information (figure 8(a)). The edge consists of pixels 4 and the center pixel and therefore pixels 5 and 7 are excluded due to the direction of the edge. Pixels 1,4,8 are excluded due to the weak edge direction degrees of the direction index shown in figure 8(a). Pixels 2 and 3 are the possible successors of which the one with the bigger similarity of its feature vector to the endpoint feature vector is chosen.

The whole tracing process is based in the fuzzy output and is applied iteratively. That means that, once the endpoints have been chosen, they are processed according to their degree of being an edge. In this way, first the pixels, having the higher degree of being edge pixels, are traced in order to be linked and then the rest in successive groups.

2.4 EDGE REFINING

After the edge-tracing stage, a final refining stage is iteratively applied in order to erase edge pixels, which violate rules of one-pixel-thick edge line, and short line segments, which are not connected to any other edge segment and also have low degree of being edges.

The aforementioned refining processes can be realized through morphological operations such as thinning and pruning [10], having as a parameter for pruning, the length of the sorted segments to be eliminated.

3. EXTRACTION OF LINEAR FEATURES

Extracting linear features from SAR images can serve two tasks as far as reconnaissance is concerned. These are the screening process and the thematic data exploitation [5]. A complete detection of all objects of interest is the objective of the screening process and therefore FED's fuzzy output can be directly used without thresholding. Instead, length and direction filtering processes help to exclude spurious responses and structures produced by the presence of speckle noise. The level, up to which these unwanted structures are eliminated, depends on the resolution of the SAR image itself, the resolution of the edge detector and the expected length of the structures to be extracted.

In order to extract linear features out of FED's output, the fuzzy information concerning the edge direction can be used. For this reason, the information resulting from FED was decomposed in:

- The fuzzy edges (three dimensional array including for each pixel the four feature-vector resulting from FEE, cf. 2.1)
- The edge map e (indicating the maximum degree of dissimilarity for each pixel).
- The direction array (indicating the direction along which the maximum degree of the certain pixel has occurred according to figure 2).
- The non-maximum suppression (NMS) stage output.
- FED's final output (refined edge-tracing process output).

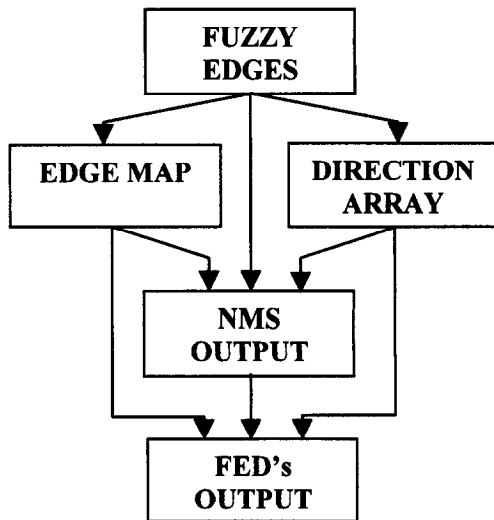


Figure 9: Interaction between the different forms of information.

Figure 9 shows the interaction between these five different forms of information, while figure 10 indicates the hierarchy according to information content between the forms. It has to be noted that the edge map and the direction array are two forms of the same information with the edge map giving the edge strength and the direction array giving the edge direction.

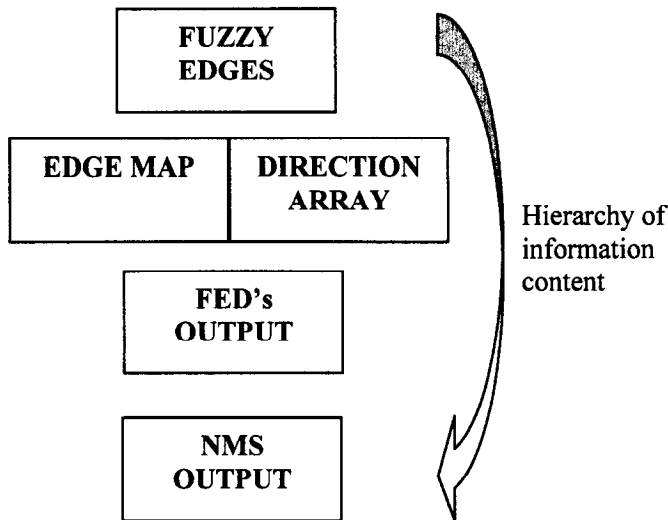


Figure 10: Hierarchy of information content among the different forms of information resulting from FED.

Once these forms of data have been produced, the procedure of figure 11 is proposed. A direction and length filtering process is applied in FED's non-maximum suppression output. This process has as parameters the length of the linear segments to be extracted, the direction to be investigated each time and the edge strength above which edge segments considered important will be extracted. For this reason, the direction array is used, in order to exclude pixels having other directions.

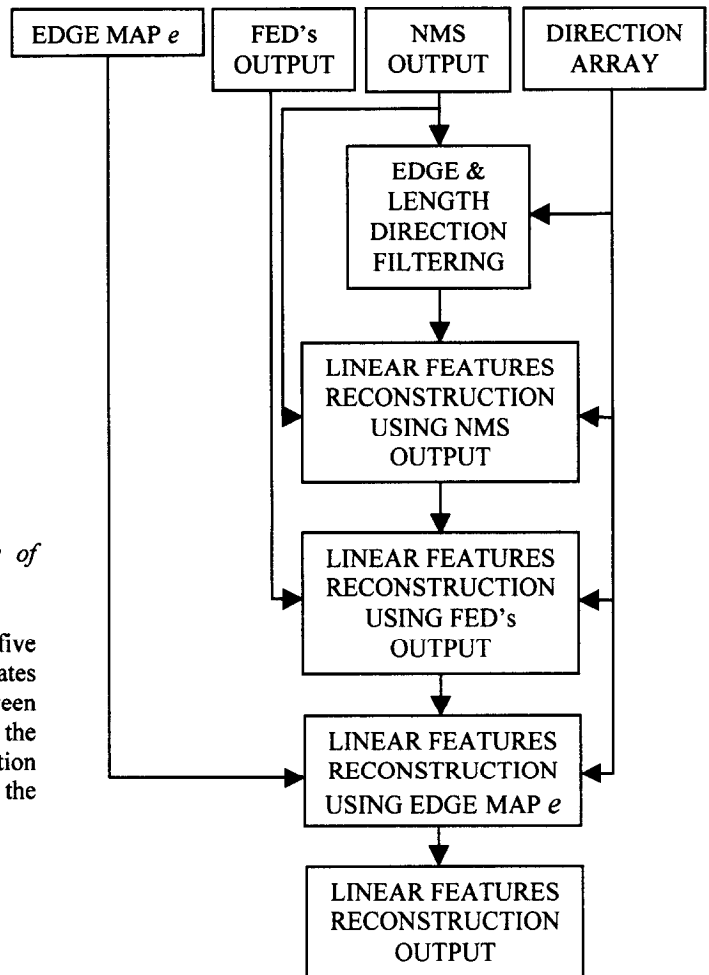


Figure 11: The proposed linear features extraction scheme.

The linear segments resulting from the direction and length filtering are considered the "seed segments" from which the linear features reconstruction process begins. The process uses as inputs the seed segments, the direction array and sequentially the NMS output, FED's final output and finally the edge map e . The used parameters are once again the edge direction and the edge strength.

The whole procedure is based on the concept that once linear seed segments are identified, linear features' reconstruction should be able to identify bigger linear segments even if they don't possess the same direction properties locally. Therefore, the reconstruction takes place sequentially in forms of increasing and more complex information according to figure 10. In this way, a hierarchical sequential reconstruction takes place but instead of the symbolic level this happens in the actual contour level. Because of this, the initial edge detection resolution is kept, but on the other hand, deviations and misconstructions due to speckle and low resolution of the image itself can not be avoided.

3.1 EDGE DIRECTION & LENGTH FILTERING

The edge direction and length filtering is applied on FED's non-maximum suppression output and additionally uses the direction array. The parameters affecting its performance are the direction and the length of the edge segments to be extracted and additionally, the edge strength of the segments to be extracted.

The *directions* used are those resulting from the direction array and correspond to the four possible edge directions, FED is incorporating to resolve edges (figure 2). The direction filtering is done sequentially along these four directions. Nominal points are considered the points that fulfil the requirement of being edge points (edge map entry) and having the certain direction (direction array entry).

The *length* of the edge segments is considered as a degree of freedom. The selected edge segments define the "seed segments" from which the linear features reconstruction will begin. The demand for small length segments will produce many seed segments and additionally, also non-linear features will be extracted, as they can be considered linear locally. This fact can be a potential advantage in the case of structures changing direction slowly, such as rivers. On the other hand, this big amount of "seed segments" will help the reconstruction process. Long length segments, are difficult to be extracted, mostly because of the random structures produced due to speckle. On the other hand, only strongly linear features will be selected and the reconstruction process will be more reliable.

The whole edge direction and length filtering process is proceeding in the following way. First, pixels fulfilling the requirements of the specific direction and edge strength are marked in the edge map. The edge strength value can be set to a very low value (~ 0.1) and therefore long edge segments expanding through different edge strengths will not be excluded. On the other hand, such a low value will allow weak edge segments to present and make the detection of the actual linear features more difficult and the whole process more computational demanding. Once the pixels have been marked, the length of the segments is assessed and those exceeding a given range are considered to be the "seed segments".

3.2 LINEAR FEATURES' RECONSTRUCTION

Once the edge direction & length filtering process has been completed, all segments having constant direction and a certain length are considered to be marked. Nevertheless, bigger segments can not be completely revealed because locally the edge direction is changing due to the shape of the feature itself and to the presence of speckle. Therefore, the linear features' reconstruction process, following this stage, should be able to overcome the difficulties resulting from the

aforementioned phenomena. Within the framework of this paper, a contour-tracing approach has been implemented as a first attempt to solve this problem.

The process should be able to trace the contour upon which lies the "seed segment" and connect the segments between them, following the edges already extracted by FED. In order to proceed more reliably, the hierarchy of information presented in figure 10 is used. Sequentially, the non-maximum suppression entries, FED's final entries and finally the edge map entries are used in order to reconstruct the missing segments between the "seed segments". The parameters affecting its performance are the direction and the edge strength of the edge segments to be extracted.

The *edge strength* of the edge segments is considered a factor of importance for the edge segment handling. Edge segments having higher degree of being an edge are considered more important and are, therefore, processed first. As mentioned before, edge segments excluded due to the weak edge strength, can be reconstructed if they fulfil the requirement of connectivity with large or strong line segments.

Although this contour tracing process is reconstructing features which many times have high irregular shape and cannot be considered to be linear, this is something to be expected. It has already been mentioned in [7] that linear man-made structures like airfields and roads present high complexity and the linear approximation can not fulfil the reconnaissance task. Additionally, it is within reconnaissance needs that auxiliary segments to the linear features such as road turns and airfields' taxiways are to be revealed. Finally, the resolution of the sensor and its nature (airborne or spaceborne) affect greatly feature extraction.

The output of the linear features' reconstruction process includes also unwanted structures depending on the number of the "seed segments" in its input. These random structures (mostly created by speckle) can be excluded either by choosing bigger edge segment length, or higher edge strength value during direction & length filtering.

4. EXPERIMENTAL RESULTS, DISCUSSION AND CONCLUSIONS

The linear features' extraction process was applied in an X-band Shuttle Radar Topographic Mission (SRTM) data set of Bayern/Germany (Munich airport area). The data set is a 4-look amplitude data set, processed by the German Aerospace Center (DLR) and it is not geometrically calibrated and not geocoded (figure 12(a)).

Dissimilarity measure D_3 , sorted pixels as feature to be extracted out of the symmetric regions and relatively small areas of investigation were used as parameters inside FED. The small areas of investigation ($5 \times 5, 7 \times 7$) were posed by the low resolution of the linear structures to be extracted (runways and taxiways of the airport). The edge map e , the non-maximum

suppression output filtered along the direction of 135 degrees according to the direction array's entries and the FED's final result were shown in figures 12(b), 12(c) and 12(d) respectively for 5×5 area of investigation. The results show that treating the data with such a small area of investigation produces too many structures, making the linear structures' extraction task harder.

The linear features reconstruction process was applied in 12(d) and the length & direction filtering was done in four different versions, namely the four combinations of edge length values of 5 and 10 pixels and an edge strength level set of 0.1 and 0.5. The "seed segments" resulting from these combinations are presented in figure 13. Once the "seed segments" have been extracted, the proposed linear structures' reconstruction process was applied. First, the NMS output then FED's final result and finally the edge map entries were used to resolve the structures. The process was applied sequentially along the four directions and iteratively until no more pixels could be reconstructed. A refining process similar to the one used inside FED (cf. 2.4) was applied in the output were it was necessary. The results are presented in figure 14 respectively. Figure 15 resumes the results with bigger area of investigation (7×7) and additionally introduces an overlaying between the two reconstructions in order to present a potential approach of overcoming the drawbacks of the two different resolutions of the edge detector, namely the sensitivity of the small area of investigation and the low feature resolving of the bigger area of investigation.

The results show that linear features' reconstruction can be achieved using the fuzzy information resulting from FED. The performance of this reconstruction is depending on the resolution of the SAR image, FED's resolution and the parameters used inside the reconstruction process. The different combinations of edge segments' length and edge segments' strength clearly outline the impact of these degrees of freedom in the final result. Higher edge segments' strength presents a bigger tension of revealing all the important features, producing though unwanted structures due to speckle and locally linear features. Bigger edge segments' length presents a higher reliability of revealing the strongly linear edge segments but the number of "seed segments" is small for the feature to be reconstructed. A good combination between the two parameters will result in an output, which will sufficiently fulfil the screening task.

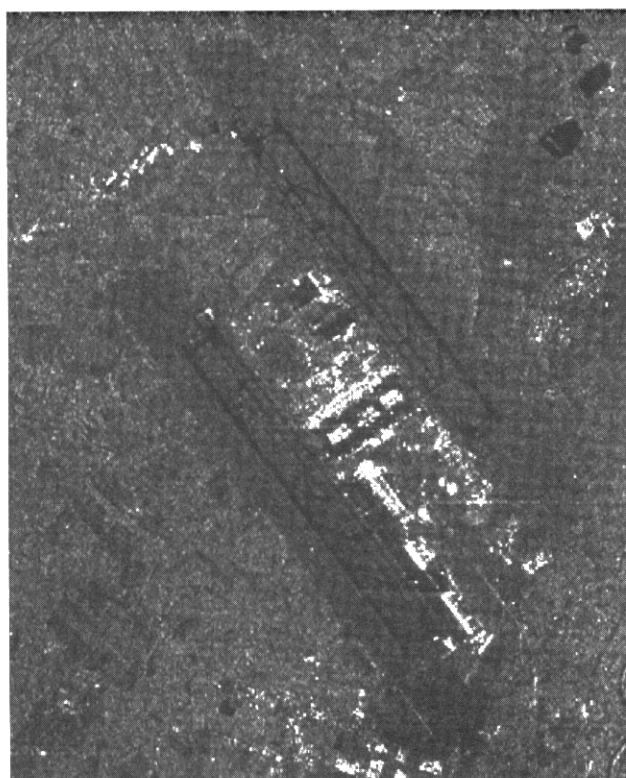
Nevertheless, the aforementioned procedure constitutes a first attempt to exploit FED's information for extracting figures of interest possessing certain properties (e.g. linearity). It was based in a contour tracing approach to investigate FED's capabilities towards features extraction out of SAR images.

5. ACKNOWLEDGEMENTS

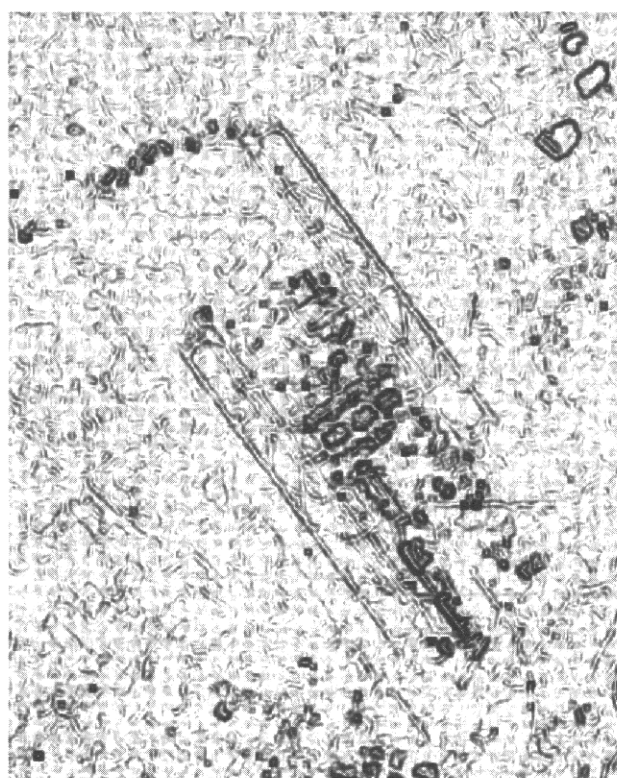
Mr. Dimou wishes to thank Prof. V. Makios of the University of Patras, Greece for his valuable remarks and DaimlerChrysler Aerospace Hellas for their financial support to his research work.

6. REFERENCES

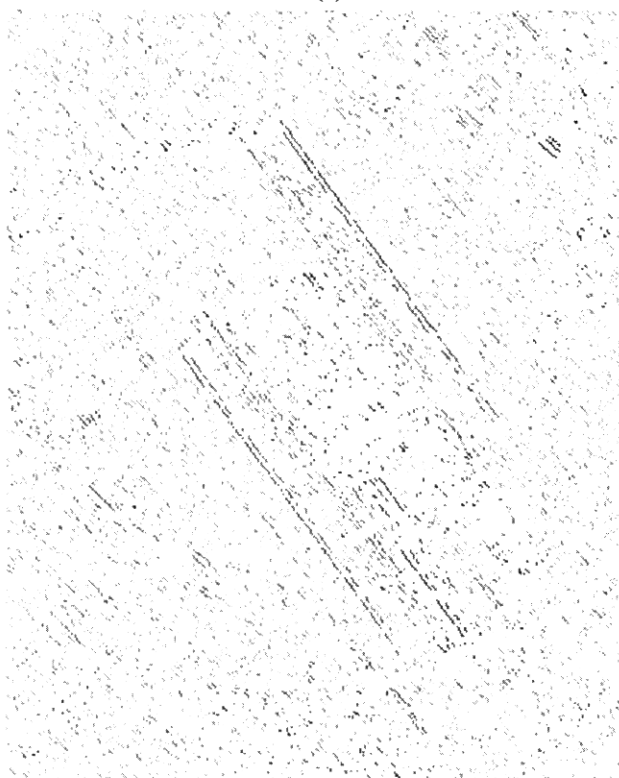
- [1] J. C. Bezdek, R. Chandrasekhar and Y. Attikiouzel: "A Geometric Approach to Edge Detection", IEEE Trans. Fuzzy Systems, Vol. 6, 1998, pp. 52-75.
- [2] R. Touzi, A. Lopés and P. Bousquet: "A Statistical and Geometrical Edge Detector for SAR Images", IEEE Trans. Geoscience and Remote Sensing, Vol. 26, 1988, pp. 764-773.
- [3] R. Fjørtoft, A. Lopés, P. Marthon and E. Cubero-Castan: "An Optimal Multiedge Detector for SAR Image Segmentation", IEEE Trans. Geoscience and Remote Sensing, Vol. 36, 1998, pp. 793-802.
- [4] R. Fjørtoft, A. Lopés, J. Bruniquel and P. Marthon: "Optimal Edge Detection and Edge Localization in Complex SAR Images with Correlated Speckle", IEEE Trans. Geoscience and Remote Sensing, Vol. 37, 1999, pp. 2272-2281.
- [5] R. Schärf, H. Schwan and U. Thönnessen: "Reconnaissance in SAR images", Proc. European Conference on Synthetic Aperture Radar, 1998, pp. 343-346, Berlin Offenbach.
- [6] H. Schwan, R. Schärf, and U. Thönnessen: "Reconnaissance of extended targets in SAR image data" Proceedings of SPIE, Vol. 3500, 1998, pp. 164-171
- [7] K. Schulz, U. Thönnessen: "Segmentation of detailed structures of extended objects in SAR images", Proc. 3rd European Conference on Synthetic Aperture Radar, 2000, pp. 339-342, Munich, Germany.
- [8] A. Dimou, G. Jäger, U. Benz and V. Makios, "A fuzzy edge detector for SAR images", Proc. 3rd European Conference on Synthetic Aperture Radar, 2000, pp. 699-702, Germany.
- [9] G. Jäger and U. Benz: "Measures of classification accuracy based on fuzzy similarity", IEEE Trans. Geoscience and Remote Sensing, vol 38, 2000, pp. 1462-1467.
- [10] R. C. Gonzalez and R. E. Woods: "Digital Image Processing", Addison-Wesley, 1992, ISBN 0-201-60078-1.
- [11] R. Bolter, M. Gelautz and F. Leberl, "SAR speckle simulation", International Archives of Photogrammetry and Remote Sensing, vol. 21, pp 20-25, 1996.
- [12] J. F. Canny: "Finding edges and lines in images", MIT Artificial Intell. Lab., Cambridge, MA, Rep. AI-TR-720, 1983.



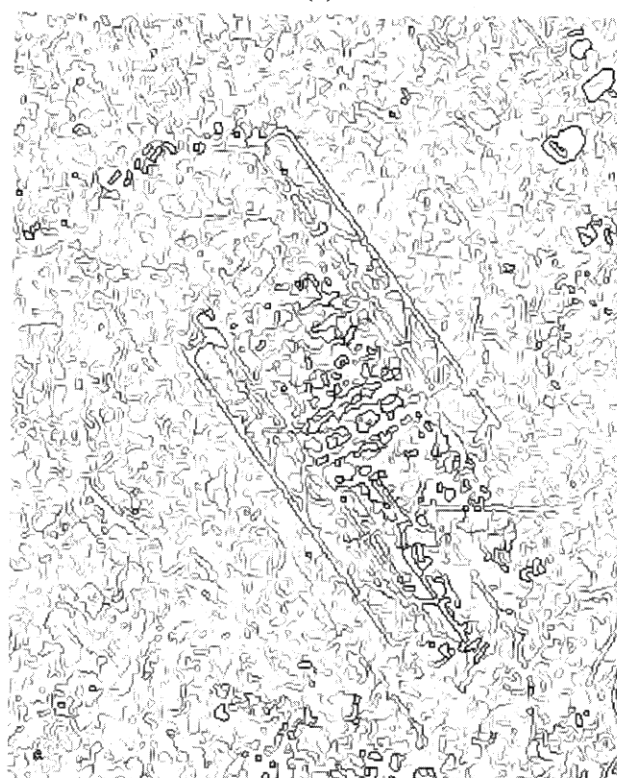
(a)



(b)



(c)



(d)

Figure 12: (a) 8-bit scaled version of the data set used. (b) Edge map of figure 12(a) using dissimilarity measure D_3 , 5×5 area of investigation and sorted pixels as feature. (c) Non maximum suppression result filtered along direction 3 (figure 2) using the direction array. (d) FED's final result after edge tracing (used iteratively three times) and refining (edge segments having length below 5 pixels were erased).

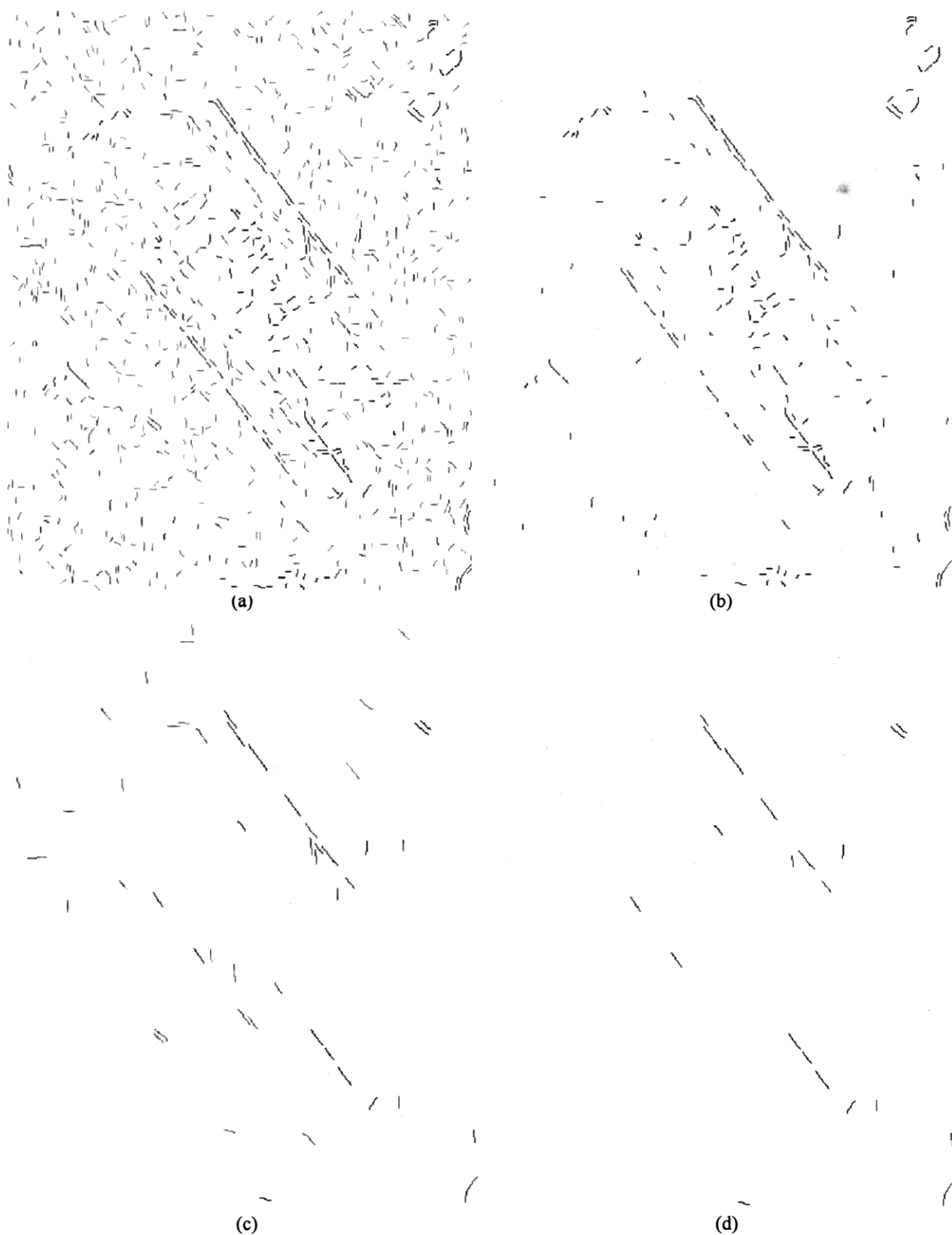


Figure 13: (a) "Seed segments" resulting from edge direction & length filtering with edge segments' length of 5 pixels and edge segments' strength above 0.1 applied on 12d, (b) "Seed segments" with edge segments' length of 5 pixels and edge segments' strength above 0.5, (c) "Seed segments" with edge segments' length of 10 pixels and edge segments' strength above 0.1, (d) "Seed segments" with edge segments' length of 5 pixels and edge segments' strength above 0.1

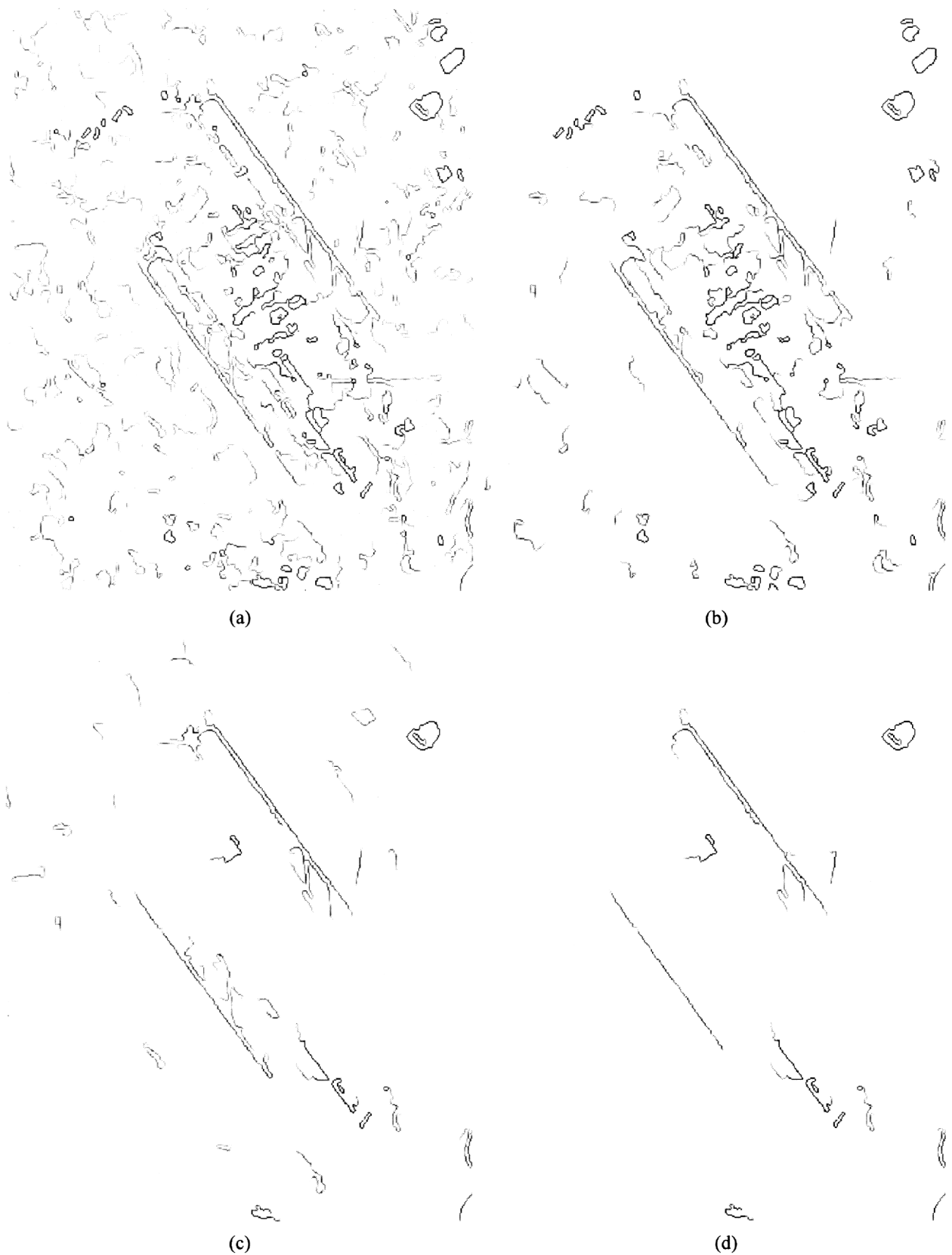


Figure 14: (a) Linear features' reconstruction based on the "seed segments" of 13(a), (b) Linear features' reconstruction based on the "seed segments" of 13(b), (c) Linear features' reconstruction based on the "seed segments" of 13(c), (d) Linear features' reconstruction based on the "seed segments" of 13(d),

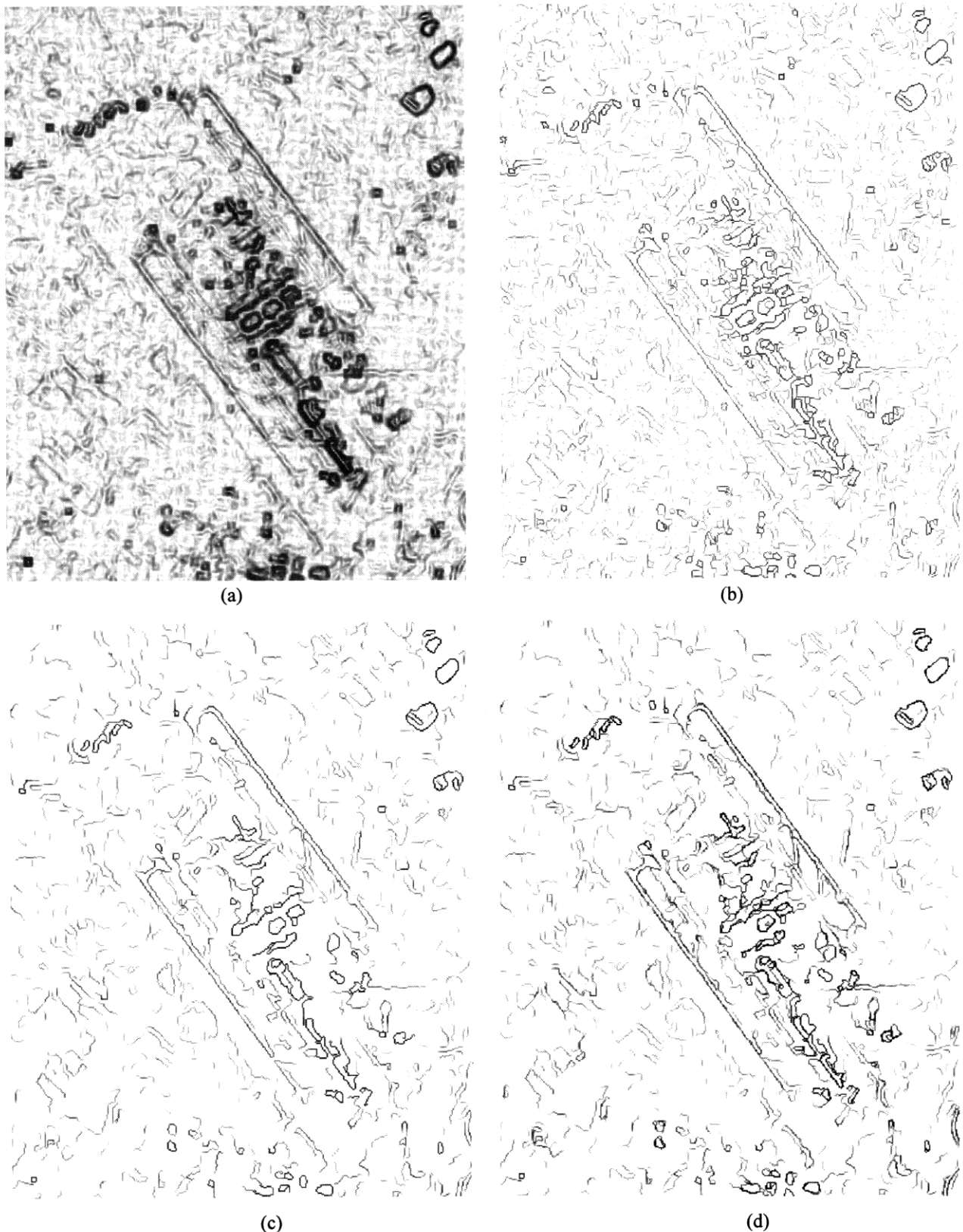


Figure 15: (a) Edge map of figure 12(a) using dissimilarity measure D_3 , 7×7 area of investigation and sorted pixels as feature, (b) FED's final result after edge tracing (used iteratively three times) and refining (edge segments having length below 5 pixels were erased), (c) Linear features' reconstruction based on the "seed segments" resulting from edge direction & length filtering with edge segments' length of 5 pixels and edge segments' strength above 0.1 applied on 15b, (d) Overlaying figures 14(b) and 15(c) results in an improved extraction of the airport.

An Embedded Fusion Processor

John Rooks, AFRL/IFTC
26 Electronic Parkway
Rome, NY 13441-4514 USA

Summary:

This paper describes an embedded High Performance Computer (HPC) designed to perform the sensor data fusion for the Discriminating Interceptor Technology Program (DITP). The HPC's electrical and physical architecture will be reviewed. The processor's architecture, FPASP5, evolved from years of Ballistic Missile Defense Organization (BMDO), and US Air Force research into wafer scale packaging and power efficient programmable signal processors for space-based applications. The processors, memory, and interface bare chips are packaged in Multichip Modules (MCMs). Our current version is designated MCM3. These MCMs can be stacked in thin layers before being inserted into the chassis level interconnect scheme. The chassis interconnect leverages a BMDO and Air Force Research Laboratory (AFRL) funded technology called Highly Integrated Packaging and Processing (HIPP). HIPP allows MCMs and two by two inch Printed Circuit Boards (PCBs) to be stacked together and interconnected with printed flexible flaps and a micro backplane. The combination of these techniques allows us to meet the strict constraints of space-based surveillance and interceptor applications.

The following description starts with the processors followed by their interface chip and communication protocols. Then continues with the MCM and chassis level packaging. Finally the Fusion Processor's (FP) integration with other components and its software environment are reviewed.

Floating Point Application Specific Processor (FPASP5):

The FPASP5 was designed by AFRL's Information Directorate for compatibility with MCM packaging and for power efficient floating point operation. The processor was kept simple to allow radiation hardening of the design. It employs external commercial SRAMs for its primary memory within each computing element. Each die contains two processors that operate independently, for highest throughput, as a processor/coprocessor pair, for lowest latency, or as a self checking pair, for fault tolerance. Having a simple core processor keeps the die costs low and yields high. Each processor has a 64 bit static memory interface and shares with its die mate a 64-bit IOBus interface and a

boundary scan test access port. All communication with the processor registers and memory from outside the die goes through the IOBus. Using the boundary scan test access port for bare die testing eliminates probing damage to the bond pads.

Each processor can perform two 32-bit multiplies and two Arithmetic Logic Unit (ALU) operations per clock cycle or one 64-bit multiply and one 64-bit ALU operation per clock cycle. The pair of processors on each die execute eight 32-bit operations per clock. Peak performance is 320 MFLOPS per die with the current generation. It is fabricated in a 0.5 μm CMOS process and runs at 40 MHz.

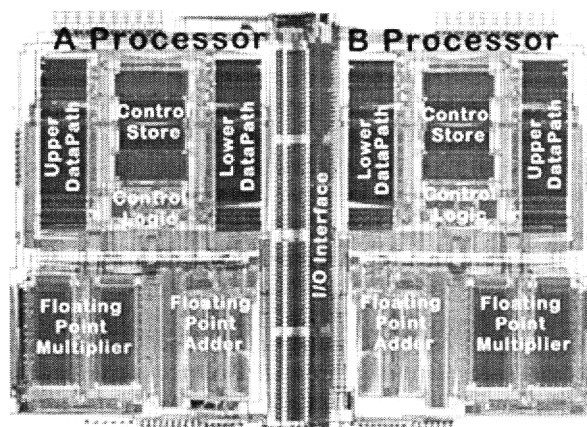


Figure 1: Floating Point Application Specific Processor

Each processor has an independent bus for its static memory. Additionally it is possible for each processor to read, write, or execute from its die mate's memory by temporarily shutting the other processor's clock off. The use of a relatively large Static Random Access Memory (SRAM) for each processor's main memory and the lack of a cache gives predictable execution times no matter where an operand is located in memory. And unlike Dynamic Random Access Memory (DRAM) there is no penalty for non-unit stride memory references frequently encountered in signal processing. Predictable memory performance simplifies program optimization. [1] [2]

In the MCM3 four processor chips (eight processors) are interconnected using their IOBus. The PCIF2.0 bridge chip among other things is the host for the processors on the IOBus, granting the bus and preempting processors to clear the bus when necessary.

PCIF2:

Messages that leave the MCM3 or originate from outside the MCM3 pass through the PCIF2 shown in figure 2. The PCIF2 in addition to being the IOBus host provides access to a 32/64-bit PCI bus, a Myrinet FI32 SAN interface chip, and Synchronous Dynamic Random Access Memory (SDRAM). Each interface has a non-blocking connection to each of the other interfaces, with all internal transfers taking place between First-In-First-Out memories (FIFOs) at the IOBus clock (or FPASP5 clock) rate.

There are eight FIFOs on the PCIF2. Four of the eight FIFOs receive data from outside the chip and the other four receive data from inside the chip (primarily other FIFOs). All FIFOs are eight bytes wide. The PCI and SDRAM FIFOs have asynchronous controllers allowing the IOBus clock to run independent of the PCI and SDRAM clocks. The interface to the FI32 chip uses the IOBus clock for convenience since the FI32 die provides the asynchronous interface to the Myrinet link. The FI32 version 1.3 has two independent channels one for inward bound messages and one for outward bound messages, each runs at 160 Mbytes per second

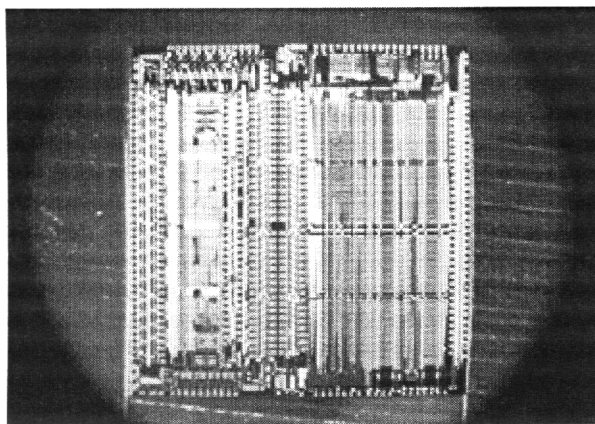


Figure 2: PCIF2.0

To maximize throughput the PCI outgoing FIFO is 8 bytes by 80 deep. Outgoing PCI messages can be stored and forwarded when the PCI bus is not available. The PCIF2 uses the PCI command "Memory Write and Invalidate" as well as the more standard "Memory Write". Standard Memory Writes cause the receiving processor to get an interrupt after the write is completed. The Memory Write and Invalidate command is received without interrupting the receiving processor. To prevent deadlocks and insure message progress is made, incoming PCI messages receive priority over outgoing PCI messages. Incoming PCI messages destined for the IOBus will preempt any current outgoing IOBus message to allow the incoming PCI message to get to its destination. The incoming PCI FIFO is 8-bytes wide by 16 deep.

Both Myrinet FIFOs are 8-bytes wide by 128 deep. This in combination with packets that are on the order of 1K-byte keeps the 160 Mbyte/sec Myrinet link from consuming excess IOBus time, since the IOBus transfer rate is 320 Mbytes/sec. Myrinet packets can exceed the 1K-byte. The only consequence is that after the FIFO is emptied the IOBus will be transferring data at 160 Mbytes per second, only using one-half of the IOBus's potential 320 MBytes/sec bandwidth. Using the 1K byte packet size allows the processing elements to keep both of the independent (in and out) Myrinet channels busy. To maximize data transfer a special packet was registered with Myricom for the FP and its associated sensors.

The AFRL Myrinet Packet (0B00 Hex) is used to reduce processing overhead and make Myrinet messages transparent to the application programmer. Various subtypes are defined. The primary subtype that the processors use is the WSSP direct write packet subtype (0000). This has the simple definition that when a packet of this type arrives it is forwarded by the PCIF2.0 to the address contained by the next 8-bytes, (those following the packet type and subtype). So an arriving packet of type and subtype 0B000000 can be written to any processor memory or register, the PCI bus, SDRAM, or the outgoing Myrinet port. If the message was addressed to a processor's SRAM it would first be held in the incoming Myrinet FIFO until the end of the packet is received or the FIFO is full. Then it would be forwarded to the outgoing IOBus FIFO where it would go onto the IOBus preempting any other activity on the IOBus except for an incoming PCI transaction. All messages except incoming Myrinet messages pass through the PCIF2 with only a few clock cycles of latency. The Myrinet messages are intentionally delayed until the end of the packet is received or the FIFO is full to maximize IOBus efficiency. [3]

The SDRAM is used to assemble smaller messages destined for the Myrinet and for data storage. For instance, a message traveling from the PCI bus to the Myrinet could become broken up as it traverses PCI-PCI bridges and other agents request the bus. By first dumping the data into the SDRAM and then issuing an instruction to the SDRAM controller to write the message to the Myrinet, you can insure that an intact Myrinet message is sent out. This is important since each Myrinet message requires the appropriate routing bytes prefixed to the packet type and packet data. When the SDRAM is used for data storage its data can be accessed by many processors without burdening an individual processor with multiple memory accesses. It is also capable of writing back its memory using a non unity stride which prevents unnecessary data transfers.

MCM3A:

General Electric's (GE's) High Density Interconnect (HDI) is used for our bare die interconnections. The GE HDI process uses copper interconnects separated with KAPTON (Dupont trademark) for a high density interconnection between the silicon chips and the package.

Our current version is designated MCM3A. It has four processor chips (eight processors), one PCIF2 interface chip, 16 8-Mbit SRAMs, 2 64-Mbit SDRAMs, a FI32 version 1.3 Myrinet chip, as well as capacitors and resistors. Figure 3 below shows that there is very little wasted space in the MCM3. The chips are interconnected with 5 layers of interconnects which include the power and ground distribution. Heat is dissipated from the back side of the MCM.

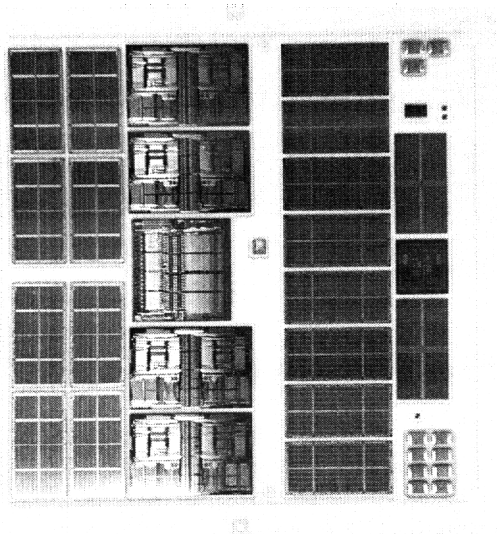


Figure 3: MCM3A

A new version of the MCM3, "MCM3B" is now in fabrication. It is similar to MCM3A except that it adds two additional layers of GE HDI. The top layer (layer 7) is a Land Grid Array (LGA), shown in figure 4a, that will be used for the I/O interconnects in place of the perimeter bond pads used in the MCM3A. The 6th layer is used to interconnect layer 5 (the old top layer) to the new top layer. This new interface was added to support HIPP packaging, which will be described later.

The MCM3B's LGA is contacted using an interposer similar to the one shown in figure 4b. The interposer has conductive compressible contacts that make a connection between two mirror image LGA surfaces. This allows easy testing at the MCM3 level on a standard PCB, and later insertion into the higher level packaging scheme.

After testing, up to four MCM3Bs can be stacked one on top of the other. Their contacts to the LGA also run to

two sides of the MCM package (not shown). The signals are connected to feed throughs in the sides of the ceramic package. Connection is then made up the side of the MCM using a single layer of GE HDI. The top MCM (with its exposed LGA), has the routing needed to take the signals from the lower 3 (buried) MCM3Bs to the appropriate LGA pad. Other than being thicker than single layer MCM3Bs, stacks have the same electrical interface, an LGA.

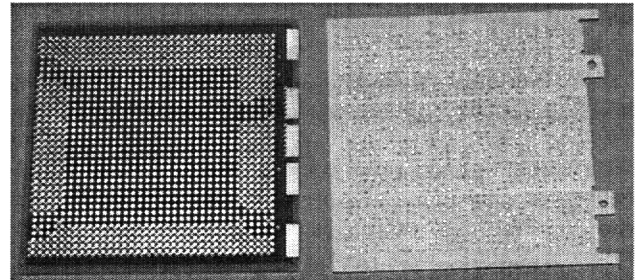


Figure 4a

Figure 4b

Highly Integrated Packaging and Processing (HIPP):

HIPP is an AFRL program to develop efficient packaging of MCMs and various other components including standard PCBs. [4] Each MCM or PCB with its mounting hardware and LGA is referred to as a segment.

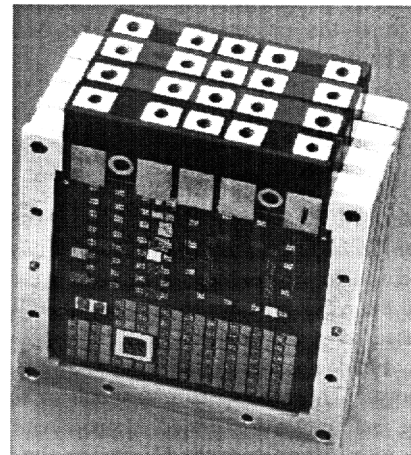


Figure 5: Highly Integrated Packaging and Processing (HIPP)

This packaging scheme brings the power in through the terminals shown at the top of fig 5. The signals are routed down a flexible printed circuit referred to as a flap. The connection between the flap and the MCM3B is made by placing an interposer between the two and compressing the contacts. One end of the flap has a ball grid array that allows the signals to make contact with a micro-back-plane. The micro-back-plane is another

flexible printed circuit that interconnects the signals from various flaps. Non MCM components can be attached to a PCB which has a LGA formed on one side and the components on the other. These two by two inch PCBs can then be inserted into the HIP structure.

Fusion Processor Segments:

In addition to 12 MCM3Bs packaged as three four-layer stacks the FP contains a 16-port Myrinet crossbar switch segment, a clock segment, and a management segment.

The Crossbar segment consists of a Myricom 16-port crossbar packaged part mounted on a two by two inch PCB with a clock and other support components. It provides non-blocking crossbar switching for internal and external communications using the Myricom System Area Network hardware protocol. This allows communication at 160 Mbytes per second in each direction for each of the 16 channels, for distances up to 10 feet.

The clock segment provides the IOBus and Myrinet clocks for the MCM3Bs. It consists of packaged parts on a two by two inch PCB.

The Management segment boots the FP. First it provides some low level boot functions by generating boundary scan signals. Then the programs are loaded by transferring data from it's Flash RAM to it's FI32 then over the Myrinet to the appropriate MCM3B. After loading each processor's memory the Management segment turns the processors on. The Management Segment's hardware is described below.

Other Segments:

AFRL's Space Vehicles Directorate has developed several other MCM based segments for Discrimination Interceptor Technology Program (DITP). These include one called the Malleable Signal Processor (MSP), and one called the MSP Management Segment. The two are usually used as a pair. The MSP contains 2 Altera 10K100A Field Programmable Gate Arrays (FPGAs) and memory. The MSP performs much of the integer processing before it's associated Management segment passes the information over the Myrinet to the FP. The Management segment contains a FI32, an Altera 10K100A, 4 Mbytes of Flash RAM, and an 8051 microprocessor with 128K of RAM and 128K of ROM. [5] [6] [7]

Sensor and Fusion Engine (SAFE):

Figure 6 shows an artist concept of the SAFE, ready for insertion into its thermal housing. It includes the fusion processor and other digital and analog circuits required for DITP. The FP alone is expected to be slightly over

two by two inches and two inches long without thermal management. In Figure 6 the thermal management is provided by a phase change material. The maximum power consumption for the FP is approximately 100 Watts. For bench operation the heat can be removed with a heat sink on one side. The system is easily customized by changing the micro-back-plane to add or remove segments. In addition to the MCM segments that are available custom two by two inch PCBs are easily added.

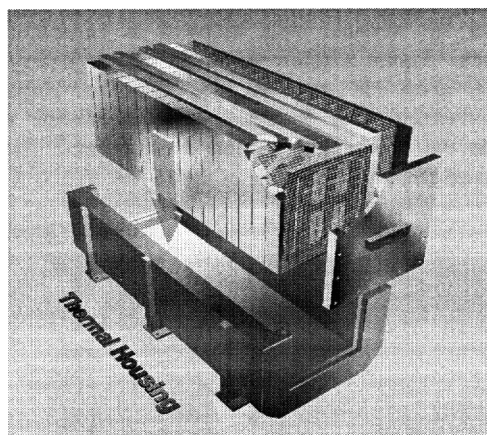


Figure 6: Sensor and Fusion Engine (Artist Conception)

Software Environment:

The GNU toolset provides the compilers (C, C++, Fortran), assembler and debugger for the FP. [8] Its operating system is the US Army developed Real-Time Executive for Microprocessor Systems (RTEMS). RTEMS provides a real-time multi-tasking operating system with open source code. [9] A simulator/communicator is available for PCs running Windows NT or LINUX, and Sun Workstations running Solaris. It simulator provides visibility into the processor operations and assists in communications with the processors for code debugging.

References:

- [1] Dr. R. Linderman, Dr. M. Linderman, R. Kohler, Maj. J. Comtois, PhD, J. Sabatini "HDI Design of a 100 MFLOPS/Watt Floating Point DSP" GOMAC 1998 pg 335-338
- [2] Capt. Figie, Y. Kinashi, B Johnson, R. Linderman, J. Fabunmi "Discrimination Interceptor Technology Program (DITP): Sensor Fusion for Improved Interceptor Seekers" 1996 AIAA/BMDO Missile Sciences Conference

[3] J. Rooks "Myrinet ARFL Packets Protocol", Version 1.2, 6/11/99, available from rooksj@rl.af.mil

[4] J. Lyke and G. Forman "Microengineering Aerospace Systems" H. Helvajian editor, The Aerospace Press 1999, Chapter 8

[5] J.C. Lyke, G.W. Donohoe, N. Anderson, "Malleable Signal Processor: A General-purpose Module for Sensor Integration", to appear, MAPLD 2000.

[6] G.W. Donohoe and J.C. Lyke, "Adaptive Computing for Space", Proc. Midwest Symposium on Circuits and Systems, Las Cruces, NM, August 8-11, 1999.

[7] G.W. Donohoe and J.C. Lyke, "Embedded, Configurable Computing for Space", Invited Graduate Seminar, Texas A&M University Analog and Mixed Signal Center, October 8, 1999.

[8] GNU web site www.gnu.org

[9] RTEMS web site www.rtems.com

Fusion of the Multi-sensor Data of the COSMO-SkyMed Mission

F. Melgani *, S. B. Serpico *

* DIBE - Dept. of Biophysical and Electronic Eng. - University of Genoa
Via Opera Pia 11a - 16145 Genova (ITALY)

F. Caltagirone **, R. Vigliotti **,

** ALENIA SPAZIO SpA - Remote Sensing Engineering
Via Saccomuro, 24 - 00131 Rome (ITALY)

Summary - The COSMO-SkyMed mission will provide remotely-sensed data of the Earth that are very interesting for two main reasons. First, the short revisit time over ground areas, made possible by the constellation of satellites involved, will allow to extract information about the territory or the sea surface on a daily basis. Second, this mission will provide data acquired by sensors of different and complementary nature: SAR, multispectral camera with high-spatial resolution (HRC), and hyperspectral camera (HYC). An appropriate signal processing, based on a synergistic use of the data that will be acquired and transmitted to ground stations, will represent a powerful and flexible tool for the investigation of the state of the soil and its changes, and for object detection. Data fusion techniques will be of primary importance in order to exploit the complementary nature of the sensors involved. The purposes may be different, such as a composite display of the information derived from different sensors, target detection, classification, change detection, etc. In this paper, after recalling some basic information about the COSMO-SkyMed mission, a brief survey of the most widespread techniques for the fusion of remote sensing data will be provided. Experimental results obtained with real data will also be presented.

INTRODUCTION

The COSMO-SkyMed mission will be based on a constellation of small satellites for Earth observation acquiring remote sensing data in such a way to cover a broad range of applications like risks management, in particular, but also resource management, land use and coastal monitoring. The ambitious objective assigned to the COSMO-SkyMed mission are allowed thanks to the intrinsic characteristics of the system. The seven satellites constellation aims at providing remote sensing data of higher quality from the spectral, temporal and spatial points of view. Three satellites of the

constellation carry optical instruments such as: a panchromatic camera, a multispectral camera and a hyperspectral camera, providing imagery with a valuable information content. The four other satellites are equipped with a Synthetic Aperture Radar (SAR) to give an insight in the microwave range and, consequently, to provide all weather and day/night acquisition capability unreachable by optical sensors, but at the price of a more limited spectral information content. A more detailed description of the COSMO-SkyMed mission instruments is given in the next section.

Because of its valuable panel of heterogeneous and complementary sensors, the COSMO-SkyMed mission belongs to the next generation of Earth observation systems for which adapted processing methodologies must be considered. The synergistic use of the numerous available sensors, which can be achieved by data fusion, allows to merge their advantages in order to obtain a richer information by enlarging the spectral view, improving the spatial resolution and/or getting a better revisit time of a given study area. Moreover, it reduces the uncertainty associated with the data from individual sensors. Data fusion can be defined as a formal framework in which are expressed means and tools for the alliance of data originating from different sources [1]. It opens a way to reach a better analysis and understanding of the remote sensing data, and consequently, to obtain information of greater quality. Aware of the limitations of analysing single sensor data whatever the processing complexity, the remote sensing community, like other scientific communities, has shown in the last few years a particular interest and motivation for data fusion. The important number of papers, conferences, workshops and special issues on data fusion are convincing indicators about its importance and usefulness. Among the current major processing targets of data fusion in remote sensing, we recall improved geometric correction, substitution of missing data, image sharpening, multisource classification for improved accuracy and change detection.

THE COSMO-SKYMED CONSTELLATION

The COSMO-SkyMed primary mission objective includes the monitoring, surveillance and intelligence applications for defence users, the management of exogenous, endogenous and anthropogenic risks. However, a broad range of other important applications, in the field of the resource management, land use and commercial products and services may be also satisfied once the primary objective is fulfilled. In particular, the fulfilment of the risk management user needs calls for the following general characteristics:

- fast response time (up to the final users)
- very good image quality, to allow a robust image interpretability at the requested scale of analysis
- all weather and day/night acquisition capability
- collection of large areas during a single pass capability
- along-track stereo during a single pass capability
- global coverage
- acquisition of a sufficiently large and interpretable image in a single pass
- acquisition of homogeneous and comparable multi-temporal data set, characterised by adequate spatial and spectral resolution suitable to perform analyses at different scales of detail

Most of the mission user needs have to be carried out through a correct mix of optical and SAR sensor observations. The most required spectral characteristics are multispectral (VIS), hyperspectral (NIR, SWIR, TIR, VIS), panchromatic (VIS) and microwave.

The sensors should be based on multi-satellite Earth observation systems combined with a fast data reception capability. Such a provision of data on an operational basis with the associated implications of continuity and quality is an essential characteristic of the system. Required resolution and revisit time imply a constellation of satellites, small in size and mass for economical reasons. Therefore, the best promising constellation has been identified and the relevant characteristics are here below summarised.

SAR Satellites Selected Orbit
Orbit: Dawn-dusk SSO
Total satellite Number: 4
Altitude: ≈ 600 km
Revisit Time: 12 hours

Optical Satellites Selected Orbit
Orbit : Near-noon SSO
Total satellite Number: 3
Altitude: ≈ 600 km
Revisit Time: 24 hours

The utilisation of X-band is suitable for flood risk management, oil-spill and small scale weather forecast on the sea, to study the content of water in the snow (for avalanches monitoring) and for on ground pollution monitoring (oil), etc... An X-band SAR instrument can be designed to meet the above needs together with the capability of measuring sub-centimetres swelling by means of differential interferometry using corner reflectors. The fundamental characteristics of the Synthetic Aperture Radar instrument operative modes (Fig. 1) are summarised as follows:

Modes with one polarisation selectable among HH, VV, HV or VH:

- HIMAGE
 - resolution: few m
 - swath width: \approx several tens of km
- WIDEREGION
 - resolution: few tens of m
 - swath width: \approx hundreds of km
- HUGEREGION
 - resolution: several tens of m
 - swath width: \approx few hundreds of km
- FRAME
 - resolution: order of the m
 - spot width: several tens of km²

Modes with two polarisation selectable among HH, VV, HV or VH:

- PING PONG
 - resolution: few m
 - swath width: \approx several tens of km

The need of a high resolution panchromatic sensor is due to different user needs. During the warning and crisis phases, the users requirements are to be in possession of images "as prompt as possible", "as accurate as possible" and "as synoptic as possible". In particular during the warning and crisis phase of earthquakes or floods, the availability of high resolution images, acquired just after and if possible just before the crisis, is of great advantage to understand where the most damaged areas are localised in order to organise the rescue operations. High resolution images with very high swath, is of great value also for off-line services requested by user needs: topography

updating, urban areas maps, land use maps at big scale. Moreover, if the sensors will have the best characteristics, interesting products could be also offered on the market for commercial purposes.

The multispectral sensor should mainly be oriented to the production of images useful during the knowledge and prevention phase of risk management. The applications are oriented to the land use determination (e.g. flood risk, seismic risk, forest fire risk), vegetation and habitat map (e.g. forest fire risk) and damage evaluation of forest fires. The TIR camera will be devoted to monitor surface, sea temperature, forest fires and volcanic activities.

The Hyperspectral camera should be mainly devoted to the water pollution management, vegetation mapping, drought evaluation, geological applications. They are of great importance to assess the vulnerability of the environment during the Knowledge and Prevention phase of natural and anthropic risks.

The fundamental characteristics of the optical instrument operative modes (Fig. 2) are summarised as follows:

High-Resolution Camera:

- Type: push broom imager operating in 6 different and simultaneous spectral channels
- Multispectral bands and resolutions:
 - 1: 0.5-0.90 μm (PAN) order of the m at nadir
 - 2: 0.45-0.52 μm (blue) few m at nadir
 - 3: 0.52-0.60 μm (green) few m at nadir
 - 4: 0.63-0.69 μm (red) few m at nadir
 - 5: 0.76-0.90 μm (NIR) few m at nadir
 - 6: 1.55-1.75 μm (SWIR) few m at nadir
- Swath : tens of Km
- Access region : $\pm 35^\circ$ (across-track)

Hyperspectral Camera:

- Operational modes:
 - Wide mode - Low resol.
 - Narrow mode - High resol.
- Resolutions: 20 m to 300 m (VIS, NIR)
50 m to 300 m (IR)
- Swaths: 20 Km to 300 Km
- Access region: $\pm 35^\circ$ (across-track)

COSMO-SKYMED AND RISK MANAGEMENT

In the field of Risk Management, one basic consideration is that all natural hazards are of multidisciplinary nature and can be typified by origin:

- exogenous (floods, drought, landslides)
- endogenous (volcanism, earthquakes)
- anthropogenic (industrial accident, water pollution & coastal management).

Risk management is evolving from pure post-accident activities to prevention, preparedness and mitigation of crisis, so increasing the role of pre-crisis activities in order to avoid or to mitigate the consequences of a disaster. In this perspective, risk management can be seen as subdivided into three major phases, each one having its own information and timeline needs. These phases can be stated as follows:

- Knowledge and Prevention Phase (K&P), which gathers all activities performed to reduce vulnerability and to perform monitoring at various levels in order to be ready in case of an emergency situation. Such a phase is characterised by the production of thematic and base maps which can be carried out with the contribution of remote sensing techniques contribution, by the conventional photo-interpretation and/or visual computer assisted techniques. The K&P phase includes the monitoring routines also effected to predict the crisis, and therefore also performed with prohibitive weather/sun illumination conditions.
- Warning and Crisis Phase (W&C), mostly pertaining to the alarm and first operation activities to mitigate and provide first aids to population. The contribution of space remote sensing techniques should be particularly valuable in such a phase. The “vision” of what is going on, during the emergency, should be assured with every weather/sun illumination conditions too.
- Post Crisis Phase (PC), to perform restoration, evaluation of the damages and lesson learning to improve the overall management of the risk. Remote Sensing techniques are also important for this phase.

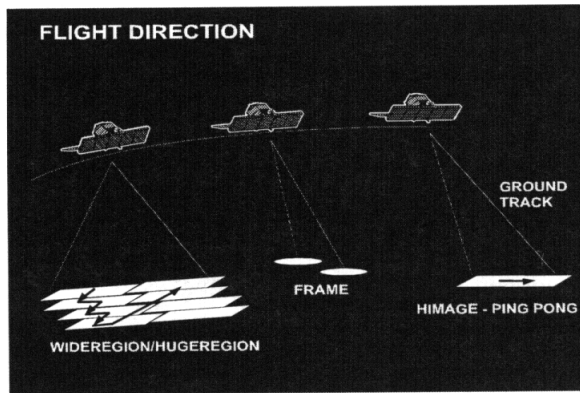


Fig. 1. Fundamental characteristics of the X-band Synthetic Aperture Radar instrument operative modes

All these phases contribute to create and exploit a knowledge base of the risk which represent the key element for the mitigation of damages and to reduce the consequences on population.

DATA FUSION TECHNIQUES

Depending on the nature of the data, several kinds of fusion can be distinguished. In our case, we will consider only the fusion aspects related to the COSMO-SkyMed mission. As mentioned above, the first kind is the fusion of multi-sensor data which plays a key role in data fusion due to the importance of the synergistic use of different sensors. The concept of satellites constellation, adopted in the COSMO-SkyMed mission, aims at opening the way to provide data with a very good revisit time (12 hours for the SAR sensors and 24 hours for the optical sensors). The exploitation of the temporal information is fundamental for risk management and change detection purposes but can be also valuable in image classification to improve the classification accuracy. This can be reached by the fusion of multi-temporal data. A third kind of fusion is the combination of multi-resolution data for which an important example of advantage is to overcome the difficulty to get high spatial and spectral resolution at the same time. In the case of the COSMO-SkyMed mission, the merging of data provided by the panchromatic and hyperspectral cameras will allow to provide imagery with both characteristics and so of higher quality.

The combination (fusion) of data can take place at three different processing levels, namely: pixel, feature and decision levels. In the pixel (low) level

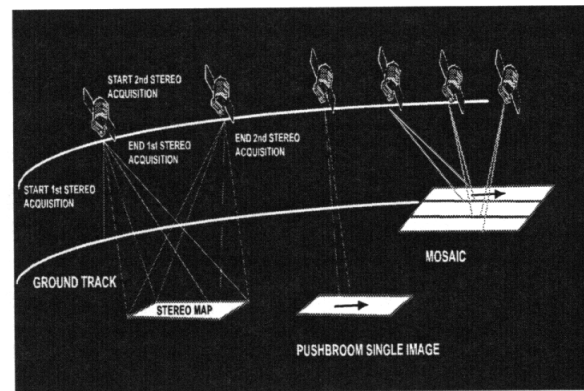


Fig. 2. Fundamental characteristics of the optical instrument operative modes

fusion, images coming from different sources are registered and then combined, pixel by pixel. In the case of feature (intermediate) level fusion, images are first processed to extract features of interest such as geometric, structural or spectral features; then the merging process is applied to such features. Finally, in the decision (high) level fusion, the data from each sensor are processed independently and the outcomes from all the sources are combined after giving them different weights of significance or reliability.

Numerous methodologies, like the probabilistic methods, the Dempster-Shafer evidence theory, neural networks and fuzzy logic, propose a solution to the problem of data fusion. The probabilistic methods include the stacked-vector method [2] characterised by a concatenation of the data from different sources in the same measurement vector. The stratification methods [3]-[4] and relaxation labeling technique [5] are generally used for the integration of ancillary data (other than remotely sensed images). The extended statistical fusion method [6] develops an original idea by introducing the concept of "reliability factors" aiming at weighing the different information sources according to their reliability. To provide a global model of probability density function for multi-sensor data, some statistical methods can be suitable such as: the dependence trees [7], based on the idea to approximate any multidimensional probability density function by a product of second order probability density functions; the Parzen approach, based on the principle of superposition of kernel functions; the expansion by basis functions or the projection pursuit density estimation [8]. Markov Random Fields [9]-[10] represents another

powerful probabilistic mathematical tool because of its remarkable ability to integrate any source of information (multi-sensor, multi-temporal, spatial contextual and/or ancillary information) in the scene model by the concept of energy functions. For the multi-temporal fusion problem, the Expectation-Maximisation algorithm was proved to be interesting to estimate the temporal information linking images separated in time [11].

The Dempster-Shafer theory of evidence [12]-[13] represent another approach to deal with the data fusion problem. In such a scheme, a conclusion (decision) is drawn according to the use of two confidence levels called respectively "belief" and "plausibility" reflecting the uncertainties related to the data sources.

Because they do not need any prior knowledge about the information sources, neural networks allow a straightforward but also efficient merging of different information sources. Among them, the MultiLayer Perceptron (MLP) trained with the error backpropagation learning algorithm is the most widely used and proved to be an effective multi-sensor fusion tool as shown by the results obtained in [14], [15]-[16]. The MLP popularity is explained by its ability to generate arbitrary decision boundaries in the feature space, provided that its two or more hidden layer architecture supports enough neurons. The Radial Basis Function (RBF) neural networks represent also an interesting alternative to the MLP due to their intrinsic simplicity and their low training cost [17]. Another neural network model is the Probabilistic Neural Network (PNN) in which statistically derived activation functions are used instead of the classical sigmoid activation function of the MLP. It can produce non-linear decision boundaries approaching the Bayes optimal ones, which can be modified in real-time due to the quasi-zero training phase it requires [18].

Fuzzy Sets theory, known as a simple and efficient mathematical tool aiming at imitating the human reasoning mechanisms, can represent a simple alternative approach for data fusion [19]-[20]. Depending on their behaviour, fuzzy operators belong to one of the three basic categories, namely: conjunctive-type (severe), disjunctive-type (indulgent) and compromise operators (cautious) like respectively the MIN, MAX and MEAN fuzzy operators. In dealing with the multi-temporal fusion aspect, the approach described in [21] starts by defining the spectral class distributions by exploiting rules based on an expert knowledge and applies a fusion of the multi-temporal data sets by carrying out a concatenation of the different bands

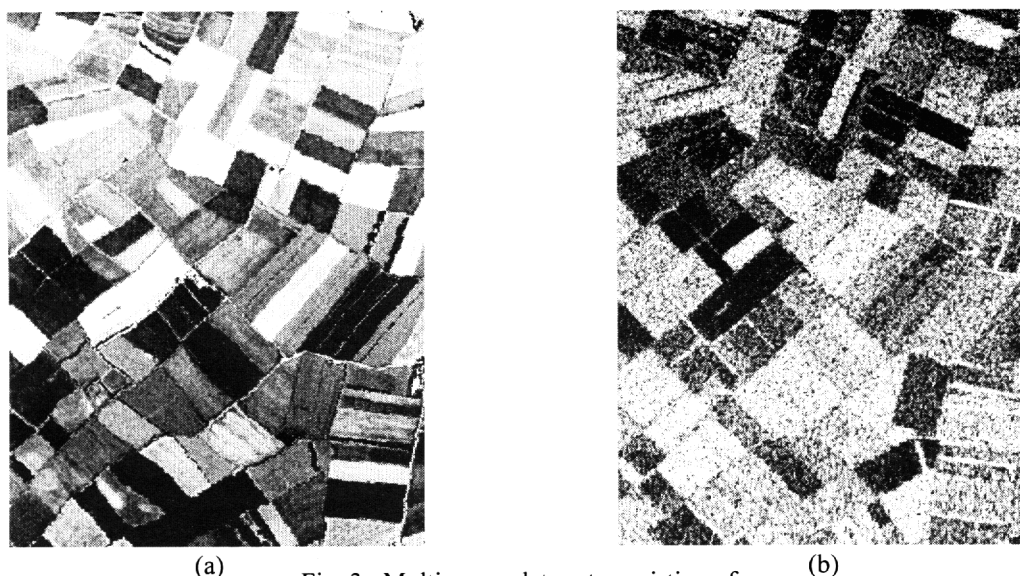
assuming no class change over time. Then a conjunctive operator is used for the class membership decision. In [22], two fuzzy-based fusion strategies of different temporal data sets aiming at obtaining a fusion that is neither purely conjunctive nor purely disjunctive are applied for linear feature detection with application to road network extraction. The first strategy is carried out by an implementation of compromise operators, while the second one consist to fuse the extreme operators.

Other mathematical tools were investigated such as the Fourier Series for the analysis of the vegetation phenology [23] and land cover classification [24]. It was observed that the Fourier Series can be useful to define some frequency characteristics from the class temporal signatures of a temporal sequence of remotely-sensed data.

The wavelet decomposition is another mathematical tool to which interest has been devoted, in particular to enhance the poor spatial resolution of multispectral data by means of a combination with images of higher resolution. Better performances (i.e. visual quality and spectral fidelity) compared to classical methods are reported in [25],[26] and [27].

TWO DATA FUSION EXPERIMENTS

Due to the unavailability of real data from the COSMO-SkyMed mission at the moment, we will present two experiments carried out with real data acquired from other remote sensors. The selection of the data sets was made in order to deal with the peculiarities of the COSMO-SkyMed missions and, in particular, on the one side the optical/radar data duality aspect and, on the other side, the multi-temporal data aspect. In the first experiment, we will show the benefit of merging both optical and SAR data together in a classification scheme. Whereas the second experiment will highlight the advantage of fusing multi-temporal data to improve significantly the classification accuracy with respect to single dates.



(a)

(b)

Fig. 3. Multisensor data set consisting of:
 (a) optical image (ATM sensor); (b) SAR image

Multi-sensor Data Fusion

The fusion of heterogeneous data, such as optical and radar data, gives rise to the difficulty of finding a common statistical model to estimate the class conditional probability density functions (pdf). Adopting a parametric approach, by assuming a specific functional form of the distribution, may be a straightforward solution, but may be also far to provide a model which fits the real distribution of data. An effective alternative to the parametric approach is the non-parametric approach which includes methods like the K-nearest neighbours, the kernel estimators and neural networks. In this experiment, we will use the K-nearest neighbours (K-nn) to fuse the multi-sensor data set described later. From a classification viewpoint, the K-nearest neighbours decision rule represents a simple way to associate to any pixel in the feature space a label corresponding to an information class. The principle is to search, for any unlabeled pixels, the K nearest labeled neighbours available from the training set and, then, the decision can be made on the basis of the majority label in the set of the K nearest neighbours for which weights can be assigned according to the distance pixel-neighbour. The main weakness of the K-nn method is the computational load involved by the distance computations which can be overcome by adapting sophisticated search algorithms (like the Kd-Trees) to speed up the search process. The K parameter depends on the training set size but is in general set empirically.

The multi-sensor data set, on which the experiment was carried out, is made of two images referencing the same ground area. The first image was taken in July 1989 by a Daedalus 1268

Airborne Thematic Mapper (ATM) scanner from which six channels were considered in this experiment (all the TM channels apart from the thermal infrared channel). The second data set is a SAR image acquired in August 1989 by a PLC-band, fully polarimetric, NASA/JPL SAR airborne sensor, yielding nine different channels corresponding to all possible combinations of bands (P, L or C) and polarisation (HH, HV or VV). The ATM and SAR images (Fig. 3), separated in time by only few days, were registered by taking the SAR image as reference. They illustrate a part of 250x350 pixel size of a scene representing an agricultural area near Feltwell, U.K, in which five land cover types are dominant, namely: sugar beets, stubble, bare soil, potatoes and carrots. Both the multi-sensor and single-sensor data sets were classified using different K values, from K=3 up to K=50. The best results on the test set with and without multi-sensor fusion are summarised in terms of Overall Accuracy (O.A.) in the following table:

SENSOR	O.A. [%]
SAR	74.0
ATM	80.5
SAR+ATM	89.8

The obtained results show well that exploiting the information from only one sensor may give poor performances (74.0[%] for SAR data only), while taking advantage from the complementarity between SAR and ATM data improves considerably the results with +15.8[%] and +9.3[%] with regard, respectively, to the single SAR and ATM images.

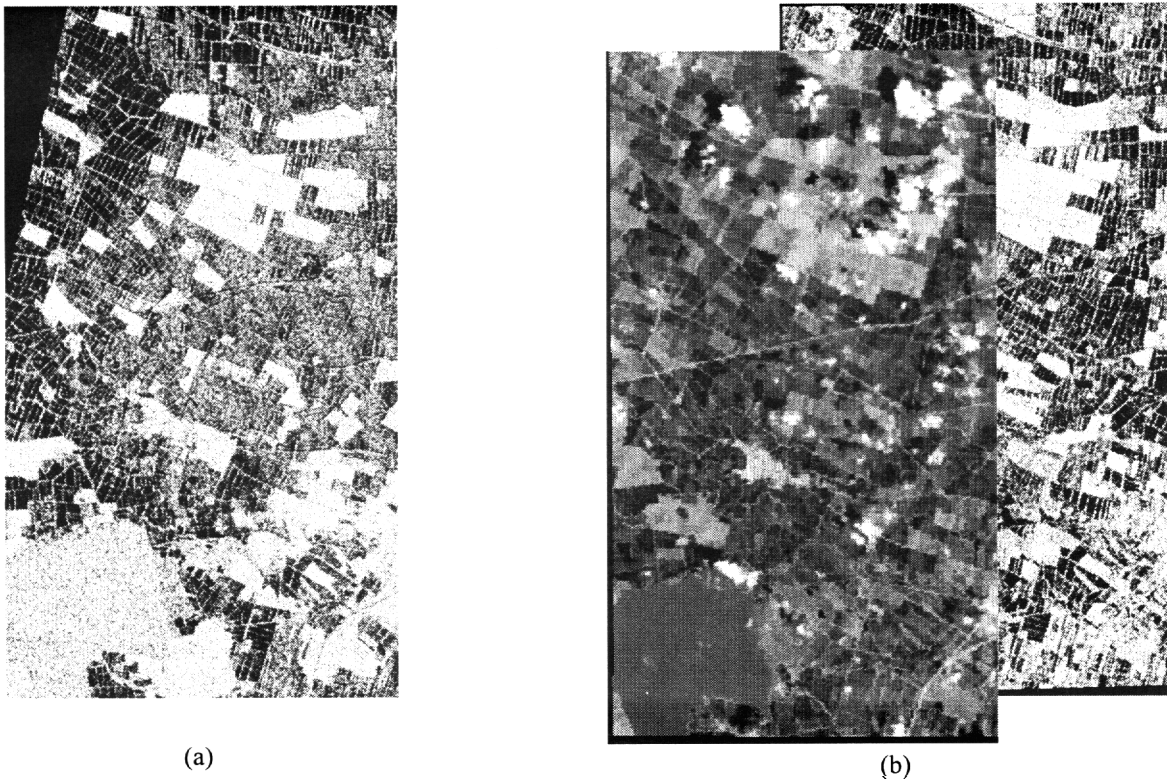


Fig. 4. Multitemporal and multisensor data set consisting of:
(a) SAR image (April 1994); (b) optical and SAR images (May 1994)

Multi-temporal and multi-sensor Data Fusion

As we mentioned above, in addition to the multi-sensor data fusion, the integration of the temporal information carried by a multi-temporal data set may represent an effective way to improve the classification accuracy. The experiment, which will be described briefly in this section, was presented in [11] to which the reader is referred for further information. The multi-sensor fusion aspect is dealt with by using a Multi-Layer Perceptron (MLP) neural network, trained with the error back-propagation algorithm according to the Minimum Square Error (MSE) criterion, for a non-parametric estimation of posterior class probabilities. The temporal correlation between the multi-sensor images acquired at two dates is captured by using the joint class probabilities related to possible land cover changes. A technique based on a specific formulation of the iterative Expectation-Maximisation (EM) algorithm is applied to compute such estimates. Then, the posterior class probabilities and joint class probabilities are exploited by the multi-temporal classification approach which is based on the application of the Bayes Rule for minimum error to the "compound classification" of pairs of multi-sensor images acquired at different dates.

For different reasons, in real applications, the available sensors at two dates may be different. For example, at one date, both optical and SAR images may be available, whereas at the other date, the optical image may convey no or few information because of cloud covering. Because of its daily revisit time, this situation will undoubtedly appear frequently for the COSMO-SkyMed mission when, for a given period of time characterised by bad weather conditions, only SAR data will be utilisable. The multi-temporal multi-sensor data set considered for this experiments (Fig. 4) refers to an agricultural area in the Basin of the Po River, in northern Italy, and is represented by two registered images acquired in April and May 1994 by, respectively, the ERS-1 SAR sensor and the Landsat TM and ERS-1 SAR sensors. The dominant land cover types in April for the study area are four, namely: wet rice fields, bare soil, cereals and wood. In May, an additional cover type (corn areas) is to be included increasing the size of the set of possible classes to five. For the May data set, 11 features were extracted: 6 intensity features from the Landsat TM image, 1 intensity feature from ERS-1 SAR (C band, VV polarisation) image and 4 texture features (entropy, difference entropy, correlation and sum variance) computed from the ERS-1 SAR image using the gray-level co-

occurrence matrix. Whereas for the April image, only 5 features were utilised (1 intensity and 4 texture features as described above). For each date, a feed-forward MLP neural network, with one hidden layer of eight neurons, is trained. The number of input and output neurons correspond, respectively, to the number of features and of classes considered for each date. The EM algorithm was applied and reached the convergence after six iterations to provide the estimate of the joint class probabilities. The classification results of the two temporal images independently (without temporal fusion) and with temporal fusion obtained by the proposed approach are illustrated in the following table. In this case, they will be expressed in terms of Average Accuracy (AA) in [%] (i.e. the mean value of the accuracy over the different classes).

	WITHOUT FUSION	WITH FUSION
April	75.16	92.16
May	89.58	89.43

A significant improvement is obtained for April image with a value of +17[%], while, for the May image, the results are almost identical. The use of the Average Accuracy to appreciate the results was adopted to show that classes which are poorly discriminated in a given date can be recovered by the use of the temporal information. In this case, the improvement is mainly due to the class "cereals" in April with an increase of accuracy from 16.67[%] (without temporal fusion) to 75[%] (with temporal fusion). The early growth of this plant in April makes difficult its discrimination and, in particular, with only one sensor (SAR). The temporal information, extracted from the May image in which the discrimination of the class "cereals" is better (+84.26[%] without temporal fusion), played a valuable role to recover the class.

CONCLUSIONS

The COSMO-SkyMed mission with its valuable panel of sensors belongs undoubtedly to the next generation of Earth observation systems, whose main objective is to contribute in increasing the weight of remote sensing in numerous real-world applications. For the COSMO-SkyMed mission, an emphasis is given to the risk management application whose interest is not to show with the increasing number of natural hazards that characterise the Earth in these last years. The

qualitative and quantitative aspects of the data acquired by the new generation of remote sensors make the data fusion a strategic way by which a better exploitation of the data can be reached. The importance of data fusion methods has been illustrated by the two experiments presented in this paper. In particular, the synergistic use of both optical and radar data and/or the integration of the temporal information can considerably improve the performances of a classification scheme. This pushes the remote sensing community to go further in the development of new data fusion methods dealing with the multi-sensor, multi-temporal and multi-resolution aspects in order to obtain optimised processing performances.

ACKNOWLEDGEMENTS

This work was supported by the Italian Space Agency (ASI) within the framework of the research project entitled "Sviluppo di metodi integrati di classificazione agroecologica tramite dati di telerilevamento per la gestione delle risorse naturali".

The authors wish to thank the Hunting Technical Services Ltd. (U.K.) for providing the ATM images used in the first experiment, and Dr. M. A. Gomasasca (C.N.R. - I.R.R.S.- Telerilevamento, Milan, Italy) for supplying the multisource images of the second experiment and for assisting in the related agronomic interpretation.

REFERENCES

- [1] L. Wald, "Some terms of reference in data fusion", IEEE Trans. Geosci. Remote Sensing, vol. 37, pp. 1190-1193, May 1999.
- [2] D. G. Leckei, "Synergism of synthetic aperture radar and visible/infrared data for forest type discrimination", Photogram. Eng. and Remote Sensing, vol. 56, pp. 1237-1246, 1990.
- [3] S. E. Franklin, "Ancillary data input to satellite remote sensing of complex terrain phenomena", Computers and Geoscience, vol 15, pp. 799-808, 1989.
- [4] C. F. Hutchinson, "Techniques for combining Landsat and ancillary data for digital classification improvement", Photogram. Eng. and Remote Sensing, vol. 48, pp. 123-130, 1982.
- [5] J. A. Richards, D. A. Landgrebe and P. H. Swain, "A means for utilizing ancillary information in multispectral classification", Remote Sens. Envir., vol. 12, pp. 463-477, 1982.

- [6] J. A. Benediktson and P. H. Swain, "A method of statistical multisource classification with a mechanism to weigh the influence of the data sources", in *Proc. IEEE Symp. Geosci. and Remote Sensing (IGARSS)*, Vancouver, Canada, July 1989, pp. 517-520.
- [7] C. K. Chow and C. N. Liu, "Approximating discrete probability distributions with dependence trees", *IEEE Trans. on Information Theory*, vol. 14, pp. 462-467, 1968.
- [8] A. J. Izenman, "Recent developments in nonparametric density estimation", *Journal of the American Statistical Association*, vol. 86, pp. 205-224, 1991.
- [9] B. Jeon and D. A. Landgrebe, "Classification with spatio-temporal interpixel class dependency contexts", *IEEE Trans. Geosci. Remote Sensing*, vol. 30, pp. 663-672, Jan. 1992.
- [10] A. H. S. Solberg, T. Taxt and A. K. Jain, "A Markov Random Field model for classification of multisource satellite imagery", *IEEE Trans. Geosci. Remote Sensing*, vol. 43, pp. 100-113, Jan. 1996.
- [11] L. Bruzzone, D. F. Prieto and S. B. Serpico, "A neural-statistical approach to multi-temporal and multisource remote-sensing image classification", *IEEE Trans. Geosci. Remote Sensing*, vol. 37, pp. 1350-1359, May 1999.
- [12] G. Shafer, *A Mathematical Theory of Evidence*. Princeton, NJ: Princeton Univ. Press, 1979.
- [13] S. Le Hégarat-Masclé, I. Bloch and D. Vidal-Madjar, "Application of the Dempster-Shafer evidence theory to unsupervised classification in multisource remote sensing", *IEEE Trans. Geosci. Remote Sensing*, vol. 35, pp. 1018-1031, July 1997.
- [14] S. B. Serpico and F. Roli, "Classification of multi-sensor remote sensing images by structured neural networks", *IEEE Trans. Geosci. Remote Sensing*, vol. 33, pp. 562-578, May 1995.
- [15] L. Bruzzone, C. Conese, F. Maselli and F. Roli, "Multisource classification of complex rural areas by statistical and neural network approaches", *Photogram. Eng. and Remote Sensing*, vol. 63, no. 5, pp. 523-533, May 1997.
- [16] L. Bruzzone and S. B. Serpico, "An iterative technique for the detection of land-cover transitions in multi-temporal remote-sensing images", *IEEE Trans. Geosci. Remote Sensing*, vol. 35, pp. 858-867, July 1997.
- [17] L. Bruzzone and D. F. Prieto, "A technique for the selection of kernel-function parameters in RBF neural networks for classification of remote-sensing images", *IEEE Trans. Geosci. Remote Sensing*, vol. 37, pp. 1179-1184, March 1999.
- [18] D. F. Specht, "Probabilistic Neural Networks", *Neural Networks*, vol. 3, pp. 109-118, 1990.
- [19] I. Bloch, "Information combination operators for data fusion: a comparative review with classification", *IEEE Trans. Syst., Man and Cybern.-Part A*, vol. 26, pp. 52-67, Jan. 1996.
- [20] J. Desachy, L. Roux and E. Zahzah, "Numeric and symbolic data fusion: A soft computing approach to remote sensing images analysis", *Pattern Recogn. Letters*, vol. 17, pp. 1361-1378, 1996.
- [21] P. N. Blonda, G. Pasquariello, S. Losito, A. Mori, F. Posa and D. Ragno, "An experiment for the interpretation of multi-temporal remotely sensed images based on a fuzzy logic approach", *Int. J. Remote Sensing*, vol. 12, pp. 463-476, 1991.
- [22] J. Chanussot, G. Mauris and P. Lambert, "Fuzzy fusion techniques for linear features detection in multi-temporal SAR images", *IEEE Trans. Geosci. Remote Sensing*, vol. 37, pp. 1292-1304, May 1999.
- [23] L. Olsson and L. Eklundh, "Fourier Series for analysis of temporal sequences of satellite sensor imagery", *Int. J. Remote Sensing*, vol. 15, pp. 3735-3741, 1994.
- [24] L. Andres, W. A. Salas and D. Skole, "Fourier analysis of multi-temporal AVHRR data applied to a land cover classification", *Int. J. Remote Sensing*, vol. 15, pp. 1115-1121, 1994.
- [25] T. Ranchin, L. Wald and M. Mangolini, "The ARSIS method: A general solution for improving spatial resolution of images by the means of sensor fusion", in *Proc. Int. Conf. Fusion of Earth Data*, T. Ranchin and L. Wald, Eds., Cannes, France, 1996, pp. 53-58.
- [26] J. Nunez, X. Otazu, O. Fors, A. Prades, V. Palà and R. Arbiol, "Multi-resolution-based image fusion with additive wavelet decomposition", *IEEE Trans. Geosci. Remote Sensing*, vol. 37, pp. 1204-1211, May 1999.
- [27] B. Aiazzi, L. Alparone, F. Argenti and S. Baronti, "Wavelet and pyramid techniques for multi-sensor data fusion: a performance comparison varying with scale ratios", in *Image and Signal Processing for Remote Sensing V*, S. B. Serpico (Ed.), *Proc. EUROPTO Series*, SPIE 3871, pp. 251-262, 1999.

REPORT DOCUMENTATION PAGE					
1. Recipient's Reference	2. Originator's References RTO-MP-61 AC/323(SET)TP/14	3. Further Reference ISBN 92-837-1050-9	4. Security Classification of Document UNCLASSIFIED/ UNLIMITED		
5. Originator	Research and Technology Organization North Atlantic Treaty Organization BP 25, 7 rue Ancelle, F-92201 Neuilly-sur-Seine Cedex, France				
6. Title	Space-Based Observation Technology				
7. Presented at/sponsored by	the RTO Sensors and Electronics Technology Panel (SET) Symposium held on the Island of Samos, Greece, 16-18 October 2000.				
8. Author(s)/Editor(s) Multiple	9. Date October 2000				
10. Author's/Editor's Address Multiple	11. Pages 244				
12. Distribution Statement	There are no restrictions on the distribution of this document. Information about the availability of this and other RTO unclassified publications is given on the back cover.				
13. Keywords/Descriptors <table border="0" style="width: 100%;"> <tr> <td style="vertical-align: top;"> Spaceborne detectors Spaceborne radar Space reconnaissance Electrooptics Optical detection Radar detection Target acquisition Target recognition Artificial satellites Real time operations </td> <td style="vertical-align: top;"> NATO Synthetic Aperture Radar Space surveillance (spaceborne) High resolution radar Imaging Image processing Optronics SBR (Space Based Radar) Remote sensing </td> </tr> </table>				Spaceborne detectors Spaceborne radar Space reconnaissance Electrooptics Optical detection Radar detection Target acquisition Target recognition Artificial satellites Real time operations	NATO Synthetic Aperture Radar Space surveillance (spaceborne) High resolution radar Imaging Image processing Optronics SBR (Space Based Radar) Remote sensing
Spaceborne detectors Spaceborne radar Space reconnaissance Electrooptics Optical detection Radar detection Target acquisition Target recognition Artificial satellites Real time operations	NATO Synthetic Aperture Radar Space surveillance (spaceborne) High resolution radar Imaging Image processing Optronics SBR (Space Based Radar) Remote sensing				
14. Abstract <p>This volume contains the unclassified papers presented at the Sensors and Electronics Technology Panel symposium held on the Island of Samos, Greece on 16, 17 and 18 October 2000.</p> <p>All aspects of space-based observation including the satellite, support systems, sensors, data handling etc.</p> <p>Topics covered included:</p> <ul style="list-style-type: none"> • Operational requirements/trade-offs • Spaceborne radar technology • On-board/real-time processing • Specific space systems issues • Special features of optronics systems 					



RESEARCH AND TECHNOLOGY ORGANIZATION

BP 25 • 7 RUE ANCELLE

F-92201 NEUILLY-SUR-SEINE CEDEX • FRANCE

Télécopie 0(1)55.61.22.99 • E-mail mailbox@rta.nato.int

DIFFUSION DES PUBLICATIONS

RTO NON CLASSIFIÉES

L'Organisation pour la recherche et la technologie de l'OTAN (RTO), détient un stock limité de certaines de ses publications récentes, ainsi que de celles de l'ancien AGARD (Groupe consultatif pour la recherche et les réalisations aérospatiales de l'OTAN). Celles-ci pourront éventuellement être obtenues sous forme de copie papier. Pour de plus amples renseignements concernant l'achat de ces ouvrages, adressez-vous par lettre ou par télécopie à l'adresse indiquée ci-dessus. Veuillez ne pas téléphoner.

Des exemplaires supplémentaires peuvent parfois être obtenus auprès des centres nationaux de distribution indiqués ci-dessous. Si vous souhaitez recevoir toutes les publications de la RTO, ou simplement celles qui concernent certains Panels, vous pouvez demander d'être inclus sur la liste d'envoi de l'un de ces centres.

Les publications de la RTO et de l'AGARD sont en vente auprès des agences de vente indiquées ci-dessous, sous forme de photocopie ou de microfiche. Certains originaux peuvent également être obtenus auprès de CASI.

CENTRES DE DIFFUSION NATIONAUX

ALLEMAGNE

Streitkräfteamt / Abteilung III
Fachinformationszentrum der
Bundeswehr, (FIZBw)
Friedrich-Ebert-Allee 34
D-53113 Bonn

BELGIQUE

Coordinateur RTO - VSL/RTO
Etat-Major de la Force Aérienne
Quartier Reine Elisabeth
Rue d'Evère, B-1140 Bruxelles

CANADA

Directeur - Recherche et développement -
Communications et gestion de
l'information - DRDCGI 3
Ministère de la Défense nationale
Ottawa, Ontario K1A 0K2

DANEMARK

Danish Defence Research Establishment
Ryvangs Allé 1, P.O. Box 2715
DK-2100 Copenhagen Ø

ESPAGNE

INTA (RTO/AGARD Publications)
Carretera de Torrejón a Ajalvir, Pk.4
28850 Torrejón de Ardoz - Madrid

ETATS-UNIS

NASA Center for AeroSpace
Information (CASI)
Parkway Center
7121 Standard Drive
Hanover, MD 21076-1320

FRANCE

O.N.E.R.A. (ISP)
29, Avenue de la Division Leclerc
BP 72, 92322 Châtillon Cedex

GRECE (Correspondant)

Hellenic Ministry of National
Defence
Defence Industry Research &
Technology General Directorate
Technological R&D Directorate
D.Soutsou 40, GR-11521, Athens

HONGRIE

Department for Scientific
Analysis
Institute of Military Technology
Ministry of Defence
H-1525 Budapest P O Box 26

ISLANDE

Director of Aviation
c/o Flugrad
Reykjavik

ITALIE

Centro di Documentazione
Tecnico-Scientifica della Difesa
Via XX Settembre 123a
00187 Roma

LUXEMBOURG

Voir Belgique

NORVEGE

Norwegian Defence Research
Establishment
Attn: Biblioteket
P.O. Box 25, NO-2007 Kjeller

PAYS-BAS

NDRCC
DGM/DWOO
P.O. Box 20701
2500 ES Den Haag

POLOGNE

Chief of International Cooperation
Division
Research & Development Department
218 Niepodleglosci Av.
00-911 Warsaw

PORTUGAL

Estado Maior da Força Aérea
SDFA - Centro de Documentação
Alfragide
P-2720 Amadora

REPUBLIQUE TCHEQUE

Distribuční a informační středisko R&T
VTÚL a PVO Praha
Mladoboleslavská ul.
197 06 Praha 9-Kbely AFB

ROYAUME-UNI

Defence Research Information Centre
Kentigern House
65 Brown Street
Glasgow G2 8EX

TURQUIE

Millî Savunma Başkanlığı (MSB)
ARGE Dairesi Başkanlığı (MSB)
06650 Bakanlıklar - Ankara

AGENCES DE VENTE

NASA Center for AeroSpace

Information (CASI)
Parkway Center
7121 Standard Drive
Hanover, MD 21076-1320
Etats-Unis

The British Library Document

Supply Centre
Boston Spa, Wetherby
West Yorkshire LS23 7BQ
Royaume-Uni

Canada Institute for Scientific and

Technical Information (CISTI)
National Research Council
Document Delivery
Montreal Road, Building M-55
Ottawa K1A 0S2, Canada

Les demandes de documents RTO ou AGARD doivent comporter la dénomination "RTO" ou "AGARD" selon le cas, suivie du numéro de série (par exemple AGARD-AG-315). Des informations analogues, telles que le titre et la date de publication sont souhaitables. Des références bibliographiques complètes ainsi que des résumés des publications RTO et AGARD figurent dans les journaux suivants:

Scientific and Technical Aerospace Reports (STAR)

STAR peut être consulté en ligne au localisateur de
ressources uniformes (URL) suivant:
<http://www.sti.nasa.gov/Pubs/star/Star.html>
STAR est édité par CASI dans le cadre du programme
NASA d'information scientifique et technique (STI)
STI Program Office, MS 157A
NASA Langley Research Center
Hampton, Virginia 23681-0001
Etats-Unis

Government Reports Announcements & Index (GRA&I)

publié par le National Technical Information Service
Springfield
Virginia 2216
Etats-Unis
(accessible également en mode interactif dans la base de
données bibliographiques en ligne du NTIS, et sur CD-ROM)



Imprimé par St-Joseph Ottawa/Hull
(Membre de la Corporation St-Joseph)

45, boul. Sacré-Cœur, Hull (Québec), Canada J8X 1C6



RESEARCH AND TECHNOLOGY ORGANIZATION

BP 25 • 7 RUE ANCELLE

F-92201 NEUILLY-SUR-SEINE CEDEX • FRANCE

Telefax 0(1)55.61.22.99 • E-mail mailbox@rta.nato.int

DISTRIBUTION OF UNCLASSIFIED
RTO PUBLICATIONS

NATO's Research and Technology Organization (RTO) holds limited quantities of some of its recent publications and those of the former AGARD (Advisory Group for Aerospace Research & Development of NATO), and these may be available for purchase in hard copy form. For more information, write or send a telefax to the address given above. **Please do not telephone.**

Further copies are sometimes available from the National Distribution Centres listed below. If you wish to receive all RTO publications, or just those relating to one or more specific RTO Panels, they may be willing to include you (or your organisation) in their distribution.

RTO and AGARD publications may be purchased from the Sales Agencies listed below, in photocopy or microfiche form. Original copies of some publications may be available from CASI.

NATIONAL DISTRIBUTION CENTRES

BELGIUM

Coordinateur RTO - VSL/RTO
Etat-Major de la Force Aérienne
Quartier Reine Elisabeth
Rue d'Evère, B-1140 Bruxelles

CANADA

Director Research & Development
Communications & Information
Management - DRDCIM 3
Dept of National Defence
Ottawa, Ontario K1A 0K2

CZECH REPUBLIC

Distribuční a informační středisko R&T
VTÚL a PVO Praha
Mladoboleslavská ul.
197 06 Praha 9-Kbely AFB

DENMARK

Danish Defence Research
Establishment
Ryvangs Allé 1, P.O. Box 2715
DK-2100 Copenhagen Ø

FRANCE

O.N.E.R.A. (ISP)
29 Avenue de la Division Leclerc
BP 72, 92322 Châtillon Cedex

GERMANY

Streitkräfteamt / Abteilung III
Fachinformationszentrum der
Bundeswehr, (FIZBw)
Friedrich-Ebert-Allee 34
D-53113 Bonn

GREECE (Point of Contact)

Hellenic Ministry of National
Defence
Defence Industry Research &
Technology General Directorate
Technological R&D Directorate
D.Soutsou 40, GR-11521, Athens

HUNGARY

Department for Scientific
Analysis
Institute of Military Technology
Ministry of Defence
H-1525 Budapest P O Box 26

ICELAND

Director of Aviation
c/o Flugrad
Reykjavik

ITALY

Centro di Documentazione
Tecnico-Scientifica della Difesa
Via XX Settembre 123a
00187 Roma

LUXEMBOURG

See Belgium

NETHERLANDS

NDRCC
DGM/DWOO
P.O. Box 20701
2500 ES Den Haag

NORWAY

Norwegian Defence Research
Establishment
Attn: Biblioteket
P.O. Box 25, NO-2007 Kjeller

POLAND

Chief of International Cooperation
Division
Research & Development
Department
218 Niepodleglosci Av.
00-911 Warsaw

PORTUGAL

Estado Maior da Força Aérea
SDFA - Centro de Documentação
Alfragide
P-2720 Amadora

SPAIN

INTA (RTO/AGARD Publications)
Carretera de Torrejón a Ajalvir, Pk.4
28850 Torrejón de Ardoz - Madrid

TURKEY

Milli Savunma Başkanlığı (MSB)
ARGE Dairesi Başkanlığı (MSB)
06650 Bakanlıklar - Ankara

UNITED KINGDOM

Defence Research Information
Centre
Kentigern House
65 Brown Street
Glasgow G2 8EX

UNITED STATES

NASA Center for AeroSpace
Information (CASI)
Parkway Center
7121 Standard Drive
Hanover, MD 21076-1320

SALES AGENCIES

**NASA Center for AeroSpace
Information (CASI)**

Parkway Center
7121 Standard Drive
Hanover, MD 21076-1320
United States

**The British Library Document
Supply Centre**

Boston Spa, Wetherby
West Yorkshire LS23 7BQ
United Kingdom

**Canada Institute for Scientific and
Technical Information (CISTI)**

National Research Council
Document Delivery
Montreal Road, Building M-55
Ottawa K1A 0S2, Canada

Requests for RTO or AGARD documents should include the word 'RTO' or 'AGARD', as appropriate, followed by the serial number (for example AGARD-AG-315). Collateral information such as title and publication date is desirable. Full bibliographical references and abstracts of RTO and AGARD publications are given in the following journals:

Scientific and Technical Aerospace Reports (STAR)

STAR is available on-line at the following uniform resource locator:

<http://www.sti.nasa.gov/Pubs/star/Star.html>

STAR is published by CASI for the NASA Scientific and Technical Information (STI) Program
STI Program Office, MS 157A
NASA Langley Research Center
Hampton, Virginia 23681-0001
United States

Government Reports Announcements & Index (GRA&I)

published by the National Technical Information Service
Springfield
Virginia 22161
United States
(also available online in the NTIS Bibliographic Database or on CD-ROM)



Printed by St. Joseph Ottawa/Hull
(A St. Joseph Corporation Company)
45 Sacré-Cœur Blvd., Hull (Québec), Canada J8X 1C6